

NASA Contractor Report 191099

N-25
160235
P.497

Measurements of Soot Formation and Hydroxyl Concentration in Near-Critical Equivalence Ratio Premixed Ethylene Flame

Michael Andrew Inbody
Purdue University
West Lafayette, Indiana

N93-25116

Unclass

G3/25 0160285

Prepared for
Lewis Research Center
Under Grant NAG3-1038

NASA
National Aeronautics and
Space Administration

(NASA-CR-191099) MEASUREMENTS OF
SOOT FORMATION AND HYDROXYL
CONCENTRATION IN NEAR CRITICAL
EQUIVALENCE RATIO PREMIXED ETHYLENE
FLAME (Purdue Univ.) 497 P



**MEASUREMENTS OF SOOT FORMATION
AND HYDROXYL CONCENTRATION
IN NEAR-CRITICAL EQUIVALENCE RATIO
PREMIXED ETHYLENE FLAMES**

**A Thesis
Submitted to the Faculty
of
Purdue University**

**by
Michael Andrew Inbody**

**In Partial Fulfillment of the
Requirements for the Degree
of**

Doctor of Philosophy

August 1992

TABLE OF CONTENTS

	Page
LIST OF TABLES	vi
LIST OF FIGURES	xiii
LIST OF SYMBOLS	xx
ABSTRACT	xxvi
CHAPTER 1: INTRODUCTION	1
1.1 Relevance	1
1.2 Objectives	4
1.3 Overview	6
CHAPTER 2: LITERATURE REVIEW - SOOT FORMATION	9
2.1 Introduction	9
2.2 Structure of Premixed Sooting Flames	13
2.3 Coagulation	16
2.4 Surface Growth	20
2.5 Particle Inception	26
2.5.1 PAH Coagulation	27
2.5.2 PAH Growth	29
2.5.3 Formation of Aromatic Hydrocarbons	35
2.5.4 Role of the H ₂ -O ₂ System Radicals	42
2.6 Modelling of Soot Formation	44
2.6.1 Chemical Kinetic Modelling of Soot Formation	45
2.6.2 Models for Incipient Soot Formation in Premixed Flames	49
2.7 Summary	55
CHAPTER 3: LITERATURE REVIEW - OPTICAL MEASUREMENTS OF SOOT AND HYDROXYL RADICAL	59
3.1 Introduction	59
3.2 Measurements of Soot Profiles with Laser Scattering-Extinction	60
3.2.1 Theory	62
3.2.1.1 Interpretation of Transmittance Measurements	64
3.2.1.2 Interpretation of Scattering Measurements	66
3.2.2 Interferences and Background Corrections	68
3.2.2.1 Molecular Scattering	68
3.2.2.2 Fluorescence	70

	Page
3.2.2.3 Gas-Phase Absorption.....	72
3.2.3 Particle Index of Refraction.....	73
3.2.4 Particle Size Distributions.....	79
3.2.5 Determination of the Number Density and Particle Size	80
3.3 Measurements of the Hydroxyl Radical in Sooting Flames	83
3.3.1 Theory	86
3.3.2 Interferences and Background Corrections.....	90
3.3.3 Quenching	92
3.3.4 Calibration	94
3.4 Summary	94
CHAPTER 4: EXPERIMENTAL APPARATUS AND METHODS	97
4.1 Introduction	97
4.2 The Flat Flame Burner System	98
4.2.1 The Flat Flame Burner	99
4.2.2 Burner Mounting and Translation System	102
4.2.3 Gas Delivery and Metering System	106
4.2.4 Subatmospheric Pressure Operation of the Burner	111
4.2.5 Atmospheric Pressure Operation of the Burner	117
4.3 Summary of Flame Conditions	118
4.4 Laser Scattering-Extinction Measurements	123
4.4.1 Optical Setup	124
4.4.2 Signal Detection and Data Acquisition Setup	128
4.4.3 Experimental Procedure	130
4.4.4 Data Analysis	134
4.5 Laser-Induced Fluorescence Measurements of the Hydroxyl Radical	142
4.5.1 Optical Setup	142
4.5.2 Signal Detection and Data Acquisition Setup.....	147
4.5.3 Experimental Procedure	148
4.5.4 Data Analysis	151
4.5.4.1 Rayleigh Scattering Background Corrections	152
4.5.4.2 Normalized Fluorescence Profiles	155
4.6 Chemical Kinetic Modelling	156
CHAPTER 5: LASER SCATTERING-EXTINCTION MEASUREMENTS OF SOOT FORMATION IN PREMIXED ETHYLENE FLAMES	163
5.1 Introduction.....	163
5.2 Results of the Laser Scattering-Extinction Measurements	165
5.2.1 Extinction Coefficient Measurements.....	167
5.2.1.1 Atmospheric-Pressure Flames	167
5.2.1.2 Subatmospheric Flames	175
5.2.2 Scattering Coefficient Measurements	176
5.2.2.1 Atmospheric-Pressure Flames	176
5.2.2.2 Subatmospheric Flames	184
5.2.3 Argon-ion Laser-Induced Fluorescence Measurements	190
5.2.4 Depolarized Scattering Measurements	192
5.2.4.1 Atmospheric-Pressure Flames	194

	Page
5.2.4.2 Subatmospheric Flames	197
5.3 Interpretation of the Laser Scattering-Extinction Measurements	199
5.3.1 Calculation of the Soot Profiles	199
5.3.2 Soot Volume Fraction, Number Density, and Particle Diameter Profiles	205
5.3.3 Implications of the Detection Limits	215
5.3.4 Comparison of Fluorescence and Extinction Coefficients	219
5.3.5 Temperature Profiles	222
5.4 Discussion	228
5.4.1 Near-Critical Equivalence Ratio Flames	229
5.4.2 Argon-ion Laser-induced Fluorescence	232
5.4.3 Sooting Flames	234
5.5 Summary	240
CHAPTER 6: LASER-INDUCED FLUORESCENCE MEASUREMENTS OF HYDROXYL RADICAL IN PREMIXED ETHYLENE FLAMES	242
6.1 Introduction	242
6.2 Results	242
6.2.1 Flame Conditions	242
6.2.2 Review of Theory and Measurements	245
6.2.3 Quenching Calculations	247
6.2.4 Calibration	252
6.2.5 OH Fluorescence Profiles	254
6.3 Discussion	259
6.4 Summary	262
CHAPTER 7: CHEMICAL KINETIC MODELLING OF PREMIXED ETHYLENE FLAMES	263
7.1 Introduction	263
7.2 Implementation of the Models	265
7.2.1 Sandia Flame Code	265
7.2.2 Reaction Mechanism of Drake and Blint (1991)	266
7.2.3 Reaction Mechanism of Miller and Melius (1992)	267
7.2.4 Flames Studied and Solution Procedure	268
7.3 Results	271
7.3.1 Comparison of OH Number Density Profiles.....	271
7.3.2 Comparison of Predicted Benzene Profiles with Profiles of Soot Formation	275
7.4 Discussion	282
7.5 Summary	285
CHAPTER 8: CONCLUSIONS AND RECOMMENDATIONS	287
8.1 Conclusions	287
8.2 Recommendations for Future Work	291
LIST OF REFERENCES	294

	Page
APPENDICES	306
Appendix A: Flow Rate Uncertainty Analysis	306
Appendix B: Details of the Laser Scattering-Extinction Measurements	316
B.1 Introduction	316
B.2 Photodetectors and Photodetector Electronics	316
B.3 Signal Conditioning and Data Acquisition	321
B.4 Data Analysis	324
B.5 Error Analysis and Detection Limits.....	330
B.5.1 Error Analysis and Detection Limit for the Extinction	331
Coefficient	
B.5.2 Error Analysis and Detection Limit for the Scattering	340
Coefficient	
Appendix C: Determination of Temperature from the Scattering	
Coefficient	347
C.1 Introduction	347
C.2 Theory and Method	348
C.3 Calculation Procedure	351
C.4 Results and Discussion	360
C.5 Conclusions and Recommendations	371
Appendix D: Summary of Scattering-Extinction Data for the	
Atmospheric-Pressure Flames	373
Appendix E: Scattering Coefficient Profiles for the 80-Torr Flames	427
Appendix F: OH Fluorescence Profiles for the Atmospheric and	
80-Torr Flames	448

LIST OF TABLES

Table		Page
2.1	Summary of incipient soot formation studies, including type of burner, fuels studied, assumptions for the model parameters, and the resulting correlation equation coefficients (adapted and expanded from Janssen and Senser, 1991).	53
3.1	Summary of soot particle index of refraction data.	74
4.1	Equivalence ratio, cold gas flow rates, cold flow velocity, and dilution ratio for the atmospheric-pressure flames used in the scattering-extinction measurements.	119
4.2	Equivalence ratio, cold gas flow rates, and cold flow velocity for the 80-torr flames used in the scattering-extinction measurements.	121
4.3	Equivalence ratio, cold gas flow rates, cold flow velocity, and dilution ratio for the atmospheric-pressure flames used in the OH measurements.	122
4.4	Equivalence ratio, cold gas flow rates, and cold flow velocity for the 80-torr flames used in the OH measurements.	123
4.5	Height interval, height range and initial height for the scattering-extinction profiles.	133
4.6	Height interval, height range and initial height for the OH fluorescence profiles.	150
5.1	Particle index of refraction and the resulting factors for the calculation of volume fraction, number density, and particle diameter.	204
5.2	Particle size distribution, equivalent geometric width, dimensionless moment ratio, and factor relating d_0 to d_{63}	204
5.3	Estimates of the volume fraction and number density detection limits based on the extinction coefficient detection limit.	217
5.4	Estimates of the particle number density detection limits based on the scattering coefficient detection limit for the atmospheric-pressure flames.	218
5.5	Estimates of the particle number density detection limits based on the scattering coefficient detection limit for the 80-torr flames.	218

Table	Page
5.6 Estimated peak temperatures, flame code energy-equation temperatures, and adiabatic flame temperatures for the atmospheric-pressure flames.	227
6.1 Equivalence ratio, cold flow velocity, and dilution ratio for the flames used in the OH measurements. Flames not duplicated in the scattering-extinction measurements are marked with an asterisk.	244
6.2 Summary of the quenching rate coefficient calculations for the atmospheric-pressure flames.	251
6.3 Summary of the quenching rate coefficient calculations for the 80-torr flames.	251
6.4 Relative maxima of the fluorescence profiles for the rich atmospheric flames and the 80-torr flames.	255
7.1 Equivalence ratio, flow rates, cold flow velocity and dilution ratio for the atmospheric flames used for the model comparisons.	270
7.2 Peak measured and predicted OH number densities for the four atmospheric-pressure flames	276
 Appendix	
Table	
A.1 Flow rate parameters with their calculated precision uncertainties for three typical flames. The fractional uncertainties are given in parentheses.	313
A.2 Estimates of the uncertainties in the independent variables in the calibrated flow rates.	314
A.3 Flow rate parameters with their calculated accuracy uncertainties for three typical flames. The fractional uncertainties are given in parentheses.	315
B.1 Component values used in the transimpedance amplifier circuits.	319
B.2 Transmittance uncertainty calculation based on the variation in the lock-in parameters.	333
B.3 Effect of variation in voltage measured at the computer interface on the variation and uncertainty in the transmittance.	335
B.4 Transmittance uncertainty based on the variation in the transmittance signal ratio.	336

Appendix Table	Page
B.5 Mean, standard deviation, and range of the transmittances measured at four heights on three days for flame A-IA-S2 ($\phi = 1.92$, $v_c = 7.73 \text{ cm}\cdot\text{sec}^{-1}$, $N_2/O_2 = 4.16$).	339
B.6 Transmittance, extinction coefficient, fractional uncertainty and uncertainty of the extinction coefficient for a range of transmittances. The assumed quantities in the uncertainty analysis are: $L = 5.6 \text{ cm}$; $\delta L = 0.2 \text{ cm}$; $\delta\tau = 0.001$	341
B.7 Uncertainties in the scattering calibration factors and the quantities used in their calculation for both the atmospheric and subatmospheric pressure measurements.	343
B.8 Typical mean values for profiles of the scattering signal ratio and its standard deviation and the resulting scattering coefficient and its uncertainties. Values are given for profiles measured from vertically polarized scattered light and horizontally polarized scattered light for both atmospheric and subatmospheric pressures and for argon-ion laser-induced fluorescence at atmospheric pressure.	346
C.1 Molar refractivity, index of refraction, depolarization ratio, and scattering cross-section at $\lambda = 488.0 \text{ nm}$ for major combustion species. The molar refractivities are taken from Table I of Gardiner, Hidaka, and Tanzawa (1981).	352
C.2 Molar refractivity, index of refraction, depolarization ratio, and scattering cross-section at $\lambda = 488.0 \text{ nm}$ for combustion species. The refractivities are calculated from atomic and bond refractivities (Table II, Gardiner, Hidaka, and Tanzawa, 1981).	353
C.3 Molar refractivity, index of refraction, depolarization ratio, and scattering cross-section at $\lambda = 488.0 \text{ nm}$ for combustion species not in the Gardiner, Hidaka, and Tanzawa (1981) compilation. The refractivities are calculated from atomic and bond refractivities (Table II, Gardiner, Hidaka, and Tanzawa, 1981).	354
C.4 Percentage contributions by the principal species to the mean differential scattering cross-section at a height of 3 mm above the burner.	370
D.1 Normalized transmittance and extinction coefficient profiles of the A-IA-R2 flame ($\phi = 1.63$, $v_c = 7.73 \text{ cm}\cdot\text{sec}^{-1}$, $D = 4.15$).	375
D.2 Normalized transmittance and extinction coefficient profiles of the A-IA-S1 flame ($\phi = 1.78$, $v_c = 7.73 \text{ cm}\cdot\text{sec}^{-1}$, $D = 4.16$).	376
D.3 Normalized transmittance and extinction coefficient profiles of the A-IA-S2 flame ($\phi = 1.92$, $v_c = 7.75 \text{ cm}\cdot\text{sec}^{-1}$, $D = 4.17$).	377

Appendix Table	Page
D.4 Normalized transmittance and extinction coefficient profiles of the A-IA-S3 flame ($\phi = 2.02$, $v_c = 7.74 \text{ cm}\cdot\text{sec}^{-1}$, $D = 4.16$).	378
D.5 Normalized transmittance and extinction coefficient profiles of the A-IA-S4 flame ($\phi = 2.17$, $v_c = 7.75 \text{ cm}\cdot\text{sec}^{-1}$, $D = 4.16$).	379
D.6 Normalized transmittance and extinction coefficient profiles of the A-IA-S5 flame ($\phi = 2.32$, $v_c = 7.75 \text{ cm}\cdot\text{sec}^{-1}$, $D = 4.16$).	381
D.7 Normalized transmittance and extinction coefficient profiles of the A-IB-C flame ($\phi = 1.67$, $v_c = 7.87 \text{ cm}\cdot\text{sec}^{-1}$, $D = 3.31$).	383
D.8 Normalized transmittance and extinction coefficient profiles of the A-IB-S2 flame ($\phi = 1.92$, $v_c = 7.78 \text{ cm}\cdot\text{sec}^{-1}$, $D = 3.54$).	385
D.9 Normalized transmittance and extinction coefficient profiles of the A-IB-S3 flame ($\phi = 2.02$, $v_c = 7.78 \text{ cm}\cdot\text{sec}^{-1}$, $D = 3.54$).	387
D.10 Normalized transmittance and extinction coefficient profiles of the A-IB-S4 flame ($\phi = 2.17$, $v_c = 7.77 \text{ cm}\cdot\text{sec}^{-1}$, $D = 3.53$).	388
D.11 Normalized transmittance and extinction coefficient profiles of the A-IIA-R2 flame ($\phi = 1.63$, $v_c = 10.42 \text{ cm}\cdot\text{sec}^{-1}$, $D = 4.29$).	390
D.12 Normalized transmittance and extinction coefficient profiles of the A-IIA-S1 flame ($\phi = 1.78$, $v_c = 10.45 \text{ cm}\cdot\text{sec}^{-1}$, $D = 4.29$).	391
D.13 Normalized transmittance and extinction coefficient profiles of the A-IIA-S2 flame ($\phi = 1.92$, $v_c = 10.45 \text{ cm}\cdot\text{sec}^{-1}$, $D = 4.28$).	393
D.14 Normalized transmittance and extinction coefficient profiles of the A-IIA-S3 flame ($\phi = 2.02$, $v_c = 10.45 \text{ cm}\cdot\text{sec}^{-1}$, $D = 4.28$).	395
D.15 Profile of the total scattering coefficient for the A-IA-R2 flame ($\phi = 1.63$, $v_c = 7.73 \text{ cm}\cdot\text{sec}^{-1}$, $D = 4.15$).	397
D.16 Profile of the total scattering coefficient and the corrected scattering coefficient for the A-IA-S1 flame ($\phi = 1.78$, $v_c = 7.73 \text{ cm}\cdot\text{sec}^{-1}$, $D = 4.16$).	399
D.17 Profile of the total scattering coefficient, the particle scattering coefficient, and the corrected particle scattering coefficient for the A-IA-S2 flame ($\phi = 1.92$, $v_c = 7.75 \text{ cm}\cdot\text{sec}^{-1}$, $D = 4.17$).	400
D.18 Profile of the total scattering coefficient, the particle scattering coefficient, and the corrected particle scattering coefficient for the A-IA-S3 flame ($\phi = 2.02$, $v_c = 7.74 \text{ cm}\cdot\text{sec}^{-1}$, $D = 4.16$).	401

Appendix Table	Page
D.19 Profile of the total scattering coefficient, the particle scattering coefficient, and the corrected particle scattering coefficient for the A-IA-S4 flame ($\phi = 2.17$, $v_c = 7.75 \text{ cm}\cdot\text{sec}^{-1}$, $D = 4.16$).	402
D.20 Profile of the total scattering coefficient and the particle scattering coefficient for the A-IA-S5 flame ($\phi = 2.32$, $v_c = 7.75 \text{ cm}\cdot\text{sec}^{-1}$, $D = 4.16$).	403
D.21 Profile of the total scattering coefficient for the A-IB-C flame ($\phi = 1.67$, $v_c = 7.87 \text{ cm}\cdot\text{sec}^{-1}$, $D = 3.31$).	405
D.22 Profile of the total scattering coefficient and the particle scattering coefficient for the A-IB-S2 flame ($\phi = 1.92$, $v_c = 7.78 \text{ cm}\cdot\text{sec}^{-1}$, $D = 3.54$).	406
D.23 Profile of the total scattering coefficient and the particle scattering coefficient for the A-IB-S3 flame ($\phi = 2.02$, $v_c = 7.78 \text{ cm}\cdot\text{sec}^{-1}$, $D = 3.54$).	408
D.24 Profile of the total scattering coefficient and the particle scattering coefficient for the A-IB-S4 flame ($\phi = 2.17$, $v_c = 7.77 \text{ cm}\cdot\text{sec}^{-1}$, $D = 3.53$).	410
D.25 Profile of the total scattering coefficient for the A-IIA-R2 flame ($\phi = 1.63$, $v_c = 10.42 \text{ cm}\cdot\text{sec}^{-1}$, $D = 4.29$).	412
D.26 Profile of the total scattering coefficient for the A-IIA-S1 flame ($\phi = 1.78$, $v_c = 10.45 \text{ cm}\cdot\text{sec}^{-1}$, $D = 4.29$).	413
D.27 Profile of the total scattering coefficient and the particle scattering coefficient for the A-IIA-S2 flame ($\phi = 1.92$, $v_c = 10.45 \text{ cm}\cdot\text{sec}^{-1}$, $D = 4.28$).	415
D.28 Profile of the total scattering coefficient and the particle scattering coefficient for the A-IIA-S3 flame ($\phi = 2.02$, $v_c = 10.45 \text{ cm}\cdot\text{sec}^{-1}$, $D = 4.28$).	417
D.29 Profiles of the fluorescence coefficient detected at 503 nm and 473 nm for the A-IA-R2 flame ($\phi = 1.63$, $v_c = 7.73 \text{ cm}\cdot\text{sec}^{-1}$, $D = 4.15$).	419
D.30 Profiles of the fluorescence coefficient detected at 503 nm and 473 nm for the A-IA-S1 flame ($\phi = 1.78$, $v_c = 7.73 \text{ cm}\cdot\text{sec}^{-1}$, $D = 4.16$).	420
D.31 Profiles of the fluorescence coefficient detected at 503 nm and 473 nm for the A-IA-S2 flame ($\phi = 1.92$, $v_c = 7.75 \text{ cm}\cdot\text{sec}^{-1}$, $D = 4.17$).	421

Appendix Table	Page
D.32 Profiles of the fluorescence coefficient detected at 503 nm and 473 nm for the A-IA-S3 flame ($\phi = 2.02$, $v_c = 7.74 \text{ cm}\cdot\text{sec}^{-1}$, $D = 4.16$).	422
D.33 Temperature profiles determined from the scattering coefficient profiles for the A-IA flames ($v_c = 7.73 \text{ cm}\cdot\text{sec}^{-1}$, $D = 4.15$).	423
D.34 Temperature profiles determined from the scattering coefficient profiles for the A-IA flames ($v_c = 7.73 \text{ cm}\cdot\text{sec}^{-1}$, $D = 4.15$).	424
D.35 Temperature profiles determined from the scattering coefficient profiles for the A-IB flames ($v_c = 7.87 \text{ cm}\cdot\text{sec}^{-1}$, $D = 3.31$).	425
D.36 Temperature profiles determined from the scattering coefficient profiles for the A-IIA flames ($v_c = 10.42 \text{ cm}\cdot\text{sec}^{-1}$, $D = 4.29$).	426
E.1 Profile of the total scattering coefficient for the L-I-R1 flame ($\phi = 2.03$, $v_c = 18.1 \text{ cm}\cdot\text{sec}^{-1}$).	428
E.2 Profile of the total scattering coefficient for the L-I-R2 flame ($\phi = 2.17$, $v_c = 18.1 \text{ cm}\cdot\text{sec}^{-1}$).	430
E.3 Profile of the total scattering coefficient and the particle scattering coefficient for the L-I-S1 flame ($\phi = 2.32$, $v_c = 18.1 \text{ cm}\cdot\text{sec}^{-1}$).	432
E.4 Profile of the total scattering coefficient and the particle scattering coefficient for the L-I-S2 flame ($\phi = 2.46$, $v_c = 18.1 \text{ cm}\cdot\text{sec}^{-1}$).	434
E.5 Profile of the total scattering coefficient and the particle scattering coefficient for the L-I-S3 flame ($\phi = 2.60$, $v_c = 18.1 \text{ cm}\cdot\text{sec}^{-1}$).	436
E.6 Profile of the total scattering coefficient for the L-II-R1 flame ($\phi = 2.03$, $v_c = 22.4 \text{ cm}\cdot\text{sec}^{-1}$).	438
E.7 Profile of the total scattering coefficient for the L-II-R2 flame ($\phi = 2.16$, $v_c = 22.4 \text{ cm}\cdot\text{sec}^{-1}$).	440
E.8 Profile of the total scattering coefficient and the particle scattering coefficient for the L-II-S1 flame ($\phi = 2.32$, $v_c = 22.4 \text{ cm}\cdot\text{sec}^{-1}$).	442
E.9 Profile of the total scattering coefficient and the particle scattering coefficient for the L-II-S2 flame ($\phi = 2.46$, $v_c = 22.4 \text{ cm}\cdot\text{sec}^{-1}$).	444
E.10 Profile of the total scattering coefficient and the particle scattering coefficient for the L-II-S3 flame ($\phi = 2.60$, $v_c = 22.4 \text{ cm}\cdot\text{sec}^{-1}$).	446
F.1 Normalized OH fluorescence profile measured on Day 1 for the lean atmospheric-pressure flame, A-0-L ($\phi = 0.97$, $v_c = 8.86 \text{ cm}\cdot\text{sec}^{-1}$, $D = 5.42$).	449

Appendix Table	Page
F.2 Normalized OH fluorescence profile measured on Day 2 for the lean atmospheric-pressure flame, A-0-L ($\phi = 0.97$, $v_c = 8.86 \text{ cm}\cdot\text{sec}^{-1}$, $D = 5.42$).	450
F.3 Normalized OH fluorescence profile measured on Day 3 for the lean atmospheric-pressure flame, A-0-L ($\phi = 0.97$, $v_c = 8.86 \text{ cm}\cdot\text{sec}^{-1}$, $D = 5.42$).	451
F.4 Normalized OH fluorescence profile of the A-IA-R1 flame ($\phi = 1.49$, $v_c = 7.73 \text{ cm}\cdot\text{sec}^{-1}$, $D = 4.15$).	452
F.5 Normalized OH fluorescence profile of the A-IA-R2 flame ($\phi = 1.63$, $v_c = 7.73 \text{ cm}\cdot\text{sec}^{-1}$, $D = 4.15$).	453
F.6 Normalized OH fluorescence profile of the A-IA-S1 flame ($\phi = 1.78$, $v_c = 7.73 \text{ cm}\cdot\text{sec}^{-1}$, $D = 4.16$).	454
F.7 Normalized OH fluorescence profile of the A-IA-S2 flame ($\phi = 1.92$, $v_c = 7.75 \text{ cm}\cdot\text{sec}^{-1}$, $D = 4.17$).	455
F.8 Normalized OH fluorescence profile of the L-II-R1 flame ($\phi = 2.03$, $v_c = 22.4 \text{ cm}\cdot\text{sec}^{-1}$, $P = 80 \text{ torr}$).	456
F.9 Normalized OH fluorescence profile of the L-II-R2 flame ($\phi = 2.16$, $v_c = 22.4 \text{ cm}\cdot\text{sec}^{-1}$, $P = 80 \text{ torr}$).	459
F.10 Normalized OH fluorescence profile of the L-II-S1 flame ($\phi = 2.32$, $v_c = 22.4 \text{ cm}\cdot\text{sec}^{-1}$, $P = 80 \text{ torr}$).	461
F.11 Normalized OH fluorescence profile of the L-II-S2 flame ($\phi = 2.46$, $v_c = 22.4 \text{ cm}\cdot\text{sec}^{-1}$, $P = 80 \text{ torr}$).	464

LIST OF FIGURES

Figure		Page
2.1	Structure of a premixed sooting flame. The features of the flame and the stages of particle formation are identified (Calcote, 1981).	14
2.2	Detailed kinetic mechanism for surface growth. Armchair site (a) on the surface of the soot particle reacts with hydrogen atom to generate a radical site (b). Acetylene reacts with the radical site to add to the soot particle (c). (Frenklach and Wang, 1990)	25
2.3	Detailed kinetic mechanism for PAH growth. Hydrogen abstraction from the initial PAH (a) generates an aryl radical (b). Acetylene reacts with the radical to add to the PAH (c). A second hydrogen abstraction creates the new aryl radical (d). A second acetylene molecule reacts with the radical site to add to the PAH (e). The two acetylenes cyclize to form an aryl radical with an added ring (f). (Frenklach et al., 1984)	31
2.4	Global model for incipient soot formation.	51
3.1	Basic structure of a laser scattering-extinction measurement system. ..	64
3.2	A laser-induced fluorescence measurement system.	87
3.3	Two-level model for the energy levels in laser-induced fluorescence. W_{12} and W_{21} are the rate coefficients for stimulated absorption and emission. A_{21} is the spontaneous emission rate coefficient and Q_{21} is the quenching rate coefficient.	87
4.1	Cutaway view of the honeycomb plug flat flame burner.	100
4.2	Side view of the translation system showing the elements of the vertical translation system. The horizontal translation mechanism elements are shown but not labelled.	103
4.3	Top view of the translation system showing the elements of the horizontal translation system. The vertical translation mechanism elements are hidden by the pressure vessel base plate.	105
4.4	Schematic of the gas delivery and metering system. Components: PR - pressure regulator; PV - plug valve; IR - instrument pressure regulator; PG - pressure gauge; F - filter; MFC - mass flow controller; CV -check valve; FA - flashback arrestor; NV - needle valve.	108

Figure	Page	
4.5	Cutaway view of the pressure vessel showing sections of the pressure vessel at 90° to each other to display the two types of window mounts.	112
4.6	Schematic of the vacuum pump driven exhaust system for subatmospheric pressure operation of the burner.	114
4.7	Schematic showing the optical setup for the laser scattering-extinction measurements. Abbreviations for components: A - aperture; M - mirror.	125
4.8	Schematic of the signal detection and data acquisition setup for the laser scattering-extinction measurements.	129
4.9	Schematic of the hydroxyl radical fluorescence measurement setup. Components: BS - beamsplitter; L - lens (focal length in mm); M - mirror; NDF - neutral density filter; UVD - ultraviolet diffuser; VD - visible diffuser.	143
5.1	Extinction coefficient profiles of the A-IA sequence of flames ($v_c = 7.7 \text{ cm}\cdot\text{sec}^{-1}$ and $D = 4.2$). The narrow range of the extinction coefficient corresponding to the transmittance range from $\tau = 1.000$ to $\tau = 0.989$ shows the detail of the profiles of the lightly sooting flames. The error bars show twice the standard deviation of the measurement.	168
5.2	Extinction coefficient profiles of the A-IA sequence of flames ($v_c = 7.7 \text{ cm}\cdot\text{sec}^{-1}$ and $D = 4.2$). The full range of the extinction coefficient profiles is shown. The error bars show twice the standard deviation of the measurement.	170
5.3	Extinction coefficient profiles of the A-IB sequence of flames ($v_c = 7.8 \text{ cm}\cdot\text{sec}^{-1}$ and $D = 3.5$). The narrow range of the extinction coefficient corresponding to the transmittance range from $\tau = 1.000$ to $\tau = 0.989$ shows the detail of the profiles of the lightly sooting flames. The error bars show twice the standard deviation of the measurement.	171
5.4	Extinction coefficient profiles of the A-IB sequence of flames ($v_c = 7.8 \text{ cm}\cdot\text{sec}^{-1}$ and $D = 3.5$). The full range of the extinction coefficient profiles is shown. The error bars show twice the standard deviation of the measurement.	173
5.5	Extinction coefficient profiles of the A-IIA sequence of flames ($v_c = 10.4 \text{ cm}\cdot\text{sec}^{-1}$ and $D = 4.3$). The full range of the extinction coefficient profiles is shown. The error bars show twice the standard deviation of the measurement.	174

Figure	Page	
5.6	Scattering coefficient profiles of the A-IA sequence of flames ($v_c = 7.7 \text{ cm}\cdot\text{sec}^{-1}$ and $D = 4.2$). The narrow range of the scattering coefficient shows the details of the lightly sooting flame profiles. The error bars show the standard deviation of the measurement.	177
5.7	Scattering coefficient profiles of the A-IA sequence of flames ($v_c = 7.7 \text{ cm}\cdot\text{sec}^{-1}$ and $D = 4.2$). The logarithmic scale is used to show the full range of the scattering coefficient measurements.	179
5.8	Scattering coefficient profiles of the A-IB sequence of flames ($v_c = 7.8 \text{ cm}\cdot\text{sec}^{-1}$ and $D = 4.3$). The narrow range of the scattering coefficient shows the details of the lightly sooting flame profiles. The error bars show the standard deviation of the measurement.	180
5.9	Scattering coefficient profiles of the A-IB sequence of flames ($v_c = 7.8 \text{ cm}\cdot\text{sec}^{-1}$ and $D = 3.5$). The logarithmic scale is used to show the full range of the scattering coefficient measurements.	181
5.10	Scattering coefficient profiles of the A-IIA sequence of flames ($v_c = 10.4 \text{ cm}\cdot\text{sec}^{-1}$ and $D = 4.3$). The narrow range of the scattering coefficient shows the details of the lightly sooting flame profiles. The error bars show the standard deviation of the measurement.	182
5.11	Scattering coefficient profiles of the A-IIA sequence of flames ($v_c = 10.4 \text{ cm}\cdot\text{sec}^{-1}$ and $D = 4.3$). The logarithmic scale is used to show the full range of the scattering coefficient measurements.	183
5.12	Scattering coefficient profiles of the L-I sequence of flames ($v_c = 18.1 \text{ cm}\cdot\text{sec}^{-1}$). The narrow range of the scattering coefficient shows the details of the profiles in the transition from nonsooting to sooting flames.	186
5.13	Scattering coefficient profiles of the L-I sequence of flames ($v_c = 18.1 \text{ cm}\cdot\text{sec}^{-1}$). The logarithmic scale is used to show the full range of the scattering coefficient measurements.	187
5.14	Scattering coefficient profiles of the L-II sequence of flames ($v_c = 22.4 \text{ cm}\cdot\text{sec}^{-1}$). The narrow range of the scattering coefficient shows the details of the profiles in the transition from nonsooting to sooting flames.	188
5.15	Scattering coefficient profiles of the L-II sequence of flames ($v_c = 22.4 \text{ cm}\cdot\text{sec}^{-1}$). The logarithmic scale is used to show the full range of the scattering coefficient measurements.	189
5.16	Spectrum of the argon-ion laser-induced fluorescence measured at 12 mm above the burner for three sooting atmospheric-pressure flames: A-IA-S1 ($\phi = 1.78$), A-IA-S2 ($\phi = 1.92$), and A-IA-S3 ($\phi = 2.02$). The fluorescence signal ratio is normalized to the peak at the excitation wavelength, $\lambda_0 = 488.0 \text{ nm}$	191

Figure	Page	
5.17	Profiles of the argon-ion laser-induced fluorescence measured in the A-IA sequence of flames ($v_c = 7.7 \text{ cm}\cdot\text{sec}^{-1}$ and $D = 4.2$). The fluorescence coefficient ($Q_f \cdot \Delta\lambda \text{ cm}^{-1}\cdot\text{sr}^{-1}$) was measured with excitation at $\lambda = 488 \text{ nm}$ and detection at $\lambda = 503 \text{ nm}$ with a spectral bandpass, $\Delta\lambda = 0.72 \text{ nm}$ FWHM. The error bars show twice the standard deviation of the measurement.	193
5.18	(a) Profiles of the horizontal scattering coefficient in three sooting atmospheric-pressure flames. (b) Profiles of the calculated depolarization ratio for the same three flames. The solid symbols represent the corresponding signals when the fluorescence background is subtracted.	196
5.19	(a) Profiles of the horizontal scattering coefficient in the sooting 80-torr flames, L-I-S2, L-I-S3, L-II-S2, and L-II-S3. (b) Profiles of the calculated depolarization ratio for the same four flames.	198
5.20	Relative volume fraction profiles of the A-IA flame sequence. The relative volume fraction profile of the A-IB-S4 flame is also shown. The scale on the right axis corresponds to the volume fraction calculated with $\bar{n} = 2.10 - i\cdot 0.55$	206
5.21	a) Comparison of the relative volume fraction profiles measured in the -S2 ($\phi = 1.92$) flame of the three flame sequences. b) Comparison of the relative volume fraction profiles measured in the -S3 ($\phi = 2.02$) flame of the three flame sequences.	207
5.22	Relative number density profiles of the A-IA flame sequence. The solid symbols represent the profiles that have been corrected for the fluorescence background.	209
5.23	a) Comparison of the relative number density profiles measured in the -S2 ($\phi = 1.92$) flame of the three flame sequences. b) Comparison of the relative number density profiles measured in the -S3 ($\phi = 2.02$) flame of the three flame sequences.	210
5.24	Comparison of the relative number density profiles measured in the A-IB-S4 and A-IA-S4 flames ($\phi = 2.17$) and the A-IA-S5 flame ($\phi = 2.32$).	211
5.25	Relative particle diameter profiles of the A-IA flame sequence. The solid symbols represent the profiles that have been corrected for the fluorescence background.	213
5.26	a) Comparison of the relative particle diameter profiles measured in the -S2 ($\phi = 1.92$) flame of the three flame sequences. b) Comparison of the relative particle diameter profiles measured in the -S3 ($\phi = 2.02$) flame of the three flame sequences.	214
5.27	Relative number density profiles representing the upper bounds on the number density profiles of the 80-torr sooting flames.	220

Figure	Page	
5.28	Fluorescence coefficient detected at 503 nm vs. the extinction coefficient for the A-IA-S2 and A-IA-S3 flames. The linear curve fit for the A-IA-S2 flame was $Q_f(\lambda_0 = 488 \text{ nm}, \lambda = 503 \text{ nm})(z) = 0.199 \cdot K_{ext}(z)$ and for the A-IA-S3 flame, $Q_f(\lambda_0 = 488 \text{ nm}, \lambda = 503 \text{ nm})(z) = 0.141 \cdot K_{ext}(z)$	221
5.29	Temperature profiles determined from the scattering coefficient profiles for the A-IA flame sequence. The -R2, -S1, and -S2 profiles are free of particle scattering interference. The -S3 profile is free of interference below 10 mm, while the -S4 and -S5 profiles may remain free of interference only through the maximum.	224
5.30	Temperature profiles determined from the scattering coefficient profiles for the A-IB flame sequence. The -C flame is free of particle scattering interference, while the other three flames may remain free of interference only through the maximum.	225
5.31	Temperature profiles determined from the scattering coefficient profiles for the A-IIA flame sequence. The -R2 and -S1 profiles are free of particle scattering interference. The -S2 profile is free of interference below 10 mm, while the -S3 profile may remain free of interference only through the maximum.	226
6.1	Comparison of the normalized OH fluorescence profiles of the A-0-L ($\phi = 0.97$) flame with the OH number density profile predicted by the flame code solution. The OH fluorescence profiles were matched to the predicted OH number density profile over the region from 4.0 to 6.0 mm.	253
6.2	OH number density profiles of the four rich atmospheric-pressure flames: A-IA-R2 ($\phi = 1.49$), A-IA-R1 ($\phi = 1.63$), A-IA-S1 ($\phi = 1.78$), and A-IA-S2 ($\phi = 1.92$). The number densities were calibrated with respect to the A-0-L ($\phi = 0.97$) flame and corrected for quenching.	256
6.3	Relative OH fluorescence profiles of the four 80-torr flames: L-II-R1 ($\phi = 2.03$), L-II-R2 ($\phi = 2.16$), L-II-S1 ($\phi = 2.32$), and L-II-S2 ($\phi = 2.46$).	257
6.4	Fluorescence profiles of the four rich atmospheric-pressure flames normalized to the maximum of the profile to show the similarity in the profile shapes.	258
6.5	Fluorescence profiles of the four 80-torr flames normalized to the maximum of the profile to show the similarity in the profile shapes. ..	258
7.1	Comparison of the measured OH number density profiles with the predicted OH number density profiles using the Drake and Blint (1991) reaction mechanism and the Miller and Melius (1992) reaction mechanism. (a) Flame A-IA-R1, $\phi = 1.49$. (b) Flame A-IA-R2, $\phi = 1.63$. Both are nonsooting flames.	272

Figure		Page
7.2	Comparison of the measured OH number density profiles with the predicted OH number density profiles using the Drake and Blint (1991) reaction mechanism and the Miller and Melius (1992) reaction mechanism. (a) Flame A-IA-S1, $\phi = 1.78$. (b) Flame A-IA-S2, $\phi = 1.92$. Both are sooting flames.	273
7.3	Temperature profiles estimated from the scattering coefficient profiles for three flames: A-IA-R2, $\phi = 1.63$; A-IA-S1, $\phi = 1.78$; A-IA-S2, $\phi = 1.92$	274
7.4	Comparison of the argon-ion laser-induced fluorescence profiles (a) with the predicted benzene number density profiles (b) for four atmospheric-pressure flames: A-IA-R2, $\phi = 1.63$, nonsooting; A-IA-S1, $\phi = 1.78$, lightly sooting; A-IA-S2, $\phi = 1.92$, sooting; A-IA-S3, $\phi = 2.02$, sooting.	278
7.5	Comparison of the relative volume fraction profiles (a) measured in the $\phi = 1.92$ (-S2) flame of the three flame sequences with the predicted benzene number density profiles (b) for the same flames. ...	280
7.6	Comparison of the relative volume fraction profiles (a) measured in the $\phi = 2.02$ (-S3) flame of the three flame sequences with the predicted benzene number density profiles (b) for the same flames. ...	281
Appendix		
Figure		
A.1	Calibration of the dry test flow meter flow rates against the bubble meter flow rates.	314
B.1	Transimpedance amplifier circuit used to convert the photodiode current output to a voltage output.	319
B.2	Schematic of the signal detection and data acquisition setup for the laser scattering-extinction measurements.	323
B.3	Block diagram showing the gains and offsets applied for detection of the reference photodiode voltage.	328
B.4	Block diagram showing the gains and offsets applied for detection of the transmittance photodiode voltage.	328
B.5	Block diagram showing the gains and offsets applied for detection of the scattering photomultiplier voltage.	328
B.6	Transmittance profiles for a lightly sooting flame (A-IA-S1, $\phi = 1.78$, $v_c = 7.73 \text{ cm}\cdot\text{sec}^{-1}$, $N_2/O_2 = 4.16$) measured on two days. The error bars indicate a variation of two standard deviations in the transmittance recorded at a given height.	337

Appendix Figure	Page
B.7 Transmittance profiles for a sooting flame (A-IA-S2, $\phi = 1.92$, $v_c = 7.73 \text{ cm}\cdot\text{sec}^{-1}$, $N_2/O_2 = 4.16$) measured on three days. The error bars indicate a variation of two standard deviations in the transmittance recorded at a given height.	338
C.1 Successive estimates of the temperature profile (upper plot) and the resulting predicted scattering coefficient profile (lower plot) for the A-IA-S1 flame ($\phi = 1.78$).	357
C.2 Comparison of the predicted scattering coefficient profile with the measured scattering coefficient profile for the A-IA-S1 flame ($\phi = 1.78$, upper plot) and the A-IA-R2 flame ($\phi = 1.63$, lower plot). Also shown are the predicted scattering coefficient profiles when the peak temperatures are varied by 20 K.	359
C.3 Variation of the mean differential scattering cross-section with height above the burner for four flames: A-IA-R2 ($\phi = 1.63$), A-IA-S1 ($\phi = 1.78$), A-IA-S2 ($\phi = 1.92$), and A-IA-S3 ($\phi = 2.02$). The mean differential scattering cross-sections at the peak of the temperature profiles are marked with filled diamonds.	361
C.4 Calculated temperature profiles for the A-IA-R2 flame ($\phi = 1.63$).	363
C.5 Calculated temperature profiles for the A-IA-S1 flame ($\phi = 1.78$).	364
C.6 Calculated temperature profiles for the A-IA-S2 flame ($\phi = 1.92$).	366
C.7 Calculated temperature profiles for the A-IA-S3 flame ($\phi = 1.92$).	368

LIST OF SYMBOLS

English Symbols

<u>Symbol</u>	<u>Description</u>	<u>Units</u>
A	Pre-exponential factor in the Arrhenius rate expression	moles·cm ⁻³ ·sec ⁻¹ units
A	Area	cm ²
A_{21}	Rate coefficient for spontaneous emission	sec ⁻¹
C_{ext}	Extinction cross-section	cm ²
C_{PP}	Differential scattering cross-section	cm ² ·sr ⁻¹
\bar{C}_{PP}	Mean differential scattering cross-section	cm ² ·sr ⁻¹
\bar{C}_{ext}	Mean extinction cross-section	cm ²
c	speed of light	cm·sec ⁻¹
D	Dilution ratio	--
d_{63}	Mean particle diameter defined in terms of the ratio of the sixth moment to the third moment of the particle size distribution (Eq. 3.2.31)	nm
d_0	Mean particle diameter	nm
E_i	Activation energy	cal·mole ⁻¹
$E(\tilde{m})$	Function of complex index of refraction (Eq. 3.2.26)	--
F	Calibration factor	--
$F(\tilde{m})$	Function of complex index of refraction (Eq. 3.2.27)	--
F_{12}	Boltzmann fraction	--

Symbol	Description	Units
f_N	Dimensionless moment ratio of the particle size distribution (Eq. 3.2.29)	--
f_V	Volume fraction	$\text{cm}^3 \text{ soot} \cdot \text{cm}^{-3} \text{ gas}$
G	Lock-in amplifier gain	voltage output/voltage input
h	Planck's constant	J·sec
I_0	Incident irradiance	$\text{W} \cdot \text{cm}^{-2}$
I_T	Transmitted irradiance	$\text{W} \cdot \text{cm}^{-2}$
i_{sh}	Photodetector short circuit current	A
K_{ext}	Local extinction coefficient	cm^{-1}
k	Imaginary part of the complex index of refraction	--
k_f	Forward rate coefficient	$\text{moles} \cdot \text{cm}^{-3} \cdot \text{sec}^{-1}$ units
L	Pathlength of the laser through the flame	cm
MW	Molecular weight	$\text{gm} \cdot \text{gmol}^{-1}$
$\bar{m} = n - ik$	Complex index of refraction	--
N_{av}	Avogadro's number	gmol^{-1}
N_0	Standard molecular number density (0 °C and 1 atm)	cm^{-3}
N_p	Particle number density	cm^{-3}
N_T	Total number density	cm^{-3}
N_1	Number density in the ground level	cm^{-3}
N_1^0	Initial number density in the ground level	cm^{-3}
N_2	Number density in the excited level	cm^{-3}
n	Real part of the complex index of refraction	--
P	Pressure	atm
$P(r)$	Particle size distribution function	--
Q	Integrated quenching rate coefficient	sec^{-1}
Q_f	Monochromatic fluorescence coefficient	$\text{cm}^{-1} \cdot \text{sr}^{-1} \cdot \text{nm}^{-1}$

<u>Symbol</u>	<u>Description</u>	<u>Units</u>
Q_{PP}	Differential scattering coefficient	$\text{cm}^{-1} \cdot \text{sr}^{-1}$
Q_{scs}	Total scattering coefficient	$\text{cm}^{-1} \cdot \text{sr}^{-1}$
Q_{21}	Rate coefficient for collisional quenching	sec^{-1}
q_m	Mass flux through burner	$\text{gm} \cdot \text{cm}^{-2} \cdot \text{sec}^{-1}$
R	Gas constant	$\text{cm}^3 \cdot \text{atm} \cdot \text{gmol}^{-1} \cdot \text{K}^{-1}$
R_L	Molar refractivity	$\text{cm}^3 \cdot \text{mol}^{-1}$
r	Particle radius	nm
r_0	Mean particle radius	nm
r_λ	Photodetector responsivity	$\text{A} \cdot \text{W}^{-1}$
S	Lock-in sensitivity	mV signal/full scale input
S_f	Fluorescence signal power	W
S_{PP}	Scattered light power	W
S_R	Rayleigh scattering light power	W
S_{scs}	Total scattered light power	W
T	Temperature	K
t	Time	sec
V	Photodetector voltage	V
V_c	Collection volume	cm^3
\dot{V}	Volume flow rate	$\text{l} \cdot \text{min}^{-1}$
v_k	Relative velocity between species k and the quenched species	$\text{cm} \cdot \text{sec}^{-1}$
v_c	Cold flow velocity	$\text{cm} \cdot \text{sec}^{-1}$
W	Molecular weight used in Sandia flame code notation	$\text{gm} \cdot \text{gmol}^{-1}$
W_{12}	Rate coefficient for stimulated absorption	sec^{-1}
W_{21}	Rate coefficient for stimulated emission	sec^{-1}
X	Mole fraction	--

<u>Symbol</u>	<u>Description</u>	<u>Units</u>
x	distance	cm
z	Height above the burner	cm

Greek Symbols

<u>Symbol</u>	<u>Description</u>	<u>Units</u>
$\alpha = 2\pi r/\lambda$	Particle size parameter	--
β	Temperature exponent in the Arrhenius rate expression	--
ϵ_f	Fluorescence emission	$\text{W}\cdot\text{cm}^{-3}\cdot\text{sr}^{-1}$
ϵ_{fB}	Broadband fluorescence emission	$\text{W}\cdot\text{cm}^{-3}\cdot\text{sr}^{-1}$
η_c	Efficiency of the collection optics	--
η_o	Optical efficiency	--
η_E	Electronic efficiency	--
θ	angle between the incident and scattered light	deg
λ	wavelength	nm
ν	wavenumber	cm^{-1}
ρ	Molar density	$\text{mol}\cdot\text{cm}^{-3}$
ρ_v	Depolarization ratio	--
τ	transmittance	--
σ	Absorption cross-section	cm^2
σ_g	Geometric width of the lognormal distribution	--
σ_Q	Quenching cross-section	cm^2
ϕ	Equivalence ratio	--
ϕ_c	Critical equivalence ratio	--
Ω_c	Collection solid angle	sr

Subscripts

<u>Symbol</u>	<u>Description</u>	<u>Units</u>
<i>A</i>	Analog processor	--
<i>c</i>	Computer interface	--
<i>cal</i>	Calibration conditions	--
<i>D</i>	Diluent	--
<i>F</i>	Fuel	--
<i>f</i>	Fluorescence	--
<i>g</i>	Gas or molecular scattering	--
<i>H</i>	Horizontal polarization	--
<i>k</i>	Species index	--
<i>m</i>	Measured	--
<i>L</i>	Laser or incident light	--
<i>N₂</i>	Nitrogen	--
<i>O</i>	Oxidizer	--
<i>O₂</i>	Oxygen	--
<i>oA</i>	Output offset of analog processor	--
<i>oL</i>	Output offset of lock-in amplifier	--
<i>os</i>	Input offset of lock-in amplifier	--
<i>PP</i>	General subscript for scattering coefficient and cross-sections. The first subscript denotes the polarization of the detected scattered light and the second denotes the polarization of the detected light.	--
<i>pd</i>	photodetector	--
<i>R</i>	Rayleigh scattering	--
<i>S</i>	Scattered	--
<i>STP</i>	Standard temperature (25 °C) and pressure (1 atm)	--
<i>T</i>	Transmittance	--
<i>TOT</i>	Total	--

Superscripts

<u>Symbol</u>	<u>Description</u>	<u>Units</u>
V	Vertical polarization	--
0	Incident	--
r	Relative, identifies the volume fraction, particle number density and particle diameter determined independent of index of refraction and particle size distribution.	--

Notation for identification of flames

First two-letter designations

A-IA-	Atmospheric-pressure flames with $v_c = 7.7 \text{ cm}\cdot\text{sec}^{-1}$ and $D \approx 4.2$
A-IB-	Atmospheric-pressure flames with $v_c = 7.8 \text{ cm}\cdot\text{sec}^{-1}$ and $D \approx 3.5$
A-IIA-	Atmospheric-pressure flames with $v_c = 10.4 \text{ cm}\cdot\text{sec}^{-1}$ and $D \approx 4.3$
L-I-	80-torr flames with $v_c = 18.1 \text{ cm}\cdot\text{sec}^{-1}$
L-II-	80-torr flames with $v_c = 22.4 \text{ cm}\cdot\text{sec}^{-1}$

Third letter designation

-L	Lean
-R	Rich nonsooting
-C	Critical equivalence ratio
-S	Sooting

ABSTRACT

The testing and development of existing global and detailed chemical kinetic models for soot formation requires measurements of soot and radical concentrations in flames. A clearer understanding of soot particle inception relies upon the evaluation and refinement of these models in comparison with such measurements.

We present measurements of soot formation and hydroxyl (OH) concentration in sequences of flat premixed atmospheric-pressure $C_2H_4/O_2/N_2$ flames and 80-torr C_2H_4/O_2 flames for a unique range of equivalence ratios bracketing the critical equivalence ratio (ϕ_c) and extending to more heavily sooting conditions. Soot volume fraction and number density profiles are measured using a laser scattering-extinction apparatus capable of resolving a 0.1% absorption. Hydroxyl number density profiles are measured using laser-induced fluorescence (LIF) with broadband detection. Temperature profiles are obtained from Rayleigh scattering measurements.

The relative volume fraction and number density profiles of the richer sooting flames exhibit the expected trends in soot formation. In near- ϕ_c visibly sooting flames, particle scattering and extinction are not detected, but an LIF signal due to polycyclic aromatic hydrocarbons (PAHs) can be detected upon excitation with an argon-ion laser. A linear correlation between the argon-ion LIF and the soot volume fraction implies a common mechanistic source for the growth of PAHs and soot particles. The peak OH number density in both the atmospheric and 80-torr flames declines with increasing equivalence ratio, but the profile shape remains unchanged in the transition to sooting, implying that the primary reaction pathways for OH remain unchanged over this transition.

Chemical kinetic modelling is demonstrated by comparing predictions using two current reaction mechanisms with the atmospheric flame data. The measured and predicted OH number density profiles show good agreement. The predicted benzene number density profiles correlate with the measured trends in soot formation, although anomalies in the benzene profiles for the richer and cooler sooting flames suggest a need for the inclusion of benzene oxidation reactions.



CHAPTER 1: INTRODUCTION

1.1 Relevance

Soot is the carbonaceous particles formed from the gas phase during the incomplete combustion of a hydrocarbon fuel. This simple definition disguises the complexity of the mechanism of soot formation. The effects of soot are the reason for seeking to unravel its complex mechanism. These effects can be seen quite literally in the world around us. The presence of soot is manifested by the yellow emission of a candle flame. Soot increases the luminosity of the flame and, in general, increases the radiative heat transfer from a combustion process. Thus, its presence can be desirable, for example, in a furnace.

The presence of soot can also be seen in the exhaust of a diesel truck or from the smokestack of a powerplant. Thus, soot is also a visual pollutant and its emission represents inefficient combustion because of the unburned carbon. Soot can remain airborne for long periods of time because of its size and thus it can disperse widely from its source and reduce atmospheric visibility.

The presence of soot was also identified as the first known cause of cancer. In 1775, chimney soot was identified as causing cancer of the scrotum in chimney sweeps in London (Pott, 1775). The carcinogenicity of soot is primarily caused by the polycyclic aromatic hydrocarbons (PAHs) which condense on the soot during its formation. Benzo(a)pyrene, fluoranthene, and cyclopenta(cd)pyrene are carcinogenic PAHs found in the soot emitted from practical combustors (Longwell, 1983).

These effects of soot are the motivation for seeking to understand the mechanism of soot formation, so that its formation can be modelled, predicted or possibly controlled. Studies of soot formation in a variety of combustion systems and for different fuels suggest a common mechanism for soot formation (Glassman, 1988). Thus, an understanding of the soot formation mechanism in complex combustion systems can be developed from investigations in simpler laboratory combustion systems where interactions between transport processes and chemical kinetics can be more easily modelled.

From previous laboratory studies, the mechanism of soot formation consists of four processes: particle inception, surface growth, coagulation, and oxidation (Haynes and Wagner, 1981). Particle inception is the formation of the soot particles from the gas phase through oxidation and pyrolysis of the fuel. Surface growth is the subsequent growth of the particles from the reactions of gas phase species with the particles. Coagulation is the growth of the particles through collision and fusion of the particles. Oxidation competes with both the growth and formation of the particles through oxidation of the particles by surface reactions or by oxidation of gas-phase species involved in particle inception.

The understanding of soot formation has advanced to the point where both coagulation and surface growth can be described well by empirical models, although the underlying mechanisms for these processes are still not fully understood. While coagulation and surface growth account for most of the particle growth in size and mass, the empirical models suggest that the number of particles formed initially is the determining factor in the final amount of soot formed. Thus, particle inception is the critical stage in soot formation.

Particle inception is a molecular growth process that is postulated to occur in three stages: formation of single-ring aromatic species, growth of polycyclic aromatic hydrocarbons, and coagulation of polycyclic aromatic hydrocarbons. The bottleneck in

the formation of soot from aliphatic fuels is thought to be the formation of single-ring aromatic species by the pyrolysis of the fuel. Once formed, the single-ring aromatic species grow through a sequence of addition and cyclization reactions to form larger multiple-ring aromatic species, PAHs. These large PAHs can either grow further or coagulate to form incipient soot particles, particles with a weight of about 2000 amu and about 2 nm in diameter.

This model of the particle inception process is based on the development of detailed chemical kinetic models that describe the formation reactions and on the comparison of model predictions with measured species profiles in nonsooting and sooting flames. However much remains unknown about the details of the individual steps. In particular, the route to the formation of the single-ring aromatic species from aliphatic fuels is still being debated. Models based upon this theory of particle inception are successful in predicting selected features of soot formation. However, further development will require testing over a wider range of flame conditions for which the data is not yet available.

Global models for incipient soot formation have been used to predict the occurrence of soot formation in flames. Specifically, these models correlate macroscopic properties of the flame such as fuel type and mixture, maximum temperature, and equilibrium OH concentration with the critical equivalence ratio, which is the equivalence ratio at which the yellow emission of soot first becomes visible as the equivalence ratio is increased from nonsooting conditions. The basis of these models is the assumption that the critical equivalence ratio occurs when the rate of formation of soot precursors by pyrolysis is balanced by their rate of oxidation by the hydroxyl radical. The success of these models in correlating critical equivalence ratio data for a variety of fuels suggests that the macroscopic properties are sufficient to describe soot formation near the onset of sooting. However, the identity of the precursors is unknown and it is also unknown whether the hydroxyl radical is directly involved as an oxidizer of precursors or if it is a marker for

other processes that occur. Further refinement of the global models is likely to come from a better understanding of the details of soot formation and from measurements of species profiles such as the hydroxyl radical near the critical equivalence ratio.

1.2 Objectives

The objective of this study is to provide a set of data that can be used in the development and testing of both global and detailed chemical kinetic models of soot formation. Soot formation and hydroxyl radical concentration are measured in a series of premixed flat ethylene flames to serve as a basis for comparison with one-dimensional flat flame models describing the formation of aromatic species and soot.

The flame conditions were selected so that they ranged from a rich non-sooting flame near the critical equivalence ratio to a visibly sooting flame at or near the critical equivalence ratio to more heavily sooting flames. Three sequences of ethylene/oxygen/nitrogen flames at atmospheric pressure were examined in which the cold flow velocity (total flow rate of the fuel/oxidizer mixture divided by the burner surface area) and the dilution ratio (ratio of nitrogen to oxygen mole fractions) were held constant, while the equivalence ratio was varied through the range of sooting conditions. Variation of the cold flow velocity and the dilution ratio between the sequences allowed measurement of the effects of temperature and fuel mixture composition on soot formation. Two sequences of ethylene/oxygen flames at 80 torr were also examined in which the cold flow velocity was held constant, while the equivalence ratio was varied. The 80-torr flames allowed the hydroxyl radical concentration profile to be measured in greater detail, while the variation in cold flow velocity allowed the assessment of the effect of temperature on soot formation.

These atmospheric and 80-torr flames serve as the basis for a systematic investigation of both soot formation and hydroxyl radical concentration in the region about the critical equivalence ratio, a region of soot formation that has not been previously

investigated with this combination of methods. Soot formation was quantified by measurements of the soot volume fraction and particle number density profiles using the laser scattering-extinction method. In addition, profiles of the argon-ion laser-induced fluorescence were measured in one flame sequence as a relative measure of the polycyclic aromatic hydrocarbon concentration. Temperature profiles were also obtained from the scattering-extinction measurements.

These profiles of soot formation then serve as the basis for identifying trends in soot formation with variation of major flame parameters. In particular, the profiles identify the change in soot formation in the region near the critical equivalence ratio. Thus, these profiles can serve as a basis for testing the ability of the models to predict both the amount of soot formed and the relative trends between flames and also their ability to predict the transition from nonsooting to sooting flames.

Hydroxyl radical concentration profiles were measured in a sequence of the atmospheric-pressure flames and in a sequence of the 80-torr flames using the laser-induced fluorescence method. These profiles can serve as the basis for testing detailed chemical kinetic models for their ability to model the hydroxyl radical concentration profile. In addition, the change in the hydroxyl radical concentration profile as the equivalence ratio is varied through the critical equivalence ratio provides a basis for evaluating the assumptions of the global models describing incipient soot formation.

Chemical kinetic modelling of these flames was demonstrated using the Sandia premixed one-dimensional flame code and two reaction mechanisms. The reaction mechanism of Drake and Blint (1991) was used for initial modelling of the hydroxyl radical concentration profiles, because the mechanism was not intended to model sooting conditions and only includes hydrocarbon species of size C_3 and smaller. The reaction mechanism of Miller and Melius (1992) incorporates the most recent hypotheses for the

formation of aromatic species in aliphatic flames and was used to model both the hydroxyl radical concentration profiles and the benzene profiles. The hydroxyl radical concentration profiles predicted with both reaction mechanisms were compared with the measured profiles to evaluate their ability to model these profiles. The trends of the benzene concentrations predicted with the Miller and Melius (1992) mechanism were compared with the observed trends in soot formation. This preliminary modelling demonstrates the use of the data in the evaluation of soot formation models.

1.3 Overview

In Chapter 2, we review the literature on soot formation with a focus on soot formation in premixed flames. We first describe current global models for coagulation and surface growth. We then discuss the three stages of particle inception, formation of aromatic species, PAH growth, and PAH coagulation, and their hypothetical mechanisms. In particular, we focus on the chemical reaction routes leading to the formation of the first aromatic ring and the possible role of the H_2-O_2 system radicals in that chemistry. Detailed chemical kinetic models that have been developed to describe the formation of aromatic species and also those that include the full range of soot formation are then described. Finally, we discuss the global models that describe incipient soot formation in premixed flames.

In Chapter 3, we review the methods that have been used to measure soot and hydroxyl radical concentrations in flames. We develop the theory for the laser scattering-extinction measurements of soot formation and the laser-induced fluorescence measurements of the hydroxyl radical. The possible interferences and concerns that may affect the interpretation of the measurements in sooting flames are identified.

In Chapter 4, we describe the experimental apparatus and our specific implementation of the measurement methods. The premixed flat flame burner system is described and the flame conditions that we examined are listed. Then, for both the laser

scattering-extinction measurements and the laser-induced fluorescence measurements, we describe the optical setup, the signal detection and data acquisition system, the experimental procedure, and the subsequent data analysis. Finally, we describe our implementation of the Sandia premixed one-dimensional flame code and the solution procedure using two reaction mechanisms that can be used to describe the oxidation and pyrolysis of ethylene.

In Chapter 5, we present the results of the laser scattering-extinction measurements of soot formation in three sequences of atmospheric-pressure $C_2H_4/O_2/N_2$ flames and two sequences of 80-torr C_2H_4/O_2 flames. Relative volume fraction, number density, and particle diameter profiles are presented for the more heavily sooting atmospheric-pressure flames, while upper bounds are established for these parameters in the 80-torr flames and the near-critical equivalence ratio atmospheric flames. These measured profiles and upper bounds are used to identify the trends in soot formation with changing equivalence ratio, temperature, and dilution ratio.

In Chapter 6, we present the laser-induced fluorescence measurements of the hydroxyl radical in a sequence of atmospheric-pressure $C_2H_4/O_2/N_2$ flames and a sequence of 80-torr C_2H_4/O_2 flames, both spanning the transition from rich nonsooting to sooting conditions. Absolute number density profiles are determined for the atmospheric flames, while only relative number density profiles could be determined for the 80-torr flames. We then examine the behavior of the OH number density profiles as the transition is made from nonsooting to sooting flame conditions.

In Chapter 7, we present results from chemical kinetic modelling of the atmospheric-pressure flames using the Sandia premixed one-dimensional flame code and two reaction mechanisms, one modelling up to the formation of C_3 hydrocarbons and one modelling up to the formation of benzene. The predicted OH number density profiles using both reaction mechanisms are compared with the measured OH number density

profiles to evaluate the ability of the mechanism to model the OH concentration over a range of equivalence ratios. The predicted benzene profiles using the second mechanism are compared with the trends in measured soot formation.

Finally, in Chapter 8, we summarize the results of this study, suggest improvements that might be made our kinetic analysis and propose directions for future research.

CHAPTER 2: LITERATURE REVIEW - SOOT FORMATION

2.1 Introduction

The literature covering the many aspects of soot formation is extensive. This reflects the importance placed on understanding and controlling soot formation because of its effect on the combustion process and its role as a pollutant. It also reflects the complicated nature of soot formation, whereby a soot particle containing a million carbon atoms forms in milliseconds during the combustion of a hydrocarbon fuel whose molecules contain just a few carbon atoms.

The process of soot formation has not been completely described because it involves fuel-rich hydrocarbon chemistry and because its formation is rate limited. Fuel-rich hydrocarbon chemistry itself has not been completely described because of difficulties in both identifying and measuring the large number of species present and also identifying and modelling the myriad reactions that take place. Because of its chemical kinetic rate-limited nature, the formation of soot in a combustion process depends on the structure of the flow and the temperature in addition to the fuel and oxidizer composition. The interactions between the transport processes and the chemical kinetics strongly influence the formation of soot and thus complicate and confound the comparisons of studies of soot formation that use different combustors. Thus, most of the knowledge on soot formation comes from laboratory studies in laminar flames and shock tubes where the interactions between the chemical kinetics and the transport processes can be reduced or easily modelled.

From previous laboratory studies, a general mechanism for the formation of soot has been postulated that consists of four processes - particle inception, surface growth, coagulation, and oxidation (Haynes and Wagner, 1981; Calcote, 1981; Glassman, 1988). Particle inception is concerned with the formation of the soot particles through the oxidation and pyrolysis of fuel molecules. The initial step in particle inception is believed to be the formation of single-ring aromatic species by the pyrolysis of fuel molecules. These single-ring aromatic species grow into larger multiple-ring aromatic species, polycyclic aromatic hydrocarbons (PAHs), through a repeated sequence of additions of acetylene, dehydrogenation, and cyclization reactions (Frenklach and Wang, 1990). The initial particles are formed from either further growth or from coagulation of these large PAH molecules. The first particles observed in a flame are small, less than 2 nm in diameter, and they represent only a small fraction of the soot mass eventually formed in a flame, even though they are present in great numbers (Haynes and Wagner, 1981).

Once they have formed, the soot particles grow through both surface growth and coagulation simultaneously. Surface growth is the addition of gas phase species to the particle surface. Acetylene is thought to be the primary growth species and may either condense on the particle surface or may join to the particle through a reaction sequence (Harris and Weiner, 1983a; 1983b). Surface growth generates the major fraction of the soot mass, but does not change the number of soot particles in the flame. Coagulation is the collision and fusion of the particles. In the early stages of soot formation, the small particles appear to coalesce to form a single sphere. In the later stages of soot formation, the particles collide and fuse together to form chains or clusters of spheres. Coagulation increases the size and reduces the number of particles without changing the total soot mass. Coagulation dominates in the later stages of soot formation as the particles age and become less reactive. The spheroidal particles grow to a size of 10 to 50 nm; the chains or clusters of the spheroidal particles can grow much larger (Haynes and Wagner, 1981).

Oxidation competes with the formation of soot by removing soot from the system through both heterogeneous and homogeneous oxidation. Heterogeneous oxidation is the oxidation of the soot particle at its surface and thus acts to remove the soot mass. It is responsible for the burn-out of soot particles in the oxygen-rich side of a diffusion flame. Homogeneous oxidation competes with particle formation by oxidizing gas-phase species that are involved in either particle inception or surface growth (Olson, Keil, and Calcote, 1984).

Models of soot formation are being developed that include submodels corresponding to the above stages of soot formation. Models describing both surface growth (Harris and Weiner, 1983a; 1983b; Harris, 1990) and coagulation (Prado and Lahaye, 1981; Harris and Kennedy, 1988; Megaridis and Dobbins, 1989) have been developed that agree well with flame measurements, although the details of the mechanisms are still being investigated. Particle inception models are more complicated and are less mature in their development. These models incorporate detailed chemical kinetics that describe the formation of aromatic species from the rich combustion of some of the simpler hydrocarbon fuels such as methane, ethylene, and acetylene. Details of these mechanisms are still being investigated (Frenklach and Wang, 1990). In particular, the route to formation of the first aromatic rings and subsequently to the first soot particle are still being debated (Westmoreland et al., 1989; Miller and Melius, 1992).

Global models have been developed that describe the sooting tendency of fuels (Janssen and Senser, 1991). These global models typically describe the onset of soot formation in terms of the temperature, fuel structure, and OH concentration. Their utility is in investigating the parameters that influence the onset of soot formation. Although they predict the onset of soot formation in premixed flames, they have not been developed to the point where they can predict soot yield.

The literature pertaining to soot formation is voluminous. Early studies of carbon formation were summarized by Palmer and Cullis (1965) and more specifically for premixed flames by Homann (1967). The comprehensive review by Haynes and Wagner (1981) summarized the research to date on soot formation in both laminar and turbulent premixed, diffusion, and spray flames. Calcote (1981) summarized the research on particle inception in flames with an emphasis on ionic mechanisms. More recent reviews have been published by Homann (1984), who reviewed the research on the formation of PAHs and soot in premixed flames, and by Glassman (1988), who reviewed the mechanism of soot formation and its application to understanding the sooting tendencies of fuels.

An important goal of our research has been to investigate the role of the OH radical in the formation of soot in premixed flames. Thus, we will focus on reviewing the aspects of soot formation in premixed flames that are pertinent to that role and also the models of soot formation that may be used to evaluate that role. We begin by describing the general structure of a sooting premixed flame to identify the stages of soot formation. The mechanism and model for the coagulation of the particles is then reviewed followed by the discussion of a mechanism and model for the surface growth of the particle. An understanding of these two processes leads to the conclusion that the particles formed in the inception stage determine the final amount of soot formed in the flame. We then review investigations of the pre-particle inception chemistry and hypotheses concerning the formation of the first soot particles. Next, we review the detailed chemical kinetic models that have been proposed to model the pre-particle inception chemistry. Global models that describe the onset of soot formation are also described. Finally, we summarize the review and suggest an approach for identifying the role of the hydroxyl radical in soot formation.

2.2 Structure of Premixed Sooting Flames

The visible structure of a flat premixed sooting flame is illustrated in Figure 2.1. A nonluminous zone directly above the burner is followed by the blue-green emission of the main reaction zone. Further above the burner, a dark space appears between the main reaction zone and the start of the yellow to orange emission of soot (Millikan, 1962; Haynes, Jander, and Wagner, 1980). However, no dark zone is observed in benzene flames as the luminous yellow emission of soot directly follows the main reaction zone (Haynes, Jander, and Wagner, 1980). Similarly, Bonne, Homann, and Wagner (1965) did not observe the dark space between the main reaction zone and the soot luminosity in any of their ethylene, acetylene, propane, or benzene flames.

The yellow emission of a premixed sooting flame signals the presence of soot particles. The two primary methods that have been used to measure soot particles are laser scattering-extinction and direct sampling of the soot followed by examination with an electron microscope. The soot particles are described by the soot volume fraction, f_v ($\text{cm}^3 \text{ soot} \cdot \text{cm}^{-3} \text{ gas}$), the particle number density, N_p (cm^{-3}), the radius of the soot particles, r (nm), and the particle size distribution function, $P(r)$. These parameters are related by

$$f_v = N_p \cdot \frac{4\pi}{3} \cdot \int_0^\infty P(r) \cdot r^3 \cdot dr \quad . \quad (2.1)$$

Usually, the volume fraction and the number density are used to describe the soot particle field. The particle size distribution is usually assumed to be either a monodisperse or lognormal distribution, except when the particle size is measured explicitly such as by direct sampling or by dynamic light scattering measurements. Non-spherical particles and chainlike agglomerates of particles are usually described by an equivalent diameter which is the diameter of a sphere with a volume equal to the particle volume.

Within a sooting premixed hydrocarbon flame, particle inception occurs in a narrow region near the main reaction zone where the temperature and radical concentrations are

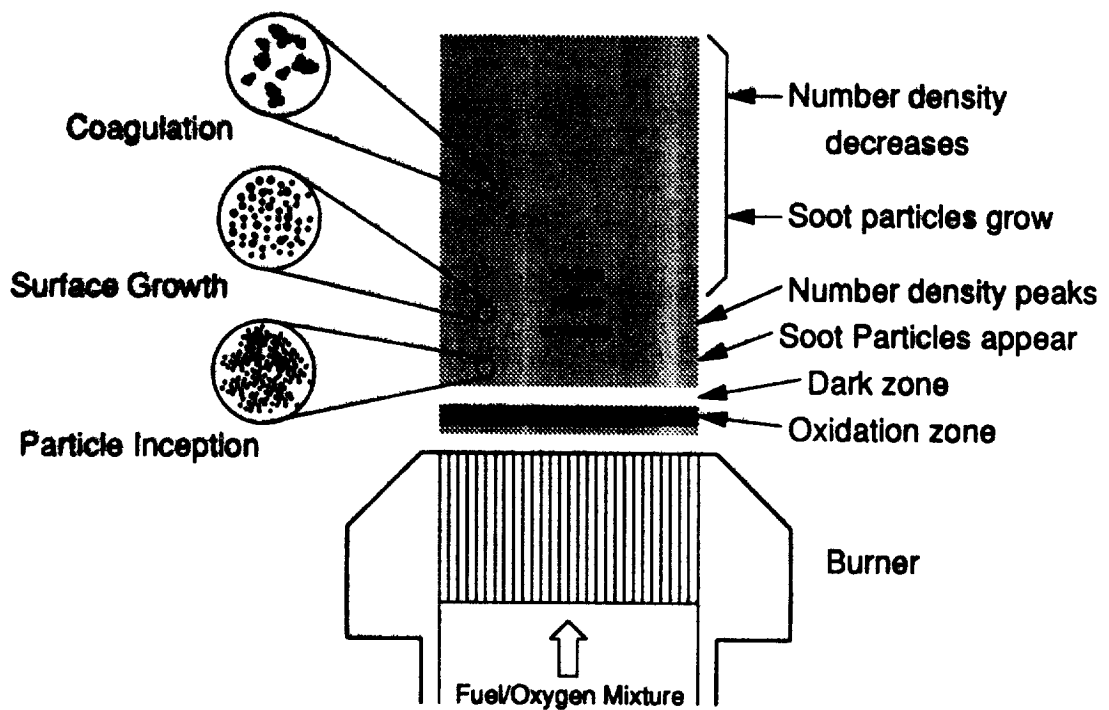


Figure 2.1 Structure of a premixed sooting flame. The features of the flame and the stages of particle formation are identified (Calcote, 1981).

high. Homann and Wagner (1967) observed that in a benzene flame carbon had already formed by the end of the oxidation zone where the O_2 concentration had dropped below their detection limit (10^{-7} mole fraction). Harris (1986) noted that particle inception occurred in an ethylene flame where the O_2 concentration was approximately 1 percent, but inception ceased when the O_2 concentration decreased below a few tenths of a percent. The number density of the newly formed particles is typically $N_p > 10^{12} \text{ cm}^{-3}$, but since their size is small (typically $d < 2 \text{ nm}$), the initial volume fraction is also small, e.g., $f_v \approx 10^{-9} \text{ cm}^3 \text{ soot} \cdot \text{cm}^{-3} \text{ gas}$ (Haynes and Wagner, 1982).

Particle inception ceases shortly after the start of surface growth and coagulation as shown by the strong decrease in number density prior to the increase in volume fraction (Bockhorn et al., 1982; 1984; Haynes and Wagner, 1982; Prado and Lahaye, 1981). Surface growth adds up to 97 percent of the final soot mass to the initial soot particles (Bockhorn, Fetting, and Heddrich, 1986). The volume fraction increases rapidly following particle inception, but the surface growth rate eventually declines to zero with increasing height above the burner as the volume fraction asymptotically approaches a final volume fraction, f_v^* . In benzene flames, the volume fraction grows rapidly at first and then remains constant (Homann and Wagner, 1967; Haynes, Jander, and Wagner, 1980), while the soot volume fraction increases more steadily with time in ethylene flames (Haynes, Jander, and Wagner, 1980). The final soot volume fraction depends strongly on fuel type, flame stoichiometry, pressure, and temperature (Haynes and Wagner, 1982). Increasing temperature strongly decreases the final soot yield. Haynes and Wagner (1982) report a negative activation energy of approximately $100 \text{ kcal} \cdot \text{mole}^{-1}$ for f_v^* in their ethylene and benzene flames at 1 atm. Bockhorn et al. (1984) found that f_v^* increased by a factor of 1.5 if the maximum temperature decreased by only 20 K.

Coagulation begins once the particles form. The number density drops rapidly at first, and then more slowly throughout the downstream regions of the flame. Flames with

different final soot yields show a similar decrease in N_p with increasing time as they approach a final number density of $N_p \approx 10^9$ to 10^{10} cm^{-3} (Haynes and Wagner, 1982; Baumgartner et al., 1984). The final number density depends weakly on the volume fraction and not at all on the initial number density (Bockhorn, Fetting, and Heddrich, 1986).

The differences in the final volume fraction among flames are manifested as differences in the final soot particle diameter since the final number densities are similar. As the mean diameter of the soot particles increases with time or height above the burner, the total surface area of the soot particles remains nearly constant. This phenomenon has been observed by Haynes and Wagner (1982), Harris and Weiner (1983a; 1983b; 1984) and Ramer et al. (1986). Apparently, a balance exists between surface growth and coagulation that keeps the surface area constant. Harris and Weiner (1983b) found that the total surface area of the particles increases substantially with C/O ratio (and thus f_v) in their ethylene flames.

2.3 Coagulation

Evidence for the coagulation of soot particles can be seen when soot collected from a flame is examined with an electron microscope. The soot produced in flames consists of spheroidal particles, so-called "elementary" soot particles, which range in diameter from 10 to 50 nm and are clustered in chainlike or branched chainlike agglomerates (Haynes and Wagner, 1981). Wersborg, Howard, and Williams (1973) collected soot from a 20-torr acetylene flame at a sequence of heights above their burner to observe the soot with an electron microscope. Particles in the early stages of formation were small and spheroidal; the smallest observed size was 1.5 nm. The particles grew, while remaining spheroidal, with increasing height until the later stages of soot formation where the particles began to form chainlike agglomerates. They observed coagulated particles at each burner height. Examination with a high-resolution electron microscope showed

that the larger spheroidal particles in the chainlike agglomerates were themselves formed from agglomerated particles. They hypothesized that the particles remained spheroidal during the early stages because surface growth rapidly obscured the chainlike structure, while the chainlike structure was not obscured in the later stages because of the larger particles and slower surface growth rate.

An alternate mechanism proposed by Haynes and Wagner (1981) suggests that the particles in the early stages of formation coalesce upon collision to form single spheroidal particles rather than chains of particles. Graham (1977) suggested that the early particles are composed of liquid-phase PAHs which slowly turn into soot in the flame. Prado et al. (1981) proposed that the early particles are highly reactive and rearrange after collision to form a sphere, while older and larger particles do not coalesce because either their viscosity has increased through dehydrogenation or the larger mass requires more time to coalesce. When the volume fraction was small ($f_v < 10^{-7}$), and thus the particle size was small ($d < 18$ nm), they did not observe agglomerated particles and thus they assumed that only coalescent collisions occurred under these conditions.

The evolution of the number density and the size distribution of the soot particles can be modelled with free molecular coagulation theory. If the soot particles are small compared to the mean free path and coalesce upon every collision to form spherical particles, the change in number density is given by

$$\frac{dN_p}{dt} = -\frac{6}{5} \cdot k_{th} \cdot f_v^{1/6} \cdot N_p^{11/6} \quad (2.2)$$

where the coagulation rate coefficient, k_{th} ($\text{cm}^{5/2} \cdot \text{sec}^{-1}$), is given by

$$k_{th} = \frac{5}{12} \cdot \left(\frac{3}{4\pi}\right)^{1/6} \cdot \left(\frac{6k_b T}{\rho_s}\right)^{1/2} \cdot G \cdot \alpha \quad (2.3)$$

and k_b is the Boltzmann constant (1.3804×10^{-23} J·K⁻¹), T is the temperature (K), ρ_s is the density of soot ($\text{gm} \cdot \text{cm}^{-3}$), G is an enhancement factor that accounts for the dispersion

forces between particles, and α is a collision integral which depends on the particle size distribution (Graham, Homer, and Rosenfeld, 1975; Prado and Lahaye, 1981; Bockhorn et al., 1984).

If Eq. (2.2) is integrated and then evaluated at long residence times for a large initial particle number density, the number density is given by (Prado et al., 1981)

$$N_p = (k_n \cdot f_V^{1/6} \cdot t)^{-6/5} \quad . \quad (2.4)$$

Thus, the model predicts that at long times the number density depends only weakly on the volume fraction and temperature and does not depend at all on the initial number density. This has been verified by the similarity of the final number densities measured in flames by Haynes and Wagner (1982) and Prado et al. (1981).

Several studies have determined that the free molecular coagulation model fits their measured number density profiles, if the coagulation rate coefficients are greater than the theoretical rate coefficient for a hard sphere, i.e., if the enhancement factor, G , is greater than one. The enhancement factor was determined to be in the range $1.5 \leq G \leq 2.5$ by Bockhorn et al. (1982), $0.6 \leq G \leq 5$ by Baumgartner et al. (1984), and $G = 2$ by Prado et al. (1981). Harris and Kennedy (1988) calculated the enhancement factor, G , based on the van der Waals forces between the particles. They determined that collisions between small particles (1 to 15 nm) of the same size were enhanced by a factor of 2.2 to 2.4, while collisions between particles of different sizes (for example, between a 15 nm particle and a 1 nm particle) were enhanced by a factor of 1.2. An average enhancement factor of $G = 2.2$ fit their measured number density profiles in an atmospheric sooting ethylene flame.

The coagulation model does not fit measured number density profiles well in the later regions of the flames owing to the formation of agglomerated particle chains. Both the size and shape of the agglomerated particles would invalidate the free molecular coagulation assumption of spherical particles that are small with respect to the mean free

path (Prado et al., 1981; Harris and Kennedy, 1988). Uncertainties in the optical measurements of number density, in the temperature measurements, and in the calculation of residence times all contribute to the uncertainty in the measured values of the enhancement factor and may account for the different values determined by the different investigators (Bockhorn et al., 1982).

Coagulation of the particles affects the particle size distribution. Since laser scattering-extinction methods measure moments of the particle size distribution, knowledge of these moments is necessary to interpret the measurements and thus determine the number density (Harris, Weiner, and Ashcraft, 1986; Dobbins and Mulholland, 1984; Hodges and Foster, 1987). Numerical (Graham and Robinson, 1976) and analytical (Frenklach, 1985) solutions of Eq.(2.2) predict that the size distribution will asymptotically approach a self-preserving size distribution (SPSD) in which the distribution of particle sizes about the instantaneous mean size is constant. However, Eq.(2.2) is based on the assumption that there is no source of particles or creation of mass within the particle system. In sooting flames, particle inception violates the first assumption and surface growth violates the second assumption. Models incorporating both particle inception and surface growth along with coagulation have been solved numerically for conditions that simulate premixed sooting flames. Both Dobbins and Mulholland (1984) and Megaridis and Dobbins (1989) found that the moment ratios during particle inception exceeded the moment ratios expected for an SPSPD, but after particle inception the ratios began to approach asymptotic values close to those for an SPSPD. Harris and Kennedy (1988) found that the moment ratios approached those of the SPSPD faster when the collisional enhancement caused by van der Waals forces was included. The models show that surface growth reduces the width of the size distribution, while coagulation controls the time dependence of the number density. Hodges and Foster (1987) determined from their model that an SPSPD based on only coagulation is not

likely, because surface growth and coagulation are strongly coupled. They suggest that a two-parameter lognormal distribution be used to describe the particle size distribution instead of an SPSD.

2.4 Surface Growth

While coagulation produces similar final number densities in sooting flames, as predicted by Eq. (2.4), the difference in surface growth rates among sooting flames produces large differences in final soot volume fraction (Haynes and Wagner, 1982). Surface growth occurs through the addition of gas-phase species to the surface of the soot particles. It generates from 90% to 97% of the final soot mass (Bockhorn, Fetting, and Heddrich, 1986; Harris, Weiner, and Ashcraft, 1986). This added mass is reflected in the growth of the soot volume fraction, which can be measured with laser scattering-extinction methods. In premixed flames, the volume fraction grows rapidly following particle inception. With increasing height above the burner, the volume fraction grows more slowly until it asymptotically approaches a final soot volume fraction, f_v^* (Homann and Wagner, 1967; Haynes, Jander, and Wagner, 1980).

Haynes and Wagner (1982) found that f_v^* differed by an order of magnitude among flames of different stoichiometry. However, if they normalized the volume fraction profiles by f_v^* , then the profiles became practically identical. The volume fraction profiles could be empirically described by a pseudo first-order rate equation,

$$\frac{df_v}{dt} = k_{sg} \cdot (f_v^* - f_v) \quad , \quad (2.5)$$

where k_{sg} (sec^{-1}) is a phenomenological rate coefficient for surface growth. The rate coefficient depended on flame temperature but was independent of fuel type, stoichiometry, pressure, and the final soot volume fraction. The temperature sensitivity was found to correspond to an activation energy of 40-50 $\text{kcal}\cdot\text{mole}^{-1}$ by Haynes and Wagner (1982) and 20-35 $\text{kcal}\cdot\text{mole}^{-1}$ by Bockhorn et al. (1984). Different methods of

selecting the flame temperature may account for the different values of the activation energy (Bockhorn et al., 1984). The final volume fraction was found to depend on the fuel type, stoichiometry, pressure, and maximum flame temperature (Haynes and Wagner, 1982; Bockhorn et al., 1984).

The primary growth species has been found to be acetylene (Harris and Weiner, 1983a; 1983b), although diacetylene may contribute up to 10 to 15% of the growth (Harris and Weiner, 1984). Acetylene and methane are the most abundant hydrocarbons found beyond the oxidation zone in fuel-rich flames and they are found in excess of equilibrium (Harris and Weiner, 1983a; Bittner and Howard, 1982). Methane may contribute to surface growth, but not significantly, since its concentration undergoes little depletion in the post-flame zone (Harris and Weiner, 1983a). In the region of the flame where particle inception and surface growth overlap, PAHs may also contribute significantly to surface growth (Harris and Weiner, 1988; Frenklach and Wang, 1990). Lam, Howard, and Longwell (1988) identified tar species as contributing to surface growth in the early stages of soot formation in a jet-stirred/plug-flow reactor. These tar species are large molecules with molecular mass in the range from 200 to 800 amu, similar to large PAHs.

The mass growth of soot by acetylene addition is described by the empirical relationship (Harris and Weiner, 1985)

$$\rho_s \cdot \frac{df_v}{dt} = k(t) \cdot S(t) \cdot [C_2H_2] \quad (2.6)$$

where $k(t)$ ($\text{gm}\cdot\text{cm}^{-2}\cdot\text{sec}^{-1}\cdot\text{molecules}^{-1}$) is the first order rate coefficient for surface growth, $S(t)$ (cm^2) is the surface area of the soot particles, and $[C_2H_2]$ ($\text{molecules}\cdot\text{cm}^{-3}$) is the acetylene concentration. Harris and Weiner (1983a; 1983b) determined from their laser scattering-extinction measurements of soot in ethylene/oxygen/argon flames that the total soot surface area, $S(t)$, remained constant throughout the flame. Coagulation reduced the total surface area, while surface growth increased the total surface area, so that the soot

surface area remained constant and could be set equal to the soot surface area at particle inception, S_0 . The acetylene concentration also remained constant in the post-flame regions of these sooting flames (Harris and Weiner, 1983a; 1983b). The decay of the surface growth rate with time is then caused by a decay of the growth rate coefficient with time. This decay can be accounted for by including an exponential decay term in the first order rate coefficient (Dasch, 1985). When this decay and the constancy of the soot surface area are included, the mass growth rate from Eq.(2.6) can be written as (Harris, 1990)

$$\rho_s \cdot \frac{df_v}{dt} = k_0 \cdot \exp(-t/\tau) \cdot S_0 \cdot [C_2H_2] \quad (2.7)$$

where k_0 ($\text{gm}\cdot\text{cm}^{-2}\cdot\text{sec}^{-1}\cdot\text{molecules}^{-1}$) is the growth rate coefficient at the end of the particle inception zone and τ (sec) is a time constant for the first order exponential decay. Equation (2.7) successfully describes mass growth using very similar values of k_0 for ethylene flames at different stoichiometries and temperatures (Harris and Weiner, 1983b), ethylene/toluene flames (Harris and Weiner, 1984) and methane flames (Ramer et al., 1986). The agreement among the rate coefficients for these different flames suggests that the growth process is similar not only for these flames, but probably for all premixed flames (Harris and Weiner, 1984; Ramer et al., 1986).

Specific surface growth rates ($1/S\cdot df_v/dt$) were observed to be similar for a series of sooting premixed ethylene/oxygen/argon flames (Harris and Weiner, 1983a; 1983b). Thus, the more heavily sooting flames produced more soot because more surface area was available for growth reactions. This dependence of the growth rate on surface area was challenged by Wieschnowsky, Bockhorn, and Fetting (1988) who measured similar surface growth rates in unseeded and seeded flames at the same flame conditions. In the flames seeded with cesium chloride, coagulation was suppressed so that surface growth

could increase the soot surface area to two to three times that of the soot in the unseeded flames. The similarity of the surface growth rates in the unseeded and seeded flames implied that the rates could not depend directly on the particle surface area.

Harris (1990) and Woods and Haynes (1991) have proposed that surface growth instead depends on the number of active surface sites for the addition reactions. The mass growth of the particles can then be expressed as

$$\rho_s \cdot \frac{df_v}{dt} = k_{as} \cdot N_{as}(t) \cdot [C_2H_2] \quad (2.8)$$

where k_{as} ($\text{gm}\cdot\text{sec}^{-1}\cdot\text{molecules}^{-1}$) is a rate coefficient per active site for acetylene addition and $N_{as}(t)$ is the number of active sites as a function of time. The decline in the surface growth rate is then modelled as an exponential decay in the number of active sites by

$$N_{as}(t) = N_{as}^0 \cdot \exp(-t/\tau) \quad (2.9)$$

where N_{as}^0 is the number of active sites leaving the inception zone (Harris, 1990). Woods and Haynes (1991) have developed a similar expression.

The active sites are thought to be mobile on the particle surface and regenerated by the surface growth process, since their number is not affected by coagulation and surface growth (Harris, 1990; Woods and Haynes, 1991). Harris (1990) proposed that the active sites are edges or defects in the graphite-like structure of the particle that are lost through a temperature-dependent annealing process. Thus, growth stops at long times because the reactivity of the particle declines. Comparing Eqs. (2.6) and (2.7) with Eqs. (2.8) and (2.9) and considering the similarity of k_0 amongst premixed flames, Harris (1990) concluded that the number of active sites per unit surface area (N_{as}^0/S^0) leaving the particle inception zone was the same for all flames.

The empirical equations for surface growth, Eqs. (2.7) and (2.8), can be written in the form of Eq. (2.5) (Dasch, 1985), i.e.,

$$\frac{df_v}{dt} = \frac{1}{\tau} \cdot (f_v^* - f_v) \quad (2.10)$$

where the time constant is related to the phenomenological rate coefficient by $k_{sg} = 1/\tau$. Expressions for the final volume fraction in terms of the initial surface area or the initial number of active sites can be determined by integrating Eq. (2.7) to give (Dasch, 1985)

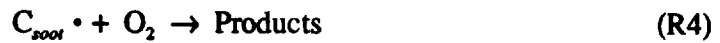
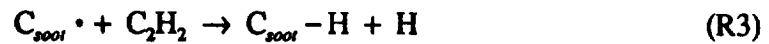
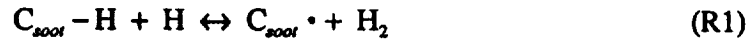
$$f_v^* = f_v^0 + k_0 \cdot [C_2H_2] \cdot S^0 \cdot \tau \cdot \rho_s^{-1} \quad (2.11a)$$

or by integrating Eqs. (2.8) and (2.9) to give (Harris, 1990)

$$f_v^* = f_v^0 + k_{ac} \cdot [C_2H_2] \cdot N_{ac}^0 \cdot \tau \cdot \rho_s^{-1} \quad (2.11b)$$

where f_v^0 is the volume fraction leaving the inception zone. Since the initial volume fraction is small, the final volume fraction of soot produced depends on the number of active sites (or the surface area) leaving the inception zone.

Frenklach and Wang (1990) have developed a detailed kinetic model for surface growth that is described by the following reactions:



where $C_{soot}-H$ represents an armchair site on the surface of the soot (Fig 2.2a) and $C_{soot} \cdot$ is a radical site on the surface of the soot (Fig. 2.2b). In this model, the radical sites are activated by a reaction with hydrogen atoms at the soot surface and thus the number of radical sites depends on the hydrogen atom concentration. Acetylene adds to the soot surface at a radical site. Oxidation of the soot proceeds by reaction of O_2 with a radical or OH with an armchair site. Their numerical simulations of premixed sooting flames

showed that the decline in surface growth rate was caused by a decline in hydrogen atom concentration. The rate of surface growth was found to be similar to that of Harris and Weiner (1983b). Also, they found that the rate of oxidation of the soot by O_2 and OH was not significant in the post-flame zone.

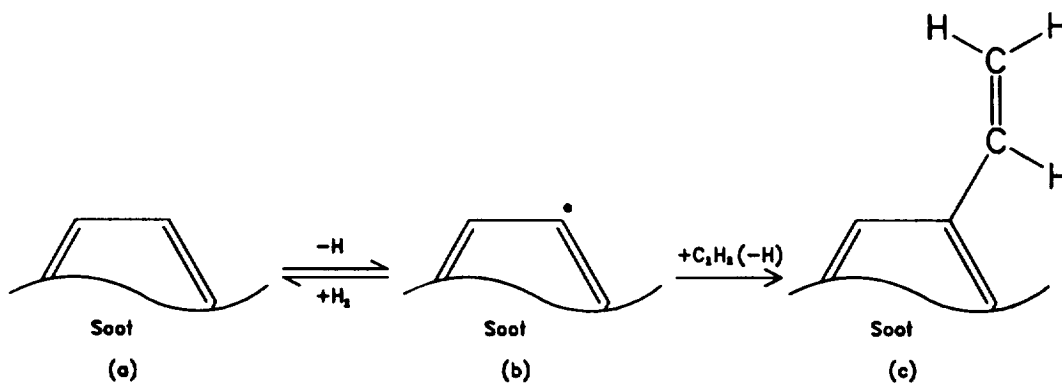


Figure 2.2 Detailed kinetic mechanism for surface growth. Armchair site (a) on the surface of the soot particle reacts with hydrogen atom to generate a radical site (b). Acetylene reacts with the radical site to add to the soot particle (c). (Frenklach and Wang, 1990)

The detailed kinetic mechanism for surface growth is similar to a model for the growth of PAHs discussed in Sec. 2.5.2. Surface growth by addition of acetylene to radical sites on the surface of soot is supported by Howard (1990). He investigated the reaction kinetics of acetylene addition to PAHs and to carbonaceous solids at radical sites and determined that the predicted reaction rate coefficients agreed with experimentally observed rates of growth.

The surface growth of soot can be successfully described by the addition of carbon to radical sites with either the detailed kinetic mechanism (R1-R5) or by the above empirical expressions (Eq. 2.6 or Eq. 2.8). The exact cause of the decay in surface growth

rate is still in question. Harris (1990) suggests that the reactivity declines because of temperature dependent annealing and not because of gas-phase chemistry. Frenklach and Wang (1990) suggest that the reactivity declines because of the gas-phase chemistry, specifically because of a decline in the hydrogen atom concentration. In either case, the study of surface growth suggests that it is the number of particles formed in the inception zone which determines the final volume fraction of soot formed.

2.5 Particle Inception

Our understanding of coagulation and surface growth points to the particle inception stage as being the determining factor in the amount of soot generated in premixed flames. Particle inception is a molecular growth process that starts from the fuel molecules and leads to the first particles observed in the flame. Although much research has been devoted to the study of particle inception, the process is still not clearly understood. Progress in understanding the process has been made through a combination of measurement and modelling. Measurement is complicated by the number of species involved in the growth process and also by the difficulty in measuring the important radicals associated with the growth process. Modelling is also complicated by the number of species, but also by the uncertainties in the thermochemical properties of the species and in the kinetic rates of the controlling elementary reactions. As a result, the understanding of particle inception has been advanced not only by studies in premixed flames, but also by studies in shock tubes where the chemical kinetics can be studied in a simpler environment and specific reactions can be isolated.

The current understanding of particle inception can be modelled as occurring in three steps (Frenklach and Wang, 1990). The first stage is the pyrolysis of the fuel molecules and the subsequent reactions to form single-ring aromatic species (for example, benzene and phenyl radical). The second stage is the formation of larger polycyclic aromatic hydrocarbons from the single-ring aromatics through addition

reactions. These larger PAHs may then coagulate to form a particle in the third stage. Coagulation and growth of the PAHs may proceed simultaneously. These stages in particle inception - aromatic inception, growth, and coagulation - are similar to the soot particle processes - particle inception, surface growth, and coagulation. The three particle-inception steps are discussed in reverse order beginning with coagulation of PAHs, followed by the growth of PAHs and finally the formation of single-ring aromatics. We then discuss the role of the H_2-O_2 system radicals in these processes.

2.5.1 PAH Coagulation

Formation of soot particles by the coagulation of large molecular weight species has been proposed by Harris and Weiner (1988). Their qualitative model of particle inception considered three size classes of high molecular weight molecules: class A molecules with a size on the order of 1000 amu, class B molecules with sizes ranging from 500 to 1000 amu, and class C molecules with a size less than 500 amu. These three classes of molecules form in the oxidation zone of the flame through formation and then growth of the aromatic species. Incipient soot particles are formed from the collisions of class A molecules which have high sticking coefficients. Incipient soot particles are defined to have a size of approximately 2000 amu, corresponding to a 1.5 nm diameter particle. This is the size of the smallest particle observed by Wersborg, Howard, and Williams (1973). Class B and C molecules do not stick upon collision because their sticking coefficients are too small. In the oxidation zone, these molecules are either oxidized or continue to grow through addition reactions.

Particle inception ceases when the class A molecules are depleted which coincides with the drop in O_2 concentration. Growth rates of the class B molecules are not high enough to produce more class A molecules. Instead, they are consumed by coagulation with the incipient soot particles and contribute to the rapid initial growth of the particles.

Particle surface growth by acetylene addition dominates once the class B molecules are consumed. The smaller class C molecules persist into the post-inception zone and may either grow through addition reactions or coagulate with the soot.

This model of particle inception is supported by experimental observations of higher molecular weight species and PAHs in flames. Absorption measurements by Weiner and Harris (1989) in a premixed sooting ethylene flame show that the absorption at 900 nm and 800 nm peaks in the oxidation zone and then declines rapidly within the inception zone. They attributed absorption at these wavelengths to molecules of the class B size. Absorption at shorter wavelengths, corresponding to absorption by smaller molecules, persisted into the post-inception zone. This supports the hypothesis that Class B molecules are depleted, while class C molecules are not.

Measurements of higher molecular weight species with a mass spectrometer also support this hypothesis. Bittner and Howard (1981) measured the rate of formation of higher molecular weight material in both a benzene and an acetylene flame. They measured species as a group with $MW > 700$ in benzene flames and $MW > 1000$ in acetylene flames. In both benzene and acetylene flames, the high MW species peaked as the PAH concentrations experienced a rapid decline. As Bittner and Howard (1981) increased the equivalence ratio past the sooting point, the peak concentration of the high MW material increased by 100. They found that the concentration peaks for benzene and the high MW material were very sensitive to changes in equivalence ratio. Bockhorn, Fetting, and Wenz (1983) also noticed that the concentration of the larger aromatics increased significantly as the equivalence ratio was increased.

More evidence to support this model of incipient soot formation by PAH coagulation comes from the structure of soot particles. The elementary spheroidal particles in the chainlike agglomerates are formed from about 10^4 benzenoid arrays, sometimes referred to as crystallites, randomly oriented in spherical annuli around a

center. These benzenoid arrays have a characteristic dimension of ~ 2 nm and contain on the order of 100 carbon atoms arranged in 5 to 10 layer planes with a structure similar to the layer planes of graphite (Palmer and Cullis, 1965; Haynes and Wagner, 1981; Ebert, Scanlon, and Clausen, 1988). The model of soot as a collection of stacked benzenoid arrays, essentially large polynuclear aromatic hydrocarbons, is supported by its X-ray diffraction patterns (Ebert, Scanlon, and Clausen, 1988).

Frenklach and Wang (1990) included coagulation of PAHs in their detailed kinetic model of soot formation. They assumed a sticking coefficient of unity for PAH collisions. Their numerical simulations of premixed sooting flames showed that the incipient particles were formed by coagulation of PAHs, but the average size of the PAH was only 20 to 50 carbon atoms (~ 240-600 amu). Miller (1990) calculated dimerization rate coefficients for PAHs and determined that coagulation rates of PAHs in flames became significant when the PAH molecules exceeded ~ 800 amu. In his global soot formation model, McKinnon (1989) considered the coagulation of PAHs as the collision between a PAH molecule and an aryl radical (a PAH radical formed by abstraction of a hydrogen atom). He used a sticking coefficient in the range of 0.2 to 0.4 to fit his measured profiles of PAH concentrations and soot.

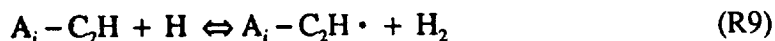
Thus, modelling and measurements of sooting flames supports PAH coagulation as the mechanism for formation of incipient particles. However, the size of the PAH necessary for coagulation and the sticking coefficient remain uncertain.

2.5.2 PAH Growth

The high molecular weight PAHs in sooting flames are thought to be formed from smaller PAHs by the sequential addition of aromatic rings. Frenklach et al. (1986) have proposed that the mechanism for the addition of aromatic rings proceeds through a

sequence of hydrogen abstractions from the aromatic, addition of acetylene, and then ring closure. Bittner and Howard (1981) and Bockhorn, Fetting, and Wenz (1983) have also proposed similar ring growth mechanisms through the addition of acetylene.

The general steps in the mechanism proposed by Frenklach et al. (1986) are given by the following set of reactions:



where A_i represents an aromatic species with i fused rings and $A_i \cdot$ represents the corresponding aryl radical. The steps in this mechanism are shown in Figure 2.3. The reaction of atomic hydrogen with the aromatic species removes a hydrogen atom to create an aryl radical. Acetylene adds to the aryl radical to form an ethynyl substituted aromatic species. A second hydrogen abstraction by atomic hydrogen creates an ethynyl substituted aryl radical which subsequently adds a second acetylene molecule. The two ethynyl groups close to form an aryl radical with an additional aromatic ring. Other routes to add aromatic rings or five-membered rings have a similar mechanism and depend on the structure of the aryl radical. Howard (1990) notes that hydrogen abstraction can also occur by reaction with atomic oxygen and the OH radical, but that their contributions can be scaled to that of atomic hydrogen by partial equilibrium.

Stein and Fahr (1985) identified the most stable isomers of the possible PAH species at 1500 to 3000 K based on their thermodynamic equilibrium with acetylene and hydrogen. Under these conditions, condensed PAH structures were favored

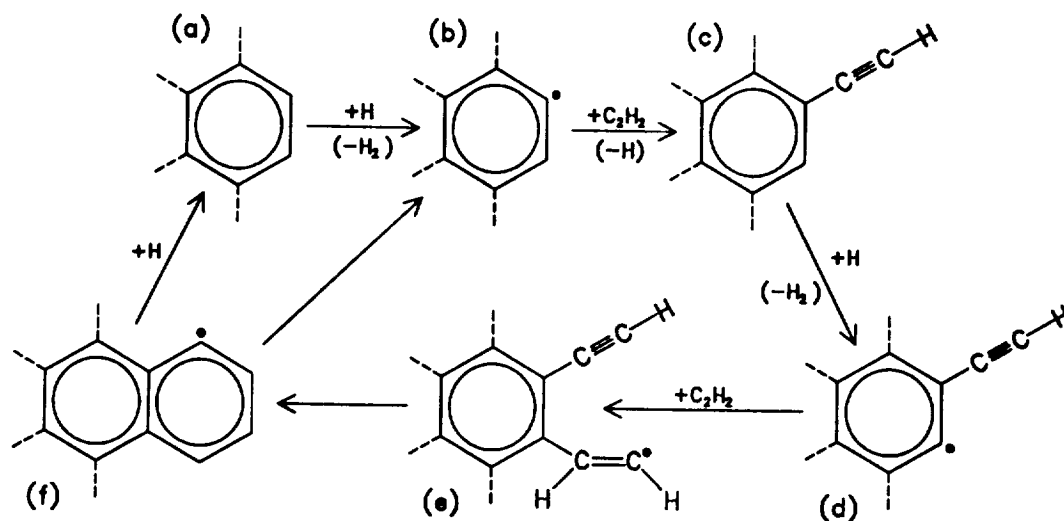


Figure 2.3 Detailed kinetic mechanism for PAH growth. Hydrogen abstraction from the initial PAH (a) generates an aryl radical (b). Acetylene reacts with the radical to add to the PAH (c). A second hydrogen abstraction creates the new aryl radical (d). A second acetylene molecule reacts with the radical site to add to the PAH (e). The two acetylenes cyclize to form an aryl radical with an added ring (f). (Frenklach et al., 1984).

thermodynamically; moreover, their thermodynamic stability increased with the size of the PAH. Thus, the formation of aromatics with an increasing number of rings proceeds through these thermodynamically favored PAHs. The increasing thermodynamic stability of the larger PAHs makes their formation by reaction (R11) practically irreversible and thus tends to displace the chain of reversible reactions (R6-R10) towards irreversible formation of larger PAHs (Frenklach et al., 1986).

Observations of PAH concentrations in sooting flames by McKinnon (1989), Bittner and Howard (1981), and Bockhorn, Fetting, and Wenz (1983) show similar trends in PAH formation. The most abundant PAH species measured in flames appear to be the stable isomers predicted by Stein and Fahr (1985). In particular, preference is given to

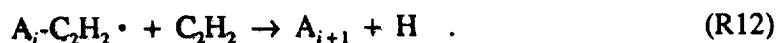
the formation of substituted PAHs. However, PAHs with a lower H content were preferentially formed for compounds with the same carbon number. Substituted PAH mole fractions were about 100 times lower than those for unsubstituted PAHs. McKinnon (1989) observed that measured PAH species with five-membered rings and the existence of ethynyl substituted naphthalene and acenaphthalene are consistent with the acetylene addition mechanism.

Measurements of PAH concentration profiles show that one to four-ring PAHs form rapidly in the oxidation zone and reach their maximum concentration at the end of the oxidation zone before the region of soot formation (Bittner and Howard, 1981; Delfau and Vovelle, 1984). In comparison, the concentrations of larger PAHs decline sharply at the end of the oxidation zone and then approach a steady-state value or increase slowly in the burned gases (Bockhorn, Fetting, and Wenz, 1983). The largest PAHs such as coronene do not show a peak, but instead increase rapidly within the oxidation zone and then more slowly in the burned gases (Bockhorn, Fetting, and Wenz, 1983; D'Alessio et al., 1972). Benzene flames have peak PAH concentrations that are 1 to 2 orders of magnitude larger than that in aliphatic flames (Homann and Wagner, 1967; Bockhorn, Fetting, and Wenz, 1983). The eventual decline in PAH concentration is also much larger in benzene flames than in aliphatic flames.

Frenklach (1988) evaluated the factors that affect PAH growth with a lumped kinetic model of a simplified version of the PAH growth mechanism (R6-R11). The three reaction growth model consisted of reversible reaction (R6) and a reversible reaction similar to (R8),



and the irreversible reaction,



The irreversibility of reaction (R12) allows a lumped kinetic model to be applied to model the growth of A_i up to an infinite size. Based on this model, Frenklach (1988) developed a simple analytic expression relating the reaction rate coefficients, the species concentrations, $[H]$, $[H_2]$, $[C_2H_2]$, and the lumped species concentrations, $\sum_i [A_i \cdot]$, $\sum_i [A_i - C_2H_2 \cdot]$, and $\sum_i [A_i]$. Frenklach (1988) determined that the rate of the initial PAH formation (one or two-ring aromatics) controlled the total PAH concentration, $\sum_i [A_i]$, and the rate of PAH growth. The PAH growth was controlled by the superequilibrium of H atoms at high temperatures. PAH growth at low temperatures in the presence of low concentrations of H_2 was proportional to the rate of hydrogen abstraction (R6), while at high concentrations of H_2 the growth rate was limited by the thermodynamics of hydrogen abstraction and the rate of acetylene addition.

Mechanisms for the destruction or size reduction of large PAHs by oxidation and pyrolysis are not well understood and have not been measured. Frenklach et al. (1986) found that oxidation reactions were needed to properly fit measured soot yields in a shock tube. Their modelling showed that the oxidation of aromatic radicals by O_2 was significant, while abstraction reactions and oxidation reactions by OH radicals and O atoms were not. McKinnon and Howard (1990) suggest that oxidation of PAHs can occur by radical recombination of an aryl radical and an OH radical. Howard (1990) analyzed destruction rates of PAHs in a sooting benzene flame and estimated that the OH reaction efficiency was 0.15 to 0.20 carbon atoms removed per collision of a PAH and an OH radical. McKinnon and Howard (1990) note that the O_2 concentration is much greater than the OH concentration in the early regions of the flame and thus oxidation by O_2 will be dominant even though its reaction efficiency is much less than that for OH radical oxidation. McKinnon (1989) concludes that the pyrolysis of the large PAHs at high temperatures (1800 to 2000 K) must also occur to account for PAH destruction in his

sooting benzene flames. He modelled the unimolecular pyrolysis reaction as the loss of two carbon atoms from the PAH, which is essentially the reverse of the acetylene addition mechanism.

A related issue to the role of PAH growth in particle inception is the formation of fullerenes (closed spherical carbon clusters with a geodesic structure) and their possible role in soot formation. Following the initial discovery by Kroto et al. (1985) of C_{60} and the identification of the truncated icosahedron as its structure, the same research group (Zhang et al., 1986) proposed that C_{60} and other spheroidal carbon clusters might grow through addition of carbon to form successive shells around the initial cluster and thus grow into the spheroidal soot particles observed in flames. Frenklach and Ebert (1988) rebutted this proposal on the basis that the kinetics and thermodynamics of PAH growth did not favor a route through growth of the spheroidal carbon clusters. However, fullerenes are now manufactured by passing high electric currents through graphite rods in a vacuum to generate a soot from which fullerenes are extracted (Huffman, 1991). Fullerenes have also been observed to form with soot in premixed benzene/oxygen/argon flames by Howard et al. (1991). They measured the yields of two fullerenes, C_{60} and C_{70} , in the soot extracted from the premixed benzene/oxygen/argon flames at different pressures and flame temperatures. The fullerene yields increased with increasing temperature and decreasing pressure, both factors which tend to decrease soot yields. In addition, fullerenes were detected in nonsooting flames. These observations led Howard et al. (1991) to conclude that the mechanism for fullerene formation may be substantially different from that for soot formation.

The modelling of PAH growth and the measurement of PAH concentrations in premixed flames suggest that PAHs grow through a series of increasingly thermodynamically stable, condensed PAHs by a sequence of hydrogen abstraction, acetylene addition, and ring closure. The concentration of H atoms has a significant effect

on the growth rate. Both the total concentration of PAHs and their rate of growth depends on the formation rate of the initial one and two-ring aromatics. The details of the mechanism are uncertain because the addition reactions and the oxidation reactions have not been measured for large PAHs and have only been extrapolated from the analogous single-ring aromatic reactions.

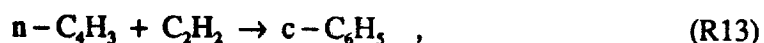
2.5.3 Formation of Aromatic Hydrocarbons

The first step in soot formation is the formation of the initial one-ring aromatic species, which serve as the basis for PAH growth. The formation of the first aromatic rings may be the thermodynamic bottleneck in the formation of soot (Frenklach et al., 1984), and thus it may also be the rate-limiting step. Frenklach (1988) noted that formation of the one and two-ring aromatic species determines the total concentration of the PAHs formed in a flame. Thus, to understand or model soot formation requires an understanding of the mechanisms through which aromatic species are formed in flames, and also an understanding of how they may be destroyed through either oxidation or pyrolysis.

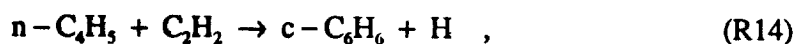
Our understanding of how aromatic species are initially formed is based upon measured species concentrations in flames and the numerical simulation of those flames with an elementary chemical kinetic reaction mechanism. The reaction pathways to form aromatics are identified from the numerical simulation by calculating the fluxes of species through the reactions (reaction pathway analysis) and the sensitivity of the species concentrations to the individual rate coefficients (sensitivity analysis). The identified pathways for the formation or destruction of a species depend on the reactions included in the reaction mechanism. Thus, reaction mechanisms that include different reactions or reaction rate coefficients may identify different pathways for the formation of a species while simulating the same flame conditions.

A number of mechanisms for the formation of benzene from smaller hydrocarbons have been proposed. Westmoreland et al. (1989) identified 18 proposed routes in their survey of the literature. However, they noted that only five studies had made quantitative comparisons between the proposed reaction mechanism and data measured in flames or shock tubes.

Westmoreland et al. (1989) identified the primary reactions that formed benzene in a 20-torr sooting $C_2H_2/O_2/Ar$ flame. The two primary reactions were

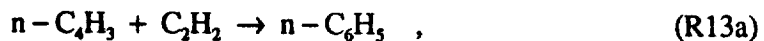


the reaction of 1-buten-3-ynyl (C_4H_3), sometimes called the vinyl acetylene radical, and acetylene (C_2H_2) to form the phenyl radical ($c-C_6H_5$), and



the reaction of 1,3-butadienyl (C_4H_5) with acetylene to form benzene ($c-C_6H_6$) and an H atom.

These two reactions are similar to the overall mechanisms identified as the main routes to form benzene by Harris, Weiner, and Blint (1986) in ethylene flames, Frenklach et al. (1986) and Bastin et al. (1988) in acetylene flames, and by Colket (1986) in the shock tube pyrolysis of acetylene. Reaction (R13) was identified as the main route at high temperatures (> 1000 K), while reaction (R14) was the main route at lower temperatures. However, the reactions, (R13) and (R14), proposed by Westmoreland et al. (1989) proceed directly from the reactants through chemically activated intermediates that react unimolecularly and rapidly to form the cyclized structures. The mechanisms proposed by the other researchers proceed through thermalized intermediates which then subsequently cyclized. For example, the equivalent reactions for reaction (R13) as used by Frenklach et al. (1986) were the formation of linear C_6H_5 ,



followed by the cyclization reaction,

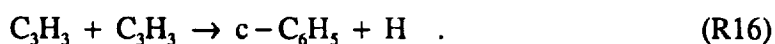


Westmoreland et al. (1989) noted that the other investigators considered their reactions to be in the high-pressure limit and thus they did not properly account for the falloff in their reaction rate coefficients. Frenklach and Wang (1990) subsequently used the rate coefficient data of Westmoreland et al. (1989) in their detailed chemical kinetic modelling of soot formation.

The recombination of propargyl radicals (C_3H_3) may be a more likely route to form benzene than reactions (R13) and (R14). The recombination of propargyl radicals was identified as a likely route by Alkemade and Homann (1989), Wu and Kern (1987), and Kern, Singh, and Wu (1988) to explain the rapid rate of benzene formation in their experimental observations. The recombination of propargyl radicals to form benzene is given by the overall reactions



or



The intermediate steps in these reactions and their rate coefficients are not clearly known and are being investigated by a number of researchers (Miller and Melius, 1992; Thomas, Communal, and Westmoreland, 1991; Kern, Xie, and Chen, 1991; Tsang and Walker, 1991; Pfefferle, Boyle, and Bermudez, 1991). Stein et al. (1990) have proposed that propargyl recombination forms 1,5-hexadiyne (C_6H_6) which then rapidly cyclizes to form 1,2-dimethylene cyclobutene. Benzene and fulvene are then the products of hydrogen migration within 1,2-dimethylene cyclobutene. They found that the product ratio of benzene to fulvene increased with temperature in their flow reactor studies of 1,5-hexadiyne pyrolysis. They also concluded that the reaction was almost irreversible,

because it was highly exothermic ($\Delta H = 100$ kcal). Stein et al. (1990) calculated the formation rate of benzene from the data of Westmoreland et al. (1989) and determined that the propargyl recombination reactions matched the data better than reactions (R12) and (R13). Miller and Melius (1992) identify the recombination reactions of propargyl radical, (R15) and (R16), to be the most likely route for the formation of benzene and phenyl. They note that the route through $n\text{-C}_4\text{H}_3$ (R13) is less likely, because its isomer, $i\text{-C}_4\text{H}_3$, is more stable and thus the concentration of $n\text{-C}_4\text{H}_3$ will be too small to account for the observed formation of benzene.

The mechanisms for the oxidation and pyrolysis of benzene are almost as uncertain as those for its formation and are still being investigated. Brezinsky (1986) reviewed the general mechanism for oxidation of aromatic hydrocarbons and identified the general pathways for benzene and phenyl destruction. Bittker (1991) and Chevalier and Warnatz (1991) have developed detailed mechanisms for the oxidation of benzene. Bittker (1991) found qualitative agreement between his predictions and shock tube ignition delay data, but quantitative agreement over the full range of conditions would require further knowledge of the important reactions in the mechanism. Chevalier and Warnatz (1991) identified the reactions of phenyl with oxygen and the reaction of benzene with O atoms as needing further study to improve their mechanism.

Vaughn, Howard, and Longwell (1991) identified the main pathway for benzene destruction in their jet-stirred reactor as hydrogen abstraction by H atoms and OH radicals to form phenyl, i.e.,



and



The phenyl radical may then be destroyed through reactions with oxygen or the OH radical to form phenoxy radical (Bittker, 1991; Chevalier and Warnatz, 1991; Miller and Melius, 1991), i.e.,



Phenoxy may then decompose to form cyclopentadienyl and carbon monoxide, i.e.,



The further decomposition of cyclopentadienyl (C_5H_5) is not well understood, but it may react with either an O atom or an OH radical through a radical-radical reaction, giving the possible end products, C_4H_3 and CO (Brezinsky, 1986). At high temperatures, phenyl may decompose unimolecularly to form 1-buten-3-ynyl and acetylene,



which is the reverse of reaction (R13) for the formation of phenyl.

The amount of benzene (or phenyl) formed depends on the difference between the formation rate and the oxidation and pyrolysis rates. The benzene formation rate depends on the concentrations of the molecular intermediates material to its formation. The concentration of these molecular intermediates, C_2H_2 , C_4H_3 , C_4H_5 , and C_3H_3 , in reactions (R13) to (R16) will depend on the initial fuel structure and also on the local temperature and species concentrations. As for the formation of benzene, the hypothetical reaction pathways that form these intermediates will depend strongly on the reaction mechanism used to simulate the flame structure.

The comprehensive reaction mechanisms developed to model the formation of aromatics for the rich combustion of ethylene and acetylene are described in Section 2.6. Flame simulations with these mechanisms suggest that in the pre-flame zone, the primary

reaction is the reaction of the fuel molecule with a hydrogen atom, which has diffused from the main reaction zone. In an acetylene flame, the reaction of acetylene with H atom creates the vinyl radical (Frenklach and Warnatz, 1987),



In an ethylene flame, hydrogen abstraction from ethylene creates the vinyl radical (Harris et al., 1986),



which can also occur by reaction with the OH radical,



Reaction of the vinyl radical with acetylene by



forms the butadienyl radical, the intermediate to aromatic formation at low temperatures (Frenklach and Warnatz, 1987).

The vinyl radical may be oxidized by reaction with oxygen to decompose into formaldehyde and the formyl radical,



The products of this reaction decompose further to form the major combustion products, CO and CO₂, and are also the major source of H atoms (Frenklach and Warnatz, 1987; Harris et al., 1986). The formation of the primary radicals in the main reaction zone occur through the two reactions (Frenklach and Warnatz, 1987),



and



The reaction of acetylene with either an OH radical or an H atom forms the ethynyl radical,



which can then react with acetylene,



to form 1-buten-3-ynyl, which is the intermediate to aromatic formation at high temperatures (Frenklach and Warnatz, 1987; Harris et al., 1986).

Miller et al. (1990) and Miller and Melius (1991; 1992) note that the dominant mechanism for the removal of acetylene is by reaction with an O atom through the reactions to form ketyl and H atom,



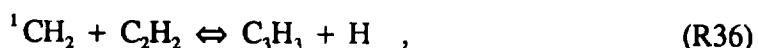
and to form methylene (triplet) and carbon monoxide,



The further reaction of ketyl with hydrogen forms singlet methylene,



Singlet methylene plays a significant role in the formation of higher hydrocarbons through its reaction with acetylene,



to form the propargyl radical, which is the intermediate for the formation of aromatics by the previous alternate route.

The difference between the mechanism of Miller et al. (1990) and the mechanisms of Frenklach and Warnatz (1987) and Harris et al. (1986) illustrates how the mechanism itself can influence the interpretation of species profiles and the possible reaction

pathways. The uncertainties in these mechanisms arise because the elementary reactions associated with the radical intermediates and also their thermochemical properties are still not fully or accurately known. These uncertainties require further investigation both by modelling and by experimental measurement before a complete detailed mechanism of particle inception can be formulated.

2.5.4 Role of the H₂-O₂ System Radicals

The species in the H₂-O₂ reaction mechanism, particularly the radicals H atom, O atom, and OH radical, have significant roles in hydrocarbon combustion. They are also hypothesized to play key roles in the formation of soot. These species are critical in the abstraction reactions that form hydrocarbon radicals for further molecular growth or oxidation. They are also involved in the oxidation reactions competing with the growth processes.

The initial reactions of the hydrocarbon fuel in a rich premixed flame are dominated by hydrogen abstraction by the H atom, which has diffused from the main reaction zone into the pre-flame zone (Frenklach and Warnatz, 1987; Harris et al., 1986). The hydrogen abstraction by the H atom is a significant reaction in the creation of hydrocarbon radicals for further growth. Frenklach and Warnatz (1987) find that aromatic ring growth in their model is correlated with the overshoot of equilibrium by H atoms. The overshoot, f , is defined as

$$f = \frac{[H]^2}{[H_2]} \cdot \frac{1}{K_{eq}} \quad (2.13)$$

where K_{eq} is the equilibrium constant for the reaction $H_2 + M \rightleftharpoons H + H + M$. The overshoot in the reaction zone is caused by the generation of H atoms through reactions such as (R29) and from the products of (R27). Aryl radicals are significant in the growth reactions. Their concentration can be related to the H atom concentration through equilibrium of the abstraction reaction $A_1 + H \rightleftharpoons A_1\cdot + H_2$, although OH radicals and O

atoms may also contribute to the aryl radical formation through abstraction reactions (Howard, 1990). The decline in the rate of surface growth is thought to be caused by the drop in H atom concentration in the post-flame gases (Frenklach and Wang, 1990).

Reaction with molecular oxygen is thought to be the major oxidation route for the aromatic species (Frenklach et al., 1986). McKinnon and Howard (1990) note that O₂ is the dominant oxidizer in the early regions of the flame where the O₂ concentration is high, but the OH radical becomes the significant oxidizer in the post-flame region. Harris et al. (1986) note that, in their flames, the concentrations of O atom and OH radical are low and the flame temperatures are low, so that O₂ and HO₂ are more important oxidizers. Molecular oxygen may also enhance soot formation. Harris (1986) noted that particle inception stopped when the O₂ concentration dropped below 1% and suggested that O₂ may be important in forming species leading to soot formation. In particular, the O₂ concentration strongly influences hydrogen superequilibrium. Hura and Glassman (1987) found that oxygen addition to ethylene in the fuel side of a counterflow diffusion flame increased the formation of soot by increasing the radical pool. Frenklach et al. (1986) found in their shock tube studies of acetylene oxidation that oxygen addition resulted in rapid generation of H atoms, thus increasing the hydrogen superequilibrium and molecular growth reactions.

The OH radical is involved in both abstraction and oxidation reactions, although these reactions tend to occur later in the flame than those with H atoms and O₂, because the OH concentration peaks later (McKinnon and Howard, 1990). The OH concentration profiles decline in the region of particle inception. Measurements of the OH concentration by Millikan (1962) and by Lucht, Sweeney, and Laurendeau (1985) show that the OH concentration peaks near the end of the oxidation zone and then declines to its equilibrium value before the visible emission of soot. Comparison of OH profiles in nonsooting and sooting flames showed that the peak OH concentration decreased as the

equivalence ratio increased, but no significant change in the profile shape occurred in the transition from a nonsooting to sooting flame. Millikan (1962) proposed that soot precursors were oxidized by the OH radical in regions where its concentration declined and soot formed only when the OH radical had reached its equilibrium level.

The reaction of acetylene with O atom is the main route for the oxidation of acetylene (Miller et al., 1990). This scavenging reaction reduces the O atom concentration as equivalence ratio is increased in rich flames, because the C_2H_2 concentration increases with increasing equivalence ratio. Removal of O atoms decreases both the OH radical and H atom concentrations as equivalence ratio is increased, owing to the fast equilibrium reached in the H_2-O_2 reactions (Burgess and Langley, 1991). Because of the rapid equilibration among the radicals of the H_2-O_2 system, measurements of a single radical profile may provide a measure of the other radicals in the system.

2.6 Modelling of Soot Formation

Modelling of soot formation may take two approaches. The first approach is to analyze the mechanism of soot formation in detail for simple flow systems. The second approach is to then take that basic understanding and apply it to the prediction of soot formation in more complicated flow systems. Detailed chemical kinetic modelling takes the first approach by modelling the elementary reactions of soot formation and evaluating the model against experiments in simple flow systems. Global modelling takes the second approach by modelling soot formation with global reactions and then using those models, for example, to predict sooting tendencies of fuels or to predict soot formation in complex flow systems. We first discuss detailed chemical kinetic models for soot formation and then the global models.

2.6.1 Chemical Kinetic Modelling of Soot Formation

Since the formation of soot has been hypothesized to begin with the formation of aromatics, the development of detailed chemical kinetic models describing soot formation has been through reaction mechanisms which describe the formation of single-ring aromatic species from the rich combustion of simple fuels such as acetylene and ethylene. Further PAH growth and formation of soot particles can be modelled by a combination of global reactions for growth and oxidation of PAHs and detailed numerical simulations of particle coagulation and surface growth.

Frenklach and Wang (1990) have developed a detailed kinetic model for soot formation in laminar premixed hydrocarbon flames. The basis of their model is a set of 337 elementary reactions with 70 species that described the oxidation and pyrolysis of acetylene, including the formation of aromatic species and the growth of PAHs up to the size of coronene. The acetylene combustion model was developed from an initial study of the shock-tube pyrolysis of acetylene (Frenklach et al., 1984) which was subsequently refined to model the shock-tube oxidation of acetylene (Frenklach et al., 1986) and then adapted to model laminar premixed acetylene flames (Frenklach and Warnatz, 1987). Their approach to developing the mechanism was to begin with a comprehensive set of reactions describing the possible reaction pathways. Thermochemical parameters of the PAH species and some of the hydrocarbon radicals were estimated based on the data of Stein and Fahr (1985). Estimates of the reaction rate coefficients were either based on a known rate from a prototype reaction or based on upper limits from collision theory. The mechanism was then evaluated against the shock-tube or flame measurements. The size of the mechanism was reduced by identifying significant and insignificant reaction pathways through a reaction pathway analysis and a sensitivity analysis.

The full range of soot formation in a flame was modelled in two steps. In the first step, the elementary reaction mechanism was used to obtain profiles of C_2H_2 , H_2 , H , O_2 ,

OH, H₂O, and PAH for input to a global mechanism in which PAH and particle nucleation and growth were modelled. PAH growth was modelled with reactions (R6) to (R11) (Sec. 2.5.2). The PAH were allowed to coagulate with unity sticking coefficients to form soot 'particles'. Surface growth of the particles was modelled with reactions (R1) to (R5) (Sec. 2.4). The method of moments was used to model particle nucleation, surface growth, and coagulation.

The model used by Frenklach and Warnatz (1987), which modelled the formation of large PAHs, but not the further steps of soot formation, predicted the general shape and relative concentrations of the measured species profiles, but could not reproduce correctly the decline in aromatic concentrations. They suggested that further data on the oxidation reactions of the aromatic hydrocarbons and of the hydrocarbon radicals was needed. Frenklach and Wang (1990) modelled the flame data of Wieschnowsky, Bockhorn, and Fetting (1988) and Harris et al. (1986). They obtained good agreement with the particle profiles, but they predicted a nucleation rate that decayed more slowly than the measured rate. In addition, they were unable to reproduce the H atom profile and the particle profile of Harris et al. (1986) unless they used the measured H, OH, H₂, O₂, H₂O, and C₆H₆ profiles as inputs to their particle formation model.

An alternate approach to that of Frenklach and Wang (1990) has been to develop a more accurate description of the oxidation chemistry in rich combustion and of the reactions leading to the formation of one to two-ring aromatics, but not to model the formation of larger PAHs, since the thermodynamic properties of PAHs can only be estimated and their reaction rates and pathways have not been measured.

Harris, Weiner, and Blint (1988) developed an elementary reaction mechanism for the formation of two-ring aromatic species in sooting ethylene flames. An initial model for rich sooting ethylene flames was assembled based on previous work and then tested against measured species concentrations in a rich nonsooting and a sooting ethylene flame

(Harris et al., 1986). The tested mechanism, which included up to C_4 species, was then expanded to consider the formation of single-ring aromatics by adding appropriate reactions with estimated rate coefficients. This mechanism successfully modelled the measured concentrations of single-ring aromatic species. Their sensitivity analysis showed that the single-ring aromatic concentrations were controlled by the estimated rate coefficient for the reaction $C_4H_3 + C_2H_2 \rightarrow C_6H_5$.

Bastin et al. (1988) refined the general hydrocarbon oxidation mechanism of Warnatz (1984) with the addition of the C_4 species reactions of Frenklach and Warnatz (1987) to predict the formation of benzene in a lightly sooting 20-torr acetylene/oxygen/argon flame. They used a molecular beam mass spectrometer technique to measure stable species profiles in the flames and also those of the radicals, OH, H, C_2H , C_2H_3 , C_4H_3 , and C_4H_5 . Their mechanism agreed well with their measured species concentrations including the radicals. In particular, their predicted benzene profile shape and position agreed with their measured benzene profile.

Miller et al. (1990) adapted their reaction mechanism to describe the rich combustion of acetylene by comparison with measurements in rich, nonsooting 25-torr acetylene/oxygen/argon flames at equivalence ratios of $\phi = 1.03$, $\phi = 1.67$, and $\phi = 2.0$. They measured CH, H, OH, and temperature with laser-induced fluorescence and stable species with a quartz microprobe. They found good agreement between their predictions and measurements for the $\phi = 1.03$ and $\phi = 1.67$ flames. For the $\phi = 2.0$ flame, they found good agreement with the CH and OH profiles, but poor agreement with the stable species profiles, possibly because the flame may have attached to the probe. They identified the reactions of singlet methylene (1CH_2) as important in the destruction of acetylene and the formation of the propargyl radical (C_3H_3). The thermochemical properties of the ethynyl radical (C_2H) also had a strong influence on hydrogen abstraction from acetylene by OH

radical and H atom. Miller and Melius (1992) updated this model to include the formation of benzene and phenyl. They found good agreement between the predictions of their model and the data of Bastin et al. (1988).

McKinnon (1989) developed a numerical model to describe the nucleation phase of soot formation in a laminar premixed flame. His model begins with already formed aromatic species and so it does not model the formation of one-ring aromatics. Four basic processes in the formation of soot were modelled based on prototype reactions for a single-ring aromatic. Mass growth of soot or PAH was modelled as acetylene addition to an aryl radical site by using the rate of acetylene addition to phenyl radical. Oxidation of soot or PAH was considered as a reaction of an aryl radical with either OH or O₂. The coagulation of PAH was modelled as the reaction between an aryl radical and a PAH. The fourth process was the thermal decomposition of aryl radicals. The pyrolysis rate for phenyl was used for single-ring aromatics, while the rate for larger PAHs was scaled to the size of the PAH. The pyrolysis rate was set to zero for a PAH with a size of 1000 amu or larger, because the pyrolysis of soot had been observed to be almost zero. The concentration of aryl radicals at a point in the flame was determined from the local hydrogen concentration and equilibration of the reaction, $\text{Aryl} + \text{H}_2 \rightleftharpoons \text{PAH} + \text{H}$.

The system of differential equations describing coagulation, growth, oxidation, and pyrolysis were solved numerically using profiles of temperature, C₂H₂, O₂, H₂, H, and OH as inputs. Reaction efficiencies and rate coefficients for the prototype reactions were adjusted to make the model fit measured PAH and soot profiles in sooting benzene flames. Disagreements between the coefficients obtained by fitting the flame profiles were attributed to the possibility that the OH, H, and aryl radical profiles were not correct, because they were inferred from other species measurements. Another possibility was that a significant process had been left out of the mechanism. The results of McKinnon

(1989) are similar to those of Frenklach and Wang (1990) in that all the reaction pathways may not have been described and measured profiles of the OH radical and H atom may be needed to model the formation process.

Review of the detailed mechanisms suggests that while they may be used to predict formation of benzene and perhaps even soot, uncertainties still abound in the mechanisms and in the thermochemical properties and reaction rates of the species in the reaction pathway to benzene. Thus far, the detailed chemical kinetic models have been applied to premixed laminar flat flames for a limited selection of fuels, primarily acetylene and ethylene. Comparisons between predictions and experimental data have been made for a small set of sooting flames. Uncertainties in the both thermochemical properties and reaction rate coefficients limit their application beyond the conditions of the original study. The size of the mechanisms also precludes their use in more complicated flows such as diffusion flames because of computational limitations.

2.6.2 Models for Incipient Soot Formation in Premixed Flames

Global models can be used to model soot formation over a wider range of fuels and conditions and for more complex flows than detailed chemical kinetic models. Global models for incipient soot formation in premixed flames relate the onset of sooting to macroscopic properties of the flame such as the fuel mixture, temperature, and equilibrium OH concentration. Incipient soot formation, the onset of sooting, soot limit, and soot threshold are all synonyms found in the literature that describe the point at which soot is first emitted from a flame. In a premixed flame, this point is described by the fuel/oxidizer ratio at which the yellow emission of soot particles first becomes visible as the ratio is increased from a nonsooting condition. The fuel/oxidizer ratio is specified by either the critical equivalence ratio, ϕ_c , based on the final combustion products, CO_2 and

H₂O, the modified critical equivalence ratio, ψ_c , based on the final combustion products, CO and H₂O, or the critical carbon to oxygen ratio, $(C/O)_c$, which would be based on the final products, CO and H₂.

The global models for incipient soot formation are derived from the initial model proposed by Millikan (1962). His model was based on the observation that soot emission first occurs in a premixed flat ethylene/air flame at a height where the OH concentration has dropped to its equilibrium value. He proposed that pyrolysis of the acetylene formed in the flame produces soot precursors. These precursors are oxidized by the OH radical. Any precursors remaining in the flame when the OH radical concentration drops to its equilibrium value form soot. Thus, the competition between the pyrolysis and oxidation reactions determines whether or not soot is formed. The point of incipient soot formation occurs when the pyrolysis and oxidation reaction rates are balanced.

The global model, in its general form (Figure 2.4), is based on three assumptions: (1) pyrolysis of the fuel forms soot precursors, (2) soot precursors form soot through growth or nucleation, and (3) soot precursors are removed by oxidation. The rate equation describing the formation of precursors for nonsooting flames can be written as

$$\frac{d[\text{Pr}]}{dt} = k_p \cdot [\text{Fu}] - k_{ox} \cdot [\text{Pr}] \cdot [\text{OH}] \quad (2.14)$$

where [Pr] is the precursor concentration, [Fu] is the fuel concentration, [OH] is the hydroxyl concentration, k_p is the rate coefficient for pyrolysis, and k_{ox} is the rate coefficient for oxidation. The rate coefficients are expressed in the Arrhenius form as

$$k_p = A_p \cdot \exp\left[\frac{-E_p}{RT}\right] \quad (2.15)$$

$$k_{ox} = A_{ox} \cdot \exp\left[\frac{-E_{ox}}{RT}\right] \quad (2.16)$$

where A_p and A_{ox} are the pre-exponential factors for pyrolysis and oxidation, E_p and E_{ox} are the activation energies for pyrolysis and oxidation, T is the temperature, and R is the gas constant. At the point of incipient soot formation, the oxidation and pyrolysis rates are balanced and thus the rate of precursor formation is zero. Then combining Eqs. (2.14), (2.15), and (2.16) gives

$$\ln\left(\frac{[Fu]}{[OH]}\right) = \frac{\Delta E}{RT} + \ln\left(\frac{A_{ox}}{A_p} \cdot [Pr]\right) \quad (2.17)$$

where $\Delta E = E_p - E_{ox}$ is the difference between the pyrolysis and activation energies. This is the general form of the equation used to correlate critical equivalence ratios in studies of incipient soot formation.

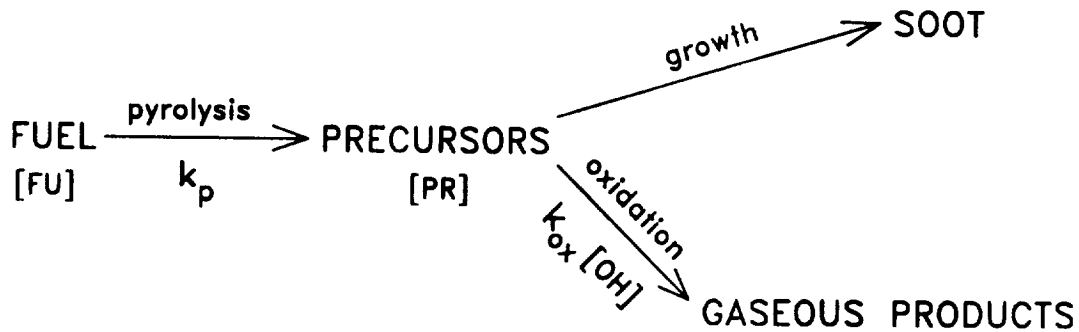


Figure 2.4 Global model for incipient soot formation.

Table 2.1 (adapted and expanded from Janssen and Senser, 1991) summarizes six studies of incipient soot formation. The type of burner and fuels studied are listed along with the assumptions for $[Fu]$, $[OH]$, and $[Pr]$. The correlation equation obtained by each of the studies can be written as

$$\ln \alpha = \frac{\Delta E}{RT} + \ln \beta \quad (2.18)$$

where the form of the coefficients α and β depend on the assumptions for $[Fu]$, $[OH]$, and $[Pr]$, and are listed in Table 2.1.

The six studies successively refined the correlation for incipient soot formation. In the first study, Millikan (1962) measured the OH radical and C_2H_2 concentrations in a series of ethylene/air flames. He assumed that the pyrolysis of acetylene produced precursors; thus $[Fu]$ was set to the measured $[C_2H_2]$. The oxidation reaction was considered to be first order in $[OH]$ at its post-flame equilibrium value.

Takahashi and Glassman (1984) examined incipient sooting behavior of 21 fuels on a Bunsen burner. Their correlation was based on the assumptions that fuel concentration was proportional to the modified equivalence ratio, ψ_c , and that the oxidizer concentration was proportional to the OH equilibrium concentration calculated at the adiabatic flame temperature.

Harris, King, and Laurendeau (1986) examined incipient soot formation for five aliphatic fuels at varying dilution ratios and maximum temperatures. They assumed that the fuel concentration was proportional to the critical equivalence ratio, ϕ_c , and that the oxidizer reaction was first order in both the precursor concentration and the equilibrium OH concentration at the measured maximum flame temperature. They also noted the importance of basing the correlation on the measured maximum temperature rather than the calculated adiabatic flame temperature.

Cummings, Sojka, and Lefebvre (1987) investigated the critical equivalence ratio dependence on pressure in turbulent premixed flames. They used the model of Harris, King, and Laurendeau (1986), but accounted for pressure effects by expressing $[Fu]$, $[Pr]$, and $[OH]_{eq}$ in terms of the mole fraction.

Janssen and Senser (1991) measured incipient soot formation in flames of methane-dichloromethane mixtures. They used the correlation equation in the form used by Cummings, Sojka, and Lefebvre (1987), but noted that the model should be evaluated

Table 2.1 Summary of incipient soot formation studies, including type of burner, fuels studied, assumptions for the model parameters, and the resulting correlation equation coefficients (adapted and expanded from Janssen and Senger, 1991).

Study	Millikan (1962)	Takahashi and Glassman (1984)	Harris, King, and Laurendeau (1986)	Cummings, Sojka, and Lefebvre (1987)	Janssen and Senger (1991)	Janssen (1991)
Burner	Flat	Bunsen	Flat	Turbulent, high-pressure (2-8 atm)	Flat	Flat
Fuels	C_2H_4	21 fuels C_2 - C_6 aliphatics, 1-2 ring aromatics	CH_4 , C_2H_2 , C_2H_4 , C_2H_6 , C_3H_4	CH_4 , C_2H_4 , C_2H_6 , C_3H_6 , $c-C_4H_8$, C_4H_8 , C_4H_{10}	$CH_4/CH_2/Cl_2$ mixtures	CH_4 , C_2H_4 , $CH_4/CH_2/Cl_2$ and $CH_4/CH_2/Br_2$ mixtures
[Fu]	$[C_2H_2]$	$b \cdot \psi_c$	$b \cdot \phi_c$	$b \cdot \phi_c \cdot \frac{P}{RT}$	$b \cdot \phi_c \cdot \frac{P}{RT}$	$b \cdot X_{CO,eq} \cdot \frac{P}{RT}$
[OH]	$[OH]_{aq}$	$a \cdot [OH]_{aq}$	$a \cdot [OH]_{aq}$	$a \cdot X_{OH,eq} \cdot \frac{P}{RT}$	$a \cdot X_{OH,eq} \cdot \frac{P}{RT}$	$a \cdot X_{OH,eq} \cdot \frac{P}{RT}$
[Pt]	N/A	N/A	constant	$X_{Pr} \cdot \frac{P}{RT}$	$X_{Pr} \cdot \frac{P}{RT}$	$X_{Pr} \cdot \frac{P}{RT}$
Temperature	maximum (Na D-line)	adiabatic (calculated)	maximum (Na D-Line)	maximum (sonic suction thermometer)	maximum (thermocouple)	maximum (thermocouple)
α	$\frac{[C_2H_2]}{[OH]}$	$\frac{\psi_c}{[OH]_{aq}}$	$\frac{\phi_c}{[OH]_{aq}}$	$T \cdot \frac{\phi_c}{X_{OH,eq}}$	$T \cdot \frac{\phi_c}{X_{OH,eq}}$	$T \cdot \frac{X_{CO,eq}}{X_{OH,eq}}$
β	$\frac{A_{ox}}{A_f}$	$\frac{a \cdot A_{ox}}{b \cdot A_f}$	$\frac{a \cdot A_{ox}}{b \cdot A_f} \cdot [Pt]$	$\frac{a \cdot A_{ox}}{b \cdot A_f} \cdot \frac{P}{R} \cdot X_{Pr}$	$\frac{a \cdot A_{ox}}{b \cdot A_f} \cdot \frac{P}{R} \cdot X_{Pr}$	$\frac{a \cdot A_{ox}}{b \cdot A_f} \cdot \frac{P}{R} \cdot X_{Pr}$

in terms of the primitive variables, ϕ_c and T , rather than the parametric variables, $\phi_c T / X_{OH,c}$ and $1/T$. The large variation of OH mole fraction relative to ϕ_c and T may give deceptively good correlations when using the parametric variables.

Janssen (1991) further analyzed the global model and noted that previous work did not account for dilution of the precursor concentration. He proposed a more realistic model in which precursor formation depended on the unoxidized carbon present in the post-flame zone. The equilibrium CO concentration was used as a measure of the unoxidized carbon in the post-flame zone because the CO is proportional to the unoxidized carbon and dilution affects the CO and the unoxidized carbon in the same way. This modification of the correlation accounted for the variation in incipient soot formation with fuel structure, but still did not fully account for dilution effects.

These global models for incipient soot formation do not identify the precursor or its nature. The models also do not include a rate of growth from precursor to soot particles that competes with the oxidation rate. The implicit assumption is that the growth rate is slow compared with the oxidation rate and can be neglected (Janssen, 1991). In fact, a negligible growth rate also may imply that the precursors are actually incipient particles, because the model presumes that precursors form soot if they are not destroyed by oxidation.

McKinnon (1989) evaluated a simple model for the critical equivalence ratio by using the assumption that the soot precursors are large PAHs (~ 900 amu). Soot particles are formed by the coagulation of the PAHs, while oxidation of PAHs competes with soot formation by removing mass from the incipient particles. The critical equivalence ratio occurs when the rate of coagulation is balanced by the rate of oxidation. Based on his analysis, he calculated that a critical $[PAH]/[OH]$ ratio would have to be exceeded for soot to form. His model did not include a rate expression for the formation of the PAHs.

The success of these global models in describing incipient soot formation for a variety of fuels and fuel mixtures in spite of the complex chemistry of soot formation suggests that a common mechanism may exist for soot formation. The detailed picture of soot formation suggests that formation of the aromatic ring is the controlling step in soot formation (Glassman, 1988). The further growth and coagulation appear to be similar for all fuels, and depend on the concentrations of acetylene and selected radicals. Thus, the effect of fuel structure on the concentrations of acetylene and the radicals (particularly H atoms) may be portrayed in the global model through a combination of the equivalence ratio or equilibrium CO concentration and the OH equilibrium concentration. The aromatic species are thought to be oxidized primarily by molecular oxygen (Frenklach and Warnatz, 1987), but the OH concentration may also provide a measure for this oxidation rate as the OH and O₂ are linked through fast reactions of the H₂-O₂ system. Further understanding and refinement of these global models are likely to come from a deeper understanding of the detailed models and from measurements in flames near the critical equivalence ratio of the important species profiles, such as those for OH, C₂H₂, and CO (Janssen, 1991).

2.7 Summary

The pathway from hydrocarbon fuel to soot particles in a flame is complicated and still not fully mapped. The stages in the formation of soot are particle inception followed by surface growth and coagulation of the particles. Coagulation of soot particles can be modelled empirically using free molecular coagulation theory, while surface growth can be modelled as acetylene addition to active sites on the particle. These empirical models describe well the measurements of soot particles in flames. However, details of the underlying mechanisms are still not fully understood. In particular, it is not known whether the decline in surface growth rate is caused by a decrease in the number of active sites or by a decline in the H atom concentration in the post-flame region.

Coagulation and surface growth begin as the soot particles are formed and account for almost all of the growth in particle size and volume fraction. However, the final volume fraction is controlled by the number of particles formed in the inception stage, because the surface growth is proportional to the initial number of active sites, which can be represented by the particle surface area. Incipient particles are thought to be about 1.5 nm in diameter with a molecular weight of about 2000 amu. They are hypothesized to form from the coagulation and growth of large PAH molecules. These large PAHs grow from single-ring aromatic species through a sequence of repeated hydrogen abstraction and acetylene addition reactions. The coagulation of the large PAHs may be through free molecular coagulation enhanced by van der Waals forces or by reactions between large aryl radicals. While these mechanisms of PAH growth and coagulation are still unconfirmed, the rate-limiting step in particle inception may be the formation of the single-ring aromatic species. Reaction pathways involving C₂, C₃, and C₄ hydrocarbon radicals have been proposed for the formation of these single-ring aromatic species. The radicals in the H₂-O₂ system play key roles in both the growth and oxidation reactions of the intermediate and aromatic species.

Our understanding of soot formation rests on the development of both empirical and detailed chemical kinetic models and on comparison of these model predictions with measurements of species concentrations and soot in flames. Detailed chemical kinetic mechanisms have been developed to describe the formation of single-ring aromatic species based on the combustion of acetylene and ethylene. The mechanism of Frenklach and Wang (1990) combined a detailed chemical kinetic model with a global model incorporating particle inception, surface growth, and coagulation. McKinnon (1989) developed a global model that described the growth, oxidation, coagulation, and pyrolysis of PAHs in the nucleation stage of soot formation. These models are successful in predicting the general shape and relative concentrations of the species profiles and also

some of the features of the soot profiles for selected flame conditions. When applied to a wider range of flame conditions, these models require either different rate coefficients for some of the reactions or an input of the measured radical profiles. Refinements to these models require further knowledge of thermochemical properties and the reaction rates of the radical species. In addition, measurements of the radical species profiles, particularly the H atom and the OH radical profiles, are required to test some of the hypotheses of these kinetic mechanisms.

The onset of soot formation can be described by simple global models in which the soot precursors are formed by pyrolysis of the fuel and are destroyed by oxidation with the OH radical. The models successfully correlate critical equivalence ratio data for a variety of fuels using such parameters as maximum temperature, equivalence ratio, and equilibrium OH and CO concentrations. Their success suggests that these parameters may be a good indicator of the soot formation process near the critical equivalence ratio. However, the relation between the global models and the detailed mechanisms of soot formation is not obvious because the precursors are not identified and the model parameters do not clearly account for the pyrolysis and oxidation chemistry of soot formation. Further refinement of the global models is likely to come from further understanding of the connection between the detailed mechanism and the global models and from measurements of species profiles near the critical equivalence ratio.

Measurements of radical species profiles and soot formation in nonsooting and sooting flames at conditions near the critical equivalence ratio can provide data for the evaluation of global and detailed chemical kinetic models. Measurements of OH radical profiles in sequences of flames that span the transition from nonsooting to sooting can provide data to establish the relationships between the OH radical concentrations and the amount of soot formed in the flame. Such data may clarify the role of the OH concentration in the global models. Models such as those of Frenklach and Wang (1990)

and McKinnon (1989) also require more accurate information about OH radical profiles in sooting flames. Soot and OH data measured in near-critical equivalence ratio flames can provide a crucial test for the ability of a detailed mechanism to model the transition from nonsooting to sooting flames. An understanding of the transition to sooting may clarify the mechanisms that initiate soot formation and may identify thermodynamic or kinetic bottlenecks in the soot formation process.

CHAPTER 3:
LITERATURE REVIEW -
OPTICAL MEASUREMENTS OF SOOT AND HYDROXYL RADICAL

3.1 Introduction

This investigation of the role of the hydroxyl radical in soot formation has taken the approach of examining the transition from nonsooting to sooting conditions in premixed flames. Profiles of soot volume fraction, number density, and particle size were measured in sequences of premixed flames with increasing equivalence ratio at a constant dilution ratio and total flow rate. Hydroxyl concentration profiles were also measured for nonsooting and sooting conditions near the critical equivalence ratio in these same flame sequences. These OH radical and soot profiles can then be used to evaluate global models and detailed chemical kinetic models that are being developed to understand soot formation in premixed flames.

In this chapter we review the methods used for measuring the soot and OH radical concentrations. The laser scattering-extinction method was used to measure the soot volume fraction and number density profiles. The OH radical concentration profiles were measured with a broadband laser-induced fluorescence technique. For the soot and OH radical measurements, we first review investigations that have reported these profiles in flames. We then discuss the theory for the measurement methods. Finally, we identify interferences and discuss specific concerns that may affect the interpretation of these measurements in sooting flames.

3.2 Measurements of Soot Profiles with Laser Scattering-Extinction

The change in the sooting behavior of flames with increasing equivalence ratio can be observed through measurements of the soot volume fraction and number density profiles. An analysis of these profiles can determine the final soot volume fraction and the rates of surface growth and coagulation as a function of the equivalence ratio. In addition, the variation of the volume fraction and number density profiles provides an indirect measurement of the particle inception rate as a function of equivalence ratio, since the final soot volume fraction depends on the number of particles formed in the inception zone. In particular, numerical simulations of these profiles using an aerosol dynamics model have been used to infer the particle inception rates (Harris, Weiner, and Ashcraft, 1986; Bockhorn, Fetting, and Heddrich, 1986).

The three primary methods that have been used to measure soot in flames are probe sampling, classical light scattering, and dynamic light scattering. In the probe sampling methods, soot particles are removed from a flame either through a probe or through deposition onto a surface and are then examined with an electron microscope. Bonne, Homann, and Wagner (1965), Wersborg, Howard, and Williams (1973), and Bockhorn, Fetting, and Heddrich (1986) all used molecular beam sampling to remove soot from a flame with minimal change in the soot structure. They measured particle size and particle size distribution as a function of height above the burner. Dobbins and Megaridis (1987) used thermophoretic sampling to extract soot from a laminar ethylene diffusion flame. They determined the overall particle size, the size of the primary particles in the soot aggregate, and the structure of the aggregates including the fractal dimension. The sampling methods give direct measurements of the particle size and morphology and are the primary source for information about the structure of soot particles.

In comparison to probe sampling methods, the light scattering methods do not perturb the flame physically and are capable of greater spatial resolution. However, the

light scattering methods measure the overall characteristics of an ensemble of particles. Charalampopoulos (1992) reviews the applications, advantages, and limitations of these light scattering methods. The classical techniques measure the extinction and the elastically scattered light from a light beam passing through a volume containing the soot particles. Typically, the volume fraction and the number density of the soot are determined from the measurements. The angular variation of the scattered intensity and the depolarization of the scattered light can provide information about the size distribution and the shape of the larger agglomerated particles. A disadvantage is that these measurements rely on an assumed value of the particle index of refraction. This method has been used extensively to measure both soot volume fraction and number density (e.g., Haynes, Jander, and Wagner, 1980; D'Alessio, 1981; Bockhorn, Fetting, and Heddrich, 1986; Harris, Weiner, and Ashcraft, 1986).

Dynamic light scattering techniques measure the particle diameter by using the spectral broadening of the scattered light caused by the brownian diffusion of the particles. If the dynamic light scattering is measured in the time domain it is termed photon correlation spectroscopy, while if it is measured in the frequency domain it is termed diffusion broadening spectroscopy. These methods are used to measure the particle size and the particle size distribution, and have the advantage that they do not depend on the particle index of refraction for small particles. Scrivner et al. (1986) and Ramer et al. (1986) used photon correlation spectroscopy along with classical laser scattering-extinction to measure particle size distribution, particle size, and number density in premixed methane/oxygen flames. Charalampopoulos and Felske (1987) and Charalampopoulos and Chang (1988) used photon correlation spectroscopy in conjunction with laser scattering-extinction to deduce the particle index of refraction along with the particle size, size distribution, and number density in premixed methane/oxygen and propane/oxygen flames.

The laser scattering-extinction method was used to measure soot volume fraction and number density in the sooting flames of this study. In this section, the theory for the method is described and equations are developed that relate the measured data to the soot volume fraction and number density. The interferences that may affect the scattered light and extinction measurements are identified. Both the particle index of refraction and the particle size distribution must be known or assumed to interpret the scattering-extinction measurements. These assumptions are discussed and then the relevant expressions are derived for the number density and particle size.

3.2.1 Theory

The laser scattering-extinction method has been applied to the study of sooting flames and its theory has been well developed. The fundamental theory of the absorption and scattering of light by particles has been discussed by Kerker (1969) and more recently by Bohren and Huffman (1983). Jones (1979) reviewed the theory and also its diagnostic applications. D'Alessio (1981) reviewed the application of the theory to the measurement of soot in flames. Detailed examples of the apparatus, methods, and interferences encountered in the measurement of soot in flames have been presented by Müller-Dethlefs (1979), D'Alessio (1981), and Charalampopoulos and Felske (1987). Our notation follows that used by D'Alessio (1981) and Charalampopoulos and Felske (1987).

The application of the laser scattering-extinction method to the measurement of soot particle volume fraction and number density in a sooting premixed flame is illustrated by the diagram of a simplified laser scattering-extinction measurement system shown in Figure 3.1. The transmittance, τ , of the flame is measured by the decrease in irradiance of a laser beam as it passes through the flame. The incident irradiance, I_0 , of the laser

beam is measured by reflecting a portion of the beam onto a detector with a beam splitter. A detector placed after the flame measures the transmitted irradiance of the laser beam, I_T . The transmittance is the ratio of the transmitted to incident irradiance,

$$\tau = \frac{I_T}{I_0} \quad (3.2.1)$$

The light scattered from the particles at an angle θ with respect to the incident laser beam is focussed onto another detector to measure the scattered light power, S_{pp} . The effective aperture of the collection optics determines the collection solid angle, Ω_c , of the scattered light. The intersection of the laser beam and the image of the detector in the flame defines the collection volume, V_c , from which the scattered light is gathered.

The parameters describing the soot particles in the flame are determined from the transmittance and scattered light measurements. These parameters are the volume fraction of the soot, f_v ($\text{cm}^3 \text{ soot} \cdot \text{cm}^{-3} \text{ gas}$), the number density of the particles, N_p (cm^{-3}), and the radius of the particles, r (cm). If there is a polydispersion of the particle sizes, they are described by a normalized particle size distribution function $P(r)$. These parameters are related by

$$f_v = N_p \cdot \frac{4\pi}{3} \cdot \int_0^\infty P(r) \cdot r^3 \cdot dr \quad (3.2.2)$$

The integral term in Eq. (3.2.2) is the third moment of the particle size distribution and is proportional to the volume of the particles.

The parameters describing the particles can be determined from the transmittance and scattered light measurements by using Mie scattering theory. Mie scattering theory gives the solution of Maxwell's equations for scattering and absorption of light by a homogeneous spherical absorbing particle (Kerker, 1969). If the particle size is small compared to the wavelength of light, λ , then the measurements can be interpreted using Rayleigh scattering theory, a much simpler analysis than Mie scattering theory. Rayleigh scattering theory is a good approximation to the Mie scattering theory for particle sizes

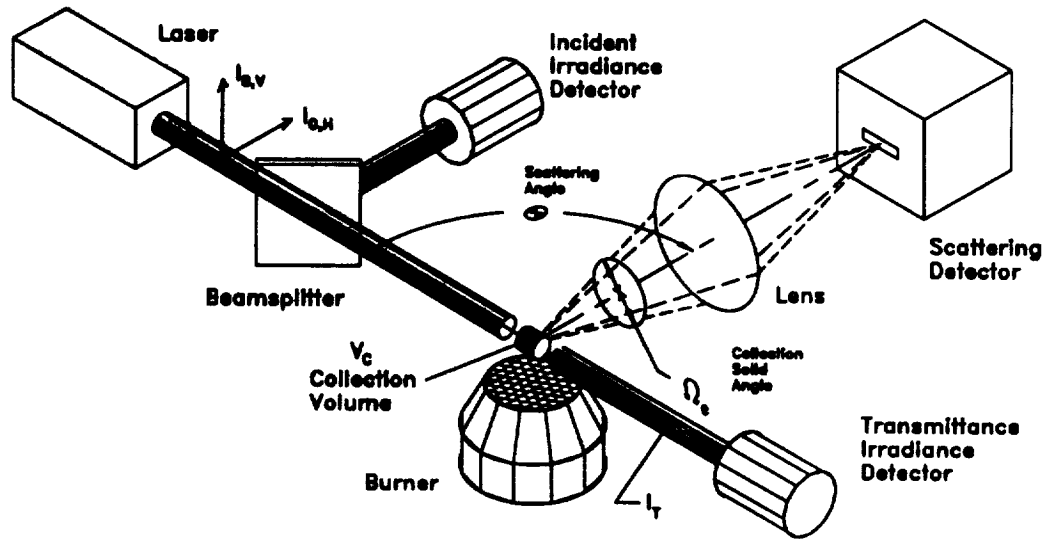


Figure 3.1 Basic structure of a laser scattering-extinction measurement system.

with $\alpha < 0.3$, where $\alpha = 2\pi r/\lambda$ is the particle size parameter (D'Alessio, 1981). This approximation is valid for particle diameters up to 47 nm, when using an argon-ion laser operating at $\lambda = 488.0$ nm. Both Rayleigh and Mie scattering theory require that the complex index of refraction of the particles, $\bar{m} = n - ik$, be known beforehand to interpret the results. In this study, the interpretation of the transmittance and scattered light measurements are based on Rayleigh scattering theory.

3.2.1.1 Interpretation of Transmittance Measurements

The transmittance of the laser beam through the flame is related to the integral of the local extinction coefficient, K_{ext} (cm^{-1}), along the path of the laser beam through the flame. The relationship is given by

$$\tau = \frac{I_T}{I_0} = \exp\left[-\int_0^x K_{ext} \cdot dx\right] \quad (3.2.3)$$

where x is the distance along the path. When the particle field is homogeneous and thus the extinction coefficient is constant along the path, Eq. (3.2.3) simplifies to

$$\tau = \frac{I_T}{I_0} = \exp[-K_{ext} \cdot L] \quad (3.2.4)$$

where L (cm) is the pathlength of the laser through the flame.

The extinction coefficient is related to the extinction cross-section of the particles and their number density by

$$K_{ext} = N_p \cdot \bar{C}_{ext} \quad (3.2.5)$$

where \bar{C}_{ext} (cm²) is the mean extinction cross-section defined as

$$\bar{C}_{ext} = \int_0^\infty C_{ext}(r) \cdot P(r) \cdot dr \quad (3.2.6)$$

When the particle size is within the Rayleigh scattering regime, the extinction cross-section of a particle is given by

$$C_{ext} = \frac{-8\pi^2 r^3}{\lambda} \cdot Im \left\{ \frac{\bar{m}^2 - 1}{\bar{m}^2 + 2} \right\} \quad (3.2.7)$$

where Im indicates the imaginary part of the complex index of refraction function, $(\bar{m}^2 - 1)/(\bar{m}^2 + 2)$. If all the particles have the same complex index of refraction, then substituting Eqs. (3.2.6) and (3.2.7) into Eq. (3.2.5) gives

$$K_{ext} = \frac{-8\pi^2}{\lambda} \cdot Im \left\{ \frac{\bar{m}^2 - 1}{\bar{m}^2 + 2} \right\} \cdot N_p \cdot \int_0^\infty P(r) \cdot r^3 \cdot dr \quad (3.2.8)$$

Substituting into Eq. (3.2.2) and rearranging gives an expression for the volume fraction in terms of the extinction coefficient,

$$f_v = -\frac{\lambda}{6\pi} \cdot \left[Im \left\{ \frac{\bar{m}^2 - 1}{\bar{m}^2 + 2} \right\} \right]^{-1} \cdot K_{ext} \quad (3.2.9)$$

Thus the particle volume fraction can be determined from measurement of the extinction coefficient and knowledge of the complex index of refraction. No knowledge is required about the particle size distribution.

3.2.1.2 Interpretation of Scattering Measurements

The light power scattered by the particles and monitored by the detector is given by

$$S_{PP} = I_{0,P} \cdot V_c \cdot \Omega_c \cdot \eta_c \cdot Q_{PP} \quad , \quad (3.2.10)$$

where S_{PP} (W) is the scattered light power and Q_{PP} ($\text{cm}^{-1} \cdot \text{sr}^{-1}$) is the differential scattering coefficient. For both of these parameters, the first subscript denotes the polarization of the detected scattered light and the second subscript denotes the polarization of the incident light. $I_{0,P}$ ($\text{W} \cdot \text{cm}^{-2}$) is the incident irradiance, where again the subscript denotes the polarization of the incident light. V_c (cm^3) is the collection volume, Ω_c (sr) is the acceptance solid angle of the collection optics, and η_c is the efficiency of the collection optics. If a significant extinction exists from the edge of the flame to the scattering volume, both the incident irradiance and the scattered light power must be adjusted for the extinction.

The differential scattering coefficient is given by

$$Q_{PP} = N_p \cdot \bar{C}_{PP} \quad (3.2.11)$$

where \bar{C}_{PP} is the mean differential scattering cross-section ($\text{cm}^2 \cdot \text{sr}^{-1}$) of the particles. It is defined in terms of the differential scattering cross-section of the individual particles and the particle size distribution as

$$\bar{C}_{PP} = \int_0^{\infty} C_{PP} \cdot P(r) \cdot dr \quad . \quad (3.2.12)$$

For Rayleigh scattering, the differential scattering cross-sections of a single particle for the various combinations of incident and scattered polarizations are given by

$$C_{VV} = \frac{16\pi^4}{\lambda^4} \cdot \left| \frac{\bar{m}^2 - 1}{\bar{m}^2 + 2} \right|^2 \cdot r^6 \quad (3.2.13a)$$

$$C_{HH} = C_{VV} \cdot \cos^2 \theta \quad (3.2.13b)$$

$$C_{VH} = C_{HV} = 0 \quad (3.2.13c)$$

Typically, the scattered light is measured at right angles to the incident beam ($\theta = 90^\circ$) using vertically polarized incident light. The scattered light with horizontal polarization (S_{HV}) can be measured to determine the depolarization ratio, ρ_v , defined as

$$\rho_v = \frac{C_{HV}}{C_{VV}} \quad (3.2.14)$$

which should be equal to zero for Rayleigh scattering conditions. A non-zero depolarization ratio could be caused by particle anisotropy or by non-spherical particles such as the chainlike agglomerates formed as the soot particles coagulate.

Combining Eqs. (3.2.11), (3.2.12), and (3.2.13a) gives the differential scattering coefficient of the particles as

$$Q_{VV} = \frac{16\pi^4}{\lambda^4} \cdot \left| \frac{\bar{m}^2 - 1}{\bar{m}^2 + 2} \right|^2 \cdot N_p \cdot \int_0^\infty P(r) \cdot r^6 \cdot dr \quad (3.2.15)$$

Thus, the scattering coefficient depends on the sixth moment of the particle size distribution and is inversely proportional to the fourth power of the wavelength.

The expressions for the scattering coefficient (Eq. 3.2.15) and the extinction coefficient (Eq. 3.2.8) can be used to determine the number density and particle size. However, the number density and the particle size will depend on the shape of the particle size distribution. Therefore, expressions for the number density and particle size for an assumed particle size distribution are developed in Section 3.2.5 after a discussion of particle size distributions in Section 3.2.4.

3.2.2 Interferences and Background Corrections

The scattered light from from soot particles is collected along with background contributions from molecular scattering by flame gases and broadband fluorescence excited at the laser wavelength. The gas-phase species which are the source of the fluorescence may also cause an absorption which adds to the extinction by the soot particles (Müller-Dethlefs, 1979; Haynes, Jander, and Wagner, 1980; D'Alessio, 1981). To determine the scattering and extinction caused by only soot particles, these background contributions must be measured and subtracted from the overall measurements. The cause of each background interference and the development of an expression describing each contribution follows.

3.2.2.1 Molecular Scattering

The scattered light contribution caused by molecular scattering from the flame gases can be expressed as a molecular scattering coefficient similar to that of the soot particles (Eq. 3.2.11) so that

$$Q_{PP,g} = N_g \cdot \bar{C}_{PP,g} \quad (3.2.16)$$

where N_g (cm^{-3}) is the number density of the gas molecules and $\bar{C}_{PP,g}$ ($\text{cm}^2 \cdot \text{sr}^{-1}$) is the average differential scattering cross-section for the gas mixture. The average differential scattering cross-sections for vertically and horizontally polarized scattered light can be determined from the molar composition of the gas by

$$\bar{C}_{VV,g} = \sum_k X_k \cdot C_{VV,k} \quad (3.2.17a)$$

$$\bar{C}_{HV,g} = \sum_k X_k \cdot \rho_{V,k} \cdot C_{VV,k} \quad (3.2.17b)$$

where X_k is the mole fraction of species k and $\rho_{V,k}$ is the depolarization ratio of species k (D'Alessio, 1981). The differential scattering cross-section of gas species k for vertical incident and detected polarization, $C_{VV,k}$ ($\text{cm}^2 \cdot \text{sr}^{-1}$), can be calculated from

$$C_{VV,k} = \frac{4\pi^2}{\lambda^4} \cdot \frac{(n_k - 1)^2}{N_o^2} \cdot \frac{3}{3 - 4\rho_{V,k}} \quad (3.2.18)$$

where n_k is the refractive index of light for species k and N_o (cm^{-3}) is a standard molecular number density (Rudder and Bach, 1968; D'Alessio, 1981). Both the refractive index and the number density are normally evaluated at 0°C and 1 atm . The measured depolarization ratio $\rho_{V,k} = C_{HV,k}/C_{VV,k}$ accounts for the anisotropy of the gas molecules.

Typically, the molecular scattering contribution is small compared to that from soot particles. Scattering cross-sections for the major combustion products are on the order of $10^{-27} \text{ cm}^2 \cdot \text{sr}^{-1}$, while those for 1 nm diameter soot particles are on the order of $10^{-25} \text{ cm}^2 \cdot \text{sr}^{-1}$ (D'Alessio, 1981). Thus, the molecular scattering contribution is likely to be significant only in the inception region of sooting flames and in lightly sooting flames. The molecular scattering coefficient in sooting flames can be estimated from the measured scattering coefficient in rich but nonsooting flames at the same cold flow velocity and dilution ratio (Harris, Weiner, and Ashcraft, 1986).

Molecular scattering from a gas with a known differential scattering cross-section can be used to calibrate the scattering measurement system (D'Alessio, 1981). For example, if the scattered signal from flowing nitrogen is measured, then the expression for the scattered light power is obtained by combining Eq. (3.2.10) and (3.2.16) so that

$$S_{VV,N_2} = V_c \cdot \Omega_c \cdot \eta_c \cdot N_{N_2} \cdot C_{VV,N_2} \cdot I_{0,N_2} \quad (3.2.19)$$

where the differential scattering cross-section for nitrogen, C_{VV,N_2} , can be found from the literature (Rudder and Bach, 1968; Bogaard et al., 1978) and the number density can be determined from the temperature and pressure. The optical system constants can then be replaced in (Eq. 3.2.10) by substituting in Eq.(3.2.19) to give the scattering coefficient

$$Q_{VV} = \frac{S_{VV}}{S_{VV,N_2}} \cdot \frac{I_{0,N_2}}{I_0} \cdot N_{N_2} \cdot C_{VV,N_2} \quad (3.2.20)$$

3.2.2.2 Fluorescence

A broadband fluorescence has been observed in premixed sooting flames, when laser scattering-extinction is measured with an argon-ion laser. Excitation at either $\lambda = 488.0$ nm or 514.5 nm produced fluorescence spectra which were broad and structureless and contained both Stokes and anti-Stokes components (Haynes, Jander, and Wagner, 1980; D'Alessio, 1981). This fluorescence is thought to be caused by PAH species. DiLorenzo et al. (1981) noted that the argon-ion excited fluorescence profiles in their sooting methane flames coincided with their sampling probe measurements of four-ring PAH concentrations. Several studies have identified acenaphthylene as the species primarily responsible for the fluorescence excited at 488.0 nm (Coe and Steinfeld, 1980; Coe, Haynes, and Steinfeld, 1981; Beretta et al., 1985). Miller, Mallard, and Smyth (1982) suggested that the argon-ion fluorescence is caused by two to four-ring PAH species and not by a single species, because the fluorescence spectral structure varied when they altered the flow structure of their diffusion flame. Since studies of PAH spectra have not been made at flame temperatures, a definitive identification of the species responsible for the argon-ion laser-induced fluorescence is not possible. However, the fluorescence may provide a measure of the relative PAH concentration and the location of PAH formation.

The argon-ion excited fluorescence is observed as a depolarized light component in Rayleigh scattering measurements in sooting flames (Haynes, Jander, and Wagner, 1980; Müller-Dethlefs, 1979). Since the fluorescence also contributes to the measured vertically-polarized scattered signal, the measured signal must be corrected for this interference. This fluorescence contribution to the total scattered light power can be expressed as

$$S_f(\lambda_0, \lambda) = I_0(\lambda_0) \cdot V_c \cdot \Omega_c \cdot \eta_c \cdot Q_f(\lambda_0, \lambda) \cdot \Delta\lambda \quad (3.2.21)$$

where $S_f(\lambda_0, \lambda)$ (W) is the broadband fluorescence power incident on the detector, λ_0 (nm) is the incident (excitation) wavelength, λ (nm) is the collection wavelength, $Q_f(\lambda_0, \lambda)$ ($\text{cm}^{-1} \cdot \text{sr}^{-1} \cdot \text{nm}^{-1}$) is the monochromatic fluorescence coefficient, $\Delta\lambda$ (nm) is the spectral bandwidth of the detector, and $I_0(\lambda_0)$ ($\text{W} \cdot \text{cm}^{-2}$) is the incident irradiance at the excitation wavelength (Beretta et al., 1985). Harris, Weiner, and Ashcraft (1986) measured the fluorescence contribution to the Rayleigh scattered signal at 488.0 nm by excitation at the 476.5 nm and 514.5 nm argon-ion laser wavelengths. Their assumption was that the fluorescence coefficients for all three excitation wavelengths were equivalent, i.e., $Q_f(\lambda_0=488.0, \lambda=488.0) = Q_f(\lambda_0=476.5, \lambda=488.0) = Q_f(\lambda_0=514.5, \lambda=488.0)$.

The contributions to the scattered light power from particle scattering, molecular scattering, and fluorescence are additive, if multiple scattering effects are not significant. The total scattered power, S_{sca} (W), incident on the detector can then be expressed as

$$S_{sca} = I_{0,v} \cdot V_c \cdot \Omega_c \cdot \eta_c \cdot (Q_{vv} + Q_{vv,g} + Q_f(\lambda_0, \lambda) \cdot \Delta\lambda) \quad (3.2.22)$$

where the term $I_{0,v} V_c \cdot \Omega_c \cdot \eta_c$ is common to the three contributions. The scattering coefficient determined from the total vertically polarized scattered power, $Q_{sca,v}$, is the sum of the scattering coefficients of the individual contributions and is defined as

$$Q_{sca,v} = Q_{vv} + Q_{vv,g} + Q_f(\lambda_0, \lambda) \cdot \Delta\lambda \quad (3.2.23)$$

The scattering coefficient for vertically polarized particle scattering, Q_{vv} , can be determined by subtracting the scattering coefficients for molecular scattering and fluorescence from the measured total scattering coefficient. Similarly, the scattering coefficient determined from the horizontally polarized scattered power is defined as

$$Q_{sca,h} = Q_{hv} + Q_{hv,g} + Q_f(\lambda_0, \lambda) \cdot \Delta\lambda \quad (3.2.24)$$

Likewise, the horizontally polarized particle scattering coefficient, Q_{hv} , can be determined by subtracting the contributions from molecular scattering and fluorescence.

3.2.2.3 Gas-Phase Absorption

A gas-phase absorption has been observed in sooting flames for extinction measurements made at UV wavelengths and also at the visible wavelengths, 488.0 nm and 514.5 nm, of an argon-ion laser (Müller-Dethlefs, 1979; Haynes, Jander, and Wagner, 1980; Harris, Weiner, and Ashcraft, 1986). The absorption was strongest in the UV region and declined toward the visible with a wavelength dependence that was greater than that expected from particle extinction. This absorption was attributed to large gaseous molecules and may be caused by the PAH species which are also responsible for the argon-ion excited fluorescence. This gas-phase absorption was observed in the nonsooting and particle inception regions of premixed sooting flames and thus it can interfere with the detection of soot particles in the early stages of soot formation.

Müller-Dethlefs (1979), Haynes, Jander, and Wagner (1980), and Harris, Weiner, and Ashcraft (1986) corrected their measured extinction coefficients to account for gas-phase absorption. In particular, Harris, Weiner, and Ashcraft (1986) corrected their extinction measurements at 488.0 nm by using extinction measurements at 1090 nm, for which the soot particles were the sole source of extinction. Müller-Dethlefs (1979) and Haynes, Jander, and Wagner (1980) estimated the magnitude of the gas-phase absorption at 488.0 nm from the magnitude of the fluorescence excited at 488.0 nm. They assumed that the fluorescence and absorption were caused by the same species and thus by estimating a quantum yield for the fluorescence, they could calculate the gas-phase absorption. Haynes, Jander, and Wagner (1980) observed that in their flat premixed flame the gas-phase absorption was significant only below the point where the soot scattering signal rose above the background, and thus it did not significantly affect their scattering-extinction measurements of soot.

3.2.3 Particle Index of Refraction

The calculation of the volume fraction, number density, and particle size from the extinction coefficient (Eq. 3.2.8) and the scattering coefficient (Eq. 3.2.15) requires that the particle index of refraction, $\bar{m} = n - ik$, be known or assumed. The assumed value of the index of refraction can have a large effect on the parameters determined from the measurements. Charalampopoulos (1992) showed that the calculated volume fraction can vary by a factor of two as the real part of the refractive index is varied over the range $1.3 \leq n \leq 2.0$ and by a factor of three when the imaginary part is varied over the range $0.3 \leq k \leq 1.0$. Table 3.1 summarizes previous measurements of the index of refraction for soot particles at wavelengths near 488.0 nm for various flame conditions and measurement methods.

The index of refraction reported by Dalzell and Sarofim (1969) is used often in the analysis of scattering-extinction measurements (e.g., Müller-Dethlefs, 1979; D'Alessio, 1981; Harris, Weiner, and Ashcraft, 1986). Dalzell and Sarofim (1969) measured the index of refraction by extracting soot from a flame, compressing it into a pellet, and then measuring the reflectance as a function of wavelength. The index of refraction was determined from the reflectance by using the Fresnel equations. Janzen (1979) noted that the results obtained with the reflectance method are likely to be artifacts of the surface roughness and not a true measure of the particle index of refraction. Janzen (1979) determined the index of refraction from light extinction measurements of carbon black particles in a dilute liquid suspension. Mullins and Williams (1987) compared soot refractive indices measured with the reflectance method for a soot pellet and the light extinction method for a liquid suspension of soot. The real parts of the refractive indices were similar, but the imaginary parts differed significantly because of a dependence on the compaction of the soot in the pellet.

Table 3.1 Summary of soot particle index of refraction data.

<u>Investigation</u>	<u>Type of soot</u>	<u>Wavelength</u>	<u>Index of refraction</u>	
Dalzell and Sarofim (1969)	Acetylene H/C = 0.068	450 nm	1.56 - i·0.48	
		550 nm	1.56 - i·0.46	
	Propane H/C = 0.22	450 nm	1.56 - i·0.50	
		550 nm	1.57 - i·0.53	
Chippet and Gray (1978)	Acetylene	550 nm	1.9(±0.1) - i·0.35(±0.05)	
Janzen (1979)	Carbon black	visible	2.0 - i·1.0	
Lee and Tien (1981)	Polystyrene, plexiglas, iso-octane	visible	1.9(±0.1) - i·0.55(±0.1)	
Mullins and Williams (1987) (extinction) (reflectance)	Toluene H/C = 0.153	450 nm	1.90 - i·0.42	
	Propane H/C = 0.106	450 nm	1.90 - i·0.42	
	Heptane H/C = 0.120	450 nm	1.88 - i·0.44	
	Methane H/C = 0.177	450 nm	1.91 - i·0.43	
	Toluene H/C = 0.153	450 nm	1.90 - i·0.54	
	Propane H/C = 0.106	450 nm	1.90 - i·0.53	
	Heptane H/C = 0.120	450 nm	1.88 - i·0.51	
	Methane H/C = 0.177	450 nm	1.91 - i·0.53	
Charalampopoulos and Felske (1987)	Methane $\phi = 1.8$			
	z = 6 mm	488.0 nm	1.38 - i·0.42	
	z = 11 mm	488.0 nm	1.81 - i·0.75	
	z = 16 mm	488.0 nm	1.64 - i·0.63	
	average	488.0 nm	1.60 - i·0.59	
Habib and Vervisch (1988)	Methane, Ethylene, Propane	H/C ≥ 0.2	500 nm	1.46 - i·0.27
		H/C ≤ 0.1	500 nm	1.83 - i·0.43

Table 3.1 continued

<u>Investigation</u>	<u>Type of soot</u>	<u>Wavelength</u>	<u>Index of refraction</u>
Charalampopoulos and Chang (1988)	Propane $\phi = 1.8$ $z = 5$ mm	488.0 nm	1.57 - i-0.65
	$z = 9$ mm	488.0 nm	1.82 - i-0.85
	$z = 13$ mm	488.0 nm	1.61 - i-0.68
Charalampopoulos, Chang, and Stagg (1989)	Propane $\phi = 1.8$ $z = 8$ mm	488.0 nm	1.81 - i-0.84
	$z = 15$ mm	488.0 nm	1.64 - i-0.70
	$\phi = 2.1$ $z = 8$ mm	488.0 nm	1.59 - i-0.66
	$z = 16$ mm	488.0 nm	1.54 - i-0.62
	$\phi = 2.4$ $z = 8$ mm	488.0 nm	1.41 - i-0.51
	$z = 16$ mm	488.0 nm	1.51 - i-0.60
	Primary particle $\phi = 1.8$	488.0 nm	1.89 - i-0.89
	$\phi = 2.1$	488.0 nm	1.84 - i-0.87
	$\phi = 2.4$	488.0 nm	1.74 - i-0.79
Dobbins, Santoro, and Semerjian (1990)	Ethylene diffusion flame, primary particle	488.0 nm	2.10 - i-0.55

The above refractive index measurements were made at room temperature. Both Lee and Tien (1981) and Charalampopoulos, Chang, and Stagg (1989) show that the index of refraction changes significantly from room to flame temperatures. Their conclusions are based on calculations of the refractive index using the dispersion equations. The key factor is that the damping constants of the electrons depend on the square root of the temperature. Both studies note that the refractive index does not vary significantly over the range from 1100 to 1500 K.

In situ measurements of the soot particle index of refraction have been made using optical methods. Chippett and Gray (1978) measured the transmitted light through a sooting flame over the range from 400 nm to 800 nm and also the soot particle size and size distribution by extracting the soot from the flame. They determined the refractive index based on that value which gave the best agreement between the two measurements. Lee and Tien (1981) measured the transmitted light through a sooting flame over a much broader wavelength range. The index of refraction was determined by fitting the data with the dispersion equations.

Habib and Vervisch (1988) measured extinction spectra over the range from 0.4 to 5.0 μm and the particle size and size distribution with diffusion broadening spectroscopy as a function of height above the burner in methane, propane, and ethylene flames. The soot index of refraction was determined by fitting the extinction spectra with the dispersion equations. Soot was extracted from the flame and analyzed to determine the H/C ratio. They found that the refractive index varied with height above the burner and also with the changing hydrogen content of the soot. They determined that increasing the H/C ratio of the soot decreased the refractive index, especially in the imaginary component.

Charalampopoulos and Felske (1987) also found a variation of refractive index with height above the burner in a methane/oxygen flame. They used photon correlation

spectroscopy to measure the particle size and size distribution and laser scattering-extinction to measure number density and volume fraction. Solution of the relevant equations relating these parameters gave the value of the index of refraction. A similar measurement of soot in a propane/oxygen flame by Charalampopoulos and Chang (1988) was made using photon correlation spectroscopy and extinction measurements over the range from 340 nm to 600 nm. The refractive index was determined by fitting the extinction measurements with the dispersion equations. Again, the refractive index was found to vary with height and thus probably with H/C ratio.

The effect of H/C ratio on the soot index of refraction was investigated theoretically by both Lee and Tien (1981) and Charalampopoulos, Chang, and Stagg (1989) by using a dispersion equation model with two bound electrons and one free electron. Increasing the hydrogen content of the soot tends to decrease the concentration of free electrons. Lee and Tien (1981) determined that decreasing the free electron number density by 30% only changed the refractive index by 5%. Thus, they concluded that the optical properties of soot were relatively independent of the H/C ratio. Charalampopoulos, Chang, and Stagg (1989), however, came to a different conclusion. They calculated that an increase in the number density of the second bound electron by a factor of two would increase the imaginary part of the refractive index by 30% at 488 nm. Thus, the composition of the soot should have a significant effect on the refractive index.

Charalampopoulos, Chang, and Stagg (1989) measured the variation of the particle index of refraction with equivalence ratio in propane/oxygen flames using the method of Charalampopoulos and Felske (1987). They found that both the real and imaginary parts of the refractive index decreased with equivalence ratio. However, they noted that their procedure only provided an 'effective' particle index of refraction, because photon correlation spectroscopy measures a diffusional diameter, which for an agglomerated particle may not be the same as the optical diameter measured with Rayleigh

scattering-extinction. The effect of agglomeration on the soot index of refraction changes with increasing equivalence ratio because the number of primary particles in the agglomerates increases at higher equivalence ratios.

Dobbins, Santoro, and Semerjian (1990) made scattering-extinction measurements of soot in an ethylene diffusion flame. They measured the scattered light at three angles to obtain a measure of the aggregate structure of the soot particles. They then determined allowable values of the index of refraction which gave the best fit between the optical measurements of particle diameter and the diameter obtained from electron microscope measurements of extracted soot particles. The index of refraction determined for the primary particles in the aggregates was $2.10 - i0.55$ which is close to that determined by Lee and Tien (1981).

Despite the number of investigations which have measured the soot particle index of refraction, the choice of which index of refraction to use in the analysis of laser scattering-extinction data is not clear. The variation of the index of refraction has been measured as a function of height above the burner and may be a function of temperature, the H/C ratio of the soot, and the agglomeration of the particles. The index of refraction is apparently only slightly affected by the temperature at flame temperatures. The effect of changing soot H/C ratio with height above the burner may be masked in part by the agglomeration of the particles. Measurements by Charalampopoulos, Chang, and Stagg (1989) and Dobbins, Santoro, and Semerjian (1990), which attempt to account for the agglomeration, find an index of refraction for the primary particles that is close to that measured by Lee and Tien (1981) and is also larger than that of the agglomerated particles. These measurements suggest that an independent determination of particle size and shape or particle index of refraction may be needed to assess the scattering-extinction measurements. In the absence of these measurements, a good assumption for the index of refraction would be the value used for the primary particles by Dobbins, Santoro, and

Semerjian (1990), since similar values were also obtained by Charalampopoulos, Chang, and Stagg (1989), Lee and Tien (1981), and for low H/C ratio by Habib and Vervisch (1988). This assumption should be particularly appropriate for lightly sooting flames where the agglomeration of the particles is reduced accordingly.

3.2.4 Particle Size Distributions

The determination of soot particle number density and particle size from the extinction coefficient (Eq. 3.2.8) and scattering coefficient (Eq. 3.2.15) depends on the moments of the particle size distribution function, $P(r)$. Soot particle size distributions have been measured by extracting the soot particles from the flame and then observing them with an electron microscope. Wersborg, Howard, and Williams (1973) found that soot particles at the early stages of soot formation had a near Gaussian size distribution. They also observed that particles near the inception stage had a narrow size distribution that could be assumed to be monodisperse. In the later stages of soot formation, as the particles begin to agglomerate to form chains, a lognormal distribution best describes the particle size distribution (Wersborg, Howard, and Williams, 1973; Prado et al., 1981). Bockhorn, Fetting, and Heddrich (1986) determined that a lognormal size distribution with $\sigma_g = 1.405$ (where σ_g is the geometric width of the lognormal distribution) best fit their measured particle sizes. The moment ratios of their particle size distribution remained constant throughout the flame after particle inception and were close to those of a self-preserving size distribution (SPSD). This experimental result agrees with the aerosol dynamics modelling studies discussed in Section 2.3 which found that, following particle inception, the particle size distribution approaches that of the SPSPD for which the distribution of particle sizes about the instantaneous mean size is constant.

In situ measurements of the soot particle size distribution have been made with the dynamic light scattering technique. Scrivner et al. (1986) used photon correlation spectroscopy to measure the particle size distribution as a function of height in premixed

methane/oxygen flames. Charalampopoulos and Felske (1987) used photon correlation spectroscopy along with laser scattering-extinction to determine the particle size distribution and complex index of refraction as a function of height in a methane/oxygen flame. Charalampopoulos and Chang (1988) used the same method for a propane/oxygen flame. The particle size distributions in these investigations was assumed to be a zeroth order lognormal distribution (ZOLD) given by

$$P(r) = \frac{1}{(2\pi)^{1/2} \cdot r_0 \cdot \ln \sigma_g} \cdot \exp\left[\frac{-(\ln \sigma_g)^2}{2}\right] \cdot \exp\left[\frac{-(\ln r/r_0)^2}{2(\ln \sigma_g)^2}\right] \quad (3.2.25)$$

where r_0 is the mean particle radius. The terms, r_0 and σ_g , are the first two moments of the particle size distribution function and can be determined from photon correlation spectroscopy.

Scrivner et al. (1986) observed a decrease in the geometric width of the distribution from $\sigma_g \approx 1.285$ at 8 mm above the burner to $\sigma_g \approx 1.214$ to 1.150 at 16 mm above the burner. Charalampopoulos and Felske (1988) observed an increase in σ_g with height above the burner from $\sigma_g = 1.139$ at 6 mm to $\sigma_g = 1.240$ at 16 mm in a flame similar to that of Scrivner et al. (1986). Charalampopoulos and Chang (1988) observed σ_g to decrease and then level off at $\sigma_g \approx 1.14$ to 1.15 in a propane/oxygen flame. These in situ measured values of σ_g are lower than the $\sigma_g = 1.405$ reported by Bockhorn, Fetting, and Heddrich (1986) and the $\sigma_g = 1.33$ for a SPSSD. A possible reason for the differences in σ_g is that the soot particles in these flames are likely to be agglomerated and the dynamic light scattering technique can only measure an average diffusional diameter for the soot particles (Charalampopoulos, 1992).

3.2.5 Determination of the Number Density and Particle Size

The number density and particle size can be determined from the extinction coefficient (Eq. 3.2.8) and the scattering coefficient (Eq. 3.2.15), once the particle size

distribution and the index of refraction are known or assumed. We will use the notation of Santoro, Semerjian, and Dobbins (1983) for the functions of the complex index of refraction, $E(\bar{m})$ and $F(\bar{m})$, which are defined as

$$E(\bar{m}) = -Im \left\{ \frac{\bar{m}^2 - 1}{\bar{m}^2 + 2} \right\} \quad (3.2.26)$$

and

$$F(\bar{m}) = \left| \frac{\bar{m}^2 - 1}{\bar{m}^2 + 2} \right|^2 \quad (3.2.27)$$

The number density of the particles can be determined from the ratio of the extinction coefficient squared to the scattering coefficient so that

$$N_p = \frac{1}{4\lambda^2} \cdot \frac{F(\bar{m})}{(E(\bar{m}))^2} \cdot f_N \cdot \frac{(K_{ext})^2}{Q_{vv}} \quad (3.2.28)$$

where f_N is a dimensionless moment ratio (Megaridis and Dobbins, 1989) given by

$$f_N = \frac{\int_0^\infty P(r) \cdot r^6 \cdot dr}{\left[\int_0^\infty P(r) \cdot r^3 \cdot dr \right]^2} \quad (3.2.29)$$

The particle size can be determined from the ratio of the scattering coefficient to the extinction coefficient. The particle diameter is given by (Santoro, Semerjian, and Dobbins, 1983)

$$d_{63} = \lambda \cdot \left(\frac{4}{\pi^2} \cdot \frac{E(\bar{m})}{F(\bar{m})} \cdot \frac{Q_{vv}}{K_{ext}} \right)^{1/3} \quad (3.2.30)$$

where the mean diameter, d_{63} , is defined in terms of the sixth moment of the particle size distribution divided by its third moment and is given by

$$d_{63} = 2 \cdot \left[\frac{\int_0^\infty P(r) \cdot r^6 \cdot dr}{\int_0^\infty P(r) \cdot r^3 \cdot dr} \right]^{1/3} \quad (3.2.31)$$

This diameter reflects the bias of the scattering coefficient measurement towards larger particle sizes.

The two commonly assumed particle size distributions for the interpretation of laser scattering-extinction measurements are the monodisperse and ZOLD size distributions. The monodisperse particle size distribution function is $P(r) = 1.0$, so that from Eqs. (3.2.29) and (3.2.31),

$$f_N = 1.0 \quad (3.2.32)$$

and

$$d_{63} = d_0 \quad (3.2.33)$$

where $d_0 = 2 \cdot r_0$ is the mean particle diameter. For the ZOLD distribution given by Eq. (3.2.25) (Charalampopoulos, 1992),

$$f_N = \exp[9(\ln \sigma_g)^2] \quad (3.2.34)$$

and

$$d_{63} = d_0 \cdot \exp\left[\frac{11}{2}(\ln \sigma_g)^2\right] \quad (3.2.35)$$

The dimensionless moment ratio for a self-preserving size distribution was determined to be $f_N = 2.079$ through numerical simulation by Graham and Robinson (1976). This moment ratio corresponds to that for a ZOLD distribution with a geometric width of $\sigma_g = 1.33$. Thus, the number density calculated for a SPSD distribution is twice that for a monodisperse distribution.

Another approach for determining the number density and particle size profiles in a flame is to use an aerosol dynamics model to interpret the data. This approach has been used by Bockhorn, Fetting, and Heddrich (1986) and Harris, Weiner, and Ashcraft (1986) to interpret their laser scattering-extinction measurements. The aerosol dynamics models include a description of particle inception, surface growth, and coagulation for discrete sizes of soot particles. The numerical solution of the system of differential equations

describing these processes for each particle size is an iterative procedure that matches the model predictions to the flame measurements. The solution includes the number density and particle size profiles and does not require prior knowledge of the particle size distribution. The accuracy of the model depends on how well the coagulation and surface growth processes are modelled and the results still depend on the assumed particle index of refraction. These models primarily serve as a tool to infer the particle inception rates and location from the scattering-extinction measurements which typically cannot resolve the incipient particles.

3.3 Measurements of the Hydroxyl Radical in Sooting Flames

Measurements of the OH radical concentration profile as the equivalence ratio is increased from nonsooting to sooting conditions are necessary to ascertain its role in soot formation. Relative OH number density profiles can be used to evaluate either global or detailed chemical kinetic models for relative comparisons, but absolute OH radical concentration profiles are necessary to evaluate predicted OH radical concentrations from detailed chemical kinetic models.

Hydroxyl concentrations have been measured in a variety of flame types and conditions because of its significant role in both general combustion chemistry and in soot formation. In particular, OH radical concentrations have been measured in rich nonsooting and sooting premixed flames using three methods: molecular beam mass spectrometry (MBMS), ultraviolet light absorption, and laser-induced fluorescence.

Measurements of the OH radical with the MBMS technique have been made in low-pressure near-sooting and sooting laminar premixed flames. Typically, the flame gases are extracted through a quartz probe, formed into a molecular beam, and then detected with a mass spectrometer. An advantage of this method is that many species can be detected simultaneously. Typically, the major stable species in hydrocarbon combustion are detected along with some of the radicals such as H, OH, CH₃, C₂H₃, C₄H₃,

and C_4H_5 . A disadvantage is that the probe physically perturbs the flame and the species profiles are typically shifted 1 to 2 probe orifice diameters upstream to account for the disturbance. Because of this perturbation, the MBMS technique cannot resolve steep concentration gradients and thus it is used primarily for low-pressure flame measurements. The near-sooting and sooting flames in which OH profiles were measured with the MBMS technique include a 20-torr, $\phi = 1.8$ near-sooting benzene/ O_2 /Ar flame by Bittner and Howard (1981;1982), a 20-torr, $\phi = 2.4$ lightly sooting C_2H_2/O_2 /Ar flame by Westmoreland, Howard, and Longwell (1986), and a 20-torr, $\phi = 2.5$ lightly sooting C_2H_2/O_2 /Ar flame by Bastin et al. (1988). One comparison of OH radical profiles between a 30-torr, $\phi = 1.6$, nonsooting and a 60-torr, $\phi = 2.0$ sooting CH_4/O_2 /Ar flame was made by Burgess and Langley (1991).

Optical methods for measuring OH concentration have a major advantage over the MBMS methods because the optical methods do not physically perturb the flame. Ultraviolet absorption has been used by Millikan (1962) to measure OH concentration profiles in a series of nonsooting and sooting atmospheric C_2H_4 /air flames and by Warchold and Reuther (1984) to measure maximum OH number densities in a series of nonsooting and sooting C_2H_6 /air flames at pressures from 0.25 to 0.75 atm. The low OH concentrations in rich and sooting flames can make absorption measurements difficult. Millikan (1962) used a two-pass absorption arrangement and a large diameter (7 cm) burner to increase the pathlength. A disadvantage of UV absorption measurements is that the measured concentration is an average over the pathlength. For example, Lucht, Sweeney, and Laurendeau (1985) noted that low OH concentrations in the center of rich premixed flat flames could be obscured by the high OH concentrations in the diffusion flame that forms at the boundary between the rich flame and the surrounding air.

Laser-induced fluorescence methods have been used to measure local concentrations in flames. Lucht, Sweeney, and Laurendeau (1985) used laser-induced

fluorescence to measure OH concentration profiles in a $\phi = 1.68$ nonsooting, a $\phi = 1.85$ nearly sooting, and a $\phi = 2.02$ sooting atmospheric premixed $\text{CH}_4/\text{O}_2/\text{N}_2$ flame. They excited the $Q_1(8)$ transition of the (0,0) band in the $A^2\Sigma^+ - X^2\Pi$ system and detected the $P_1(9)$ transition with narrowband temporal detection. The dependence on electronic quenching was reduced by saturating the transition. Absolute concentration profiles were obtained by calibrating the OH fluorescence measurements in a lean $\text{CH}_4/\text{O}_2/\text{N}_2$ flame where the OH concentration was measured with UV absorption.

Harris, Weiner, and Blint (1986) measured relative OH concentration profiles with laser-induced fluorescence in a $\phi = 1.68$ nonsooting and a $\phi = 2.76$ sooting atmospheric premixed $\text{C}_2\text{H}_4/\text{O}_2/\text{Ar}$ flame. They excited the $R_1(5)$ transition (~ 281 nm) of the (1,0) band and detected fluorescence at 315 nm, the bandhead of the (1,1) band. Their profiles were not corrected for electronic quenching.

Miller et al. (1990) measured absolute OH concentration profiles in three 25-torr rich, nonsooting ($\phi = 1.03, 1.67,$ and 2.0) $\text{C}_2\text{H}_2/\text{O}_2/\text{Ar}$ premixed flames. They excited the OH transition by scanning across the (1,0) and (0,0) bands and detected the broadband fluorescence from the (0,0) and (1,1) bands using a 10-nm bandpass. They calibrated the fluorescence measurements by using an $\text{H}_2/\text{O}_2/\text{Ar}$ flame, for which they could accurately calculate the OH concentration. They also determined the OH rotational temperature from the spectral scans.

The spatial resolution of LIF measurements is crucial in determining the structure of diffusion flames. Smyth et al. (1990) have used LIF to measure absolute OH concentration measurements in a sooting laminar CH_4/air diffusion flame. They excited the $P_1(9)$ transition in the (1,0) band and detected the fluorescence in the (1,1) band with a 4-nm bandpass at 314 nm. They corrected for quenching variations using previously measured major species concentration profiles. An absorption measurement in a nonsooting region of the flame was used to calibrate the fluorescence measurements.

In this investigation, we used the laser-induced fluorescence method to measure relative OH concentration profiles. We first develop the theory for the measurements. The possible interferences with OH fluorescence measurements in sooting flames are then discussed, along with methods for reducing them. Finally, we discuss the effect of quenching variations and methods of calibration.

3.3.1 Theory

The OH fluorescence profiles were measured using laser-induced fluorescence (LIF) with broadband spectral and temporal detection. We used the SPF(0,0) method described by Laurendeau and Goldsmith (1989). The $Q_1(8)$ transition in the (0,0) band of the $A^2\Sigma^+ - X^2\Pi$ system of OH was excited with the UV output of a frequency-doubled Nd:YAG pumped dye laser. The OH fluorescence was detected over a spectral range encompassing most of the (0,0) band and the fluorescence signal was temporally integrated over the laser pulse. Broadband spectral and temporal detection were used to measure OH fluorescence in these rich nonsooting and sooting flames to increase the measured fluorescence signal and to obtain a better detection limit than would be possible using saturated LIF which uses narrowband spectral and temporal detection. The general theory and implementation of LIF to measure species concentrations has been presented by Eckbreth (1988). The theory and method presented here follows that of Laurendeau and Goldsmith (1989).

A basic laser-induced fluorescence system for the measurement of species concentrations in a flame is illustrated in Figure 3.2. The LIF method can be understood by considering a simple two-level energy model, as shown in Figure 3.3. The laser wavelength is tuned to the energy difference between a rovibronic level in the ground electronic state (level 1) and a rovibronic level in the excited electronic state (level 2). Absorption of laser energy produces a population in the excited state. The fluorescence

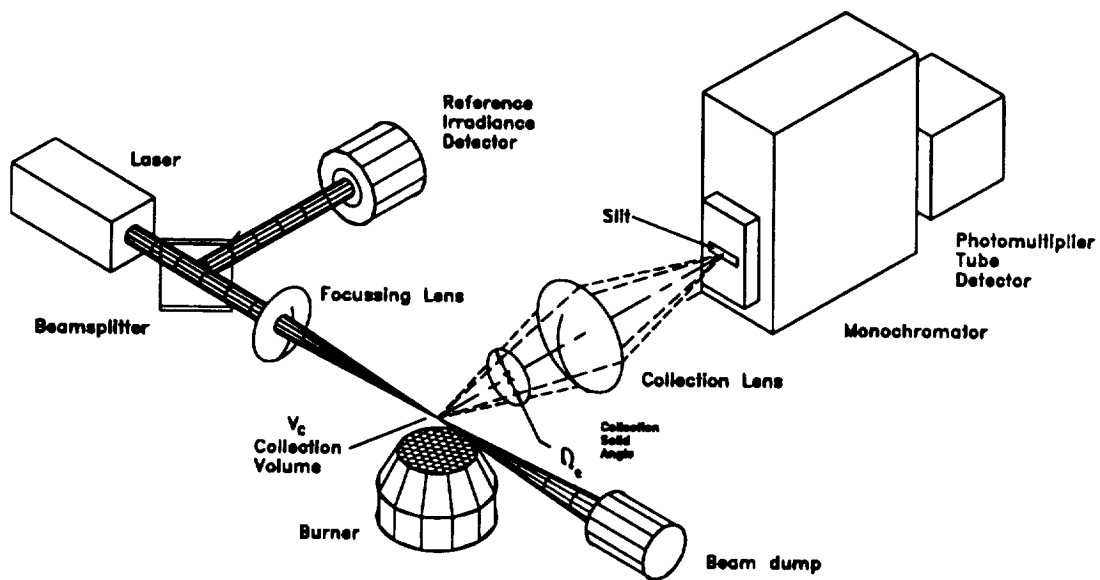


Figure 3.2 A laser-induced fluorescence measurement system.

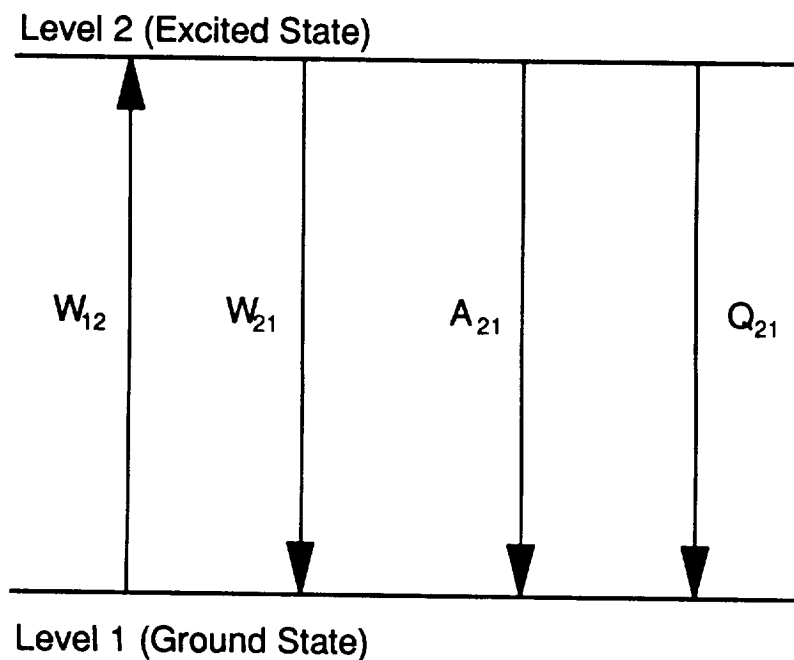


Figure 3.3 Two-level model for the energy levels in laser-induced fluorescence. W_{12} and W_{21} are the rate coefficients for stimulated absorption and emission. A_{21} is the spontaneous emission rate coefficient and Q_{21} is the quenching rate coefficient.

emitted from molecules in the excited state is collected by a lens and focussed on a detector. The collection optics fix both the collection volume, V_c (cm^3), and the solid angle, Ω_c (sr), over which the fluorescence is gathered.

The fluorescence emission, ϵ_f ($\text{W}\cdot\text{cm}^{-3}\cdot\text{sr}^{-1}$), at a single wavelength due to spontaneous emission from level 2 to 1 is a measure of the number density of the molecules in the excited level, N_2 (cm^{-3}). The emission is given by

$$\epsilon_f = \frac{hc\nu_f}{4\pi} \cdot A_{21} \cdot N_2 \quad (3.3.1)$$

where ν_f is the wavenumber of the fluorescence (cm^{-1}), h is Planck's constant (6.6256×10^{-34} J·sec), c is the speed of light (2.998×10^{10} $\text{cm}\cdot\text{sec}^{-1}$), and A_{21} is the rate coefficient for spontaneous emission (sec^{-1}).

The number density in the excited level, N_2 , is related to the number density in the ground level, N_1 , through the rate equation

$$\frac{dN_2}{dt} = N_1 \cdot W_{12} - N_2 \cdot (W_{21} + A_{21} + Q_{21}) \quad (3.3.2)$$

where W_{12} and W_{21} are the stimulated absorption and emission rate coefficients (sec^{-1}), respectively, and Q_{21} is the rate coefficient for collisional quenching (sec^{-1}). The number density in the excited level prior to excitation will be negligible if the energy difference between the two levels is large. Thus the number densities after excitation are related to the initial number density in the ground level by

$$N_1^0 = N_1 + N_2 \quad (3.3.3)$$

The population in the excited level can be assumed to be in steady-state when the quenching rates are high enough so that the temporal behavior of the laser and fluorescence pulses are nearly identical (Laurendeau and Goldsmith, 1989). With this assumption, the excited level number density from Eqs. (3.3.2) and (3.3.3) becomes

$$N_2 = \frac{1}{1 + (W_{21} + A_{21} + Q_{21})/W_{12}} \cdot N_1^0 \quad (3.3.4)$$

When the laser irradiance is small, the terms W_{12} and W_{21} are small (non-saturated conditions) and Eq. (3.3.4) simplifies to

$$N_2 = \frac{W_{12}}{A_{21} + Q_{21}} \cdot N_1^0 \quad (3.3.5)$$

The stimulated absorption rate coefficient for single-photon absorption is given by

$$W_{12} = \frac{\sigma I_L}{h c \nu_L} \quad (3.3.6)$$

where σ is the absorption cross-section (cm^2), I_L is the incident laser irradiance ($\text{W}\cdot\text{cm}^{-2}$), and ν_L is the wavenumber of the laser (cm^{-1}). The fluorescence emission is obtained by combining Eqs. (3.3.1), (3.3.5) and (3.3.6) and is given by

$$\epsilon_f = \alpha \cdot \frac{A_{21}}{A_{21} + Q_{21}} \cdot N_1^0 \cdot I_L \quad (3.3.7)$$

where the constant α is defined by

$$\alpha = \frac{\nu_f}{\nu_L} \cdot \frac{\sigma}{4\pi} \quad (3.3.8)$$

When the species concentration is small (e.g., the OH concentration in a sooting flame), the fluorescence emission captured with narrowband spectral and temporal detection (Eq. 3.3.7) may not be measurable. However, the measured fluorescence signal can be increased if the fluorescence emission is collected over the temporal width of the laser pulse and also over a spectral range encompassing the manifold of transitions from the rovibronic levels in the upper electronic state to the rovibronic levels in the lower electronic state. The fluorescence emission for broadband spectral and temporal detection, ϵ_{fB} , is given by (Laurendeau and Goldsmith, 1989)

$$\epsilon_{fB} = \alpha \cdot \left[\frac{A}{A + Q} \right] \cdot N_1^0 \cdot \int I_L(t) \cdot dt \quad (3.3.9)$$

where A and Q are the rate coefficients for spontaneous emission and quenching obtained by integrating A_{21} and Q_{21} over the manifold of rovibronic levels in the excited and ground electronic states. The fraction of the fluorescence emission gathered by the collection optics and measured by the detector is then given by

$$S_f = \eta_o \cdot \Omega_c \cdot V_c \cdot \epsilon_{fB} \quad (3.3.10)$$

where S_f is the fluorescence signal power (W) and η_o is the optical efficiency of the detection optics.

The initial number density in the ground state, N_1^o , can be determined from the fluorescence signal power through Eqs. (3.3.9) and (3.3.10). The optical system constants in Eqs. (3.3.9) and (3.3.10) can be determined through calibration. The irradiance term in Eq. (3.3.9) may be accounted for by either measuring a reference irradiance or by calibration, if the laser irradiance is invariant with time. The quenching term may be accounted for by either assuming constant quenching or by calculating the quenching rate coefficient. These calibrations and corrections are discussed in Sections 3.3.2 to 3.3.4.

The object of the measurement, the total number density, N_T , can be determined from the initial number density in the ground state, N_1^o , by

$$N_T = \frac{N_1^o}{F_{1B}} \quad (3.3.11)$$

where F_{1B} is the Boltzmann fraction at the local flame temperature. The sensitivity to temperature can be reduced by choosing a ground state rovibronic level whose population depends only weakly on temperature.

3.3.2 Interferences and Background Corrections

OH fluorescence measurements in sooting flames are complicated by possible interferences that can become significant because the OH concentrations are so low in such flames. Possible interferences were identified by Lucht, Sweeney, and Laurendeau

(1985) as fluorescence from the soot particles and PAHs, scattering from the flame gases and soot particles, and background emission from the flame and soot. The major limitation in their saturated fluorescence measurements in sooting methane flames was the background contribution from rotational Raman scattering from nitrogen. Many of the other potential interferences were reduced because of the narrowband spectral and temporal detection used with laser-saturated fluorescence. However, narrowband spectral or temporal detection reduces the fluorescence signal which can be disadvantageous when monitoring small OH concentrations. For broadband detection, scattering interferences may be eliminated by excitation of the OH radical in the (1,0) band followed by fluorescence detection in the (1,1) band away from the laser wavelength. Both Harris et al. (1986) and Smyth et al. (1990) used this method. They also limited their spectral detection bandwidth to discriminate against fluorescence and background emission from other species. Smyth et al. (1990) noted that excitation at ~ 286 nm in the (1,0) band can excite a broadband UV fluorescence in the pyrolysis regions of diffusion flames.

In the SPF(0,0) method, the spectral bandwidth of the detector includes the laser excitation along with the OH fluorescence from the (0,0) band. Thus, potential interferences can arise from scattering of the laser by flame gases and particles and possibly from broadband fluorescence from PAHs and soot particles. The Rayleigh scattering profiles measured with the laser scattering-extinction method can be used to identify where particulate scattering and PAH fluorescence might arise. Typically, in premixed sooting flames, the OH concentration profile declines to its equilibrium value before the region of visible soot emission (Millikan, 1962; Lucht, Sweeney, and Laurendeau, 1985). Thus, measurements near the peak of the OH concentration profile in the oxidation zone are unlikely to be affected by particulate scattering; the same is not true for the near equilibrium OH concentrations in the post-flame zone. Since the

particulate volume fractions in the near-critical equivalence ratio flames of this study are low, the associated interferences tend to be insignificant. Thus, the principal interference for the OH fluorescence measurements will be Rayleigh scattering from the flame gases.

The Rayleigh scattering background can be measured by tuning the laser wavelength away from the OH transition. Possible interferences from PAH fluorescence and particulate scattering are included in the background when it is measured in this way. The power, S_R (W), for Rayleigh scattering measured by the detector is given by

$$S_R = \eta_O \cdot \Omega_c \cdot V_c \cdot Q_{VV,g} \cdot I_L \quad (3.3.12)$$

where $Q_{VV,g}$ is the differential scattering coefficient of the gases ($\text{cm}^{-1} \cdot \text{sr}^{-1}$). From Sec. 3.2.1, the differential scattering coefficient is given by

$$Q_{VV,g} = N_g \cdot \sum_k X_k \cdot C_{VV,k} \quad (3.3.13)$$

where N_g is the number density of the gases (cm^{-3}), X_k is the mole fraction of species k , and $C_{VV,k}$ is the differential scattering cross-section of species k . The fluorescence signal, S_f , is then determined by subtracting the Rayleigh background signal from the signal measured when the laser wavelength is tuned to the OH transition.

The Rayleigh scattering interference can be reduced by one to two orders of magnitude if the incident laser irradiance is horizontally polarized. The differential scattering cross-sections for horizontally polarized incident light and for scattering measured at 90° are $C_{HH} = 0$ (Eq. 3.2.13b) and $C_{HV} = \rho_v \cdot C_{VV}$ (Eq. 3.2.14). The depolarization ratio, ρ_v , for flame gases is in the range from 0.0 to 0.05 (D'Alessio, 1981; Bogaard et al., 1978). Thus, the scattered signal from horizontally polarized incident light would be at most 5% of the scattered signal from vertically polarized incident light.

3.3.3 Quenching

Relative OH number density profiles can be determined from the measured OH fluorescence profiles if the quenching rate coefficient is known throughout the flame. The

optical system constants and the laser irradiance terms in the expression for the fluorescence signal (Eqs. 3.3.9 and 3.3.10) are assumed to remain constant throughout the flame or to be known from experimental measurement. Comparisons between relative OH number density profiles measured in different flames can be made if the variation in quenching rate coefficient between flames is known.

The total quenching rate coefficient can be calculated by (Garland and Crosley, 1986)

$$Q = \sum_k N_k \cdot \sigma_{Qk} \cdot v_k \quad (3.3.14)$$

where N_k (cm^{-3}) is the number density of species k , σ_{Qk} (cm^2) is the quenching cross-section for species k , and v_k ($\text{cm}\cdot\text{sec}^{-1}$) is the relative velocity between species k and the quenched species. The quenching rate coefficient depends on the flame environment through the temperature and the local concentrations of the quenching species. In addition, the quenching cross-sections vary with both rotational level and temperature (Garland and Crosley, 1986). Since quenching cross-sections have been measured for only a few major combustion species at flame temperatures, calculations of the quenching rate coefficient using Eq. (3.3.14) can only be approximate.

Measurements suggest that the quenching rate coefficient for the OH radical remains approximately constant throughout a single flame and among similar flames. Stepowski and Cottereau (1981) measured the collisional lifetimes of OH in propane/oxygen flames at pressures from 15 to 80 torr to determine profiles of the quenching rate coefficient. They concluded that a mean constant quenching rate coefficient could be used through the reaction and burnt gas zones in a given flame. Anderson, Decker, and Kotlar (1982) suggested that the overall quenching rate coefficient was constant in atmospheric pressure $\text{CH}_4/\text{N}_2\text{O}$ flames based on agreement between OH concentration profiles measured by absorption and fluorescence. Schwarzwald,

Monkhouse, and Wolfrum (1988) measured collisional lifetimes of OH in atmospheric pressure methane/air flames for equivalence ratios from 0.77 to 1.43. They found that the lifetimes were constant throughout each flame and did not vary with equivalence ratio.

These studies suggest that the assumption of a constant quenching rate coefficient can be justified for the flames of this study. If this assumption is correct, then the measured fluorescence profiles can be considered to be relative OH number density profiles.

3.3.4 Calibration

Conversion of the relative OH number density profiles to absolute OH number density profiles requires a calibration to determine the constants in the equations for the fluorescence signal voltage, Eqs. (3.3.9) and (3.3.10). This calibration can be done by measuring the fluorescence signal with the same optical and electronic detection system for a flame with a known OH number density. Lucht, Sweeney, and Laurendeau (1985) calibrated their fluorescence signal in a lean methane flame where the OH concentration had been measured with UV absorption. Miller et al. (1990) calibrated their fluorescence signal in a hydrogen/oxygen flame for which they could calculate the OH concentration accurately with a numerical simulation of the flame using a detailed chemical kinetics model. An OH number density could also be obtained in a rich flame by calculating the equilibrium OH concentration in the post-flame region. This method of calibration may be subject to error because the OH concentrations are low in the post-flame zone and thus the signal to background ratio may be too low.

3.4 Summary

We have reviewed methods for measurement of the soot and OH radical concentration profiles in the transition from nonsooting to sooting conditions in premixed flames. The laser scattering-extinction method can be used to measure profiles of soot

volume fraction, number density, and particle size in these flames. We have presented the theory of the laser scattering-extinction method when the particle sizes are in the Rayleigh regime. The volume fraction of the soot in the flame can be determined from the extinction coefficient. The soot particle number density and particle size can be determined from the extinction coefficient and the scattering coefficient. Molecular scattering, fluorescence, and gas-phase absorption interfere with the measurement of particle scattering and extinction in sooting flames. However, these background interferences can be quantified and subtracted from the overall signal to obtain the contributions caused by the soot particles alone. The relative concentration and location of unidentified PAH species can be measured using argon-ion laser induced fluorescence.

Both the particle size distribution and the particle index of refraction must be assumed in this analysis to determine the volume fraction, number density, and particle size. The particle size distribution may be assumed to be lognormal, because previous work indicates that this distribution fits the measured particle size distributions in premixed sooting flames. Beyond the particle inception stage, the moment ratios of the particle size distribution approach those of a self-preserving size distribution.

The appropriate particle index of refraction is not as clear-cut, because the index of refraction depends on the H/C ratio of the soot and the degree of agglomeration. A good assumption for the index of refraction is the value determined for the primary particles of the agglomerate by Dobbins, Santoro, and Semerjian (1990), since agglomeration is reduced in lightly sooting flames near the critical equivalence ratio. Comparison of volume fraction profiles should consider the possible errors introduced by the assumption of a particle index of refraction.

The OH radical concentration profiles can be measured with a broadband laser-induced fluorescence technique. We have presented the equations that relate the measured OH fluorescence signal to the OH concentration. Background interferences

from laser scattering or broadband fluorescence from other species can be quantified and subtracted from the signal. The relative OH fluorescence profiles may be considered to be relative OH concentration profiles because the overall quenching rate coefficient remains approximately constant throughout a premixed flame and also as a function of the equivalence ratio. The absolute OH concentration can be determined from the relative OH concentration by calibrating the measurement system using a known OH concentration.

CHAPTER 4: EXPERIMENTAL APPARATUS AND METHODS

4.1 Introduction

Incipient soot formation was investigated by examining a set of laminar flat premixed ethylene flames at both atmospheric and subatmospheric (80 torr) pressures. The equivalence ratio, total flow rate, and dilution ratio ($\dot{V}_{N_2}/\dot{V}_{O_2}$) were varied to produce a sequence of flame conditions ranging from rich nonsooting to sooting. The laser scattering-extinction method was used to measure the soot volume fraction and number density profiles (i.e., as a function of height above the burner) in each flame. Scattering-extinction measurements in nonsooting regions of the flames were used to estimate the temperature profile. Broadband argon-ion laser-induced fluorescence profiles were used to estimate relative polycyclic aromatic hydrocarbon (PAH) concentrations.

The OH radical concentration profiles were measured with a broadband laser-induced fluorescence technique. These measurements were made in a subset of the flames examined with the laser scattering-extinction method. The absolute concentration profiles were determined from the measured relative fluorescence profiles by calibration in a lean flame.

Chemical kinetic modelling of these flames was used to calibrate the OH fluorescence measurements and to estimate the flame temperature profiles. For the initial modelling studies, an existing reaction mechanism for ethylene oxidation was used with the Sandia premixed one-dimensional flame code to predict the temperature and species

concentration profiles. The initial modelling studies served as the basis for further modelling using a reaction mechanism that modelled the formation of single-ring aromatic species.

In this chapter, we first describe the premixed flat-flame burner system used in all the experiments. This description includes the design of the flat-flame burner, the mounting of the burner in the computer-controlled two-axis translation system, and the gas flow delivery system. The differences between the burner system configuration used at atmospheric pressure and that used at subatmospheric pressure are also described. We then summarize the flame conditions examined in this study.

Next, the laser scattering-extinction measurements and the broadband laser-induced fluorescence measurements are described. For both techniques, the implementation of the method is discussed, the optical and the electronic data acquisition setups are described, and then the procedures used in the experiments and in the subsequent data analyses are outlined.

Finally, we describe the implementation of the Sandia premixed one-dimensional flame code and the solution procedure to obtain the species concentration profiles for our flame conditions.

4.2 The Flat Flame Burner System

The flat-flame burner system consisted of (1) a premixed honeycomb frit burner, (2) a mounting system for the burner with accurate computer-controlled positioning in both the vertical and horizontal directions, (3) a gas delivery system to supply accurate metered flow of the feed gases, (4) a pressure vessel and a vacuum-pump driven exhaust system to operate the burner at subatmospheric pressures, and (5) a flame stabilizer and a blower-driven exhaust system to operate the burner at atmospheric pressures. These components of the burner system are described in order in the following sections.

4.2.1 The Flat Flame Burner

The premixed flat-flame burner consisted of a honeycomb flameholder within a sintered bronze guard flow ring mounted in a stainless steel guard flow housing. The burner and housing were mounted on a plenum tube which mixed and straightened the flow of the feed gases before they entered the burner. A cutaway view of the burner is shown in Figure 4.1.

The burner design was a modification of a burner used in a study of the critical equivalence ratio of premixed flames (Harris, King, and Laurendeau, 1986) and in a set of preliminary measurements of the OH concentration in subatmospheric sooting flames (Inbody et al., 1986). The design was modified to operate leaktight at subatmospheric pressures and to work with a new translation system to more accurately position the burner.

The flameholder was a 5.9 cm diameter, 3.8 cm (1.5 in.) thick honeycomb plug cut from a Hastelloy-X honeycomb fabricated by Kentucky Metals, Inc., New Albany, IN. The honeycomb was made of 0.05 mm (0.002 in.) thick metal formed into a pattern of 0.8 mm (1/32 in.) hexagonal tubes (as measured across the flats of the hexagons). The honeycomb plug was held in a stainless steel sleeve and was pressed against the upper lip of the sleeve by a threaded retainer ring. The inside diameter of the sleeve's upper lip (5.6 cm) defined the flow area of the burner (24.6 cm²), which was used for calculations of the cold flow velocity and the mass fluxes required by the flame code.

The original purpose for using the honeycomb burner instead of a more commonly used sintered-metal burner was so that the flame could be seeded with sodium chloride to measure flame temperatures with the sodium d-line reversal technique. The honeycomb burner also had a further advantage in that when used for sooting flames it would become clogged with soot and could be easily cleaned. A disadvantage of the honeycomb plug was that the flame could stabilize in the burner since the hole size was too large to quench

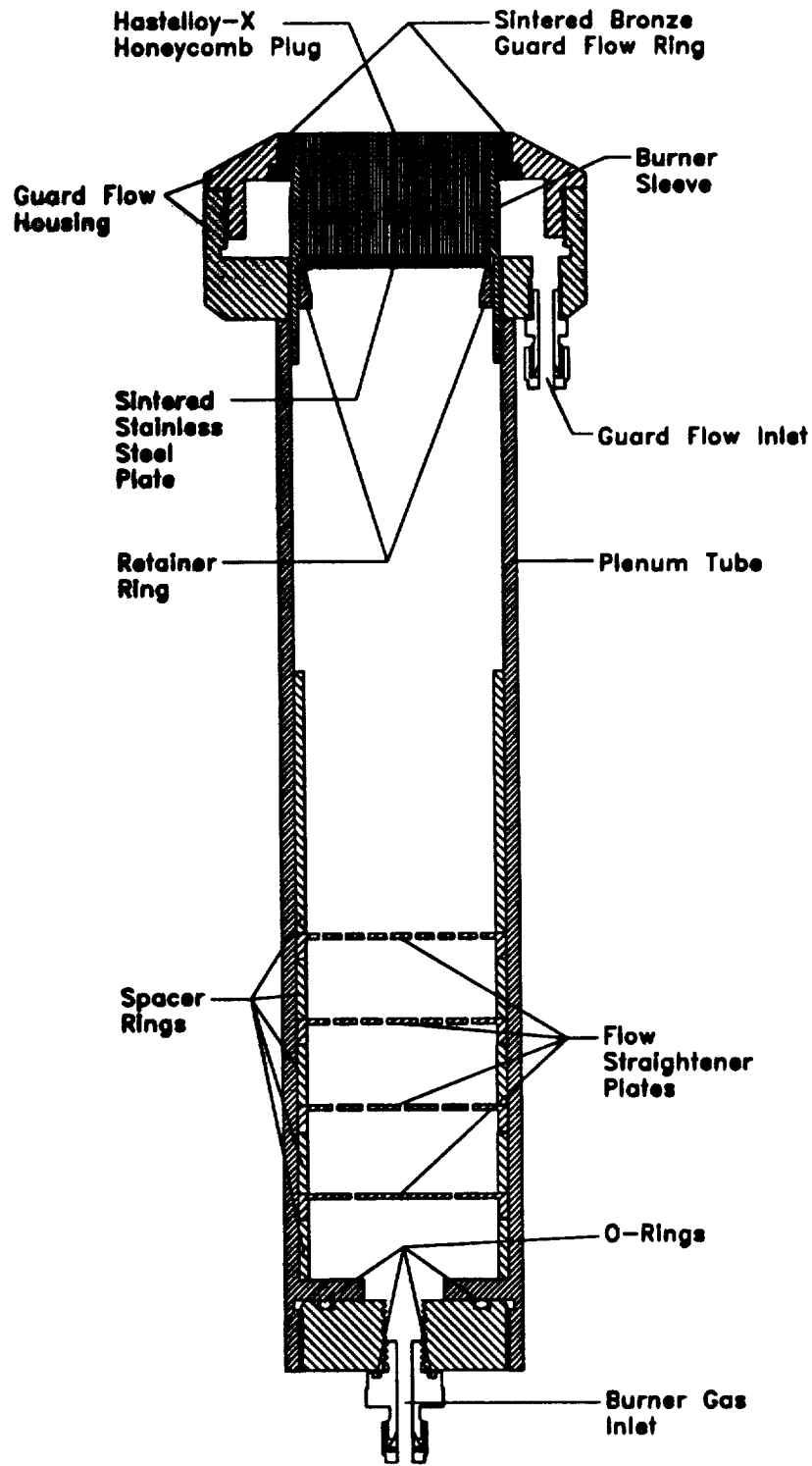


Figure 4.1 Cutaway view of the honeycomb plug flat flame burner.

the flame and thus the flame could flashback into the plenum chamber. To prevent flashback, a 3.2 cm (1/8 in.) thick sintered stainless steel disk (100 μ m pore size) was placed below the honeycomb plug and held in place by the threaded retainer ring. When seeding flames, the sintered disk could easily be removed from the burner.

The guard flow around the flame was supplied through a 1.3 cm (1/2 in.) width sintered bronze guard flow ring (McKenna Products, Inc., Pittsburg, CA). The guard flow ring was held even with the burner surface by the stainless steel guard flow housing. The lower half of the housing screwed onto the burner sleeve. The upper half screwed into the lower half and thus pressed and sealed the guard flow ring against the burner sleeve. The nitrogen flow through the guard ring was supplied through a 1/4 in. Swagelok male connector into the plenum of the guard flow housing. The design of the guard flow housing was similar to that of a 6.0 cm diameter McKenna Burner.

The head of the burner, consisting of the guard flow housing and the burner sleeve containing the flameholder, screwed into the top of an aluminum plenum tube 33.0 cm (13 in.) long with a 7.56 cm (2.975 in.) outside diameter and a 6.67 cm (2.625 in.) inside diameter. A 2.23 cm (7/8 in.) thick aluminum plug screwed into the bottom of the plenum tube and sealed the tube with an O-ring. The burner feed gases entered the plenum tube through a 1/4 in. O-ring sealed Swagelok fitting in this bottom plug.

Within the plenum tube, four flow straightener disks mixed and smoothed the flow of the burner feed gases. The 1.59 mm (1/16 in.) thick, 6.65 cm (2.620 in.) diameter brass disks were held apart at 2.54 cm (1 in.) intervals with brass spacer rings starting at 2.54 cm (1 in.) above the bottom plug. The gases passed through 1.59 mm (1/16 in.) diameter holes drilled in each disk. The number of holes in each disk increased from 4 to 8 to 17 to 33 holes from the bottom disk to the top disk. An 8.25 cm (3 1/4 in.) long spacer ring placed above the top disk kept the plates from floating up to the base of the burner plug during operation of the burner at subatmospheric pressures.

4.2.2 Burner Mounting and Translation System

The plenum tube connected the burner into the computer-controlled translation system that moved the burner both vertically and horizontally relative to the optical measurement axis. The translation system was designed to work within the constraints of an existing pressure vessel for subatmospheric pressure experiments. The vertical translation range was realized by translating the burner through a sliding O-ring seal within the pressure vessel, while both the burner and the vessel were translated horizontally to realize the necessary horizontal range. Both the horizontal and vertical translation mechanisms used linear bearings riding on rigidly fixed bearing shafts to reduce the friction and the required torque to move the burner and also to maintain the rigidity of the system necessary for precision positioning. Computer-controlled stepper motor-driven worm gear drives positioned the burner both vertically and horizontally. A side view of the translation system in Figure 4.2 shows the elements of the vertical translation mechanism. The elements of the horizontal translation mechanism are shown in the top view of the translation system in Figure 4.3.

The mounting point for the translation mechanisms was the pressure vessel base plate, a 25.4 cm (10 in.) by 30.5 cm (12 in.) by 1.91 cm (3/4 in.) thick aluminum plate. The horizontal translation mechanism mounted the pressure vessel base plate on the optical table. The vertical translation mechanism was attached to the bottom of the base plate and thus moved with it when the base plate was translated horizontally.

The burner was moved vertically by moving the plenum tube through a double O-ring seal in a flange bolted to the center of the base plate. Since the plenum tube was the sliding surface in the O-ring seal, the aluminum tube was hard anodized to prevent surface scratches that would defeat the seal and increase the sliding friction. The plenum tube was rigidly constrained to be vertically aligned with the flange O-ring seal by fixing the bottom of the tube to a bearing mount with three linear bearings riding on three

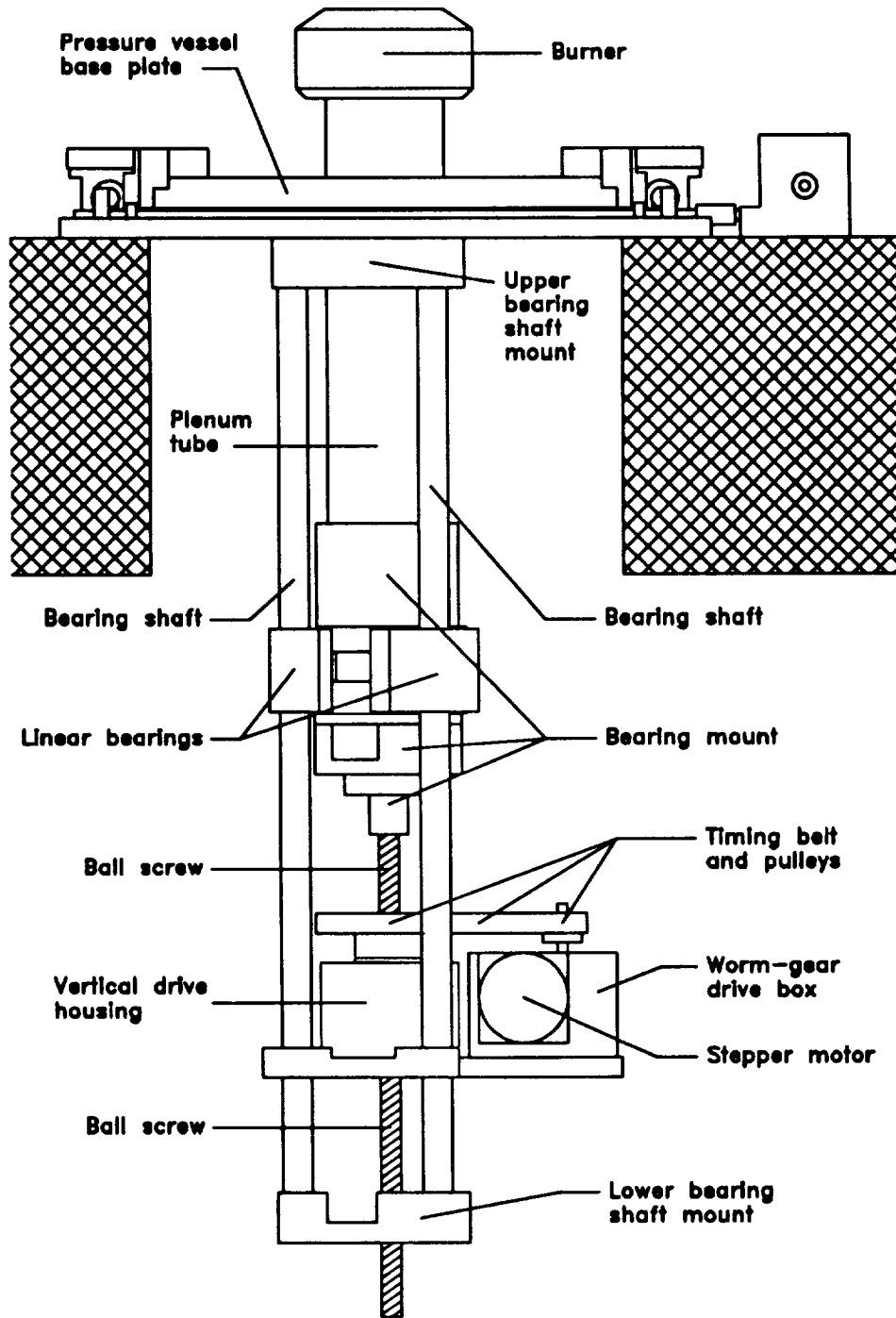


Figure 4.2 Side view of the translation system showing the elements of the vertical translation system. The horizontal translation mechanism elements are shown but not labelled.

parallel 1.91 cm (3/4 in.) diameter, 61.0 cm (24 in.) long shafts. These bearing shafts formed a triangular frame held at the ends by bearing shaft mounts. The top of the frame bolted to the flange in the base plate. The linear bearings constrained the lateral movement while reducing the friction in the vertical direction so that the dominant resistance to the vertical movement of the burner was the friction of the O-ring seal.

The plenum tube and the burner were positioned vertically with a precision ball screw manufactured by Thomson Industries, Inc., Port Washington, NY. The Thomson Star ball screw, 305 mm long with a 16 mm diameter and a 5 mm per revolution lead, was used because of its lead accuracy (lead error: 50 μm per 300 mm length) and because its ball screw nut could be preloaded to reduce backlash. The top end of the ball screw bolted to the base of the bearing mount, while the bottom end floated free; the ball screw nut was held between two angular contact bearings in the vertical drive housing. The ball screw was moved vertically by rotating the ball screw nut with a 3/8-inch pitch Flex-E-Grip timing belt-pulley mechanism (Winfred M. Berg, Inc., East Rockaway, NY). A 30-tooth pulley was fixed to the ball screw nut with an adapter and was driven by the timing belt with a 10-tooth pulley. A stepper motor (Superior Electric Slo-Syn model M061-FC08; 200 steps per revolution) drove the drive pulley through a precision four-thread worm and a 100-tooth anti-backlash worm gear mounted in a drive box. This combination of gears required 3000 steps of the stepper motor to move the burner vertically 1 mm for an effective resolution of 0.33 μm per step.

The ball screw vertical drive housing and the gear drive box were mounted on a plate attached to the bearing shaft frame with adjustable clamps. The position of the plate could be moved to adjust the center of the vertical translation range. The burner vertical position was read from a dial indicator with a 150 mm range and a 0.01 mm resolution. The dial indicator was clamped onto a bearing shaft and sensed the position of the bearing mount holding the burner.

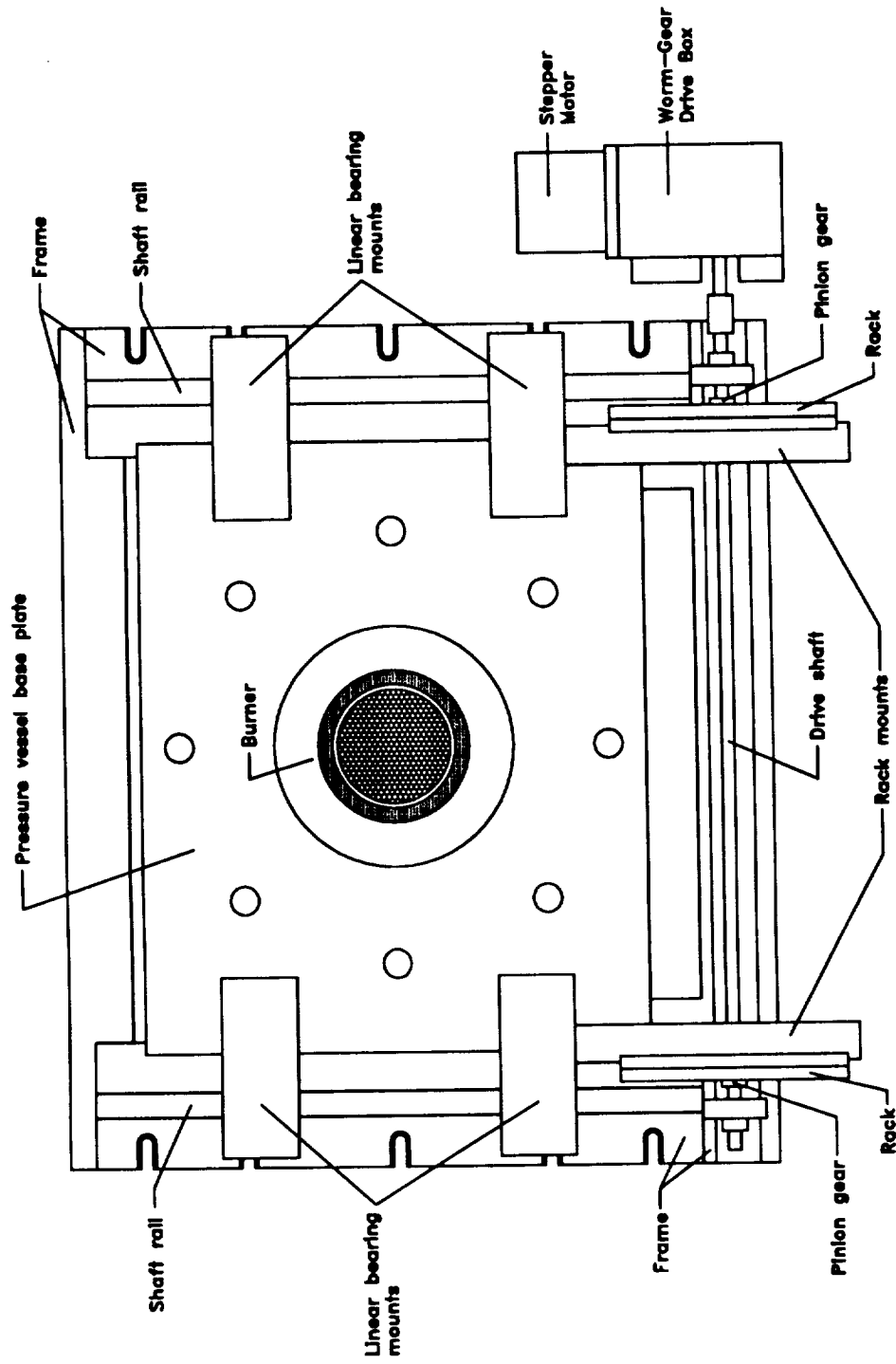


Figure 4.3 Top view of the translation system showing the elements of the horizontal translation system. The vertical translation mechanism elements are hidden by the pressure vessel base plate.

The horizontal translation mechanism (Fig. 4.3) supported the pressure vessel base plate on two 12 inch long, 1/2 inch diameter bearing shaft rails mounted on an aluminum frame bolted to the optical table. The base plate rode on linear bearings on these rails, so that the weight of the burner, pressure vessel, and the vertical translation mechanism was supported with only a minimal frictional resistance to horizontal movement. The frame was bolted to the optical table with the base plate centered over a 12 inch diameter hole in the optical table, so that the vertical translation mechanism hung down below the table.

The burner was moved horizontally by moving the base plate relative to the frame with a rack and pinion drive system assembled from parts manufactured by Winfred M. Berg, Inc. Two precision racks, each 4 inches long with a 1/20 inch pitch and mounted on one end of the surface plate, were driven by pinion gears (40 teeth, 1/20 inch pitch) mounted on a 1/4 inch drive shaft running the length of the frame. The shaft was rotated on one end by a stepper-motor worm-gear drive box containing a stepper motor (Superior Electric Slo-Syn model M061-FC08; 200 steps per revolution), a double-thread worm and a 64-tooth, anti-backlash worm gear. The translation mechanism required 126 steps of the stepper motor to move the burner 1 mm horizontally for an effective horizontal resolution of 8 μm per step. The effective horizontal translation range was 7.6 cm (3 in.), about the diameter of the pressure vessel windows. The horizontal position of the base plate and, thus, the burner was read from a dial indicator with a 100 mm range and a 0.01 mm resolution.

4.2.3 Gas Delivery and Metering System

The fuel, oxidizer, diluent and guard flows were supplied to the burner by the gas delivery and metering system. This system also supplied a nitrogen flow for purging of the pressure vessel windows during subatmospheric operation of the burner.

The gas delivery and metering system used electronic mass flow controllers to achieve repeatable flow rates for the fuel, oxidizer, and diluent flows. In a set of preliminary experiments, rotameters were used to control the flow rates. Scattering-extinction measurements made in these flames showed significant variations in the soot concentration in what were thought to be the same flame conditions (i.e., at the same flow rate settings) despite care in setting the flow rates. These variations were attributed to a lack of precision of the rotameters. To achieve the desired repeatability in the flame conditions, electronic mass flow controllers were used to set the flow rates more precisely and to achieve a better repeatability ($\pm 0.25\%$) in the flow rates compared to that of the rotameters ($\pm 1.0\%$). The schematic of the gas delivery and metering system is shown in Figure 4.4. A description of the system follows.

In all the experiments, the fuel was ethylene, C.P. grade (99.5% pure, minimum), in cylinders obtained from Matheson Gas Products, Inc.. The oxidizer was oxygen, commercial grade (99.5% pure). The diluent and guard flows were supplied by nitrogen, high purity dry (99.995% pure). Both the oxygen and nitrogen were supplied through the Purdue University Materials Management and Distribution system.

Both the ethylene and oxygen flows were supplied and metered through similar setups. The cylinder pressure regulators were typically set to 150-180 psig. From the cylinders, the gases were supplied to a control panel through 1/4 inch stainless steel tubing. At the control panel, a plug valve was used for positive on/off flow control. Downstream from the plug valve, an instrument pressure regulator (Linde SG4820 0-200 psig single-stage low pressure instrument regulator) accurately regulated the inlet pressure to the mass flow controller. A pressure gage downstream from the instrument regulator was used to set the regulator outlet pressure to 120 psig. A 2-micron filter (Nupro TF tee type removable filter) at the inlet to the mass flow controller trapped particles that might otherwise clog the capillary tube in the mass flow controller. The

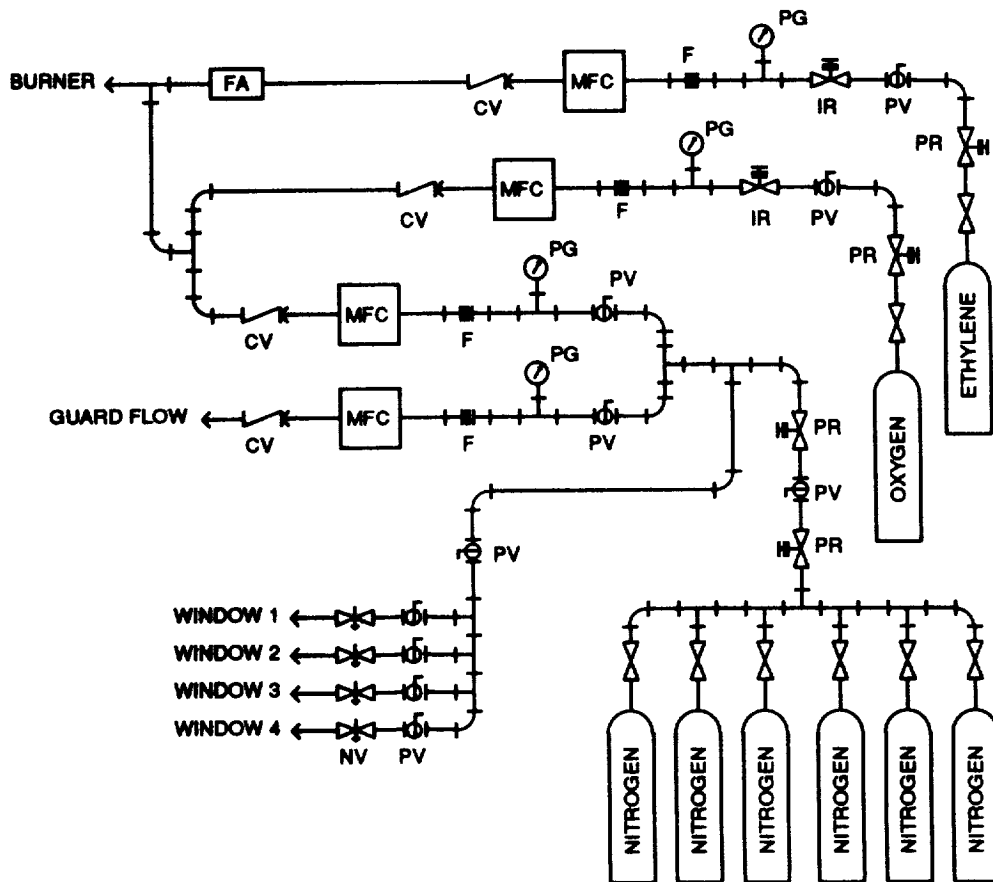


Figure 4.4 Schematic of the gas delivery and metering system. Components: PR - pressure regulator; PV - plug valve; IR - instrument pressure regulator; PG - pressure gauge; F - filter; MFC - mass flow controller; CV - check valve; FA - flashback arrestor; NV - needle valve.

mass flow controllers used were Linde Standard Mass Flow Control Modules controlled by a Linde FM 4575 Mass Flowmeter/Flow Controller. The oxygen mass flow controller was a module 13C rated and calibrated at a maximum of $5000 \text{ cm}^3 \cdot \text{min}^{-1}$ (STP) of oxygen. The ethylene mass flow controller module was a module 13C rated and calibrated at a maximum of $2000 \text{ cm}^3 \cdot \text{min}^{-1}$ (STP) of ethane. A check valve (Nupro inline check valve 1/3 psi) at the outlet of each mass flow controller prevented back flow from the other gas supply lines. The gases then flowed through 1/4 inch stainless steel tubing to the burner.

The nitrogen for the diluent, guard, and window purge flows was supplied from a 6-cylinder manifold. The nitrogen was supplied to the control panel through 1/4 inch stainless steel tubing at approximately 200 psig as set by the manifold pressure regulator. At the control panel, a plug valve was used for positive on/off control of the nitrogen flow. A single-stage pressure regulator (Linde SG3800 single-stage low-flow regulator) was used to control and set the inlet pressure at 140 psig to the diluent flow, guard flow, and window purge flow lines. Downstream from the pressure regulator, the diluent flow, guard flow, and window purge flow lines were split off from each other.

The diluent flow and the guard flow were supplied and metered through similar setups. A plug valve was used to turn on and off the flow and to provide positive shut-off of the flow. Downstream from the plug valves, pressure gages monitored the inlet pressure to the mass flow controllers. At the inlet of the mass flow controllers, 2-micron filters prevented particulates from entering the controller. A Linde Standard Flow Control Module 16C rated at $0\text{-}20 \text{ l} \cdot \text{min}^{-1}$ (STP) for nitrogen controlled the diluent flow rate. A Standard Flow Control Module 18C rated at $0\text{-}50 \text{ l} \cdot \text{min}^{-1}$ (STP) for nitrogen controlled the guard flow rate. Check valves at the outlet of the flow controllers prevented backflow through the mass flow controllers. Similar to the oxygen and ethylene flows, the diluent and guard flows were transported to the burner through 1/4 inch stainless steel tubing.

Before entering the burner, the diluent and oxygen flows were combined. The ethylene flow passed through a flashback arrestor (Matheson series 6103 flash arrestor) and then combined with the diluent and oxygen flows. The three combined flows then flowed into the base of the burner plenum chamber through a stainless steel flexible hose.

The guard flow was routed in a 1/4 inch Tygon hose through the pressure vessel base plate and then to the Swagelok connector on the burner guard flow housing. The feedthrough in the base plate was a 1/4 inch Swagelok connector drilled out to a 1/4 inch clearance. The Swagelok connector sealed against the Tygon hose backed by a 1/2 inch long section of 3/16 inch outside diameter brass tube inserted into the Tygon hose.

The window purge flow was used only when the burner was operated at subatmospheric pressures. The window purge flow was routed separately from the diluent and guard flow lines to its own control panel. A plug valve at the inlet to the control panel was used to turn on and off the flow to all four windows. The flow was then split into a flow for each of the four windows. For each window flow, a shut-off valve controlled the flow and a needle valve (Nupro S-series 1/8 inch fine-metering valve) set the flow rate to the window. The flows from the control panel went through 1/4 inch polyethylene tubing to each window.

The mass flow controllers were calibrated at the inlet and outlet pressure settings and over the range of flow rates used in the experiments. This calibration was necessary because the pressure settings used in the experiments were different from the factory calibration settings and also because the fuel mass flow controller was originally calibrated for ethane instead of ethylene, the fuel used in these experiments.

The flow controllers were calibrated with a dry test meter (Singer-American DTM-115) for flow rates greater than $0.6 \text{ l}\cdot\text{min}^{-1}$ and with a 500 ml bubble flow meter (Supelco) for flow rates less than $1.2 \text{ l}\cdot\text{min}^{-1}$. The temperature of the gas flow was

measured with a thermocouple and the exhaust pressure was measured with an absolute pressure gauge. The measured temperature and pressure were used to correct the measured flow rates to STP flow rates (at 25°C and 1 atm).

The calibrations obtained using the dry test meter and the bubble meter were compared by measuring a series of flow rates from 0.6 l·min⁻¹ to 1.2 l·min⁻¹ with both meters. The calibrations showed that the dry test meter measured flow rates were consistently 4% lower than the flow rates measured with the bubble flow meter. The dry test meter flow rates were then adjusted based on the comparison between the bubble flow meter and the dry test meter.

4.2.4 Subatmospheric Pressure Operation of the Burner

To examine flames at subatmospheric pressure conditions, the burner was enclosed in a pressure vessel connected to a vacuum pump driven exhaust system. A cutaway view of the pressure vessel is shown in Figure 4.5. Figure 4.6 is a schematic of the exhaust system.

The pressure vessel was an aluminum tube, 45.1 cm (17.75 in.) tall with a 15.24 cm (6 in.) inside diameter and a 20.32 cm (8 in.) outside diameter, welded to flanges at both ends. The 24.13 cm (9 1/2 in.) diameter bottom flange bolted to the pressure vessel base plate. A 27.94 cm (11 in.) diameter, 2.54 cm (1 in.) thick blind aluminum flange bolted to the top flange of the vessel. The flange connections were sealed with O-ring seals. The vessel exhaust exited through the top blind flange through a 1 in. stainless steel Swagelok connector. Four 1/4 in. NPT threaded holes in the top blind flange allowed access to the vessel chamber for two pressure gauges, a thermocouple, and a pressure relief valve.

The pressure vessel windows were mounted on four 7.62 cm (3.0 in.) diameter access ports 90° apart and centered 22.23 cm (8.75 in.) above the base plane of the vessel. A nitrogen purging system, based on a design by Crumley and Gole (1986), was built into the window mounts to prevent deposition of soot or other condensates on the windows.

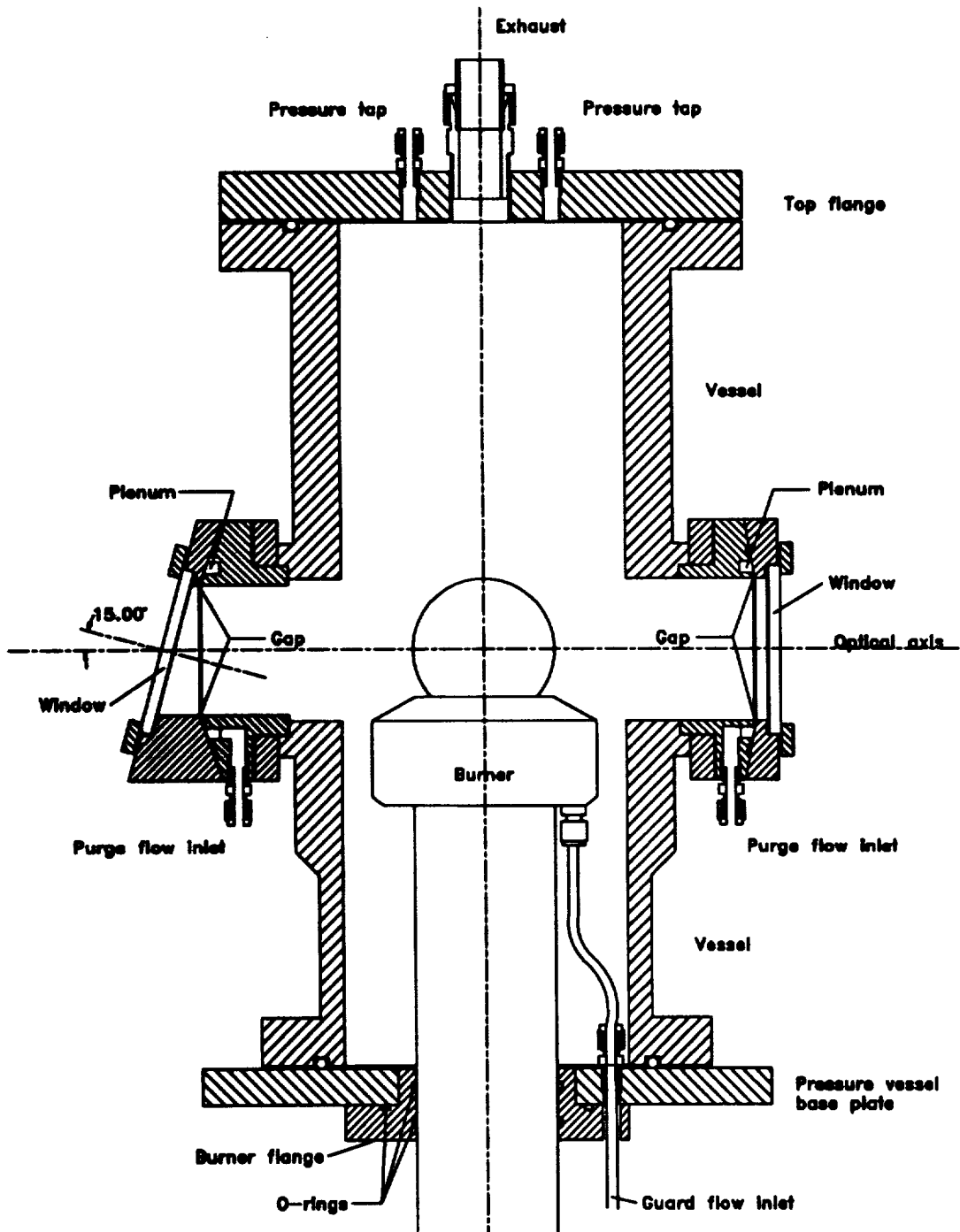


Figure 4.5 Cutaway view of the pressure vessel showing sections of the pressure vessel at 90° to each other to display the two types of window mounts.

A cross-section of these window mounts can be seen in Figure 4.5. Each window mount consisted of two circular flanges with their mating faces having matching conical surfaces. A circumferential slot was cut into the inner conical surface to form a plenum between the mating surfaces of the flanges. Nitrogen fed into this slot flowed to the window surface through a 0.076 mm (0.003 in.) gap between the conical surfaces. The angle of the conical faces directed the nitrogen flow toward the center of the window. The windows were 90.8 mm (3.575 in.) diameter, 6.35 mm (1/4 in.) thick optical flats made of either A1 quartz or fused silica. Retainer rings held the windows in place against the O-ring seals in the window mounts. The two windows where the laser beam entered and exited the vessel were tilted at a 15° angle to reduce back reflections of the laser beam.

The nitrogen purging of the windows prevented soot build-up on three of the windows, but could not prevent a deposit from forming on the window where the laser beam exited from the vessel. This deposit may have been caused by an uneven flow pattern which allowed soot to reach the window and might have been prevented by significantly increasing the nitrogen flow, but that would also have disturbed the flame.

The exhaust from the pressure vessel was drawn through 1 in. O.D. brass tubing and was routed to a control panel. A manually-operated stainless steel regulating valve with an 0.437 in. orifice regulated the exhaust flow and thus controlled the pressure in the vessel. Upstream from the regulating valve, a tee in the line allowed atmospheric pressure air to bleed into the system. A regulating valve in this line controlled the amount of bleed air let into the exhaust stream. A toggle shut-off valve in the bleed air line also was used to bring the pressure vessel back up to atmospheric pressure.

Downstream from the exhaust regulating valve, a ball valve with a 0.406 in. orifice provided positive shut-off of the vessel from the vacuum system. From the ball valve the

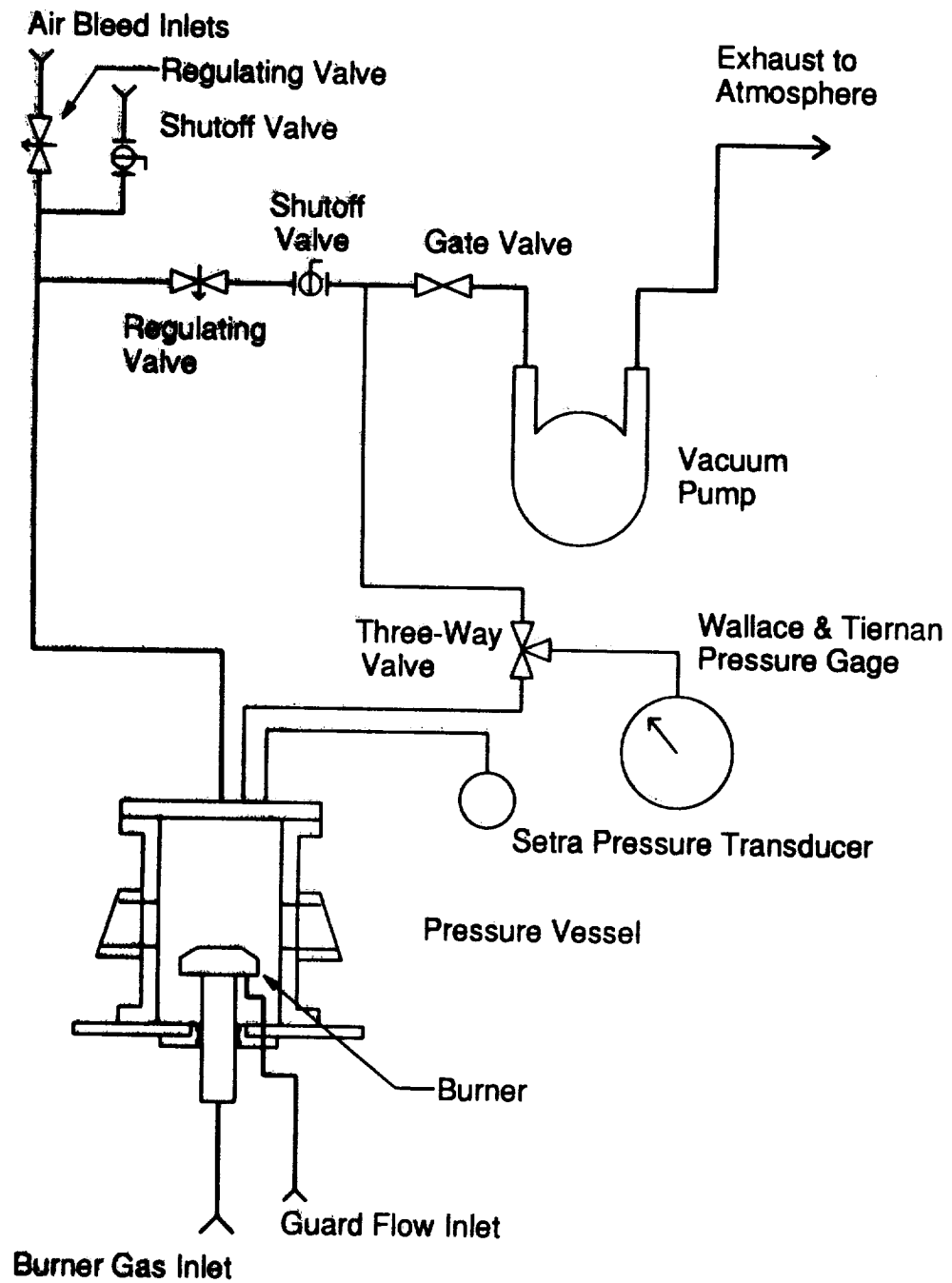


Figure 4.6 Schematic of the vacuum pump driven exhaust system for subatmospheric pressure operation of the burner.

exhaust passed through 1 in. O.D. tubing to the 2 in. piping of the inlet header and then through an inlet gate valve to the vacuum pump. The vacuum pump was a Kinney KDH-80 rotary piston vacuum pump.

Two pressure gauges monitored the pressure in the pressure vessel. A Wallace and Tiernan Series 300 absolute pressure gauge with a range of 0 to 800 torr monitored the pressure through 1/4 in. tubing connected to the top of the pressure vessel. This gauge had a specified accuracy of 0.33% full scale (2.6 torr) and a specified sensitivity of 0.2% full scale (1.6 torr). The second pressure gauge, a Setra Model 205-2 Pressure transducer with a range of 0 to 25 psia, was connected to a tap in the top of the pressure vessel through a 6 in. length of 3/8 in. tubing. This transducer output was monitored with a voltmeter. The specified accuracy of the pressure transducer was $\pm 0.11\%$ full scale (± 1.4 torr) with a non-repeatability of $\pm 0.02\%$ (± 0.3 torr).

The pressure in the vessel was controlled by adjusting the regulating valve and observing the pressure with the pressure gauges. The pressure for the 80-torr flames was set by adjusting the regulating valve until the Wallace and Tiernan pressure gauge read 80 torr. Then, at that pressure, the voltage output was read from the Setra pressure gauge and used as the setpoint when the regulating valve was adjusted to maintain the pressure at 80 torr. The nonsooting and lightly sooting flames usually did not require valve adjustments to maintain the pressure. However, heavier sooting flames required frequent adjustments of the valve as the soot depositing on the internal surfaces of the valve effectively changed its orifice size. Control of the bleed air flow could be used to partly alleviate the problem by diluting the exhaust stream passing through the valve.

During preliminary experiments, the scattering signal from sooting flames varied significantly if the pressure varied by as little as two torr. Because of this observed pressure dependence, the pressure was controlled to keep it within ± 0.5 torr of the 80-torr

setpoint. An automatic pressure control with an absolute accuracy better than ± 0.5 torr would circumvent this problem and would also improve the reproducibility of the pressure setting from day to day.

The apparatus for subatmospheric pressure operation of the burner was not well adapted for handling sooting flames. Soot deposition within the exhaust system, particularly in the constricted flow regions of the valves, made it difficult to hold the pressure constant. Because of soot deposition, the exhaust system required frequent cleaning. Since the soot was not removed from the exhaust, it contaminated the vacuum pump oil, and caused additional wear on the vacuum pump.

During experiments on the more heavily sooting flames, a cloud of soot particles would build up in the stagnant regions of the pressure vessel. This soot 'fog' would increase the deposition of soot on the windows and would also contribute to the extinction of the laser beam passing through the vessel, and thus interfere with the extinction measurements.

Problems with the soot 'fog' and soot deposition could be alleviated through some major modifications to the system. The soot 'fog' might be prevented if a bath flow of nitrogen was added at the bottom of the pressure vessel. This extra flow would help prevent buildup of soot on the windows, but it would place an extra load on the vacuum pump.

Typical design practice for the inlet plumbing of vacuum pumps suggests that the inlet piping should be the same diameter as that of the vacuum pump. To implement this, the pressure vessel exhaust piping should be changed from 1 in. tubing to 2 in. piping. Although this would make the system more physically cumbersome, it would decrease the pressure losses and would also decrease the effects of soot deposition within the system. Larger diameter piping would also require larger control valves.

An obvious solution to prevent soot build-up within the piping, valves, and vacuum pump oil would be to install a filter or trap to remove the soot from the exhaust. An alternative might be to change to a liquid jet vacuum pump that would tolerate a contaminated exhaust stream better than the rotary piston vacuum pump.

A final suggestion that would not improve the experiment itself, but that would improve the environment outside the laboratory would be to include an oil mist eliminator on the exhaust of the vacuum pump. During experiments, the pump would emit a cloud of fine oil droplets much like the exhaust of a car that is burning oil. The oil mist could be removed by installing an oil mist eliminator on the exhaust of the vacuum pump.

4.2.5 Atmospheric Pressure Operation of the Burner

The configuration of the burner system was simpler for atmospheric pressure operation than for subatmospheric pressure operation. The pressure vessel was removed and the burner was operated open to the room. The burner exhaust gases were drawn into a sheet metal duct by a blower (a portable fume exhauster) and then exhausted to the outside of the laboratory.

To stabilize the atmospheric pressure flames, a 7.62 cm (3 in.) square by 1.27 cm (1/2 in.) thick Hastelloy-X honeycomb (the same material as the burner's honeycomb plug) was mounted 40 mm above the burner surface with a mounting fixture attached to the burner guard flow housing. The fixture consisted of a mounting ring held in place by bolts screwed against the guard flow housing. Four optical posts, 3 in. long, screwed into the mounting ring. The honeycomb was suspended over the burner with hooks made from piano wire which bolted to the four optical posts. The height of the stabilizer above the burner could be varied by moving the position of the mounting ring on the guard flow housing.

4.3 Summary of Flame Conditions

In this study, a series of flat, premixed, laminar ethylene/oxygen/nitrogen flames was examined with conditions ranging from rich nonsooting to sooting at both atmospheric and subatmospheric (80 torr) pressures. The flow rates of ethylene, oxygen, and nitrogen were chosen to obtain a specific equivalence ratio, cold flow velocity, and dilution ratio for each flame.

The equivalence ratio is defined as the actual ratio of the ethylene to oxygen flow rates divided by the stoichiometric ratio. The cold flow velocity (v_c , $\text{cm}\cdot\text{sec}^{-1}$) is defined as the total flow rate of the ethylene, oxygen, and nitrogen flows at 25 °C and at the pressure of the experiment divided by the cross-sectional area of the burner (24.6 cm^2). The dilution ratio (D) is the ratio of the flow rate of nitrogen to the flow rate of oxygen.

The goal of the experiments was to measure the change in the soot and hydroxyl concentration profiles as the flames changed from rich nonsooting to heavily sooting conditions. To do this, the general approach was to examine a sequence of flames in which the cold flow velocity and dilution ratio were held constant, while the equivalence ratio was varied.

The equivalence ratios, cold gas flow rates, cold flow velocities, and dilution ratios of the flames that were examined are listed in Tables 4.1 to 4.4. Table 4.1 lists the atmospheric pressure flame conditions for which the soot concentrations were measured with the laser scattering-extinction method. Three sequences of equivalence ratios were examined. The first and second sequences had approximately the same cold flow velocity, but different dilution ratios. The first and third sequences had approximately the same dilution ratio, but different cold flow velocities. Table 4.3 lists the atmospheric pressure flame conditions for which OH radical concentration profiles were measured.

Table 4.1 Equivalence ratio, cold gas flow rates, cold flow velocity, and dilution ratio for the atmospheric-pressure flames used in the scattering-extinction measurements.

Flame	Equivalence Ratio	Flow Rates (slpm)				Cold Flow Velocity (cm·s ⁻¹)	Dilution Ratio
		C ₂ H ₄	O ₂	N ₂	Total		
A-IA-R2	1.63	1.089	2.002	8.32	11.41	7.73	4.15
A-IA-C	1.70	1.126	1.991	8.29	11.41	7.73	4.16
A-IA-S1	1.78	1.176	1.984	8.25	11.41	7.73	4.16
A-IA-S2	1.92	1.263	1.968	8.20	11.43	7.75	4.17
A-IA-S3	2.02	1.320	1.958	8.14	11.42	7.74	4.16
A-IA-S4	2.17	1.406	1.943	8.09	11.43	7.75	4.16
A-IA-S5	2.32	1.489	1.929	8.03	11.44	7.75	4.16
A-IB-C	1.67	1.326	2.383	7.90	11.61	7.87	3.31
A-IB-S2	1.92	1.421	2.218	7.84	11.48	7.78	3.54
A-IB-S3	2.02	1.485	2.204	7.79	11.48	7.78	3.54
A-IB-S4	2.17	1.578	2.185	7.71	11.47	7.77	3.53
A-IIA-R2	1.63	1.432	2.640	11.31	15.39	10.42	4.29
A-IIA-S1	1.78	1.556	2.623	11.25	15.43	10.45	4.29
A-IIA-S2	1.92	1.667	2.604	11.15	15.42	10.45	4.28
A-IIA-S3	2.02	1.742	2.589	11.09	15.42	10.45	4.28

The rich flames had the same cold flow velocity and dilution ratio as the first sequence examined with the scattering-extinction measurements. The lean atmospheric flame was used in the calibration of the OH fluorescence measurements.

Soot concentrations were measured with the laser scattering-extinction method for the 80-torr flames listed in Table 4.2. Two sequences of equivalence ratios with different cold flow velocities were examined. These flames were not diluted with nitrogen and thus the dilution ratio was zero. OH fluorescence profiles were measured in one subset of an equivalence ratio sequence. These conditions are listed in Table 4.4.

An uncertainty analysis of the flow rates, equivalence ratios, dilution ratios, and cold flow velocities is given in Appendix A. The precision of the mass flow controllers cause an uncertainty in the flow rates that is less than 0.3%, but the uncertainty caused by the calibration increases the uncertainty in the flow rates to approximately 0.90%. The uncertainties in the equivalence ratios and dilution ratios are about 0.35% and are affected only by the precision of the mass flow controllers. The uncertainties in the cold flow velocities are somewhat larger, approximately 2.0%, because of the uncertainty in the burner diameter.

The flames in the tables are labeled with a three part code to aid in identifying the flames and to aid in comparing the measurements from the flames. The code consists of three letter-number combinations separated by hyphens. The first letter indicates whether the flame is an atmospheric (A) or an 80-torr (L) flame. For the second number-letter combination, the roman numeral indicates a sequence of flames that have the same cold flow velocity, while the letter indicates a sequence of flames that have the same dilution ratio. Thus, at atmospheric pressure, flames with a cold flow velocity of $7.7 \text{ cm}\cdot\text{sec}^{-1}$ are designated with the numeral 'I' and flames with a cold flow velocity of $10.4 \text{ cm}\cdot\text{sec}^{-1}$ are designated with the numeral 'II'. Flames with a dilution ratio of 4.2 are designated with the letter 'A' and those with a dilution ratio of 3.5 are designated with the letter 'B'. At

Table 4.2 Equivalence ratio, cold gas flow rates, and cold flow velocity for the 80-torr flames used in the scattering-extinction measurements.

Flame	Equivalence Ratio	Flow Rates (slpm)			Cold Flow Velocity (cm·s ⁻¹)
		C ₂ H ₄	O ₂	Total	
L-I-R1	2.03	1.132	1.675	2.807	18.1
L-I-R2	2.17	1.179	1.629	2.808	18.1
L-I-S1	2.32	1.222	1.584	2.806	18.1
L-I-S2	2.46	1.265	1.541	2.806	18.1
L-I-S3	2.60	1.303	1.502	2.806	18.1
L-II-R1	2.03	1.400	2.074	3.474	22.4
L-II-R2	2.16	1.460	2.023	3.483	22.4
L-II-S1	2.32	1.515	1.962	3.477	22.4
L-II-S2	2.46	1.567	1.913	3.480	22.4
L-II-S3	2.60	1.616	1.863	3.479	22.4

80 torr, flames with a cold flow velocity of $18.1 \text{ cm}\cdot\text{sec}^{-1}$ are designated with the numeral 'I' and those with a cold flow velocity of $22.4 \text{ cm}\cdot\text{sec}^{-1}$ are designated with the numeral 'II'.

The third letter-number combination indicates the equivalence ratio of the flame. The letter indicates the nature of the flame; 'L' indicates a lean flame, 'R' a rich but nonsooting flame, 'S' a sooting flame, and 'C' a flame at the critical equivalence ratio. The number increases with the equivalence ratio. Flames with the same number have the same equivalence ratio.

Table 4.3 Equivalence ratio, cold gas flow rates, cold flow velocity, and dilution ratio for the atmospheric-pressure flames used in the OH measurements.

Flame	Equivalence Ratio	Flow Rates (slpm)				Cold Flow Velocity ($\text{cm}\cdot\text{s}^{-1}$)	Dilution Ratio
		C_2H_4	O_2	N_2	Total		
A-0-L	0.97	0.627	1.941	10.52	13.08	8.86	5.42
A-IA-R1	1.49	1.001	2.020	8.39	11.41	7.73	4.15
A-IA-R2	1.63	1.089	2.002	8.32	11.41	7.73	4.15
A-IA-S1	1.78	1.176	1.984	8.25	11.41	7.73	4.16
A-IA-S2	1.92	1.263	1.968	8.20	11.43	7.75	4.17

Table 4.4 Equivalence ratio, cold gas flow rates, and cold flow velocity for the 80-torr flames used in the OH measurements.

Flame	Equivalence Ratio	Flow Rates (slpm)			Cold Flow Velocity (cm·s ⁻¹)
		C ₂ H ₄	O ₂	Total	
L-II-R1	2.03	1.400	2.074	3.474	22.4
L-II-R2	2.16	1.460	2.023	3.483	22.4
L-II-S1	2.32	1.515	1.962	3.477	22.4
L-II-S2	2.46	1.567	1.913	3.480	22.4

4.4 Laser Scattering-Extinction Measurements

The laser scattering-extinction method was used to measure soot formation in sequences of flames at both atmospheric and subatmospheric pressures. The laser scattering-extinction apparatus was used to measure profiles of the scattering and extinction coefficients. For the sooting flames, these profiles were used to calculate profiles of the soot volume fraction, particle number density, and mean particle diameter. For the nonsooting flames, the scattering coefficient profiles were a measure of the background contribution from molecular scattering of the flame gases. In addition, the scattering coefficient profiles for nonsooting flames and for nonsooting regions of sooting flames were used to estimate temperature profiles. The depolarized component of the scattered light was measured to determine the extent of anisotropic scattering by the particles and particle agglomeration. The broadband fluorescence induced by the argon-ion laser was measured to quantify its background contribution and also to monitor the presence of PAH species or perhaps other soot-related species.

The theory for the laser scattering-extinction method was presented in Section 3.2. The implementation of the method is presented here by first describing the optical setup and then the signal detection and data acquisition setup. We then describe the experimental procedure used to calibrate the measurements and to acquire the raw data for the scattering and extinction coefficient profiles. We conclude with a description of the analysis procedures to determine the scattering and extinction coefficient profiles from the raw data.

4.4.1 Optical Setup

The basic structure of a laser scattering-extinction measurement system was described in Section 3.2.1 and was shown in Figure 3.1. The basic measurement system consists of a laser, the output of which is directed through the flame parallel to the burner surface, and three detectors to measure the laser irradiance and scattered light power. A 'reference' detector measures the incident laser irradiance on the flame, a 'transmittance' detector measures the laser irradiance transmitted through the flame, and a 'scattering' detector measures the scattered light power from the particles and gases in the flame. The implementation of this laser scattering-extinction measurement system to measure scattering and extinction coefficient profiles in flames near the critical equivalence ratio is shown in Figure 4.7.

The light source was a Lexel Model 95 argon-ion laser tuned to 488.0 nm with a vertically polarized output. The laser was set to run in the light control mode to provide feedback stabilization of the output power. The output of the laser was directed to and aligned with the optical axis of the burner by four beam-steering mirrors. The optical axis of the burner was defined by two apertures placed on opposite sides of the burner equidistant from the burner centerline. The height of the apertures was set to the centerline height of the burner pressure vessel windows using a cathetometer.

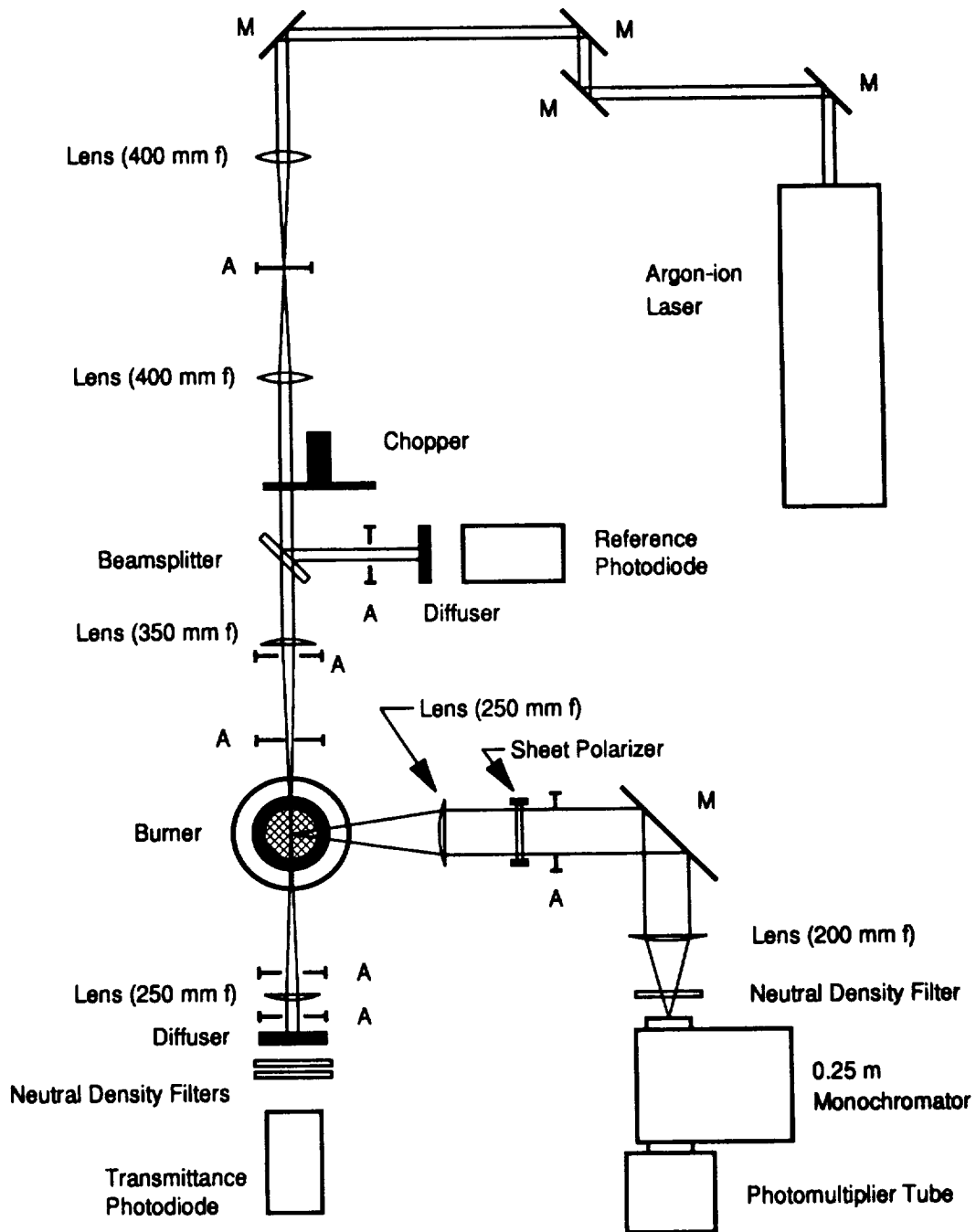


Figure 4.7 Schematic showing the optical setup for the laser scattering-extinction measurements. Abbreviations for components: A - aperture; M - mirror.

After the beam-steering mirrors, the laser beam was focussed onto an aperture by a 400 mm focal length lens to spatially filter the laser output. A second 400 mm focal length lens recollimated the laser beam. A Stanford Research Systems SR540 Optical Chopper modulated the laser beam at 1.00 kHz for phase-sensitive detection of the signals from the transmittance, reference, and scattering detectors.

After the chopper, the reference intensity of the laser beam was measured by reflecting a portion of the laser beam onto a photodiode (henceforth called the 'reference photodiode') using a 50.8 mm square 6.2 mm thick quartz plate placed in the laser beam. A flashed opal diffuser was placed in the reflected beam in front of the photodiode to reduce the laser intensity and also to reduce the sensitivity of the photodiode signal to beam wander.

The laser beam was focussed over the center of the burner by a 350 mm focal length lens. After passing over the burner, the laser beam was recollimated by a 250 mm focal length lens and then directed onto a flashed opal diffuser placed in front of the photodiode measuring the transmitted intensity of the laser beam (henceforth called the 'transmittance photodiode'). This diffuser reduced the sensitivity of the measured intensity to beam wander and to beam steering by the flame. Two Schott neutral density glass filters (NG-9 and NG-5) were placed between the diffuser and the photodiode to further reduce the laser beam intensity to within the linear range of the photodiode. The spot size at the center of the burner was measured by scanning a razor blade across the laser beam and measuring the transmitted laser intensity. The spot size was measured to be 0.104 mm between 10% and 90% of the full intensity.

The scattered light at a right angle to the incident laser beam was collected and collimated by a 50.8 mm diameter 250 mm focal length lens. The collimated light was reflected 90° by a 76.2 mm diameter mirror and focussed onto the entrance slit of a monochromator by a 50.8 mm diameter 200 mm focal length lens. The monochromator

was a Schoeffel GM252 0.25-m monochromator mounted vertically so that its entrance slit was in the same plane as the laser beam. A Hamamatsu R955 photomultiplier tube detected the light leaving the exit slit of the monochromator. The entrance and exit slit widths were set to 0.15 mm giving a measured bandpass of 0.58 nm FWHM. For the argon-ion fluorescence measurements, the entrance and exit slit widths were 0.15 mm and 0.20 mm, respectively, for a measured bandpass of 0.72 nm FWHM. The entrance slit height was generally set to 2.5 mm for the atmospheric pressure experiments. The slit height was set to 6.5 mm for the subatmospheric pressure experiments and for the atmospheric pressure horizontal polarization and fluorescence measurements.

The polarization of the detected scattered light was selected by a 50-mm diameter dichroic sheet polarizer (mounted in a rotational translation stage) placed in the collimated portion of the scattered light beam. The polarizer was removed for measurements of the fluorescence excited by the argon-ion laser. Melles-Griot precision metallic neutral density filters (50.8 mm square) were placed in front of the monochromator entrance slit to reduce the scattered light intensity from the more heavily sooting flames.

Several precautions were taken to minimize stray light that might be detected by the scattered signal detection system. Apertures were placed along the laser beam path to block scattering from lens surfaces and to block back reflections, therefore ensuring that only the incident laser beam crossed over the burner. The scattering collection optics were shielded from the rest of the optical system by dense black felt curtains. A hole in the curtain at the collection lens allowed the scattered light from the collection volume to pass through to the collection system.

The flashed opal diffusers were used to reduce the effects of beam steering because, during preliminary experiments, steering of the laser beam by the flame moved the incident laser beam position on the transmittance photodiode surface. The incident

position shift would change the photodiode signal measurably, indicating a false extinction or, in some cases, indicating an increased transmittance. The transmittance measurements would have been impossible to make without the diffusers. To further reduce the magnitude of any beam displacement, we also minimized the distance between the transmittance photodiode and the burner.

The same optical setup was used for both the atmospheric and subatmospheric pressure experiments. The pressure vessel was added for the subatmospheric pressure experiments. The vessel windows at the entrance and exit of the laser beam were tilted 15° from the vertical to reduce back reflections from the laser into the scattering collection volume. Although the windows were flushed with nitrogen, the transmittance signal was monitored for soot deposition on the windows. The window through which the laser beam exited was particularly susceptible to soot deposition.

4.4.2 Signal Detection and Data Acquisition Setup

The signal detection and data acquisition setup is shown in Figure 4.8. All three signals, the transmittance, reference, and scattered signals, were acquired electronically with lock-in amplifier (phase-sensitive) detection of the chopper modulated signals.

The reference intensity was measured with a Hamamatsu S1336-5BQ photodiode. The transmittance intensity was measured with a Newport Research model 820 photodiode. Both the transmittance and reference photodiodes were wired in transimpedance amplifier circuits (see Appendix B) to convert the photodiode current to a voltage output. The reference voltage output was detected with a Stanford Research Systems Model SR510 Lock-in amplifier. The transmittance voltage output was detected with an EG&G PARC Model 128 Lock-in amplifier. Both of these lock-in amplifiers were set using the input offset to null out the majority of the input signal so that the detection sensitivity could be increased by a factor of 10.

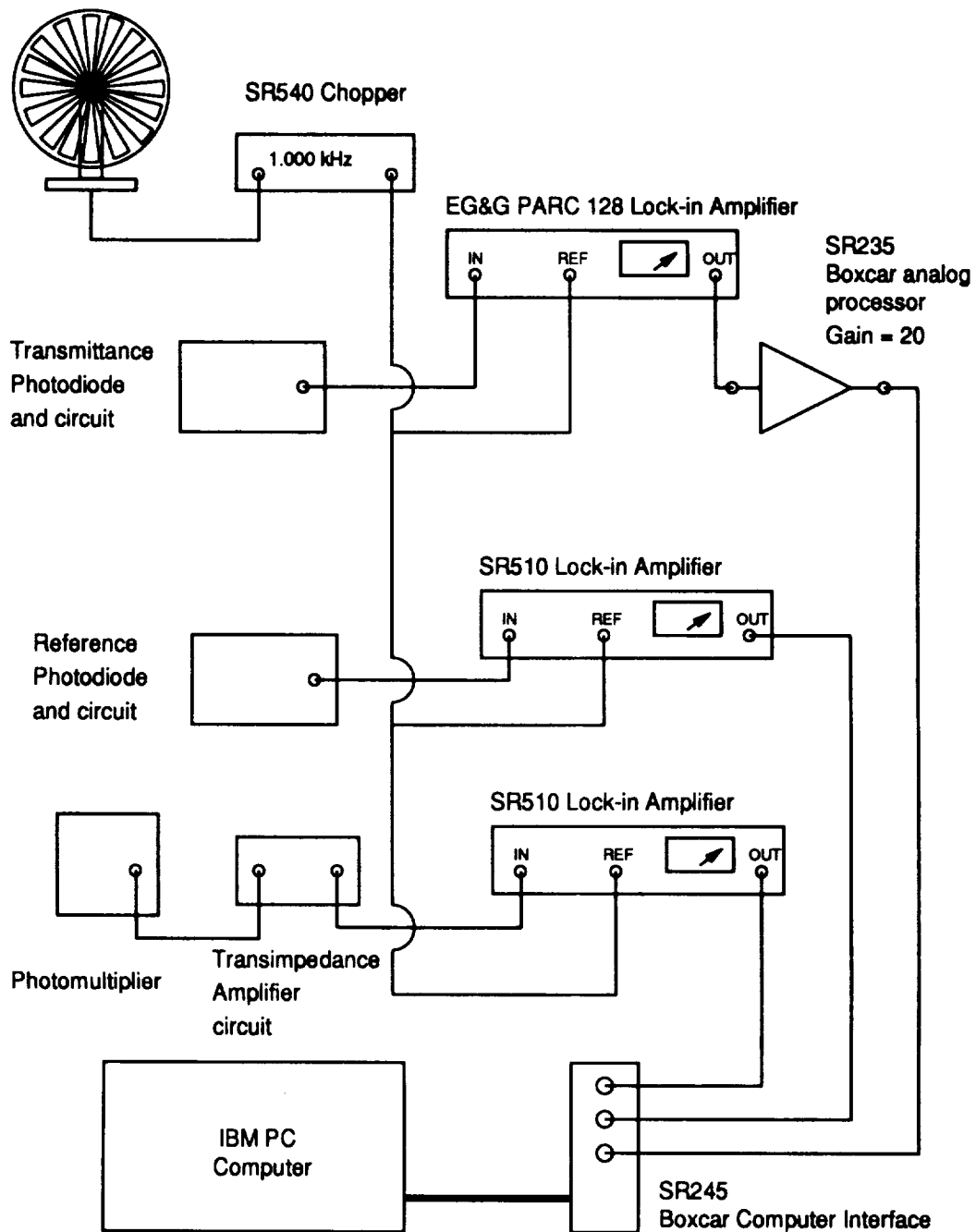


Figure 4.8 Schematic of the signal detection and data acquisition setup for the laser scattering-extinction measurements.

The scattered light at the output of the monochromator was detected by a Hamamatsu R955 photomultiplier. A transimpedance amplifier circuit (see Appendix B) converted the photomultiplier current output into a voltage output which was detected by a Stanford Research Systems Model SR510 Lock-in amplifier.

The three lock-in amplifier output signals were sent to a Stanford Research Systems Model SR245 computer interface module for analog-to-digital conversion. A Stanford Research Systems Model SR235 analog processor module amplified the output of the transmittance lock-in amplifier with a gain of 20 to more closely match the ± 1.0 volt output range of the EG&G PARC Model 128 Lock-in amplifier to the ± 10.24 volt input range of the computer interface module.

An IBM PC computer controlled the data acquisition and the experiment through a modified version of the Stanford Research Systems SR265 software program (Stanford Research Systems, 1988) for controlling the computer interface module. Carter (1990) added an interface for the stepper motor controller to the SR265 program, so that the data acquisition could be coupled to the stepper motor-driven vertical and horizontal translation of the burner and also to the wavelength translation of the monochromator.

Vertical profiles of the transmittance, reference, and scattering signals were measured in flames by setting up the program to sample the signals for 10 seconds at a 100 Hz rate (1000 samples) at each height in a sequence of heights above the burner. The signal voltage data acquired by the computer interface was stored on the hard disk of the IBM PC in binary format for later analysis.

4.4.3 Experimental Procedure

The general sequence of steps in the experimental procedure was alignment of the optics, measurement of the calibration factors, setting of the flame conditions, measurement of the transmittance and scattered light profiles, and at the end of the

experiment, a check of the calibration factors. The alignment and calibration were repeated before each experiment to assure the repeatability and accuracy of the measurements from day to day. A description of the experimental procedure follows.

The output power of the argon-ion laser was set to 800 mW. The laser beam was centered on the alignment apertures on either side of the burner and then centered on the reference and transmittance photodiodes by adjusting the position of the lenses and mirrors in the reference and transmittance optics. This alignment assured the reproducibility of the position of the laser beam relative to the burner surface.

The reference height of the burner, i.e., the burner height at which the laser beam intersects the burner surface, was determined by sampling the transmittance and reference signal voltages as the surface of the burner was scanned through the laser beam. The height at which the midpoint occurred between the minimum and maximum of the transmittance signal voltages was defined to be the reference height of the burner for subsequent determinations of the height of the laser beam above the burner surface. For the subatmospheric pressure experiments, the burner reference height was measured while the pressure was at 80 torr or less, because the burner reference height would shift slightly as the pressure was reduced below 1 atm.

Scattered light from a nitrogen flow from the burner was used to align the scattering collection lenses and to tune the monochromator wavelength to the laser wavelength. The transmittance, reference, and scattered light signals were then sampled to determine the transmittance and scattering calibration factors. The number density of the nitrogen flow was determined from the temperature measured with a K-type thermocouple in the flow above the burner and from the pressure read from the Wallace & Tiernan pressure gauge. The calibration data were measured for each neutral density filter likely to be used to reduce the scattered signal level. For the subatmospheric pressure experiments, the calibration data were measured with the pressure set to 80 torr. Because of the variation

in transmittance across the pressure vessel windows, the transmittance and scattering calibrations were also repeated at horizontal positions 2.0 mm and 4.0 mm on either side of the burner centerline.

After the calibration data were measured, the start-up flows of nitrogen, oxygen, and ethylene were set and the flame was ignited with a propane torch. The flow rates for a particular flame were set by adjusting the flow rates in small increments from the previous flame to prevent the flame from either blowing off or flashing back into the burner and also to avoid large overshoots in the flow rates caused by the mass flow controllers. For the subatmospheric pressure flames, the pressure was decreased from atmospheric pressure in small increments for the same reasons.

For each flame, typically three profiles of the transmittance, reference, and scattered signal voltages were measured with different height resolutions and ranges. A fine resolution profile was measured near the burner surface to resolve the change in temperature through the flame front. A larger range through the flame far downstream from the flame front was measured with two successively coarser resolution profiles. The starting height and height resolution and range of the three types of profiles are listed in Table 4.5. Between the measurements of the successive profiles in a flame, the burner was moved back to the starting height to monitor a reference point that could be compared with previous measurements to check for signal drift or for deposition of soot on the windows.

When switching between flame conditions, the calibration was checked by sampling the three signal voltages at a condition for which there was no extinction. In the atmospheric pressure experiments, the burner was moved horizontally so that the laser beam passed through the guard flow gases. In the subatmospheric pressure experiments, the flow rates were adjusted to a rich but nonsmoking flame and the burner was moved to the standard starting height (about 1.0 mm above the burner surface). If the calibration

Table 4.5 Height interval, height range and initial height for the scattering-extinction profiles.

Experiment and Type of Profile	Height Interval (mm)	Height Range (mm)	Initial Height (mm)
<u>80 Torr pressure</u>			
Fine resolution	0.25	5.0	0.5
Medium resolution	0.50	10.0	1.0
Coarse resolution	2.00	60.0	1.0
Depolarization	2.00	60.0	1.0
<u>Atmospheric pressure</u>			
Fine resolution	0.20	6.0	0.4
Medium resolution	0.50	15.0	1.0
Coarse resolution	1.00	20.0	1.0
Depolarization	0.50	20.0	1.0
Fluorescence	0.50	20.0	1.0

check suggested a soot build-up on the window, the burner was moved to a horizontal position 2.0 or 4.0 mm from the previous position and the calibration was rechecked. Subsequent profiles were measured at the new horizontal position.

After the flame was extinguished, the three signal voltages were measured to check the transmittance calibration in a nitrogen flow through the burner. The burner head was still cooling off from the flame and so the heated nitrogen flow was not suitable for checking the scattered light calibration.

The depolarization of the scattered light from the vertically polarized incident laser light was measured in one sequence of atmospheric-pressure sooting flames (A-IA-S2, S3, S4) and two sequences of 80-torr sooting flames (L-I-S1, S2, S3 and L-II-S1, S2, S3). The horizontally polarized component of the scattered light was measured by rotating the dichroic sheet polarizer in the scattering collection optics 90° from the setting used to measure the vertically polarized component. For each flame examined, a profile was measured of the vertically polarized scattered light and then a profile was measured of the horizontally polarized scattered light. The starting height, height resolution and range for the depolarization profiles are listed in Table 4.5.

The broadband fluorescence signal excited by the argon-ion laser was measured in one sequence of atmospheric-pressure sooting flames (A-IA-R2, S1, S2, S3). In each flame, a profile was measured of 1) the Rayleigh scattering at 488.0 nm, 2) the Stokes fluorescence at 503 nm, and 3) the anti-Stokes fluorescence at 473 nm. The polarizer was removed from the scattered light collection optics to increase the light throughput. The fluorescence wavelengths, 473 nm and 503 nm, were selected to reduce interference from the Rayleigh scattered light. The rejection of scattered light was verified by measuring the scattered signal from atmospheric, room-temperature nitrogen at these wavelengths.

4.4.4 Data Analysis

The scattering and extinction coefficient profiles were calculated from the voltage outputs of the three detectors recorded as a function of height above the burner. The reference photodiode measured the irradiance of the incident laser beam, I_0 ($\text{W}\cdot\text{cm}^{-2}$). The transmittance photodiode measured the irradiance of the laser beam after it passed through the flame, I_T ($\text{W}\cdot\text{cm}^{-2}$). The scattering photomultiplier tube measured the scattered light power, S_{scat} (W), from the flame. The measured signal voltages of these three detectors can be expressed as

$$V_0(z) = \eta_{00} \cdot \eta_{E0} \cdot I_0(z) \quad (4.4.1a)$$

$$V_T(z) = \eta_{0T} \cdot \eta_{ET} \cdot I_T(z) \quad (4.4.1b)$$

$$V_S(z) = \eta_{0S} \cdot \eta_{ES} \cdot S_{sca}(z) \quad (4.4.1c)$$

where V_0 , V_T , and V_S are the reference, transmittance, and scattering signal voltages (V), respectively. These are written as a function of the height above the burner, z , to indicate that they were recorded as profiles. The terms η_{00} , η_{0T} , and η_{0S} are optical efficiencies (dimensionless) for the reference, transmittance, and scattering detection optics, respectively. These efficiencies account for the transmittances and reflectances of the lenses, filters, and other optical elements within the detection optics. The terms η_{E0} ($V \cdot cm^2 \cdot W^{-1}$), η_{ET} ($V \cdot cm^2 \cdot W^{-1}$), and η_{ES} ($V \cdot W^{-1}$) are electronic conversion efficiencies (or gains) for the reference, transmittance, and scattering detectors, respectively. These efficiencies account for the conversion from a light signal to an electronic signal and also for the gains in the subsequent detection electronics.

The transmittance, τ , is determined from the ratio of the transmittance signal voltage (Eq. 4.4.1b) to the reference signal voltage (Eq. 4.4.1a), i.e.,

$$\tau(z) = \frac{I_T(z)}{I_0(z)} = \frac{1}{F_T} \cdot \frac{V_T(z)}{V_0(z)} \quad (4.4.2)$$

where the transmittance calibration factor, F_T , is defined as

$$F_T = \frac{\eta_{0T} \cdot \eta_{ET}}{\eta_{00} \cdot \eta_{E0}} \quad (4.4.3)$$

The total scattering coefficient, Q_{sca} , is determined from the scattered light power. The scattered light power can be expressed by combining Eqs. (3.2.22) and (3.2.23) as

$$S_{sca}(z) = V_c \cdot \Omega_c \cdot \eta_c \cdot Q_{sca}(z) \cdot I_0(z) \quad (4.4.4)$$

where V_c is the collection volume, Ω_c is the solid angle of the collection optics, and η_c is the efficiency of the collection optics. The total scattering coefficient can then be

determined from the ratio of the scattering signal voltage (Eq. 4.4.1c) to the reference signal voltage (Eq. 4.4.1a). Combining Eqs. (4.4.1a), (4.4.1c), and (4.4.4) gives the expression for the total scattering coefficient as

$$Q_{sca}(z) = \frac{1}{F_{sca}} \cdot \frac{V_s(z)}{V_0(z)} \quad (4.4.5)$$

where the scattering calibration factor, F_{sca} , is defined as

$$F_{sca} = \frac{\eta_{OS} \cdot \eta_{ES}}{\eta_{O0} \cdot \eta_{E0}} \cdot V_c \cdot \Omega_c \cdot \eta_c \quad (4.4.6)$$

The transmittance signal ratio profile, $V_T(z)/V_0(z)$, and the scattering signal ratio profile, $V_s(z)/V_0(z)$, were calculated from the voltage data recorded by the SR265 program during the measurement of the calibration factors and the scattering-extinction profiles using a set of programs written in the ASYST version 3.10 scientific programming language (ASYST Software Technologies, Inc., Rochester, NY). These programs first read the stored binary-format voltage data acquired by the computer interface and then calculated the photodetector signal voltages, V_0 , V_T , and V_s , based on the measured gains and offsets of the lock-in amplifiers used to detect them. Since the photodetector voltages were sampled for 10 seconds at each height, the means of the voltages at each height were used to calculate the signal ratio profiles, $V_T(z)/V_0(z)$ and $V_s(z)/V_0(z)$. The standard deviations of these signal ratios were also calculated to evaluate their variation during the measurement. The details of this analysis are given in Appendix B.

The transmittance and scattering calibration factors were calculated from the transmittance and scattering signal ratios measured for nitrogen flowing through the burner. The transmittance calibration factor can be determined from

$$F_T = \frac{1}{\tau_{cal}} \cdot \left(\frac{V_T}{V_0} \right)_{cal} \quad (4.4.7)$$

where the subscript *cal* indicates the measurement made at the calibration conditions. We assumed that $\tau_{cal} = 1$ for the measurements made in the nitrogen flow and also in the rich nonsooting flames. However, the transmittance calibration factors measured during the course of a single day were found to vary. This variation was caused by a variation in the laser intensity that did not cancel out of the transmittance voltage ratio because of inaccuracies in determining the offsets of the lock-in amplifiers. Because of this drift, the transmittance profiles were normalized by setting $\tau = 1$ at the maximum of the transmittance signal ratio profile, i.e., the transmittance calibration factor is given by

$$F_T = \max\left(\frac{V_T(z)}{V_0(z)}\right) . \quad (4.4.8)$$

The transmittance measurement is then calibrated based on the transmittance in the nonsooting region of a sooting flame. Any absorption by gas-phase species in this nonsooting region is then considered to be a background absorption that is not caused by soot particles and is thus effectively cancelled out by the normalization.

The scattering calibration factor was determined from the scattering signal ratio measured for flowing nitrogen by

$$F_{sca} = \frac{R \cdot T}{P \cdot N_{av}} \cdot \frac{1}{C_{VV,N_2}} \cdot \left(\frac{V_s}{V_0}\right)_{cal} \quad (4.4.9)$$

where R ($82.055 \text{ cm}^3 \cdot \text{atm} \cdot \text{gmol}^{-1} \cdot \text{K}^{-1}$) is the gas constant and N_{av} ($6.023 \times 10^{23} \text{ gmol}^{-1}$) is Avogadro's constant. The temperature, T (K), and the pressure, P (atm), of the flowing nitrogen were measured during the calibration. The differential scattering cross-section of nitrogen at 488.0 nm is $C_{VV,N_2} = 8.873 \times 10^{-28} \text{ cm}^2 \cdot \text{sr}^{-1}$. This value was determined from the data of Gardiner, Hidaka, and Tanzawa (1981) and agrees well with $C_{VV,N_2} = 8.69 \times 10^{-28} \text{ cm}^2 \cdot \text{sr}^{-1}$ extrapolated from the data of Rudder and Bach (1968) at 694.3 nm, with $C_{VV,N_2} = 8.78 \times 10^{-28} \text{ cm}^2 \cdot \text{sr}^{-1}$ used by Müller-Dethlefs (1979) at 488.0 nm, and with $C_{VV,N_2} = 8.865 \times 10^{-28} \text{ cm}^2 \cdot \text{sr}^{-1}$ determined from the data of Bogaard et al. (1978) at

488.0 nm. The data of Gardiner, Hidaka, and Tanzawa (1981) was used to be consistent with the calculations of the scattering coefficient and the cross-section using the flame code. The scattering calibration factor was also determined for each neutral density filter used to reduce the scattered light intensity in an experiment.

Normalized transmittance profiles were calculated from the transmittance signal ratio profile using Eqs. (4.4.2) and (4.4.8). The extinction coefficient profiles were calculated from the normalized transmittance profiles by

$$K_{ext}(z) = -\frac{1}{L} \cdot \ln[\tau(z)] \quad (4.4.10)$$

where L (cm) is the pathlength of the laser through the flame. The pathlength was not measured in these flames and, instead, was assumed to be the diameter of the burner, $L = 5.6$ cm. The pathlength could have been determined from transmittance measurements made at several horizontal positions (Harris, Weiner, and Ashcraft, 1986), but the procedure would likely have been inaccurate, because the transmittances were near unity in these lightly sooting flames. The pathlength could also have been determined from a measurement of the scattering coefficient across the burner width at the same height; however, this was not done. Nonetheless, the extinction coefficient profiles remain valid on a relative basis, as the cold flow velocity and dilution ratio were held constant while the equivalence ratio was varied in small increments for a given flame sequence, thus ensuring similar pathlengths. An accurate measurement of the pathlength would be warranted for a more accurate measurement of the extinction coefficient.

The measured scattering coefficient (Q_{scd}) profiles were determined from the scattering signal ratio profiles and the scattering calibration factor using Eq. (4.4.5). The measured scattering coefficient can be expressed as the sum of the particle scattering, molecular scattering, and fluorescence coefficient (Sec. 3.2.2.2) and is given by (Eq. 3.2.23),

$$Q_{sca} = Q_{vv} + Q_{vv,g} + Q_f(\lambda_0, \lambda) \cdot \Delta\lambda \quad , \quad (4.4.11)$$

where Q_{vv} ($\text{cm}^{-1} \cdot \text{sr}^{-1}$) is the particle scattering coefficient, $Q_{vv,g}$ ($\text{cm}^{-1} \cdot \text{sr}^{-1}$) is the molecular scattering coefficient, $Q_f(\lambda_0, \lambda)$ ($\text{cm}^{-1} \cdot \text{sr}^{-1} \cdot \text{nm}^{-1}$) is the fluorescence coefficient, and $\Delta\lambda$ (nm) is the detector spectral bandwidth. The particle scattering coefficient was obtained by subtracting the molecular scattering coefficient and the fluorescence coefficient from the measured scattering coefficient.

The Stokes fluorescence at 503 nm and the anti-Stokes fluorescence at 473 nm were measured in a sequence of atmospheric pressure flames (A-IA-R2, S1, S2, S3). At these wavelengths, the measured signal from the scattering photodetector was solely caused by the fluorescence and thus the fluorescence coefficient profiles could be determined from $Q_f(\lambda_0, \lambda) \cdot \Delta\lambda = Q_{sca}$. A spectral scan of the fluorescence determined that it was featureless and that the fluorescence signal rose approximately linearly from 473 nm to 503 nm. The background contribution of the fluorescence at 488.0 nm could then be calculated from the average of the fluorescence coefficients at 473 nm and 503 nm. The fluorescence contribution was not more than 1% of the total scattering signal in the early regions of the flames (less than 3 to 5 mm above the burner). In the lightly sooting flame (A-IA-S1), the fluorescence background reached a maximum of 2%, while the maximum contributions reached 11% (A-IA-S2) and 15% (A-IA-S3) in the more heavily sooting flames. Thus, in the atmospheric flames for which the fluorescence background was not measured, the fluorescence background is not likely to be significant in the lightly sooting flames, but could cause an overprediction of the scattering coefficient in the more heavily sooting flames.

The background contribution caused by molecular scattering for a sooting flame was estimated to have the same shape as the scattering coefficient profile of the nonsooting flame within its sequence but with an offset equal to the minimum of the scattering coefficient profile in the sooting flame. Equating the background to the

minimum in the scattering coefficient profile accounts for the increase in the molecular scattering coefficient as the peak temperature decreases with increasing equivalence ratio. The assumption that the molecular scattering coefficient profiles of the sooting and nonsooting flames had similar shapes was based on the similarity of their molecular scattering coefficient profiles in the region near the surface of the burner. The molecular scattering coefficient profile in nonsooting flames increased only slightly with height above the burner as the flame gases cooled off. This increase was typically less than $0.3 \times 10^9 \text{ cm}^{-1} \cdot \text{sr}^{-1}$ from a minimum of $Q_{\text{VV},g} \approx 4.0 \times 10^9 \text{ cm}^{-1} \cdot \text{sr}^{-1}$. This increase was small relative to the increases of ~ 3 to $\sim 100 \times 10^9 \text{ cm}^{-1} \cdot \text{sr}^{-1}$ observed in the sooting flames.

Finally, the soot volume fraction profiles can be calculated from the measured extinction coefficient profiles and an assumed particle index of refraction. Once the particle scattering coefficient profiles have been determined and corrected for the background contributions they can be used along with the extinction coefficient profiles to calculate the particle number density and particle diameter profiles. These further analyses are described in Chapter 5.

The molecular scattering coefficient profile was also used to estimate a temperature profile. In nonsooting flames and in the region of sooting flames where soot has not yet formed, the measured scattering coefficient profile is that caused by molecular scattering and is given by Eq. (3.2.16), i.e.,

$$Q_{\text{scat}}(z) = Q_{\text{VV},g}(z) = N_g(z) \cdot \bar{C}_{\text{VV},g}(z) \quad (4.4.12)$$

where N_g (cm^{-3}) is the number density of the gas molecules and $\bar{C}_{\text{VV},g}$ ($\text{cm}^2 \cdot \text{sr}^{-1}$) is the mean differential scattering cross-section of the gas mixture. The mean differential scattering cross-section is determined from the molar composition of the gas by Eq. (3.2.17), so that

$$\bar{C}_{\text{VV},g}(z) = \sum_k X_k(z) \cdot C_{\text{VV},k} \quad (4.4.13)$$

where X_k is the mole fraction of species k and $C_{vv,k}$ ($\text{cm}^2\cdot\text{sr}^{-1}$) is the differential scattering cross-section of species k . The temperature profile can be determined from Eq. (4.4.12) by using the ideal gas law to express the number density in terms of the temperature. The expression for the temperature profile, T (K), is then

$$T(z) = \frac{P}{R} \cdot N_{av} \cdot \frac{\overline{C}_{vv,g}(z)}{Q_{vv,g}(z)} \quad (4.4.14)$$

The calculation of the temperature profile requires that the mean differential scattering cross-section of the gases, $\overline{C}_{vv,g}$, be known or estimated. To do this, we must know the molar composition of the gas and the differential scattering cross-sections of the major species (Eq. 4.4.13). The molar compositions were estimated using the predictions of the Sandia premixed one-dimensional flame code (Kee et al., 1985) with the reaction mechanism of Drake and Blint (1991). The differential scattering cross-sections of the major species were determined using Eq. (3.2.18). The refractive indices of the gas species were calculated using the data and formulas of Gardiner, Hidaka, and Tanzawa (1981).

An iterative procedure was used to estimate the flame temperature profile from the measured scattering coefficient data. We first estimated the flame temperature profile. The molar composition profile was then determined from the flame code solution for the estimated temperature profile. The molar composition profile was in turn used to calculate the mean differential scattering cross-section profile and the scattering coefficient profile. The predicted scattering coefficient profile was then compared with the measured scattering coefficient profile. If the profiles did not agree within a given tolerance, the next estimate of the temperature profile was determined from the comparison and the procedure was repeated. The details of this procedure and the calculations are in Appendix C. The implementation of the flame code is discussed in Section 4.6.

4.5 Laser-Induced Fluorescence Measurements of the Hydroxyl Radical

Laser-induced fluorescence was used to measure relative OH concentration profiles in one sequence of flames at atmospheric pressure and in a sequence of flames at 80 torr. The theory of the laser-induced fluorescence method to measure OH radical concentrations in sooting flames was presented in Section 3.3. We present here the implementation of this method by first describing the optical setup and the signal detection and data acquisition setup. We then describe the experimental procedure and the subsequent analysis of the data.

4.5.1 Optical Setup

The experimental setup for the laser-induced fluorescence measurements of the hydroxyl radical is shown in Figure 4.9. The setup was the same for the atmospheric pressure and the subatmospheric pressure experiments, except that the burner was enclosed in a pressure vessel for the subatmospheric pressure experiments.

The UV excitation source for the OH radical was a Nd:YAG-pumped dye laser system. The Nd:YAG laser was a Molelectron MY-34-10 laser retrofitted with a Laser Photonics resonator. The typical output pulse energy ranged from 150 to 200 mJ at the Nd:YAG second harmonic wavelength of 532 nm. The second harmonic output was directed into the dye laser by two laser mirrors coated for maximum reflectivity at 532 nm.

The temporal pulse shape of the Nd:YAG laser output was monitored with a specially-wired silicon avalanche photodiode (Texas Instruments TIED56; Harris et al., 1980). The photodiode detected a portion of the 532 nm beam that passed through the second laser mirror and fell on a flashed opal diffuser. The photodiode output was observed with a Hewlett-Packard HP54502A digital sampling oscilloscope. The typical pulse shape contained two or three lobes each with a FWHM of about 4 nsec. The relative

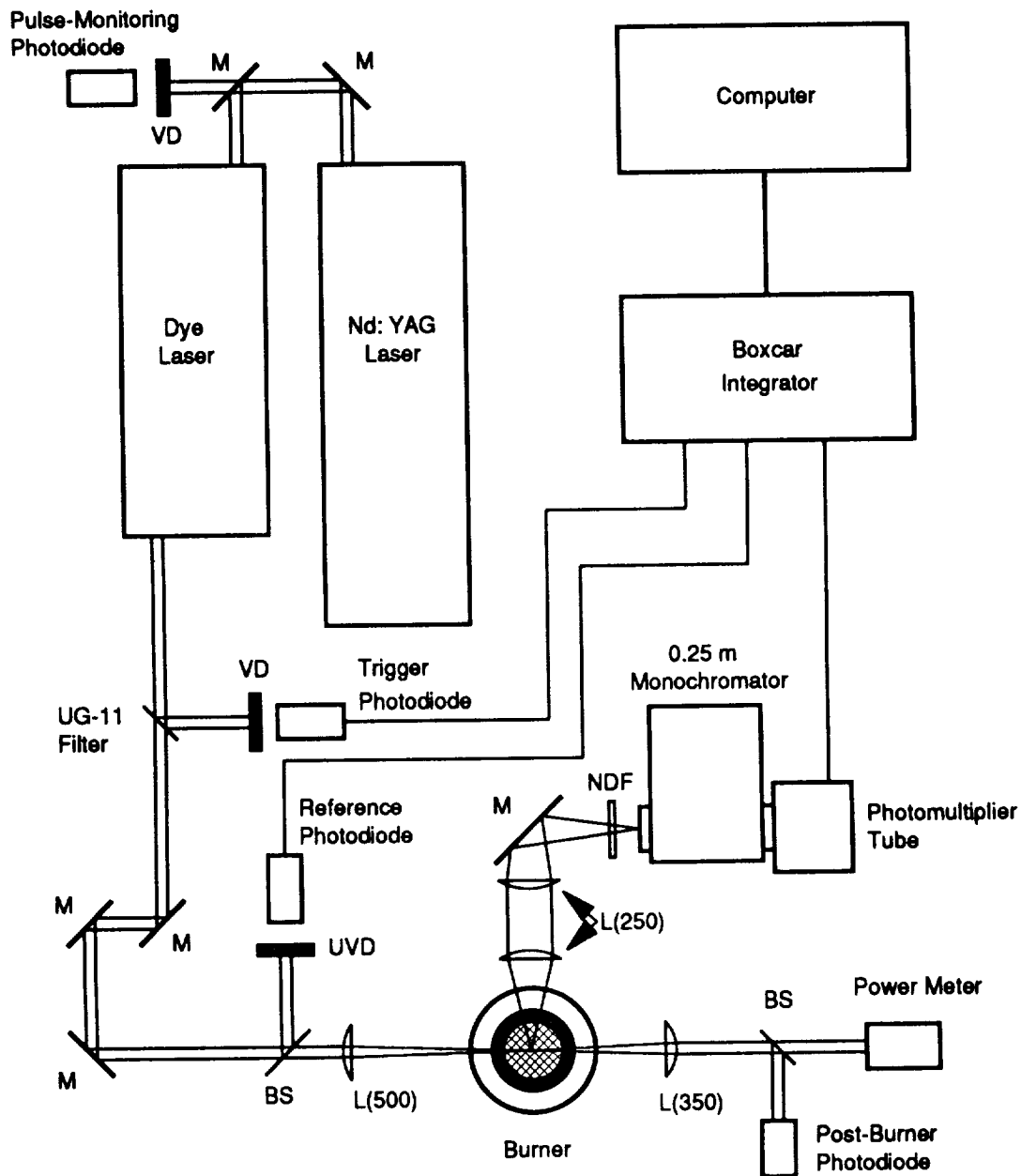


Figure 4.9 Schematic of the hydroxyl radical fluorescence measurement setup. Components: BS - beamsplitter; L - lens (focal length in mm); M - mirror; NDF - neutral density filter; UVD - ultraviolet diffuser; VD - visible diffuser.

height of the first lobe peak was adjusted to be about twice the height of the second lobe peak by making slight adjustments to the input energy of the Nd:YAG oscillator flashlamps.

The Nd:YAG second harmonic output pumped a Molelectron DL-18 dye laser to produce an output wavelength at ~ 618 nm. The dye mixtures used in both the oscillator and amplifier flowing dye cells were DCM in ethanol solutions to which a concentrated SR640 (Sulfarhodamine 640) in ethanol solution was added to maximize the output at ~ 618 nm. The procedure described by Carter (1990) was followed to maximize the output. The final oscillator dye solution was estimated to be 1.18 mM DCM and 0.236 mM SR640 in ethanol and the final amplifier solution was estimated to be 29 μ M DCM and 18 μ M SR640 in ethanol.

The dye laser output at ~ 618 nm was frequency doubled using a KDP crystal to produce the UV laser beam output at ~ 309 nm. The frequency doubled output passed through a Schott UG-11 UV-transmitting filter to attenuate the ~ 618 nm radiation. The UG-11 filter was oriented at 45° to reflect a portion of the ~ 618 nm light onto a Scientech Model 301-020 high speed photodetector (the 'trigger photodiode') placed behind another flashed opal diffuser. The output of this photodetector triggered the detection electronics.

The UV laser output was directed and aligned with the optical axis of the burner by three 309 nm dielectric mirrors. The optical axis of the burner was defined by two apertures (closed down iris diaphragms) placed 40 cm from the burner centerline on either side of the burner. The height of the apertures was set to the centerline height of the burner pressure vessel windows using a cathetometer.

The reference intensity of the UV laser beam was measured by reflecting a portion of the beam onto a photodiode with a 50.8-mm square, 1-mm thick fused silica optical flat. The 'reference' photodiode was a Hamamatsu S1722-02 PIN photodiode wired for

fast response. A UV disk diffuser was placed in the reflected beam in front of the photodiode to reduce the sensitivity of the signal to the alignment of the UV beam. The distance between the diffuser and the photodiode was adjusted to ensure that the photodiode signal was within its linear range.

The UV laser beam was focussed over the center of the burner with a 500-mm focal length fused silica lens. The spot size of the UV beam was measured to be 0.135 mm at the center of the burner and 0.175 mm at the front edge of the burner by scanning a razor blade vertically across the laser beam. The width was based on the 10% and 90% points of the transmitted intensity.

After passing over the burner, the UV laser beam was recollimated with a 350-mm focal length fused silica lens. The collimated UV beam was split with a 50-mm square, 5-mm thick quartz optical flat. The major portion of the UV beam passed through the quartz flat and was monitored with a Scientech Model 36-0001 surface absorbing disc calorimeter. This power meter was used to observe the average UV laser power. The reflected portion of the UV beam was monitored with a Hamamatsu S1722-02 PIN photodiode wired for fast response. This 'post-burner' photodiode was used to measure the transmitted UV intensity when the burner surface was scanned to determine the burner reference height.

The broadband fluorescence from the OH radical was collected at a right angle to the incident UV laser beam and collimated by a 50.8-mm diameter, 250-mm focal length fused silica collection lens. The collimated fluorescence was focussed onto the entrance slit of the monochromator by a 50.8-mm diameter, 250-mm focal length lens. A 50.8-mm diameter UV-enhanced reflectivity mirror was placed between the focussing lens and the monochromator entrance slit to turn the optical path by 90°. The mirror was used to fit the fluorescence collection optics on the optical table.

The monochromator was a Schoeffel GM 252 0.25-m monochromator mounted vertically so that its entrance slit was in the same plane as the laser beam passing through the flame. The monochromator grating was blazed at 240 nm with 1180 lines/mm. For the experiments with $Q_1(8)$ excitation, the monochromator entrance and exit slit widths were set to 0.25 mm and 3.00 mm, respectively, to give a measured bandwidth of 9.4 nm FWHM centered at 311 nm. For the experiments with $P_1(8)$ excitation, the monochromator entrance and exit slit widths were set to 0.25 mm and 2.00 mm, respectively, to give a measured bandwidth of 6.4 nm FWHM centered at 308.6 nm. The slit height was set to 15 mm for both experiments. An RCA 1P28B photomultiplier tube wired in a fast response circuit (Harris, Lytle, and McCain, 1976) detected the light leaving the exit slit of the monochromator. The photomultiplier voltage was set to 1150 V.

The voltage output of the photomultiplier tube was kept within its linear range by attenuating the fluorescence with calibrated neutral density filters (Melles-Griot 50.8 mm square precision metallic fused silica) placed in front of the monochromator entrance slit. Vignetting of the fluorescence by the burner surface was observed when the incident UV beam was less than 2 mm above the burner surface. The lower half of the collection lens was blocked with an aluminum plate to avoid vignetting in profiles measured near the burner surface.

Because the laser wavelength was within the detection bandwidth of the monochromator, the interference from stray scattered light had to be reduced. Apertures were placed along the beam to prevent stray light or back reflections from crossing the burner surface. The fluorescence collection optics were shielded from the rest of the experimental setup by dense black felt curtains. An entrance hole in the curtains at the collection lens allowed the fluorescence to pass from the flame to the fluorescence collection optics.

4.5.2 Signal Detection and Data Acquisition Setup

The output of the reference photodiode was measured with a Stanford Research Systems Model SR250 gated integrator and boxcar averager module. A second Model SR250 gated integrator and boxcar averager was used to measure the output of the photomultiplier tube (PMT). For scans of the burner surface to determine the reference height, the output of the post-burner photodiode was measured with the second gated integrator and boxcar averager. Both gated integrators and boxcar averagers were triggered by the trigger photodiode that monitored the dye laser output.

The delay and width of the boxcar gate were determined by observing the gate output and either the photodiode and PMT signals on a Hewlett-Packard HP54502A digital sampling oscilloscope. The gate width and delay were set to integrate over the signal corresponding to the first lobe of the laser pulse.

The output of the two gated integrators and boxcar averagers were sent to a Stanford Research Systems Model SR245 computer interface module for analog-to-digital conversion. The same modified SR265 program used for the scattering-extinction measurements (Sec. 4.4.2) was used to acquire the data for the OH LIF measurements. Vertical profiles of the OH fluorescence or Rayleigh scattering were measured by setting up the program to sample the reference photodiode and PMT signals for 600 samples (equivalent to one minute at a 10 Hz repetition rate). The voltage data acquired by the computer interface were stored on the IBM PC's hard disk in binary format for later analysis.

The modified SR265 program was also used to measure both fluorescence excitation and detection scans. For an excitation scan, the program was set up to drive the dye laser grating through a stepper-motor gear box. The reference photodiode and the PMT signals were sampled for each step of the stepper motor. The sampling and the movement of the stepper motor were triggered by the trigger photodiode signal at the

10 Hz laser repetition rate. The range of the wavelength scan was determined by the number of samples recorded. Detection scans were set up in a similar manner, except that the program moved the monochromator grating through a stepper-motor gear drive.

4.5.3 Experimental Procedure

Prior to the measurement of the OH fluorescence profiles in the flames, the monochromator and the dye laser grating wavelengths were calibrated and the linear range of the photomultiplier tube (PMT) voltage was verified. The monochromator wavelength readout was calibrated using the spectral lines from a mercury lamp over the range from 284.7 nm to 329.2 nm. The dye laser grating wavelength readout was calibrated by using a laser excitation scan of the (0,0) band of OH in a rich nonsooting flame. The monochromator was set to monitor a 1-nm bandwidth from 306.5 nm to 307.5 nm to capture the fluorescence from the major R-branch lines. The OH fluorescence was measured as the dye laser grating was scanned over the wavelength range from 305.0 nm to 316.75 nm. The measured OH fluorescence spectrum was compared with a previously measured absorption spectrum from another experiment (Carter, 1990) and the known OH wavelengths in the (0,0) band of OH (Dieke and Crosswhite, 1962; Coxon, 1980) to determine the wavelengths of the spectral peaks. The dye laser grating readouts were fit to their corresponding wavelengths with a linear least squares curve fit to obtain the final calibration for the dye laser grating readout.

The linear range of the PMT output voltage was verified using Rayleigh scattering from nitrogen flow and the calibrated neutral density filters to attenuate the scattering signal. The spectral bandwidth of the monochromator was measured by scanning the wavelength of the monochromator while measuring Rayleigh scattering from flowing nitrogen.

The procedure for measurement of the OH fluorescence profiles began with alignment of the dye laser beam by centering it on the alignment apertures on either side of the burner and on the reference photodiode. The reference height of the burner was measured by sampling the reference and post-burner photodiode signal voltages as the burner was scanned through the laser beam. The reference height was chosen to be the height at which the midpoint occurred between the maximum and minimum of the ratio of the post-burner to reference signals. The reference height was measured while the pressure was at 80 torr for the subatmospheric experiments.

The fluorescence collection lenses were aligned to maximize the scattered signal from nitrogen flowing from the burner. This alignment was satisfactory for the fluorescence measurements since the monochromator spectral bandwidth included the excitation wavelength. The PMT and reference photodiode signals were then sampled to determine a Rayleigh scattering calibration factor. For the subatmospheric pressure experiments, the Rayleigh scattering calibration factor was measured for flowing nitrogen at 80 torr. Vertical profiles of the Rayleigh scattering signal from flowing nitrogen were measured above the burner, one with the lower half of the collection lens blocked, and one with the lens unblocked, to determine the calibration factors for both setups and also to determine the magnitude and location of the vignetting by the burner surface.

Following the Rayleigh scattering calibration, the start-up flows of nitrogen, oxygen, and ethylene were set and the flame was ignited with a propane torch. The flow rates were adjusted for an atmospheric pressure lean flame with an equivalence ratio $\phi = 0.97$ (flame A-0-L in Table 4.2). This flame was used as the calibration standard for the OH fluorescence measurements.

The dye laser wavelength was tuned to the peak of the $Q_1(8)$ line by scanning the dye laser grating through a 0.25 nm range encompassing the $P_1(3)$ (309.2089 nm), $Q_2(5)$ (309.2260 nm), $Q_1(8)$ (309.3294 nm), and the $Q_2(6)$ (309.3688 nm) lines. For the set of

measurements made with $P_1(8)$ excitation, the dye laser wavelength was set to the peak of the $P_1(8)$ line by scanning the dye laser grating through a 0.25 nm range encompassing the $P_2(7)$ (311.8098 nm) and the $P_1(8)$ (311.8793 nm) lines. Once the laser was tuned to the $Q_1(8)$ line (or to the $P_1(8)$ line), the fluorescence collection optics were aligned to obtain the maximum fluorescence signal.

For each flame, two vertical profiles of the broadband OH fluorescence voltage and the reference photodiode voltage were measured with different height resolutions and ranges. A fine resolution profile was measured near the burner surface to measure the change in OH fluorescence through the flame front, A coarser resolution profile was measured to observe the fall-off of the OH fluorescence signal in the post-flame region. The parameters for these profiles are listed in Table 4.6.

Table 4.6 Height interval, height range and initial height for the OH fluorescence profiles.

Experiment and Type of Profile	Height Interval (mm)	Height Range (mm)	Initial Height (mm)
<u>80 Torr pressure</u>			
Fine resolution	0.50	10.0	0.5
Coarse resolution	1.00	30.0	0.5
<u>Atmospheric pressure</u>			
Fine resolution	0.25	5.0	0.5
Coarse resolution	1.00	20.0	0.5

The Rayleigh scattering background was measured in the flame by tuning the laser wavelength off of the Q₁(8) (or the P₁(8)) line. Vertical profiles of the Rayleigh scattering voltage and the reference photodiode voltage were measured with the same height resolution and range as the OH fluorescence profiles.

4.5.4 Data Analysis

The OH fluorescence and OH number density profiles were calculated from the measured voltage outputs of the photomultiplier and reference photodiode recorded as a function of height above the burner. The light detected at the output of the monochromator by the photomultiplier contained contributions from the OH fluorescence and from Rayleigh scattering by the flame gases, since the spectral bandwidth of the detector included the laser excitation as well as OH fluorescence from the (0,0) band. If the incident light is kept within the linear range of the photomultiplier, then the measured output of the photomultiplier, $V_m(V)$, can be expressed as the sum of the voltage caused by the fluorescence, $V_f(V)$, and a voltage caused by the Rayleigh scattering, $V_R(V)$. The output of the photomultiplier is

$$V_m(z) = V_f(z) + V_R(z) = \eta_{Em} \cdot (S_f(z) + S_R(z)) \quad (4.5.1)$$

where η_{Em} is an electronic conversion efficiency ($V \cdot W^{-1}$) that accounts for the conversion from a light signal to an electronic signal and also for the gains in the subsequent detection electronics. The voltages are written as a function of z to indicate that they are recorded as profiles. Recall from Section 3.3 that the fluorescence signal, $S_f(W)$, is given by Eq. (3.3.10) as

$$S_f(z) = \eta_o \cdot \Omega_c \cdot V_c \cdot \epsilon_{fB}(z) \quad (4.5.2)$$

where η_o is the optical efficiency of the detector optics, Ω_c (sr) is the solid collection angle, V_c (cm³) is the collection volume, and ϵ_{fB} ($W \cdot \text{cm}^{-3} \cdot \text{sr}$) is the fluorescence emission. The Rayleigh scattering signal, $S_R(W)$, is given by Eq. (3.3.12) as

$$S_R(z) = \eta_o \cdot \Omega_c \cdot V_c \cdot Q_{VV,g} \cdot I_L(z) \quad (4.5.3)$$

where $Q_{VV,g}$ ($\text{cm}^{-1} \cdot \text{sr}^{-1}$) is the differential scattering coefficient of the gases and I_L ($\text{W} \cdot \text{cm}^{-2}$) is the incident laser irradiance.

The incident laser irradiance was measured by the reference photodiode and its measured output voltage, V_o (V), is given by

$$V_o(z) = \eta_{o0} \cdot \eta_{E0} \cdot I_L(z) \quad (4.5.4)$$

where η_{o0} is the optical efficiency of the reference detection optics and η_{E0} ($\text{V} \cdot \text{cm}^2 \cdot \text{W}^{-1}$) is the electronic conversion efficiency of the reference detector electronics.

The profiles of the measured photomultiplier voltage, $V_m(z)$, and the reference photodiode voltage, $V_o(z)$, were calculated from the voltage data recorded by the SR265 program during the measurement of the OH fluorescence profiles, the Rayleigh scattering background profiles, and the calibration factors. These calculations were made using a set of programs (similar to those written for the scattering-extinction data analysis) written in the ASYST version 3.10 scientific programming language (ASYST Software Technologies, Inc., Rochester, NY).

These programs first read the stored binary-format voltage data acquired by the computer interface and then calculated the photomultiplier voltage, V_m , and the reference photodiode voltage, V_o , based on the gains and offsets of the gated integrators and boxcar averagers used to detect them. Since these voltages were sampled for a minute (600 samples) at each height, the means of the sampled voltages at each height were calculated to determine the profiles, $V_m(z)$ and $V_o(z)$. The standard deviations of the voltages at each height were also calculated to evaluate their variation during the measurement.

4.5.4.1 Rayleigh Scattering Background Corrections

The first step in the analysis of the OH fluorescence profiles was the correction for the Rayleigh scattering background. The Rayleigh scattering background to the

fluorescence signal was calculated from the scattering coefficient of the flame gases, which was measured by tuning the laser away from the OH transition. The measured photomultiplier voltage was thus caused only by Rayleigh scattering and $V_m = V_R$. From Eqs. (4.5.1), (4.5.3), and (4.5.4), the molecular scattering coefficient can be determined from the ratio of the photomultiplier to the reference photodiode voltages by

$$Q_{vv,s}(z) = \frac{1}{F_R} \cdot \frac{V_m(z)}{V_0(z)} \quad (4.5.5)$$

where the Rayleigh scattering calibration factor, F_R , is defined as

$$F_R = \frac{\eta_{Em} \cdot \eta_{O}}{\eta_{O0} \cdot \eta_{E0}} \cdot \Omega_c \cdot V_c \quad (4.5.6)$$

The Rayleigh scattering calibration factor was determined by measuring the ratio of the photomultiplier signal to the reference photodiode signal from a nitrogen flow in the same manner as for the scattering-extinction measurements (Eq. 4.4.9). The calibration factor was determined from

$$F_R = \frac{R \cdot T}{P \cdot N_{av}} \cdot \frac{1}{C_{vv,N_2}} \cdot \left(\frac{V_m}{V_0} \right)_{cal} \quad (4.5.7)$$

where R ($82.055 \text{ cm}^3 \cdot \text{atm} \cdot \text{gmol}^{-1} \cdot \text{K}^{-1}$) is the gas constant, N_{av} ($6.023 \times 10^{23} \text{ gmol}^{-1}$) is Avogadro's constant and C_{vv,N_2} is the differential scattering cross-section for nitrogen. The temperature, T (K), and the pressure, P (atm), of the flowing nitrogen were measured during the calibration. The differential scattering cross-section for nitrogen is $C_{vv,N_2} = 5.882 \times 10^{-27} \text{ cm}^2 \cdot \text{sr}^{-1}$ at the $Q_1(8)$ wavelength, $\lambda = 309.329 \text{ nm}$, and $C_{vv,N_2} = 5.681 \times 10^{-27} \text{ cm}^2 \cdot \text{sr}^{-1}$ at the $P_1(8)$ wavelength, $\lambda = 311.879 \text{ nm}$. Both cross-sections were determined from the data of Gardiner, Hidaka, and Tanzawa (1981).

The Rayleigh scattering coefficient profiles were determined from the profiles of the photomultiplier signal to the reference photodiode signal and the scattering calibration factor using Eq. (4.5.5). Although the Rayleigh scattering coefficient profiles were

measured by tuning the dye laser away from the peak of the $Q_1(8)$ line, some of the profiles contained a peak at the same location as the OH fluorescence peak. The behavior of the profiles suggests that some fluorescence was still excited by the laser and thus, the measured Rayleigh scattering coefficient profiles did not give a true measure of the background. Nevertheless, they were still used in the following manner to determine a good estimate of the background signal. Rayleigh scattering coefficients measured far downstream from the flame front in rich flames showed no significant interference from OH fluorescence because the OH concentrations have dropped significantly. Scattering coefficients predicted from an adiabatic solution of the flame equations agree well with the measured scattering coefficients downstream. The scattering-extinction measurements made at 488.0 nm show that the scattering coefficients of the flame gases remain constant throughout the flame except for a small region near the surface of the burner. Thus, the Rayleigh scattering coefficients measured far downstream were used as an estimate of the mean Rayleigh scattering coefficient for the flame. The use of a mean value should be valid except for the region near the burner surface, but there the OH concentrations are high and the Rayleigh scattering background does not pose a significant interference to the fluorescence signal.

The Rayleigh scattering background contribution to the measured fluorescence signal was calculated using the measured scattering calibration factor, the estimated mean scattering coefficient, and the reference photodiode voltage using the expression

$$V_R(z) = F_R \cdot Q_{VV,R} \cdot V_0(z) \quad . \quad (4.5.8)$$

The fluorescence voltage profile was then determined by subtracting the calculated Rayleigh scattering background contribution from the measured photomultiplier signal, i.e.,

$$V_f(z) = V_m(z) - V_R(z) \quad . \quad (4.5.9)$$

4.5.4.2 Normalized Fluorescence Profiles

The fluorescence voltage profile in a flame can be related to the fluorescence emission profile by combining Eqs. (4.5.1) and (4.5.2) to obtain

$$V_f(\phi, z) = \eta_{Em} \cdot \eta_O \cdot \Omega_c \cdot V_c \cdot \epsilon_{fB}(\phi, z) \quad (4.5.10)$$

where the fluorescence voltage and emission have been written as a function of the flame stoichiometry, ϕ , and height above the burner, z . The dependence of the voltage profiles on the optical constants and efficiencies can be removed by normalizing the fluorescence voltage profile to a fluorescence voltage measured in a calibration flame with the same optical setup. Then the fluorescence emission profiles are related to the normalized voltage profiles by

$$\frac{\epsilon_{fB}(\phi, z)}{\epsilon_{fB}(\phi_{cal}, z_{cal})} = \frac{V_f(\phi, z)}{V_f(\phi_{cal}, z_{cal})} \quad (4.5.11)$$

From Section 3.3.1 the fluorescence emission for broadband spectral and temporal detection is given by Eq. (3.3.9) as

$$\epsilon_{fB} = \alpha \cdot \left[\frac{A}{A + Q} \right] \cdot N_1^0 \cdot \int I_L(t) \cdot dt \quad (4.5.12)$$

where α is a constant that depends on the laser and fluorescence wavenumbers and the absorption cross-section, A and Q are integrated rate coefficients for spontaneous emission and quenching, and N_1^0 is the ground state number density. Combining Eqs. (4.5.11) and (4.5.12) and rearranging gives an expression for the ground state number density profile as

$$N_1^0(\phi, z) = N_1^0(\phi_{cal}, z_{cal}) \cdot \left[\frac{A}{A + Q} \right]_{\phi_{cal}, z_{cal}} \cdot \left[\frac{A}{A + Q} \right]_{\phi, z}^{-1} \cdot \frac{V_f(\phi, z)}{V_f(\phi_{cal}, z_{cal})} \quad (4.5.13)$$

The influence on the laser irradiance was neglected by assuming that the temporal laser irradiance remained the same between the calibration and measurement conditions. This assumption is reasonable since the laser energy and pulse shape were observed to remain constant over the period of the tests on a single day.

The relative fluorescence profiles measured in the atmospheric pressure flames were normalized to the fluorescence signal voltage measured on the same day in the post-flame region of the lean flame (flame A-0-L, $\phi = 0.97$). The relative fluorescence profiles measured in the 80-torr flames were normalized to the fluorescence signal voltage measured on the same day in the post-flame region of the leanest rich nonsooting flame (flame L-II-R1, $\phi = 2.03$). The conversion of the normalized relative OH fluorescence profiles to absolute OH number density profiles is discussed in Chapter 6.

4.6 Chemical Kinetic Modelling

The flame chemistry in this study was modelled with the Sandia laminar premixed one-dimensional flame code (Kee et al., 1985) and its associated programs. The flame code was used to evaluate chemical kinetic reaction mechanisms describing the oxidation and pyrolysis of ethylene. The chemical kinetic modelling studies were used to compare the measured and predicted OH concentration profiles to evaluate postulated fuel-rich reaction mechanisms. These studies were also used to estimate the molar composition profiles of the flames, so that the temperature profiles could be estimated from the measured scattering coefficient profiles. The results from the chemical kinetic modelling studies could subsequently be used in a sensitivity analysis and a reaction pathway analysis to identify the role of particular species and reactions in the creation and destruction of other species, particularly PAHs and soot.

The Sandia flame code solved the mass, species, and energy equations for a constant-pressure steady laminar premixed one-dimensional flame to determine the species and temperature profiles. The equations were solved for a burner-stabilized flame

with the following boundary conditions: fixed constant mass flow rate, specified temperature and species mass flux fractions at the burner surface, and vanishing species and temperature gradients at the hot boundary (far downstream from the flame front). The production rates of the species were calculated by summing the production rates from the rate expressions for the elementary reactions in the reaction mechanism. The thermal conductivities and the diffusion coefficients were calculated from the thermodynamic and transport properties of the species entered from the thermodynamic and transport property databases.

The flame code program calculates the solution to the system of algebraic equations generated from the finite difference approximation of the mass, species, and energy conservation equations. A damped modified Newton algorithm was used to find the solution. When the Newton algorithm failed to converge, the program used time integration methods to calculate a better solution estimate for the Newton algorithm. The program first found the solution on a coarse mesh of flame positions and then refined the solution by adding positions to the profile where the solution or the gradients changed most rapidly.

The flame code program required input from a keywords file that described the flame problem to be solved and from two binary link files, one that contained the thermodynamic properties of the species and the reaction rate data and one that contained the transport properties of the species.

The binary link file containing the thermodynamic properties and reaction rates was generated by the Chemkin-II Interpreter program (version 1.6 April 1990; Kee, Rupley, and Miller, 1989) from two input files, a reaction mechanism description file and a thermodynamic property database file. The reaction mechanism description file

contained a list of the elements and species in the mechanism and a list of the elementary reactions with their forward reaction rate coefficients. The forward reaction rate coefficients were determined from the modified Arrhenius rate expression:

$$k_f = A \cdot T^\beta \cdot \exp\left(\frac{-E_i}{RT}\right) \quad (4.6.1)$$

where k_f is the forward rate coefficient (moles·cm⁻³·sec⁻¹ units), A is the pre-exponential factor, β is the temperature exponent, E_i is the activation energy (cal·mole⁻¹), R is the gas constant (1.987 cal·mole⁻¹·K⁻¹), and T is the temperature (K). The thermodynamic property database file contained the specific heat, enthalpy, and entropy of each species in the form of two seven coefficient polynomial fits over an upper and lower temperature range. Each species entry also contained the species name, its elemental composition, its phase, and the temperature range for the polynomial fits. We used the Chemkin thermodynamic database reported by Kee, Rupley, and Miller (1987).

The binary link file containing the transport properties was generated by the Chemkin-II transport property fitting program (version 1.5 August 1989; Kee, Warnatz, and Miller, 1983) from two input files, a transport property database file and the binary link file generated by the Chemkin Interpreter. The transport property fitting program calculated the polynomial fits for the viscosities, thermal conductivities, and binary diffusion coefficients for each species from the molecular parameters stored in the transport property database file and the thermodynamic data in the interpreter link file. The transport property database used in these calculations was supplied along with the transport property subroutines by Kee et al. (1986).

The flame code program (version 1.6, February 1990) was compiled with the Chemkin-II chemical kinetics subroutine library (version 2.0, January 1990; described by Kee, Rupley, and Miller, 1989) and the Chemkin-II multicomponent transport subroutine library (version 1.3 February 1990; described by Kee et al., 1986). The multicomponent

transport subroutines were used to guarantee mass conservation and to calculate the diffusion coefficients, viscosities, and thermal conductivities more accurately than transport subroutines using approximate mixture averaging rules. The double precision versions of the flame code program, the preprocessor programs, and the subroutine libraries were compiled and run on a Sun Microsystems Sparcstation 1 and a Gould PN9080. Both computers are 32-bit machines and use the UNIX operating system. The calling programs for the flame code and the preprocessor programs were modified to access files within the UNIX filesystem.

The species and temperature profiles calculated by the flame code were written to an ASCII file and to two binary files. The formatted ASCII output contained the record of the interim calculations in the solution procedure and then the final solution with the position, temperature, velocity, and mass density profiles along with the mole fraction profiles of each species. The binary files contained the pressure, mass flux, the number of species and the number of grid points and an array containing the position, temperature, and species mass fraction profiles. The binary 'restart' file was written when a final solution was found. The binary 'recover' file was written every time an interim solution was found. The binary restart and recover files could be read by the flame code program to generate an initial solution estimate that typically converged faster to the final solution than if the program guessed the initial solution. This feature could be used to refine the mesh of a previous solution for a set of flame conditions or to start from an interim solution should the computer fail in the middle of a solution calculation. It could also be used as a starting point for solutions for different flame conditions or for solutions with the same flame conditions but with a different reaction mechanism.

A set of computer programs were written to extract and analyze data from the flame code solution. These programs were written using the Chemkin-II subroutine library (Kee, Rupley, and Miller, 1989) to access the Chemkin interpreter link file and the binary

restart file. One set of programs was written to read the mass fraction profiles from the binary restart file to generate a file containing the mole fraction profiles or a file containing the number density profiles. Another program could then read these files and then extract the species profiles for plotting.

To use a solution from one reaction mechanism as an initial solution for another reaction mechanism, a program was written to convert the mass fraction profiles in the restart file by either subtracting species profiles not present in the new mechanism or by adding zero mass fraction profiles for species in the new mechanism but not in the old mechanism. Another program was written to calculate scattering cross-section and scattering coefficient profiles from the temperature and species mole fraction profiles. This program was used to estimate temperature profiles from the measured scattering coefficient data as outlined in Sec. 4.4.4 and discussed in detail in Appendix C.

Preliminary temperature and species profiles for the flames in this study were calculated with the flame code using the reaction mechanism of Drake and Blint (1991). The nitrogen chemistry reactions (reactions 124 through 202 in Table I of Drake and Blint, 1991) were removed to reduce the mechanism size to 32 species and 144 reactions and, thus, speed the solution time. The Drake and Blint mechanism was derived from the Glarborg, Miller, and Kee (1986) mechanism (henceforth called the GMK mechanism) which was developed to model NO_x formation during methane combustion. Drake and Blint modified the reaction rate coefficients for the methyl and ethyl recombination reactions in addition to modifying some of the nitrogen chemistry. Vaughn et al. (1991) found that the GMK mechanism predictions for the stable species concentrations showed good agreement with their measurements of rich ethylene combustion in a jet-stirred reactor. Thus, this mechanism was deemed to be a good starting point for the modelling of these flames. It could be used to obtain the initial solutions for these flames and to predict the major species profiles for the estimation of the scattering coefficient profiles.

The preliminary temperature and species profiles for the sequences of flames were calculated using the energy equation to determine the temperature profile. The solutions were found in the following manner:

1. The solution was calculated on a coarse mesh of 16 to 23 grid points (positions in the profile) for the leanest flame in a sequence of flames with the same cold flow velocity and dilution ratio. This coarse mesh solution was saved in a binary restart file.
2. The solution for the flame was restarted from the coarse binary restart file and refined to a final mesh of 80 to 125 grid points by setting the upper bounds on the solution gradient and curvature to 0.10 and 0.20, respectively.
3. The solution for the next richer flame in the sequence was calculated on a coarse mesh of 16 to 23 grid points. This solution used the previous flame's solution on a coarse mesh (contained in the binary restart file) as the initial solution estimate. The final coarse mesh solution was saved in a binary restart file to be refined further and to be used for the next richer flame solution.

Steps 2 and 3 were repeated for each successively richer flame in a sequence to obtain the refined solution for each flame. This procedure of using the previous flame's solution as the starting point for the next flame's solution was much faster than if each solution had been found from scratch.

These flame code solutions based on the Drake and Blint mechanism were used to predict the major species profiles for estimation of the temperature profile from the measured scattering coefficient profile as described in Sec. 4.4.4 and Appendix C. Determination of the temperature profile for these flames can speed up subsequent flame code calculations using different reaction mechanisms by removing the need to use the energy conservation equation to calculate the temperature profile.

The solutions obtained using the Drake and Blint mechanism were then used as the starting point for flame code solutions using the reaction mechanism of Miller and Melius (1992). Their mechanism models the rich combustion of acetylene and includes the formation of the single-ring aromatic species, benzene and phenyl radical. The aromatic formation mechanism includes the reaction pathways through both the C₃ and C₄ intermediate species. They report that the mechanism modelled well the measured species profiles of Bastin et al. (1988) for a lightly sooting 20-torr acetylene/oxygen/argon flame. The Miller and Melius mechanism containing 50 species and 221 reactions was used without further modification to model the flames in this study. Updated Chemkin thermodynamic property and transport property databases (Miller and Melius, 1992) were used because some of the C₃ and C₄ species were not present in our earlier versions of these databases. The flame code solutions obtained with this mechanism were used to compare the predicted with the measured OH concentration profiles. They were also used to investigate the behavior of the aromatic species profiles in the flames as the equivalence ratio was increased from nonsooting to sooting conditions.

CHAPTER 5:
LASER SCATTERING-EXTINCTION MEASUREMENTS
OF SOOT FORMATION IN PREMIXED ETHYLENE FLAMES

5.1 Introduction

In this chapter, we report on measured vertical profiles of soot particle volume fraction, number density, and particle size in sequences of flat flames as their equivalence ratio is increased from nonsooting conditions to lightly sooting conditions near the critical equivalence ratio through more heavily sooting conditions. These measurements of soot formation can serve as a basis for evaluating chemical kinetic models that have been developed to describe and predict soot formation in flat laminar premixed flames. When combined with profiles of the OH radical concentration measured in the same sequences of flames (described in Chapter 6), such measurements can serve as a basis for investigating the role of the OH radical in soot formation.

Three sequences of atmospheric pressure, flat $C_2H_4/O_2/N_2$ flames were examined in which the equivalence ratio was varied within the sequence, while the cold flow velocity (v_c) and the dilution ratio ($D = \dot{V}_{N_2}/\dot{V}_{O_2}$) were held constant. Two of the flame sequences had the same cold flow velocity ($v_c = 7.7 \text{ cm}\cdot\text{sec}^{-1}$), but different dilution ratios ($D = 4.2$ for flames in the A-IA sequence and $D = 3.5$ for flames in the A-IB sequence). The third flame sequence (A-IIA) had a higher cold flow velocity ($v_c = 10.4 \text{ cm}\cdot\text{sec}^{-1}$), but approximately the same dilution ratio ($D = 4.3$) as the first sequence (A-IA). Two sequences of 80-torr, flat C_2H_4/O_2 flames were also examined in which the equivalence ratio was varied while the cold flow velocity was held constant. Since no nitrogen diluent was used in these sequences of flames, their dilution ratio was zero. The two sequences

of 80-torr flames had different cold flow velocities ($v_c = 18.1 \text{ cm}\cdot\text{sec}^{-1}$ for the flames in the L-I sequence and $v_c = 22.4 \text{ cm}\cdot\text{sec}^{-1}$ for the flames in the L-II sequence). The flow rates, equivalence ratios, cold flow velocities, and dilution ratios of these flames are listed in Tables 4.1 and 4.2 in Section 4.3.

The profiles of soot volume fraction, particle number density, and particle size for these flames were measured with the laser scattering-extinction method. The theory of the laser scattering-extinction method and its application to sooting flames is described in Section 3.2. Profiles of the scattering coefficient and the extinction coefficient were measured with the experimental apparatus described in Section 4.4. The soot volume fraction, particle number density, and particle size profiles were then calculated from the measured scattering and extinction coefficient profiles. In addition to the scattering and extinction coefficient profiles, the laser scattering-extinction apparatus was used to measure profiles of the depolarized scattered light signal and the argon-ion laser-induced fluorescence. These additional measurements were used to quantify background contributions to the scattering and extinction measurements and also to interpret the behavior of sooting flames near the critical equivalence ratio.

We first present and describe the features of the extinction coefficient and the scattering coefficient profiles measured in the sequences of the atmospheric-pressure flames. We then present and describe the scattering coefficient profiles measured in the 80-torr flames. Measurements of the argon-ion laser-induced fluorescence are described next for the atmospheric sooting flames. Profiles of the horizontally polarized component of the scattered light are then presented for both the atmospheric and subatmospheric pressure flames.

Our interpretation of these results follows. We first identify the considerations and assumptions needed to calculate the volume fraction, number density, and particle size profiles from the extinction and scattering coefficient profiles. The volume fraction,

number density, and particle size profiles are then shown for the atmospheric-pressure flames. Based on these measurements, we then identify upper bounds on the soot formed in the flames near the critical equivalence ratio. The extinction coefficient and the fluorescence coefficient profiles are then compared. The temperature profiles estimated from the molecular scattering contribution to the scattering coefficient are presented next. Finally, we examine and discuss the behavior of the sooting flames based on these measured profiles and suggest methods for improving the measurements.

5.2 Results of the Laser Scattering-Extinction Measurements

The laser scattering-extinction method is used to measure two quantities, the transmittance of the laser beam through the flame and the scattered light from the particles and gases in the flame. From these measurements and the calibration, the two primary quantities determined are the extinction coefficient and the scattering coefficient.

The extinction coefficient (K_{ext} cm⁻¹) profile was calculated from the transmittance profile using

$$K_{ext}(z) = -\frac{1}{L} \cdot \ln[\tau(z)] \quad (5.2.1)$$

where L (cm) is the pathlength of the laser through the flame. The extinction coefficient profiles presented here are relative profiles based on the assumed pathlength, $L = 5.6$ cm, equal to the diameter of the burner. The relative extinction coefficient profiles measured in different flames within the same sequence can still be compared, however, because the pathlength remains approximately the same, since the cold flow velocity and dilution ratio were held constant while the equivalence ratio was varied in small increments. The transmittance profiles were normalized to their maximums before the extinction coefficient was calculated. This normalization is equivalent to subtracting an extinction coefficient corresponding to the background extinction at the location of the maximum of the transmittance profile.

The measured scattering coefficient ($Q_{sca} \text{ cm}^{-1}\cdot\text{sr}^{-1}$) is the sum of the possible contributions from particle scattering (Q_{VV}), molecular scattering from the flame gases ($Q_{VV,g}$), and argon-ion laser-induced fluorescence (Q_f) and thus, can be expressed as

$$Q_{sca}(z) = Q_{VV}(z) + Q_{VV,g}(z) + Q_f(\lambda_0, \lambda)(z) \cdot \Delta\lambda \quad . \quad (5.2.2)$$

These individual contributions cannot be identified from a single measurement of the scattering coefficient. Estimates of the molecular scattering contribution were obtained by measuring the scattering coefficient profiles of nonsooting flames with the same cold flow velocity and dilution ratio. Estimates of the fluorescence contribution were obtained by measuring the fluorescence at 473 nm and 503 nm excited by the argon-ion laser at 488.0 nm. The particle scattering contribution can then be calculated by subtracting the estimates of the molecular scattering and fluorescence contributions from the measured scattering coefficient.

The scattering and extinction coefficient profiles were measured in sequences of flames whose range of equivalence ratios spanned the transition from nonsooting to sooting. This systematic approach was undertaken to examine the change in the scattering and extinction coefficient profiles through the soot threshold. Profiles of nonsooting flames provided a baseline for comparison with the profiles of sooting flames. The scattering coefficient profiles for the nonsooting flames were also used to quantify the molecular scattering contribution. The profiles of the sooting flames near ϕ_c were measured to identify how much soot is present in lightly sooting flames and to evaluate the laser scattering-extinction method for measuring the critical equivalence ratio. The profiles of sooting flames at richer equivalence ratios were measured to quantify the trends of soot formation growth with equivalence ratio.

5.2.1 Extinction Coefficient Measurements

5.2.1.1 Atmospheric-Pressure Flames

The extinction coefficient profiles of the three sequences of atmospheric-pressure $C_2H_4/O_2/N_2$ flames are shown in Figures 5.1 to 5.5. The measured range in height above the burner was from approximately 0.5 mm to 15 mm or 20 mm, approximately half the distance from the burner surface to the flame stabilizer. The extinction coefficient profiles presented here represent the average of multiple measurements, though the number of measurements included in the average varies from one to five.

The extinction coefficient profiles of the A-IA sequence of flames are shown in Figures 5.1 and 5.2. The equivalence ratios within this sequence were varied from $\phi = 1.63$ to $\phi = 2.32$, while the cold flow velocity was held constant at $v_c = 7.7 \text{ cm}\cdot\text{sec}^{-1}$ and the dilution ratio was held constant at $D = 4.2$. Within this sequence, the critical equivalence ratio was observed at $\phi_c \sim 1.70$.

The behavior of the profiles as the equivalence ratio is increased from nonsooting to lightly sooting conditions is shown in Figure 5.1, which displays a narrow range of the extinction coefficient profiles corresponding to the transmittance range from $\tau = 1.000$ to $\tau = 0.989$. Based on the error analysis of the transmittance measurements presented in Appendix B, the detection limit for the extinction coefficient was estimated to be $K_{ext} = 1.8 \times 10^{-4} \text{ cm}^{-1}$, which corresponds to a detection limit for the transmittance of $\tau = 0.999$. The extinction coefficient profiles of both the nonsooting flame A-IA-R2 ($\phi = 1.63$) and the lightly sooting flame A-IA-S1 ($\phi = 1.78$, slightly greater than ϕ_c) are approximately flat and fall below this detection limit. The extinction coefficient profile of the next richer flame A-IA-S2 ($\phi = 1.92$) is the first which shows a measurable increase above the detection limit. However, the final extinction coefficient measured at 20 mm above the burner is small, $K_{ext} \sim 11 \times 10^{-4} \text{ cm}^{-1}$, and corresponds to a change in the transmittance of 0.6%.

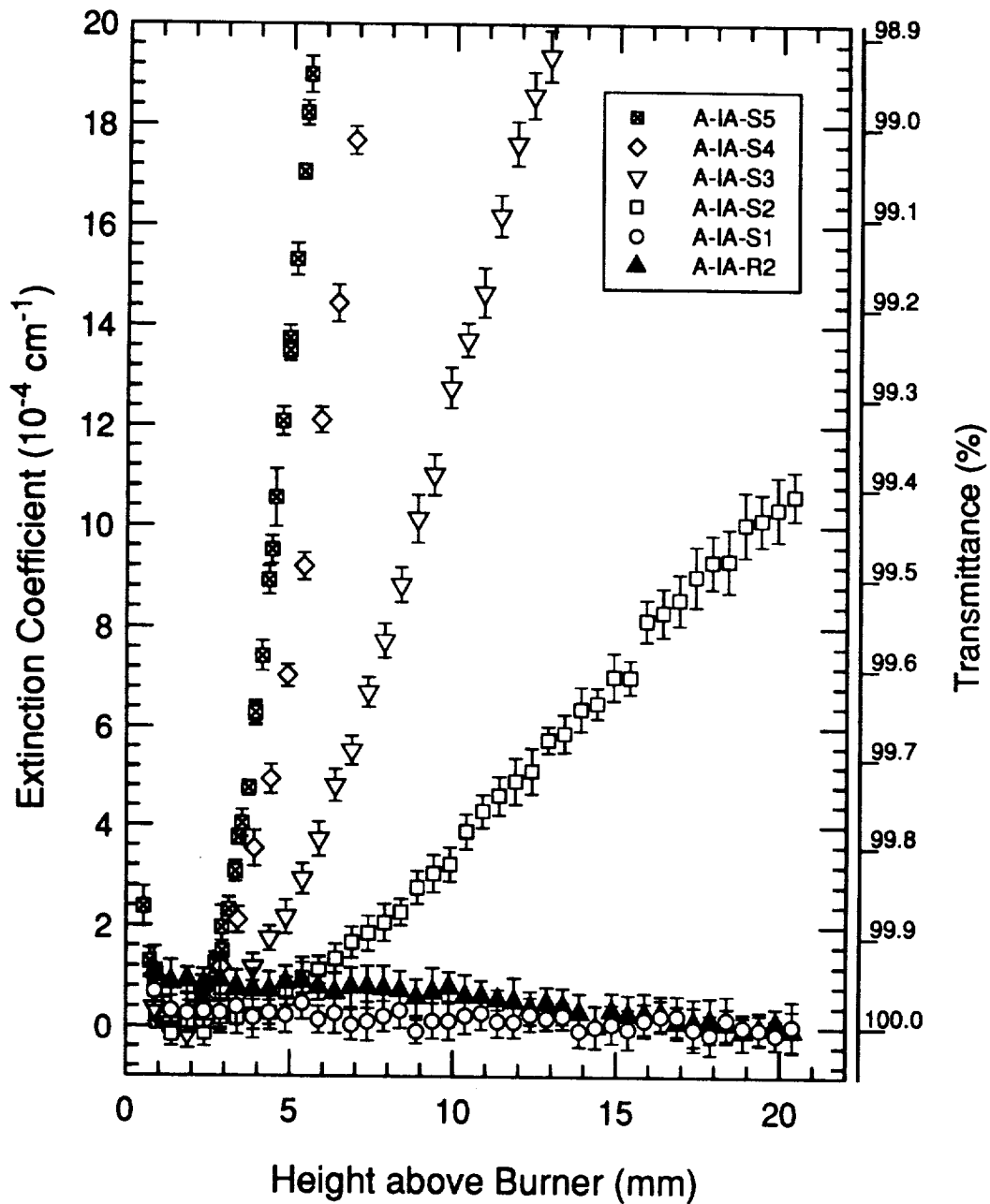


Figure 5.1 Extinction coefficient profiles of the A-IA sequence of flames ($v_c = 7.7 \text{ cm}\cdot\text{sec}^{-1}$ and $D = 4.2$). The narrow range of the extinction coefficient corresponding to the transmittance range from $\tau = 1.000$ to $\tau = 0.989$ shows the detail of the profiles of the lightly sooting flames. The error bars show twice the standard deviation of the measurement.

As the equivalence ratio within this sequence is increased still further, the measured extinction coefficients at a given height increase significantly. The full range of the extinction coefficient profiles for the A-IA sequence of flames is shown in Figure 5.2. The extinction coefficient profiles of the richer sooting flames increase linearly with height over the 20 mm range in height above the burner. In the richer flames (A-IA-S5 and A-IA-S4), the noise in the extinction coefficient measurement increases at heights near 15 mm above the burner as indicated by the increase in the standard deviation of the measurement. This increased noise was probably caused by the flame flicker observed in the less stable richer flames.

The extinction coefficient profiles of the A-IB sequence of flames are shown in Figures 5.3 and 5.4. The equivalence ratios within this sequence were varied from $\phi = 1.67$ to $\phi = 2.17$, while the cold flow velocity was held constant at $v_c = 7.8 \text{ cm}\cdot\text{sec}^{-1}$, approximately the same as that of the A-IA sequence, and the dilution ratio was held constant at $D = 3.5$, 17% lower than that of the A-IA sequence. Within this sequence, a flame at the critical equivalence ratio, $\phi_c \sim 1.67$, was measured, although its $v_c = 7.9 \text{ cm}\cdot\text{sec}^{-1}$ and $D = 3.3$ differ slightly from the remainder of the flames within the sequence.

The behavior of the extinction coefficient profiles as the equivalence ratio is increased from the critical equivalence ratio is shown in Figure 5.3, which shows the narrow range of the extinction coefficient profiles corresponding to the transmittance range from $\tau = 1.000$ to $\tau = 0.989$. The behavior of these extinction coefficient profiles is similar to that of the A-IA flames. The extinction coefficient profile of the flame at the critical equivalence ratio (A-IB-C $\phi = 1.67$) is approximately flat and falls below the detection limit. The extinction coefficient profile increases measurably above the detection limit in the A-IB-S2 ($\phi = 1.92$) flame, but the extinction coefficient at 15 mm is still small, $K_{ext} \sim 9.5 \times 10^{-4} \text{ cm}^{-1}$, and corresponds to a change in the transmittance of 0.5%.

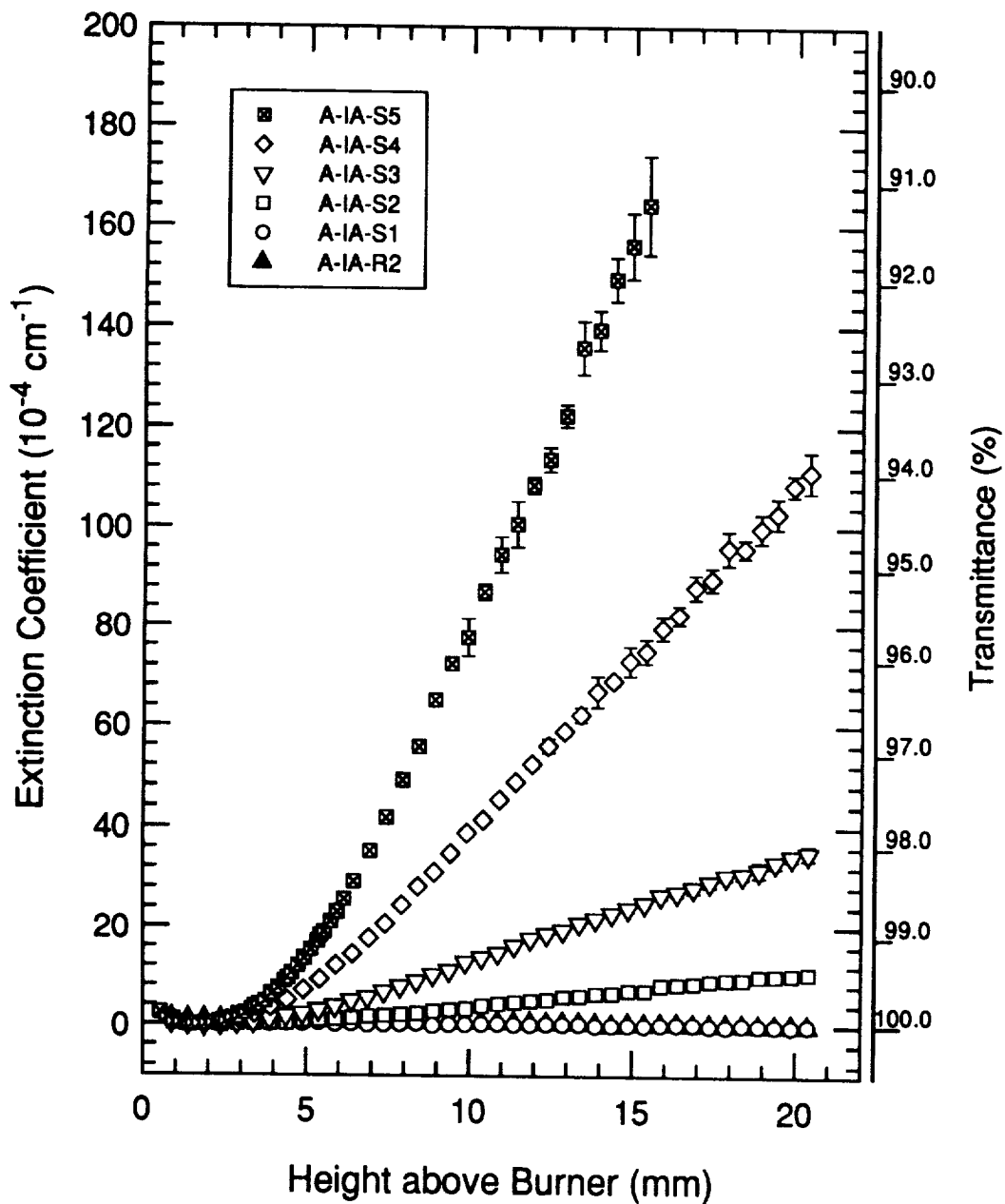


Figure 5.2 Extinction coefficient profiles of the A-IA sequence of flames ($v_c = 7.7 \text{ cm}\cdot\text{sec}^{-1}$ and $D = 4.2$). The full range of the extinction coefficient profiles is shown. The error bars show twice the standard deviation of the measurement.

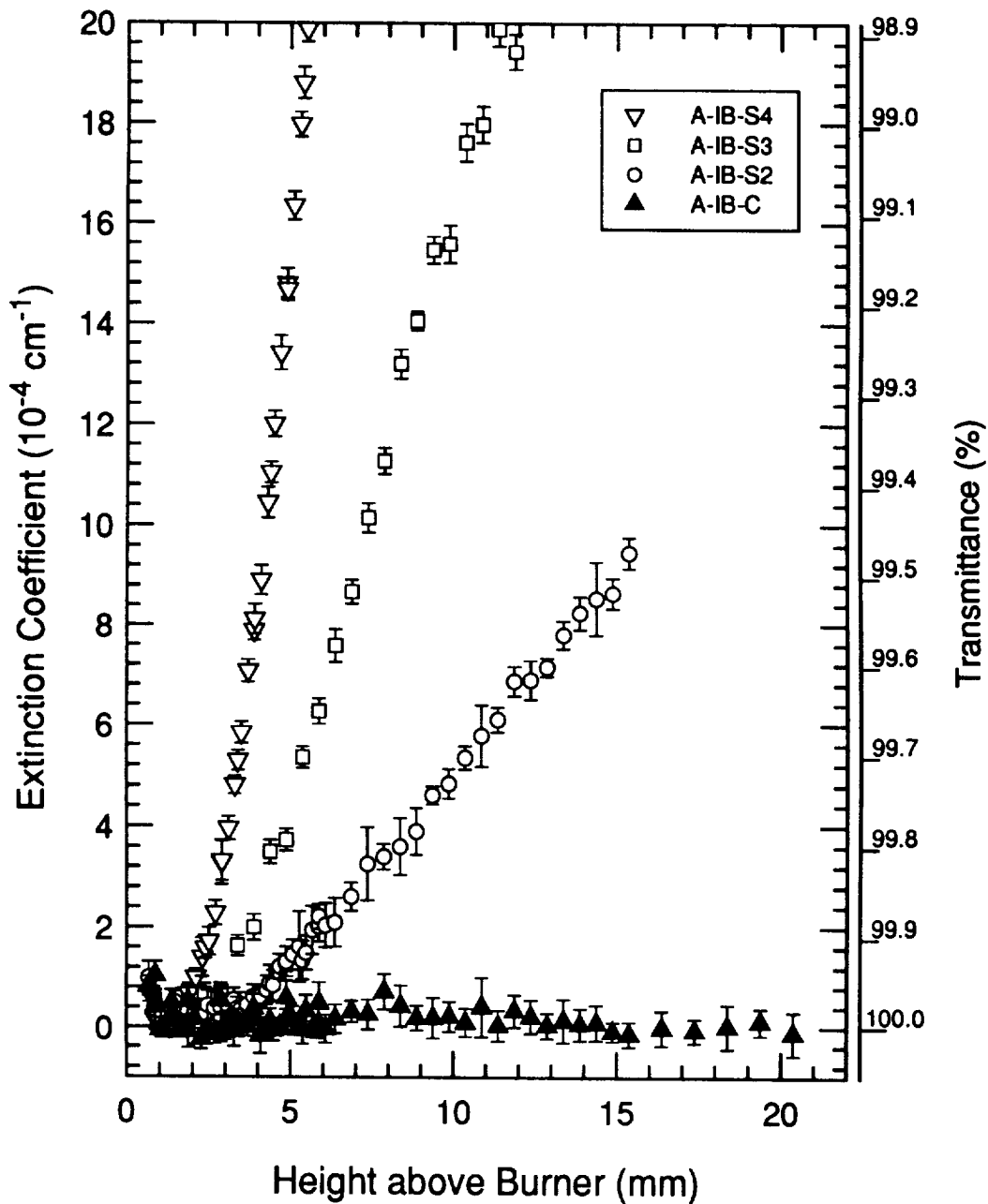


Figure 5.3 Extinction coefficient profiles of the A-IB sequence of flames ($v_c = 7.8 \text{ cm}\cdot\text{sec}^{-1}$ and $D = 3.5$). The narrow range of the extinction coefficient corresponding to the transmittance range from $\tau = 1.000$ to $\tau = 0.989$ shows the detail of the profiles of the lightly sooting flames. The error bars show twice the standard deviation of the measurement.

The full range of the extinction coefficient profiles of the A-IB flames is shown in Figure 5.4. Again, as the equivalence ratio is increased above $\phi = 1.92$, the extinction coefficient increases significantly at a given height. The extinction coefficient profiles increase approximately linearly with height above the burner. The range of extinction coefficients is not as great as that for the A-IA flames, because the richest equivalence ratio investigated in the A-IB sequence was $\phi = 2.17$, while that in the A-IA sequence was $\phi = 2.32$.

The extinction coefficient profiles of the A-IIA flames are shown in Figure 5.5. The equivalence ratios within this sequence were varied from $\phi = 1.63$ to $\phi = 2.02$. The cold flow velocity was kept constant at $v_c = 7.7 \text{ cm}\cdot\text{sec}^{-1}$, which is 35% higher than that of the A-IA sequence, while the dilution ratio was kept constant at $D = 4.3$, approximately the same as that for the A-IA sequence. The A-IIA-S1 flame ($\phi = 1.78$) is at the critical equivalence ratio for this flame sequence.

The full range of the extinction coefficient profiles for the A-IIA flame sequence is shown in Figure 5.5 and falls within the transmittance range from $\tau = 1.000$ to $\tau = 0.989$. Compared with the A-IA flames (Fig. 5.2) and the A-IB flames (Fig. 5.4), the A-IIA flames distinctly produce less soot over the same range of equivalence ratios. However, the behavior of the profiles near the critical equivalence ratio is similar to that of the other flame sequences. The extinction coefficient profiles of both the nonsooting flame (A-IIA-R2) and the flame at or near ϕ_c (A-IIA-S1) are approximately flat and fall below the detection limit. Similar to the other flame sequences, the extinction coefficient profile rises above the detection limit at $\phi = 1.92$ (A-IIA-S2), but only slightly, since $K_{ext} \sim 2.0 \times 10^{-4} \text{ cm}^{-1}$ at 15 mm above the burner. The extinction coefficient increases significantly in the next richer flame (A-IIA-S3 $\phi = 2.02$). Further increases in the equivalence ratio were not possible for this flame sequence since the flame lifted off the burner as the equivalence ratio was increased beyond $\phi = 2.02$.

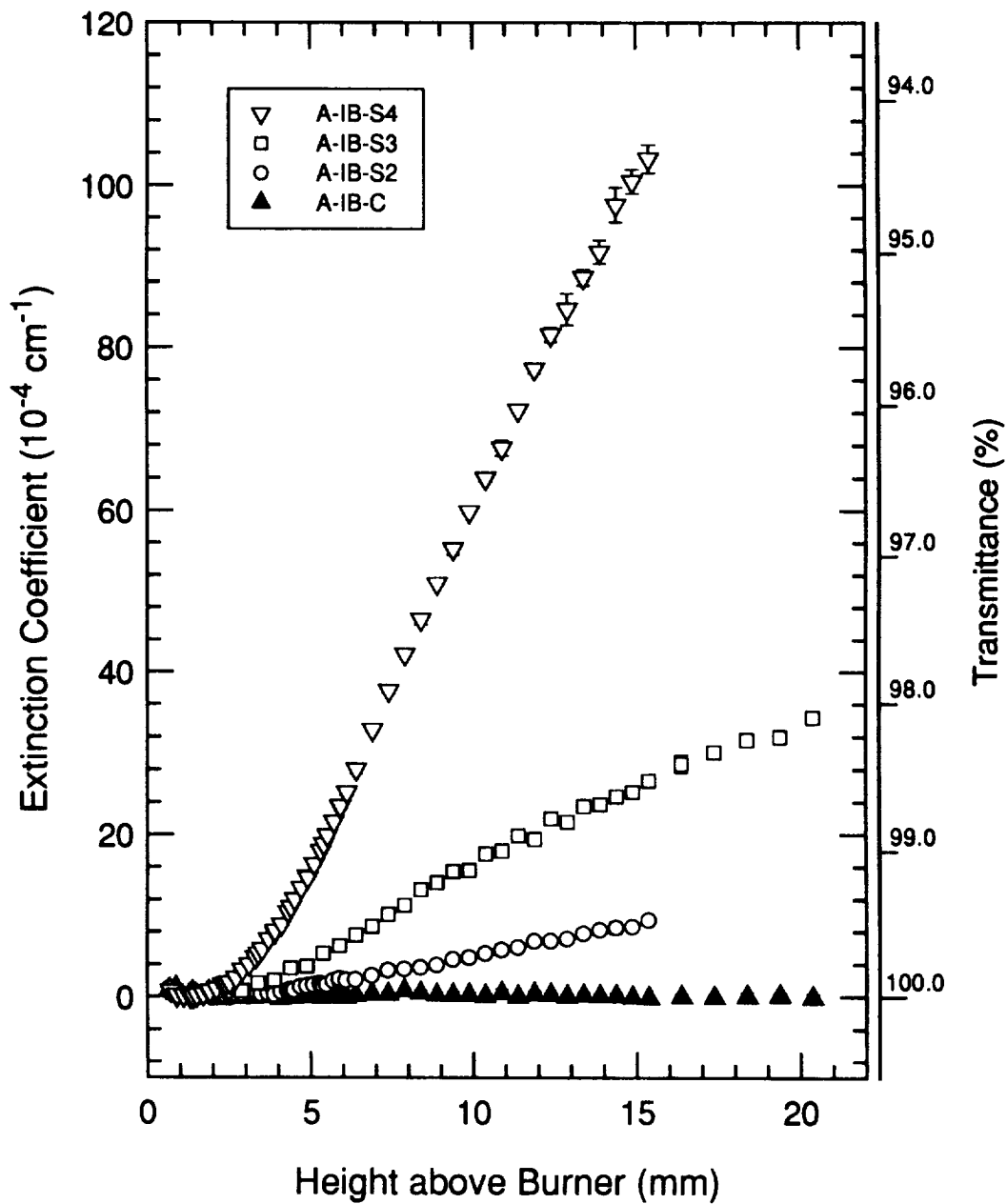


Figure 5.4 Extinction coefficient profiles of the A-IB sequence of flames ($v_c = 7.8 \text{ cm} \cdot \text{sec}^{-1}$ and $D = 3.5$). The full range of the extinction coefficient profiles is shown. The error bars show twice the standard deviation of the measurement.

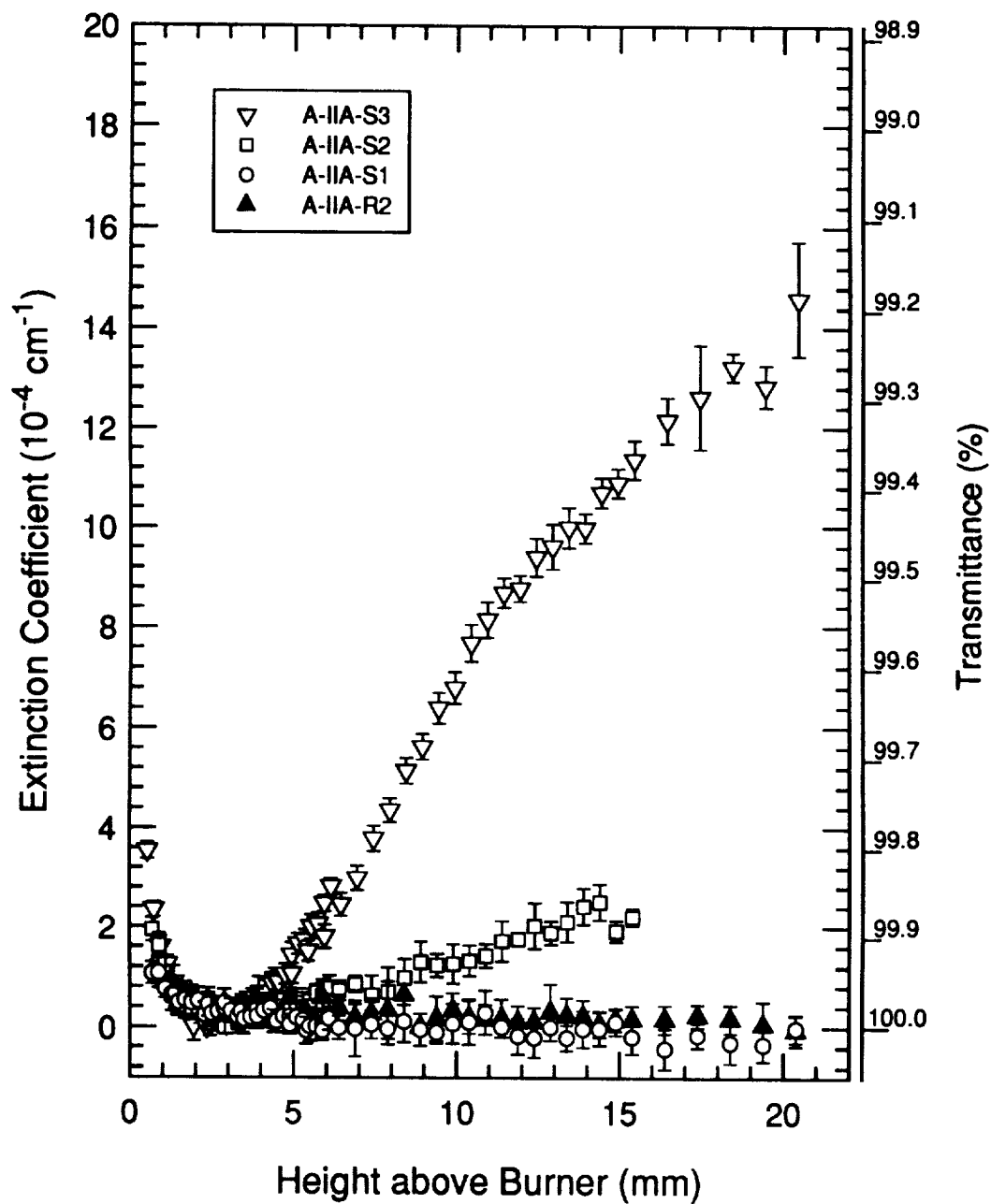


Figure 5.5 Extinction coefficient profiles of the A-IIA sequence of flames ($v_c = 10.4 \text{ cm}\cdot\text{sec}^{-1}$ and $D = 4.3$). The full range of the extinction coefficient profiles is shown. The error bars show twice the standard deviation of the measurement.

The extinction coefficient profiles of the three atmospheric-pressure flame sequences provide a range of sooting conditions to investigate the effects of equivalence ratio, cold flow velocity, and dilution ratio on soot formation. Based on these three flame sequences, the extinction coefficient profile does not increase above the estimated detection limit of $K_{ext} \sim 1.8 \times 10^{-4} \text{ cm}^{-1}$ until the equivalence ratio has been increased beyond the critical equivalence ratio. The smoothness of the measured extinction coefficient profiles, particularly in the lightly sooting flames (-S2 flames, $\phi = 1.92$), suggests that this detection limit may be too conservative.

5.2.1.2 Subatmospheric Flames

We were not able to measure extinction coefficient profiles for the two 80-torr flame sequences. Similar to the atmospheric-pressure flames, we could not detect an extinction coefficient profile in the flames near the critical equivalence ratio. At richer equivalence ratios, false extinction coefficient profiles were observed that were caused by a buildup of a brownish deposit on the window where the laser beam exited the pressure vessel. This was confirmed by switching to a nonsooting flame and observing the same decrease in transmittance as for the sooting flame. The brownish deposit on the window was confined to the spot where the laser beam passed through the window. The exact cause of this deposit is not known. All the windows of the pressure vessel were nitrogen-purged to prevent soot buildup on the windows and with the exception of the exit window, no soot buildup was observed on the windows after running the experiment for several hours. A possible explanation is that the nitrogen purge flow pattern of the exit window may have been uneven and may have blown soot towards the window instead of away from it.

A second difficulty encountered in measuring extinction coefficients for the 80-torr sooting flames was that a soot 'fog' would build up in the stagnant regions within the pressure vessel. The presence of the soot fog would render an extinction coefficient measurement meaningless, because the extinction would no longer be confined to the

flame. In fact, the extinction caused by the fog was likely to be greater than that caused by the flame, because the fog was cooler and thus denser and also had a longer pathlength. We restricted our measurements of the sooting flames to equivalence ratios less than those which generated the soot fog and thus could not examine more heavily sooting flames that might have had a detectable extinction coefficient profile.

Both the soot fog and the window deposits are related problems that would have required a redesign of the pressure vessel and the vacuum exhaust system to solve, as was discussed in Section 4.2.4.

5.2.2 Scattering Coefficient Measurements

5.2.2.1 Atmospheric-Pressure Flames

The scattering coefficient profiles of the three sequences of atmospheric-pressure $C_2H_4/O_2/N_2$ flames are shown in Figures 5.6 to 5.11. Since the scattering coefficient profiles were measured coincident with the extinction coefficient profiles, the same range in height above the burner was measured, i.e., from approximately 0.5 mm to 15 or 20 mm, approximately half the distance from the burner surface to the flame stabilizer.

The scattering coefficient profiles of the A-IA flames are shown in Figures 5.6 and 5.7. Figure 5.6 shows the details of the profiles over a narrow range of the scattering coefficient as the equivalence ratio is increased from nonsooting to sooting conditions. The scattering coefficient profile of the nonsooting flame, A-IA-R2 ($\phi = 1.63$), serves as a baseline for comparison with the sooting flame profiles, since its profile is caused solely by molecular scattering. The scattering coefficient profile of the first visibly sooting flame (A-IA-S1) has an identical shape to that of the nonsooting flame, except that it is displaced by a small increase in the scattering coefficient. Thus, it shows no obvious evidence of the presence of soot. As the equivalence ratio is increased further, the presence of soot formation produces a steep increase in the scattering coefficient with

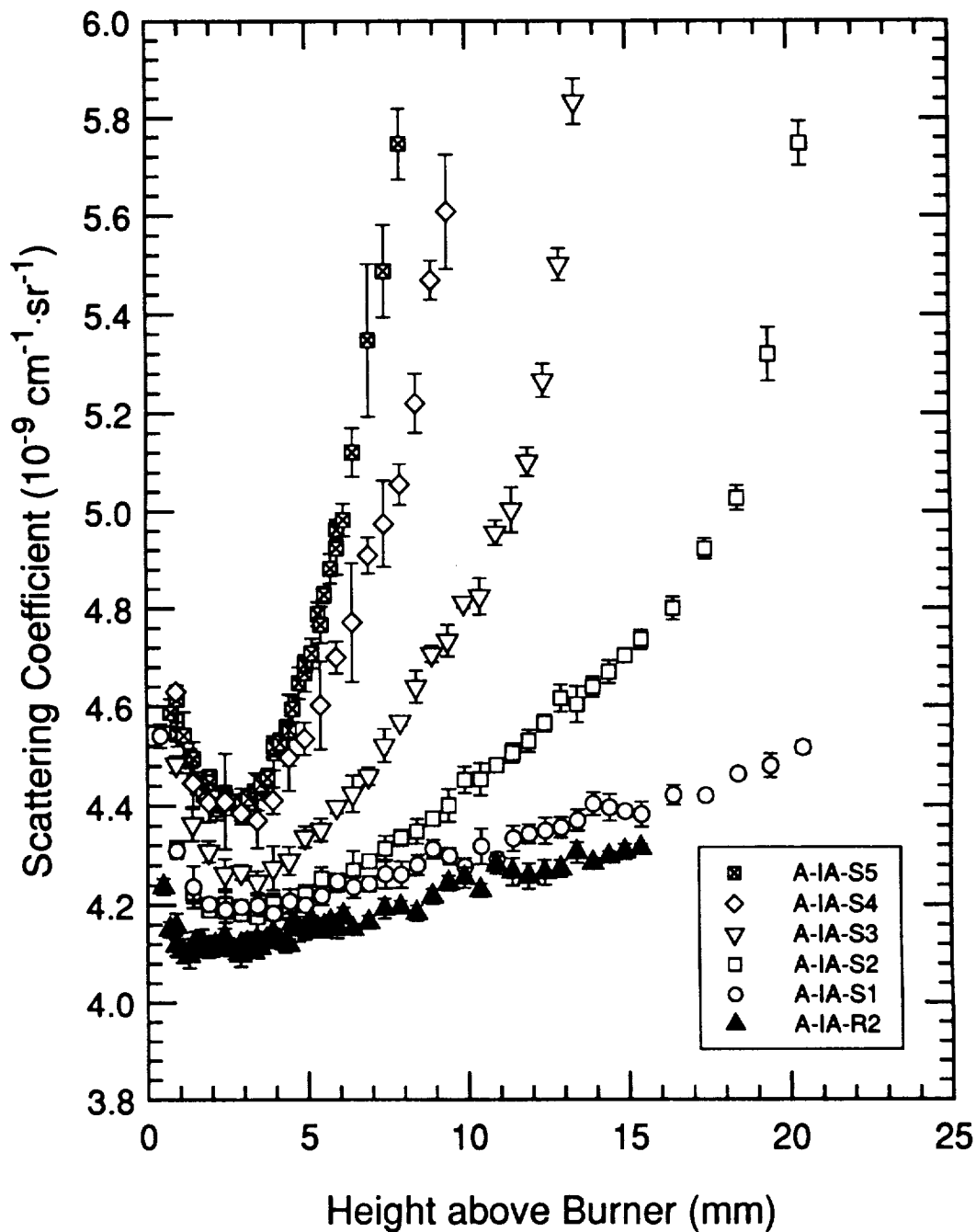


Figure 5.6 Scattering coefficient profiles of the A-IA sequence of flames ($v_c = 7.7 \text{ cm}\cdot\text{sec}^{-1}$ and $D = 4.2$). The narrow range of the scattering coefficient shows the details of the lightly sooting flame profiles. The error bars show the standard deviation of the measurement.

height. For the A-IA-S2 flame, this steep increase begins at a height of about 18 mm. The corresponding height for the remaining flames decreases as the equivalence ratio is increased. This trend is shown more clearly in Figure 5.7 which shows the full range of the scattering coefficient profiles. The steep increase in the scattering coefficient is caused by its dependence on the sixth power of the particle radius.

The scattering coefficient profiles of the A-IB sequence of flames are shown in Figures 5.8 and 5.9. Figure 5.8 shows the details of the profiles over a narrow range of the scattering coefficient as the equivalence ratio is increased from the flame at the critical equivalence ratio (A-IB-C) to more heavily sooting flames. The profile of the A-IB-C flame is similar to that of the A-IA-R2 and A-IA-S1 flames; the scattering coefficient is caused primarily by molecular scattering and thus soot cannot be detected. Similar to the A-IA flame sequence, the presence of soot can be detected beginning at an equivalence ratio of $\phi = 1.92$ by a steep increase in the scattering coefficient profile beginning at a height of 12 mm in the A-IB-S2 flame. The full range of the scattering coefficient profiles of the A-IB flames is shown in Figure 5.9. The behavior of the scattering coefficient profiles is similar to that of the A-IA flames, except that the steep increase in the scattering coefficient begins at a lower height for the A-IB flames than for the A-IA flames at the same equivalence ratio.

The scattering coefficient profiles of the A-IIA sequence of flames are shown in Figures 5.10 and 5.11. The details of the scattering coefficient profiles over a narrow range of the scattering coefficient are shown in Figure 5.10. Similar to the other two atmospheric flame sequences, the scattering coefficient profile of the visibly sooting flame near the critical equivalence ratio (A-IIA-S1) appears identical to that of the nonsooting flame (A-IIA-R2) and thus does not show any evidence of soot formation. When the equivalence ratio is increased to $\phi = 1.92$ (A-IIA-S2), the scattering coefficient profile again increases steeply indicating the presence of soot particles. The full range of

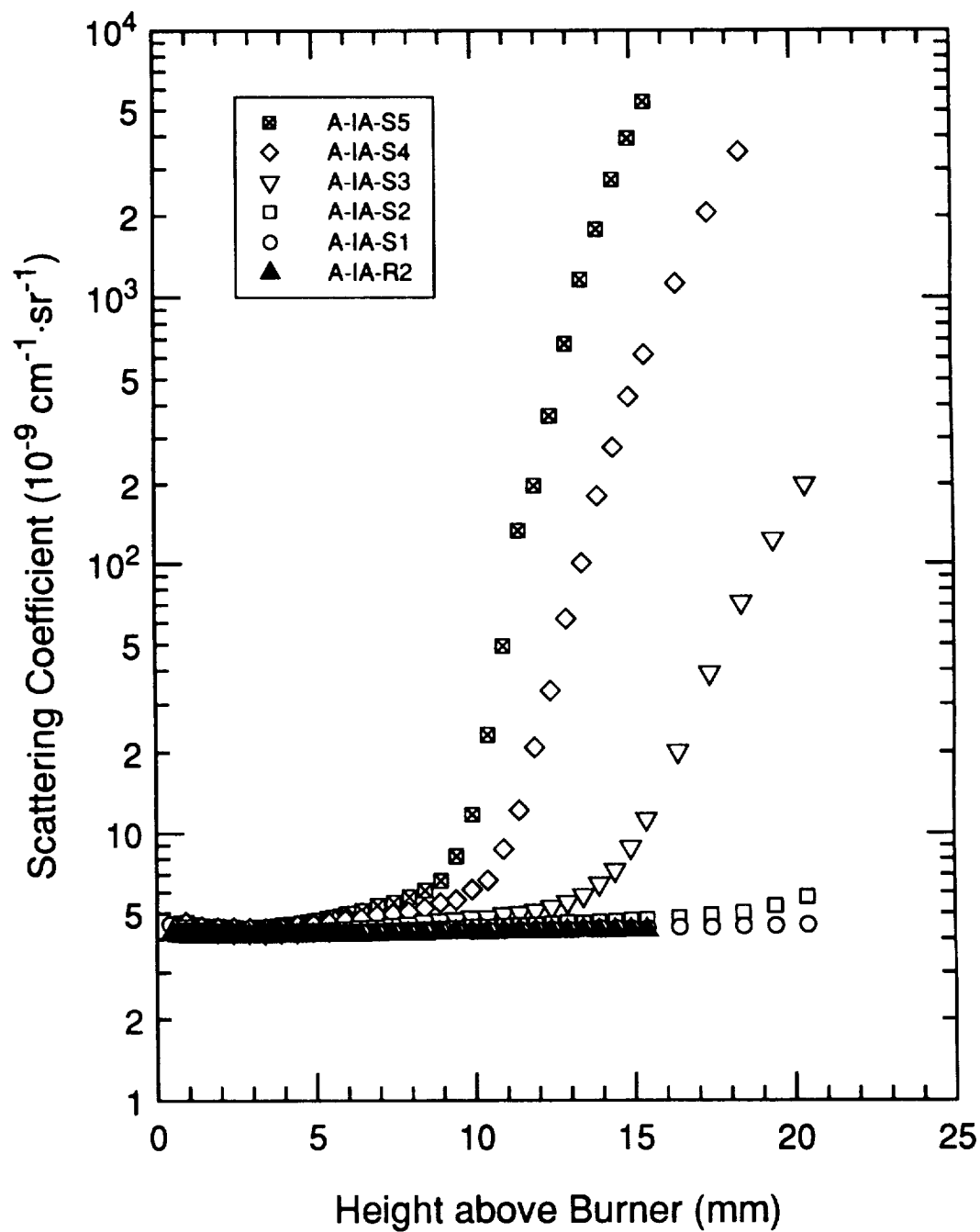


Figure 5.7 Scattering coefficient profiles of the A-IA sequence of flames ($v_c = 7.7 \text{ cm}\cdot\text{sec}^{-1}$ and $D = 4.2$). The logarithmic scale is used to show the full range of the scattering coefficient measurements.

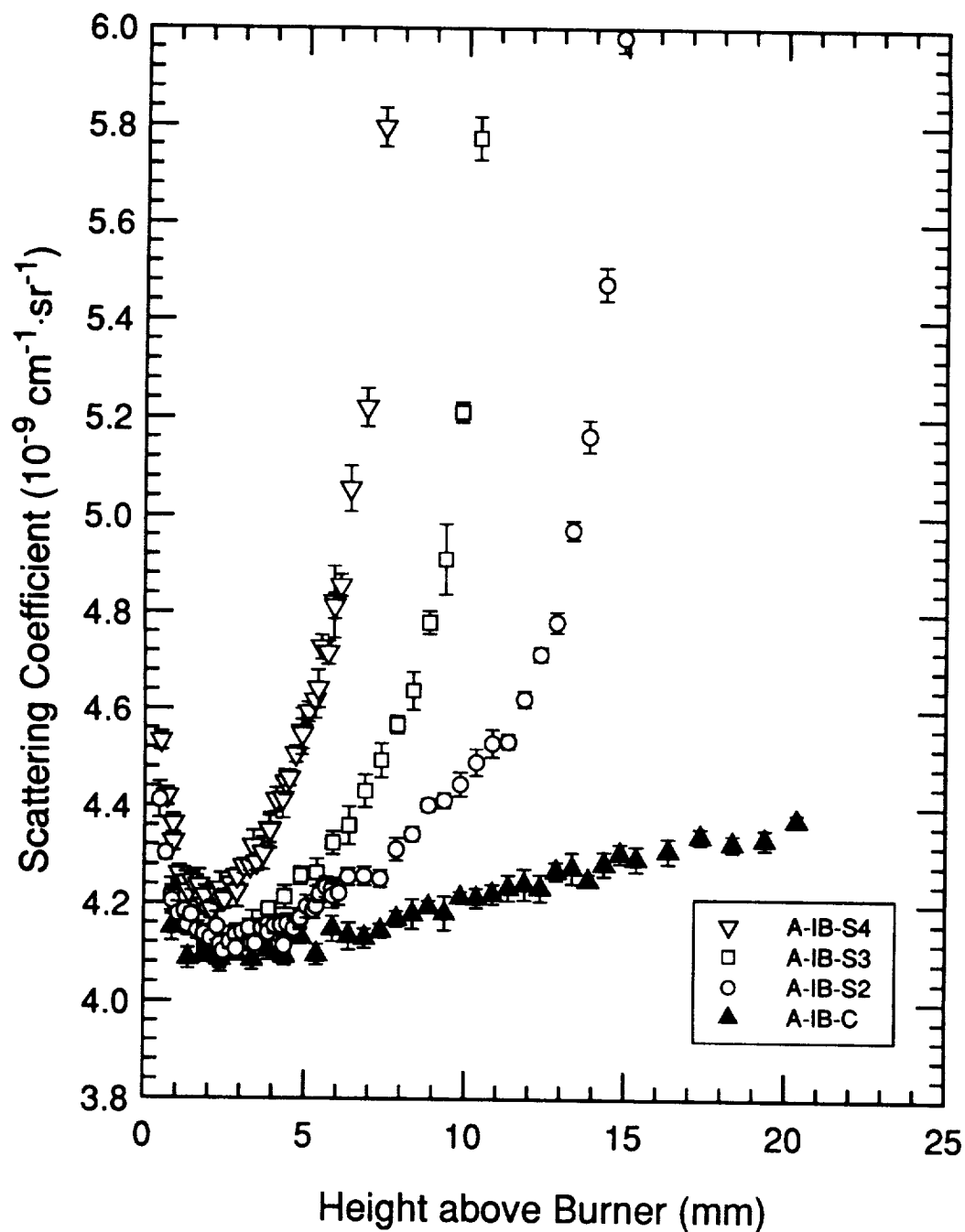


Figure 5.8 Scattering coefficient profiles of the A-IB sequence of flames ($v_c = 7.8 \text{ cm}\cdot\text{sec}^{-1}$ and $D = 4.3$). The narrow range of the scattering coefficient shows the details of the lightly sooting flame profiles. The error bars show the standard deviation of the measurement.

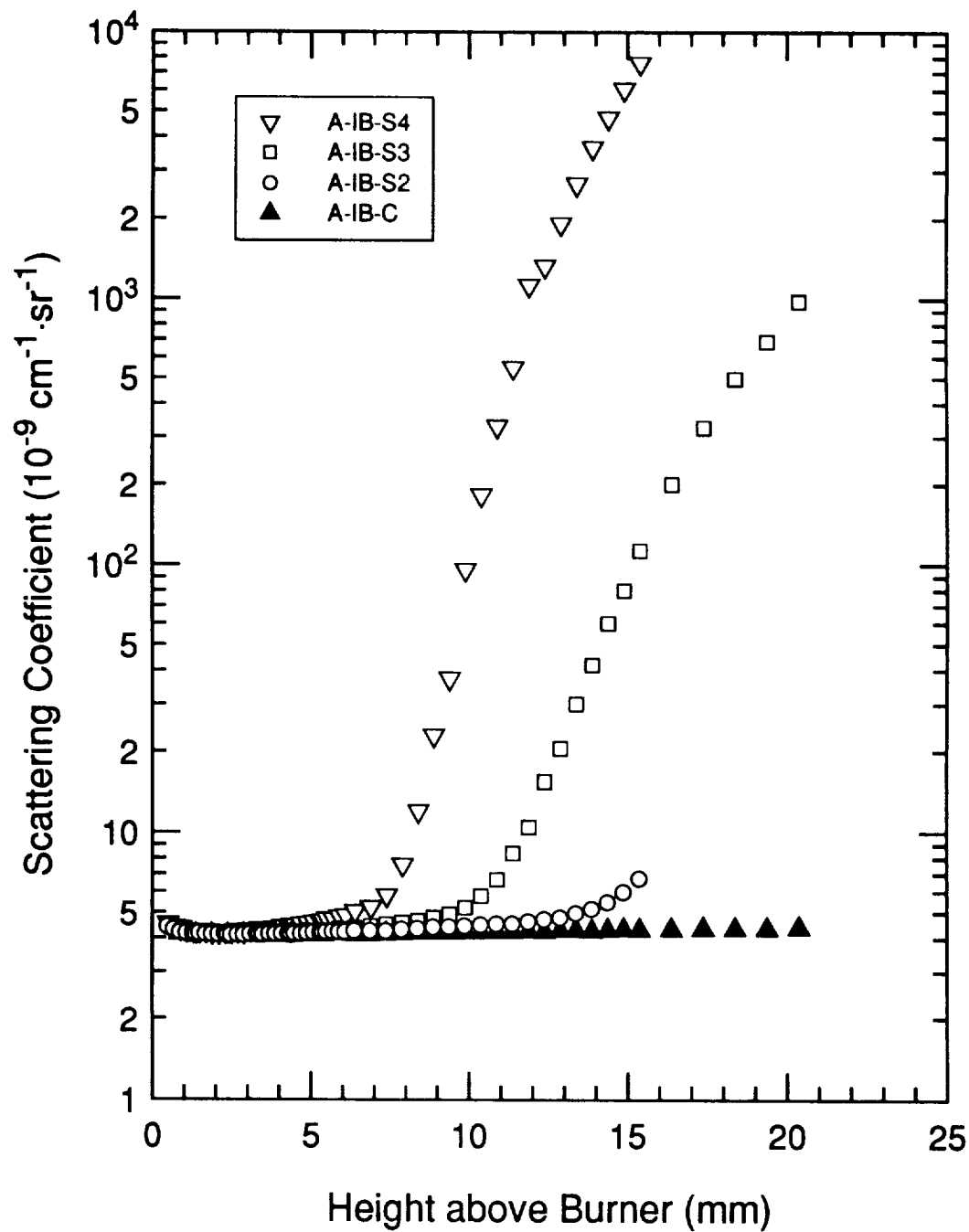


Figure 5.9 Scattering coefficient profiles of the A-IB sequence of flames ($v_c = 7.8 \text{ cm}\cdot\text{sec}^{-1}$ and $D = 3.5$). The logarithmic scale is used to show the full range of the scattering coefficient measurements.

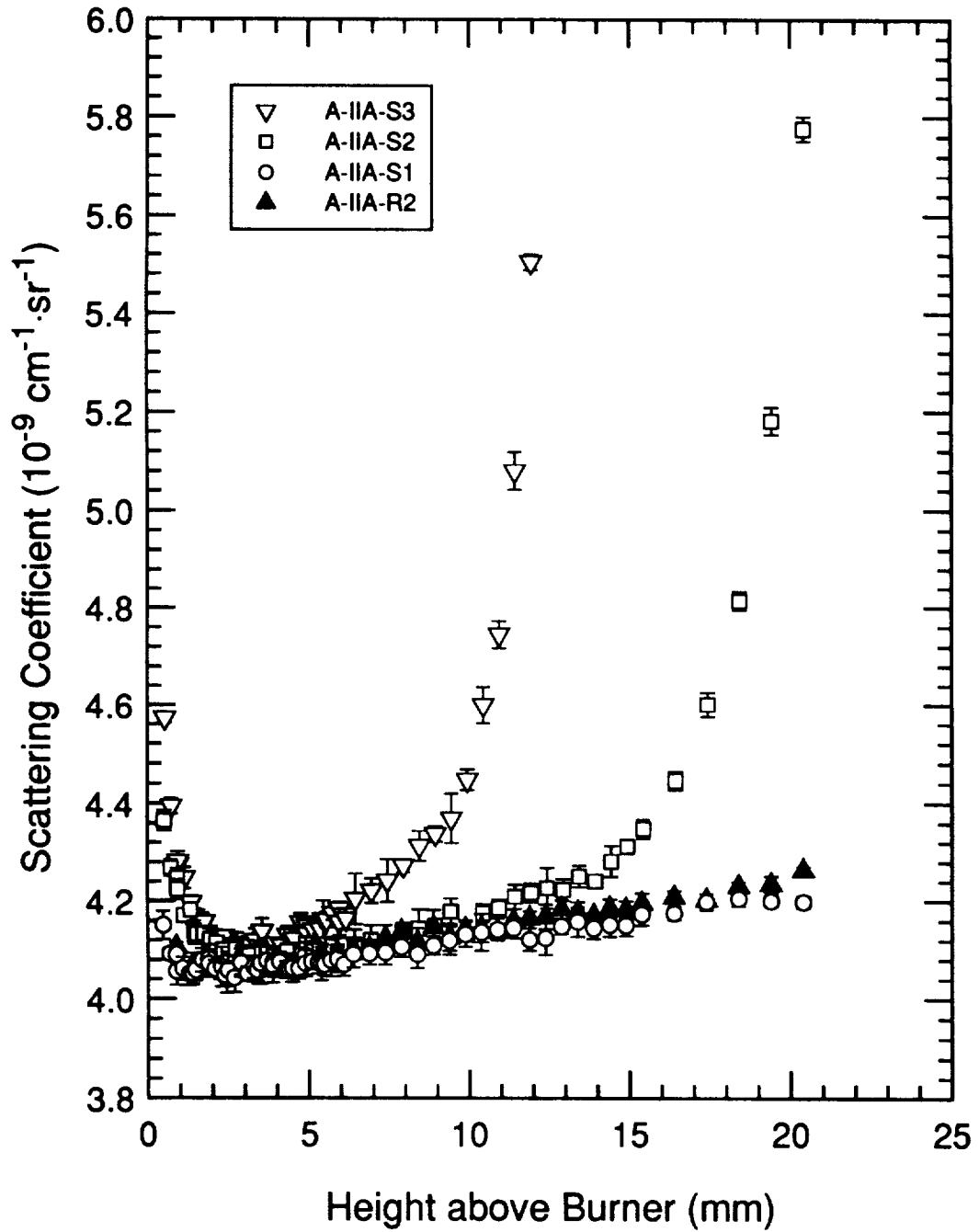


Figure 5.10 Scattering coefficient profiles of the A-IIA sequence of flames ($v_c = 10.4 \text{ cm}\cdot\text{sec}^{-1}$ and $D = 4.3$). The narrow range of the scattering coefficient shows the details of the lightly sooting flame profiles. The error bars show the standard deviation of the measurement.

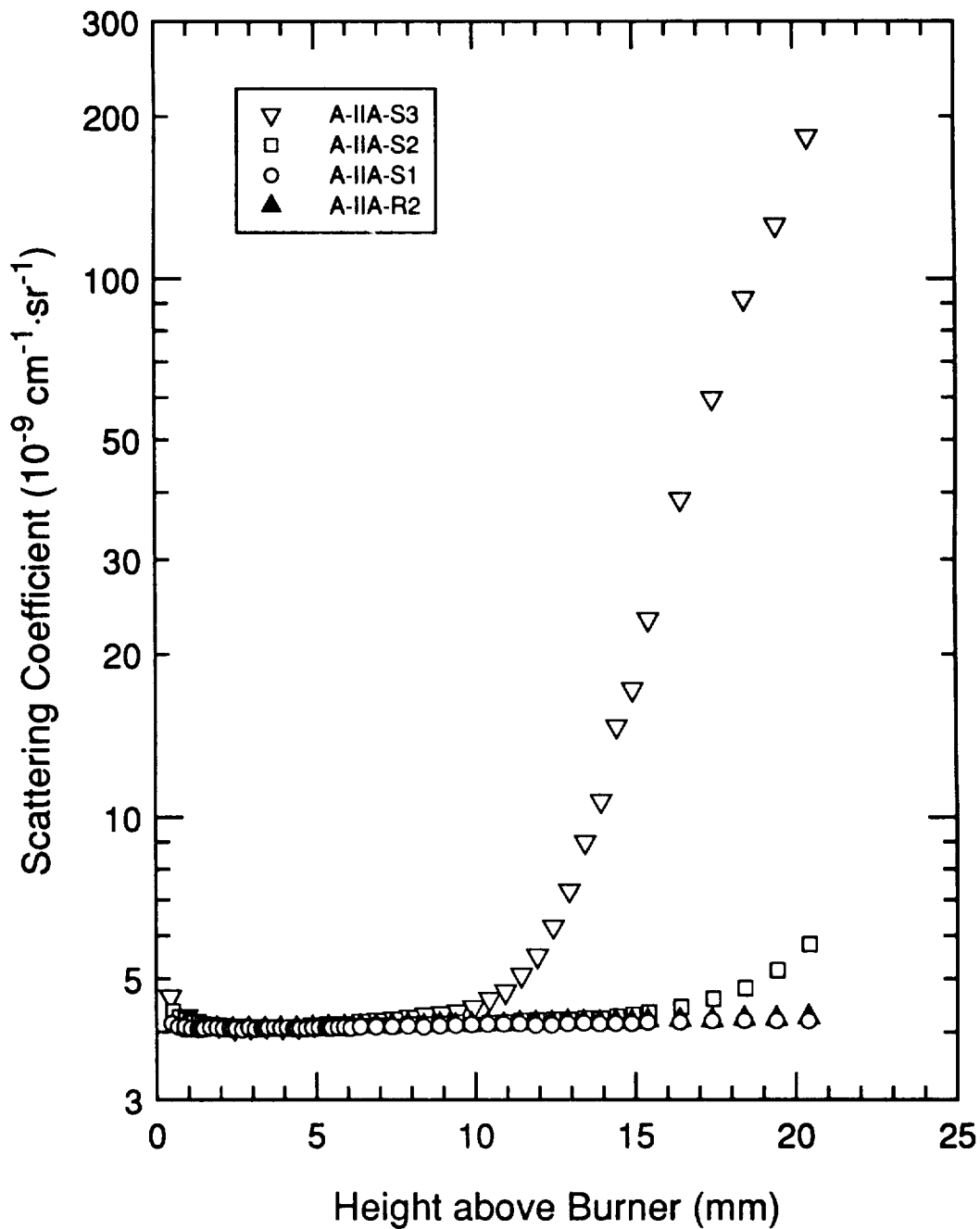


Figure 5.11 Scattering coefficient profiles of the A-IIA sequence of flames ($v_c = 10.4 \text{ cm}\cdot\text{sec}^{-1}$ and $D = 4.3$). The logarithmic scale is used to show the full range of the scattering coefficient measurements.

the scattering coefficient profiles is shown in Figure 5.11. The range of the A-IIA flames is much less than that of the A-IA flames (Fig. 5.7) and the A-IB flames (Fig. 5.9). This confirms our previous observation deduced from the extinction coefficient profiles that the A-IIA flames produce less soot than the A-IA and A-IB flames at the same equivalence ratio.

As for the extinction coefficient profiles, the scattering coefficient profiles for the sooting flames near the critical equivalence ratio do not show the presence of soot. However, when the equivalence ratio is increased further to $\phi = 1.92$ and greater, the presence of soot is clearly indicated by the steep increase in the scattering coefficient profiles. The range in the scattering coefficient profiles for the three atmospheric flame sequences provides a basis to investigate the effects of equivalence ratio, cold flow velocity, and dilution ratio on soot formation.

5.2.2.2 Subatmospheric Flames

Although we were unable to measure extinction coefficient profiles for the two 80-torr flame sequences, we were able to measure the scattering coefficient profiles of these flames. The scattering coefficient profiles of the L-I sequence of flames are shown in Figures 5.12 and 5.13. Those of the L-II sequence of flames are shown in Figures 5.14 and 5.15. The only difference in these two flame sequences is that the cold flow velocity of the L-I sequence is $v_c = 18.1 \text{ cm}\cdot\text{sec}^{-1}$ and that of the L-II sequence is $v_c = 22.4 \text{ cm}\cdot\text{sec}^{-1}$. Within the flame sequences, both the $\phi = 2.03$ (-R1) and $\phi = 2.17$ (-R2) flames are nonsooting. The transition to a visibly sooting flame occurs between $\phi = 2.17$ (-R2) and $\phi = 2.32$ (-S1) for each flame sequence. However, the critical equivalence ratio was not measured because of difficulties associated with incrementing the flow rates while keeping the total flow rate constant. More heavily sooting conditions were investigated at equivalence ratios of $\phi = 2.46$ (-S2) and $\phi = 2.60$ (-S3).

The details of the scattering coefficient profiles as the equivalence ratio is increased from nonsooting to sooting are shown in Figure 5.12 for the L-I sequence of flames and in Figure 5.14 for the L-II sequence of flames. The measured range in height above the burner for these scattering coefficient profiles was from 1.0 mm to 60 mm. The increase in range reflects the expansion of the flame profile at 80 torr when compared to that at atmospheric pressure. In these 80-torr flames, the decline of the scattering coefficient profile in the region immediately above the burner surface is clearly measured. This decline reflects the increase in temperature with height and also the formation of combustion products with smaller scattering cross-sections than the parent fuel.

A comparison of the two visibly sooting flames at $\phi = 2.32$ (-S1) with the nonsooting flames indicates the different sooting behavior of the two sequences. The L-I-S1 flame shows a significant increase in the scattering coefficient with height, while the profile of the L-II-S1 flame is basically identical in shape to that of the nonsooting flames. This behavior suggests that the L-II-S1 flame may be closer to the critical equivalence ratio than the L-I-S1 flame. This conclusion is further supported by the scattering coefficient profiles of the richer sooting flames. The full range of these scattering coefficient profiles is shown in Figure 5.13 for the L-I sequence of flames and in Figure 5.15 for the L-II sequence of flames. The L-I sooting flames distinctly produce more soot than the L-II flames as can be seen by comparing the magnitudes of the final scattering coefficients in the flames.

Although the utility of the 80-torr scattering coefficient profiles is limited by the absence of measured extinction coefficient profiles, the scattering coefficient profiles of these two flame sequences do provide a basis for comparing the effects of equivalence ratio and cold flow velocity on soot formation.

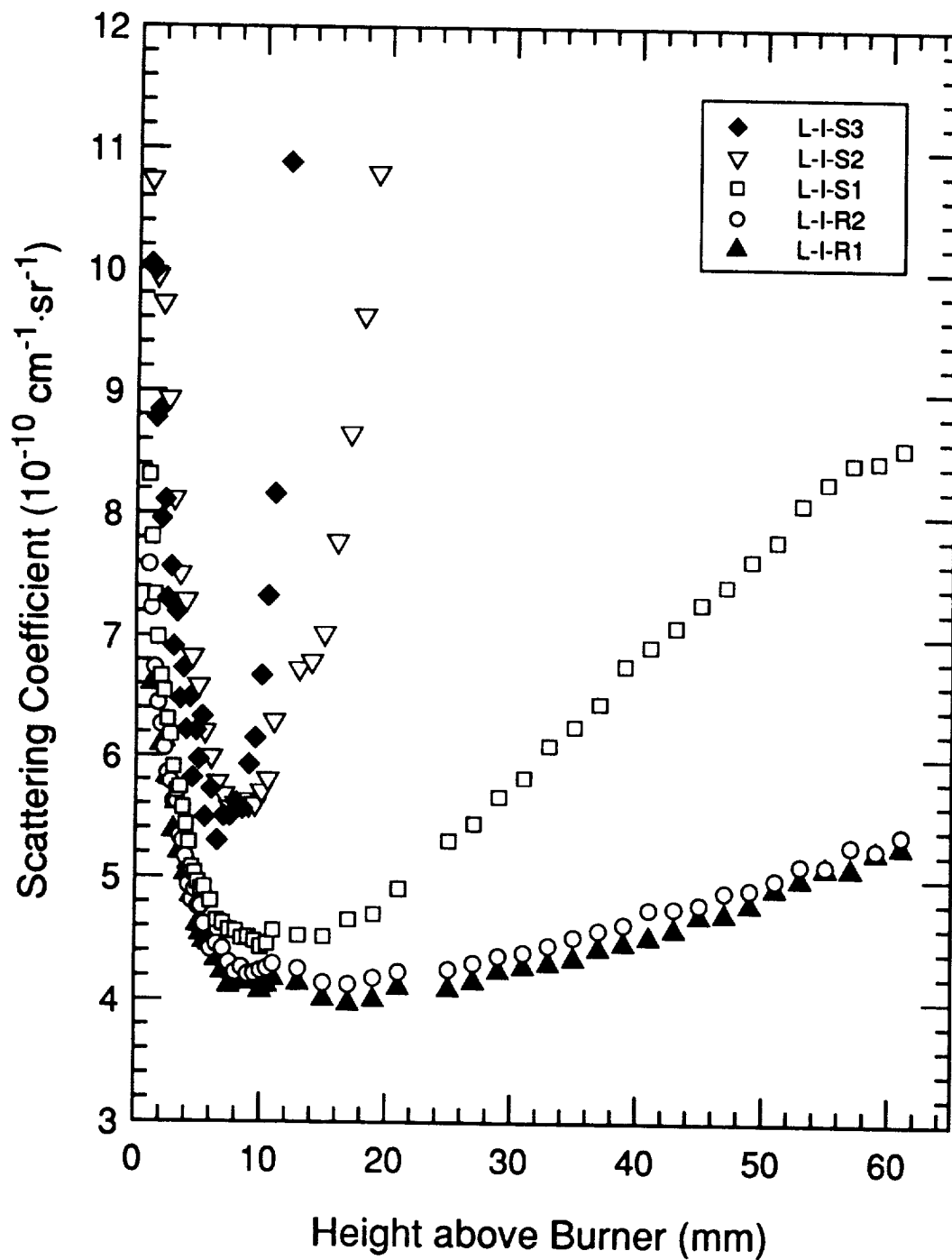


Figure 5.12 Scattering coefficient profiles of the L-I sequence of flames ($v_c = 18.1 \text{ cm}\cdot\text{sec}^{-1}$). The narrow range of the scattering coefficient shows the details of the profiles in the transition from nonsooting to sooting flames.

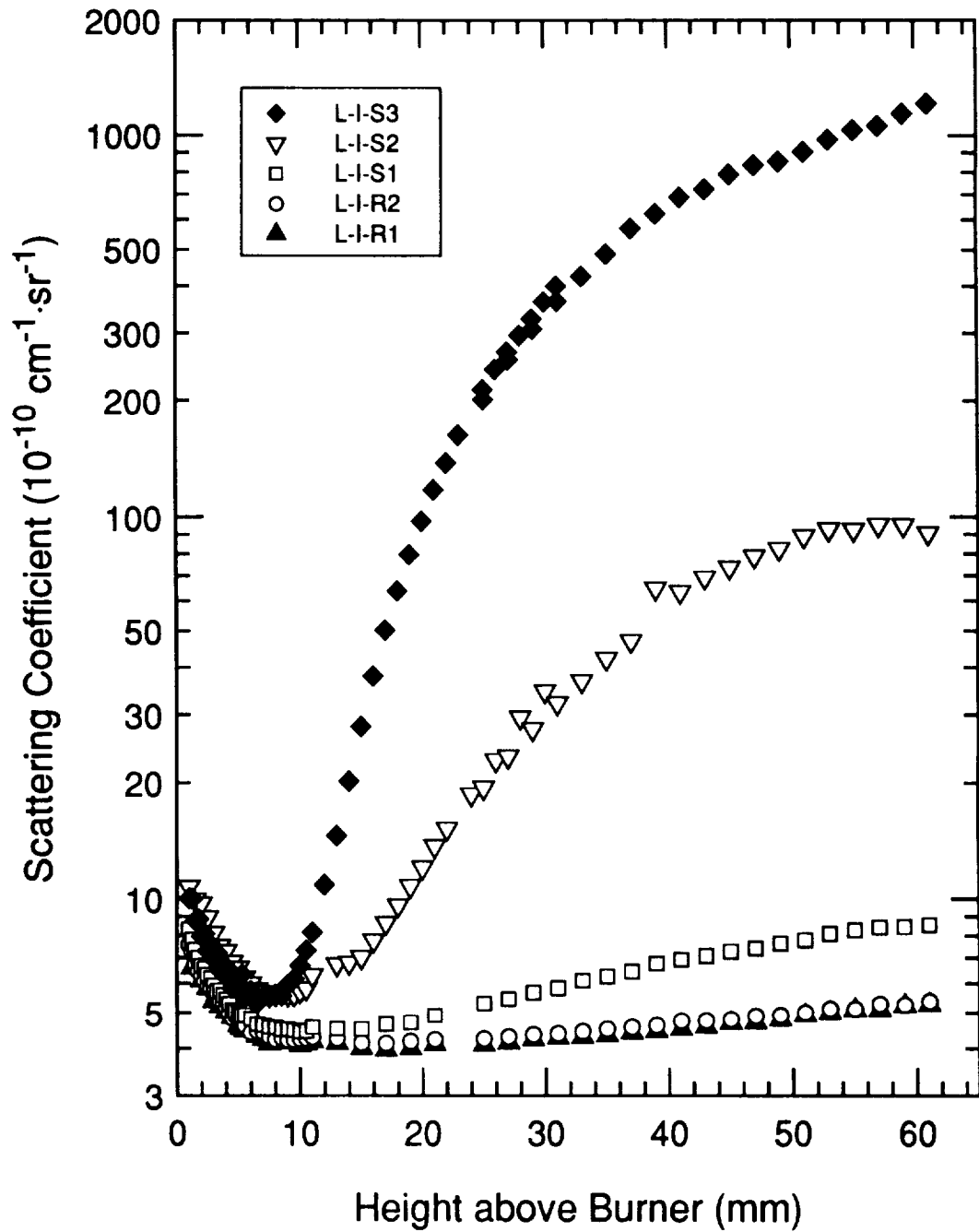


Figure 5.13 Scattering coefficient profiles of the L-I sequence of flames ($v_c = 18.1 \text{ cm}\cdot\text{sec}^{-1}$). The logarithmic scale is used to show the full range of the scattering coefficient measurements.

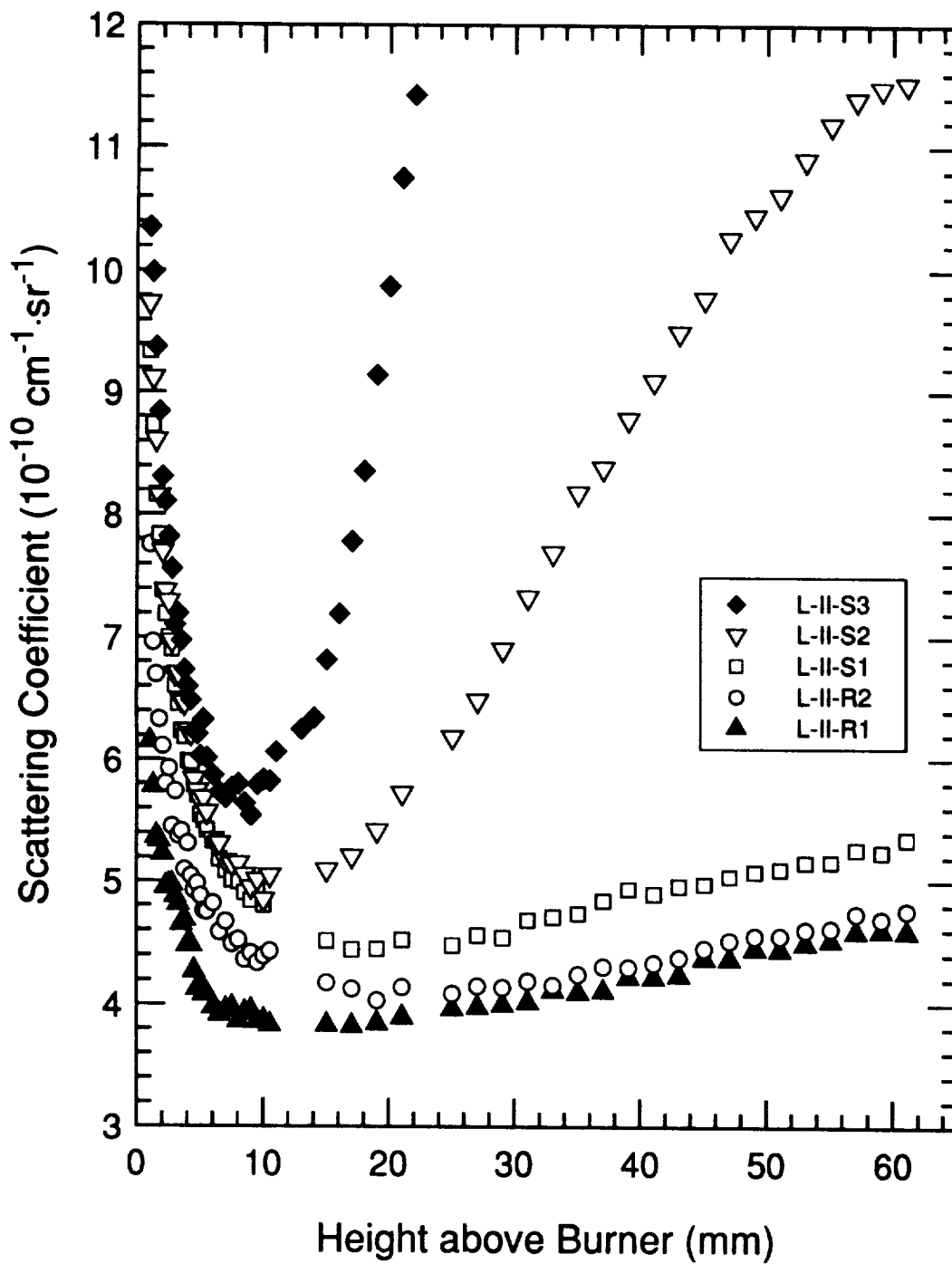


Figure 5.14 Scattering coefficient profiles of the L-II sequence of flames ($v_c = 22.4 \text{ cm}\cdot\text{sec}^{-1}$). The narrow range of the scattering coefficient shows the details of the profiles in the transition from nonsooting to sooting flames.

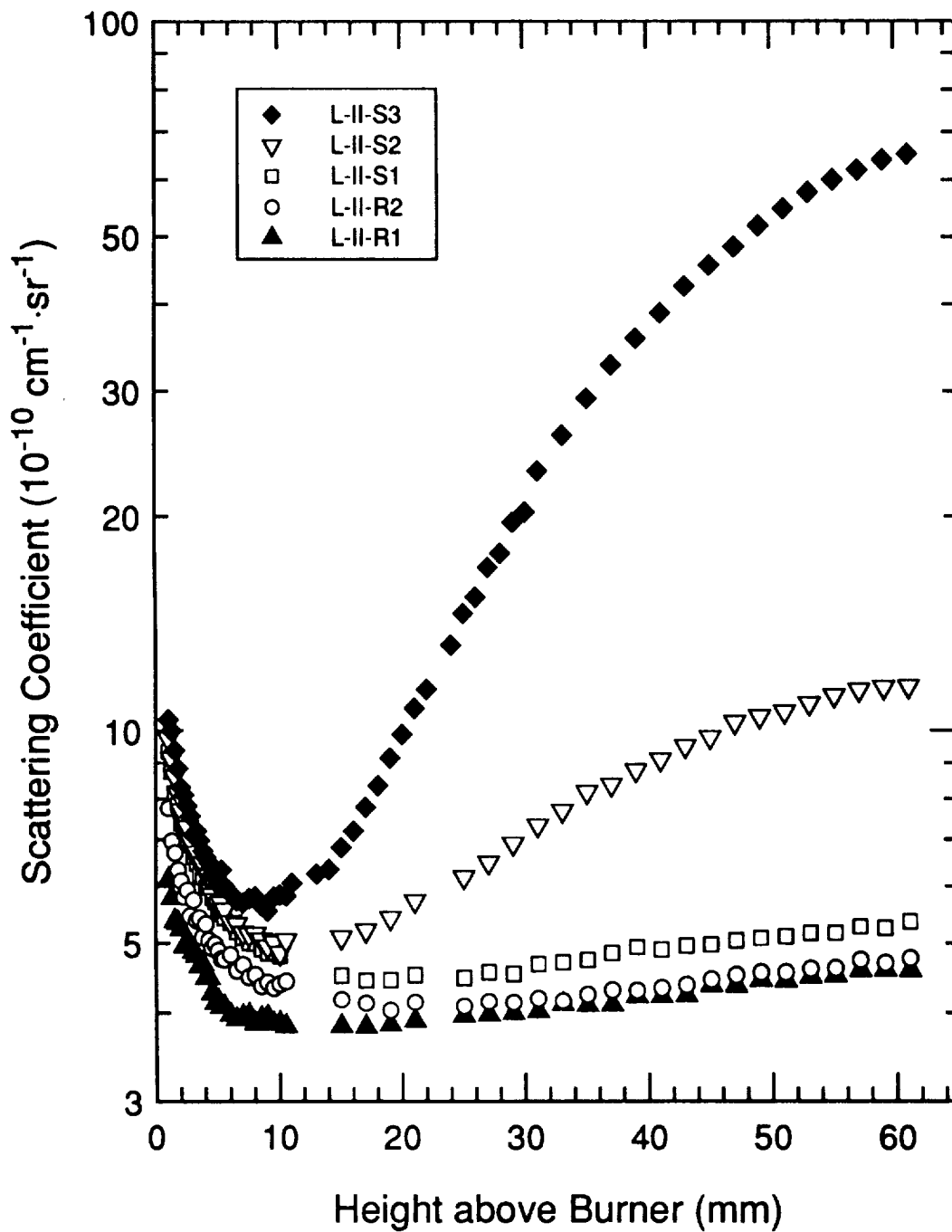


Figure 5.15 Scattering coefficient profiles of the L-II sequence of flames ($v_c = 22.4 \text{ cm}\cdot\text{sec}^{-1}$). The logarithmic scale is used to show the full range of the scattering coefficient measurements.

5.2.3 Argon-ion Laser-Induced Fluorescence Measurements

We investigated the fluorescence excited by the argon-ion laser in five flames within the A-IA flame sequence. The argon-ion laser-induced fluorescence was measured by tuning the monochromator wavelength away from the laser excitation wavelength, $\lambda = 488.0$ nm. The spectral detection bandpass of the monochromator was widened to $\Delta\lambda = 0.72$ nm FWHM and the entrance slit height of the monochromator was increased to gather more light from the flame. The rejection of Rayleigh scattered light from the laser was verified by measuring the scattering from a nitrogen flow at room temperature. The rejection ratio was determined to be greater than 10^4 at wavelengths at least 5 nm away from the laser excitation wavelength.

Figure 5.16 shows spectra of the argon-ion laser-induced fluorescence in three of the sooting A-IA flames at a height of 12 mm above the burner, which is within the visibly sooting region of all three flames. The spectra were measured by scanning the monochromator detection wavelength from 448 to 528 nm. The spectra of all three flames are broad, essentially featureless, and show both Stokes and Anti-Stokes components. The magnitude of the fluorescence increases steadily with wavelength in this measured wavelength range. The fluorescence signal also increases with equivalence ratio at this height, which is similar to the increase of the extinction coefficient with equivalence ratio in the same flames. However, the fluorescence spectrum is also observed in the A-IA-S1 ($\phi = 1.78$) flame, for which the scattering and extinction coefficient profiles do not show evidence of soot formation.

Vertical profiles of the fluorescence were measured in four of the flames within the A-IA flame sequence at two detection wavelengths, $\lambda = 473$ nm and $\lambda = 503$ nm, 15 nm on either side of the excitation wavelength, $\lambda = 488.0$ nm. These profiles were measured to observe the behavior of the fluorescence profiles in the transition from a nonsooting flame (A-IA-R2) to more heavily sooting conditions (A-IA-S3) and also to quantify the

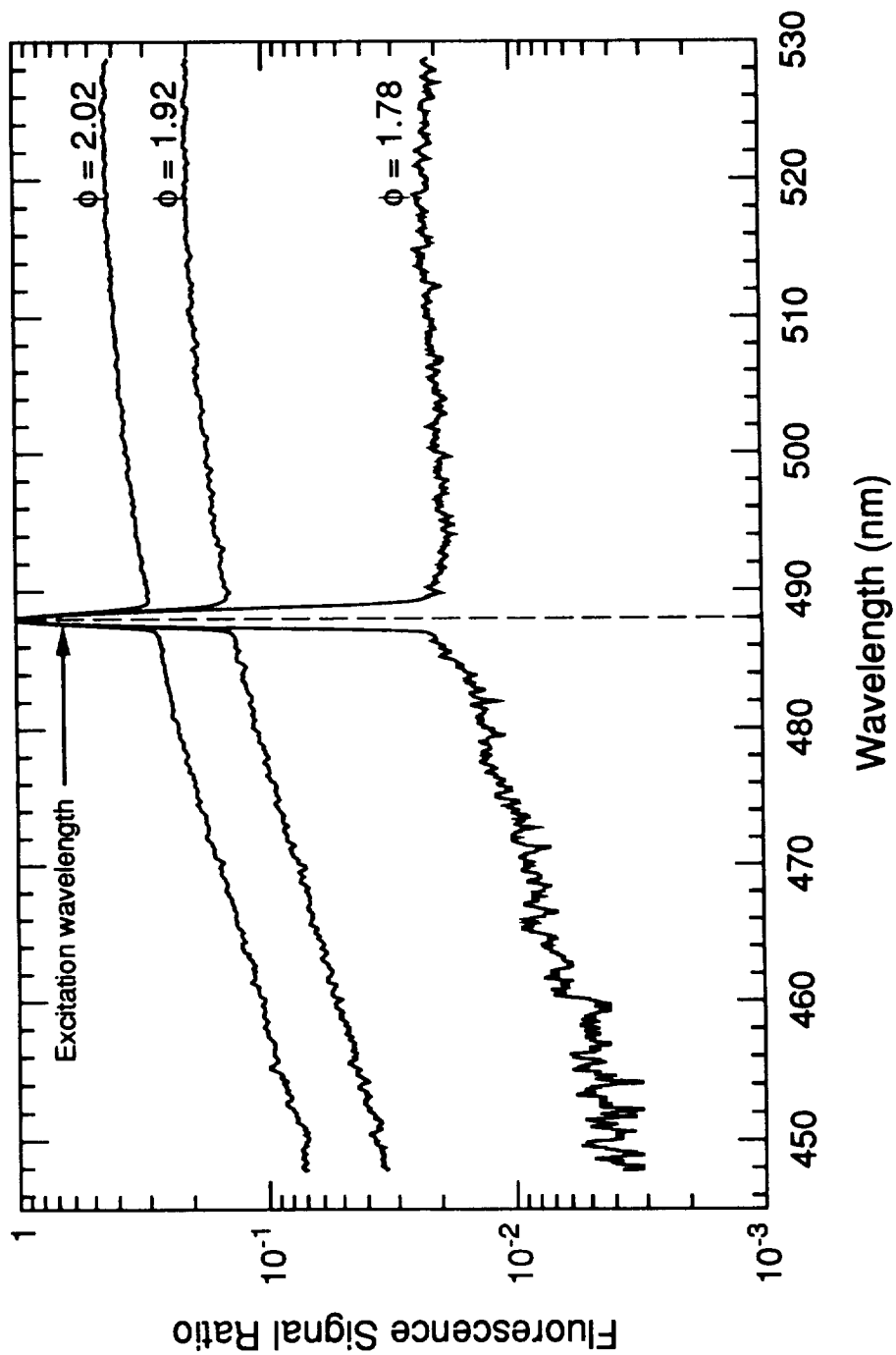


Figure 5.16 Spectrum of the argon-ion laser-induced fluorescence measured at 12 mm above the burner for three sooting atmospheric-pressure flames: A-IA-S1 ($\phi = 1.78$), A-IA-S2 ($\phi = 1.92$), and A-IA-S3 ($\phi = 2.02$). The fluorescence signal ratio is normalized to the peak at the excitation wavelength, $\lambda_0 = 488.0$ nm.

fluorescence background contribution to the scattering coefficient at 488.0 nm. The fluorescence coefficient ($Q_f \cdot \Delta\lambda \text{ cm}^{-1} \cdot \text{sr}^{-1}$) profiles measured at the detection wavelength of $\lambda = 503 \text{ nm}$ are shown in Figure 5.17. The fluorescence profiles measured at the detection wavelength of 473 nm were identical in shape and their magnitude was half of that measured at 503 nm.

The three sooting flames, A-IA-S1, A-IA-S2, and A-IA-S3, show distinctly measurable fluorescence coefficient profiles which rise steadily with height in the flame and also increase in magnitude with equivalence ratio. The observation of a measurable profile in the A-IA-S1 flame is striking, because, although the flame is visibly sooting, the presence of soot was not indicated by either the extinction or scattering coefficient profiles. To investigate this effect further, we measured the fluorescence at 503 nm at a height of 20 mm above the burner at the critical equivalence ratio (A-IB-C) and were able to measure a fluorescence coefficient above the estimated detection limit (Fig. 5.17). Thus, a measurable fluorescence coefficient appears to correlate with the visible yellow emission of soot from a flame.

We were not able to measure a fluorescence coefficient profile for the nonsooting A-IA-R2 flame. However, a signal at the estimated detection limit of the experimental apparatus was observed at heights of 15 mm and above, suggesting that the fluorescence might be present and may be measurable if more fluorescence could be collected from the flame. On the other hand, as might be expected, we were not able to detect a fluorescence signal from the 80-torr sooting flames.

5.2.4 Depolarized Scattering Measurements

Profiles of the horizontally polarized scattered light from vertically polarized incident light at 488 nm were measured in three sooting atmospheric-pressure flames in the A-IA sequence and in the sooting 80-torr flames in both the L-I and L-II sequences.

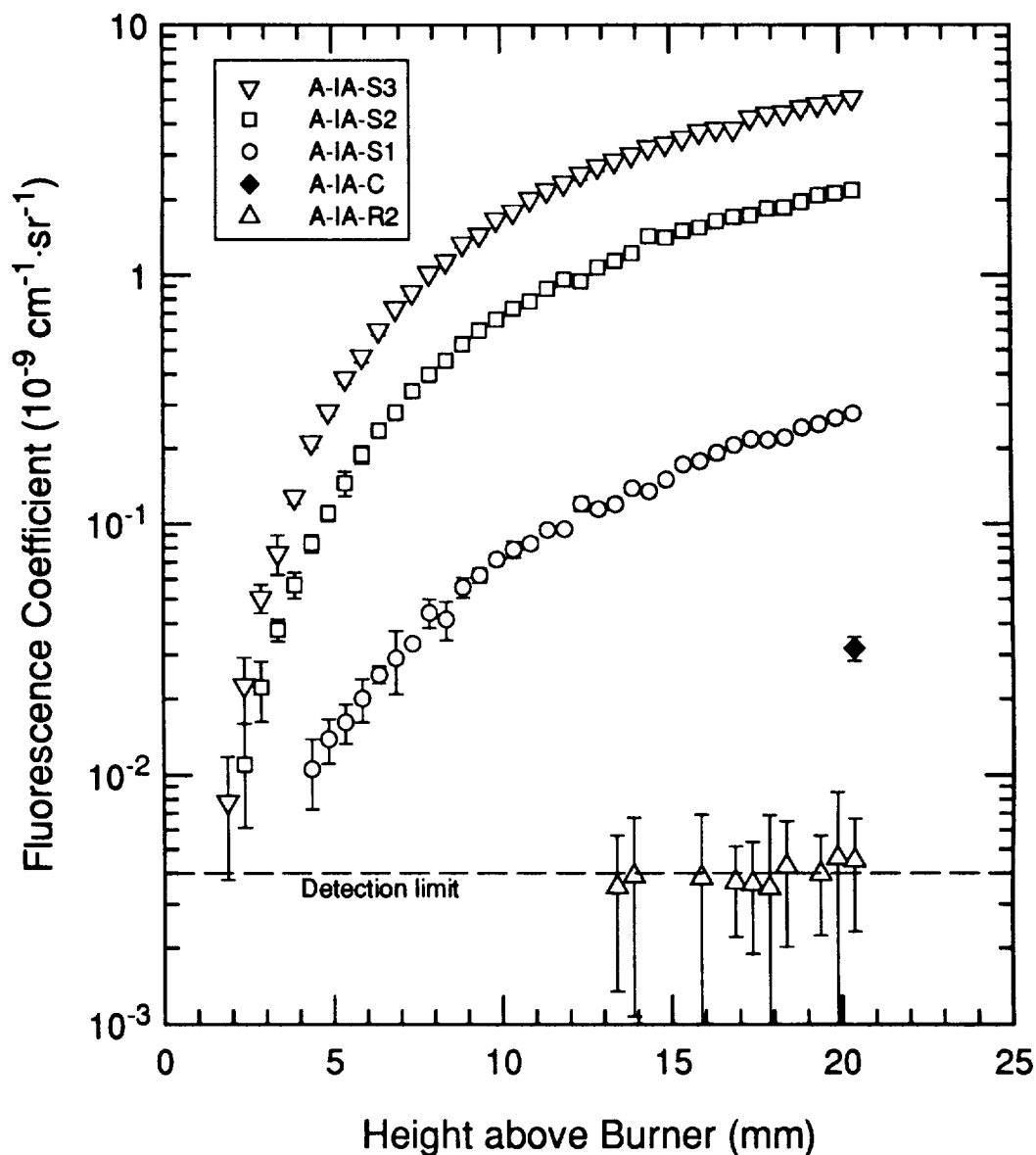


Figure 5.17 Profiles of the argon-ion laser-induced fluorescence measured in the A-IA sequence of flames ($v_c = 7.7 \text{ cm} \cdot \text{sec}^{-1}$ and $D = 4.2$). The fluorescence coefficient ($Q_f \cdot \Delta\lambda \text{ cm}^{-1} \cdot \text{sr}^{-1}$) was measured with excitation at $\lambda = 488 \text{ nm}$ and detection at $\lambda = 503 \text{ nm}$ with a spectral bandpass, $\Delta\lambda = 0.72 \text{ nm}$ FWHM. The error bars show twice the standard deviation of the measurement.

From these measurements, we determined profiles of the horizontal scattering coefficient, $Q_{HV}(z)$. Profiles of the depolarization ratio were then calculated using

$$\rho_v(z) = \frac{Q_{HV}(z)}{Q_{VV}(z)} \quad (5.2.3)$$

The depolarization ratio provides a measure of the anisotropy of the scattering. The scattering cross-section for horizontally polarized scattered light and vertically polarized incident light is $C_{HV} = 0$ for Rayleigh scattering (D'Alessio, 1981). A non-zero depolarization ratio thus indicates a departure from Rayleigh scattering theory.

The horizontally polarized scattered light contains contributions from the same sources as the vertically polarized scattered light. The measured scattering coefficient for horizontally polarized scattered light, $Q_{sca,H}$, is given by Eq. (3.2.24) as

$$Q_{sca,H} = Q_{HV} + Q_{HV,g} + Q_f(\lambda_0, \lambda) \cdot \Delta\lambda \quad (5.2.4)$$

The horizontally polarized particle scattering coefficient, $Q_{HV} = \rho_v \cdot Q_{VV}$, where ρ_v is the depolarization ratio of the particles. The horizontally polarized scattering coefficient, $Q_{HV,g}$, is on the order of 1% of $Q_{VV,g}$, since the depolarization ratios of the major exhaust gases are on the order of 1% (e.g., $\rho_v(\text{CO}) = 0.521\%$, $\rho_v(\text{CO}_2) = 4.12\%$, $\rho_v(\text{N}_2) = 1.042\%$; Bogaard et al., 1978). The fluorescence coefficient, $Q_f(\lambda_0, \lambda) \cdot \Delta\lambda$, is the same for both vertically and horizontally polarized scattered light, since the argon-ion laser-induced fluorescence is isotropic (Haynes, Jander, and Wagner, 1980).

5.2.4.1 Atmospheric-Pressure Flames

Profiles of the measured horizontal scattering coefficient, $Q_{sca,H}$, are shown in Figure 5.18(a) for three sooting atmospheric-pressure flames, A-IA-S2, A-IA-S3, and A-IA-S4. The calculated depolarization ratio profiles are shown in Figure 5.18(b). Profiles of the fluorescence coefficient were measured in two of these flames, A-IA-S2 and A-IA-S3, and the resulting horizontal scattering coefficient profiles after subtraction of the fluorescence background are shown in Figure 5.18(a) by the filled symbols.

The $Q_{sca,H}$ profile of the A-IA-S2 flame after correction for the fluorescence background remains approximately constant with height above the burner. This constant scattering coefficient corresponds to the horizontal molecular scattering coefficient, $Q_{HV,g}(z)$. Thus, fluorescence contributes the remainder of the depolarized scattered signal and the horizontal scattering coefficient due to the particles is not detected.

The $Q_{sca,H}$ profile of the A-IA-S3 flame after correction for the fluorescence background remains constant at the same value of $Q_{HV,g}$ as for the A-IA-S2 flame up to a height of 15 mm. Above 15 mm, the steep increase in $Q_{sca,H}$ can be attributed to depolarized scattered light from soot particles. Below 15 mm the fluorescence contributes the major portion of the depolarized scattered light. The point at which the relative contribution of particle scattering becomes significant occurs as an inflection point in the uncorrected $Q_{sca,H}$ profile at ~ 17 mm.

Although the fluorescence coefficient was not measured for the A-IA-S4 flame, the inflection point at ~ 12 mm suggests that above 12 mm depolarized particle scattering contributes the major fraction of the depolarized light, while below 12 mm the fluorescence is the major fraction of the depolarized light.

The effect of the fluorescence can be seen clearly in the depolarization ratio profiles shown in Figure 5.18(b) for the same three flames. The $Q_{HV,g}$ component was removed so that the $\rho_v(z)$ profiles contain only fluorescence and particle contributions. The fluorescence contribution causes the peak in the ρ_v profile. Following the peak, ρ_v declines with height because of the increasing contribution from particle scattering and approaches a constant $\rho_v \approx 2\%$ at a height of 20 mm. The solid symbols in Figure 5.18(b) represent the ρ_v profile caused by the particles only. For the A-IA-S2 flame, $\rho_v \sim 0$ throughout the flame, while for the A-IA-S3 flame ρ_v increases above zero at 15 mm and then approaches a constant $\rho_v \sim 1.5\%$ at 20 mm.

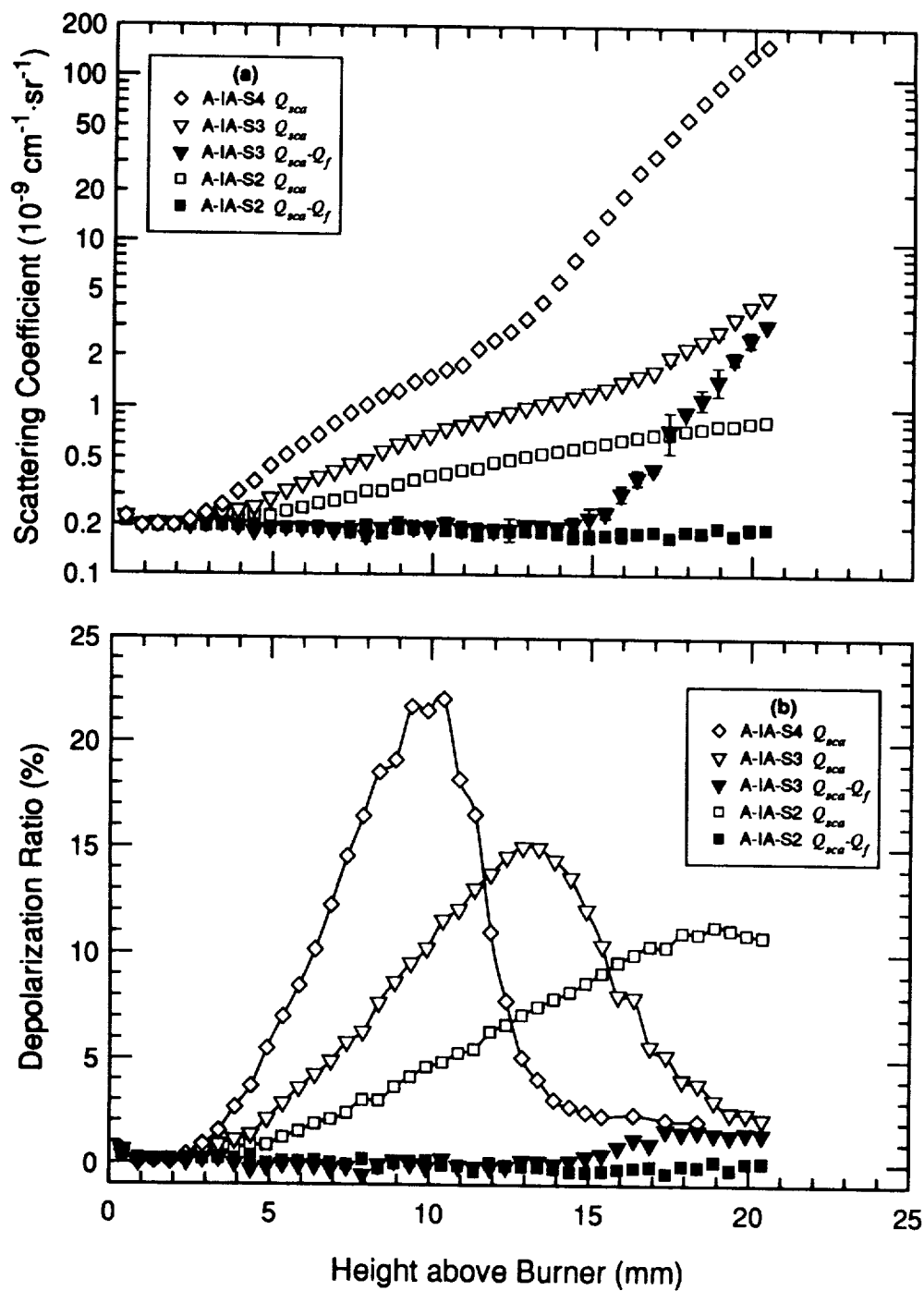


Figure 5.18 (a) Profiles of the horizontal scattering coefficient in three sooting atmospheric-pressure flames. (b) Profiles of the calculated depolarization ratio for the same three flames. The solid symbols represent the corresponding signals when the fluorescence background is subtracted.

The behavior of the depolarization profiles in these flames is similar to that observed by Haynes, Jander, and Wagner (1980) in their atmospheric-pressure ethylene flames. They concluded that the constant depolarization ratio caused by the particles was due to an intrinsic anisotropy in the particles and was not caused by anisotropy in their shape owing to agglomeration. If the depolarization ratio were caused by shape anisotropy of the particles, ρ_v would increase with height instead of remaining constant because the degree of agglomeration of the particles increases with height.

5.2.4.2 Subatmospheric Flames

Horizontal scattering coefficient profiles were also measured for the sooting 80-torr flame sequences, L-I and L-II. Figure 5.19(a) shows the horizontal scattering coefficient profiles of the four more heavily sooting flames, L-I-S2, L-I-S3, L-II-S2, and L-II-S3. The $Q_{sca,H}$ profiles of the lightly sooting flames, L-I-S1 and L-II-S1, are not shown because they remained at zero or below the detection limit of the scattering system. Recall that the argon-ion laser-induced fluorescence was not detected in the 80-torr flames. In addition, the contribution to the horizontal scattering coefficient from molecular scattering was below the detection limit. Thus, the profiles shown in Figure 5.19(a) only represent the contribution of the soot particles.

The profiles of the depolarization ratio for the four sooting flames are shown in Figure 5.19(b). The ρ_v profiles of all four flames remain approximately constant at $\rho_v \approx 1\%$ above a height of 30 mm. This behavior is similar to that of the atmospheric-pressure flames and suggests a similar conclusion, i.e., the depolarization ratio is caused by an intrinsic anisotropy in the particles rather than by a shape anisotropy.

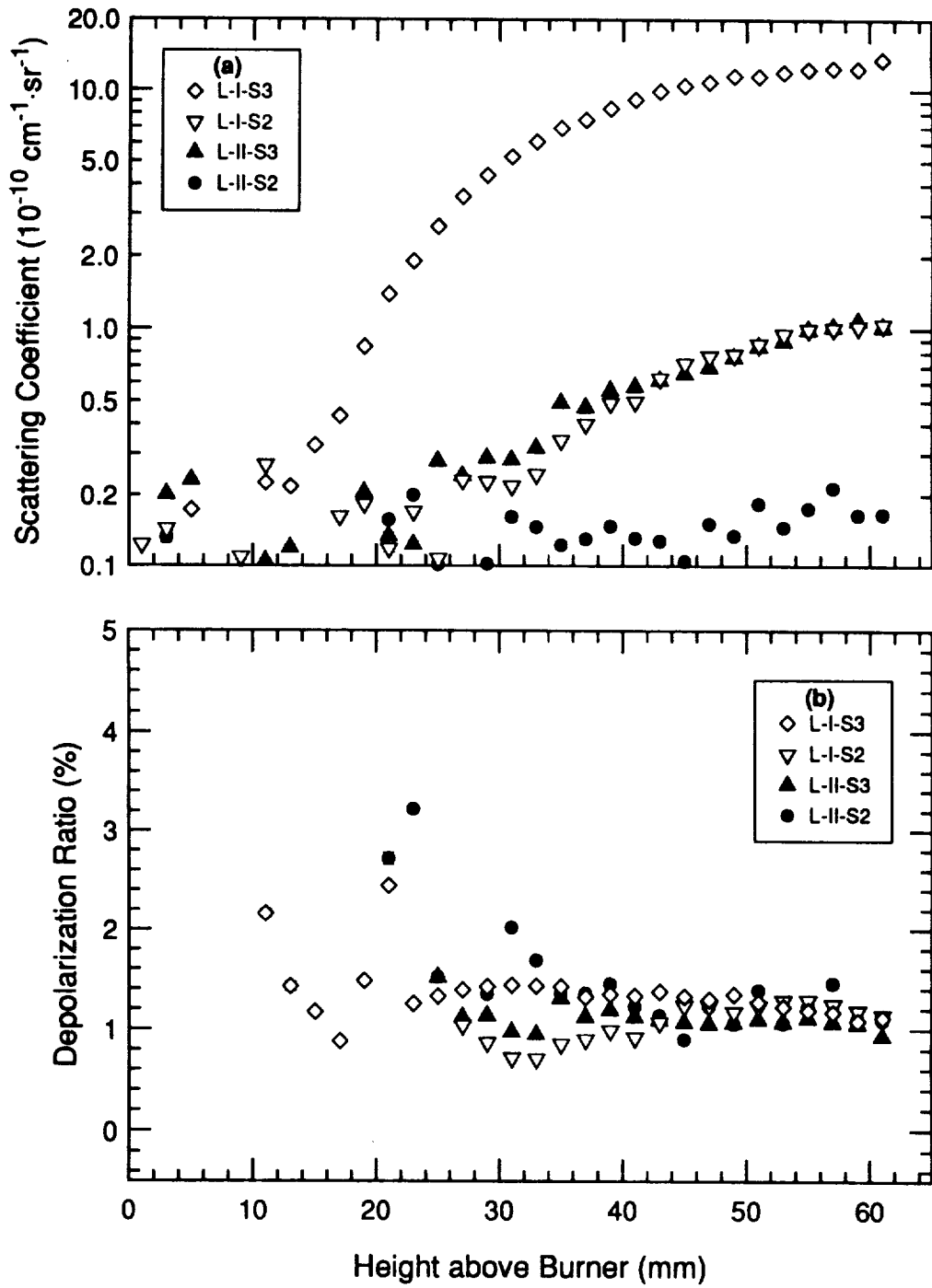


Figure 5.19 (a) Profiles of the horizontal scattering coefficient in the sooting 80-torr flames, L-I-S2, L-I-S3, L-II-S2, and L-II-S3. (b) Profiles of the calculated depolarization ratio for the same four flames.

5.3 Interpretation of the Laser Scattering-Extinction Measurements

5.3.1 Calculation of Soot Profiles

The soot volume fraction, number density, and particle diameter profiles were calculated from the scattering and extinction coefficient profiles for those flames for which the scattering and extinction coefficients caused by the particles rose above the detection limit. Thus, we were only able to calculate the profiles for those atmospheric-pressure flames with equivalence ratios $\phi \geq 1.92$ (the -S2, -S3, -S4, and -S5 flames).

The first step in the calculation of the various particle profiles was to determine the extinction and scattering coefficients due to only the particles by accounting for the background and interfering signals. We assumed that the extinction coefficient profile calculated from the normalized transmittance profile was that caused by soot particles and do not make any further corrections for gas-phase absorption. Thus we assume that the absorption present at the maximum of the transmittance profile is equivalent to the absorption created by the gas-phase species. Any further gas-phase absorption is included in the extinction coefficient. Thus our measurement of the extinction at 488 nm will include contributions from soot and also from larger molecular weight hydrocarbons down to the size of acenaphthylene which absorbs slightly at 488 nm (Beretta et al., 1985; Weiner and Harris, 1989).

The extent of gas-phase absorption could be determined by measuring the extinction at longer wavelengths. Harris, Weiner, and Ashcraft (1986) determined the extent of gas-phase absorption at 488 nm by measuring the extinction at 1090 nm. They assumed that only soot particles absorbed light at 1090 nm and calculated the extinction due to soot at 488 nm assuming a constant index of refraction and a $1/\lambda$ dependence for the extinction. Their assumption that soot particles absorb at 1090 nm effectively defines a lower bound on the size of the particles which they estimate to be 2000 amu.

The particle scattering coefficients were obtained by subtracting the estimated molecular scattering coefficient and the fluorescence coefficient (for those cases where they were both measured) from the total scattering coefficient. The background caused by the molecular scattering coefficient was subtracted from the measured scattering coefficient by first subtracting the minimum in the total scattering coefficient profile. We assume that the minimum is still in the nonsooting region of the flame and thus represents the molecular scattering coefficient background at the peak temperature. This procedure also accounts for the increase in the molecular scattering coefficient caused by the decrease in peak temperature at increasing equivalence ratio.

For each flame sequence, these subtracted profiles were then plotted and compared. The nonsooting region of the profiles were similar. In addition, the profile of the nonsooting (-R2) and the lightly sooting (-S1) flames of both the A-IA and A-IIA sequences overlaid each other, thus confirming that the scattering coefficient profiles for the lightly sooting flames showed no evidence of particle scattering. Based on this comparison, we identified the shape of the residual molecular scattering coefficient profile as that for the nonsooting flame for all the flames in a given sequence. We then subtracted the molecular scattering coefficient profile of the nonsooting flame from the measured scattering coefficient profiles of the other flames within its sequence. This last correction was minimal, since the subtracted portion of the molecular scattering coefficient background reached a maximum of $\sim 0.3 \times 10^{-9} \text{ cm}^{-1} \cdot \text{sr}^{-1}$ at a height of 20 mm above the burner. Thus, the correction was only significant in the lightly sooting flames for which the particle scattering coefficients remain small.

The measured scattering coefficient profiles were corrected for fluorescence only for those flames in which the fluorescence profiles were measured. No attempts were made to estimate the fluorescence background in the other flames. The fluorescence coefficient background at 488.0 nm was calculated from the average of the fluorescence

coefficients at 473 nm and 503 nm because the argon-ion laser-induced fluorescence appeared to be linear over this wavelength range (Fig. 5.16). The subtraction process also accounted for the difference in the spectral bandpass of the monochromator between the fluorescence and the scattering measurements. The accuracy of the subtraction is confirmed by the depolarization ratio measurements.

Given the particle extinction and scattering coefficient profiles, the volume fraction, number density, and particle diameter profiles were then calculated. These calculations required two additional parameters, the particle index of refraction, \bar{m} , and the particle size distribution, $P(r)$, both of which were assumed, since they could not be measured with our experimental apparatus. The equations to calculate these profiles were developed in Section 3.2. Here we reiterate those equations to define a relative volume fraction, number density, and particle diameter, which do not depend on the particle index of refraction and the size distribution. The volume fraction is calculated from the extinction coefficient and is determined from Eq. (3.2.9) and (3.2.25) to give

$$f_V(z) = \frac{\lambda}{6\pi} \cdot (E(\bar{m}))^{-1} \cdot K_{ext}(z) = (E(\bar{m}))^{-1} \cdot f_V^r(z) \quad (5.3.1)$$

where f_V^r is the relative volume fraction given by

$$f_V^r(z) = \frac{\lambda}{6\pi} \cdot K_{ext}(z) \quad . \quad (5.3.2)$$

The number density is calculated from the ratio of the extinction coefficient squared to the scattering coefficient and is determined from Eq. (3.2.27) to obtain

$$N_p(z) = \frac{1}{4\lambda^2} \cdot \frac{F(\bar{m})}{(E(\bar{m}))^2} \cdot f_N \cdot \frac{(K_{ext}(z))^2}{Q_{VV}(z)} = \frac{F(\bar{m})}{(E(\bar{m}))^2} \cdot f_N \cdot N_p^r(z) \quad (5.3.3)$$

where N_p^r is the relative number density given by

$$N_p^r(z) = \frac{1}{4\lambda^2} \cdot \frac{(K_{ext}(z))^2}{Q_{VV}(z)} \quad . \quad (5.3.4)$$

The particle diameter is calculated from the ratio of the scattering coefficient to the extinction coefficient and is determined from Eq. (3.2.29) to give

$$d_{63} = \lambda \cdot \left(\frac{4}{\pi^2} \cdot \frac{E(\bar{m})}{F(\bar{m})} \cdot \frac{Q_{vv}(z)}{K_{ext}(z)} \right)^{1/3} = \left(\frac{E(\bar{m})}{F(\bar{m})} \right)^{1/3} \cdot d_{63}^r \quad (5.3.5)$$

where d_{63}^r is the relative particle diameter given by

$$d_{63}^r = \lambda \cdot \left(\frac{4}{\pi^2} \cdot \frac{Q_{vv}(z)}{K_{ext}(z)} \right)^{1/3} \quad (5.3.6)$$

We have taken the approach of calculating the relative profiles, $f_v'(z)$, $N_p'(z)$, and $d_{63}'(z)$, because they can be calculated directly from the extinction coefficient and scattering coefficient profiles. Assumptions for the particle refractive index and the particle size distribution can then be applied as multiplicative factors to the relative profiles. Also, any comparison of the relative profiles is equivalent to a comparison of profiles evaluated at a constant index of refraction and particle size distribution.

An important reason for calculating relative profiles is that the choice of an index of refraction for soot is not clear. Measurements of the index of refraction and the factors affecting it were discussed in Section 3.2.3. Briefly, the index of refraction may depend on the H/C ratio of the soot, the equivalence ratio of the flame, and also the height within the flame. The latter two factors may result from the dependence of \bar{m} on the degree of agglomeration of the soot particles.

Table 5.1 lists values of the index of refraction that have been assumed or measured in previous studies and also the resulting factors used to calculate the f_v , N_p , and d_{63} profiles from the corresponding relative profiles. The values of \bar{m} include that measured by Dobbins, Santoro, and Semerjian (1990) for the primary particles within the soot aggregates produced by an ethylene diffusion flame. The \bar{m} values of Lee and Tien (1981) and Dalzell and Sarofim (1969) are often referenced. The $\bar{m} = 1.57 - i0.56$ value is that quoted from Dalzell and Sarofim (1969) and used by Harris, Weiner, and Ashcraft

(1986), D'Alessio (1981), and Haynes, Jander, and Wagner (1980). The two \bar{m} values of Charalampopoulos, Chang, and Stagg (1989) represent the range of values they measured in propane flames over a range of equivalence ratios and heights. The value of Habib and Vervisch (1988) was measured for soot with a high H/C ratio and may be more applicable for soot in the early stages of formation.

The range in the factors illustrates that the assumed value of \bar{m} can have a significant effect on the calculated values of f_v , N_p , and d_{63} . For the range of factors shown in Table 5.1, the volume fraction can range over a factor of 2.2, the number density over a factor of 6, and the particle diameter over a factor of 1.5.

For the evaluation of the profiles presented here, the $\bar{m} = 2.10 - i \cdot 0.55$ measured by Dobbins, Santoro, and Semerjian (1990) is probably most appropriate. Since the resulting factors lie near the upper extreme of the values in Table 5.1, the calculated profiles would define upper bounds for the volume fraction and number density profiles and a lower bound on the diameter profile. Since this \bar{m} is for the primary particles within the soot aggregates, it should be more applicable for the lightly sooting flames we have examined here, because the degree of agglomeration is small when the volume fraction and the final diameters are small (Prado et al., 1981). Also, this \bar{m} is an upper bound because agglomeration decreases the effective index of refraction (Dobbins and Megaridis, 1991).

The assumption of a particle size distribution also significantly affects the calculated values of the number density and the mean particle diameter. These effects are discussed in Section 3.2.4. Table 5.2 lists for three particle size distributions the equivalent geometric width, the dimensionless moment ratio, and the factor (Eq. 3.2.35) relating the mean diameter, d_0 , to the diameter, d_{63} , determined from the scattering-extinction measurements. These factors are for a monodisperse distribution, a self-preserving size distribution (SPSD) (Graham and Robinson, 1976) and for the zero-order lognormal distribution measured by Bockhorn, Fetting, and Heddrich (1986). Here, the choice of the

Table 5.1 Particle index of refraction and the resulting factors for the calculation of volume fraction, number density, and particle diameter.

	\bar{m}	$E(\bar{m})$	$F(\bar{m})$	$(E(\bar{m}))^{-1}$	$\frac{F(\bar{m})}{(E(\bar{m}))^2}$	$\left(\frac{E(\bar{m})}{F(\bar{m})}\right)^{1/3}$
1)	2.10 - i-0.55	0.163	0.352	6.15	13.3	0.773
2)	1.90 - i-0.55	0.193	0.280	5.19	8.02	0.865
3)	1.56 - i-0.48	0.226	0.185	4.43	3.64	1.07
4)	1.57 - i-0.56	0.260	0.217	3.85	3.23	1.06
5)	1.81 - i-0.84	0.303	0.389	3.30	3.77	0.953
6)	1.41 - i-0.51	0.270	0.163	3.70	2.23	1.18
7)	1.46 - i-0.27	0.138	0.102	7.23	5.32	1.11

1) Dobbins, Santoro, and Semerjian (1990)

2) Lee and Tien (1981)

3) Dalzell and Sarofim (1969)

4) Dalzell and Sarofim (1969) referenced by Haynes, Jander, and Wagner (1980), D'Alessio (1981), and Harris, Weiner, and Ashcraft (1986)

5) & 6) Charalampopoulos, Chang, and Stagg (1989)

7) Habib and Vervisch (1988)

Table 5.2 Particle size distribution, equivalent geometric width, dimensionless moment ratio, and factor relating d_0 to d_{63} .

	Size Distribution	σ_g	f_N	$\exp\left[-\frac{11}{2}(\ln \sigma_g)^2\right]$
1)	Monodisperse	1.0	1.0	1.0
2)	Self-preserving	1.33	2.079	0.639
3)	Zeroth order lognormal	1.405	2.831	0.530

2) Graham and Robinson (1976)

3) Bockhorn, Fetting, and Heddrich (1986)

SPSD should be appropriate, because the size distribution rapidly approaches that of the SPSP following particle inception (Dobbins and Mulholland, 1984; Megaridis and Dobbins, 1989; Harris and Kennedy, 1988). Typically, the number density and diameter cannot be calculated until after particle inception, since the scattering coefficient does not rise above the detection limit until then because of the small initial particle sizes.

5.3.2 Soot Volume Fraction, Number Density, and Particle Diameter Profiles

The relative volume fraction profiles of the atmospheric-pressure flames are shown in Figures 5.20 and 5.21. Figure 5.20 shows the relative volume fraction profiles of the A-IA sequence of flames. The volume fraction profile of the A-IB-S4 flame is included for comparison with the A-IA-S4 flame. The volume fraction profiles of flames with the same equivalence ratio from each of the flame sequences are compared for the -S2 ($\phi = 1.92$) and the -S3 ($\phi = 2.02$) flames in Figure 5.21. In both figures, the right axis has been scaled to show the volume fraction for an assumed index of refraction, $\bar{m} = 2.0 - i0.55$, which should give an upper bound for the volume fraction profiles of these flames.

Within all three flame sequences, the volume fraction increases with equivalence ratio at a given height. The relative volume fraction profiles increase approximately linearly with height above the burner over the range of heights investigated. The growth in the volume fraction profiles for the A-IB and A-IIA flames declines slightly as the profiles depart from linearity ~ 15 to 20 mm above the burner.

Comparing the A-IB flames with A-IA flames at the same equivalence ratio shows that a decrease in dilution ratio increases the soot volume fraction significantly. However, the volume fraction profiles of the A-IA-S3 and the A-IB-S3 flames reach the same volume fraction above a height of 15 mm. Comparing the A-IIA flames with the A-IA

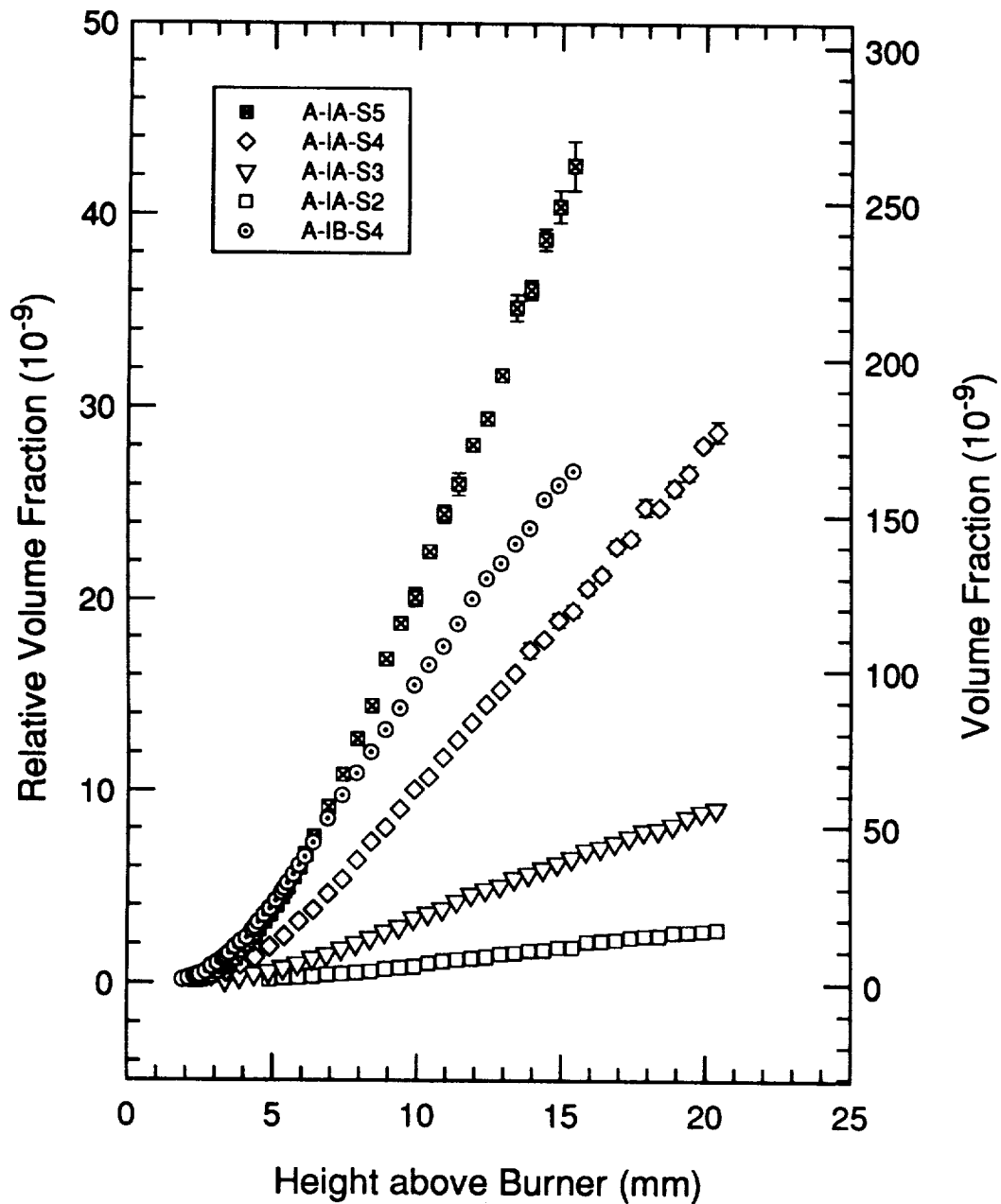


Figure 5.20 Relative volume fraction profiles of the A-IA flame sequence. The relative volume fraction profile of the A-IB-S4 flame is also shown. The scale on the right axis corresponds to the volume fraction calculated with $\bar{m} = 2.10 - i \cdot 0.55$.

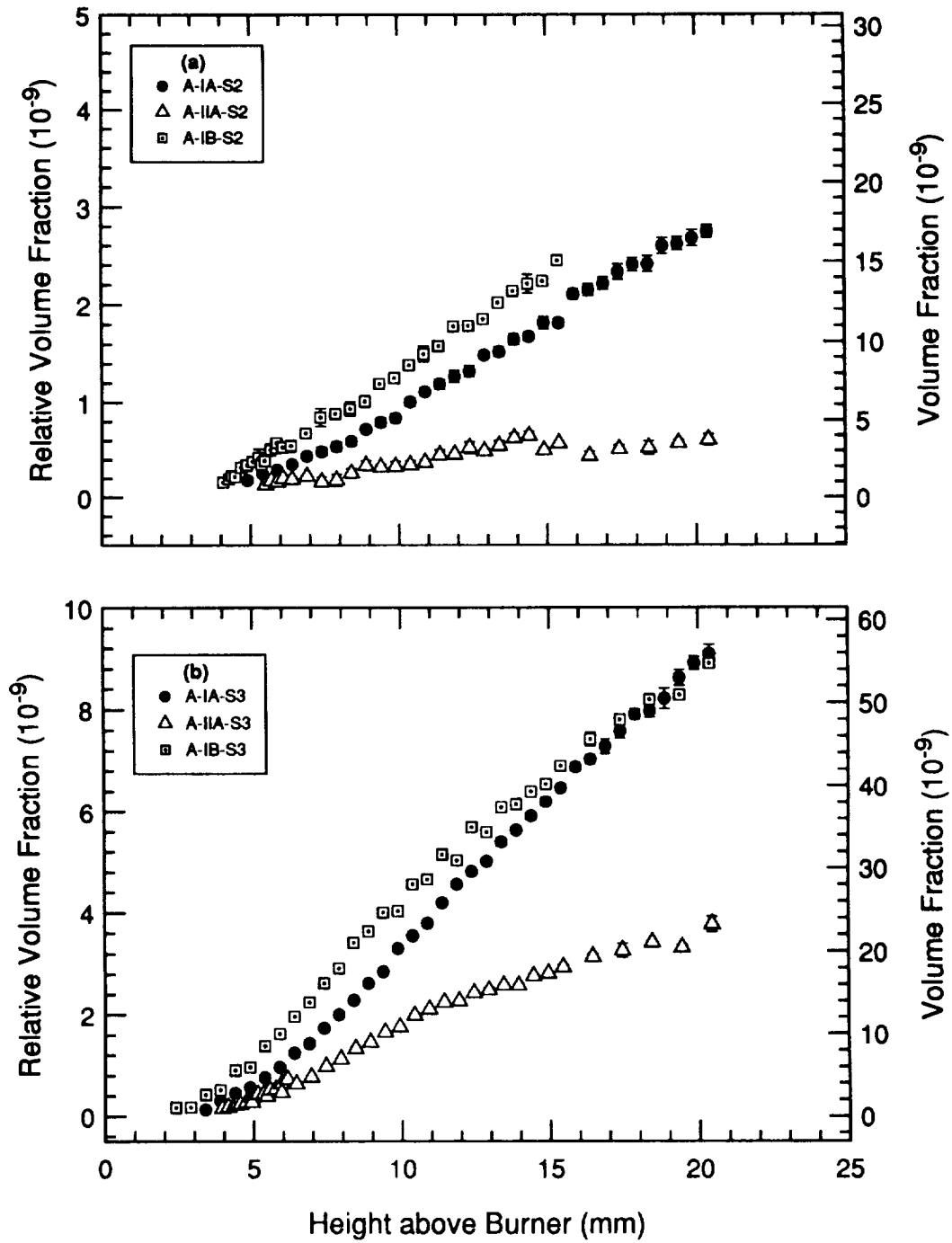


Figure 5.21 a) Comparison of the relative volume fraction profiles measured in the -S2 ($\phi = 1.92$) flame of the three flame sequences. b) Comparison of the relative volume fraction profiles measured in the -S3 ($\phi = 2.02$) flame of the three flame sequences.

flames at the same equivalence ratio shows that an increase in the cold flow velocity decreases the volume fraction significantly, almost by a factor of three for these conditions.

Relative number density profiles for the three flame sequences are shown in Figures 5.22 to 5.24. The relative number density profiles of the A-IA sequence of flames are shown in Figure 5.22. As the equivalence ratio within the A-IA flame sequence increases, the number density peaks at a lower height and then declines so that the number density at a given height well above the burner decreases with increasing equivalence ratio. The decline in number density following the peak appears to have a similar slope for all the flames.

To show the effect of the argon-ion laser-induced fluorescence on the number density profile, the profiles calculated from the scattering coefficient with and without the fluorescence background subtracted are compared in Figure 5.22. The peaks in the number density profile can be underestimated, if the fluorescence is not accounted for properly. The magnitude of this underestimation decreases as the equivalence ratio increases. The peak number densities should be considered with caution because the number density is inversely proportional to the particle scattering coefficient, and the peak number densities occur in a region where the particle scattering coefficient is small relative to the molecular scattering background. Small errors in subtracting the estimated molecular scattering coefficient background can thus produce large errors in the calculated number density.

The relative number density profiles of the flames with the same equivalence ratio from each flame sequence are compared in Figures 5.23 and 5.24. The decline in number density again appears to have a similar shape for both the -S3 ($\phi = 2.02$) and -S4 ($\phi = 2.17$) flames. The decline in number density in the -S2 ($\phi = 1.92$) flames is not as well resolved because the scattering coefficient does not increase until above a height of

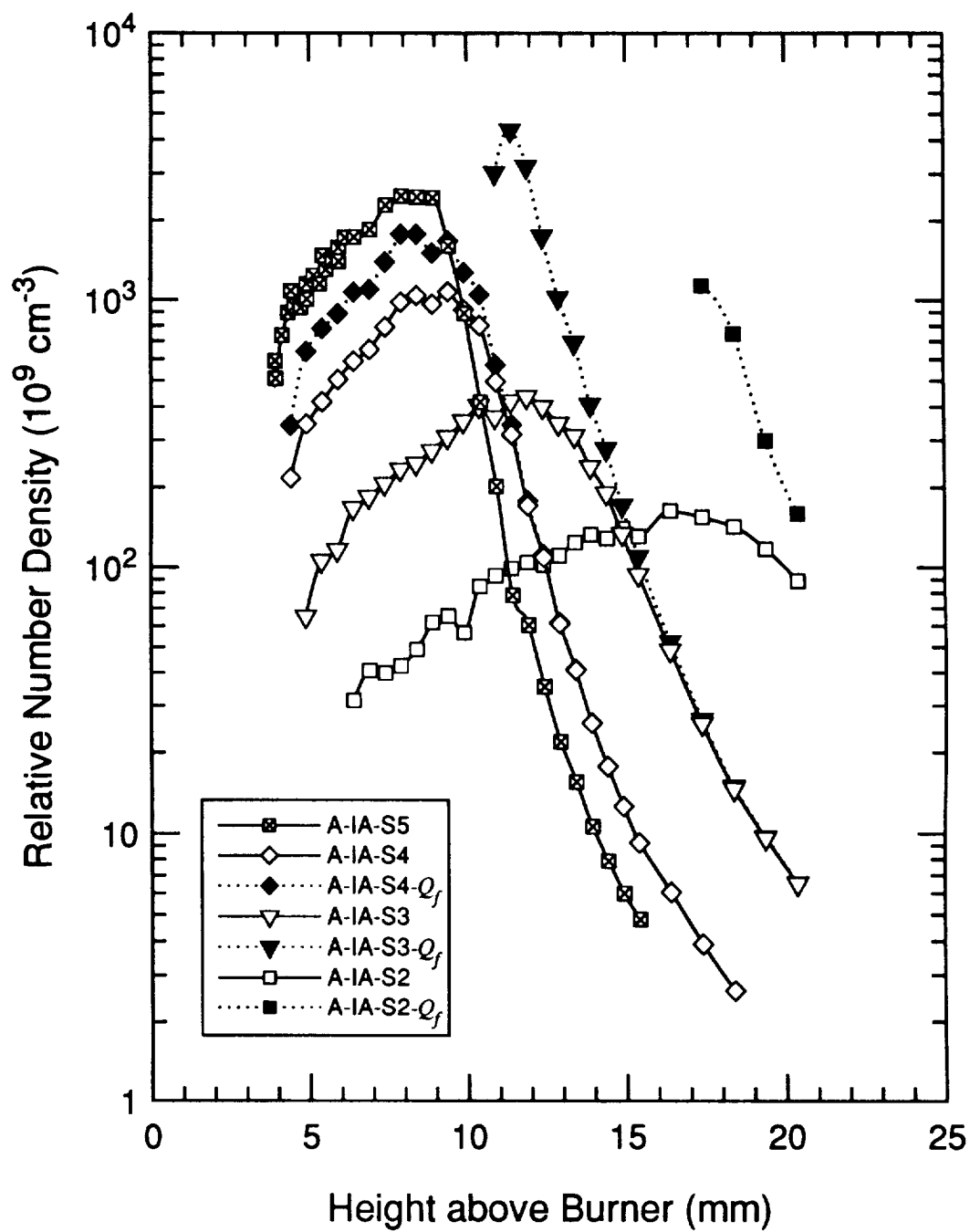


Figure 5.22 Relative number density profiles of the A-IA flame sequence. The solid symbols represent the profiles that have been corrected for the fluorescence background.

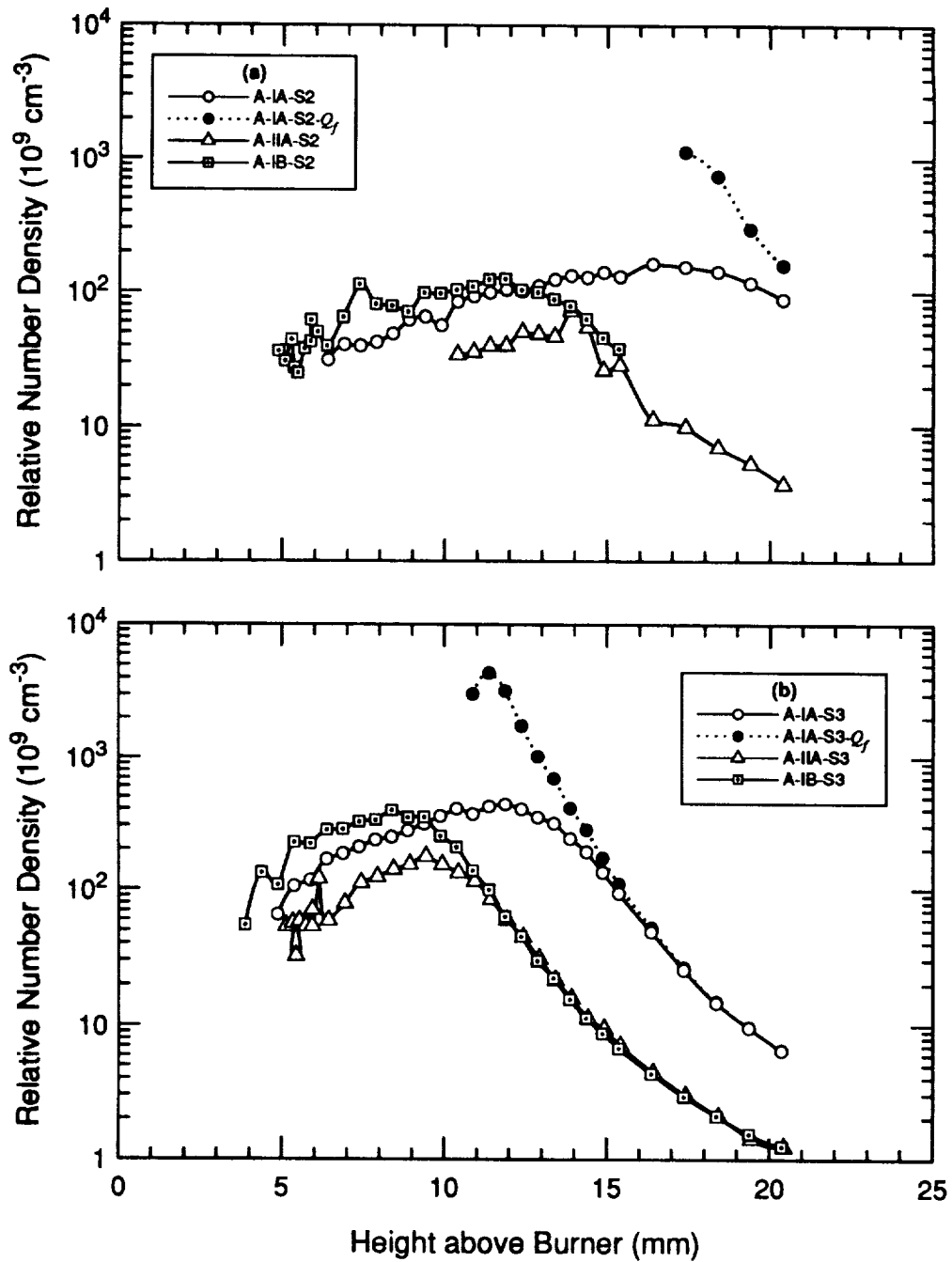


Figure 5.23 a) Comparison of the relative number density profiles measured in the -S2 ($\phi = 1.92$) flame of the three flame sequences. b) Comparison of the relative number density profiles measured in the -S3 ($\phi = 2.02$) flame of the three flame sequences.

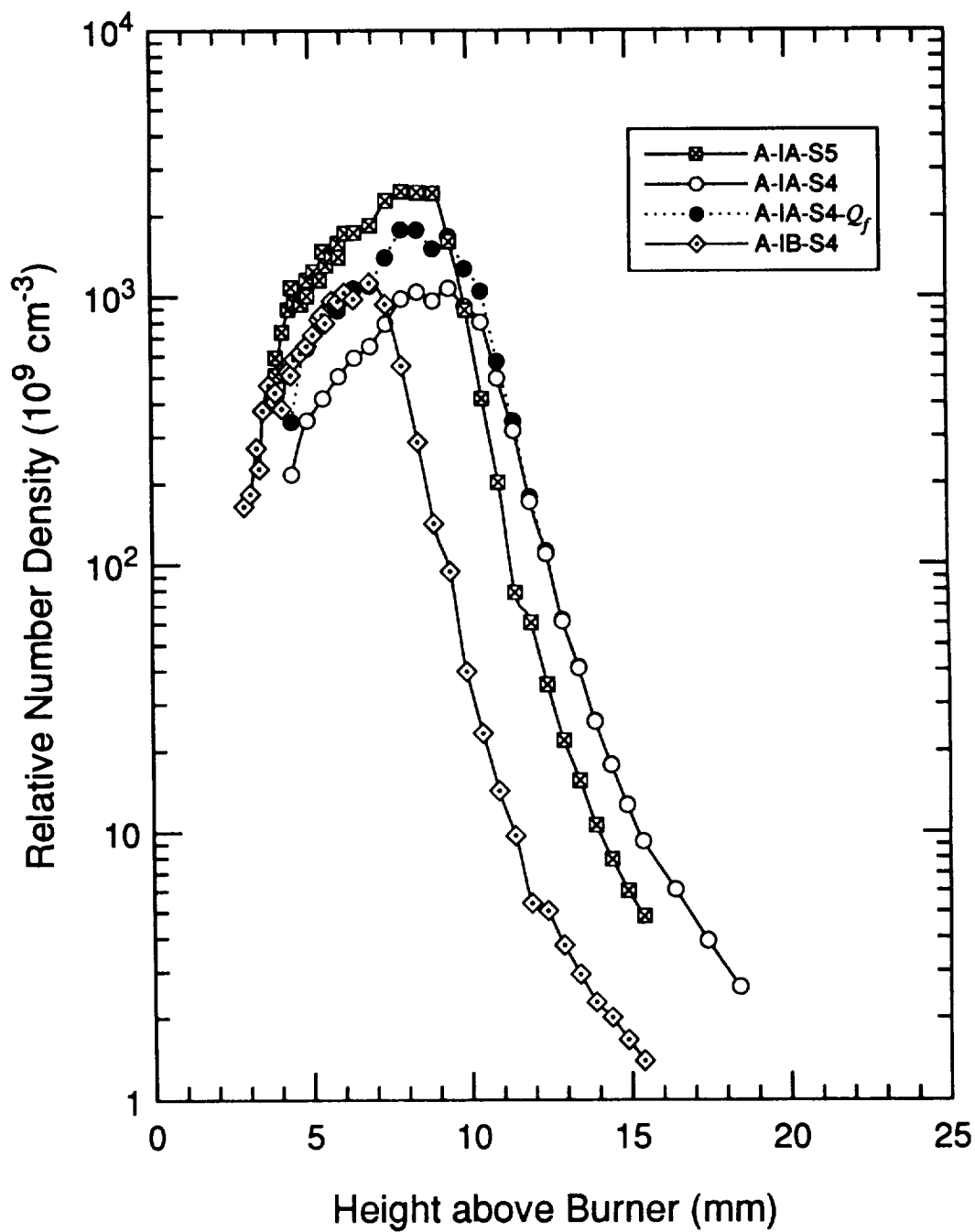


Figure 5.24 Comparison of the relative number density profiles measured in the A-IB-S4 and A-IA-S4 flames ($\phi = 2.17$) and the A-IA-S5 flame ($\phi = 2.32$).

~ 12 to 15 mm. The relative number density profiles of both the A-IB and the A-IIA flames peak and decline at a lower height above the burner than the A-IA flames. The decline in the relative number density profiles of the A-IB-S3 and A-IIA-S3 flames overlay each other. The trends of the A-IB-S2 and A-IIA-S2 flames suggest that they may also overlay each other. The argon-ion laser-induced fluorescence was not measured in either the A-IB or A-IIA flames; thus the peak number densities may not be a true measure of the peak particle number density. The uncorrected peak number densities of the A-IA and A-IB flames are approximately the same, while those of the A-IIA flames are almost a factor of two lower.

Figures 5.25 and 5.26 show the relative particle diameter profiles of the flame sequences. The relative particle diameter profiles of the A-IA flames are shown in Figure 5.25, which also includes the profile of the A-IB-S4 flame to compare with that of the A-IA-S4 flame. The relative particle diameter profiles appear to remain flat at a particle diameter of ~ 2.2 nm until the height at which the particle diameter begins to increase linearly. The flat section of the profile is an artifact of the resolution of both the extinction coefficient and the particle scattering coefficient. Smaller particle diameters are observed with the fluorescence background correction because of a reduction in the scattering coefficient.

Within a flame sequence, the final particle diameter increases with increasing equivalence ratio. The relative particle diameters also appear to increase linearly with height, a trend which is observed in all three flame sequences. Comparing the relative particle diameter profiles of flames at the same equivalence ratio (Fig. 5.26) indicates that the final particle diameter increases in the order, A-IA, A-IIA, A-IB, for both the -S2 and -S3 flames.

Since the factors relating the mean particle diameter, d_0 , to the relative particle diameter, d'_{03} , in Table 5.2 are on the order of 1 or less, the relative particle diameter

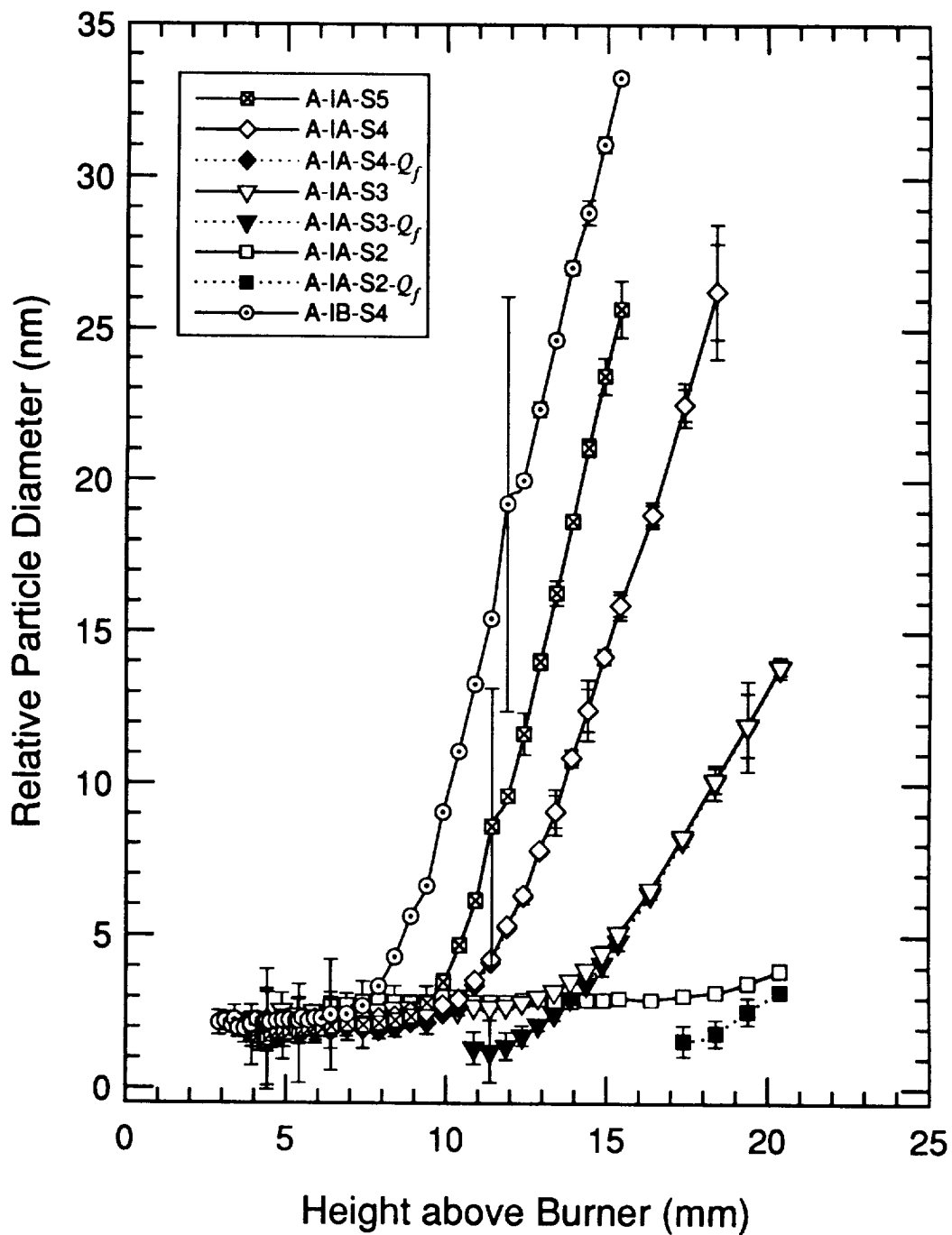


Figure 5.25 Relative particle diameter profiles of the A-IA flame sequence. The solid symbols represent the profiles that have been corrected for the fluorescence background.

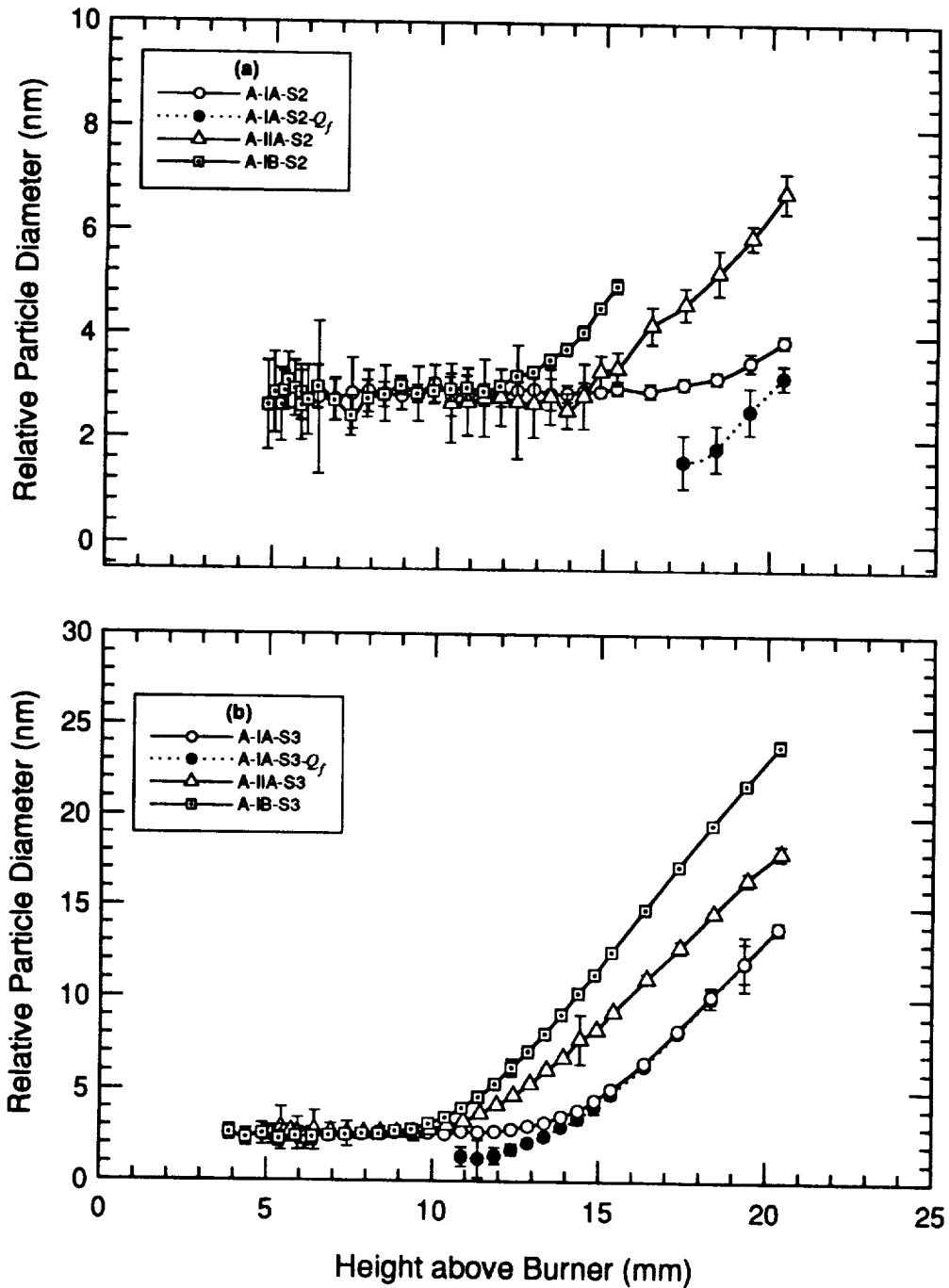


Figure 5.26 a) Comparison of the relative particle diameter profiles measured in the -S2 ($\phi = 1.92$) flame of the three flame sequences. b) Comparison of the relative particle diameter profiles measured in the -S3 ($\phi = 2.02$) flame of the three flame sequences.

represents an upper bound on the mean particle size. The particle diameters measured here fall below the Rayleigh limit of $d_0 < 47$ nm defined by the relation, $\alpha = 2\pi d_0/\lambda < 0.3$ (D'Alessio, 1981). Thus, the assumptions of Rayleigh scattering are valid for the scattering-extinction measurements in these flames.

5.3.3 Implications of the Detection Limits

Although the scattering and extinction coefficient profiles due to the soot could not be measured in the atmospheric sooting flames near the critical equivalence ratio, an upper bound on the soot volume fraction and number density within these flames can be estimated from the detection limits of the experimental apparatus. Similarly, since the extinction coefficient profile could not be detected in the 80-torr sooting flames, we can estimate an upper bound for their volume fractions. As the scattering coefficient profile due to the particles was measured in the 80-torr flames, we can also infer an upper bound on their number density profiles.

The analysis to determine the detection limits for both the scattering and extinction coefficients is presented in Appendix B. The detection limit for the extinction coefficient was the same for both the atmospheric-pressure and the 80-torr flames. This detection limit can be used to estimate an upper bound on the soot volume fraction present in those sooting flames for which the extinction coefficient could not be measured.

The upper bounds on the volume fraction are listed in Table 5.3 for three values of the index of refraction. The index of refraction of Dobbins, Santoro, and Semerjian (1990) gives a conservative estimate of the volume fraction, which is likely to be appropriate for a small degree of agglomeration. The limits on the volume fraction using the refractive index value of Dalzell and Sarofim (1969) can be compared with results from other studies which used that value. The index of refraction from Habib and Vervisch (1988) was measured for soot with a higher hydrogen content and may be more appropriate for defining the upper bounds during the early stages of soot formation.

The upper bounds on the volume fraction imply an upper bound on the particle number density for particles of a given diameter. The upper bounds on the number density are listed in Table 5.3 for three particle diameters assuming a monodisperse size distribution and three refractive indices. The assumption of a self-preserving size distribution reduces these calculated number densities by a factor of ~ 2 . If incipient particles have a 2-nm diameter, then an upper bound can be placed on the number of incipient particles formed when the extinction coefficient falls below the detection limit.

The detection limit for the scattering coefficient implies an upper bound on the product of the number density and the sixth power of the particle diameter. Thus, for a given particle diameter, the scattering coefficient detection limit implies an upper bound on the number density of the particles. Tables 5.4 and 5.5 list the scattering coefficient detection limits for both the atmospheric and 80-torr flames and the resulting upper bounds on the number densities for three particle diameters. The detection limit for the scattering coefficient at 80 torr was about half that at atmospheric pressure. We again assume a monodisperse particle size distribution and employ the same refractive indices as used in the extinction coefficient evaluation.

The detection limit for the number density based on the scattering coefficient is the same order of magnitude as that based on the extinction coefficient for 2-nm particles (incipient particles), but the detection limit based on the scattering coefficient improves by two orders of magnitude over that based on the extinction coefficient for 10-nm particles. This decrease in the number density detection limit for the scattering coefficient is the reason why the scattering coefficient could be detected while the extinction coefficient could not for the 80-torr sooting flames.

The particle scattering coefficient profiles for the sooting 80-torr flames can be used to calculate relative number density profiles that define upper bounds on the relative number density profiles of these flames. These relative number density profiles were

Table 5.3 Estimates of the volume fraction and number density detection limits based on the extinction coefficient detection limit.

Index of refraction	2.10 - i-0.55	1.57 - i-0.56	1.46 - i-0.27
Extinction coefficient, K_{ext} (cm^{-1})	1.8×10^4	1.8×10^4	1.8×10^4
Relative volume fraction, f'_v	4.7×10^{-10}	4.7×10^{-10}	4.7×10^{-10}
Volume fraction, f_v	2.9×10^{-9}	1.8×10^{-9}	3.4×10^{-9}
Particle number density (cm^{-3})			
$N_p(d_0 = 1 \text{ nm})$	5.5×10^{12}	3.4×10^{12}	6.4×10^{12}
$N_p(d_0 = 2 \text{ nm})$	6.8×10^{11}	4.3×10^{11}	8.0×10^{11}
$N_p(d_0 = 10 \text{ nm})$	5.5×10^9	3.4×10^9	6.4×10^9

Table 5.4 Estimates of the particle number density detection limits based on the scattering coefficient detection limit for the atmospheric-pressure flames.

Scattering Coefficient	$4.2 \times 10^{-11} \text{ cm}^{-1} \cdot \text{sr}^{-1}$		
Index of refraction	2.10 - i-0.55	1.57 - i-0.56	1.46 - i-0.27
Number Density (cm^{-3})			
$N_p(d_0 = 1 \text{ nm})$	2.8×10^{13}	4.5×10^{13}	9.6×10^{13}
$N_p(d_0 = 2 \text{ nm})$	4.3×10^{11}	7.0×10^{11}	1.5×10^{12}
$N_p(d_0 = 10 \text{ nm})$	2.8×10^7	4.5×10^7	9.6×10^7

Table 5.5 Estimates of the particle number density detection limits based on the scattering coefficient detection limit for the 80-torr flames.

Scattering Coefficient	$1.9 \times 10^{-11} \text{ cm}^{-1} \cdot \text{sr}^{-1}$		
Index of refraction	2.10 - i-0.55	1.57 - i-0.56	1.46 - i-0.27
Number Density (cm^{-3})			
$N_p(d_0 = 1 \text{ nm})$	1.3×10^{13}	2.1×10^{13}	4.3×10^{13}
$N_p(d_0 = 2 \text{ nm})$	2.0×10^{11}	3.2×10^{11}	6.8×10^{11}
$N_p(d_0 = 10 \text{ nm})$	1.3×10^7	2.0×10^7	4.3×10^7

calculated from the scattering coefficient profile using Eq. (5.3.4) by assuming a constant extinction coefficient profile at the detection limit, $K_{ext} = 1.8 \times 10^{-4} \text{ cm}^{-1}$. These relative number density profiles for the five sooting 80-torr flames are shown in Figure 5.27. These profiles can serve to identify the relative trends in soot formation for these flames. These profiles exhibit similar trends to those of the atmospheric-pressure flames. As the equivalence ratio increases, the decline in the number density moves closer to the burner surface indicating that the location of particle inception moves closer to the burner surface.

5.3.4 Comparison of Fluorescence and Extinction Coefficients

The argon-ion laser-induced fluorescence coefficient was compared to the extinction coefficient profiles for both the A-IA-S2 ($\phi = 1.92$) and the A-IA-S3 ($\phi = 2.02$) flames, the only two flames for which both the fluorescence was measured and a measurable particle extinction coefficient was observed. The correlation between the fluorescence and extinction coefficients was investigated by plotting the fluorescence coefficient detected at 503 nm against the extinction coefficient at the same height for the A-IA-S2 and A-IA-S3 flames and then fitting the curves with a linear least squares curve fit. The linear relationship between the fluorescence coefficient and the extinction coefficient is shown in Figure 5.28 for both flames. The linear curve fit for the A-IA-S2 flame is given by

$$Q_f(\lambda_0 = 488\text{nm}, \lambda = 503\text{nm}) \cdot \Delta\lambda(z) = 0.199 \cdot K_{ext}(z) \quad (5.3.7)$$

and that for the A-IA-S3 flame is given by

$$Q_f(\lambda_0 = 488\text{nm}, \lambda = 503\text{nm}) \cdot \Delta\lambda(z) = 0.141 \cdot K_{ext}(z) \quad (5.3.8)$$

The linear relationship also holds between the fluorescence coefficient detected at 473 nm and the extinction coefficient; however, the slopes in this case are half those for the fluorescence detected at 503 nm. A correlation could not be established between

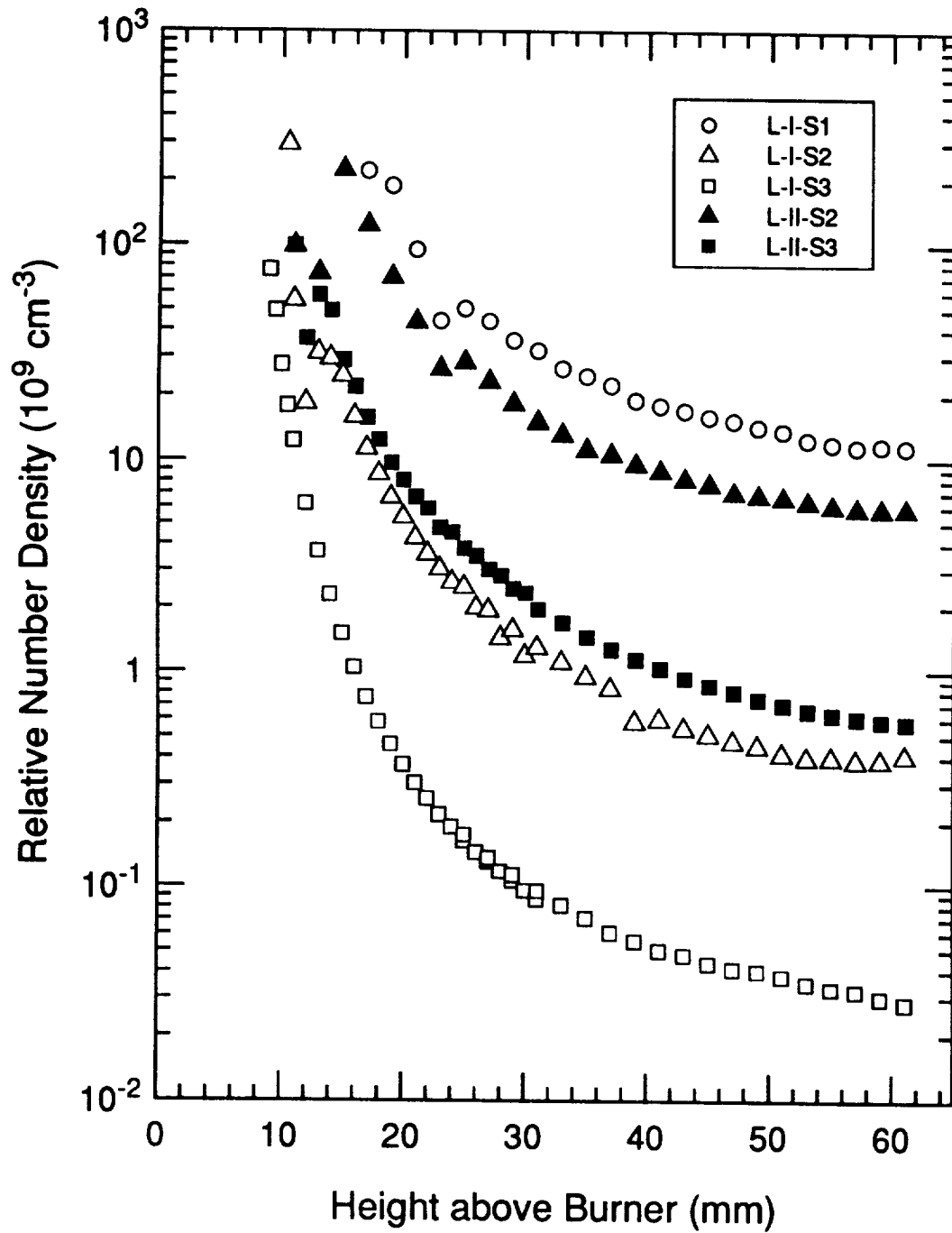


Figure 5.27 Relative number density profiles representing the upper bounds on the number density profiles of the 80-torr sooting flames.

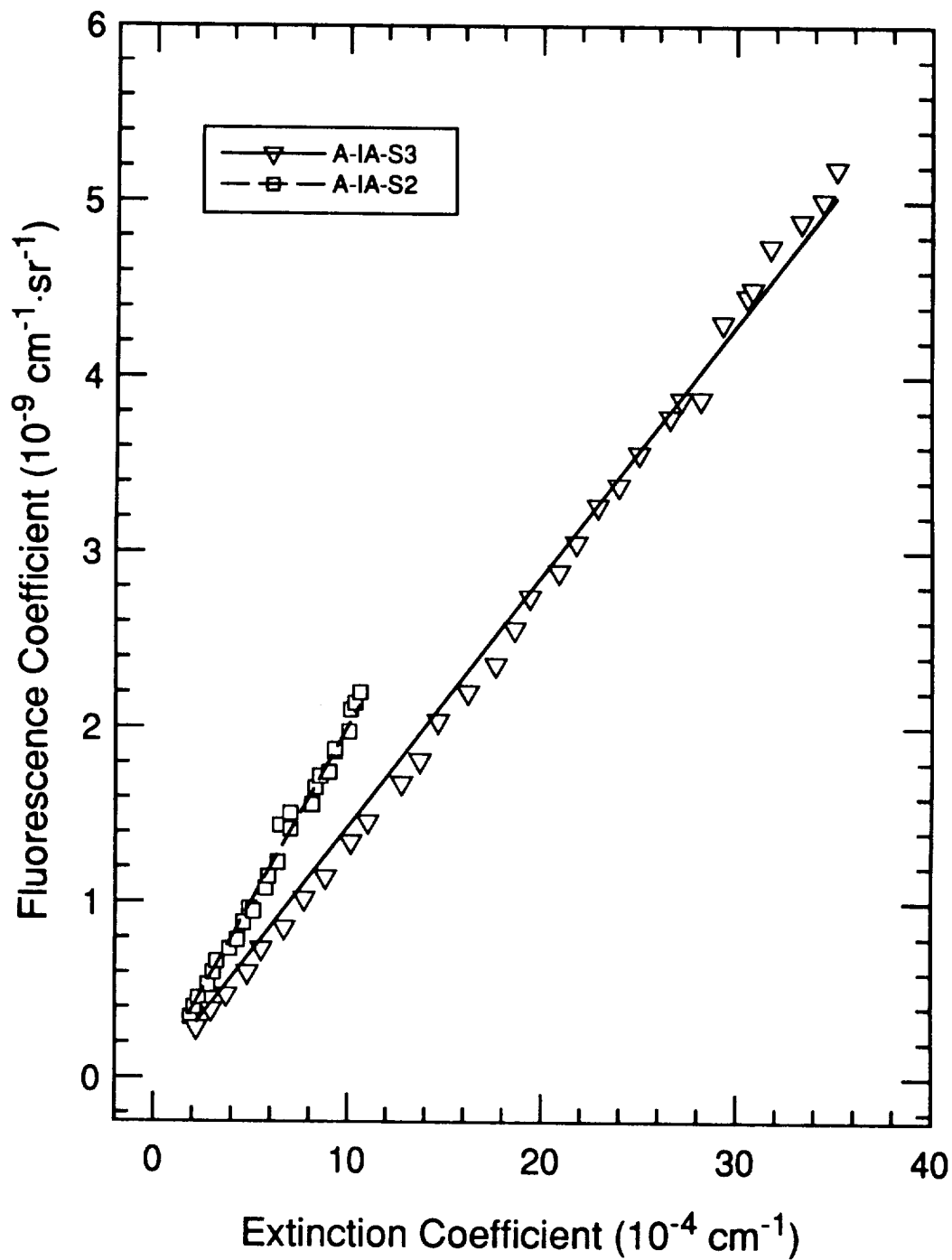


Figure 5.28 Fluorescence coefficient detected at 503 nm vs. the extinction coefficient for the A-IA-S2 and A-IA-S3 flames. The linear curve fit for the A-IA-S2 flame was $Q_f(\lambda_0 = 488 \text{ nm}, \lambda = 503 \text{ nm})(z) = 0.199 \cdot K_{ext}(z)$ and for the A-IA-S3 flame, $Q_f(\lambda_0 = 488 \text{ nm}, \lambda = 503 \text{ nm})(z) = 0.141 \cdot K_{ext}(z)$.

the fluorescence coefficient and the extinction coefficient for the A-IA-S1 flame because the extinction coefficient remained below the detection limit throughout the measured range in the flame.

If we assume the linear correlation between the fluorescence coefficient and the extinction coefficient remains valid for the regions of the flame where the extinction coefficient can not be detected, then we can extrapolate the extinction coefficient profile into this region based on the fluorescence coefficient profile. The detection limit for this extrapolated extinction coefficient can then be based on the detection limit for the fluorescence coefficient, which we estimate conservatively at $Q_f \cdot \Delta\lambda = 1.0 \times 10^{-11} \text{ cm}^{-1} \cdot \text{sr}^{-1}$ (Appendix B). Hence, for the A-IA-S2 flame, the detection limit for the extinction coefficient would be $K_{ext} > 5.0 \times 10^{-6} \text{ cm}^{-1}$ and for the A-IA-S3 flame, $K_{ext} > 7.1 \times 10^{-6} \text{ cm}^{-1}$. These limits would correspond to an equivalent decrease in the transmittance of 0.0028% and 0.0040%. Thus, the linear correlation between the fluorescence and extinction coefficient allows the possibility of increasing the sensitivity of the extinction coefficient by over an order of magnitude. Because the relationship between the extinction coefficient and the fluorescence coefficient changes with equivalence ratio, we cannot extrapolate these results to the A-IA-S1 flame.

5.3.5 Temperature Profiles

The temperature profiles of the atmospheric-pressure flames were determined from their scattering coefficient profiles. The theory relating the temperature to the molecular scattering coefficient and the method to estimate the temperature profile are described in Appendix C.

The determination of the temperature profile was an iterative procedure in which a predicted scattering coefficient profile from the solution of the Sandia flame code was matched to the measured scattering coefficient profile. The match between the predicted and measured scattering coefficient profiles was sensitive to a variation of $\pm 15 \text{ K}$ in the

estimated temperature. The method was thus very precise but its accuracy was not checked by a comparison with another thermometric method. The accuracy depends on how well the flame code and reaction mechanism model the actual molar composition profile of the flame and also on the accuracy of the differential scattering cross-sections of the major gas species. Since the reaction mechanism is most accurate in predicting the major combustion gas products that comprise nearly all of the scattering cross-section, the estimated temperatures are expected to be reasonably accurate and thus relative comparisons between flame temperatures should be valid.

This thermometric method only works when the scattering coefficient is that caused by the flame gases. Contributions from either particle scattering or fluorescence will decrease the apparent temperature determined from the scattering coefficient. Thus, this method is only valid for determining the temperature profiles for the nonsooting flames and for nonsooting regions of the sooting flames, which is usually sufficient to resolve the maximum in the temperature profile. The effect of particle scattering on the temperature profile causes a rapid decline following the peak of the temperature profile in the more heavily sooting flames.

The temperature profiles of the atmospheric-pressure flames are shown in Figures 5.29 to 5.31. The peak temperatures of the estimated profiles are listed in Table 5.6. For comparison, the peak temperatures determined from the solution of the energy conservation equation by the Sandia flame code for both the Drake and Blint (1991) reaction mechanism and the Miller and Melius (1992) reaction mechanism are included in Table 5.6 along with the adiabatic flame temperatures calculated with the NASA equilibrium code (Gordon and McBride, 1971).

A comparison of the peak temperatures of the A-IIA flames with the A-IA flames shows that increasing the cold flow velocity while keeping the dilution ratio constant increases the peak temperature. The A-IIA flames are 22 to 65 K hotter than the A-IA

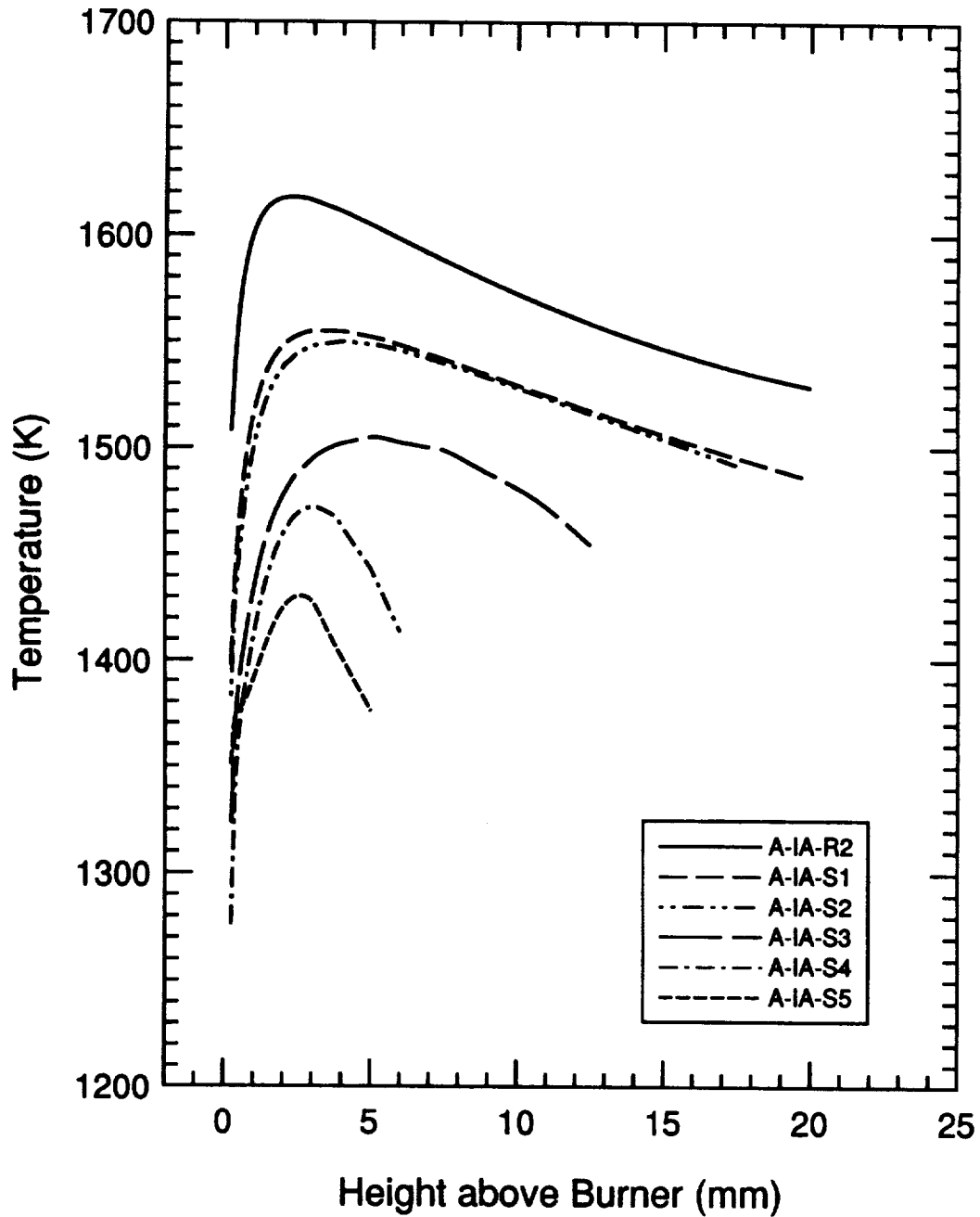


Figure 5.29 Temperature profiles determined from the scattering coefficient profiles for the A-IA flame sequence. The -R2, -S1, and -S2 profiles are free of particle scattering interference. The -S3 profile is free of interference below 10 mm, while the -S4 and -S5 profiles may remain free of interference only through the maximum.

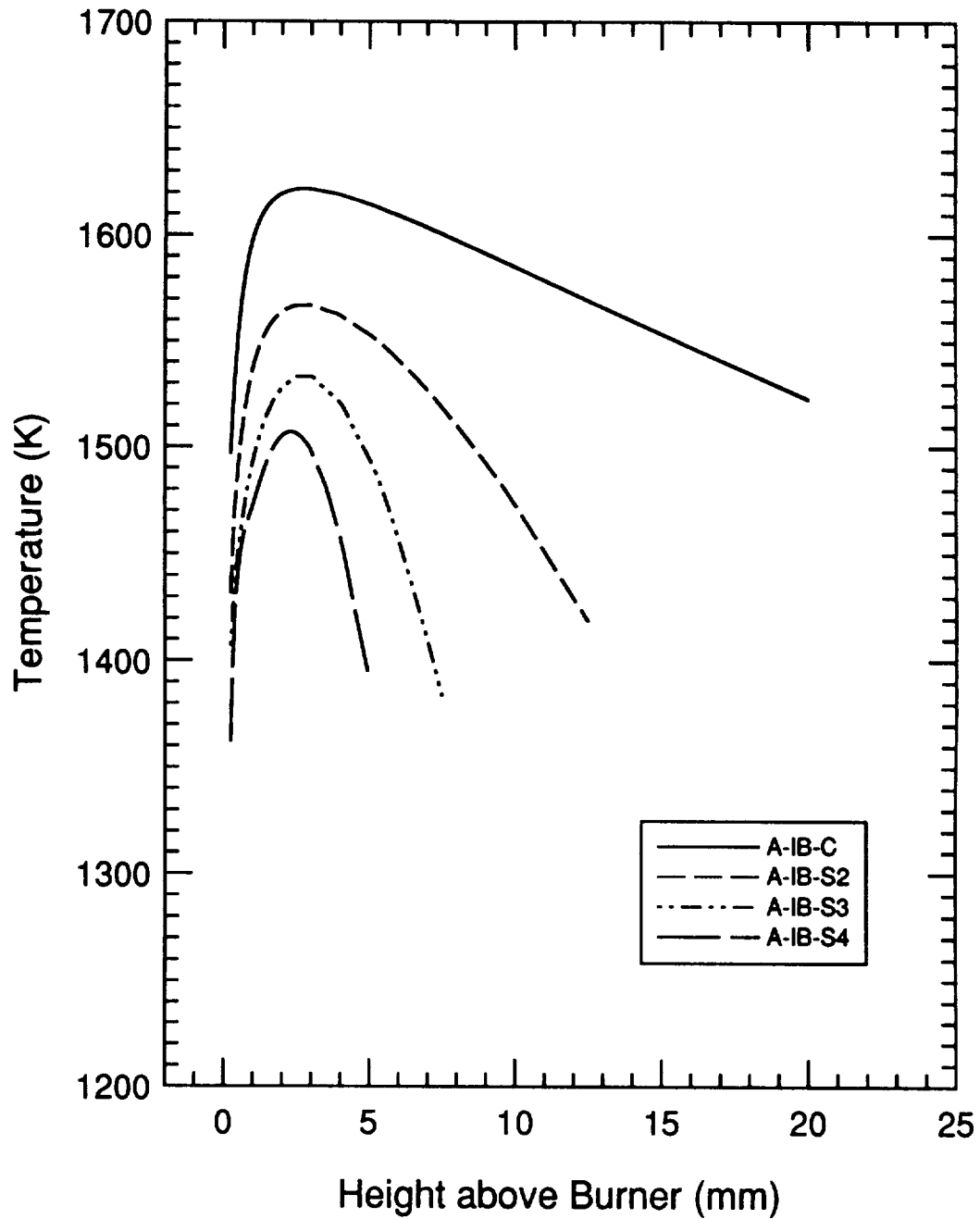


Figure 5.30 Temperature profiles determined from the scattering coefficient profiles for the A-IB flame sequence. The -C flame is free of particle scattering interference, while the other three flames may remain free of interference only through the maximum.

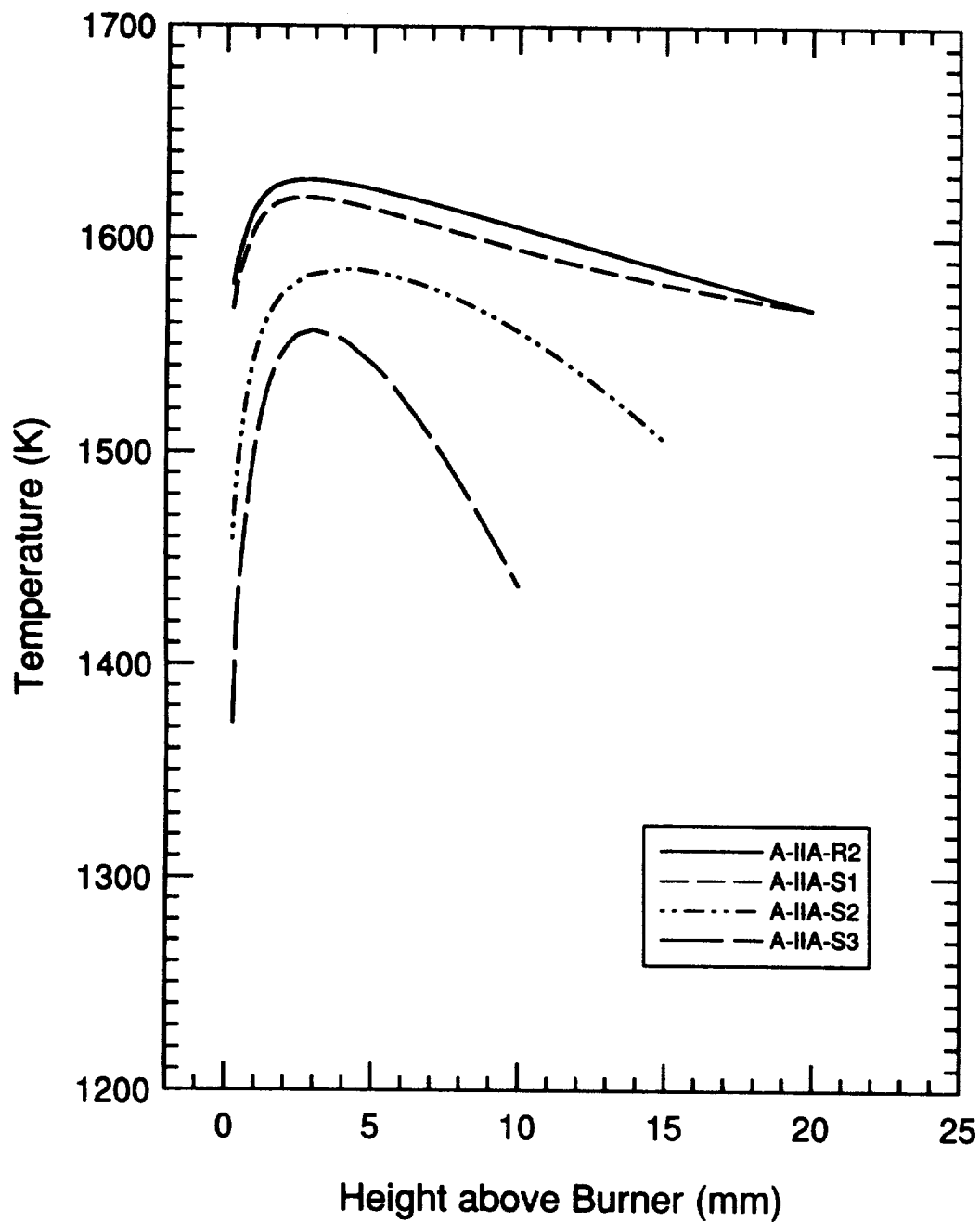


Figure 5.31 Temperature profiles determined from the scattering coefficient profiles for the A-IIA flame sequence. The -R2 and -S1 profiles are free of particle scattering interference. The -S2 profile is free of interference below 10 mm, while the -S3 profile may remain free of interference only through the maximum.

Table 5.6 Estimated peak temperatures, flame code energy-equation temperatures, and adiabatic flame temperatures for the atmospheric-pressure flames.

Flame	Temperature (K)			
	Estimated Peak	Energy Equation solution		Adiabatic
		Drake & Blint	Miller & Melius	
A-IA-R2	1617	1610	1604	2019
A-IA-S1	1554	1616	1603	1938
A-IA-S2	1550	1614	1598	1860
A-IA-S3	1505	1612	1593	1811
A-IA-S4	1472	1602	1578	1738
A-IA-S5	1430	1595	1572	1669
A-IB-C	1622	1646	1637	2206
A-IB-S2	1567	1636	1621	1998
A-IB-S3	1553	1634	1613	1941
A-IB-S4	1521	1627	1603	1863
A-IIA-R2	1639	1656	1650	1993
A-IIA-S1	1619	1665	1655	1911
A-IIA-S2	1585	1667	1651	1839
A-IIA-S3	1559	1665	1647	1790

flames at the same equivalence ratio. Decreasing the dilution ratio while keeping the cold flow velocity constant also increases the peak temperature. The peak temperatures of the A-IB-S3 and A-IB-S4 flames are ~ 50 K hotter than the A-IA-S3 and A-IA-S4 flames, while the peak of the A-IB-S2 flame is only 17 K greater than the A-IA-S2 flame.

The relative trends in the peak temperatures among the flame sequences are reflected in the peak temperatures obtained by solving the energy equation with the flame code. However, the peak temperatures of the flames within a sequence determined from the flame code decrease only slightly (or not at all in the case of the A-IIA flames) with equivalence ratio. In contrast, the estimated peak temperatures decrease on the order of 100 K over the range of equivalence ratios. A related effect is that the peak temperatures of the nonsooting flames are within 25 K of the flame code solution, while those of the lightly sooting flames differ by 50 K. These temperature differences are caused by the fact that the increased radiative heat loss from the soot is not modelled in the energy equation of the Sandia flame code. Thus, only the nonsooting flames will be well approximated by the energy equation solutions obtained from the flame code.

5.4 Discussion

We measured the scattering and extinction coefficient profiles of the atmospheric-pressure and the 80-torr flames to provide a wide range of sooting conditions. Our intention was to develop a unique data set that can be used to test predictions of soot formation models, including the amount of soot formed and the transition from nonsooting to sooting flames. The experimental data were obtained by measuring the scattering and extinction coefficient profiles of a rich nonsooting flame and of a related sequence of sooting flames so that the critical equivalence ratio was bracketed by a narrow range of equivalence ratios. The critical equivalence ratio is defined as that for which the yellow emission from soot first becomes visible as the equivalence ratio is increased from nonsooting conditions.

5.4.1 Near-Critical Equivalence Ratio Flames

The yellow emission of soot was visible in the A-IA-S1, A-IB-C, and A-IIA-S1 flames. The A-IB-C ($\phi = 1.67$) and the A-IIA-S1 ($\phi = 1.78$) flames were at or near the critical equivalence ratio for their flame sequences, while the equivalence ratio for the A-IA-S1 ($\phi = 1.78$) flame was somewhat greater than the critical value for its flame sequence ($\phi_c \sim 1.70$). The extinction coefficient profiles for these flames showed no evidence of particle extinction that was greater than the detection limit of $K_{ext} = 1.8 \times 10^{-4} \text{ cm}^{-1}$. The scattering coefficient profiles of the A-IA-S1 and A-IIA-S1 flames were essentially equivalent to the molecular scattering coefficient profiles of their associated nonsooting flames. A nonsooting reference flame was not measured for the A-IB-C flame; however, its profile was nearly the same as the nonsooting profile for the A-IA-R2 and the A-IIA-R2 flames. Thus, while the yellow emission attributed to soot was visible within these flames, the scattering and extinction coefficient measurements did not show the presence of soot.

The scattering and extinction coefficient measurements do begin to show the presence of soot when the equivalence ratio is incremented about $\Delta\phi \sim 0.14$ to approximately $\phi = 1.92$ for the three atmospheric flame sequences. Based on this behavior, we can crudely estimate that the scattering-extinction measurements can resolve the critical equivalence ratio to within $\Delta\phi \sim 0.14$.

The behavior of the scattering coefficient profiles for the 80-torr flames about the critical equivalence ratio is similar to that of the atmospheric-pressure flames. The critical equivalence ratio was not measured for these flames, but it was bracketed by the nonsooting R2 ($\phi = 2.17$) and the visibly sooting S1 flames ($\phi = 2.32$). The scattering coefficient profile of the L-II-S1 flame showed no significant difference from that of its associated nonsooting flame except for an overall increase in the scattering coefficient

that may be attributed to a decrease in temperature. However, the L-I-S1 flame did show the presence of particle scattering when compared with the profile of the nonsooting flame.

The detection limits for both the scattering and extinction coefficients define an upper bound on the volume fraction and number density that may be present in the atmospheric flames near the critical equivalence ratio. The detection limit for the extinction coefficient defines the upper bound on the soot volume fraction to be $f_v < 1.8$ to $3.4 \times 10^{-9} \text{ cm}^3 \text{ soot-cm}^{-3} \text{ gas}$ for typical values of the index of refraction. If we define an incipient particle to be 2 nm in diameter, then the upper bound on the number density defined by the extinction coefficient is $N_p(d_0 = 2 \text{ nm}) < 4.3$ to $8.0 \times 10^{11} \text{ cm}^{-3}$. The upper bound on the number density of 2-nm particles defined by the detection limit for the particle scattering coefficient is of the same magnitude. However, the scattering coefficient is much more sensitive to larger particles, so that the upper bound on the number density falls to $N_p(d_0 = 10 \text{ nm}) \sim 2.8$ to $9.6 \times 10^7 \text{ cm}^{-3}$ for 10-nm diameter particles. The 80-torr flames provide an example of this sensitivity. Although the number densities in the 80-torr flames are insufficient to cause measurable extinction, the particle diameters grow and can eventually be detected because of their increased scattering coefficient. Thus, the absence of a measurable scattering coefficient implies that the particle diameters remain too small for significant signal detection.

A possible reason that both the extinction and scattering could not be detected is that the yellow emission is not caused by soot, but by other species. Böhm et al. (1988) rejected this argument and attributed the yellow emission to a carbonaceous aerosol based on their observations of the depolarization ratio and their measurements of PAH concentrations in flames near the critical equivalence ratio. They suggest that the index of refraction may differ for soot in near- ϕ_c flames because of its higher hydrogen content. Habib and Vervisch (1988) note that the increase in the H/C ratio of the soot will reduce

the imaginary component of the index of refraction and thus the volume fraction may be underestimated, if a typical index of refraction is assumed. Thus, the upper bounds of $f_v < 3.4 \times 10^{-9} \text{ cm}^3 \text{ soot-cm}^{-3} \text{ gas}$ and $N_p(d_0 = 2 \text{ nm}) < 8.0 \times 10^{11} \text{ cm}^{-3}$ may be more appropriate for our near- ϕ_c flames. Because the measured extinction at 488 nm will also include absorption from large hydrocarbons that may be precursors to soot (Weiner and Harris, 1989), the concentrations of these species probably do not become large enough to cause a measurable extinction.

The critical equivalence ratio, since it is defined as the equivalence ratio where the yellow emission of soot first becomes visible, is based on a luminosity threshold that depends on the response of the human eye (Janssen, 1991). Based on our scattering-extinction measurements for these flames, the visibility of the emission is more sensitive to the presence of soot than either the extinction coefficient or the scattering coefficient. However, the luminosity will be a function of both the soot volume fraction and the temperature (Janssen, 1991). Böhm et al. (1988) note that the volume fraction varies by a factor of 40 to produce the same luminosity at both 1400 K and 1900 K. Janssen (1991) determined that the volume fraction at the visible threshold was a function of T^{-11} . Thus, the volume fraction of soot present in flames at the critical equivalence ratio may differ depending on flame conditions and perhaps also on the person judging the visibility. A more appropriate definition of the critical equivalence ratio may be that equivalence ratio that produces a given volume fraction. Such a definition would be more appropriate for comparison with chemical kinetic models which predict species concentrations and are being adapted to model soot formation (Frenklach and Wang, 1990).

Since we can observe yellow emission in the near- ϕ_c flames, an emission measurement at a visible wavelength could also be used as a more objective measurement of the critical equivalence ratio. In addition, a measurement of the emission spectrum in

the region of visible yellow emission may identify whether the emission has the structure of blackbody emission or has a more defined structure which might suggest a specific species or combination of species. An additional suggested experiment would be to use probe sampling to determine the nature of particles in these flames or whether such particles are even present.

5.4.2 Argon-ion Laser-induced Fluorescence

Argon-ion laser-induced fluorescence is a more sensitive measure of the critical equivalence ratio in the atmospheric-pressure flames than either the scattering or the extinction measurements. The detectability of the fluorescence coincided with the visible yellow emission in the A-IA-S1, A-IA-S2, and the A-IA-S3 flames and also with the yellow emission in a flame adjusted to be at the critical equivalence ratio (A-IA-C). This behavior with respect to the critical equivalence ratio is similar to that observed by Haynes, Jander, and Wagner (1980). They were not able to detect fluorescence in their nonsooting flat premixed benzene and ethylene flames. Our fluorescence spectra (Fig. 5.16) are similar to those observed by Haynes, Jander, and Wagner (1980), Müller-Dethlefs (1979), and Miller, Mallard, and Smyth (1982).

The argon-ion laser-induced fluorescence is thought to be caused by two to four-ring PAH species (Miller, Mallard, and Smyth, 1982), although the primary species may be acenaphthylene (Coe and Steinfeld, 1980; Coe, Haynes, and Steinfeld, 1981; Beretta et al., 1985). Thus, the fluorescence profile is a relative measure of the formation of these PAH species in the flames. The fluorescing species are also thought to be those species which are responsible for gas-phase absorption at 488 nm (Haynes, Jander, and Wagner, 1980; Müller-Dethlefs, 1979). Both Haynes and Wagner (1980) and Müller-Dethlefs (1979) measured a linear correlation between the fluorescence excited at 488 nm and the absorption in nonsooting regions of diffusion flames.

We observe a linear correlation between the fluorescence coefficient and the extinction coefficient throughout the measured 20-mm range in the A-IA-S2 and A-IA-S3 flames. The slope of the linear least-squares curve fit is lower for the A-IA-S3 flame than for the A-IA-S2 flame. Since the extinction in these flames will contain contributions from both soot and gas-phase absorbing species, if we assume that the absorbing and fluorescing species are the same and have a constant quantum yield for fluorescence, then the difference in slopes for these two flames would imply different relative proportions of soot and gaseous species. In this case, the soot concentration relative to the absorbing-fluorescing species concentration in the A-IA-S3 flame is larger than in the A-IA-S2 flame.

The linearity of the fluorescence coefficient vs. the extinction coefficient throughout the measured height range suggests that the number density of the fluorescing species grows in proportion to the soot volume fraction (see Eq. 5.3.1). Hence, the linear relationship between the fluorescence and extinction coefficients implies a similarity between the surface growth rate and the increase in the number density of the fluorescing species. This is not a surprising result, if the fluorescing species are PAHs, because the proposed growth mechanism for PAHs (Frenklach et al., 1986; discussed in Section 2.5.2) and for soot particles (Frenklach and Wang, 1990; discussed in Section 2.4) is similar. Both involve addition of acetylene to a radical site possibly created by abstraction via a hydrogen atom. The growth of the fluorescing species may then provide an indirect measure of the surface growth rate of the particles and may indicate the chemical environment for surface growth. The presence of the fluorescing species at the critical equivalence ratio may thus be related to the growth process required to form the first particles and to the volume fraction of soot that produces the visible yellow emission.

These observations on the association between the fluorescence and extinction coefficients are revelatory and further investigations should be made to check the linear

relationship over a wider range of flame conditions. The extinction coefficient due to only soot particles should be determined by measuring the extinction at a longer wavelength where the gas-phase species are less likely to absorb. A more direct relationship could then be made between the fluorescing species and the extinction coefficient due to soot particles.

As an aside, the linear relationship between the fluorescence and the extinction coefficient may provide the basis for an accurate measurement of the extinction pathlength, which otherwise would be difficult to determine in a lightly sooting flame. A horizontal profile of the fluorescence along the path of the laser through the flame would identify the relative extinction coefficient profile along the laser path. The relative extinction coefficient profile could then be integrated to calculate an effective pathlength using the method used by Lucht, Sweeney, and Laurendeau (1985) to determine the effective pathlength for OH absorption.

5.4.3 Sooting Flames

We continued the measurements of the scattering and extinction coefficient profiles to quantify the behavior of the sooting flames as the conditions changed from lightly sooting to more heavily sooting flames. At atmospheric pressure, the equivalence ratios were incremented in the order $\phi = 1.92$, $\phi = 2.02$, $\phi = 2.17$ (and $\phi = 2.32$ for the A-IA sequence), while keeping the dilution ratio and cold flow velocity constant for each sequence. Within these sequences, the peak temperature declined with increasing equivalence ratio. The declining temperature complicates comparisons among flames within a sequence, because of the strong temperature dependence of soot formation. A more desirable approach might be to keep the maximum temperature constant while varying the equivalence ratio. However, this would have been difficult, because we did not have direct control over the flame temperature. We only have direct control over the fuel, oxygen, and nitrogen flow rates and are limited to the range of flow rates that

produce stable flat flames on our burner. However, we can make comparisons among flames at the same equivalence ratio to see the effects of temperature and dilution on soot formation. The variation in cold flow velocity between the A-IA and A-IIA sequences, while keeping the dilution ratio approximately constant, allows a comparison to be made between flames with a similar composition, but with different peak temperatures. The variation in dilution between the A-IA and A-IB sequences, while keeping the cold flow velocity approximately constant, allows a comparison to be made between flames with different compositions.

At 80 torr, the equivalence ratios were incremented from the near- ϕ_c flames at $\phi = 2.32$ to more heavily sooting conditions at $\phi = 2.46$ and $\phi = 2.60$. The difference in cold flow velocity between the L-I and L-II sequences provides a comparison between flames with similar compositions, but different peak temperatures.

The relative volume fraction profiles of the atmospheric sooting flames (Figs. 5.20 and 5.21) provide a basis for comparing the relative quantities of soot formed at different flame conditions. In all three flame sequences, the volume fraction at a given height increases with equivalence ratio. The temperature decrease with increasing equivalence ratio will also affect the volume fraction, since decreasing temperature will increase the final soot yield (Haynes and Wagner, 1982; Bockhorn et al., 1984).

The relative volume fraction profiles increase linearly with height over much of the 20-mm measured range above the burner. This continued growth in the volume fraction differs from the results of Haynes and Wagner (1982) who observe a decline in the growth rate as the volume fraction approaches a final volume fraction in their ethylene/air flames. However, Bengtsson and Aldén (1991) report volume fraction profiles that remain linear over a 15-mm range for $C_2H_4/O_2/N_2$ flames similar to ours on a porous plug burner. Böhm et al. (1988) note that at lower temperatures (below 1600 K) the volume fraction approaches the final volume fraction further above the burner surface. The continued

growth of the volume fraction in our flames is consistent with the inverse temperature dependence of the time constant for surface growth (Eq. 2.7; Dasch, 1985; Harris, 1990). The peak temperatures in our flames are about 100 K to 200 K less than those in the flames of Haynes and Wagner (1982). Thus, our volume fraction profiles may not curve over until a height beyond 20 mm above the burner.

The relative volume fraction profiles assume a constant index of refraction throughout the profile and among profiles. The effect of any variation in the refractive index throughout a flame would be to change the shape of the profile. If the imaginary component of the index of refraction is reduced in the early stages of soot formation because of the higher hydrogen content of the soot (Habib and Vervisch, 1988), then the profile would be increased near the burner surface relative to higher positions above the burner.

The comparison between the volume fraction profiles of the A-IA and A-IIA flames shows primarily the effect of temperature on the profiles, since the molar composition of the $C_2H_4/O_2/N_2$ mixtures are similar. The lower volume fractions in the A-IIA flames result from the higher peak temperatures in these flames compared to the A-IA flames. Again, this behavior is consistent with the observation that increasing temperature strongly decreases soot yield (Haynes and Wagner, 1982; Bockhorn et al., 1984). Similarly, the higher temperatures in the A-IIA flames may cause the slight decline in the growth of the volume fraction observed above 15 mm, as the growth rate decays faster at higher temperatures.

The comparison between the volume fraction profiles of the A-IA and A-IB flames is not as straightforward because both the peak temperature and the mixture composition are affected by the variation in dilution ratio. Although the peak temperatures are somewhat higher in the A-IB flames than in the A-IA flames, the volume fractions are also higher. This runs counter to the usual observation that increasing temperature

decreases soot yield. However, the ethylene mole fraction in the A-IB flames is greater than that in the A-IA flames because of the decreased dilution ratio of the A-IB flames. The increase in ethylene concentration increases the pyrolysis rate, which is observed to increase the volume fraction at a lower height than in the A-IA flames. The decline in the growth rate above 15 mm in the A-IB-S3 flame relative to the A-IA-S3 flame may again be caused by its higher temperature.

The relative number density profiles of the atmospheric-pressure flames (Figs. 5.22 to 5.24) provide a basis for comparing the number of particles formed in the flames and also the relative locations of their formation. The slope of the number density profiles following the peak number density is similar for those flames with $\phi \geq 2.02$ and indicates a similar coagulation rate. This behavior has been observed by other researchers (Haynes and Wagner, 1982; Prado and Lahaye, 1981; Bockhorn et al., 1984) in a variety of sooting flame conditions. The change in particle number density is predicted well by free molecular coagulation theory and, for a large initial particle number density and long residence times, the theory indicates that the number density is only a weak function of the volume fraction and temperature (Prado et al., 1981). The behavior we observe is consistent with that theory.

The peak number densities occur in a region where both the particle scattering and extinction coefficients are small; thus the fluorescence and gas-phase absorption may contribute errors that are magnified in the calculation of the number density. This effect can be seen in our calculation of the number density with and without the fluorescence correction for the A-IA flames. Although the peak number densities may be in error, the increase in the uncorrected peak number density corresponds to the increase in the volume fraction. This agrees with the hypothesis that the number of soot particles formed in the inception zone (and thus the number of active sites for surface growth) determines the final soot volume fraction (Harris, 1990).

The errors due to fluorescence and gas-phase absorption are small relative to the total extinction and scattering coefficients in the region of decreasing particle number density and thus the decline can be more accurately measured than the peak. Within all three flame sequences, the location of declining number density moves closer to the burner surface as the equivalence ratio is increased. This implies that the peak of the number density profile and the region of particle inception also move closer to the burner surface with increasing equivalence ratio.

The comparison between the number density profiles of the A-IA and A-IIA flames suggests that the increase in peak temperature at a fixed equivalence ratio moves the particle inception region closer to the burner surface, as the decline in the number density occurs at a lower height in the A-IIA flames than in the A-IA flames. The uncorrected peak number densities are smaller in the A-IIA flames than in the A-IA flames and are consistent with the smaller volume fractions in the A-IIA flames. This relationship between the peak number densities is likely to remain the same when corrected for the fluorescence background because the smaller extinction coefficient in the A-IIA flames implies a smaller fluorescence signal.

Similar to the A-IIA flames, the decline in the number density in the A-IB flames occurs at a lower height than in the A-IA flames implying that the inception region also occurs at a lower height. However, in this case, the effect may be caused by both the increased temperature and by the greater ethylene concentration. The greater ethylene concentration may have an effect similar to increasing the equivalence ratio which also acts to move the particle inception region closer to the burner. The uncorrected peak number densities of the A-IA and A-IB flames are of similar magnitude. However, the fluorescence background might be expected to be larger for the A-IB flames since the magnitude of their extinction coefficient profiles are larger.

We can draw fewer conclusions about the behavior of the 80-torr sooting flames because of a lack of extinction coefficient data. The lack of a measurable extinction coefficient implies that the volume fraction remains small, below $f_v \sim 1.8$ to 3.4×10^{-9} cm^3 soot- cm^{-3} gas, in all the flames. Thus, the relative quantities of soot formed cannot be compared. The scattering coefficient profiles allow determination of an upper bound for the number density profiles. Similar to the atmospheric-pressure flames, these can be used to identify approximate regions for the location of particle inception. The trends within the flame sequences are similar to the atmospheric flame sequences in that as the equivalence ratio is increased the location of particle inception moves closer to the burner surface.

Our detection limit of a 0.1% change in the transmittance is at the limit of prior studies. Haynes, Jander, and Wagner (1980) reported that their absorption measurement could resolve a 0.1% absorption using a tungsten strip lamp as the extinction light source. In their case, the limit was defined by the stability of their light source. In our experiment, the incident laser irradiance was monitored to account for any variations in the laser irradiance with time. The resulting resolution in the transmittance has allowed us to use the laser scattering-extinction method to investigate soot formation in flames at equivalence ratios much closer to the critical equivalence ratio than those of previous studies. The resolution in the transmittance also increases the resolution of the profile, so that the location of soot formation can be more closely defined.

These particle number density and volume fraction profiles can be used as the basis for testing models of soot formation. Global comparisons can be made between simpler models and the trends in the volume fraction and number density profiles. For example, detailed chemical kinetic models that predict the formation of single-ring aromatics (Harris, Weiner, and Blint, 1988; Miller and Melius, 1992) could be examined quite easily using our experimental data. Since the formation of these simple aromatics may be the

bottleneck in soot formation, trends in the aromatic concentration profiles can be compared with measured trends in soot volume fraction and with the location of the particle inception region. More direct comparisons can be made with the experimental particle number density and volume fraction profiles using models such as that of Frenklach and Wang (1990), which uses a detailed chemical kinetic scheme to model the formation of PAHs and a global scheme to model the formation of particles and their subsequent coagulation and growth. Both types of models can also be tested to see how well they predict the transition from nonsooting to sooting flames.

5.5 Summary

We have used the laser scattering-extinction method to measure the scattering and extinction coefficient profiles of sequences of atmospheric-pressure and 80-torr $C_2H_4/O_2/N_2$ flames for equivalence ratios that span the transition from nonsooting to sooting flames. Although the resolution of the extinction coefficient is high, equivalent to an absorption of 0.1%, the extinction coefficient and also the scattering coefficient profiles do not show evidence of particle formation in flames at or near the critical equivalence ratio.

The argon-ion laser-induced fluorescence correlates with the visible yellow emission and may provide a more sensitive measure of the critical equivalence ratio than the scattering and extinction measurements. The linear correlation between the fluorescence and the extinction coefficient also offers a more sensitive measure of the extinction coefficient and could provide further insight into the PAH and surface growth mechanisms.

Scattering and extinction coefficient profiles caused by particles can be resolved in the atmospheric-pressure flames at the higher equivalence ratios and these are used to calculate relative volume fraction, number density, and particle diameter profiles. In the 80-torr flames, the scattering coefficient profiles are used to calculate upper bounds on the

particle number density profiles. The trends in these profiles can be explained based on our current understanding of soot formation. The trends in volume fraction and the location of particle inception can also be compared with the predictions of detailed chemical kinetic models that model aromatic formation. More specific comparisons can be made using combined detailed-global models that include particle formation and evolution.

CHAPTER 6:
LASER-INDUCED FLUORESCENCE MEASUREMENTS OF
HYDROXYL RADICAL IN PREMIXED ETHYLENE FLAMES

6.1 Introduction

In this chapter, we report on the laser-induced fluorescence measurements of the hydroxyl radical under near-sooting conditions in a sequence of atmospheric-pressure $C_2H_4/O_2/N_2$ flames and a sequence of 80-torr C_2H_4/O_2 flames. Vertical relative profiles of the OH fluorescence were measured to observe the change in the OH concentration, both within the flames and between flames as the equivalence ratio was varied from rich nonsooting to sooting conditions near the critical equivalence ratio. In conjunction with the measurements of soot formation in the same flames (Chapter 5), the OH fluorescence profiles can serve as a test for detailed chemical kinetic models of soot formation and also as a test for the assumptions of the global models for incipient soot formation.

In this chapter, we first identify the flame conditions and then briefly review the theory and method of the measurements. The effects of quenching and the calibration method are discussed. We then present and discuss the relative OH concentration profiles for both the atmospheric and 80-torr flames.

6.2 Results

6.2.1 Flame Conditions

The equivalence ratio, cold flow velocity (v_c), and dilution ratio ($\dot{V}_{N_2}/\dot{V}_{O_2}$) for the sequence of atmospheric flames and the sequence of 80-torr flames are listed in Table 6.1. The three richest flames (-R2, -S1, and -S2) of the atmospheric-pressure sequence were

examined in the laser scattering-extinction experiments. A fourth flame (A-IA-R1) was added to this sequence with the same cold flow velocity and dilution ratio to extend the range of equivalence ratios farther to the lean side of the critical equivalence ratio. A lean atmospheric-pressure flame (A-0-L) was also added for calibration of the OH fluorescence measurements. For this flame, a higher cold flow velocity and dilution ratio than that for the rich atmospheric flames were necessary to produce a stable flat flame above the burner surface. The four 80-torr flames were also examined in the laser scattering-extinction experiments.

From our laser scattering-extinction measurements and observations (Chapter 5), we know that within the atmospheric flame sequence (A-IA) with cold flow velocity, $v_c = 7.7 \text{ cm}\cdot\text{sec}^{-1}$, and dilution ratio, $D = 4.2$, the critical equivalence ratio occurs at $\phi_c \approx 1.70$. The visible yellow emission attributed to soot was observed in the A-IA-S1 ($\phi = 1.78$) flame, but the presence of soot could not be detected by the scattering and extinction measurements. However, an argon-ion laser-induced fluorescence profile was measured that suggests that PAHs are present, although the extinction coefficient profile remains below the detection limit. The richer A-IA-S2 ($\phi = 1.92$) flame had measurable scattering and extinction coefficient profiles and thus in this case volume fraction and number density profiles could be determined for the soot particles.

At 80 torr, the critical equivalence ratio within the L-II sequence was bracketed by the L-II-R2 ($\phi = 2.16$) and the L-II-S1 ($\phi = 2.32$) flames. Similar to the visibly sooting atmospheric flame A-IA-S1, the yellow emission from soot could be observed in the L-II-S1 flame, but the scattering and extinction coefficient measurements did not show evidence of soot. A particle scattering coefficient profile, but not an extinction coefficient profile, was measured in the L-II-S2 flame, indicating that soot particles were present, but that their volume fraction was still small.

Table 6.1 Equivalence ratio, cold flow velocity, and dilution ratio for the flames used in the OH measurements. Flames not duplicated in the scattering-extinction measurements are marked with an asterisk.

Flame	Pressure	Equivalence Ratio	Cold Flow Velocity (cm·sec ⁻¹)	Dilution Ratio
A-0-L*	1 atm	0.97	8.86	5.42
A-IA-R1*	1 atm	1.49	7.73	4.15
A-IA-R2	1 atm	1.63	7.73	4.15
A-IA-S1	1 atm	1.78	7.73	4.16
A-IA-S2	1 atm	1.92	7.75	4.17
L-II-R1	80 torr	2.03	22.4	0.0
L-II-R2	80 torr	2.16	22.4	0.0
L-II-S1	80 torr	2.32	22.4	0.0
L-II-S2	80 torr	2.46	22.4	0.0

Temperature profiles for the A-IA-R2, A-IA-S1, and A-IA-S2 flames were determined from the measured scattering coefficient profiles. Although temperature profiles for the 80-torr flames might be determined from their measured scattering coefficient profiles, we were not able to calculate such profiles due to difficulties in modelling these flames in the region below the peak temperature.

6.2.2 Review of Theory and Measurements

The OH fluorescence profiles were measured using the SPF(0,0) laser-induced fluorescence method described by Laurendeau and Goldsmith (1989). Specifically, the $Q_1(8)$ transition in the (0,0) band of the $A^2\Sigma^+ - X^2\Pi$ system of OH was excited with the UV output of a frequency-doubled Nd:YAG pumped dye laser. The OH fluorescence was detected over a spectral range encompassing most of the (0,0) band and the fluorescence signal was temporally integrated over the laser pulse. Broadband spectral and temporal detection were used to increase the measured fluorescence signal over that obtained with methods such as laser-saturated fluorescence which uses narrowband spectral and temporal detection. The increased sensitivity was desirable because of the small OH concentrations in these rich nonsooting and sooting flames. However, the sensitivity is compromised to some extent by the increased background signal caused by Rayleigh scattering, since the spectral detection bandwidth includes the laser excitation wavelength. The theory for the laser-induced fluorescence measurements and the SPF(0,0) method are reviewed in Section 3.3. The experimental apparatus, procedure, and data analysis are described in Section 4.5.

The measured fluorescence voltage profiles were corrected for the Rayleigh scattering background. The resulting fluorescence profiles, $V_f(\phi, z)$, are proportional to the fluorescence emission profile, $\epsilon_{fB}(\phi, z)$ ($W \cdot cm^{-3} \cdot sr^{-1}$), through the relationship given by Eq. (4.5.10) as

$$V_f(\phi, z) = \eta_{Em} \cdot \eta_O \cdot \Omega_c \cdot V_c \cdot \epsilon_{fB}(\phi, z) \quad (6.2.1)$$

where η_{Em} and η_O are the electronic and optical efficiencies, Ω_c (sr) is the solid collection angle, and V_c (cm³) is the collection volume. The fluorescence emission for broadband spectral and temporal detection is given by Eq. (3.3.9) as

$$\epsilon_{fB} = \alpha \cdot \left[\frac{A}{A+Q} \right] \cdot N_1^0 \cdot \int I_L(t) \cdot dt \quad (6.2.2)$$

where α (cm²) is a constant that depends on the laser and fluorescence wavenumbers plus the absorption cross-section, A and Q (sec⁻¹) are integrated rate coefficients for spontaneous emission and quenching, N_1^0 (cm⁻³) is the ground state number density, and I_L (W·cm⁻²) is the incident laser irradiance as a function of time. By normalizing the profile with respect to the fluorescence voltage measured in a reference or calibration flame with the same optical and electronic setup, the dependence of the profiles on the optical constants and efficiencies can be removed. The resulting expression for the ground state number density profile is given by Eq. (4.5.13) as

$$N_1^0(\phi, z) = N_1^0(\phi_{cal}, z_{cal}) \cdot \left[\frac{A}{A+Q} \right]_{\phi_{cal}, z_{cal}} \cdot \left[\frac{A}{A+Q} \right]_{\phi, z}^{-1} \cdot \frac{V_f(\phi, z)}{V_f(\phi_{cal}, z_{cal})} \quad (6.2.3)$$

where the subscript *cal* indicates the parameters for the location in the calibration flame. The dependence on the laser irradiance was neglected by assuming that the temporal laser irradiance remained the same between the calibration and measurement conditions. This assumption is reasonable since the laser energy and pulse shape were observed to remain constant over the period of the tests on a single day.

The relative fluorescence profiles measured in the atmospheric-pressure flames were normalized to the fluorescence signal voltage measured on the same day in the post-flame region of the lean flame (A-0-L, $\phi = 0.97$). The relative fluorescence profiles

measured in the 80-torr flames were normalized to the fluorescence signal voltage measured on the same day in the post-flame region of the leanest rich nonsooting flame (L-II-R1, $\phi = 2.03$).

The total number density, N_T (cm^{-3}), is determined from the initial number density in the ground state, N_1^0 , from Eq. (3.3.11) as

$$N_T = \frac{N_1^0}{F_{1B}} \quad (6.2.4)$$

where F_{1B} is the Boltzmann fraction at the local flame temperature. We reduced the sensitivity to temperature variation by exciting the $Q_1(8)$ transition, whose ground state population varies by only $\pm 5\%$ over the temperature range from 1000 to 2600 K (Drake and Pitz, 1985). The sensitivity to temperature is further reduced by the small temperature range (< 200 K) between the calibration conditions and the measured flame conditions.

The normalized fluorescence profiles given by Eq. (6.2.3) can represent relative OH number density profiles if both the quenching variation within the profile and the quenching variation between the calibration condition and the measured condition can be accounted for or assumed constant. A subsequent determination of the number density in the calibration flames can then be used to determine absolute number density profiles from the relative number density profiles.

6.2.3 Quenching Calculations

Previous investigations that have measured the variation in quenching rate coefficient for hydrocarbon flames (Stepowski and Cottreau, 1981; Anderson, Decker, and Kotlar, 1982; Schwarzwald, Monkhouse, and Wolfrum, 1988; reviewed in Section 3.3.3) suggest that the quenching rate coefficient remains constant throughout the profile of the flame and also between flames over a range of equivalence ratios. However, Drake and Pitz (1985) note that the quenching rate coefficient varies significantly from lean to rich conditions in H_2/air diffusion flames. We investigated the validity of the assumption

of a constant quenching rate coefficient by calculating the variation in the quenching rate coefficient among the flames and also within the flames relative to the mean quenching rate coefficient.

The variation in the quenching terms of Eq. (6.2.3) was evaluated by first recognizing that at atmospheric pressure, $Q \gg A$ (Eckbreth, 1988). Thus, we assume

$$\frac{Q(\phi, z)}{Q(\phi_{cal}, z_{cal})} \approx \left[\frac{A}{A + Q} \right]_{\phi_{cal}, z_{cal}} \cdot \left[\frac{A}{A + Q} \right]_{\phi, z}^{-1} \quad (6.2.5)$$

where $Q(\phi, z)$ represents the quenching rate coefficient for a given flame condition and $Q(\phi_{cal}, z_{cal})$ represents the quenching rate coefficient at the calibration condition. The total quenching rate coefficient can be calculated from (Garland and Crosley, 1986)

$$Q = \sum_k N_k \cdot \sigma_{Qk} \cdot v_k \quad (6.2.6)$$

where N_k (cm^{-3}) is the number density of species k , σ_{Qk} (cm^2) is the quenching cross-section for species k , and v_k ($\text{cm}\cdot\text{sec}^{-1}$) is the relative velocity between species k and the quenched species. To calculate the ratio of the quenching rate coefficients (Eq. 6.2.5), we use the approach of Drake and Pitz (1985) and assume that the relative quenching rate coefficient is proportional to

$$Q \propto \sum_k \left(\frac{X_k}{T} \right) \cdot \left(\frac{T}{MW_k} \right)^{1/2} \cdot \sigma_{Qk}(T) \quad (6.2.7)$$

where X_k is the mole fraction of species k , T is the temperature, and MW_k is the molecular weight of species k .

The quenching cross-sections of the species as a function of temperature, $\sigma_{Qk}(T)$, were evaluated from the data of Garland and Crosley (1986) for the temperature range from 500 K to 2500 K for the species H_2 , N_2 , O_2 , H_2O , CO , CO_2 , and CH_4 . The quenching cross-sections for the species C_2H_2 , C_2H_4 , and C_2H_6 measured at 1100 K

(Smith and Crosley, 1986) were also included in the calculation, since these species are present in rich flames. However, for our approximate calculations, no further temperature corrections were made to the quenching cross-sections of these last three species.

To calculate approximate profiles of the relative quenching rate coefficient, we used the temperature profiles and the molar composition profiles determined from the modelling of these flames using the Sandia premixed one-dimensional flame code (Kee et al., 1985) and the reaction mechanism of Miller and Melius (1992). The details of the setup and solution procedure for the flame code are described in Section 4.6. The application of the model of Miller and Melius (1992) to these flames is discussed in Chapter 7.

Profiles of the relative quenching rate coefficient in the five atmospheric-pressure flames were calculated for the height range from 1.0 mm to 20 mm. The variation in the relative quenching rate coefficient over the profile was calculated by ratioing the quenching rate coefficient profile to its mean value. The change in quenching rate coefficient relative to the lean flame was calculated at the height at which the profiles were normalized (5.0 mm) by using the ratio of the relative quenching rate coefficient in the rich flame to that in the lean flame. These results are summarized in Table 6.2 for the atmospheric-pressure flames.

Within a flame, the ratio of the quenching rate coefficient to the mean of the quenching rate coefficient profile varies in the range from +6% to -3% for the four rich atmospheric-pressure flames. Thus, we can assume that the quenching rate coefficient remains approximately constant over the measured range of the profile and that the profiles represent relative profiles of the OH number density. The relative quenching rate coefficients of the rich flames are 28% to 40% higher than those in the lean flame. Thus, if the relative number density profiles of the rich flames are to be calibrated based on the

lean flame, then a quenching correction is necessary or the number density in the rich flames will be underpredicted.

Profiles of the relative quenching rate coefficient in the 80-torr flames were calculated for the height range from 1 mm to 30 mm. Since the temperature profiles for these flames were not available, the molar composition profiles were obtained from the flame code solution with the temperature profile based on the solution of the energy conservation equation. Thus, only approximate comparisons can be made, as the temperature profile from the energy-equation solution is thought to exceed the actual temperature profile. Since a lean 80-torr flame was not investigated, the quenching rate coefficients are compared to the L-II-R1 ($\phi = 2.03$) flame.

The results of the quenching rate coefficients for the 80-torr flames are summarized in Table 6.3. The variation of the quenching rate coefficient within the profile is much larger than at atmospheric pressure. However, much of this variation occurs below 5 mm above the burner, in the reaction zone and below, where the molar composition of the flame is changing significantly. Above 5 mm, the variation in the quenching rate coefficient falls in the range from +6% to -5% and the quenching rate coefficient can be assumed to be constant in this range. The variation in the quenching rate coefficient among the flames is small, less than 8% between the L-II-R1 ($\phi = 2.03$) and L-II-S2 ($\phi = 2.46$) flames. However, the actual variation is likely to be greater than that estimated using the temperature from the solution of the energy equation because the actual temperature difference between flames is likely to be larger due to the increased radiative heat loss from the sooting flames.

Table 6.2 Summary of the quenching rate coefficient calculations for the atmospheric-pressure flames.

Flame	A-IA-R1	A-IA-R2	A-IA-S1	A-IA-S2
Variation within profile				
$Q(\phi, z)/\overline{Q}(\phi, z)$				
maximum	1.05	1.05	1.06	1.06
minimum	0.97	0.97	0.97	0.97
Variation relative to A-0-L				
$Q(\phi, 5.0\text{mm})/Q(\phi_{cal}, 5.0\text{mm})$	1.28	1.31	1.38	1.40

Table 6.3 Summary of the quenching rate coefficient calculations for the 80-torr flames.

Flame	L-II-R1	L-II-R2	L-II-S1	L-II-S2
Variation within profile				
$Q(\phi, z)/\overline{Q}(\phi, z)$ (1 mm to 30 mm)				
maximum	1.60	1.69	1.75	1.81
minimum	0.87	0.89	0.89	0.89
Variation within profile				
$Q(\phi, z)/\overline{Q}(\phi, z)$ (5 mm to 30 mm)				
maximum	1.05	1.06	1.05	1.05
minimum	0.95	0.96	0.97	0.97
Variation relative to L-II-R1				
$Q(\phi, 10\text{mm})/Q(\phi_{cal}, 10\text{mm})$	--	1.02	1.05	1.08

6.2.4 Calibration

The relative OH number density profiles of the atmospheric-pressure flames were calibrated based on a comparison of the OH fluorescence profiles of the A-0-L ($\phi = 0.97$) flame with the OH number density profile predicted using the Sandia premixed one-dimensional flame code (Kee et al., 1985) and the reaction mechanism of Drake and Blint (1991).

Since the temperature profile of the A-0-L flame was not measured, we used the flame code solution obtained when the energy conservation equation was solved for the temperature profile. The temperature profile obtained from the energy equation solution is a good approximation to the actual temperature profile for atmospheric nonsooting flames on this burner. Comparison of the energy equation temperature profile and the estimated temperature profile from the scattering coefficient profile of the A-IA-R2 ($\phi = 1.63$) flame showed agreement within 20 K over the region from about 2 to 7 mm (Appendix C, Figure C.4). The difference between the profiles increased to 50 K at 15 mm. This agreement is within the accuracy that could be measured by a thermocouple.

The relative OH number density profiles of the A-0-L flame were matched to the predicted OH number density profiles by ratioing the values over the region from 4.0 to 6.0 mm to obtain the calibration factor. Figure 6.1 shows a comparison of the relative OH number density profiles with the predicted OH number density profile when the profiles are matched in this way. The agreement between the profiles is good from about 3 mm to 20 mm above the burner. The peak values differ because the actual temperature profile peaks closer to the burner surface than the energy-equation temperature profile (Appendix C). The peak values may also differ because the measured OH number density represents a spatial average over the collection volume, while the flame code solution gives the number density at a point.

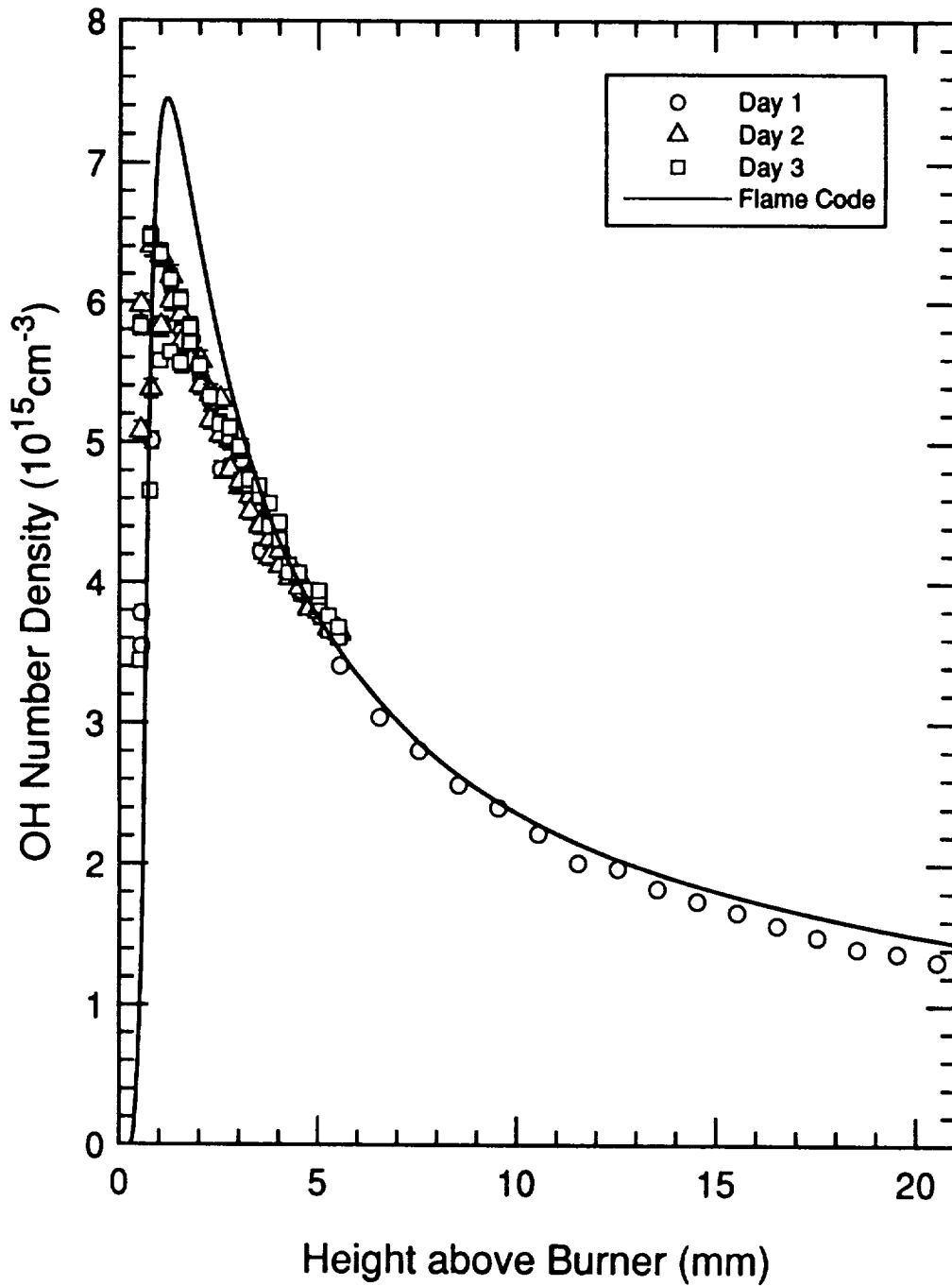


Figure 6.1 Comparison of the normalized OH fluorescence profiles of the A-0-L ($\phi = 0.97$) flame with the OH number density profile predicted by the flame code solution. The OH fluorescence profiles were matched to the predicted OH number density profile over the region from 4.0 to 6.0 mm.

The 80-torr flames were not calibrated because an OH fluorescence profile was not measured in a lean 80-torr flame. A possible calibration method similar to the atmospheric-pressure flames was investigated using the flame code energy equation solution for the L-II-R1 ($\phi = 2.03$) flame. However, comparison of the estimated scattering coefficient profile from the flame code energy-equation solution and the measured scattering coefficient profile showed that the estimated temperature was significantly higher (> 100 K) than the flame temperature. Furthermore, the shapes of the OH profiles also differed in the post-flame regions suggesting that the energy-equation solution is not a good approximation for the temperature profiles of the 80-torr flames. Thus, we abstained from calibrating the OH fluorescence profiles of the 80-torr flames.

6.2.5 OH Fluorescence Profiles

The OH number density profiles of the four rich atmospheric-pressure flames are shown in Figure 6.2. The number densities shown are based on the calibration of the number density in the A-0-L flame and the correction for the variation of the quenching rate coefficient given in Table 6.2. A logarithmic scale is used to display the declining region of the profiles and also the similarity in profile shapes. The OH number densities for all four flames peak near 1 mm above the burner.

The relative OH fluorescence profiles of the four 80-torr flames are shown in Figure 6.3. The profiles were normalized with respect to the fluorescence signal of the L-II-R1 ($\phi = 2.03$) flame at a height of 10 mm. A logarithmic scale is again used to show the declining region of the profiles and also the similarity in profile shapes. The OH fluorescence peaks in the region from 4 to 5 mm above the burner for all four flames.

For both the atmospheric-pressure and 80-torr flames, the peak fluorescence signal or number density declines with increasing equivalence ratio. The ratio of the peak heights for all flames to that of the leanest flame in each sequence for both the

atmospheric-pressure and 80-torr flames is listed in Table 6.4. The range in the relative peaks of the OH fluorescence is about a factor of five for the atmospheric-pressure flames and about a factor of two for the 80-torr flames.

The OH fluorescence profiles scale with the peak fluorescence signal. If the fluorescence profiles are normalized to their maximum, then the profiles overlay each other. This feature of the OH fluorescence profiles is shown in Figure 6.4, which shows the normalized fluorescence profiles for the atmospheric-pressure flames, and in Figure 6.5, which shows the normalized fluorescence profiles for the 80-torr flames. Thus, the magnitude of the OH fluorescence decreases, but the overall shape of the profile does not change significantly as the equivalence ratio is increased through the transition to a sooting flame.

Table 6.4 Relative maxima of the fluorescence profiles for the rich atmospheric flames and the 80-torr flames.

Flame	Equivalence Ratio	Relative Maximum	Maximum OH Number Density (10^{14} cm^{-3})
A-IA-R1	1.49	1.000	5.03
A-IA-R2	1.63	0.545	2.74
A-IA-S1	1.78	0.334	1.68
A-IA-S2	1.92	0.210	1.06
L-II-R1	2.03	1.000	--
L-II-R2	2.16	0.694	--
L-II-S1	2.32	0.531	--
L-II-S2	2.46	0.435	--

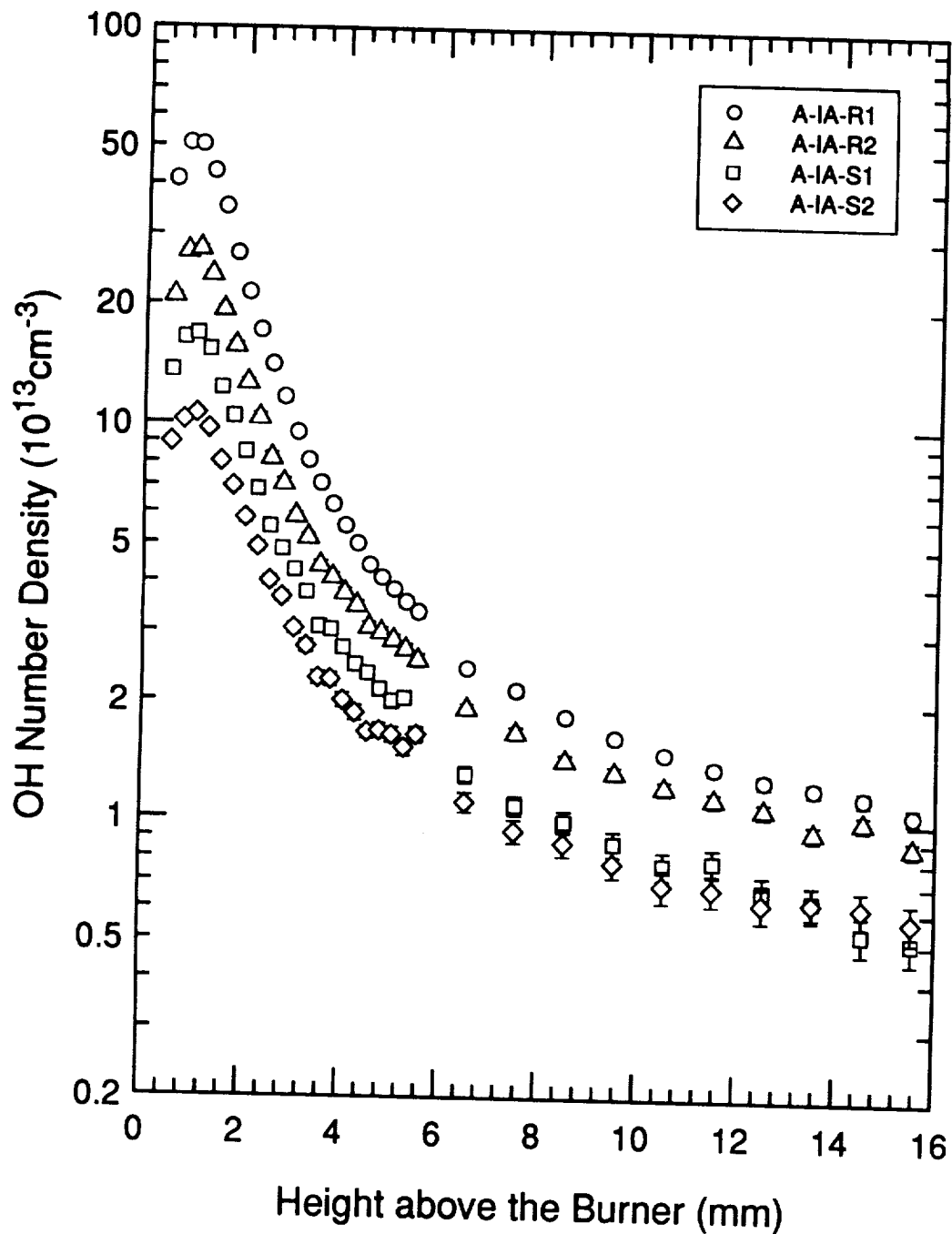


Figure 6.2 OH number density profiles of the four rich atmospheric-pressure flames: A-IA-R2 ($\phi = 1.49$), A-IA-R1 ($\phi = 1.63$), A-IA-S1 ($\phi = 1.78$), and A-IA-S2 ($\phi = 1.92$). The number densities were calibrated with respect to the A-0-L ($\phi = 0.97$) flame and corrected for quenching.

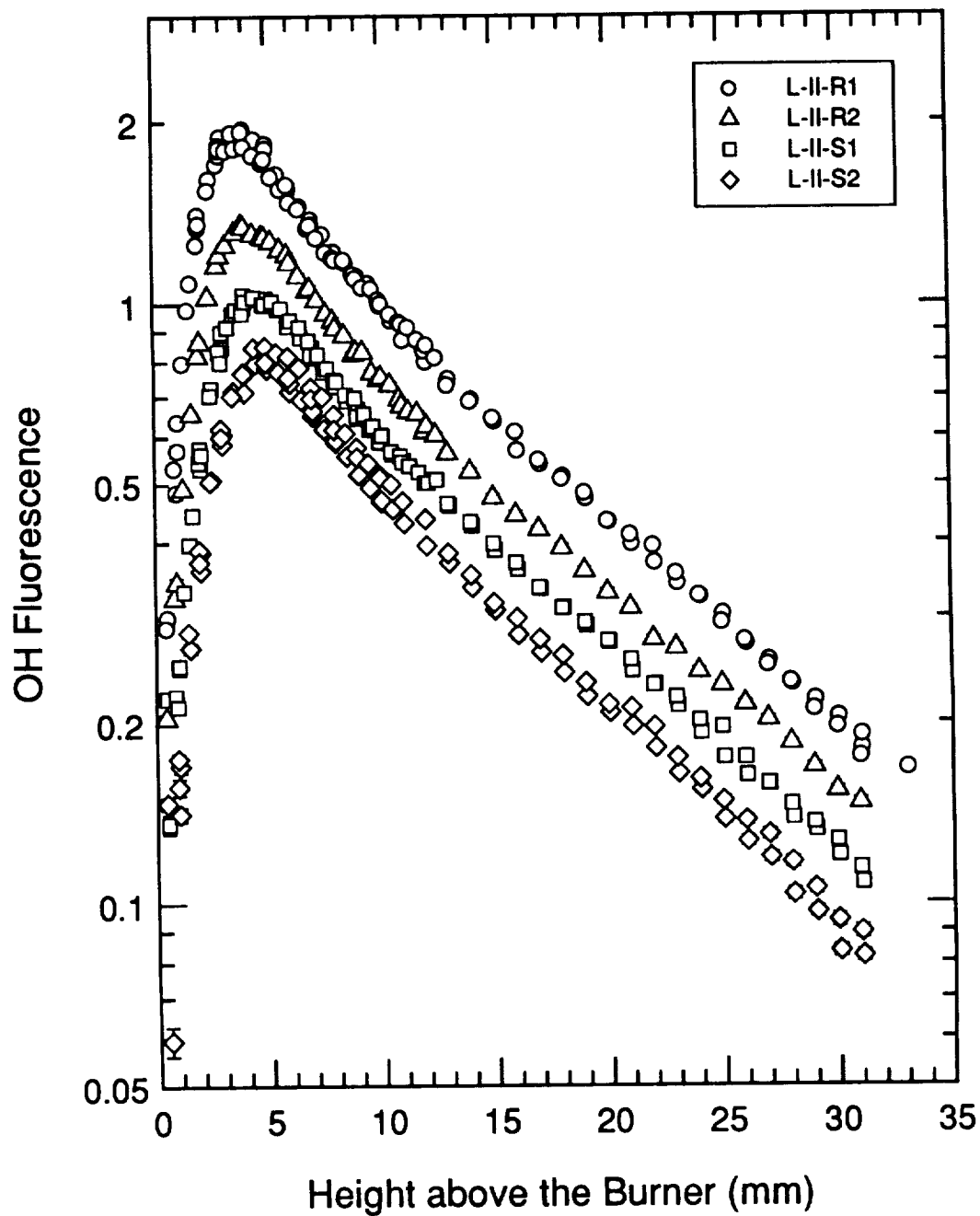


Figure 6.3 Relative OH fluorescence profiles of the four 80-torr flames: L-II-R1 ($\phi = 2.03$), L-II-R2 ($\phi = 2.16$), L-II-S1 ($\phi = 2.32$), and L-II-S2 ($\phi = 2.46$).

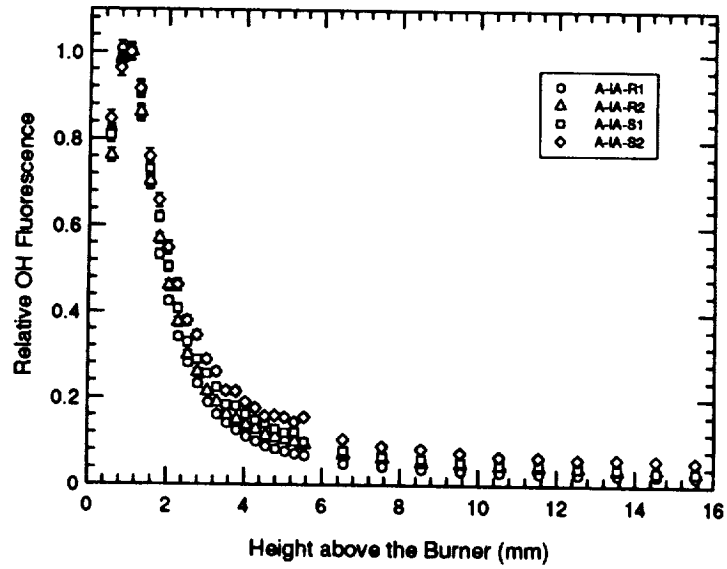


Figure 6.4 Fluorescence profiles of the four rich atmospheric-pressure flames normalized to the maximum of the profile to show the similarity in the profile shapes.

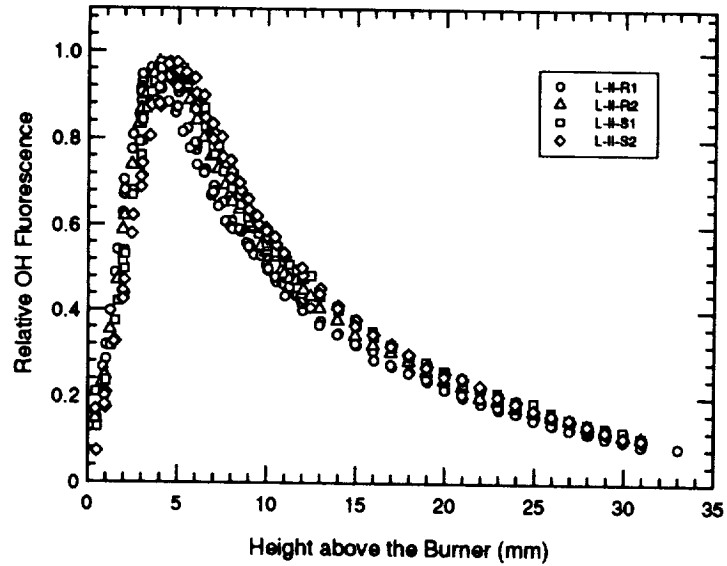


Figure 6.5 Fluorescence profiles of the four 80-torr flames normalized to the maximum of the profile to show the similarity in the profile shapes.

6.3 Discussion

We have measured relative OH fluorescence profiles in both atmospheric and 80-torr flames to measure the change in the OH number density profile as the transition is made from a rich nonsooting flame to a sooting near-critical equivalence ratio flame and then to a more heavily sooting flame. Since the variation in the quenching rate coefficient is either small or can be accounted for, relative OH number density profiles can be determined from the measured relative OH fluorescence profiles. Absolute OH number density profiles were obtained for the atmospheric-pressure flames by calibration with an atmospheric lean flame.

The peak OH number density declines with increasing equivalence ratio for both the atmospheric and 80-torr flames. The declining number density is a function of decreasing temperature as well as increasing equivalence ratio since the maximum temperature declines with increasing equivalence ratio for these flames, while the cold flow velocity and dilution ratio are held constant.

The relative OH number density profiles scale with the maximum OH number density, so that the profiles have a similar shape. Thus, only the magnitude of the OH number density profile, but not its shape or peak location, changes in the transition from nonsooting to sooting flames. Lucht, Sweeney, and Laurendeau (1985) observed a similar behavior for the OH number density profiles in the transition from nonsooting to sooting $\text{CH}_4/\text{O}_2/\text{N}_2$ flames.

The similarity of the OH number density profiles through the transition to sooting implies that the mechanisms for the formation and destruction of OH do not change significantly during that transition. In other words, the formation of higher molecular weight hydrocarbons that accompanies the transition to a sooting flame does not open up a significant new reaction pathway for removal of OH by reaction with these higher molecular weight hydrocarbons. If such a path were to be present, we would expect the

OH number density to decline at a faster rate. Instead, the smooth change in profile would imply that the main flux of OH is through reactions with species whose behavior also does not change significantly as the transition to sooting occurs. Smaller hydrocarbons such as acetylene and methane are formed in rich nonsooting flames and their concentration also changes smoothly in the transition to sooting (Harris and Weiner, 1983a; Harris et al., 1986). The smooth change in the OH profiles would then suggest that the major reaction pathways for OH involving hydrocarbons are with these smaller hydrocarbons.

The global model first proposed by Millikan (1962) hypothesized that incipient soot formation is a balance between the rate of formation of soot precursors by fuel pyrolysis and their rate of oxidation by OH. The supposed implication that OH primarily reacts with smaller hydrocarbons such as acetylene would either imply that acetylene is a precursor or that reactions of OH with acetylene or small hydrocarbons directly affects soot formation. Janssen (1991) proposed that the precursor formation rate may depend on the difference between the concentration of acetylene and OH, based on his analysis of global models for incipient soot formation in hydrocarbon flames and halogenated hydrocarbon flames. A key link between the acetylene concentration and the formation of soot is to be expected because of its proposed role in the formation of aromatics (Westmoreland et al., 1989), growth of PAHs (Frenklach et al., 1986), and the surface growth of soot particles (Harris and Weiner, 1983a; 1983b).

The identification of the main reaction pathways for OH, their relationship to the smaller hydrocarbons, and how these may change in the transition to sooting conditions may be accomplished through the application and analysis of detailed chemical kinetic models that have been developed to model aromatic formation (Harris, Weiner, and Blint, 1988; Miller and Melius, 1992) or soot formation (Frenklach and Wang, 1990). The relative OH number density profiles presented here provide a basis for verification of detailed chemical kinetic models and for exploration of the mechanism over the range of

equivalence ratios bracketing the critical equivalence ratio. These measurements are unique in their examination of the range of equivalence ratios spanning the transition to sooting for similar cold flow velocities and dilution ratios. They are also unique because of their combination with scattering-extinction measurements of soot formation. Prior OH concentration measurements in premixed flames have either been made in a few select flame conditions or have not been accompanied with soot measurements (Bittner and Howard, 1981; 1982; Westmoreland, Howard, and Longwell, 1986; Bastin et al., 1988; Millikan, 1962; Lucht, Sweeney, and Laurendeau, 1985; Harris, Weiner, and Blint, 1986).

A possible improvement to the design of the experiment would be to isolate the effects of temperature and equivalence ratio on the OH number density profile. Maintaining a constant maximum temperature while varying the equivalence ratio is difficult, since the temperature can only be controlled indirectly through variation of the flow rates. However, varying the temperature while holding equivalence ratio constant can be accomplished by varying the total flow rate. This method was used in the laser scattering-extinction measurements, i.e., the total flow rate was varied while dilution ratio and equivalence ratio were kept constant for the comparison between the A-IA and A-IIA sequences and between the L-II and L-I sequences. A logical extension to these fluorescence measurements would be to include OH measurements of the L-I and A-IIA flame sequences.

Several improvements are possible in the method for measuring OH number density in these near-critical equivalence ratio flames. The detection limit for the OH fluorescence could be lowered and the sensitivity improved in the sooting flames by changing to a horizontally polarized incident UV beam to reduce the Rayleigh scattering background by over a factor of 10. This improvement would be necessary before extending these measurements to more heavily sooting flames where particle scattering would become significant.

An alternate approach to improving the detection limit and removing the interference due to Rayleigh scattering would be to use the SPF(1,1) laser-induced fluorescence method described by Laurendeau and Goldsmith (1989). In this method, the excitation of the OH is in the (1,0) band at ~ 281 nm with broadband detection of the fluorescence from the (1,1) band in the region of 312-326 nm. The separation of the excitation and detection wavelengths would eliminate interferences from Rayleigh scattering.

Calibration of the relative number density profile in the lean atmospheric-pressure flame by a UV absorption method would provide a check on the estimated number density determined from the flame code. A similar approach could be investigated using a lean 80-torr flame for calibration of the number density profile of the 80-torr flames.

6.4 Summary

We have measured relative OH number density profiles in a sequence of atmospheric-pressure $C_2H_4/O_2/N_2$ flames and a sequence of 80-torr C_2H_4/O_2 flames. At both pressures, the equivalence ratio was varied from nonsooting to sooting conditions to examine the change in OH number density profile over this transition. The measured OH number density profiles decline in magnitude, but retain their profile shape and location, as the equivalence ratio is increased and the transition to sooting occurs. The similarity of the profiles over this transition may imply that the role of OH in soot formation is primarily through reactions with smaller hydrocarbons such as acetylene. However, this conjecture can only be investigated through detailed chemical kinetic models. The OH number density profiles presented here in conjunction with the scattering-extinction measurements for the same flames presented in Chapter 5 provide a unique set of measurements for testing of detailed chemical kinetic models in the equivalence ratio range bracketing the critical equivalence ratio.

CHAPTER 7:
CHEMICAL KINETIC MODELLING OF PREMIXED ETHYLENE FLAMES

7.1 Introduction

In this chapter, we provide results from a chemical kinetic modelling study based on three sequences of atmospheric-pressure $C_2H_4/O_2/N_2$ flames in which the cold flow velocity and dilution ratio were held constant, while the equivalence ratio was varied from nonsooting through sooting conditions. The laser scattering-extinction measurements presented in Chapter 5 identify both the location and amount of soot formed in these flames. The same measurements also define upper bounds on the soot volume fraction and number density for the near-critical equivalence ratio flames. In addition, the argon-ion laser-induced fluorescence measurements provide a measure of the relative PAH concentrations. The OH number density profiles described in Chapter 6 were obtained using laser-induced fluorescence in four flames from one sequence of the atmospheric-pressure $C_2H_4/O_2/N_2$ flames. These profiles indicate the behavior of the OH number density profiles through the transition from nonsooting to sooting conditions. Although the soot and OH measurements might be used to evaluate global soot formation models such as those describing incipient soot formation, our focus will be on comparison of these profiles with the predictions of detailed chemical kinetic models.

Comprehensive chemical kinetic models for soot formation describe the elementary reactions occurring in the rich combustion of hydrocarbon fuels (e.g., acetylene and ethylene) that lead to the formation of aromatic species, the first step in particle inception. Models developed by Bastin et al. (1988) and Miller and Melius (1992) describe the formation of single-ring aromatics, e.g., benzene and phenyl radical. The formation of

multiple-ring aromatic species (PAHs) has been modelled by Harris, Weiner, and Blint (1988), whose mechanism includes formation of two-ring PAHs, and by Frenklach and Warnatz (1987), whose mechanism includes formation of six-ring PAHs. The extension of detailed chemical kinetic models to the formation of larger PAHs and then to particle formation through growth and coagulation of PAHs becomes too computationally intensive to be modelled fully because of the large number of reactive species. Frenklach and Wang (1990) couple a detailed chemical kinetic model describing PAH formation with a global model describing both growth and coagulation of PAHs to form incipient soot particles and then the subsequent growth and coagulation of these particles.

Since the route to the formation of the single-ring aromatic species is still under investigation (Westmoreland et al., 1989; Miller and Melius, 1992) and the reactions and thermodynamic properties of PAHs must be estimated, the above models may not accurately describe the reactions leading to soot formation. However, a comparison of model predictions with measured species concentrations combined with both a reaction pathway and sensitivity analysis can identify both key species and elementary reactions for subsequent refinement of the model and for development of further experiments.

In this study, we compare our measurements with the predictions of two detailed chemical kinetic models. The model of Drake and Blint (1991) includes the formation of C_3 species and was used primarily for preliminary modelling studies which included calibration of the OH number density profiles (Chapter 6) and estimation of the temperature profiles (Appendix C). Our primary attention was focused on the model of Miller and Melius (1992) which describes the formation of the single-ring aromatics, benzene and phenyl radical, starting from the rich combustion of simple aliphatic fuels. We compare the measured OH number density profiles with the predictions of both models. A less direct comparison can be made between the predictions of the Miller and Melius (1992) model and the measured profiles of soot formation. However, since the

formation of the single-ring aromatic species is the first step in particle inception, the trends in predicted aromatic species concentrations can be compared with the trends in the experimental volume fraction profiles. In particular, the behavior of the aromatic species concentrations can be examined in the transition from nonsooting to sooting flames.

In this chapter, we first describe the flame code, the two reaction mechanisms, and the solution procedure to obtain the predicted profiles. We next compare the predicted OH number density profiles of both reaction mechanisms with the measured OH number density profiles. The predicted trends in the aromatic species profiles using the Miller and Melius (1992) mechanism are then compared with the measured trends in the soot volume fraction and the relative PAH concentration profiles. These comparisons are discussed and possible analyses are outlined for the model results.

7.2 Implementation of the Models

7.2.1 Sandia Flame Code

The predicted species concentration profiles for the two reaction mechanisms were computed with the Sandia laminar premixed one-dimensional flame code (Kee et al., 1985). The Sandia flame code solves the mass, species, and energy conservation equations for a constant-pressure steady laminar premixed one-dimensional flame to determine the species and temperature profiles. The detailed implementation of this computer program is described in Section 4.6. Briefly, the flame code was compiled with the Chemkin-II chemical kinetics subroutine library (Kee, Rupley, and Miller, 1989) and the Chemkin-II multicomponent transport subroutine library (Kee et al., 1986). The multicomponent transport subroutines were used to guarantee mass conservation and to calculate the diffusion coefficients, viscosities, and thermal conductivities more accurately than transport subroutines using approximate mixture-averaging rules. The program was compiled using the double precision version and was run on two 32-bit

computers using the UNIX operating system, a Sun Microsystems Sparcstation 1 and a Gould PN9080. The solution of the flame problem is stored as a binary format file containing the pressure, mass flux, and an array of the position, temperature, and species mass fraction profiles. A set of Fortran programs were written using subroutines from the Chemkin-II chemical kinetics subroutine library (Kee, Rupley, and Miller, 1989) to analyze the stored flame code solutions, to generate species mole fraction and number density profiles, and also to estimate scattering coefficient profiles (Appendix C).

7.2.2 Reaction Mechanism of Drake and Blint (1991)

We used the reaction mechanism of Drake and Blint (1991) for prediction of the OH number density profiles and also to estimate temperature profiles from the scattering coefficient profiles measured using laser scattering-extinction. We implemented a reduced version of their mechanism by removing the nitrogen reactions (reactions 124 through 202 in Table I of Drake and Blint, 1991), so that our version contained 32 species and 144 reactions. Removing the nitrogen reactions reduced the solution time without affecting either predicted OH concentrations or the estimated temperature profiles.

The Drake and Blint (1991) mechanism was derived from the Glarborg, Miller, and Kee (1986) mechanism which was originally developed to model NO_x formation during methane combustion. Drake and Blint (1991) modified the reaction rate coefficients for the methyl and ethyl recombination reactions, modified some of the nitrogen chemistry, and included oxidation reactions of propane. The Drake and Blint (1991) mechanism was used to model NO formation in premixed CH₄/air flames and also to model NO formation and superequilibrium OH concentrations in premixed C₂H₆/O₂/N₂ flames over the range from 1 to 9 atm (Drake et al., 1990). Drake et al. (1990) reported that their mechanism predicted the peak location and shape of the OH concentration profile well, but noted that the peak OH concentrations were 50% higher than the measured peak OH concentrations.

Vaughn et al. (1991) found that predicted stable species profiles using the Glarborg, Miller, and Kee (1986) mechanism showed good agreement with their measurements of rich ethylene combustion in a jet-stirred reactor.

Since the Drake and Blint (1991) mechanism is expected to model the stable species profiles well, it is well suited for estimating the temperature profiles because the scattering coefficient is determined from the stable species profiles (Appendix C). However, based on the results of Drake et al. (1990), we expect the OH number density profiles to be overpredicted.

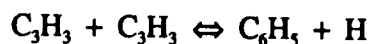
7.2.3 Reaction Mechanism of Miller and Melius (1992)

We used the reaction mechanism of Miller and Melius (1992) to predict OH number density profiles for direct comparison with the measured OH number density profiles and also to predict benzene profiles for comparison with the measured trends in soot formation. We implemented the mechanism containing 50 species and 221 reactions without modification. The mechanism was used with an updated thermodynamic and transport properties database (Miller and Melius, 1992) because some of the C₃ and C₄ species were not present in our older versions of these databases.

The mechanism was developed to model the rich combustion of simple aliphatic fuels (e.g., acetylene and ethylene) and includes hydrocarbon growth reactions up to the formation of the single-ring aromatic species, benzene and phenyl radical. Their mechanism differs from those of others who have modelled the formation of aromatics, such as Bastin et al. (1988), Frenklach and Warnatz (1987), and Harris, Weiner, and Blint (1988). One significant difference is that the Miller and Melius mechanism includes reactions of singlet methylene, ¹CH₂, which they identify as a key species in the formation of C₃H₃ and C₄H₃, which in turn are key intermediates in the formation of aromatic species. In addition, they identify the reactions of the propargyl radical (C₃H₃) to form benzene,



and to form phenyl radical,



as the most likely routes to formation of aromatic species. Oxidation of the aromatic species is only modelled by reaction of phenyl with O_2 and OH to produce the phenoxy radical, $\text{C}_6\text{H}_5\text{O}$. Further decomposition of the phenoxy radical is not included in the mechanism.

Miller and Melius (1992) note that they obtain favorable agreement with the measured stable species and radical species profiles of the lightly sooting, $\phi = 2.5$, 20-torr $\text{C}_2\text{H}_2/\text{O}_2/\text{Ar}$ flame of Bastin et al. (1988). The peak location of their predicted OH mole fraction profile agrees with the measured OH mole fraction profile, but overpredicts the magnitude of the peak mole fraction by a factor of two. In addition, Miller et al. (1990) used the same mechanism to model stable species profiles plus OH and CH radical profiles measured in $\phi = 1.03$, $\phi = 1.67$, and $\phi = 2.00$ nonsooting 25-torr $\text{C}_2\text{H}_2/\text{O}_2/\text{Ar}$ flames. They found good agreement with their predictions for the $\phi = 1.03$ and $\phi = 1.67$ flames. For the $\phi = 2.00$ flame, they found good agreement for the CH and OH profiles, but not with the stable species profiles, possibly because the flame may have attached to the probe.

7.2.4 Flames Studied and Solution Procedure

Flame code solutions were obtained using both reaction mechanisms for the 15 flames listed in Table 7.1. These flame conditions include the atmospheric-pressure flames in which measurements of soot formation were made with laser scattering-extinction and also the atmospheric-pressure flames in which OH number densities were measured with laser-induced fluorescence. The equivalence ratio, flow rates, cold flow velocity and dilution ratio for these flames are given in Table 7.1.

Flame code solutions were first computed using the Drake and Blint (1991) mechanism because of its smaller size. The iterative procedure described in Appendix C was used to match the predicted scattering coefficient profile from the flame code solution to the measured scattering coefficient profiles, so that the temperature profile could be determined. The resulting temperature profiles for these flames are shown in Section 5.3.5.

Once the temperature profile and the flame code solution using the Drake and Blint (1991) mechanism were obtained, the flame code solutions using the Miller and Melius (1992) mechanism were then computed. For a given flame, the flame code solution using the Drake and Blint mechanism was used as the first estimate for the flame code solution using the Miller and Melius mechanism. The mass fraction profiles were set to zero for those species in the Miller and Melius mechanism that were not in the Drake and Blint mechanism. This procedure greatly reduced the overall time spent in computing the solution. The estimate of the temperature profile was checked with the flame code solutions using the Miller and Melius mechanism. The predicted scattering coefficient profiles agreed with the measured scattering coefficient profiles within the tolerance of ± 20 K used in the calculation of the temperature profile.

Once obtained, the flame code solutions containing the temperature and mass fraction profiles can be further analyzed. Possibilities for further analysis include a reaction pathway analysis, in which the key reactions involved in the creation and destruction of a species can be identified, and a sensitivity analysis, which identifies the reaction rate coefficients which have the greatest impact on a species concentration. In this study, our analysis is limited to the calculation of number density and mole fraction profiles from the mass fraction profiles for comparison with the measured OH number density profiles and the trends in soot formation.

Table 7.1 Equivalence ratio, flow rates, cold flow velocity and dilution ratio for the atmospheric flames used for the model comparisons.

Flame	Equivalence Ratio	Flow Rates (slpm)				Cold Flow Velocity (cm·s ⁻¹)	Dilution Ratio
		C ₂ H ₄	O ₂	N ₂	Total		
A-IA-R1	1.49	1.001	2.020	8.39	11.41	7.73	4.15
A-IA-R2	1.63	1.089	2.002	8.32	11.41	7.73	4.15
A-IA-S1	1.78	1.176	1.984	8.25	11.41	7.73	4.16
A-IA-S2	1.92	1.263	1.968	8.20	11.43	7.75	4.17
A-IA-S3	2.02	1.320	1.958	8.14	11.42	7.74	4.16
A-IA-S4	2.17	1.406	1.943	8.09	11.43	7.75	4.16
A-IA-S5	2.32	1.489	1.929	8.03	11.44	7.75	4.16
A-IB-C	1.67	1.326	2.383	7.90	11.61	7.87	3.31
A-IB-S2	1.92	1.421	2.218	7.84	11.48	7.78	3.54
A-IB-S3	2.02	1.485	2.204	7.79	11.48	7.78	3.54
A-IB-S4	2.17	1.578	2.185	7.71	11.47	7.77	3.53
A-IIA-R2	1.63	1.432	2.640	11.31	15.39	10.42	4.29
A-IIA-S1	1.78	1.556	2.623	11.25	15.43	10.45	4.29
A-IIA-S2	1.92	1.667	2.604	11.15	15.42	10.45	4.28
A-IIA-S3	2.02	1.742	2.589	11.09	15.42	10.45	4.28

7.3 Results

7.3.1 Comparison of OH Number Density Profiles

The comparison of the measured OH number density profiles with the predicted profiles using the Drake and Blint (1991) mechanism and the Miller and Melius (1992) mechanism are shown in Figures 7.1 and 7.2. Figure 7.1 shows a comparison for the two rich nonsooting flames, A-IA-R1 ($\phi = 1.49$) and A-IA-R2 ($\phi = 1.63$), over the first 6 mm above the burner. Figure 7.2 shows a comparison for the two sooting flames, A-IA-S1 ($\phi = 1.78$) and A-IA-S2 ($\phi = 1.92$), over the same range.

The predicted OH number density profiles were calculated using temperature profiles obtained from the measured scattering coefficient profiles. These temperature profiles are shown in Figure 7.3. Because the scattering coefficient profile of the A-IA-R1 flame was not measured, its temperature profile was set equal to that of the A-IA-R2 flame as an approximation. Setting the two profiles equal is a reasonable approximation because both are nonsooting flames and thus their radiative heat losses are likely to be similar. Also, the temperature profiles for both flames determined from the flame code solution of the energy conservation equation are within 10 K of each other, thus indicating that the flame chemistry does not significantly change the temperature between the two flames. Although both the A-IA-S1 and A-IA-S2 flames are sooting, significant particle scattering is not observed until a height of about 15 mm in the A-IA-S2 flame and not at all in the A-IA-S1 flame. The molecular scattering coefficient profiles of both flames were corrected for the fluorescence background so that the corrected molecular scattering coefficient profile should reflect the temperature profile in these flames.

The comparison of the measured and predicted OH number density profiles indicates that the peak OH number density is overpredicted in all four flames, but that the difference decreases with increasing equivalence ratio. A comparison of the measured and predicted peak OH number densities is listed in Table 7.1. The ratio of the predicted

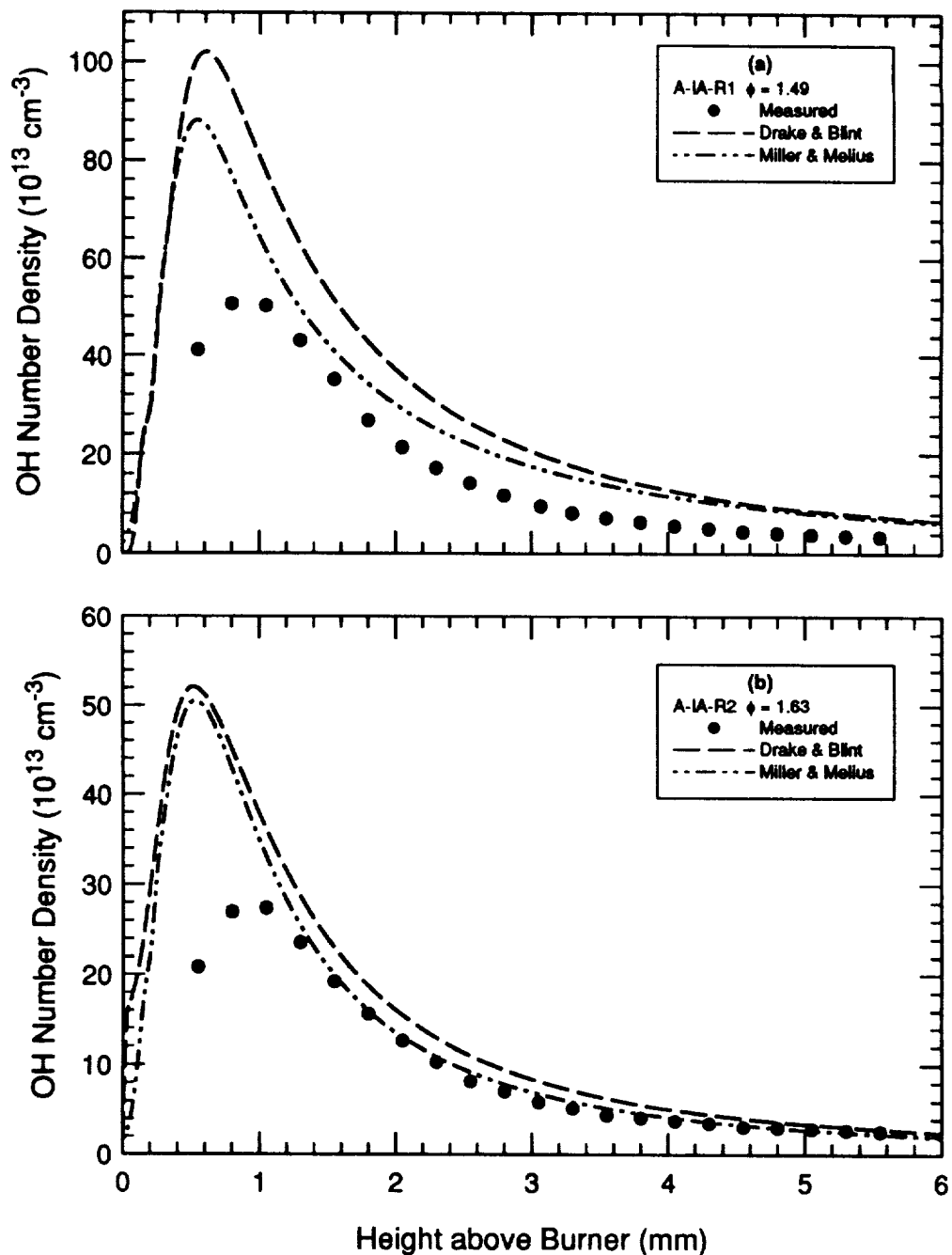


Figure 7.1 Comparison of the measured OH number density profiles with the predicted OH number density profiles using the Drake and Blint (1991) reaction mechanism and the Miller and Melius (1992) reaction mechanism. (a) Flame A-IA-R1, $\phi = 1.49$. (b) Flame A-IA-R2, $\phi = 1.63$. Both are nonsooting flames.

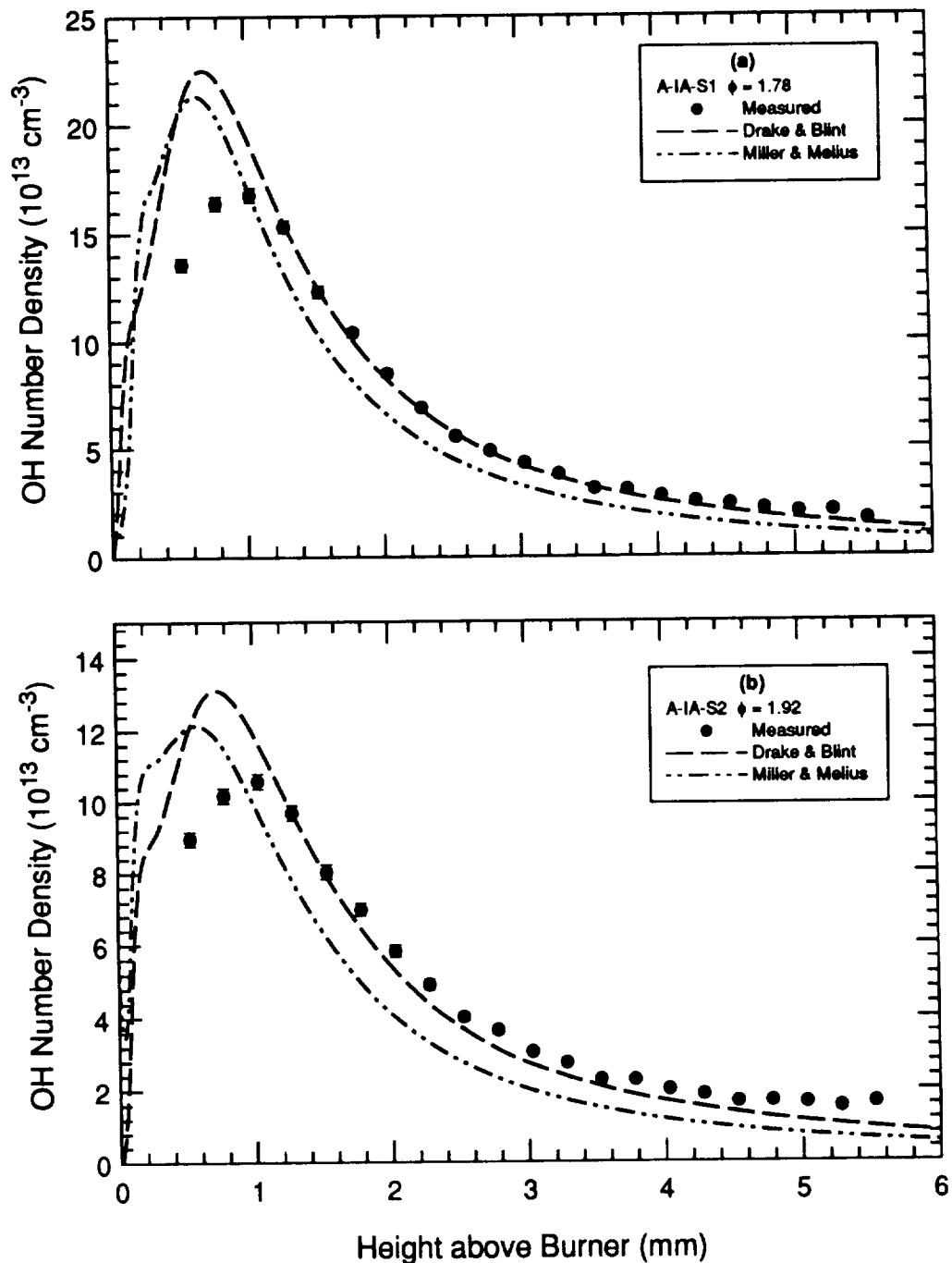


Figure 7.2 Comparison of the measured OH number density profiles with the predicted OH number density profiles using the Drake and Blint (1991) reaction mechanism and the Miller and Melius (1992) reaction mechanism. (a) Flame A-IA-S1, $\phi = 1.78$. (b) Flame A-IA-S2, $\phi = 1.92$. Both are sooting flames.

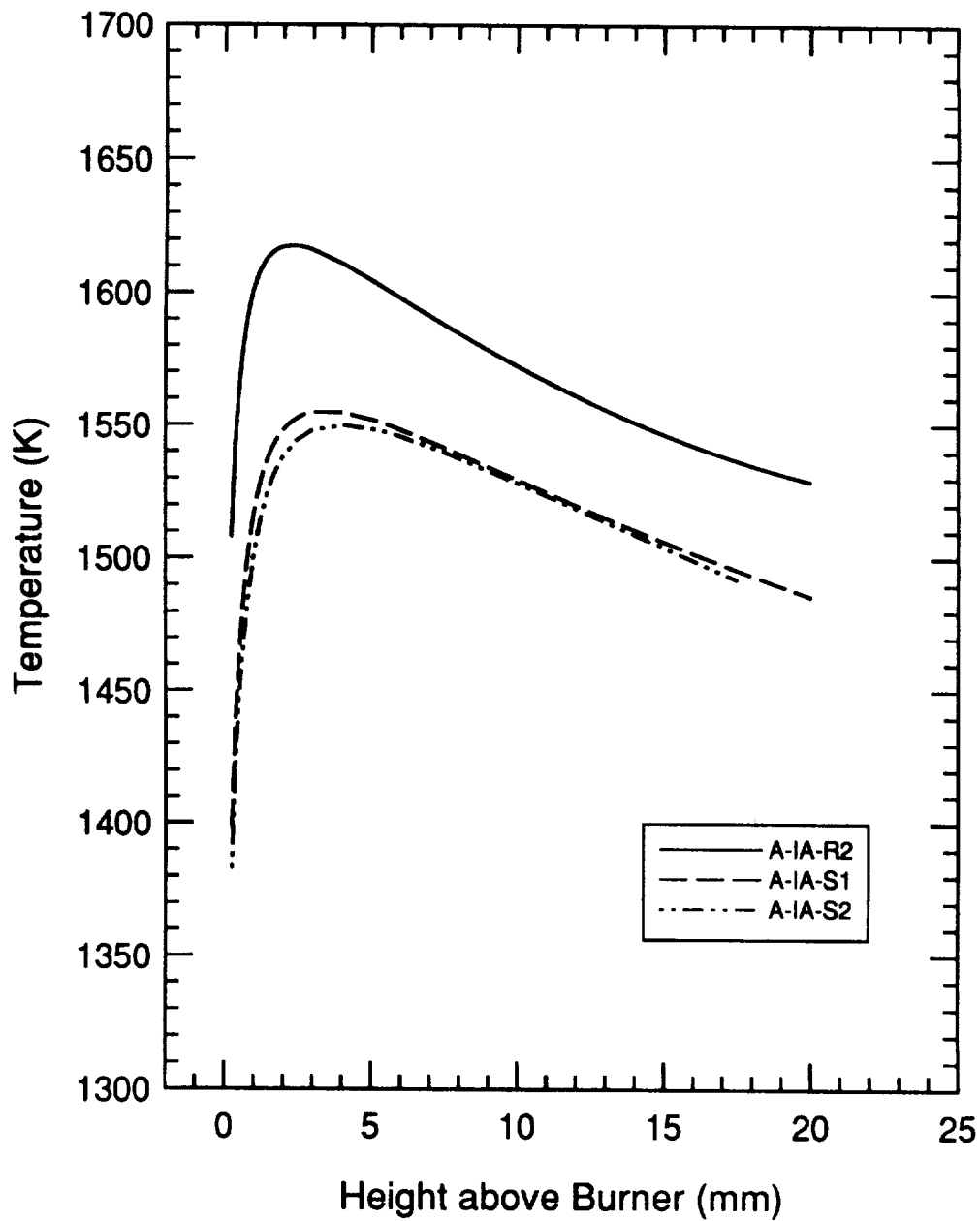


Figure 7.3 Temperature profiles estimated from the scattering coefficient profiles for three flames: A-IA-R2, $\phi = 1.63$; A-IA-S1, $\phi = 1.78$; A-IA-S2, $\phi = 1.92$.

peak number density to the measured number density decreases significantly from about 2.5 in the nonsooting flames to about 1.85 to 1.7 in the sooting flames. The maximum temperature also decreases about 60 K in the transition from nonsooting to sooting conditions.

The peak of the measured number density profiles occurs in the range of ~ 0.9 mm to ~ 1.0 mm. The resolution of the peak is limited by the resolution of the profile, which was measured at 0.25 mm intervals, and by the spatial averaging over the laser beam diameter, which was 0.135 mm. The predicted OH number density profiles peak lower in the flame at ~ 0.5 to ~ 0.7 mm above the burner.

The agreement between the measured and predicted OH number density profiles improves at heights greater than 1.4 mm. The measured and predicted profiles agree closely in this region. As equivalence ratio increases, the comparison of the predicted to the measured OH number density in this region progresses from an overprediction to an underprediction of the OH number density.

Comparing the predictions of the two mechanisms, the OH number density profiles predicted using the Miller and Melius mechanism are lower and also peak at a lower height above the burner. The difference between the predicted peak number densities of the two mechanisms is greatest at about 16% in the A-IA-R1 flame and is less than 10% for the other flame conditions.

7.3.2 Comparison of Predicted Benzene Profiles with Profiles of Soot Formation

The predicted benzene number density profiles using the Miller and Melius (1992) mechanism are compared with the measured trends for soot formation in Figures 7.4 through 7.6. The change in the predicted benzene number density profiles as the equivalence ratio is varied from nonsooting to sooting conditions is shown in Figure 7.4.

Table 7.2 Peak measured and predicted OH number densities for the four atmospheric-pressure flames.

Flame	A-IA-R1	A-IA-R2	A-IA-S1	A-IA-S2
Equivalence Ratio	1.49	1.63	1.78	1.92
Maximum Temperature	1617 K	1617 K	1554 K	1550 K
Peak OH Number Density (cm^{-3})				
Measured	5.03×10^{14}	2.74×10^{14}	1.68×10^{14}	1.06×10^{14}
Drake and Blint	1.02×10^{15}	5.21×10^{14}	2.25×10^{14}	1.31×10^{14}
Miller and Melius	8.81×10^{14}	5.05×10^{14}	2.13×10^{14}	1.22×10^{14}
Ratio of Predicted to Measured				
Drake and Blint	2.6	2.48	1.85	1.73
Miller and Melius	2.24	2.41	1.75	1.60

The predicted benzene number density profiles (Fig. 7.4b) are also compared with measured profiles of the argon-ion laser-induced fluorescence (Fig. 7.4a) for four flames with the same cold flow velocity and dilution ratio.

The profiles of argon-ion laser-induced fluorescence are thought to provide a measure of the relative PAH concentration. In addition, they have been shown to be a more sensitive measure of the presence of soot and also have been shown to be proportional to the soot volume fraction (Chapter 5). Within this sequence of flames, the A-IA-R2 ($\phi = 1.63$) flame was observed to be nonsooting, the A-IA-S1 ($\phi = 1.78$) flame was visibly sooting, but did not have a measurable particle scattering and extinction coefficient, and both the A-IA-S2 ($\phi = 1.92$) and A-IA-S3 ($\phi = 2.02$) flames were visibly sooting and had measurable particle scattering and extinction coefficient profiles.

The predicted benzene number density profiles for these same four flames show an initial high concentration near the burner surface followed by a decline to a minimum number density about 2 to 5 mm above the burner and then a slower growth in number density with increasing height. The minimum number density in the nonsooting flame (A-IA-R2) is over an order of magnitude smaller than that in the first visibly sooting flame (A-IA-S1). However, their respective number densities at a height of 25 mm differ by a factor of only 2.5. The minimum number density increases by an order of magnitude with each increment in equivalence ratio, but the growth rate of the number density following the minimum declines so that in the richest flame (A-IA-S3) the benzene number density remains almost constant throughout the profile. Hence, for these four flames, the minimum benzene number densities vary by over three orders of magnitude while at 25 mm the number densities vary by little more than an order of magnitude.

The profiles of benzene number density are compared with the profiles of soot volume fraction for flames with the same equivalence ratio, but different cold flow velocities and dilution ratios, in Figures 7.5 and 7.6. The three atmospheric-pressure

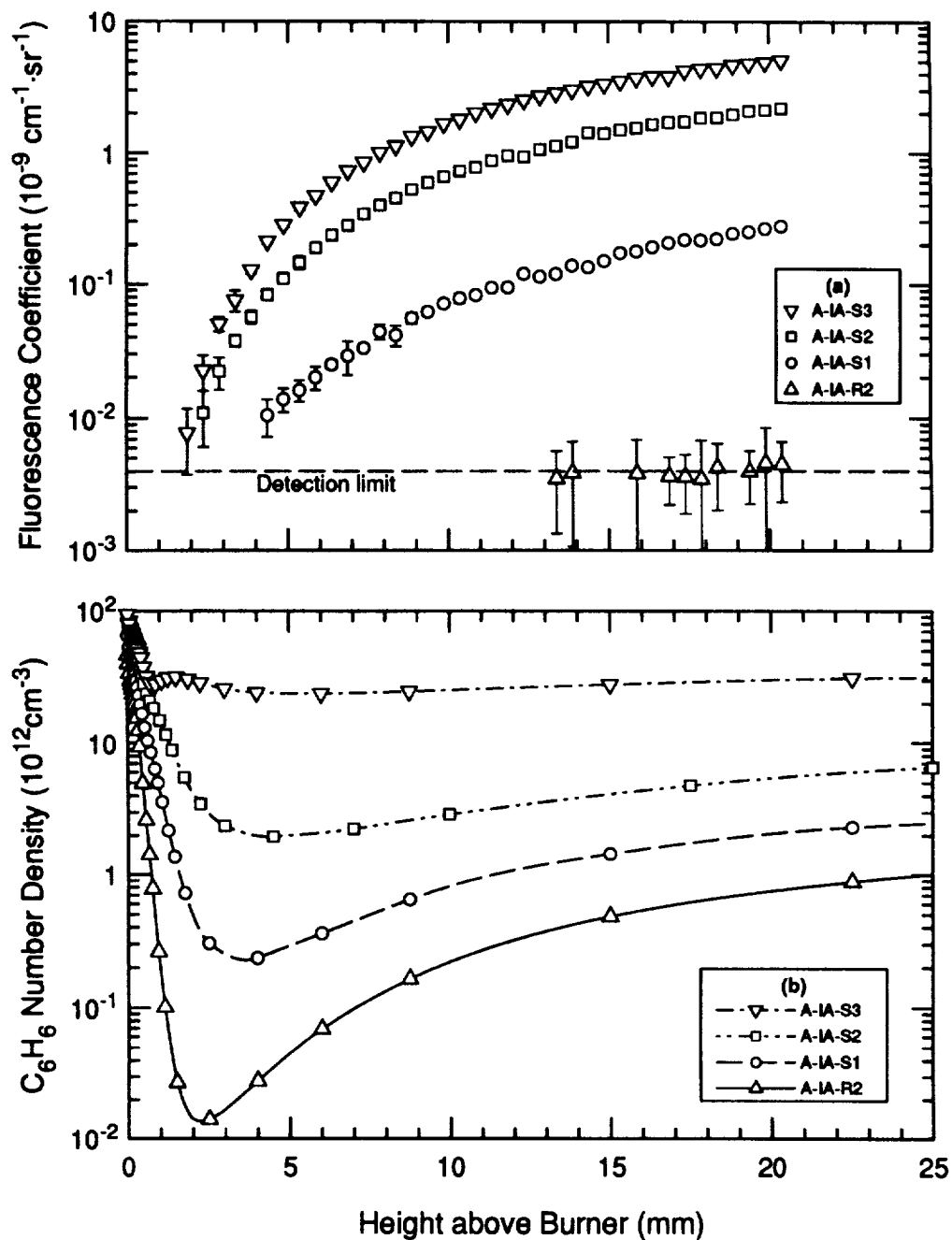


Figure 7.4 Comparison of the argon-ion laser-induced fluorescence profiles (a) with the predicted benzene number density profiles (b) for four atmospheric-pressure flames: A-IA-R2, $\phi = 1.63$, nonsooting; A-IA-S1, $\phi = 1.78$, lightly sooting; A-IA-S2, $\phi = 1.92$, sooting; A-IA-S3, $\phi = 2.02$, sooting.

flames with equivalence ratio, $\phi = 1.92$, are compared in Figure 7.5, while the three atmospheric flames with equivalence ratio, $\phi = 2.02$, are compared in Figure 7.6.

The volume fraction profiles of the $\phi = 1.92$ (-S2) flames (Fig. 7.5a) show that these are lightly sooting flames. The predicted benzene number density profiles of these flames have a similar profile shape and, in fact, have similar number densities at 25 mm above the burner. The difference in the profiles is in the magnitude and position of the minimum number density. The comparison between flames A-IA-S2 and A-IIA-S2, which have different cold flow velocities but a similar dilution ratio, shows that the flame, A-IIA-S2, with the higher cold flow velocity (and also higher temperature) has a smaller minimum benzene number density and also a smaller soot volume fraction. The comparison between flames A-IA-S2 and A-IB-S2, which have the same cold flow velocity but different dilution ratios, shows that their minimum number densities are of similar magnitude, but that the minimum of the A-IB-S2 flame occurs earlier and its subsequent growth rate is greater. This corresponds to the greater volume fraction in the A-IB-S2 flame which has a smaller dilution ratio and thus a larger fuel mole fraction than the A-IA-S2 flame.

The behavior of the benzene number density profiles is quite different for the comparison of the $\phi = 2.02$ (-S3) flames in Figure 7.6. The trends in volume fraction for these flames (Fig. 7.6a) are similar to those of the $\phi = 1.92$ flames, but the trends in the benzene volume fraction profiles (Fig 7.6b) differ significantly. The number density profiles show an order of magnitude variation in the minimum number density and also a significant variation in the number density at 25 mm. The A-IIA-S3 flame, which has the same dilution ratio but higher cold flow velocity than the A-IA-S3 flame, has a minimum benzene number density an order of magnitude smaller than the A-IA-S3 flame and also

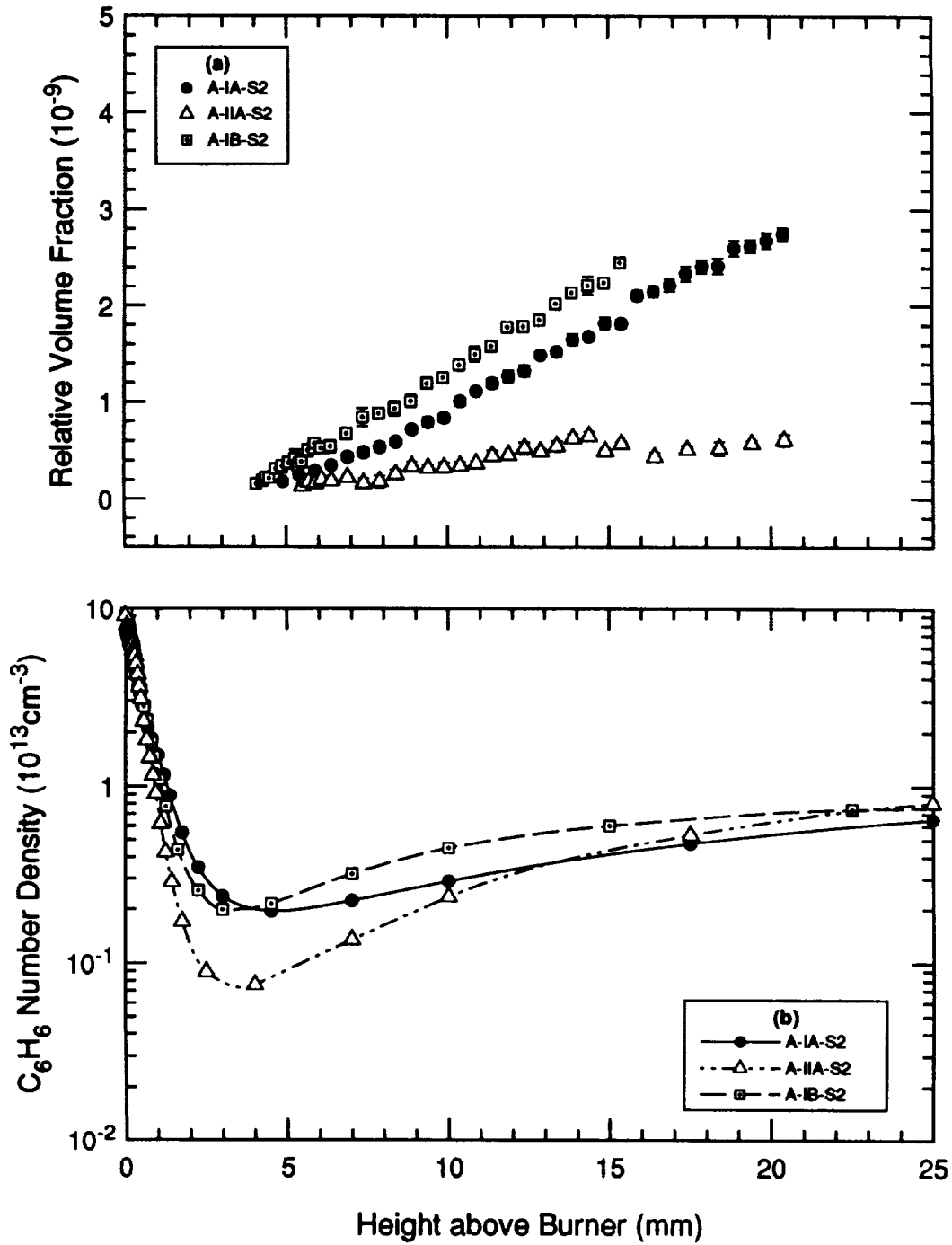


Figure 7.5 Comparison of the relative volume fraction profiles (a) measured in the $\phi = 1.92$ (-S2) flame of the three flame sequences with the predicted benzene number density profiles (b) for the same flames.

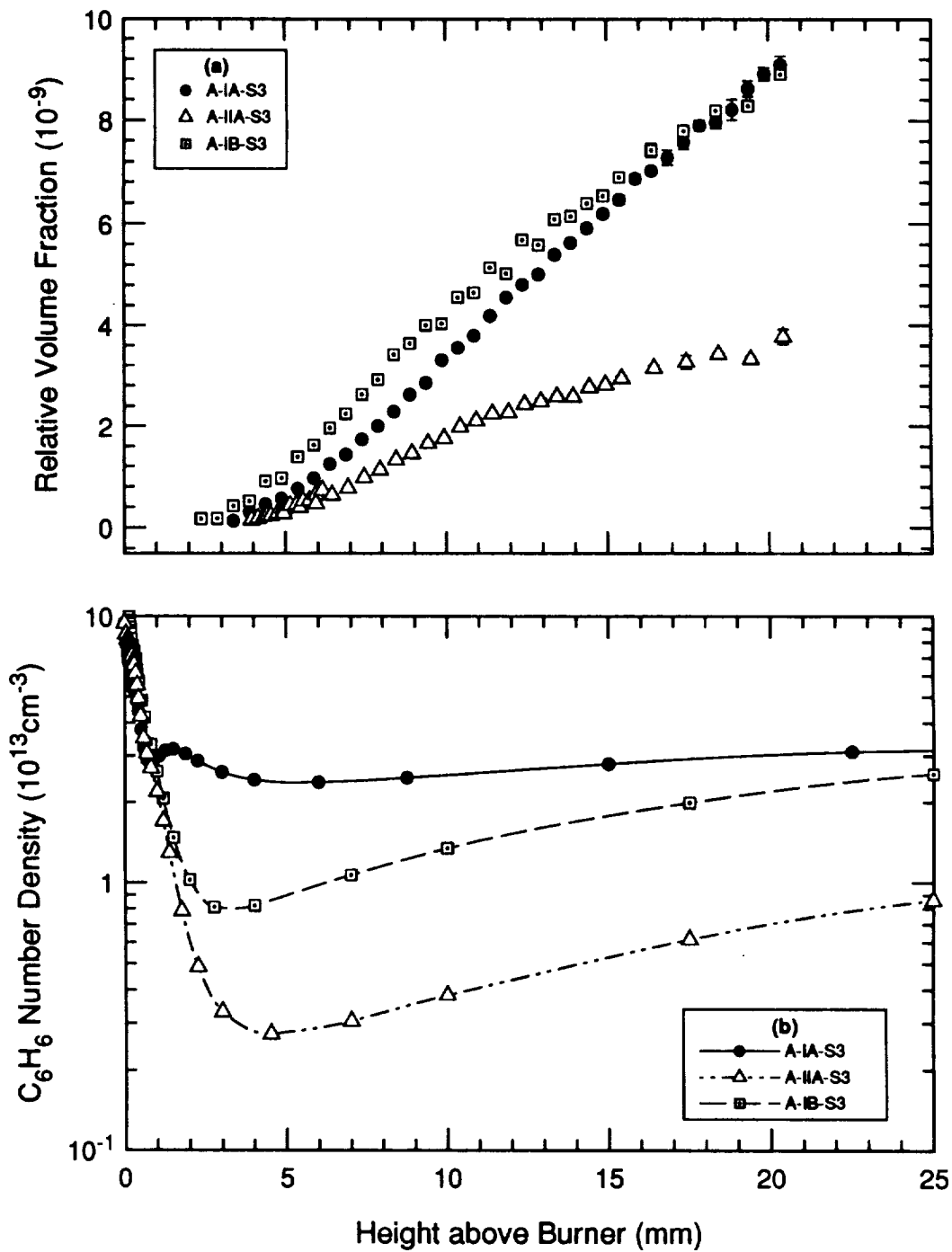


Figure 7.6 Comparison of the relative volume fraction profiles (a) measured in the $\phi = 2.02$ (-S3) flame of the three flame sequences with the predicted benzene number density profiles (b) for the same flames.

a smaller volume fraction. The A-IB-S3 flame, which has the same cold flow velocity but a smaller dilution ratio than the A-IA-S3 flame, has a minimum benzene number density which is a factor of three smaller than the A-IA-S3 flame. However, its soot volume fraction profile remains greater than that of the A-IA-S3 flame throughout the first 15 mm above the burner.

7.4 Discussion

The predicted and measured OH number density profiles of the four flames, A-IA-R1, A-IA-R2, A-IA-S1, and A-IA-S2, agree closely at heights above 1.4 mm, which is greater than the height corresponding to the peak OH number density. The agreement between the predicted and measured peak OH number densities is not as good. The predicted OH number density profiles overpredict the measured peak by a factor of ~ 2.5 in the nonsooting flames and by a factor of ~ 1.7 in the sooting flames. However, this difference between the measured and predicted peak OH number densities may still be considered reasonable agreement because of the uncertainties in the model and also because similar agreement between measured and predicted profiles is observed by other researchers (Miller et al., 1990; Drake et al., 1990). Spatial averaging over the laser beam diameter may account in part for the smaller measured OH number density compared to the predicted OH number density.

Recall that the measured OH number densities were calibrated (Chapter 6) based on a comparison between the measured relative OH number density profile for a lean flame (A-0-L, $\phi = 0.97$) and the predicted OH number density profile using the Drake and Blint (1991) mechanism. The agreement between the measured and predicted profiles in the rich flame implies that the reaction mechanisms describe well the relative behavior of the OH number density over this range of equivalence ratios. However, the accuracy of the prediction for the rich flames depends on the accuracy of the prediction for the lean flame.

The agreement between the predicted and measured peak OH number densities improves significantly in the sooting flames over that in the nonsooting flames. This improvement corresponds with the ~ 60 K decrease in maximum temperature in the sooting flames compared to that in the nonsooting flames. The relative change between the measured and predicted OH number densities through this transition may indicate that the reaction mechanisms have a different sensitivity to temperature than the actual mechanism creating or destroying OH in the flame. The slight disagreement between the location of the peak OH number densities for the predicted and measured profiles may be caused by the estimated temperature profile near the burner surface. The location of the predicted peak number density and, to a lesser extent, the magnitude of the peak depend on the shape of the estimated temperature profile in the region below the peak. The temperature profile is difficult to measure by any means in this region (<1 mm) because of the proximity to the burner surface. Thus, a small difference between the predicted and measured peak locations may not be significant for these atmospheric-pressure flames.

The similarities in the predicted OH number density profiles for both mechanisms suggests that the chemistry of OH formation and destruction is similar for both mechanisms. The addition of the C₃, C₄, and aromatic formation reactions in the Miller and Melius (1992) mechanism apparently does not affect the OH number density profile significantly. However, to state conclusively that the mechanisms for OH formation and destruction are similar for both mechanisms would require a reaction pathway analysis to identify the reactions through which the main flux of OH passes.

The trends in the minimum of the predicted benzene number density correlate with the observed trends for soot formation as shown in Figures 7.4 and 7.5. As the predicted minimum benzene number density increases, the measured soot volume fraction increases. An exception to this trend is the $\phi = 2.02$ (-S3) flames shown in Figure 7.6. This correlation of benzene number density with soot volume fraction is consistent with

the hypothesized mechanism of soot formation discussed in Chapter 2. The formation of single-ring aromatics such as benzene is the first step in particle inception. If we consider that the benzene number density at the minimum is related to the number density of soot particles leaving the inception stage, then the minimum benzene number density is likely to be related to the volume fraction because the final volume fraction depends on the number of particles leaving the inception stage. Consequently, this correlation is only likely to apply for benzene number densities in the immediate region of the minimum, where the benzene number density varies by over an order of magnitude for an increment in the equivalence ratio of $\Delta\phi \approx 0.15$. The variation in the benzene number density at a height of 25 mm is much smaller.

The process of benzene formation can still occur in the post-flame region as can be seen in the profile for the nonsooting flame A-IA-R2 in Figure 7.4. The further growth of the benzene in the region above 10 mm to form PAHs would account for the observation of argon-ion laser-induced fluorescence signals at the detection limit in this flame.

The initial high concentrations of benzene near the burner surface are in part caused by the lower temperatures there, and thus the greater overall number density of the gases. However, the presence of the benzene concentrations near the burner surface suggest that benzene is formed initially from pyrolysis of the fuel because of the relatively steep increase in the temperature profile near the burner surface. This behavior may have been measured in the extinction coefficient profiles, but not noted in the discussion of these measurements in Chapter 5. The extinction coefficient profile (this can be best seen in Figure 5.5) shows an initial extinction near the burner surface that is too far above the burner to be caused by clipping from the burner surface. Gas-phase absorption by PAHs would account for this initial extinction. The extinction coefficient profile declines to a minimum at approximately the same height as the predicted benzene number density profiles.

The exception to the observed correlation between minimum benzene number density and the measured soot volume fraction is the $\phi = 2.02$ (-S3) flames (Fig. 7.6). The A-IB-S3 flame has a much smaller minimum benzene number density, but a larger volume fraction than the A-IA-S3 flame. In addition, the shape of the benzene number density profile is significantly different for the A-IA-S3 flame than for either the A-IB-S3 or the A-IIA-S3 flame. The A-IA-S3 flame exhibits a slight peak in the number density profile whereas the other flames have a minimum. This change in behavior implies that a significant route for the destruction of benzene has been shut off in this flame that is present in the A-IB-S3 and the A-IIA-S3 flames. A major difference among these flames is that the peak temperatures of the A-IB-S3 and A-IIA-S3 flames are both about 50 K higher than that of the A-IA-S3 flame. Since the oxidation reactions of benzene are not fully modelled in the Miller and Melius reaction mechanism (e.g., the reaction of benzene with oxygen is not included), the larger benzene number density in the A-IA-S3 flame may be overpredicted because of the missing oxidation reactions. The benzene number densities of the A-IB-S3 and A-IIA-S3 flames may be more accurately modelled since pyrolysis of benzene may be the dominant path for benzene destruction in these flames because of their higher temperatures. However, a reaction pathway analysis would be required to investigate this conjecture.

In this study, we have made qualitative comparisons between the predicted benzene number density profiles and the trends in soot formation. More direct comparisons with the trends in soot formation could be made using a model such as that of Frenklach and Wang (1990) which combines a detailed chemical kinetic model for PAH formation with global models to describe the formation of soot from the PAHs.

7.5 Summary

We have used the Sandia flame code and two reaction mechanisms to model the species and temperature profiles of the atmospheric-pressure flames. The Drake and Blint

(1991) reaction mechanism was used to estimate the temperature profiles and to calculate OH number density profiles for these flames. Similarly, OH number density and benzene number density profiles were calculated for these flames using the Miller and Melius (1992) mechanism.

The comparison between the predicted and measured OH number density profiles showed good agreement for heights above 1.4 mm; however, the peak OH number densities were overpredicted. Both reaction mechanisms predict similar OH number density profiles, implying that their description of the OH chemistry is similar.

The trends in the predicted benzene number density profiles correlate with the observed trends in soot formation. The increase in the minimum benzene number density correlates with the increase in measured soot volume fraction in accordance with the hypothesis that the number of particles formed in the inception zone determines the final soot volume fraction. An exception to the observed correlation occurs in the richer and cooler sooting flames for which the mechanism of benzene destruction appears to stop. The apparent disagreement with the trends in soot formation may imply that benzene oxidation reactions must be included in the Miller and Melius (1992) reaction mechanism to more accurately model these flames. Further analysis of the data would require a reaction pathway analysis to investigate the mechanisms for the formation and destruction of both OH and benzene.

CHAPTER 8: CONCLUSIONS AND RECOMMENDATIONS

8.1 Conclusions

In this study, we have provided a set of data which can be used in the development and testing of global and detailed chemical kinetic models for soot formation. Profiles of soot and hydroxyl concentrations were measured for sequences of flat premixed atmospheric-pressure $C_2H_4/O_2/N_2$ flames and 80-torr C_2H_4/O_2 flames. The measured profiles were compared with the predictions of detailed chemical kinetic models including the formation of aromatics. The accomplishments and conclusions related to the measurement, analysis, and modelling of this data follow.

First, we have developed and refined a laser scattering-extinction measurement system capable of resolving a 0.1% change in the transmittance, which is at the limit of prior studies. This increased resolution was applied to more closely define the location of soot formation in a flame, and, more importantly, to allow the measurement of soot formation at conditions much closer to the critical equivalence ratio than those of previous flame studies.

Scattering and extinction coefficient profiles were measured in three sequences of atmospheric-pressure flat premixed $C_2H_4/O_2/N_2$ flames and two sequences of 80-torr flat premixed C_2H_4/O_2 flames. Within a sequence, the cold flow velocity and dilution ratio were held constant, while the equivalence ratio was varied from a rich nonsooting condition to a sooting condition either at the critical equivalence ratio or near the critical equivalence ratio to sequentially more heavily sooting conditions. The cold flow velocity and dilution ratio were varied between sequences of the atmospheric flames and the cold

flow velocity was varied between sequences of the 80-torr flames. The variation in cold flow velocity and dilution ratio allowed measurements of the effects of temperature and reactant composition on soot formation. These measurements in a sequence of flames near the critical equivalence ratio provide a unique data set that can be used to evaluate models of soot formation with respect to their predictions of the onset of soot formation and also the amount of soot formed in sooting flames.

The measured scattering and extinction coefficient profiles for both the 80-torr and atmospheric-pressure flames at or near the critical equivalence ratio did not show evidence of particle scattering or extinction, even though the yellow emission attributed to soot was visible. Thus, the scattering-extinction method could not resolve the critical equivalence ratio to closer than $\Delta\phi \sim 0.15$. However, the detection limits could be used to determine upper bounds on both the volume fraction and number density of particles present in the near-sooting flames.

The detection of argon-ion laser-induced fluorescence coincided with the visible yellow emission of soot and thus was a more sensitive measure of the critical equivalence ratio than the scattering-extinction method in the atmospheric-pressure flames. The linear correlation between the fluorescence and the extinction coefficients implies that the concentration of PAHs is related to the soot volume fraction and also grows at the same rate, possibly because the growth mechanism for soot is the same as that for the PAHs causing the fluorescence. The fluorescence signal thus offers the possibility of a more sensitive diagnostic for measuring changes in the soot volume fraction.

For atmospheric-pressure flames at equivalence ratios richer than the critical equivalence ratio, volume fraction, number density and particle diameter profiles were calculated from the extinction and scattering coefficient profiles. The observed trends in the relative profiles are in accord with the existing theories of soot formation. In particular, the volume fraction increases with increasing equivalence ratio. At the same

equivalence ratio, the volume fraction decreases at higher temperatures for the same reactant composition, while for a higher fuel mole fraction the volume fraction can increase at higher temperatures. The relative particle number density profiles decline similarly beyond their peaks indicating that they are governed by the same coagulation rate as has been observed by other researchers. The peak number density occurs at particle inception and although the location of the peak cannot be measured directly, its relative location can be inferred from the location of the subsequent decline in the profile. In these flames, the particle inception region moves closer to the burner surface with increases in either the equivalence ratio or the peak temperature.

Profiles of OH number density were measured using broadband laser-induced fluorescence in a sequence of four atmospheric-pressure $C_2H_4/O_2/N_2$ flames and in a sequence of four 80-torr C_2H_4/O_2 flames. These flames were a subset of the flames examined with the laser scattering-extinction method. The equivalence ratios within each sequence bracketed the critical equivalence ratio so that the change in the OH number density profile could be measured as the equivalence ratio was changed from nonsooting to sooting.

For both atmospheric pressure and 80 torr, the peak in the OH number density profile declines with increasing equivalence ratio. However, each profile scales with the maximum number density so that the normalized profiles overlay each other. Thus, the OH number density profiles do not change shape during the transition to sooting. This behavior implies that the reaction pathways for OH do not change significantly in the transition from nonsooting to sooting flames. Therefore, the major reaction pathways for OH are probably limited to smaller hydrocarbons such as acetylene which are present in rich nonsooting flames and whose concentration also does not change significantly in the transition to sooting flames. Since OH is identified as the oxidizer of soot precursors in

the global models describing incipient soot formation, the implied precursor may then be acetylene. On the other hand, the reactions of OH with acetylene could also indirectly influence soot formation.

These implications about the major reaction pathways for OH and the role of OH in the global models can be investigated through the application and analysis of detailed chemical kinetic models describing those reactions leading to aromatic or soot formation. The OH number density profiles measured in conjunction with the scattering-extinction measurements in the same flames provide a unique basis for testing such detailed chemical kinetic models over the range of equivalence ratios bracketing the critical equivalence ratio.

We have demonstrated the application of detailed kinetic models to the measured OH number density profiles and also to the prediction of benzene number density profiles for comparison with the measured trends in soot formation. The Sandia premixed one-dimensional flame code was used to obtain the predicted species profiles for the atmospheric-pressure flames using two reaction mechanisms. The reaction mechanism of Drake and Blint (1991) models rich combustion only up to the formation of C₃ hydrocarbons and was used to predict OH number density profiles and to obtain temperature profiles. The second reaction mechanism, that of Miller and Melius (1992), also models rich combustion, but includes the formation of single-ring aromatics such as benzene and phenyl radical. It also incorporates the most recent reaction rate coefficients, thermodynamic properties, and hypothesized reactions leading to the formation of aromatics. This second mechanism was used to predict OH and benzene number density profiles.

The predicted and measured OH number density profiles using both reaction mechanisms agree closely for heights above that corresponding to the peak OH number density, although the peak OH number densities are overpredicted by about a factor of two. Overall, the agreement in the shape of the profiles is quite good.

The trends in the predicted benzene number density profiles correlate with the measured trends in soot formation. Typically, the benzene number density profiles display an initial high concentration at the burner surface followed by a decline to a minimum at around 2 to 5 mm above the burner and then a subsequent slow growth throughout the remainder of the flame. The magnitude of the minimum benzene number density appears to correlate with the measured soot volume fraction. The minimum number density increases by an order of magnitude in the transition from a nonsooting flame to a sooting flame and then increases by another order of magnitude with further increases in equivalence ratio. The proposed correlation between soot formation and benzene number density appears to fail in richer and cooler sooting flames for which the benzene number density profile changes shape and no longer exhibits a defined minimum. A possible cause for this change in the profile is that the benzene destruction mechanism stops at lower temperatures thus leading to overprediction of the benzene concentration. The inclusion of benzene oxidation reactions may be needed to more accurately model these lower-temperature flames.

8.2 Recommendations for Future Work

Improvements to the measurements and apparatus have been suggested in previous chapters. A lower detection limit for the OH fluorescence measurement would allow more heavily sooting flames to be investigated to confirm the behavior of the OH profile at successively richer equivalence ratios. Calibration of the OH number density with a UV absorption measurement at both atmospheric and subatmospheric pressures would allow a more direct evaluation of the predicted OH number density profiles.

For the measurements of soot formation, an extension of the extinction measurement to longer wavelengths in the near-IR region (700 - 1100 nm) could be used to identify incipient particles or high molecular weight hydrocarbons of different sizes (Weiner and Harris, 1989). Such measurements should be used to explore the relationship between the soot volume fraction and the argon-ion laser-induced fluorescence attributed to PAHs. A better understanding of the source for the fluorescence and its relationship to the soot volume fraction could be used to develop the fluorescence as a more sensitive diagnostic for point measurements of the volume fraction. A similar method has been proposed by Bengtsson and Aldén (1991) using the fluorescence of C_2 radicals produced by the laser vaporization of soot.

An extension of the range of flame conditions to include sooting flames with higher maximum temperatures would be valuable for the testing of mechanisms because of the strong influence of temperature on soot formation. The current set of atmospheric pressure data has a relatively narrow range of maximum temperatures (~ 50 K) among flames with the same equivalence ratio. The maximum temperatures of these flames (~ 1500 to 1600 K) are also at the low end of the range of temperatures that have been investigated for sooting flames. Additional measurements in flames with peak temperatures in the range of 1700 to 1800 K would provide a basis for testing different aspects of the soot mechanism such as pyrolysis reactions that may become more significant with an increase in temperature.

Perhaps the most fruitful area for expanding on this work is to use the measured data for its intended purpose, i.e., the evaluation of existing detailed chemical kinetic models and global models for soot formation. The most immediate possibility is to continue the application and analysis of the Miller and Melius (1992) reaction mechanism to our flame conditions. Since the reaction mechanism is current, it has only been applied to a few

flame conditions at pressures of 20 to 25 torr. Here, we have a range of flame conditions at both atmospheric pressure and 80 torr that span the transition from nonsooting to sooting conditions.

Two methods are typically used in analyzing a mechanism. A sensitivity analysis is used to identify the sensitivity of a given species concentration to variations in selected reaction rate coefficients. A reaction pathway analysis identifies the main reactions through which the flux of a particular species passes. A reaction pathway analysis could, for example, be used to identify the main route for the formation of benzene. A sensitivity analysis could then be used to identify the sensitivity of the benzene concentration to the rate of acetylene oxidation by OH.

Since the flame code solutions for the atmospheric-pressure flames have already been obtained with the Miller and Melius (1992) mechanism, the groundwork for such analyses is already in place. One possibility would be to examine the change in the reaction pathways as the equivalence ratio is changed from nonsooting to sooting conditions. A reaction pathway analysis could also be used to determine the cause for the predicted change in the benzene profile shape as the equivalence ratio increases to more heavily sooting conditions.

The modelling study could be extended further to consider models such as that of Frenklach and Wang (1990) which incorporates the full range of soot formation by combining a reaction mechanism for combustion of acetylene, including the formation of PAHs, with global models for particle inception, growth and coagulation. The predictions of such a model could be compared directly with the measured profiles of soot number density. The range of sooting conditions in this study could provide an exhaustive test of such mechanisms. The evaluation of comprehensive models for soot formation could then be used to identify experiments that might further clarify the mechanism of soot formation.



LIST OF REFERENCES

LIST OF REFERENCES

- Alkemade, U., and K.H. Homann (1989). Formation of C_6H_6 isomers by recombination of propynyl in the system sodium vapour/propynylhalide. *Z. Phys. Chem. N.F.*, **161**, 19-34.
- Analog Devices, Inc. (1990). *Analog Devices 1990/1991 Linear Products Databook*. Analog Devices, Inc., One Technology Way, P.O. Box 9106, Norwood, MA 02062, pp. 2-83 to 2-93.
- Anderson, W.R., L.J. Decker, and A.J. Kotlar (1982). Concentration profiles of NH and OH in a stoichiometric CH_4/N_2O flame by laser excited fluorescence and absorption. *Combust. Flame*, **48**, 179-190.
- Bastin, E., J.L. Delfau, M. Reuillon, and C. Vovelle (1988). Experimental and computational investigation of the structure of a sooting $C_2H_2-O_2-Ar$ flame. *Twenty-second Symposium (International) on Combustion*, The Combustion Institute, Pittsburgh, PA, 313-322.
- Baumgartner, L., D. Hesse, H. Jander, and H.Gg. Wagner (1984). Rate of soot growth in atmospheric premixed laminar flames. *Twentieth Symposium (International) on Combustion*, The Combustion Institute, Pittsburgh, PA, 959-967.
- Bengtsson, P.E., and M. Aldén (1991). C_2 production and excitation in sooting flames using visible laser radiation: implications for diagnostics in sooting flames. *Combust. Sci. Tech.*, **77**, 307-318.
- Beretta, F., V. Cincotti, A. D'Alessio, and P. Menna (1985). Ultraviolet and visible fluorescence in the fuel pyrolysis regions of gaseous diffusion flames. *Combust. Flame*, **61**, 211-218.
- Bittker, D.A. (1991). Detailed mechanism for oxidation of benzene. *Combust. Sci. Tech.*, **79**, 49-72.
- Bittner, J.D., and J.B. Howard (1981). Composition profiles and reaction mechanisms in a near-sooting premixed benzene/oxygen/argon flame. *Eighteenth Symposium (International) on Combustion*, The Combustion Institute, Pittsburgh, PA, 1105-1116.
- Bittner, J.D., and J.B. Howard (1982). Mechanism of hydrocarbon decay in fuel-rich secondary reaction zones. *Nineteenth Symposium (International) on Combustion*, The Combustion Institute, Pittsburgh, PA, 211-221.
- Bockhorn, H., F. Fetting, and H. Heddrich (1986). Investigation of particle inception in sooting premixed hydrocarbon oxygen low pressure flames. *Twenty-first Symposium (International) on Combustion*, The Combustion Institute, Pittsburgh, PA, 1001-1012.

- Bockhorn, H., F. Fetting, H. Heddrich, and G. Wannemacher (1984). Investigation of the surface growth of soot in flat low pressure hydrocarbon oxygen flames. *Twentieth Symposium (International) on Combustion*, The Combustion Institute, Pittsburgh, PA, 979-988.
- Bockhorn, H., F. Fetting, G. Wannemacher, and H.W. Wenz (1982). Optical studies of soot particle growth in hydrocarbon oxygen flames. *Nineteenth Symposium (International) on Combustion*, The Combustion Institute, Pittsburgh, PA, 1413-1420.
- Bockhorn, H., F. Fetting, and H.W. Wenz (1983). Investigation of the formation of high molecular hydrocarbons and soot in premixed hydrocarbon-oxygen flames. *Ber. Bunsenges. Phys. Chem.*, **87**, 1067-1073.
- Bogaard, M.P., A.D. Buckingham, R.K. Pierens, and A.H. White (1978). Rayleigh scattering depolarization ratio and molecular polarizability anisotropy for gases. *J. Chem. Soc. Faraday Trans. I*, **74**, 3008-3015.
- Bohren, C.F. and D.R. Huffman (1983). *Absorption and Scattering of Light by Small Particles*. John Wiley & Sons, New York.
- Böhm, H., D. Hesse, H. Jander, B. Lüers, J. Pietscher, H.Gg. Wagner, and M. Weis (1988). The influence of pressure and temperature on soot formation in premixed flames. *Twenty-second Symposium (International) on Combustion*, The Combustion Institute, Pittsburgh, PA, 403-411.
- Bonne, U., K.H. Homann, and H.Gg. Wagner (1965). Carbon formation in premixed flames. *Tenth Symposium (International) on Combustion*, The Combustion Institute, Pittsburgh, PA, 503-512.
- Brezinsky, K. (1986). The high temperature oxidation of aromatic hydrocarbons. *Prog. Energy Combust. Sci.*, **12**, 1-24.
- Bridge, N.J., and A.D. Buckingham (1966). The polarization of laser light scattered by gases. *Proc. R. Soc. Lond. A*, **295**, 334-349.
- Burgess, A.R., and C.J. Langley (1991). The chemical structure of premixed fuel-rich methane flames: the effect of hydrocarbon species in the secondary reaction zone. *Proc. R. Soc. Lond. A*, **433**, 1-21.
- Calcote, H.F. (1981). Mechanisms of soot nucleation in flames - a critical review. *Combust. Flame*, **42**, 215-242.
- Carter, C.D. (1990). Saturated fluorescence measurements of the hydroxyl radical in laminar high-pressure flames. Ph.D. dissertation, School of Mechanical Engineering, Purdue University, West Lafayette, Indiana.
- Charalampopoulos, T.T. (1992). Morphology and dynamics of agglomerated particulates in combustion systems using light scattering techniques. *Prog. Energy Combust. Sci.*, **18**, 13-45.
- Charalampopolous, T.T., and H. Chang (1988). In situ optical properties of soot particles in the wavelength range from 340 nm to 600 nm. *Combust. Sci. Tech.*, **59**, 401-421.

- Charalampopoulos, T.T., H. Chang, and B. Stagg (1989). The effects of temperature and composition on the complex refractive index of flame soot. *Fuel*, **68**, 1173-1179.
- Charalampopoulos, T.T., and J.D. Felske (1987). Refractive indices of soot particles deduced from in-situ laser light scattering measurements. *Combust. Flame*, **68**, 283-294.
- Chevalier, C., and J. Warnatz (1991). A tentative detailed chemical scheme for the oxidation of benzene-air mixtures. American Chemical Society, Preprints, Fuel Chemistry Division, **36**, 1486-1493.
- Chippett, S., and W.A. Gray (1978). The size and optical properties of soot particles. *Combust. Flame*, **31**, 149-159.
- Coe, D.S., and J.I. Steinfeld (1980). Fluorescence excitation and emission spectra of polycyclic aromatic hydrocarbons at flame temperatures. *Chem. Phys. Lett.*, **76**, 485-489.
- Coe, D.S., B.S. Haynes, and J.I. Steinfeld (1981). Identification of a source of argon-ion-laser excited fluorescence in sooting flames. *Combust. Flame*, **43**, 211-214.
- Coleman, H.W., and W.G. Steele, Jr. (1989). *Experimentation and Uncertainty Analysis for Engineers*. John Wiley & Sons, New York.
- Colket, M.B. (1986). The pyrolysis of acetylene and vinylacetylene in a single-pulse shock tube. *Twenty-first Symposium (International) on Combustion*, The Combustion Institute, Pittsburgh, PA, 851-864.
- Coxon, J.A. (1980). Optimum molecular constants and term values for the $X^2\Pi(v \leq 5)$ and $A^2\Sigma^+(v \leq 3)$ states of OH. *Can. J. Phys.*, **58**, 933-949.
- Crumley, W.H., and J.L. Gole (1986). Self-flushing optical window to prevent collection of condensates. *Rev. Sci. Instrumen.*, **57**, 1692-1693.
- Cummings, W.G., P.E. Sojka, and A.H. Lefebvre (1987). The influence of temperature and pressure on incipient soot formation in premixed flames. Presented at Spring meeting, Central States Section, The Combustion Institute, Argonne, Illinois.
- D'Alessio, A. (1981). Laser light scattering and fluorescence diagnostics of rich flames produced by gaseous and liquid fuels. In *Particulate Carbon Formation During Combustion*, D.C. Siegl and G.W. Smith, ed. Plenum Press, New York, 207-259.
- D'Alessio, A., A. DiLorenzo, F. Beretta, and C. Venitozzi (1972). Optical and chemical investigations on fuel rich methane-oxygen premixed flames at atmospheric pressure. *Fourteenth Symposium (International) on Combustion*, The Combustion Institute, Pittsburgh, PA, 941-953.
- Dalzell, W.H., and A.F. Sarofim (1969). Optical constants of soot and their application to heat-flux calculations. *J. Heat Transfer*, **91**, 100-104.
- Dasch, C.J. (1985). The decay of soot surface growth reactivity and its importance in total soot formation. *Combust. Flame*, **61**, 219-235.

- Delfau, J.L., and C. Vovelle (1984). Mechanism of soot formation in premixed C_2H_2/O_2 flames. *Combust. Sci. Tech.*, **41**, 1-15.
- Dibble, R.W., and R.E. Hollenbach (1981). Laser Rayleigh thermometry in turbulent flames. *Eighteenth Symposium (International) on Combustion*, The Combustion Institute, Pittsburgh, PA, 1489-1499.
- Dieke, G.H., and H.M. Crosswhite (1962). The ultraviolet bands of OH: fundamental data. *J. Quant. Spectrosc. Radiat. Transfer*, **2**, 97-199.
- DiLorenzo, A., A. D'Alessio, V. Cincotti, S. Masi, P. Menna, and C. Venitozzi (1981). UV absorption, laser excited fluorescence, and direct sampling in the study of the formation of polycyclic aromatic hydrocarbons in rich CH_4/O_2 flames. *Eighteenth Symposium (International) on Combustion*, The Combustion Institute, Pittsburgh, PA, 485-491.
- Dobbins, R.A., and C.M. Megaridis (1987). Morphology of flame-generated soot as determined by thermophoretic sampling. *Langmuir*, **3**, 254-259.
- Dobbins, R.A., and C.M. Megaridis (1991). Absorption and scattering of light by polydisperse aggregates. *Appl. Opt.*, **30**, 4747-4754.
- Dobbins, R.A., and G.W. Mulholland (1984). Interpretation of optical measurements of flame generated particles. *Combust. Sci. Tech.*, **40**, 175-191.
- Dobbins, R.A., R.J. Santoro, and H.G. Semerjian (1990). Analysis of light scattering from soot using optical cross-sections for aggregates. *Twenty-third Symposium (International) on Combustion*, The Combustion Institute, Pittsburgh, PA, 1525-1532.
- Drake, M.C., and R.J. Blint (1991). Calculations of NO_x formation pathways in propagating laminar, high pressure premixed CH_4 /air flames. *Combust. Sci. Tech.*, **75**, 261-285.
- Drake, M.C., and R.W. Pitz (1985). Comparison of turbulent diffusion flame measurements of OH by planar fluorescence and saturated fluorescence. *Experiments in Fluids*, **3**, 283-292.
- Drake, M.C., J.W. Ratcliffe, R.J. Blint, C.D. Carter, and N.M. Laurendeau (1990). Measurements and modeling of flamefront NO formation and superequilibrium radical concentrations in laminar high-pressure premixed flames. *Twenty-third Symposium (International) on Combustion*, The Combustion Institute, Pittsburgh, PA, 387-395.
- Ebert, L.B., J.C. Scanlon, and C.A. Clausen (1988). Combustion tube soot from a diesel fuel/air mixture: issues in structure reactivity. *Energy and Fuels*, **2**, 438-445.
- Eckbreth, A.C. (1988). *Laser Diagnostics for combustion temperature and species*. Abacus Press, Cambridge, Massachusetts, 305-325.
- Frenklach, M. (1985). Dynamics of discrete distribution for Smoluchowski coagulation model. *J. Colloid Interface Sci.*, **108**, 237-242.

- Frenklach, M. (1988). On the driving force of PAH production. *Twenty-second Symposium (International) on Combustion*, The Combustion Institute, Pittsburgh, PA, 1075-1082.
- Frenklach, M., and L.B. Ebert (1988). Comment on the proposed role of spheroidal carbon clusters in soot formation. *J. Phys. Chem.*, **92**, 561-563.
- Frenklach, M., D.W. Clary, W.C. Gardiner, Jr., and S.E. Stein (1984). Detailed kinetic modeling of soot formation in shock-tube pyrolysis of acetylene. *Twentieth Symposium (International) on Combustion*, The Combustion Institute, Pittsburgh, PA, 887-901.
- Frenklach, M., D.W. Clary, T. Yuan, W.C. Gardiner, Jr., and S.E. Stein (1986). Mechanism of soot formation in acetylene-oxygen mixtures. *Combust. Sci. Tech.*, **50**, 79-115.
- Frenklach, M., and H. Wang (1990). Detailed modeling of soot particle nucleation and growth. *Twenty-third Symposium (International) on Combustion*, The Combustion Institute, Pittsburgh, PA, 1559-1566.
- Frenklach, M., and J. Warnatz (1987). Detailed modeling in PAH profiles in a sooting low-pressure acetylene flame. *Combust. Sci. Tech.*, **51**, 265-283.
- Gardiner, W.C., Jr., Y. Hidaka, and T. Tazawa (1981). Refractivity of combustion gases. *Combust. Flame*, **40**, 213-219.
- Garland, N.L., and D.R. Crosley (1986). On the collisional quenching of electronically excited OH, NH and CH in flames. *Twenty-first Symposium (International) on Combustion*, The Combustion Institute, Pittsburgh, PA, 1693-1702.
- Glarborg, P., J.A. Miller, and R.J. Kee (1986). Kinetic modeling and sensitivity analysis of nitrogen oxide formation in well-stirred reactors. *Combust. Flame*, **65**, 177-202.
- Glassman, I. (1988). Soot formation in combustion processes. *Twenty-second Symposium (International) on Combustion*, The Combustion Institute, Pittsburgh, PA, 295-311.
- Gordon, S. and B.J. McBride (1971). Computer program for calculation of complex chemical equilibrium compositions, rocket performance, incident and reflected shocks, and Chapman-Jouget detonations. NASA SP-273.
- Graham, S.C. (1977). The collisional growth of soot particles at high temperatures. *Sixteenth Symposium (International) on Combustion*, The Combustion Institute, Pittsburgh, PA, 663-669.
- Graham, S.C., J.B. Homer, and J.L.J. Rosenfeld (1975). The formation and coagulation of soot aerosols generated by the pyrolysis of aromatic hydrocarbons. *Proc. R. Soc. Lond. A*, **344**, 259-285.
- Graham, S.C., and A. Robinson (1976). A comparison of numerical solutions to the self-preserving size distribution for aerosol coagulation in the free-molecule regime. *J. Aerosol Sci.*, **7**, 261-273.

- Habib, Z.G., and P. Vervisch (1988). On the refractive index of soot at flame temperature. *Combust. Sci. Tech.*, **59**, 261-274.
- Harris, J.M., F.E. Lytle, and T.C. McCain (1976). Squirrel-cage photomultiplier base design for measurement of nanosecond fluorescence decays. *Anal. Chem.*, **48**, 2095-2098.
- Harris, J.M., W.T. Barnes Jr., T.L. Gustafson, T.H. Bushaw, and F.E. Lytle (1980). Simple, inexpensive photodetector for subnanosecond sources. *Rev. Sci. Instrum.*, **51**, 988-989.
- Harris, M.M., G.B. King, and N.M. Laurendeau (1986). Influence of temperature and hydroxyl radical concentration on incipient soot formation in premixed flames. *Combust. Flame*, **64**, 99-112.
- Harris, S.J. (1986). Soot particle inception profiles and O₂ profiles in premixed ethylene flames. *Combust. Flame*, **66**, 211-214.
- Harris, S.J. (1990). Surface growth and particle reactivity. *Combust. Sci. Tech.*, **72**, 67-77.
- Harris, S.J., and I.M. Kennedy (1988). The coagulation of soot particles with van der Waals forces. *Combust. Sci. Tech.*, **59**, 443-454.
- Harris, S.J., and A.M. Weiner (1983a). Surface growth of soot particles in premixed ethylene/air flames. *Combust. Sci. Tech.*, **31**, 155-167.
- Harris, S.J., and A.M. Weiner (1983b). Determination of the rate constant for soot surface growth. *Combust. Sci. Tech.*, **32**, 267-275.
- Harris, S.J., and A.M. Weiner (1984). Soot particle growth in premixed toluene/ethylene flames. *Combust. Sci. Tech.*, **38**, 75-87.
- Harris, S.J., and A.M. Weiner (1985). Chemical kinetics of soot particle growth. *Ann. Rev. Phys. Chem.*, **36**, 31-52.
- Harris, S.J., and A.M. Weiner (1988). A picture of soot particle inception. *Twenty-second Symposium (International) on Combustion*, The Combustion Institute, Pittsburgh, PA, 333-342.
- Harris, S.J., A.M. Weiner, and C.C. Ashcraft (1986). Soot particle inception kinetics in a premixed ethylene flame. *Combust. Flame*, **64**, 65-81.
- Harris, S.J., A.M. Weiner, and R.J. Blint (1988). Formation of small aromatic molecules in a sooting ethylene flame. *Combust. Flame*, **72**, 91-109.
- Harris, S.J., A.M. Weiner, R.J. Blint, and J.E.M. Goldsmith (1986). Concentration profiles in rich and sooting ethylene flames. *Twenty-first Symposium (International) on Combustion*, The Combustion Institute, Pittsburgh, PA, 1033-1045.
- Haynes, B.S., H. Jander, and H.Gg. Wagner (1980). Optical studies of soot-formation processes in premixed flames. *Ber. Bunsenges. Phys. Chem.*, **84**, 585-592.

- Haynes, B.S., and H.Gg. Wagner (1980). Sooting structure in a laminar diffusion flame. *Ber. Bunsenges. Phys. Chem.*, **84**, 449-506.
- Haynes, B.S., and H.Gg. Wagner (1981). Soot formation. *Prog. Energy Combust. Sci.*, **7**, 229-273.
- Haynes, B.S., and H.Gg. Wagner (1982). The surface growth phenomenon in soot formation. *Zeitschrift für Physikalische Chemie Neue Folge*, **133**, 201-213.
- Hodges, J., and D. Foster (1987). Soot coagulation with surface growth kinetics. *Combust. Sci. Tech.*, **51**, 235-249.
- Homann, K.H. (1967). Carbon formation in premixed flames. *Combust. Flame*, **11**, 265-287.
- Homann, K.H. (1984). Formation of large molecules, particulates, and ions in premixed hydrocarbon flames: progress and unresolved questions. *Twentieth Symposium (International) on Combustion*, The Combustion Institute, Pittsburgh, PA, 857-870.
- Homann, K.H., and H.Gg. Wagner (1967). Some new aspects of the mechanism of carbon formation in premixed flames. *Eleventh Symposium (International) on Combustion*, The Combustion Institute, Pittsburgh, PA, 371-379.
- Horowitz, P., and W. Hill (1989). *The Art of Electronics*. Cambridge University Press, New York.
- Howard, J.B. (1990). Carbon addition and oxidation reactions in heterogeneous combustion and soot formation. *Twenty-third Symposium (International) on Combustion*, The Combustion Institute, Pittsburgh, PA, 1107-1127.
- Howard, J.B., J.T. McKinnon, Y. Makarovskiy, A.L. Lafleur, and M.E. Johnson (1991). Fullerenes C₆₀ and C₇₀ in flames. *Nature*, **352**, 139-141.
- Huffman, D.R. (1991). Solid C₆₀. *Physics Today*, **44**, 22-29.
- Hura, H.S., and I. Glassman (1987). Fuel oxygen effects on soot formation in counterflow diffusion flames. *Combust. Sci. Tech.*, **53**, 1-21.
- Inbody, M.A., M.M. Harris, G.B. King, and N.M. Laurendeau (1986). Measurement of hydroxyl radical concentration profiles by laser saturated fluorescence in subatmospheric, nonsooting and sooting acetylene and ethylene flames. Presented at Spring Meeting, Central States Section, The Combustion Institute, Cleveland OH, Paper 10-C1
- Janssen, J.M. (1991). Incipient soot formation in halogen bearing premixed laminar flames. Ph.D. dissertation, School of Mechanical Engineering, Purdue University, West Lafayette, Indiana.
- Janssen, J.M., and D.W. Senser (1991). Incipient soot formation in dichloromethane-methane-air premixed flames. *Combust. Flame*, **84**, 265-276.
- Janzen, J. (1979). The refractive index of colloidal carbon. *J. Colloid. Int. Sci.*, **69**, 436-447.

- Jones, A.R. (1979). Scattering of electromagnetic radiation in particulate laden fluids. *Prog. Energy Combust. Sci.*, **5**, 73-96.
- Kee, R.J., F.M. Rupley, and J.A. Miller (1987). The Chemkin thermodynamic data base. Sandia National Laboratories report SAND87-8215B.
- Kee, R.J., F.M. Rupley, and J.A. Miller (1989). Chemkin-II: a Fortran chemical kinetics package for the analysis of gas-phase chemical kinetics. Sandia National Laboratories report SAND89-8009.
- Kee, R.J., G. Dixon-Lewis, J. Warnatz, M.E. Coltrin, and J.A. Miller (1986). A Fortran computer code package for the evaluation of gas-phase multicomponent transport properties. Sandia National Laboratories report SAND86-8246.
- Kee, R.J., J.F. Grcar, M.D. Smooke, and J.A. Miller (1985). A Fortran program for modeling steady laminar one-dimensional premixed flames. Sandia National Laboratories report SAND85-8240.
- Kee, R.J., J. Warnatz, and J.A. Miller (1983). A Fortran computer program package for the evaluation of gas-phase viscosities, conductivities, and diffusion coefficients. Sandia National Laboratories report SAND83-8209.
- Kerker, M. (1969). *The Scattering of Light and Other Electromagnetic Radiation*. Academic Press, New York.
- Kern, R.D., H.J. Singh, and C.H. Wu (1988). Thermal decomposition of 1,2 butadiene. *Int. J. Chem. Kin.*, **20**, 731-747.
- Kern, R.D., K. Xie, and H. Chen (1991). The reactions of propargyl chloride and 1,5 hexadiyne behind reflected shock waves. American Chemical Society, Preprints, Fuel Chemistry Division, **36**, 1423-1432.
- Kroto, H.W., J.R. Heath, S.C. O'Brien, R.F. Curl, and R.E. Smalley (1985). C₆₀: buckminsterfullerene. *Nature*, **318**, 162-163.
- Lam, F.W., J.B. Howard, and J.P. Longwell (1988). The behavior of polycyclic aromatic hydrocarbons during the early stages of soot formation. *Twenty-second Symposium (International) on Combustion*, The Combustion Institute, Pittsburgh, PA, 323-332.
- Laurendeau, N.M., and J.E.M. Goldsmith (1989). Comparison of hydroxyl concentration profiles using five laser-induced fluorescence methods in a lean subatmospheric-pressure H₂/O₂/Ar flame. *Combust. Sci. Tech.*, **63**, 139-152.
- Lee, S.C., and C.L. Tien (1981). Optical constants of soot in hydrocarbon flames. *Eighteenth Symposium (International) on Combustion*, The Combustion Institute, Pittsburgh, PA, 1159-1166.
- Longwell, J.P. (1983). Polycyclic aromatic hydrocarbons and soot from practical combustion systems. In *Soot in Combustion Systems and its Toxic Properties* J. Lahaye and G. Prado, ed. Plenum Press, New York, 37-56.

- Lucht, R.P., D.W. Sweeney, and N.M. Laurendeau (1985). Laser-saturated fluorescence measurements of OH in atmospheric pressure $\text{CH}_4/\text{O}_2/\text{N}_2$ flames under sooting and nonsooting conditions. *Combust. Sci. Tech.*, **42**, 259-281.
- McKinnon, J.T. (1989). Chemical and physical mechanisms of soot formation. Ph.D. dissertation. Department of Chemical Engineering, Massachusetts Institute of Technology, Cambridge, Massachusetts.
- McKinnon, J.T., and J.B. Howard (1990). Application of soot formation model: effects of chlorine. *Combust. Sci. Tech.*, **74**, 175-197.
- Megaridis, C.M., and R.A. Dobbins (1989). An integral solution of the aerosol dynamic equation including surface growth reactions. *Combust. Sci. Tech.*, **63**, 153-167.
- Miller, J.A., and C.F. Melius (1991). The formation of benzene in flames. American Chemical Society, Preprints, Fuel Chemistry Division, **36**, 1440-1447.
- Miller, J.A., and C.F. Melius (1992). Kinetic and thermodynamic issues in the formation of aromatic compounds in flames of aliphatic fuels. *Combust. Flame*, submitted.
- Miller, J.A., J.V. Volponi, J.L. Durant, Jr., J.E.M. Goldsmith, G.A. Fisk, and R.J. Kee (1990). The structure and reaction mechanism of rich, non-sooting $\text{C}_2\text{H}_2/\text{O}_2/\text{Ar}$ flames. *Twenty-third Symposium (International) on Combustion*, The Combustion Institute, Pittsburgh, PA, 187-194.
- Miller, J.H. (1990). The kinetics of polynuclear aromatic hydrocarbon agglomeration in flames. *Twenty-third Symposium (International) on Combustion*, The Combustion Institute, Pittsburgh, PA, 91-98.
- Miller, J.H., W.G. Mallard, and K.C. Smyth (1982). The observation of laser-induced visible fluorescence in sooting diffusion flames. *Combust. Flame*, **47**, 205-214.
- Millikan, R.C. (1962). Non-equilibrium soot formation in premixed flames. *J. Phys. Chem.*, **66**, 794-799.
- Müller-Dethlefs, K. (1979). Optical studies of soot formation and the addition of organic peroxides to flames. Ph.D. dissertation, Imperial College, London.
- Mullins, J., and A. Williams (1987). The optical properties of soot: a comparison between experimental and theoretical values. *Fuel*, **66**, 277-280.
- Olson, D.B., D.G. Keil, and H.F. Calcote (1984). The mechanism of soot formation: a workshop held 14, 15 June 1984 at Aerochem Research Laboratories. Aerochem Report TP-445, September 1984.
- Palmer, H.B., and C.F. Cullis (1965). The formation of carbon from gases. In *Chemistry and Physics of Carbon*, Vol. 1. P.L. Walker, Jr. ed. Marcel Dekker, New York, 265-325.
- Pfefferle, L.D., J. Boyle, and G. Bermudez (1991). Benzene formation during allene pyrolysis: possible implications for soot formation. American Chemical Society, Preprints, Fuel Chemistry Division, **36**, 1433-1439.

- Pott, P. (1775). *Chirurgical Observations*, reprinted in *National Cancer Inst. Monogr.*, **10**, 7, (1963).
- Prado, G., J. Jagoda, K. Neoh, and J. Lahaye (1981). A study of soot formation in premixed propane/oxygen flames by in-situ optical techniques and sampling probes. *Eighteenth Symposium (International) on Combustion*, The Combustion Institute, Pittsburgh, PA, 1127-1136.
- Prado, G., and J. Lahaye (1981). Physical aspects of nucleation and growth of soot particles. In *Particulate Carbon Formation during Combustion* D.C. Siegla and G.W. Smith, ed. Plenum Press, New York, 143-175.
- Rajan, S., J.R. Smith, and G.D. Rambach (1984). Internal structure of a turbulent premixed flame using Rayleigh scattering. *Combust. Flame*, **57**, 95-107.
- Ramer, E.R., J.F. Merklin, C.M. Sorenson, and T.W. Taylor (1986). Chemical and optical probing of premixed methane/oxygen flames. *Combust. Sci. Tech.*, **48**, 241-255.
- Rudder, R.R., and D.R. Bach (1968). Rayleigh scattering of ruby-laser light by neutral gases. *J. Opt. Soc. Am.*, **58**, 1260-1266.
- Santoro, R.J., H.G. Semerjian, and R.A. Dobbins (1983). Soot particle measurements in diffusion flames. *Combust. Flame*, **51**, 203-218.
- Schwarzwald, R., P. Monkhouse, and J. Wolfrum (1988). Fluorescence studies of OH and CN radicals in atmospheric pressure flames using picosecond excitation. *Twenty-second Symposium (International) on Combustion*, The Combustion Institute, Pittsburgh, 1413-1422.
- Scrivner, S.M., T.W. Taylor, C.M. Sorenson, and J.F. Merklin (1986). Soot particle size distribution measurements in a premixed flame using photon correlation spectroscopy. *Appl. Opt.*, **25**, 291-297.
- Smith, G.P., and D.R. Crosley (1986). Quenching of OH ($A^2\Sigma^+$, $v' = 0$) by H_2 , N_2O , and hydrocarbons at elevated temperatures. *J. Chem. Phys.*, **85**, 3896-3901.
- Smyth, K.C., P.J.H. Tjossem, A. Hamins, and J.H. Miller (1990). Concentration measurements of OH- and equilibrium analysis in a laminar methane-air diffusion flame. *Combust. Flame*, **79**, 366-380.
- Stanford Research Systems (1988). Fast gated integrators and boxcar averagers. Stanford Research Systems, 1290 D Reamwood Ave., Sunnyvale, CA 94089.
- Stein, S.E., and A. Fahr (1985). High-temperature stabilities of hydrocarbons. *J. Phys. Chem.*, **89**, 3714-3725.
- Stein, S.E., J.A. Walker, M.M. Suryan, and A. Fahr (1990). A new path to benzene in flames. *Twenty-third Symposium (International) on Combustion*, The Combustion Institute, Pittsburgh, PA, 85-90.
- Stepowski, D. and M.J. Cottureau (1981). Study of the collisional lifetime of hydroxyl ($^2\Sigma^+$, $v' = 0$) radicals in flames by time-resolved laser-induced fluorescence. *Combust. Flame*, **40**, 65-70.

- Takahashi, F., and I. Glassman (1984). Sooting correlations for premixed flames. *Combust. Sci. Tech.*, **37**, 1-19.
- Thomas, S.D., F. Communal, and P.R. Westmoreland (1991). C_3H_3 reaction kinetics in fuel-rich combustion. American Chemical Society, Preprints, Fuel Chemistry Division, **36**, 1448-1455.
- Tsang, W., and J.A. Walker (1991). The thermal decomposition of 1,7 octadiyne as a source of propargyl radicals. American Chemical Society, Preprints, Fuel Chemistry Division, **36**, 1415-1422.
- Vaughn, C.B., J.B. Howard, and J.P. Longwell (1991). Benzene destruction in fuel-rich jet-stirred reactor combustion. *Combust. Flame*, **87**, 278-288.
- Vaughn, C.B., W.H. Sun, J.B. Howard, and J.P. Longwell (1991). Measurement and modeling of light hydrocarbons in rich C_2H_4 combustion in a jet-stirred reactor. *Combust. Flame*, **84**, 38-46.
- Warchold, J.J., and J.J. Reuther (1984). Effect of sub-atmospheric pressure on soot and hydroxyl concentrations in quenched, premixed ethane/air flat flames. *Combust. Sci. Tech.*, **38**, 325-336.
- Warnatz, J. (1984). Chemistry of high temperature combustion of alkanes up to octane. *Twentieth Symposium (International) on Combustion*, The Combustion Institute, Pittsburgh, PA, 845-856.
- Weiner, A.M., and S.J. Harris (1989). Optical detection of large soot precursors. *Combust. Flame*, **77**, 261-266.
- Wersborg, B.L., J.B. Howard, and G.C. Williams (1973). Physical mechanisms in carbon formation in flames. *Fourteenth Symposium (International) on Combustion*, The Combustion Institute, Pittsburgh, PA, 929-940.
- Westmoreland, P.R., A.M. Dean, J.B. Howard, and J.P. Longwell (1989). Forming benzene in flames by chemically activated isomerization. *J. Phys. Chem.*, **93**, 8171-8180.
- Westmoreland, P.R., J.B. Howard, and J.P. Longwell (1986). Tests of published mechanisms by comparison with measured laminar flame structure in fuel-rich acetylene combustion. *Twenty-first Symposium (International) on Combustion*, The Combustion Institute, Pittsburgh, PA, 773-782.
- Wieschnowsky, U., H. Bockhorn, and F. Fetting (1988). Some new observations concerning the mass growth of soot in premixed hydrocarbon-oxygen flames. *Twenty-second Symposium (International) on Combustion*, The Combustion Institute, Pittsburgh, PA, 343-352.
- Woods, I.T., and B.S. Haynes (1991). Soot surface growth at active sites. *Combust. Flame*, **85**, 523-525.
- Wu, H.C., and R.D. Kern (1987). Shock-tube study of allene. *J. Phys. Chem.*, **91**, 6291-6296.

Zhang, Q.L., S.C. O'Brien, J.R. Heath, Y. Liu, R.F. Curl, H.W. Kroto, and R.E. Smalley (1986). Reactivity of large carbon clusters: spheroidal carbon shells and their possible relevance to the formation and morphology of soot. *J. Phys. Chem.*, **90**, 525-528.



APPENDICES

Appendix A: Flow Rate Uncertainty Analysis

Our experimental approach was to measure soot and hydroxyl concentrations in sequences of flames where we varied the equivalence ratio from nonsooting to sooting while keeping the cold flow velocity and dilution ratio constant. The equivalence ratio, cold flow velocity, and dilution ratio for a flame were set by setting the flow rates of the fuel (ethylene), oxidizer (oxygen), and diluent (nitrogen). These flow rates along with the pressure were the variables that could be controlled directly. The uncertainties in these flow rates and also in the equivalence ratio, cold flow velocity, and dilution ratio are important when comparing the results from the flames. They are equally important in the flame code simulations, because they can also be used to establish the uncertainties in those results.

Because the measurements of the hydroxyl concentration and the soot concentration were made on different days, the uncertainty in reproducibility of the flow rates indicates the extent to which the separate measurements were made in the same flame. This uncertainty depends on the precision of the flow rates set by the electronic mass flow controllers. We selected the mass flow controllers for their high precision to achieve a better reproducibility of the flow rates than was possible using rotameters. We are also interested in the accuracy of the flow rates set by the mass flow controllers. The mass flow controllers were calibrated for the conditions of our experiments which were not the same as the conditions of the factory calibration. The accuracy of the flow rates will then depend on the uncertainty in the calibration at the conditions of our experiments. However, since the flow controllers were calibrated against the same standard, the accuracy of the individual flow rates has only a minimal effect on the accuracy of the equivalence ratio and the dilution ratio, because they are ratios of flow rates.

The uncertainty (or error) in an experimental result can be evaluated by considering the uncertainties of its independent variables. An experimental result can be expressed as a function, f , of the independent experimental variables, x_1, x_2, \dots, x_n , i.e.,

$$f = f(x_1, x_2, \dots, x_n) \quad . \quad (\text{A.1})$$

If the variables x_i and the uncertainties in those variables are independent of each other, then the uncertainty in the experimental result, δf , is (Coleman and Steele, 1989)

$$\delta f = \left[\left(\frac{\partial f}{\partial x_1} \cdot \delta x_1 \right)^2 + \left(\frac{\partial f}{\partial x_2} \cdot \delta x_2 \right)^2 + \dots + \left(\frac{\partial f}{\partial x_n} \cdot \delta x_n \right)^2 \right]^{1/2} \quad (\text{A.2})$$

where δx_i , $i = 1, \dots, n$, are the uncertainties in the variables evaluated at the same confidence level.

We define the total flow rate through the burner, \dot{V}_{TOT} , as the sum of the fuel flow rate, \dot{V}_F , the oxidizer flow rate, \dot{V}_O , and the diluent flow rate, \dot{V}_D , and, thus,

$$\dot{V}_{TOT} = \dot{V}_F + \dot{V}_O + \dot{V}_D \quad . \quad (\text{A.3})$$

These flow rates ($\text{l}\cdot\text{min}^{-1}$) are at standard temperature (25°C) and pressure (760 torr). The uncertainty in the total flow rate is then

$$\delta \dot{V}_{TOT} = [(\delta \dot{V}_F)^2 + (\delta \dot{V}_O)^2 + (\delta \dot{V}_D)^2]^{1/2} \quad . \quad (\text{A.4})$$

The cold flow velocity is defined as the total flow rate at standard temperature (25°C) and the pressure of the experiment divided by the cross-sectional area of the burner. The cold flow velocity, v_c ($\text{cm}\cdot\text{sec}^{-1}$) is given by

$$v_c = \dot{V}_{TOT} \cdot \frac{P_{STP}}{P_{exp}} \cdot \frac{4}{\pi d^2} \quad (\text{A.5})$$

where P_{STP} is the standard pressure (760 torr), P_{exp} (torr) is the pressure of the experiment, and d (cm) is the diameter of the burner. The uncertainty in the cold flow velocity can be expressed in terms of the fractional uncertainties as

$$\frac{\delta v_c}{v_c} = \left[\left(\frac{\delta \dot{V}_{TOT}}{\dot{V}_{TOT}} \right)^2 + \left(\frac{\delta P_{exp}}{P_{exp}} \right)^2 + \left(2 \frac{\delta d}{d} \right)^2 \right]^{1/2} \quad . \quad (\text{A.6})$$

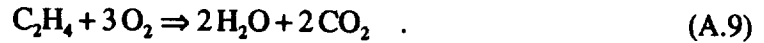
The equivalence ratio is the actual ratio of the fuel to oxidizer flow rates divided by the stoichiometric ratio and is given by

$$\phi = \left(\frac{\dot{V}_F}{\dot{V}_O} \right)_{actual} \cdot \left(\frac{\dot{V}_F}{\dot{V}_O} \right)_{stoich}^{-1} \quad (A.7)$$

where the stoichiometric ratio for ethylene,

$$\left(\frac{\dot{V}_F}{\dot{V}_O} \right)_{stoich} = \frac{1}{3} \quad (A.8)$$

is based on the stoichiometric equation for ethylene combustion,



The uncertainty in the equivalence ratio when expressed as a fractional uncertainty is

$$\frac{\delta\phi}{\phi} = \left[\left(\frac{\delta\dot{V}_F}{\dot{V}_F} \right)^2 + \left(\frac{\delta\dot{V}_O}{\dot{V}_O} \right)^2 \right]^{1/2} \quad (A.10)$$

We have defined the dilution ratio to be the ratio of the diluent flow rate to the oxidizer flow rate, and thus,

$$D = \frac{\dot{V}_D}{\dot{V}_O} \quad (A.11)$$

where D is the dilution ratio. The fractional uncertainty in the dilution ratio is

$$\frac{\delta D}{D} = \left[\left(\frac{\delta\dot{V}_D}{\dot{V}_D} \right)^2 + \left(\frac{\delta\dot{V}_O}{\dot{V}_O} \right)^2 \right]^{1/2} \quad (A.11)$$

The flow rates are also used to determine the inlet boundary conditions for the differential equations solved by the Sandia premixed one-dimensional flame code (Kee et al., 1985). The mole fractions of the reactants and the mass flux through the burner are the required inputs to determine the boundary conditions. The mole fractions for the reactants are given by

$$X_F = \frac{\dot{V}_F}{\dot{V}_{TOT}} \quad (A.12)$$

where X_F is the fuel mole fraction,

$$X_O = \frac{\dot{V}_O}{\dot{V}_{TOT}} \quad (\text{A.13})$$

where X_O is the oxidizer mole fraction, and

$$X_D = \frac{\dot{V}_D}{\dot{V}_{TOT}} \quad (\text{A.14})$$

where X_D is the diluent mole fraction. The fractional uncertainty in the fuel mole fraction is

$$\frac{\delta X_F}{X_F} = \left[\left(\frac{\delta \dot{V}_F}{\dot{V}_F} \right)^2 + \left(\frac{\delta \dot{V}_{TOT}}{\dot{V}_{TOT}} \right)^2 \right]^{1/2} \quad (\text{A.15})$$

The fractional uncertainties for the oxidizer and diluent mole fractions are similar. The mass flux through the burner is the total mass flow rate of the reactants divided by the area of the burner and is given by

$$q_m = \frac{4}{\pi d^2} \cdot \frac{P_{STP}}{RT_{STP}} \cdot (\dot{V}_F \cdot W_F + \dot{V}_O \cdot W_O + \dot{V}_D \cdot W_D) \quad (\text{A.16})$$

where q_m is the mass flux ($\text{gm}\cdot\text{cm}^{-2}\cdot\text{sec}^{-1}$), P_{STP} (atm) is the standard pressure and T_{STP} (K) is the standard temperature, R is the gas constant ($\text{cm}^3\cdot\text{atm}\cdot\text{K}^{-1}\cdot\text{gmole}^{-1}$), and W_F , W_O , and W_D are the molecular weights ($\text{gm}\cdot\text{gmole}^{-1}$) of the fuel, oxidizer, and diluent, respectively.

The uncertainty in the mass flux is then given by

$$\delta q_m = \frac{4}{\pi d^2} \cdot \frac{P_{STP}}{RT_{STP}} \cdot [(\dot{V}_F \cdot W_F + \dot{V}_O \cdot W_O + \dot{V}_D \cdot W_D)^2 \cdot \left(2 \frac{\delta d}{d} \right)^2 + (W_F \cdot \delta \dot{V}_F)^2 + (W_O \cdot \delta \dot{V}_O)^2 + (W_D \cdot \delta \dot{V}_D)^2]^{1/2} \quad (\text{A.17})$$

The mass flow controllers were calibrated by measuring the volume flow rates with a Singer-American DT-115M dry-test meter for flow rates greater than $1.0 \text{ l}\cdot\text{min}^{-1}$ and with a 500 ml Supelco bubble flow meter for flow rates less than $1.0 \text{ l}\cdot\text{min}^{-1}$. Each mass flow controller was calibrated at a flow rate setting by measuring the time for a given

volume to flow through the meter. The flow rates were corrected to STP conditions by measuring the temperature and pressure of the gas flow during the calibration. The flow rate determined from the calibration, V_{STP} ($\text{l}\cdot\text{min}^{-1}$), is given by

$$\dot{V}_{STP} = \frac{n \cdot V_{fm}}{t} \cdot \frac{P_c}{P_{STP}} \cdot \frac{T_{STP}}{T_c} \quad (\text{A.18})$$

where V_{fm} is the volume of the flow meter (l), n is the number of flow meter volumes measured (revolutions of the flow meter), t is the time (min), P_c and T_c are the pressure (torr) and temperature (K) of the gas flow during calibration, and P_{STP} and T_{STP} are the standard pressure (760 torr) and temperature (298 K). Expressing the flow rate in this way allows us to calculate the uncertainty of the flow rate based on the uncertainty in the flow meter volume. The fractional uncertainty in the calibrated flow rate is given by

$$\frac{\delta \dot{V}_{STP}}{\dot{V}_{STP}} = \left[\left(\frac{\delta n}{n} \right)^2 + \left(\frac{\delta V_{fm}}{V_{fm}} \right)^2 + \left(\frac{\delta t}{t} \right)^2 + \left(\frac{\delta P_c}{P_c} \right)^2 + \left(\frac{\delta T_c}{T_c} \right)^2 \right]^{1/2} \quad (\text{A.19})$$

Although the flow rates may have an error caused by the flow meter volume, the ratios of the flow rates will not as shown by the expression for the equivalence ratio in terms of the calibrated flow rates,

$$\phi = \frac{n_F}{n_O} \cdot \frac{t_O}{t_F} \cdot \frac{P_{cF}}{P_{cO}} \cdot \frac{T_{cO}}{T_{cF}} \quad (\text{A.20})$$

where the F subscript indicates the fuel and the O subscript indicates the oxidizer. Since most of the calibrations were made using the same number of flow meter revolutions, the terms n_F and n_O also cancel out. In addition, since the calibrations were made at very similar pressures and temperatures, the fractional uncertainties in those terms are approximately the same. The fractional uncertainty in the equivalence ratio caused by the flowmeter calibration is then given by

$$\frac{\delta \phi}{\phi} = \left[\left(\frac{\delta t_O}{t_O} \right)^2 + \left(\frac{\delta t_F}{t_F} \right)^2 + 2 \cdot \left(\frac{\delta P_c}{P_c} \right)^2 + 2 \cdot \left(\frac{\delta T_c}{T_c} \right)^2 \right]^{1/2} \quad (\text{A.22})$$

The fractional uncertainty in the dilution ratio will be similar.

We will consider the uncertainty in the precision of the above flow rate parameters separately from the uncertainty in the accuracy of those parameters. The uncertainty in the precision of the flow rates is a measure of the reproducibility of the experiments and is directly related to the precision of the flow rates set by the mass flow controllers. The manufacturer's specification for the repeatability of the flow rates is 0.25% of the mass flow controller reading and this is used as an estimate of the fractional uncertainty in the flow rates. The uncertainty in the experiment pressure is estimated to be 0.5 torr and is based on the ability to control the experiment pressure as stated in Sec. 3.2.4. The uncertainty in the burner diameter is set to zero for the precision calculation, because the same burner was used in all the experiments.

The flow rate parameters for three typical flames are listed in Table A.1 along with the uncertainty in the precision of those parameters. The three flames are the atmospheric lean flame (A-0-L) used for the OH fluorescence calibration, an atmospheric lightly sooting flame (A-IA-S1) and an 80-torr lightly sooting flame (L-II-S1). The uncertainties for the other flames will be similar to these typical flames, because the total flow rates and dilution ratio were held constant, while the equivalence ratio was varied. For these flames, the uncertainties in the precision of the flow rates are equal to or less than 0.25%. The uncertainties in the parameters calculated from the flow rates such as the equivalence ratio and the dilution ratio are equal to or less than 0.35%. The uncertainty in the cold flow velocities of the low pressure flames is higher ($\approx 0.65\%$) because the fractional uncertainty of the pressure is larger at lower pressures.

The uncertainties in the calibration of the flow rates are calculated from Eq. (A.19). The estimated uncertainties in the required independent variables are listed in Table A.2. The dry test meter was calibrated against the bubble flow meter by measuring a series of flow rates from $0.6 \text{ l}\cdot\text{min}^{-1}$ to $1.2 \text{ l}\cdot\text{min}^{-1}$ with both meters. The results of the calibration are shown in Figure A.1 and show that the dry test meter measured flow rates that were consistently 4% lower than those measured with the bubble flow meter. The volume of

the bubble flow meter was verified and thus the dry test meter flow rates were suitably corrected. The uncertainty in this correction is the root-sum-square of the uncertainties in the flow rate measurements of the two meters. This uncertainty is used as the uncertainty in the volume of the flow meter, V_{fm} .

The flow rate parameters of the three typical flames are listed again in Table A.3 along with the uncertainty in the accuracy of those parameters. The uncertainty in the accuracies of the flow rates are equal to or less than 0.90%. The uncertainty in the accuracy of the equivalence ratio and dilution ratio calculated from Eq. (A.22) is slightly less than the uncertainty in the precision of those terms ($\sim 0.35\%$). Since the accuracy cannot be better than the precision, the precision of the equivalence ratio and dilution ratio are listed in Table A.3. The accuracy uncertainties of the cold flow velocities and the mass fluxes are approximately 2.0%, because of the large uncertainty in the burner diameter.

In summary, the precision of the mass flow controllers ensured the reproducibility of the experiments. The accuracy of the flow rates, however, was not as good as the precision, primarily because of uncertainties in the calibration. The uncertainties in the calibration could be reduced by calibrating the mass flow controllers over the full range of flow rates with a more accurate flow meter such as a wet-test meter.

Table A.1 Flow rate parameters with their calculated precision uncertainties for three typical flames. The fractional uncertainties are given in parentheses.

Flame	A-O-L	A-IA-S1	L-II-S1
Flow Rates (l·min⁻¹)			
Fuel	0.627 ± 0.002 (0.25%)	1.176 ± 0.003 (0.25%)	1.515 ± 0.004 (0.25%)
Oxygen	1.941 ± 0.005 (0.25%)	1.984 ± 0.005 (0.25%)	1.962 ± 0.005 (0.25%)
Diluent	10.52 ± 0.026 (0.25%)	8.25 ± 0.021 (0.25%)	0.0
Total	13.08 ± 0.027 (0.20%)	11.41 ± 0.022 (0.19%)	3.477 ± 0.006 (0.18%)
Cold flow velocity (cm·sec ⁻¹)	8.86 ± 0.02 (0.21%)	7.73 ± 0.02 (0.21%)	22.4 ± 0.2 (0.65%)
Equivalence ratio	0.969 ± 0.003 (0.35%)	1.778 ± 0.006 (0.35%)	2.317 ± 0.008 (0.35%)
Dilution ratio	5.42 ± 0.02 (0.35%)	4.16 ± 0.02 (0.35%)	0.0
Mass flux (gm·cm ⁻² ·sec ⁻¹)	0.01036 ± 0.00002 (0.20%)	0.009061 ± 0.000017 (0.18%)	0.002916 ± 0.000005 (0.19%)
Mole fractions			
Fuel	0.0479 ± 0.0002 (0.32%)	0.1031 ± 0.0003 (0.32%)	0.4357 ± 0.0013 (0.30%)
Oxidizer	0.1483 ± 0.0005 (0.32%)	0.1739 ± 0.0006 (0.32%)	0.5643 ± 0.0017 (0.30%)
Diluent	0.8038 ± 0.0026 (0.32%)	0.7230 ± 0.0023 (0.32%)	0.0

Table A.2 Estimates of the uncertainties in the independent variables in the calibrated flow rates.

Variable	Typical value	Estimated Uncertainty	Fractional Uncertainty
n (rev)	16.0	0.02	0.00125
t (sec)	90 to 1530	0.1	0.0011 to 0.000065
P_c (torr)	749 to 754	1.5	0.002
T_c (K)	295	0.2	0.00068
V_{fm} (l)	1.0	0.008	0.008
d (cm)	5.6	0.05	0.0089

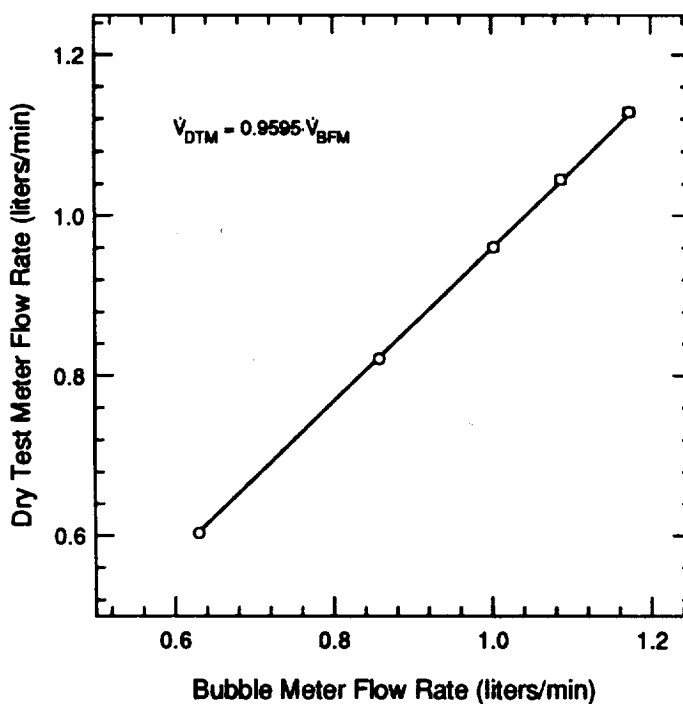


Figure A.1 Calibration of the dry test flow meter flow rates against the bubble meter flow rates.

Table A.3 Flow rate parameters with their calculated accuracy uncertainties for three typical flames. The fractional uncertainties are given in parentheses.

Flame	A-O-L	A-IA-S1	L-II-S1
Flow Rates (l·min ⁻¹)			
Fuel	0.627 ± 0.006 (0.90%)	1.176 ± 0.011 (0.90%)	1.515 ± 0.014 (0.90%)
Oxygen	1.941 ± 0.017 (0.90%)	1.984 ± 0.018 (0.90%)	1.962 ± 0.018 (0.90%)
Diluent	10.52 ± 0.045 (0.90%)	8.25 ± 0.074 (0.90%)	0.0
Total	13.08 ± 0.097 (0.74%)	11.41 ± 0.077 (0.67%)	3.477 ± 0.023 (0.66%)
Cold flow velocity (cm·sec ⁻¹)	8.86 ± 0.18 (2.03%)	7.73 ± 0.15 (2.00%)	22.4 ± 0.6 (2.67%)
Equivalence ratio	0.969 ± 0.003 (0.35%)	1.778 ± 0.006 (0.35%)	2.317 ± 0.008 (0.35%)
Dilution ratio	5.42 ± 0.02 (0.35%)	4.16 ± 0.02 (0.35%)	0.0
Mass flux (gm·cm ⁻² ·sec ⁻¹)	0.01036 ± 0.0002 (1.92%)	0.009061 ± 0.00017 (1.90%)	0.002916 ± 0.000055 (1.90%)
Mole fractions			
Fuel	0.0479 ± 0.0006 (1.17%)	0.1031 ± 0.0016 (1.12%)	0.4357 ± 0.0049 (1.12%)
Oxidizer	0.1483 ± 0.0017 (1.17%)	0.1739 ± 0.0020 (1.12%)	0.5643 ± 0.0063 (1.12%)
Diluent	0.8038 ± 0.0094 (1.17%)	0.7230 ± 0.0081 (1.12%)	0.0

Appendix B: Details of the Laser Scattering-Extinction Measurements

B.1 Introduction

In this appendix, we present the details of the laser scattering-extinction experimental apparatus and the data analysis. We first describe the photodetectors and the electronic circuits used to convert their current outputs to voltage outputs. We then describe the signal conditioning applied to the photodetector signals and then the acquisition of those signals by the computer. The analyses of the voltage signals to determine the extinction and scattering coefficients are presented next. Finally, we present the uncertainties and detection limits for the extinction and scattering coefficients.

B.2 Photodetectors and Photodetector Electronics

Three detectors were used in the laser scattering-extinction measurements. A 'reference' photodiode monitored the incident laser irradiance. A 'transmittance' photodiode monitored the transmitted laser irradiance. A photomultiplier detected the scattered light at the output of the monochromator. Photodiodes were used to measure the laser irradiance because a photodiode has a greater linear range than a photomultiplier. A photomultiplier was used to measure the scattered light because of its greater sensitivity to lower light levels compared to a photodiode.

The reference photodiode was a Hamamatsu S1336-5BQ silicon photodiode with an effective photosensitive area of 5.6 mm^2 . The transmittance photodiode was a Newport Research Model 820 silicon photodiode with an effective photosensitive area of 1.0 cm^2 . The photodiode with a larger effective area was used in an effort to reduce the effects of beam steering on the transmittance signal. During initial experiments with the laser scattering-extinction measurement system, the location of the incident laser spot on the transmittance photodiode varied depending on the pressure within the vessel, the presence of a flame, and the height within the flame. This beam steering was attributed to slight movements in the vessel and its windows as the pressure within the vessel changed and

to index of refraction gradients caused by the flame gases. A larger area photodiode reduces the possibility that beam steering will move the laser spot away from the active area. However, the transmittance photodiode output was still found to vary even if the spot remained in the active area, but moved to a slightly different location. Our final solution to reduce the sensitivity to beam steering was to place a flashed opal diffuser (Oriol Model No. 48010) in front of the photodiode to diffuse the incident laser beam.

A Hamamatsu R955 photomultiplier was used to detect scattered light at the output of the monochromator. This Hamamatsu R955 photomultiplier was used instead of the RCA 1P28B photomultiplier we typically use for fluorescence measurements because the Hamamatsu R955 photomultiplier has a greater responsivity at 488 nm than the RCA 1P28B ($\sim 60 \text{ mA}\cdot\text{W}^{-1}$ vs. $\sim 30 \text{ mA}\cdot\text{W}^{-1}$). The responsivity of the Hamamatsu R955 photomultiplier also extends further into the red, so it would have been more suitable for possible scattering measurements using a helium-neon laser at 632.8 nm. The photomultiplier was wired into a conventional voltage divider network to supply the voltage to the dynodes. The supply voltage was 900 V.

The output of all three detectors, the two photodiodes and the photomultiplier, is a current that is proportional to the incident irradiance. The current output of each detector is given by

$$i_{sh} = r_{\lambda} \cdot I_{pd} \cdot A_{pd} \quad (\text{B.1})$$

where i_{sh} (A) is the short circuit current (the current produced with no load across the photodetector terminals), I_{pd} ($\text{W}\cdot\text{cm}^{-2}$) is the incident irradiance, A_{pd} (cm^2) is the effective photosensitive area, and r_{λ} ($\text{A}\cdot\text{W}^{-1}$) is the responsivity of the photodetector, which is a function of the incident wavelength.

The output currents of the three detectors were converted to voltage using transimpedance amplifier circuits. A schematic of the transimpedance amplifier circuit used for conversion of the photodiode output current to voltage is shown in Figure B.1.

The transimpedance amplifier circuit for the photomultiplier was the same as that for the photodiodes except that the photomultiplier output was connected into the amplifier circuit through a BNC coaxial connector in place of the photodiode.

The operational amplifier used in all three circuits was an Analog Devices AD549KH with ultralow input bias current. The data sheets for this operational amplifier identify it as an excellent preamplifier for photodiodes and photomultipliers. The suggested circuit configuration for a photodiode transimpedance amplifier was used as a basis for the circuit used here. The configuration of the power supply connections and the power supply component values (not shown in Figure B.1) were as suggested by the data sheets (Analog Devices, 1991). The component values used in the transimpedance amplifier circuits are listed in Table B.1.

The voltage divider was added at the output of the transimpedance amplifier to reduce the output signal voltage and to place a constant load on the output of the op-amp. The feedback resistor and the voltage divider resistors were selected to keep the output signal voltage within the input voltage range of the lock-in amplifiers. The feedback capacitor was included to add a high-pass filter. The cutoff frequencies were selected using available capacitor values to be at least ten times greater than the 1.0 kHz modulation of the laser beam.

Metal film resistors (1%) were used for precise selection of resistor values and because they have better stability with temperature and humidity variations than carbon composition resistors (Horowitz and Hill, 1989). Mica capacitors were used because they were available through the campus stores and they have good accuracy, although either polycarbonate or Teflon capacitors would provide better temperature stability (Horowitz and Hill, 1989).

The voltage output, V_{out} (V), of the transimpedance amplifier circuit as shown in Figure B.1 is given by

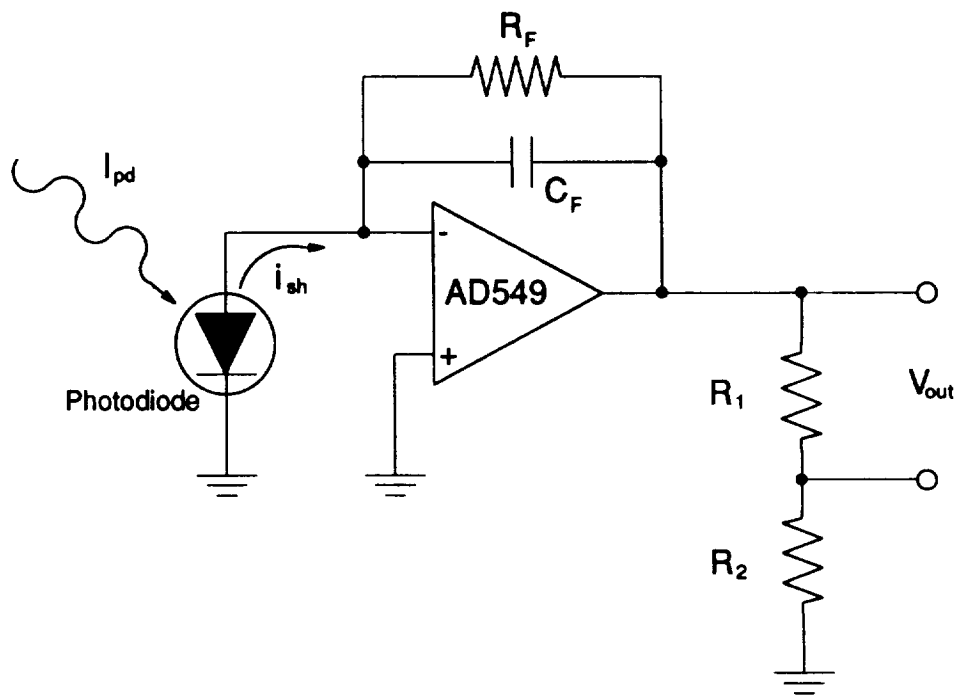


Figure B.1 Transimpedance amplifier circuit used to convert the photodiode current output to a voltage output.

Table B.1 Component values used in the transimpedance amplifier circuits.

Detector	Feedback Resistor R_F (k Ω)	Feedback Capacitor C_F (pF)	Cutoff Frequency (kHz)	Voltage Divider Resistors (k Ω)
Photodiodes	20.0	500	15.9	10.2
Photomultiplier	22.1	220	32.7	10.2

$$V_{out} = \frac{-R_F}{1 + j \cdot \omega \cdot R_F \cdot C_F} \cdot \frac{R_1}{R_1 + R_2} \cdot i_{sh} \quad (B.2)$$

where ω (rad·sec⁻¹) is the angular frequency and $j = \sqrt{-1}$. Combining Eqs. (B.1) and (B.2) gives

$$V_{out} = \frac{-R_F}{1 + j \cdot \omega \cdot R_F \cdot C_F} \cdot \frac{R_1}{R_1 + R_2} \cdot r_\lambda \cdot I_{pd} \cdot A_{pd} \quad , \quad (B.3)$$

which relates the incident irradiance on the photodetector to the voltage output of the photodetector circuit. The output offset of the amplifier circuit has been neglected in Eq. (B.2) because it can be adjusted to be near zero; moreover, since it is a small DC voltage, it will be filtered out by the lock-in amplifiers.

We assume that the resistor and capacitor values remain constant over the time of the experiment (i.e., we let the circuit warm up), that the frequency of the chopper modulation remains constant, and that we operate within the linear range of the photodetector at a constant laser wavelength. With these assumptions, the voltage output of the photodetector is linearly proportional to the laser irradiance and Eq. (B.2) can be written as

$$V_{out} = \eta_E \cdot \eta_O \cdot I_{pd} \quad (B.4)$$

where η_E is an electronic conversion efficiency (V·cm²·W⁻¹) which includes the resistance and capacitance terms along with the responsivity and the active area of the photodetector. The optical efficiency, η_O (dimensionless), accounts for the transmittance and reflectance of the optical elements within the detection optics as well as the fraction of the total light that is incident on the photodetector active surface. The equations that describe the voltage outputs of the three photodetectors are then

$$V_0 = \eta_{E0} \cdot \eta_{O0} \cdot I_0 \quad (B.5a)$$

$$V_T = \eta_{ET} \cdot \eta_{OT} \cdot I_T \quad (B.5b)$$

$$V_S = \eta_{ES} \cdot \eta_{OS} \cdot S_{sca} \quad (B.5c)$$

where V_0 (V) is the reference photodiode voltage, V_T (V) is the transmittance photodiode voltage, and V_S (V) is the scattering photomultiplier voltage, I_0 ($\text{W}\cdot\text{cm}^{-2}$) is the incident laser irradiance, I_T ($\text{W}\cdot\text{cm}^{-2}$) is the transmitted laser irradiance, and S_{scat} (W) is the scattered light power. The optical and electronic efficiencies are denoted with a T subscript to indicate transmittance, 0 to indicate reference, and S to indicate scattered. Since the scattered light power is measured, the scattering electronic efficiency, η_{ES} , does not include the area term from Eq. (B.3) and thus its units are $\text{V}\cdot\text{W}^{-1}$. Equations (B.5a-c) are the source for equations (4.1a-c) in Section 4.4.4 on the laser scattering-extinction data analysis.

B.3 Signal Conditioning and Data Acquisition

The photodetector voltage outputs were acquired with the signal conditioning and computer-controlled data acquisition system shown in Figure B.2. Lock-in amplifiers were used to detect the chopper-modulated photodetector voltage outputs to eliminate the flame and room light background. Both the reference photodiode and scattering photomultiplier voltage outputs were detected with Stanford Research Systems Model SR510 Lock-in amplifiers. The transmittance photodiode voltage output was detected with an EG&G PARC Model 128 lock-in amplifier. The output voltages of the lock-in amplifiers were acquired and converted to digital signals by a Stanford Research Systems Model SR245 computer interface module for subsequent computer storage and analysis. The computer interface module has an input range of ± 10.24 V with a 13-bit analog-to-digital converter and a maximum conversion rate of 2 kHz. The resolution of the analog-to-digital conversion was 2.5 mV.

The output voltage range of the SR510 lock-in amplifiers was ± 10.24 volts per full scale input, while that of the PARC 128 lock-in amplifier was ± 1.0 volts per full scale input. The output of the PARC 128 lock-in was amplified by a Stanford Research Systems Model SR235 Analog Processor module to more closely match the ± 10.24 V input range of the computer interface.

The object of the transmittance measurement is to monitor the small change in the laser irradiance caused by absorption and scattering of the beam as it passes through the flame. To measure this change, which may be as small as 0.1% of the photodiode signal produced by the laser beam, the major fraction of the measured transmittance and reference signal voltages were subtracted out using the input offsets of the lock-in amplifiers. This allowed the sensitivity of the lock-in amplifiers to be increased by a factor of 10. The combination of lock-in amplifier sensitivity and output voltage gain were set for both the transmittance and reference lock-in amplifiers so that the overall sensitivity to variation in the laser irradiance was the same for both the transmittance and reference measurements. The scattering signal was not superimposed on a large background and thus did not require an input offset to increase the sensitivity of the lock-in amplifier to the signal.

The SR245 computer interface module was controlled by a modified version of the Stanford Research Systems SR265 software program (Stanford Research Systems, 1988) running on an IBM PC computer. The SR265 program was modified by Carter (1990) to add an interface to the stepper-motor controller, so that data acquisition could be coupled to the stepper-motor driven vertical and horizontal translation of the burner and also to the wavelength translation of the monochromator.

Vertical profiles of the transmittance, reference, and scattering signal voltages were measured in flames by setting up the SR265 program to sample the three signals for 10 seconds at a 100 Hz rate (1000 samples) at each height in a sequence of heights above the burner. The signal voltage data acquired by the computer interface was stored on the hard

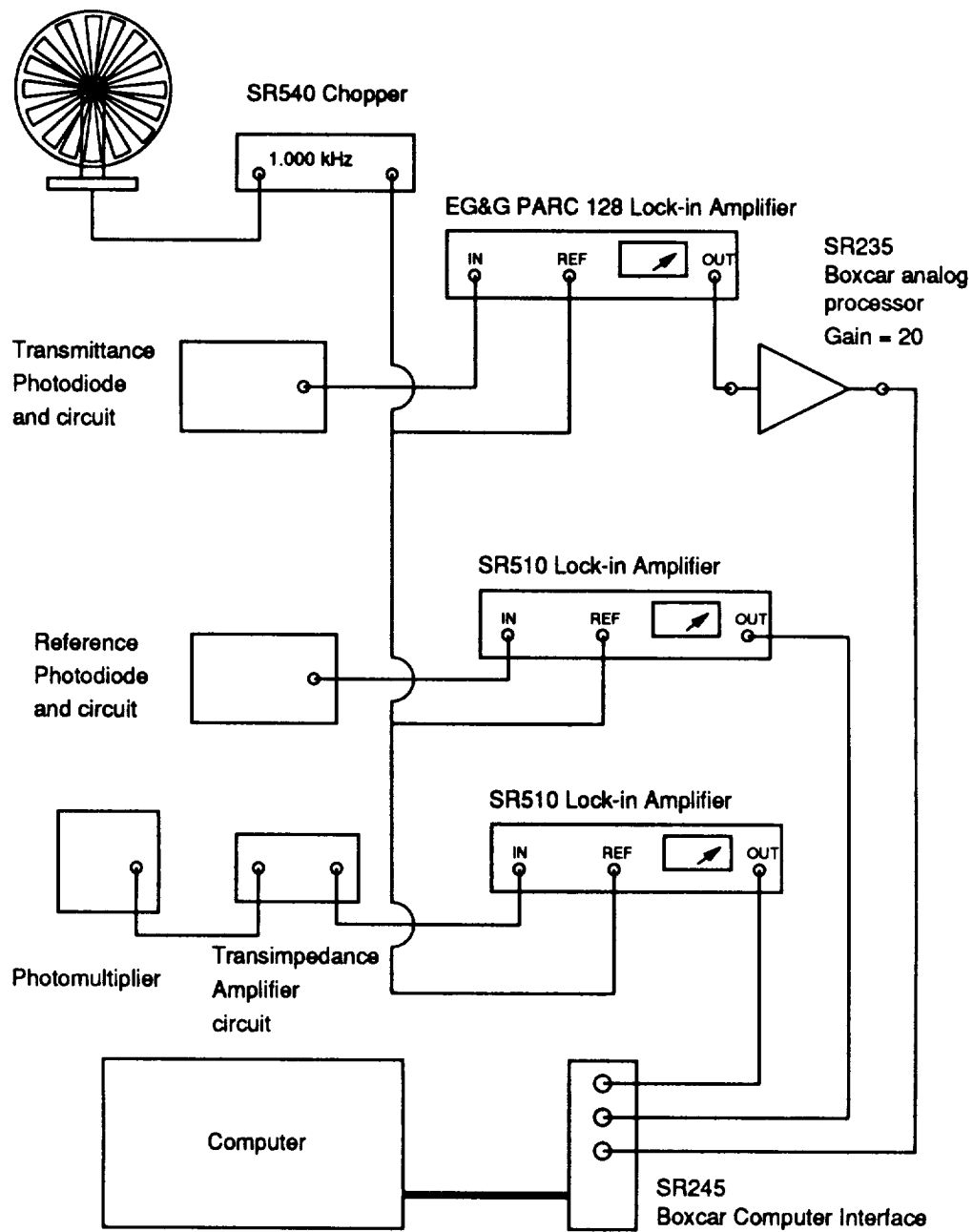


Figure B.2 Schematic of the signal detection and data acquisition setup for the laser scattering-extinction measurements.

disk of the IBM PC in binary format. The storage format for a vertical profile was such that the data from each height was stored in a data file. Each file then contained 1000 samples of the signal voltage for each of the three signals with 4 bytes required to represent each sample of the voltage. Thus, the data from each height in a profile produced a 12,000 byte file.

The calibration measurement, in which the three signal voltages were measured with nitrogen flowing through the burner, was made with the same program setup as the vertical profiles, except that the measurements were all made at a single height above the burner.

B.4 Data Analysis

The objective of the laser scattering-extinction measurements is to measure the scattering and extinction coefficients as a function of height above the burner. These profiles are calculated from the voltage data acquired and stored in binary format by the SR265 program during the experiments.

The extinction coefficient, K_{ext} (cm^{-1}), is determined from the transmittance, τ , as a function of the height above the burner, z , by

$$K_{ext}(z) = -\frac{1}{L} \cdot \ln[\tau(z)] \quad (\text{B.6})$$

where L (cm) is the pathlength of the laser beam through the flame. The transmittance is determined from the ratio of the transmittance photodiode voltage to the reference photodiode voltage by

$$\tau(z) = \frac{I_T(z)}{I_0(z)} = \frac{1}{F_T} \cdot \frac{V_T(z)}{V_0(z)} \quad (\text{B.7})$$

where the transmittance calibration factor, F_T , is defined as

$$F_T = \frac{\eta_{OT} \cdot \eta_{ET}}{\eta_{O0} \cdot \eta_{E0}} \quad (\text{B.8})$$

The total scattering coefficient, Q_{sca} ($\text{cm}^{-1}\cdot\text{sr}^{-1}$), is determined from the ratio of the scattering photomultiplier voltage to the reference photodiode voltage by

$$Q_{sca}(z) = \frac{1}{F_{sca}} \cdot \frac{V_s(z)}{V_0(z)} \quad (\text{B.9})$$

where the scattering calibration factor, F_{sca} , is defined as

$$F_{sca} = \frac{\eta_{OS} \cdot \eta_{ES}}{\eta_{OO} \cdot \eta_{EO}} \cdot V_c \cdot \Omega_c \cdot \eta_c \quad (\text{B.10})$$

and V_c (cm^3) is the collection volume, Ω_c (sr) is the solid angle of the collection optics, and η_c is the efficiency of the collection optics.

Both the transmittance and scattering calibration factors were determined by measuring the three photodetector voltages for a nitrogen flow from the burner. The transmittance calibration is determined from

$$F_T = \frac{1}{\tau_{cal}} \cdot \left(\frac{V_T}{V_0} \right)_{cal} \quad (\text{B.11})$$

where τ_{cal} is the transmittance at the calibration conditions and the subscript *cal* indicates that the measurement was made at the calibration conditions. We assume that $\tau_{cal} = 1$ for a nitrogen flow. The scattering calibration factor is determined from

$$F_{sca} = \frac{R \cdot T}{P \cdot N_{av}} \cdot \frac{1}{C_{VV,N_2}} \cdot \left(\frac{V_s}{V_0} \right)_{cal} \quad (\text{B.12})$$

where R ($82.055 \text{ cm}^3\cdot\text{atm}\cdot\text{gmol}^{-1}\cdot\text{K}^{-1}$) is the gas constant, N_{av} ($6.023 \times 10^{23} \text{ gmol}^{-1}$) is Avogadro's number, T (K) is the temperature, P (atm) is the pressure, and C_{VV,N_2} ($\text{cm}^2\cdot\text{sr}^{-1}$) is the differential scattering cross-section of nitrogen for vertically polarized incident and scattered light. The temperature and pressure of the nitrogen flow are measured during calibration, so that its number density is $P \cdot N_{av} / RT$. The differential scattering cross-section of a gas is given by Eq. (3.2.18) as

$$C_{VV,g} = \frac{4\pi^2}{\lambda^4} \cdot \frac{(n_g - 1)^2}{N_0^2} \cdot \frac{3}{3 - 4 \cdot \rho_V} \quad (\text{B.13})$$

where λ (cm) is the wavelength, n_g is the refractive index of light for the gas, N_0 (cm^{-3}) is a standard molecular number density (evaluated at the same temperature and pressure as the refractive index), and ρ_v is the depolarization ratio (Rudder and Bach, 1968; D'Alessio, 1981). This expression was evaluated for nitrogen at a wavelength, $\lambda = 488.0$ nm, with the index of refraction term, $n_g - 1 = 301.2 \times 10^{-6}$, at 0° C and 1 atm (Gardiner, Hidaka, and Tanzawa, 1981) and the depolarization ratio, $\rho_v = 1.042 \times 10^{-2}$ (Bogaard et al., 1978), to obtain the differential scattering cross-section for nitrogen, $C_{vv,N_2} = 8.873 \times 10^{-28} \text{ cm}^2 \cdot \text{sr}^{-1}$. Since the scattering calibration factor is inversely proportional to C_{vv,N_2} , the subsequently calculated scattering coefficient profiles are directly proportional to C_{vv,N_2} .

The transmittance and transmittance calibration factor are calculated from the ratio of the transmittance photodiode voltage to the reference photodiode voltage (transmittance signal ratio), V_T/V_0 . The scattering coefficient and scattering calibration factor are calculated from the ratio of the scattering photomultiplier voltage to the reference photodiode voltage (scattering signal ratio), V_s/V_0 . These signal ratios were determined from the voltages sampled at the computer interface. However, calculation of the individual signal voltages required that account be taken of the gains and offsets applied by the lock-in amplifiers in the detection of all three signals.

These gains and offsets are shown schematically in the block diagrams for the reference (Fig. B.3), transmittance (Fig. B.4), and scattering (Fig. B.5) signal detection. The parameters in the block diagrams are defined as follows. The magnitude of the photodetector voltage is given by V (mV). This voltage signal is detected by a lock-in amplifier. The gain applied by the lock-in amplifier to the photodetector voltage is K which is defined as

$$K = \frac{1}{S} \cdot \cos \phi \quad (\text{B.14})$$

where S (mV signal/full scale input) is the sensitivity of the lock-in amplifier, and ϕ is the phase angle between the input signal and the lock-in reference. We adjust the phase angle to obtain the maximum signal, so that $\cos \phi = 1$. The input offset that can be applied to the signal is V_{os} (fraction of full scale input). This offset was used to subtract out the majority of the transmittance and reference signals. The output gain of the lock-in amplifier is G (voltage out/full scale input). The output offset voltage of the lock-in amplifier is V_{ol} (V), which is the output voltage when the lock-in amplifier inputs are shorted and the input offset is set to zero. The voltage measured at the computer interface is V_c (V). For the transmittance signal detection, the gain of the SR235 analog processor is G_A (voltage output/voltage input) and its output offset voltage is V_{oA} (V). The subscripts are defined as before, 0 for reference, T for transmittance, and S for scattering.

Given that the sensitivities, gains, and offsets are known or measured, then the photodetector voltages can be determined from the voltages sampled at the computer interface by the following equations for the reference photodiode voltage,

$$V_0 = S_0 \cdot \left[\frac{1}{G_0} \cdot (V_{c,0} - V_{ol,0}) - V_{os,0} \right] , \quad (\text{B.15})$$

for the transmittance photodiode voltage,

$$V_T = S_T \cdot \left(\frac{1}{G_T \cdot G_{A,T}} \cdot [V_{c,T} - (G_{A,T} \cdot V_{ol,T} + V_{oA,T})] - V_{os,T} \right) , \quad (\text{B.16})$$

and for the scattering photomultiplier voltage,

$$V_S = S_S \cdot \left[\frac{1}{G_S} \cdot (V_{c,S} - V_{ol,S}) - V_{os,S} \right] . \quad (\text{B.17})$$

The data files containing the sampled voltage data from the calibration and profile measurements were analyzed with a series of programs written in the ASYST version 3.10 scientific programming language (ASYST Software Technologies, Inc., Rochester, NY). In the first stage of the data analysis, the sampled voltages were read from the

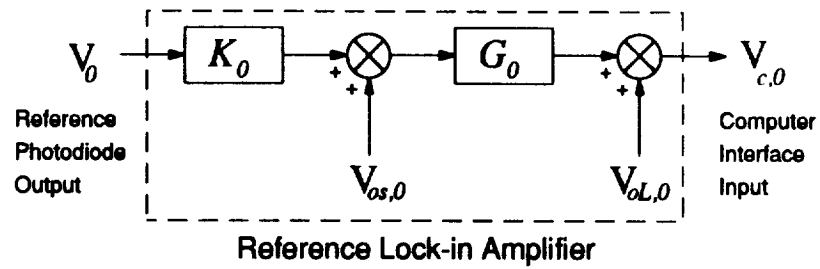


Figure B.3 Block diagram showing the gains and offsets applied for detection of the reference photodiode voltage.

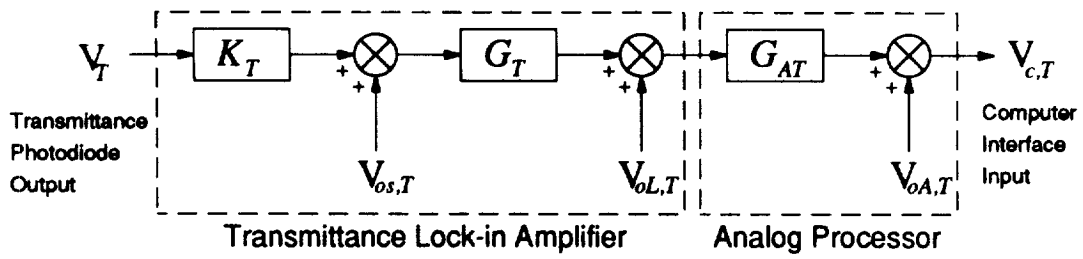


Figure B.4 Block diagram showing the gains and offsets applied for detection of the transmittance photodiode voltage.

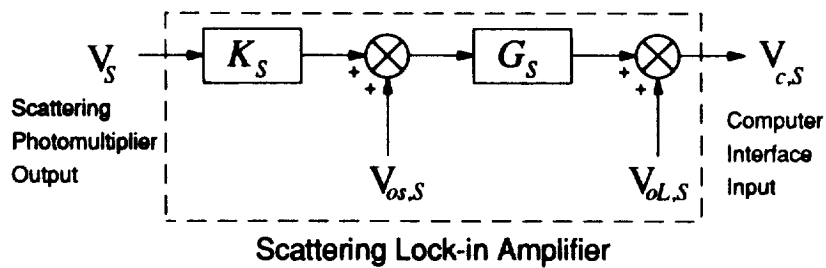


Figure B.5 Block diagram showing the gains and offsets applied for detection of the scattering photomultiplier voltage.

sequences of data files containing the calibration or profile data and then the transmittance and scattering signal ratio profiles were calculated and stored for the next stage of the data analysis. The steps in the first stage data analysis program were as follows:

- 1) The sequence of data files containing the particular profile or calibration data was specified.
- 2) The gains and offsets applied to the photodetector voltages were entered.
- 3) The starting height above the burner and height interval between measurements was entered, so that the height above the burner for each point in the profile could be calculated.
- 4) For each data file in the sequence of the profile or calibration:
 - a) The 1000 samples of the reference, transmittance, and scattering voltages measured at the computer interface were read from the file and placed in arrays.
 - b) From these arrays, the arrays of photodetector voltages were calculated using Eqs. (B.15) to (B.17).
 - c) From these photodetector voltage arrays, the arrays of the transmittance and the scattering signal ratios were calculated.
 - d) The mean and standard deviation of the photodetector signal voltages and signal ratios in the arrays were calculated.
- 5) The mean and standard deviation data for each point in the profile were then written to both ASCII and ASYST binary format data files for subsequent data analysis. Thus, all of the data for the profile was consolidated into two smaller data files.

From the calibration data, the transmittance calibration factor was calculated from the transmittance signal ratio using Eq. (B.11) and the scattering calibration factor was

calculated from the scattering signal ratio using Eq. (B.12). With the calibration factors determined, the profiles of the scattering and extinction coefficients were determined in the second stage of the data analysis. The steps in this second stage were as follows:

- 1) The data file containing the profile data calculated in the first stage was specified.
- 2) The transmittance and scattering calibration factors and the pathlength were entered.
- 3) The transmittance and scattering signal ratio profile data were read from the data file.
- 4) The transmittance profile was calculated from the transmittance signal ratio profile using Eq. (B.7) and then the extinction coefficient profile was calculated using Eq. (B.6).
- 5) The scattering coefficient profile was calculated from the scattering signal ratio profile using Eq. (B.9).
- 6) The extinction and scattering coefficient profile data were written to an ASCII data file.

The extinction and scattering coefficient profile data were then imported into a spreadsheet program to do the further calculations needed to determine the volume fraction, number density, and particle radius profiles.

B.5 Error Analysis and Detection Limits

Since the goal of this study is to develop a set of data for comparison with models of soot formation, the uncertainties and detection limits of the extinction coefficient and the scattering coefficient are necessary to make those comparisons. Knowledge of the uncertainties in these parameters allows comparisons to be made between flames and with predictions from models. Knowledge of the detection limits allows us to specify the minimum amount of soot that can be detected in flames near the critical equivalence ratio.

In this section, we first evaluate the uncertainty in the extinction coefficient and then its detection limit. Then we evaluate the uncertainty and detection limit for the scattering coefficient.

B.5.1 Error Analysis and Detection Limit for the Extinction Coefficient

Since the extinction coefficient is calculated from the transmittance profile using Eq. (B.6), we will first evaluate the uncertainty in the transmittance measurement. The transmittance at a height is calculated from the transmittance signal ratio (Eq. B.7). This ratio is calculated for each of the 1000 samples of the photodetector voltages recorded at a given height and the mean of this ratio is used to calculate the transmittance. Since the transmittance is normalized to the maximum of the transmittance profile, the calibration factor, F_T , is simply the transmittance signal ratio at the height corresponding to the maximum in the transmittance profile. The equation for the transmittance at any height is then

$$\tau(z) = \left(\frac{V_0}{V_T} \right)_{cal} \cdot \left(\frac{V_T}{V_0} \right)_z \quad (B.18)$$

The transmittance and reference signal voltages are calculated from the measured voltages using Eqs. (B.16) and (B.15). Substituting these expressions into Eq. (B.18) gives the expression for the transmittance as

$$\tau(z) = \frac{S_0 \cdot [((V_{c,0})_{cal} - V_{oL,0})/G_0 - V_{os,0}]}{S_T \cdot [((V_{c,T})_{cal} - V_{B,T})/G_\tau - V_{os,T}]} \cdot \frac{S_T \cdot [((V_{c,T})_z - V_{B,T})/G_\tau - V_{os,T}]}{S_0 \cdot [((V_{c,0})_z - V_{oL,0})/G_0 - V_{os,0}]} \quad (B.19)$$

where the subscript *cal* indicates the voltages measured at the calibration point (or the maximum of the profile) and *z* indicates the voltages measured at any height in the profile. We have defined the terms, $G_\tau = G_T G_{A,T}$ and $V_{B,T} = G_{A,T} V_{oL,T} + V_{oA,T}$, to simplify the expression from Eq. (B.16). The uncertainty in the transmittance then depends on the uncertainties in the sensitivities, gains, and offsets of the lock-in amplifiers and could be evaluated using the general expression for the uncertainty given in Eq. (A.2) (Appendix

A). However, the resulting expression would be cumbersome to derive and evaluate. Instead, we will use an approximation suggested by Coleman and Steele (1989). They suggest that when the function is sufficiently complex such that the partial derivatives of the experimental result, f , with respect to the independent variables, x_1, x_2, \dots, x_n , are difficult to evaluate, then the partial derivatives can be approximated by the forward-difference finite-difference equation given by

$$\left. \frac{\partial f}{\partial x_1} \right|_{x_2, \dots, x_n, \text{constant}} = \frac{\Delta f}{\Delta x_1} = \frac{f(x_1 + \Delta x_1, x_2, \dots, x_n) - f(x_1, x_2, \dots, x_n)}{\Delta x_1} \quad . \quad (\text{B.20})$$

The uncertainty in the experimental result is then approximated by

$$(\delta f)^2 \approx \left(\frac{\Delta f}{\Delta x_1} \cdot \delta x_1 \right)^2 + \left(\frac{\Delta f}{\Delta x_2} \cdot \delta x_2 \right)^2 + \dots + \left(\frac{\Delta f}{\Delta x_n} \cdot \delta x_n \right)^2 \quad . \quad (\text{B.21})$$

The uncertainty in the transmittance (Eq. B.19) was evaluated using the finite-difference approach (Eqs. B.20 and B.21) with the data acquired for a transmittance profile of Flame A-IA-S2, an atmospheric-pressure sooting flame at $\phi = 1.92$ with a measurable extinction coefficient profile. The parameters and results of this uncertainty analysis are listed in Table B.2.

The input offsets, gains, and output offsets used to calculate the signals are listed in Table B.2. The input offsets and gains were each varied by 1% to evaluate the variation in the transmittance, $\Delta\tau$, produced by each parameter. The variation in the input offsets, $V_{\alpha_s,0}$ and $V_{\alpha_s,T}$, produced the largest variations in the transmittance. However, both offsets were measured to better than 0.5%, so the 1% variation is a conservative estimate. The variation in the gains, G_0 and G_τ , is also conservative, but the resulting variation in transmittance is small. The output offsets, $V_{\alpha_l,0}$ and $V_{\alpha_l,T}$, were varied by 50%, because their magnitude was close to that of the computer interface resolution and thus their measurements had a larger standard deviation. Their effect on the transmittance calculation was miniscule and thus they probably could have been neglected. The total

Table B.2 Transmittance uncertainty calculation based on the variation in the lock-in parameters.

Lock-in Parameter	Parameter		Variation in Transmittance	
	Value	Variation	$ \Delta\tau _{\max}$	$\left(\frac{\Delta\tau}{\Delta r} \cdot \delta x\right)^2$
<u>Reference</u>				
Input Offset	$V_{os,0} = -0.5808$	$\Delta V_{os,0} = 0.0581$	1.09×10^{-4}	1.20×10^{-8}
Gain	$G_0 = 101.4$	$\Delta G_0 = 1.0$	9.65×10^{-6}	9.30×10^{-11}
Output Offset	$V_{ol,0} = 0.0136 \text{ V}$	$\Delta V_{ol,0} = 0.007 \text{ V}$	1.17×10^{-7}	1.38×10^{-14}
<u>Transmittance</u>				
Input Offset	$V_{os,T} = -3.248$	$\Delta V_{os,T} = 0.0325$	3.16×10^{-5}	9.98×10^{-10}
Gain	$G_\tau = 19.94$	$\Delta G_\tau = 0.2$	3.11×10^{-5}	9.67×10^{-10}
Output Offset	$V_{ol,T} = 0.0551 \text{ V}$	$\Delta V_{ol,T} = 0.028 \text{ V}$	1.35×10^{-6}	1.83×10^{-12}
<u>Combined Uncertainty</u>		$\delta\tau = 1.19 \times 10^{-4}$		

uncertainty produced by the sum of these variations is small, $\delta\tau = 1.19 \times 10^{-4}$, and thus, uncertainties in the values of the lock-in parameters are not a significant source of uncertainty in the calculation of the transmittance.

The uncertainty in the transmittance was also evaluated based on the variation in the transmittance and reference voltages, $V_{c,T}$ and $V_{c,0}$, measured at the computer interface. During the 10-second sampling of the voltages at each height, the sampled voltages exhibited variations caused by drift of the laser intensity and other unidentified noise sources. These variations were quantified during the data analysis by calculating the standard deviation of the sampled voltages at each height. The uncertainty in the transmittance produced by these variations was calculated using the finite-difference approach (Eqs. B.20 and B.21) for the voltage data at each height in the transmittance profile (the same profile as used for the calculation of Table B.2). The mean of these measured voltages in the profile, their variation, and the resulting variation produced in the transmittance are listed in Table B.3. The variation in the voltages used in the calculation was twice the standard deviation of the sampled voltages. The combined uncertainty caused by the voltage variation is $\delta\tau = 5.5 \times 10^{-4}$, about five times larger than that caused by the variation in the lock-in parameters.

An alternate way to calculate the uncertainty in the transmittance is to calculate the fractional uncertainty based on the expressions for the transmittance in Eq. (B.7) and the observed variation in the transmittance signal ratio at a single height. The expression for the uncertainty in the transmittance is

$$\left(\frac{\delta\tau}{\tau}\right)^2 = 2 \cdot \left(\frac{\delta\left(\frac{V_T}{V_0}\right)}{\left(\frac{V_T}{V_0}\right)}\right)^2 \quad (\text{B.22})$$

where $\delta(V_T/V_0)$ represents the uncertainty in the transmittance signal ratio at a single height. For this analysis, we set the uncertainty at twice the standard deviation of the transmittance signal ratio determined at a single height. The factor of two in Eq. (B.22)

accounts for the uncertainty in the calibration factor, since it is also determined from a transmittance signal ratio. The results of this uncertainty analysis are listed in Table B.4 for the same transmittance profile as in the previous analyses. The mean of the transmittance signal ratio profile and the mean of the standard deviations of the signal ratios are listed. The uncertainty in the transmittance, $\delta\tau = 3.68 \times 10^{-4}$, is of the same order as that for the other methods.

Table B.3 Effect of variation in voltage measured at the computer interface on the variation and uncertainty in the transmittance.

Signal	Computer Interface Voltage	Voltage Variation	Transmittance Variation
Reference	$V_{c,0} = 1.2482 \text{ V}$	$\Delta V_{c,0} = 0.0175 \text{ V}$	$\Delta\tau = 2.03 \times 10^{-4}$
Transmittance	$V_{c,T} = 7.3123 \text{ V}$	$\Delta V_{c,T} = 0.0136 \text{ V}$	$\Delta\tau = 5.11 \times 10^{-4}$
Combined Uncertainty	$\delta\tau = 5.50 \times 10^{-4}$		

Based on these uncertainty analyses, a conservative estimate for the uncertainty in the transmittance is of the order of $\delta\tau \sim 0.001$, i.e., we could measure a change in transmittance of 0.1%. This detection limit is illustrated in Figures B.6 and B.7 which show the variation in the transmittance profiles measured in the same flames on different days. Figure B.6 shows the transmittance profile measured on two days for a lightly sooting flame (A-IA-S1, $\phi = 1.78$). Figure B.7 shows the transmittance profiles measured on three days for a more heavily sooting flame (A-IA-S2, $\phi = 1.92$).

Table B.4 Transmittance uncertainty based on the variation in the transmittance signal ratio.

<u>Parameter</u>	<u>Value</u>
Mean Transmittance Signal Ratio	$\frac{V_T}{V_0} = 1.21537$
Mean standard deviation	$\sigma = 1.58 \times 10^{-4}$
Transmittance Uncertainty	$\Delta\tau = 3.68 \times 10^{-4}$

In the lightly sooting flame (A-IA-S1, Fig. B.6), no change in the transmittance occurs that is larger than the uncertainty and the measured transmittances vary within 0.001. The more heavily sooting flame (A-IA-S2, Fig. B.7) has a measurable, but still small change (~ 0.005% at 20 mm above the burner) in transmittance. For this flame, the variation in the transmittance is quantified in Table B.5 which lists the mean, standard deviation, and the range of transmittances measured at four heights for the profiles recorded on the three days. The standard deviation of the transmittance increases with height, but remains on the order of the uncertainty in the transmittance measurements. An additional factor involved in the variation of the transmittance from day to day is the reproducibility of the flame conditions. Although the reproducibility of the flames was shown to be excellent in Appendix A, the sensitivity of soot formation to slight variations in the flame conditions, particularly near the critical equivalence ratio, is not known. Thus, the increased variation in transmittance observed in the A-IA-S2 flame may be caused in part by variations in the amount of observed soot.

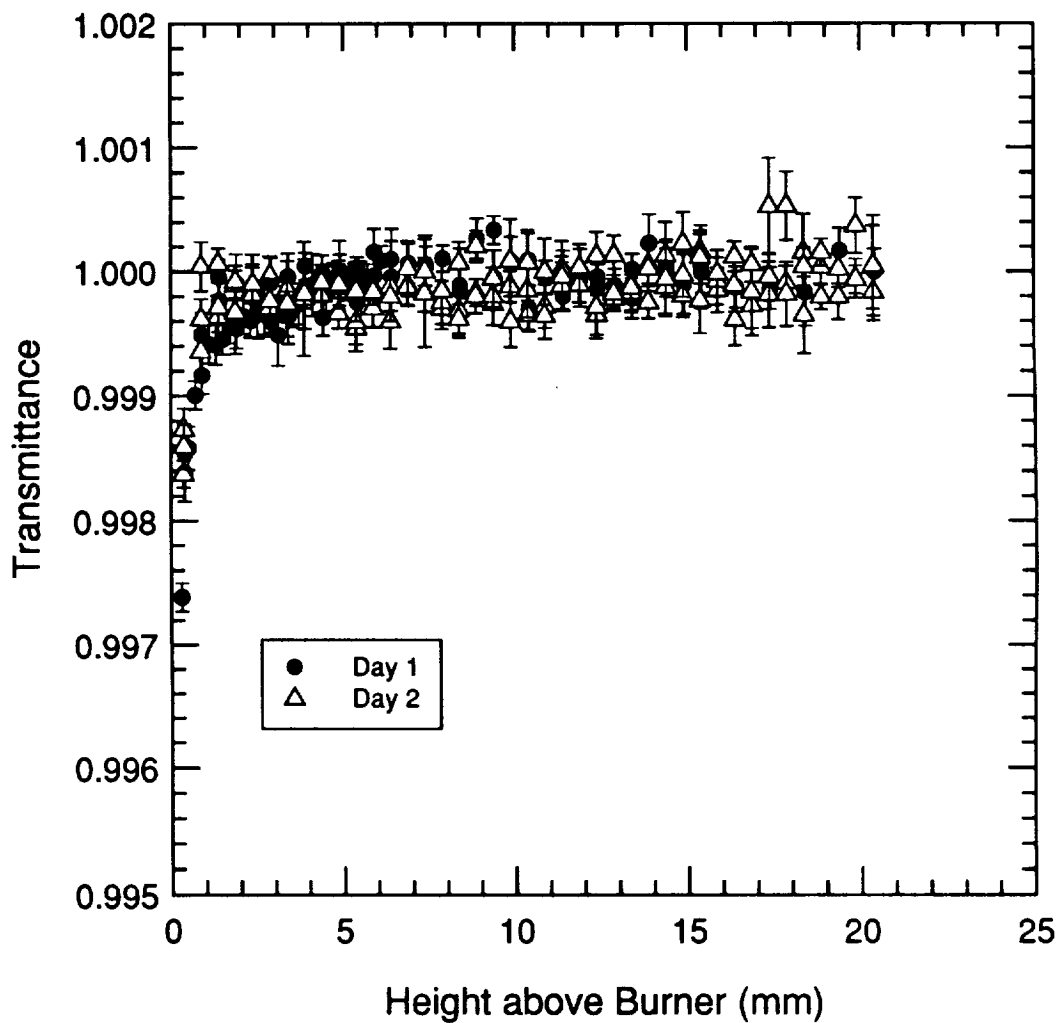


Figure B.6 Transmittance profiles for a lightly sooting flame (A-IA-S1, $\phi = 1.78$, $v_c = 7.73 \text{ cm}\cdot\text{sec}^{-1}$, $N_2/O_2 = 4.16$) measured on two days. The error bars indicate a variation of two standard deviations in the transmittance recorded at a given height.

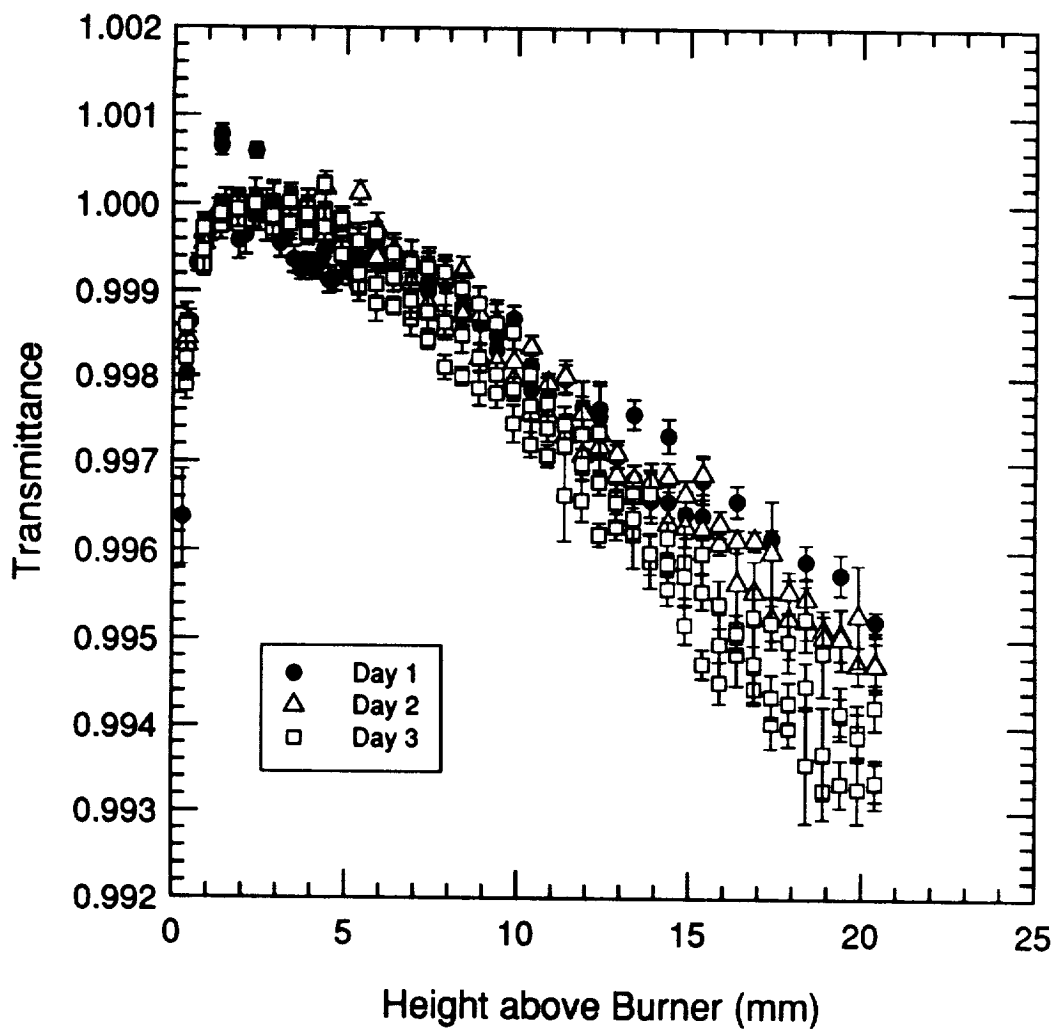


Figure B.7 Transmittance profiles for a sooting flame (A-IA-S2, $\phi = 1.92$, $v_c = 7.73 \text{ cm}\cdot\text{sec}^{-1}$, $N_2/O_2 = 4.16$) measured on three days. The error bars indicate a variation of two standard deviations in the transmittance recorded at a given height.

Table B.5 Mean, standard deviation, and range of the transmittances measured at four heights on three days for flame A-IA-S2 ($\phi = 1.92$, $v_c = 7.73 \text{ cm}\cdot\text{sec}^{-1}$, $N_2/O_2 = 4.16$).

Height above Burner (mm)	Number of Measurements	Transmittance		
		Mean $\bar{\tau}$	Standard Deviation σ_τ	Range $\Delta\tau = \tau_{\max} - \tau_{\min}$
5.4	8	0.9994	0.00034	0.0011
10.4	7	0.9978	0.00038	0.0011
15.4	7	0.9961	0.00075	0.0021
20.4	6	0.9943	0.00078	0.0019

Given the uncertainty in the transmittance, the uncertainty in the extinction coefficient can then be calculated. The fractional uncertainty in the extinction coefficient can be derived using Eqs. (A.2) and (B.6) and is given by

$$\left(\frac{\delta K_{ext}}{K_{ext}}\right)^2 = \left(\frac{\delta L}{L}\right)^2 + \left(\frac{\delta\tau}{\tau \cdot \ln \tau}\right)^2 \quad (B.23)$$

Table B.6 lists the transmittances, the extinction coefficient, the fractional uncertainty, and the uncertainty in the extinction coefficient obtained from Eq. (B.23) for a range of transmittances from $\tau = 0.999$ to $\tau = 0.90$. The uncertainty in the transmittance was assumed to be $\delta\tau = 0.001$.

The pathlength for all flames was assumed to be $L = 5.6 \text{ cm}$, the diameter of the burner. Since the pathlength was not directly measured, the extinction coefficient profiles can be considered to be relative profiles. For purposes of the uncertainty calculation, the uncertainty in the pathlength was assumed to be $\delta L = 0.2 \text{ cm}$. Any uncertainty in the pathlength appears as a constant fractional uncertainty in the extinction coefficient. In

contrast, the effect of uncertainty in the transmittance is to produce an almost constant uncertainty in the extinction coefficient because of the $\ln \tau$ term in Eq. (B.23). Thus, for the transmittance range, $\tau = 0.999$ to $\tau = 0.99$, the uncertainty, δK_{ext} , remains approximately constant, while the fractional uncertainty decreases from 100% to $\sim 10\%$. As the transmittance decreases below $\tau = 0.99$, the significance of the pathlength uncertainty increases, so that the fractional uncertainty approaches a constant, $\delta L/L$. These results imply that to measure K_{ext} to within 10% for a transmittance of $\tau = 0.999$, the uncertainty in the transmittance would have to be reduced to $\delta\tau = 0.0001$.

Based on the results of the uncertainty analysis, the resolution in the transmittance is $\Delta\tau = 0.001$, and thus the detection limit for the transmittance is $\tau = 0.999$. The resolution and detection limit for the extinction coefficient is then $K_{ext} = 1.8 \times 10^{-4} \text{ cm}^{-1}$ for the assumed pathlength of $L = 5.6 \text{ cm}$.

B.5.2 Error Analysis and Detection Limit for the Scattering Coefficient

The fractional uncertainty in the scattering coefficient is derived from the expression for the scattering coefficient (Eq. B.9) and the general uncertainty equation (Eq. A.2) and is given by

$$\left(\frac{\delta Q_{sca}}{Q_{sca}} \right)^2 = \left(\frac{\delta F_{sca}}{F_{sca}} \right)^2 + \left(\frac{\delta \left(\frac{v_s}{v_0} \right)}{\frac{v_s}{v_0}} \right)^2 . \quad (\text{B.23})$$

The fractional uncertainty in the scattering calibration factor is derived in a similar manner from Eq. (B.12) and is given by

$$\left(\frac{\delta F_{sca}}{F_{sca}} \right)^2 = \left(\frac{\delta T}{T} \right)^2 + \left(\frac{\delta P}{P} \right)^2 + \left(\frac{\delta \left(\frac{v_s}{v_0} \right)_{cal}}{\left(\frac{v_s}{v_0} \right)_{cal}} \right)^2 . \quad (\text{B.24})$$

Table B.6 Transmittance, extinction coefficient, fractional uncertainty and uncertainty of the extinction coefficient for a range of transmittances. The assumed quantities in the uncertainty analysis are: $L = 5.6$ cm; $\delta L = 0.2$ cm; $\delta\tau = 0.001$.

Transmittance τ	Extinction Coefficient K_{ext} (cm ⁻¹)	Fractional Uncertainty $\delta K_{ext}/K_{ext}$	Uncertainty δK_{ext} (cm ⁻¹)
0.999	1.79×10^{-4}	1.00	1.79×10^{-4}
0.998	3.58×10^{-4}	0.502	1.79×10^{-4}
0.9975	4.47×10^{-4}	0.402	1.79×10^{-4}
0.995	8.95×10^{-4}	0.204	1.82×10^{-4}
0.9925	1.34×10^{-3}	0.139	1.86×10^{-4}
0.990	1.79×10^{-3}	0.107	1.91×10^{-4}
0.985	2.70×10^{-3}	0.076	2.05×10^{-4}
0.980	3.61×10^{-3}	0.062	2.23×10^{-4}
0.975	4.52×10^{-3}	0.054	2.44×10^{-4}
0.950	9.16×10^{-3}	0.041	3.77×10^{-4}
0.925	1.39×10^{-2}	0.038	5.33×10^{-4}
0.900	1.88×10^{-2}	0.037	7.01×10^{-4}

These uncertainties are evaluated in terms of the uncertainty in the calculated scattering signal ratio, V_s/V_0 , instead of considering the uncertainties in the individual signal voltages, V_s and V_0 , or the uncertainties in the lock-in parameters used to calculate them. We can make this simplification because the analysis of the uncertainties in the transmittance (Sec. B.5.1) showed that the uncertainties calculated using the final signal ratio (Eq. B.22) were of the same magnitude as those calculated with the individual signal voltages (Eq. B.19). The uncertainty of the differential scattering cross-section of nitrogen is also not considered in the uncertainty of the scattering calibration factor (Eq. B.24) because the scattering cross-section of nitrogen is based on literature values and serves as a reference for the scattering measurements.

The uncertainties in the scattering calibration factors and the quantities used in their calculation are listed in Table B.7 for the measurements at both atmospheric and subatmospheric pressure. The estimates for the uncertainties in the temperature and pressure are the same as those used for the flow rate error analysis in Appendix A and are based on the manufacturer's specifications for those instruments. The uncertainty in the scattering signal ratio was estimated to be twice the standard deviation of the scattering signal ratio recorded during the calibration. The resulting fractional uncertainty in the calibration factor is small, $\sim 0.5\%$ at atmospheric pressure and $\sim 2.0\%$ at 80 torr. The larger uncertainty at 80 torr is caused by the increase in the fractional uncertainty of the pressure at subatmospheric pressures.

Typical values of the scattering coefficient and its uncertainties are listed in Table B.8 for profiles of the vertically polarized scattered light and the horizontally polarized scattered light measured in both the atmospheric and subatmospheric pressure experiments and also for the profiles of the argon-ion laser-induced fluorescence measured in the atmospheric pressure experiments. Mean values of typical profiles are presented to show the order of magnitude of the uncertainty for these measurements. The uncertainty in the scattering signal ratio, V_s/V_0 , was estimated to be twice the standard

Table B.7 Uncertainties in the scattering calibration factors and the quantities used in their calculation for both the atmospheric and subatmospheric pressure measurements.

Factor	Symbol	Atmospheric Pressure	Subatmospheric Pressure
Temperature	T (K)	295.0	295.0
Uncertainty	δT (K)	0.2	0.2
Pressure	P (torr)	750.	80.
Uncertainty	δP (torr)	1.5	1.5
Scattering signal ratio	V_s/V_0	0.5642	0.1425
Standard deviation	σ	1.33×10^{-3}	5.75×10^{-4}
Calibration factor	F_{sca} (cm·sr)	2.575×10^7	5.957×10^7
Fractional uncertainty	$\delta F_{sca}/F_{sca}$	5.20×10^{-3}	2.04×10^{-2}
Uncertainty	δF_{sca} (cm·sr)	1.34×10^5	1.22×10^6

deviation of the scattering signal ratio measured at a given height. For the atmospheric pressure experiments, the uncertainty in the scattering coefficient for vertically polarized light is ~ 1% and is larger, ~ 3 to 5%, for horizontally polarized scattered light and laser-induced fluorescence. For the subatmospheric pressure experiments, the uncertainty in the scattering coefficient for vertically polarized scattered light is ~ 3% and that for horizontally polarized scattered light is ~ 10%. The increased uncertainty for the horizontally polarized scattered light and for the fluorescence profiles is caused in part by their lower signal levels. The larger uncertainty in the scattering calibration factor also contributes to the larger uncertainty in the scattering coefficient for the subatmospheric pressure measurements compared to the atmospheric pressure measurements.

The particle scattering coefficients were obtained by subtracting the molecular scattering coefficient, $Q_{VV,g}$, from the measured scattering coefficients, i.e.,

$$Q_{VV} = Q_{sca} - Q_{VV,g} \quad . \quad (B.25)$$

The uncertainty in the particle scattering coefficient is then given by

$$(\delta Q_{VV})^2 = (\delta Q_{sca})^2 + (\delta Q_{VV,g})^2 \quad . \quad (B.26)$$

Since the molecular scattering coefficients were determined from the measured scattering coefficients in the rich nonsooting flame or from the nonsooting region of a sooting flame, the uncertainty in the molecular scattering coefficient is the same as that for the measured scattering coefficient. Thus, the uncertainty in the particle scattering coefficient is given by

$$\delta Q_{VV} = 1.41 \cdot \delta Q_{sca} \quad . \quad (B.27)$$

If we consider the uncertainty in the scattering coefficient to be the limit on the experimental resolution, then the resolution in the scattering coefficient for vertically polarized scattered light at atmospheric pressure is $4.2 \times 10^{-11} \text{ cm}^{-1} \cdot \text{sr}^{-1}$. The resolution in the scattering coefficient for vertically polarized scattered light at 80 torr is $1.9 \times 10^{-11} \text{ cm}^{-1} \cdot \text{sr}^{-1}$. The background for the horizontally polarized scattered light and

fluorescence measurements is small, so the above uncertainty is also a measure of the detection limit. The resolution of the scattering coefficient for horizontally polarized scattered light is $1.3 \times 10^{-11} \text{ cm}^{-1} \cdot \text{sr}^{-1}$ at atmospheric pressure and $1.2 \times 10^{-11} \text{ cm}^{-1} \cdot \text{sr}^{-1}$ at 80 torr. The resolution and detection limit for the fluorescence measurements is $\sim 6.0 \times 10^{-12} \text{ cm}^{-1} \cdot \text{sr}^{-1}$.

Table B.8 Typical mean values for profiles of the scattering signal ratio and its standard deviation and the resulting scattering coefficient and its uncertainties. Values are given for profiles measured of vertically polarized scattered light and horizontally polarized scattered light for both atmospheric and subatmospheric pressures and for argon-ion laser-induced fluorescence at atmospheric pressure.

Factor	Symbol	Atmospheric Pressure			Subatmospheric Pressure		
		Vertical Polarization	Horizontal Polarization	Fluorescence	Vertical Polarization	Horizontal Polarization	Fluorescence
Scattering signal ratio	V_s/V_0	1.133×10^{-1}	2.482×10^{-2}	1.303×10^{-2}	3.499×10^{-2}	4.383×10^{-3}	
Standard deviation	σ	4.44×10^{-4}	3.54×10^{-4}	3.41×10^{-4}	4.37×10^{-4}	2.38×10^{-4}	
Scattering coefficient	$Q_{sca} \text{ (cm}^{-1} \cdot \text{sr}^{-1}\text{)}$	4.398×10^{-9}	4.443×10^{-10}	1.135×10^{-10}	5.873×10^{-10}	1.041×10^{-10}	
Fractional uncertainty	$\delta Q_{sca}/Q_{sca}$	9.52×10^{-3}	3.15×10^{-2}	5.25×10^{-2}	3.26×10^{-2}	1.10×10^{-1}	
Uncertainty	$\delta Q_{sca} \text{ (cm}^{-1} \cdot \text{sr}^{-1}\text{)}$	4.19×10^{-11}	1.29×10^{-11}	5.96×10^{-12}	1.91×10^{-11}	1.16×10^{-11}	

Appendix C: Determination of Temperature from the Scattering Coefficient

C.1 Introduction

Measurement of Rayleigh scattering from the flame gases can be used to determine the local temperature (Eckbreth, 1988). The method is complicated by the dependence of the scattered signal on both the total number density and the mean scattering cross-section which is a function of the gas composition. Since determining the gas composition is an additional and sometimes complicated procedure, the gas composition can either be estimated or the experiment can be designed to reduce its effects on the variation in scattering cross-section. Dibble and Hollenbach (1981) demonstrated the application of Rayleigh scattering to measurement of temperatures in turbulent flames. They reduced the sensitivity of the method to variations in the gas scattering cross-section by adjusting the stoichiometry of the flame, so that the mean scattering cross-section variation was less than 2%. Rajan, Smith, and Rambach (1984) used Rayleigh scattering to investigate flame-turbulence interactions in a rod-stabilized propane-air flame. They used a detailed chemical kinetics code to estimate the species composition and thus the mean scattering cross-section as a function of the progress of reaction.

We take a similar approach to determine the temperature in our premixed laminar flames. We use the Sandia premixed one-dimensional flame code to solve a detailed chemical kinetic model and to determine the flame gas composition, which can then be used to calculate the scattering coefficient. The temperature is determined from a trial and error procedure which matches the predicted scattering coefficients from the solution of the flame code with the measured scattering coefficients. In this appendix, we first describe the theory for determining temperature from a Rayleigh scattering measurement. We then describe the calculation of the scattering cross-sections for the individual gas species. The implementation of the flame code to determine the gas composition and the subsequent calculation of the mean scattering cross-section and the scattering coefficient

are then discussed. We illustrate the trial-and-error procedure for a flame temperature profile and then show temperature profiles for some of our flames. Finally, we discuss possible errors in the temperature estimation and make suggestions for improving the method.

C.2 Theory and Method

The theory for Rayleigh scattering is discussed in Chapter 3. Here, we only restate those portions of the theory that are pertinent to the temperature measurement. The temperature profile can be calculated from the measured scattering coefficient profile if the scattered light is from the flame gases and not from soot particles. The scattering coefficient for the flame gases is given by

$$Q_{VV,g}(z) = N_g(z) \cdot \bar{C}_{VV,g}(z) \quad (C.1)$$

where $Q_{VV,g}$ ($\text{cm}^{-1} \cdot \text{sr}^{-1}$) is the molecular scattering coefficient, N_g (cm^{-3}) is the local gas number density, and $\bar{C}_{VV,g}$ ($\text{cm}^2 \cdot \text{sr}^{-1}$) is the mean differential scattering cross-section. The subscript VV indicates that both the incident and scattered light are vertically polarized. The molecular scattering coefficient, the local gas number density, and the mean differential scattering cross-section are functions of the height above the burner, z (cm).

We can assume that the scattering is from molecules, and not from particles, in nonsooting flames and in regions of sooting flames where soot has not yet formed. However, in flat premixed sooting flames, the height where particle scattering becomes significant is ill-defined. Fortunately, the location of significant particle scattering occurs after the peak temperature and thus, the temperature profile can at least be determined through the reaction zone.

The temperature profile can be determined from the local gas number density profile using the ideal gas law and is given by

$$T(z) = \frac{P}{R} \cdot \frac{N_m}{N_g(z)} \quad (C.2)$$

where T (K) is the temperature, P (atm) is the pressure, R ($82.055 \text{ cm}^3 \cdot \text{atm} \cdot \text{gmol}^{-1} \cdot \text{K}^{-1}$) is the gas constant, and N_{av} ($6.02252 \times 10^{23} \text{ gmol}^{-1}$) is Avogadro's number. The temperature profile can then be calculated from the measured scattering coefficient profile by combining Eqs. (C.1) and (C.2) to obtain

$$T(z) = \frac{P}{R} \cdot N_{av} \cdot \frac{\overline{C}_{vv,g}(z)}{Q_{vv,g}(z)} \quad (\text{C.3})$$

The mean differential scattering cross-section, required to calculate the temperature in Eq. (C.3), can be determined from the molar composition of the gas by

$$\overline{C}_{vv,g}(z) = \sum_k X_k(z) \cdot C_{vv,k} \quad (\text{C.4})$$

where X_k is the mole fraction and $C_{vv,k}$ ($\text{cm}^2 \cdot \text{sr}^{-1}$) is the differential scattering cross-section of species k , respectively (D'Alessio, 1981). The differential scattering cross-section of species k is given by

$$C_{vv,k} = \frac{4\pi^2}{\lambda^4} \cdot \frac{(n_k - 1)^2}{N_0^2} \cdot \frac{3}{3 - 4\rho_{v,k}} \quad (\text{C.5})$$

where λ (cm) is the wavelength of the incident light, n_k is the refractive index of the gas, N_0 (cm^{-3}) is the number density of the molecules, and $\rho_{v,k}$ is the depolarization ratio (Rudder and Bach, 1968; D'Alessio, 1981). The index of refraction and the number density must be evaluated at the same temperature and pressure. The depolarization ratio is the ratio of the horizontally polarized scattered light to the vertically polarized light and is given by $\rho_{v,k} = C_{Hv,k}/C_{Vv,k}$.

We calculated the index of refraction for the individual gas species in the chemical kinetic mechanism using the data for common combustion gases compiled by Gardiner, Hidaka, and Tanzawa (1981) from their survey and analysis of literature data. Their data is presented as the molar refractivity of the gas, R_L ($\text{cm}^3 \cdot \text{mol}^{-1}$), defined as

$$R_L = \frac{n^2 - 1}{n^2 + 2} \cdot \frac{1}{\rho} \quad (\text{C.6})$$

where ρ ($\text{mol}\cdot\text{cm}^{-3}$) is the molar density of the gas at the temperature and pressure of the refractive index measurement. For species that were common to both our reaction mechanism and the Gardiner, Hidaka, and Tanzawa (1981) compilation, we used their molar refractivity data at $\lambda = 488.0$ nm to calculate the index of refraction. For species in our reaction mechanism, but not in their compilation, we calculated the molar refractivities by summing up the atomic and bond refractivities at $\lambda = 488.0$ nm according to the structure of the species (Gardiner, Hidaka, and Tanzawa, 1981). Since the species not included in their compilation were present in only minor concentrations in the flame simulations, these species will not contribute significantly to the mean scattering cross-section and thus, any inaccuracy in the molar refractivity will be insignificant. The index of refraction is then determined from the molar refractivity by

$$n = \left(\frac{1 + 2\rho \cdot R_L}{1 - \rho \cdot R_L} \right)^{1/2} \quad (\text{C.7})$$

We evaluated the index of refraction at 0 °C and 1 atm ($\rho = 4.4615 \times 10^{-5}$ $\text{mol}\cdot\text{cm}^{-3}$) to be consistent with previous scattering-extinction measurements (Müller-Dethlefs, 1980; D'Alessio, 1981). Gardiner, Hidaka, and Tanzawa (1981) also present the index of refraction data in the form of a curve-fitted expression

$$n - 1 = \frac{a}{b - \lambda^{-2}} \quad (\text{C.8})$$

where a and b are the curve-fit coefficients. This equation and their curve-fit coefficients can be used to evaluate the index of refraction at wavelengths not in their table. We used this expression to estimate the index of refraction at $\lambda = 309$ nm, the wavelength used in the OH fluorescence measurements.

The depolarization ratios were based on data from four sources: Bogaard et al. (1978), Bridge and Buckingham (1966), Rudder and Bach (1968), and D'Alessio (1981). Data was not available for all of the species we considered in the reaction mechanisms. The depolarization ratio is a function of the electronic structure of the molecule and of

intermolecular forces in the gases. It is weakly dependent on the wavelength through the wavelength dependence of the index of refraction (Rudder and Bach, 1968). The weak dependence on wavelength allows us to estimate ρ_v at $\lambda = 488$ nm from measurements at other wavelengths. Measured depolarization ratios also include contributions caused by Raman scattering (Bridge and Buckingham, 1966). Most of the depolarization ratios are less than 5% and so their contributions to the scattering cross-sections are typically less than 7%. Missing depolarization data for minor combustion species is thus unlikely to affect the accuracy of the calculated mean differential scattering cross-sections.

Tables C.1 to C.3 list the molar refractivities, index of refraction, depolarization ratio, and the calculated differential scattering cross-sections for the species in our reaction mechanisms. Table C.1 lists the data for which Gardiner, Hidaka, and Tanzawa (1981) reported molar refractivities based on experimental measurements. Table C.2 lists the data for species for which they calculated the molar refractivities based on atomic and bond refractivities. Table C.3 lists the data for species which are not in their compilation and for which we calculated the molar refractivities based on the atomic and bond refractivities.

C.3 Calculation Procedure

The procedure to determine the temperature profile of a flame from its scattering coefficient profile used the Sandia premixed one-dimensional flame code (Kee et al., 1985) to determine the molar gas composition profile. Given the reactant composition, the mass flow rate of the reactants, the pressure, and a temperature profile, the Sandia flame code solves the conservation of mass, species, and energy equations for a constant-pressure, steady laminar, premixed one-dimensional flame to determine the species profiles. The reaction rates and properties of the species are specified through a chemical kinetic reaction mechanism. Our implementation of the flame code is described in Chapter 4 (Section 4.6). We adopted a chemical kinetic reaction mechanism reported

Table C.1 Molar refractivity, index of refraction, depolarization ratio, and scattering cross-section at $\lambda = 488.0$ nm for major combustion species. The molar refractivities are taken from Table I of Gardiner, Hidaka, and Tanzawa (1981).

Species	Molar Refractivity (mol·cm ⁻³)	Index of Refraction (n - 1)·10 ⁶	Depolarization Ratio 100· ρ_V	Cross-Section C_{VV} (10 ²⁸ cm ² ·sr ⁻¹)
O ₂	4.085	273.4	3.02 ^b	7.51
CO	5.062	338.8	0.521 ^a	11.14
CO ₂	6.720	449.8	4.12 ^a	20.64
H ₂ O	3.804	254.6	1.0 ^d	6.33
H ₂	2.097	140.3	0.339 ^c	1.91
N ₂	4.500	301.2	1.042 ^a	8.868
CH ₄ (methane)	6.665	446.1	0.0	19.18
C ₂ H ₂ (acetylene)	8.975	600.7	1.897 ^a	35.69
C ₂ H ₄ (ethylene)	10.864	727.1	1.266 ^a	51.85
C ₂ H ₆ (ethane)	11.424	764.6	0.190 ^a	56.51
C ₃ H ₄ (allene)	16.034	1073.2	4.22 ^a	117.67
C ₃ H ₆ (propylene)	15.948	1067.5	-	109.87
C ₃ H ₈ (propane)	16.254	1088.0	0.214 ^a	114.44
C ₆ H ₆ (benzene)	26.901	1800.8	1.98 ^a	321.15
OH (hydroxyl)	5.665	379.1	-	13.86
H (hydrogen atom)	1.752	117.3	-	1.32
O (oxygen atom)	1.902	127.3	-	1.56

^aBogaard et al. (1978), ^bBridge and Buckingham (1966), ^cRudder and Bach (1968), ^dD'Alessio (1981)

Table C.2 Molar refractivity, index of refraction, depolarization ratio, and scattering cross-section at $\lambda = 488.0$ nm for combustion species. The refractivities are calculated from atomic and bond refractivities (Table II, Gardiner, Hidaka, and Tanzawa, 1981).

Species	Molar Refractivity (mol·cm ⁻³)	Index of Refraction (n - 1)·10 ⁶	Depolarization Ratio 100· ρ_v	Cross-Section C_{vv} (10 ²⁸ cm ² ·sr ⁻¹)
C (carbon atom)	2.617	175.1	-	2.96
CH (methyldiyne)	3.654	244.5	-	5.77
CH ₂ (methylene)	4.691	313.9	-	9.50
CH ₃ (methyl)	5.728	383.4	-	14.17
C ₂ H (ethynyl)	8.314	556.4	-	29.85
C ₂ H ₃ (vinyl)	9.999	669.2	-	43.18
C ₂ H ₅ (ethyl)	10.420	697.4	-	46.90

Table C.3 Molar refractivity, index of refraction, depolarization ratio, and scattering cross-section at $\lambda = 488.0$ nm for combustion species not in the Gardiner, Hidaka, and Tanzawa (1981) compilation. The refractivities are calculated from atomic and bond refractivities (Table II, Gardiner, Hidaka, and Tanzawa, 1981).

Species	Molar Refractivity (mol·cm ⁻³)	Index of Refraction (n - 1)·10 ⁶	Depolarization Ratio 100· ρ_v	Cross-Section C_{vv} (10 ²⁸ cm ² ·sr ⁻¹)
H ₂ O ₂ (hydrogen peroxide)	5.282	353.5	-	12.05
HO ₂ (hydroperoxy)	4.245	284.1	-	7.78
CH ₂ O (formaldehyde)	7.173	480.1	-	22.22
HCO (formyl)	6.136	410.7	-	16.26
CH ₃ O (methoxy)	7.433	497.5	-	23.86
CH ₂ CO (ketene)	11.120	744.3	-	53.41
HCCO (ketyl)	10.083	674.9	-	43.91
C ₃ H ₂	11.968	801.0	-	61.87
C ₃ H ₇ (i)	15.110	1011.4	-	98.62
C ₃ H ₇ (n)	15.110	1011.4	-	98.62

by Drake and Blint (1991) to describe the oxidation and pyrolysis reactions of ethylene. We reduced the size of their mechanism to 32 species and 144 reactions by removing those reactions involving nitrogen chemistry. Removing these reactions and species decreased the computational time without affecting the concentrations of the major combustion species. We specified a temperature profile as an input to the flame code, instead of using the flame code to solve the energy equation to determine the temperature profile. The solutions obtained by the flame code contained the temperature and species mass fraction profiles and were stored in a binary format file for later analysis.

The temperature estimation procedure used a computer program which extracted the temperature and mass fraction profiles from the file containing the flame code solution and then calculated the predicted scattering coefficient profile. This program was written using subroutines from the Chemkin-II subroutine library (Kee, Rupley, and Miller, 1989), which read the Chemkin interpreter link file for information about the reaction mechanism and also the binary file containing the flame code solution for the temperature and molar composition profiles. This program reads the molar refractivity and depolarization ratio data for each species, calculates the index of refraction for each species using Eq. (C.7), and then calculates the differential scattering cross-section for each species using Eq. (C.5). The mean differential scattering cross-section profile, $\bar{C}_{vv}(z)$, is then calculated from the molar composition profile, $X_k(z)$, and the differential scattering cross-section for each species using Eq. (C.4). The temperature profile and the molar composition profile are then used to calculate the number density profile. Finally, the predicted scattering coefficient profile is calculated from the number density profile and the mean differential scattering cross-section profile using Eq. (C.1).

We determine the temperature profile for a flame through a trial-and-error procedure in which we use successively refined estimates of the input temperature profile until we closely match the predicted scattering coefficient profile to the measured scattering coefficient profile. A sequence of successive estimates for the temperature

profile and the resulting predicted scattering coefficient profiles are shown for the A-IA-S1 flame ($\phi = 1.78$) in Figure C.1. The match of the predicted to measured scattering coefficient profiles for the A-IA-R2 ($\phi = 1.63$) and A-IA-S1 ($\phi = 1.78$) flames are shown in Figure C.2. Figure C.2 also shows the predicted scattering coefficient profiles for both flames when the temperature profile is adjusted proportionally to an increase and decrease by 20 K in the peak temperature.

The initial estimate of the temperature profile for a flame can be determined by calculating the temperature profile from the measured scattering coefficient profile using Eq. (C.3) and a constant scattering cross-section for the burnt gas region determined from a solution of the energy equation. This procedure was used for the initial temperature profile estimate, (A), in Figure C.1. An alternate initial estimate can be obtained by using the temperature profile from a leaner flame at the same total flow rate and dilution ratio. After the flame code solution with the initial estimate is determined, the next estimate of the temperature profile can be obtained by comparing the predicted scattering coefficient profile to the measured scattering coefficient profile. We judged the fit of the predicted to the measured scattering coefficient profile by plotting both profiles using a logarithmic scale for the height above the burner as in Figure C.2. Using a logarithmic scale made it easier to compare the profiles in the region below the minimum of the scattering coefficient profile, where the decline in the scattering coefficient is steep when shown on a linear scale. Because of the scatter in the measured scattering coefficient data, we fit the measured scattering coefficient profile with a polynomial of the form

$$Q_{vv}(z) = a_{-1} \cdot z^{-1} + a_0 + a_1 \cdot z + a_2 \cdot z^2 \quad (\text{C.9})$$

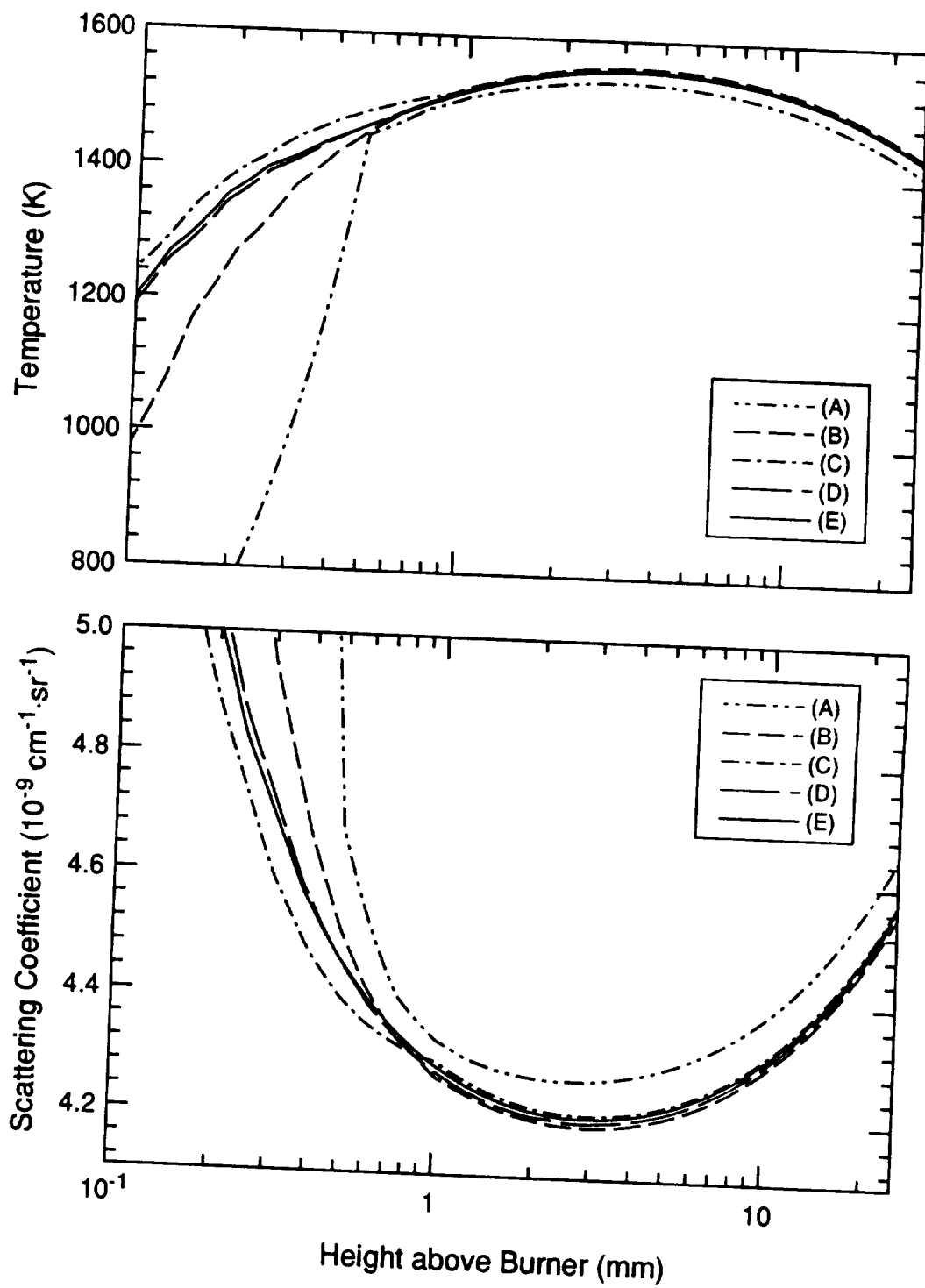


Figure C.1 Successive estimates of the temperature profile (upper plot) and the resulting predicted scattering coefficient profile (lower plot) for the A-IA-S1 flame ($\phi = 1.78$).

where a_{-1} , a_0 , a_1 , and a_2 are the curve fit coefficients to obtain a smooth profile. A visual judgment of the discrepancy between the predicted and measured scattering coefficient profile was deemed sufficient because of the scatter of the measured scattering coefficients and because of the relatively narrow temperature range (± 20 K) over which the predicted profiles bracket the measured data (Figure C.2).

When the predicted profile did not match the measured profile, the next estimate of the temperature profile was estimated from the previous temperature profile by using the equation

$$T(z) = \frac{Q_{vv,p}(z)}{Q_{vv,m}(z)} \cdot T_p(z) \quad (C.10)$$

where $T_p(z)$ is the previous estimate of the temperature profile, $Q_{vv,p}(z)$ is the previous predicted scattering coefficient profile, and $Q_{vv,m}(z)$ is the measured scattering coefficient profile. This equation was obtained from Eq. (C.3) by assuming little variation in the mean scattering cross-section. Thus, this method worked well for estimating temperatures at the peak of the temperature profile and higher, where the scattering cross-section varies little with height. However, good estimates are not always obtained in the region below the peak of the temperature profile where the scattering cross-section varies significantly. Figure C.3 shows the variation of cross-section with height for four atmospheric pressure flames with increasing equivalence ratio, but with the same cold flow velocity and dilution ratio. We used our best judgment to estimate the temperature profile in the region of the flame below the peak temperature. A more sophisticated approach might take into account the variation of cross-section with temperature and include that in a temperature estimation equation.

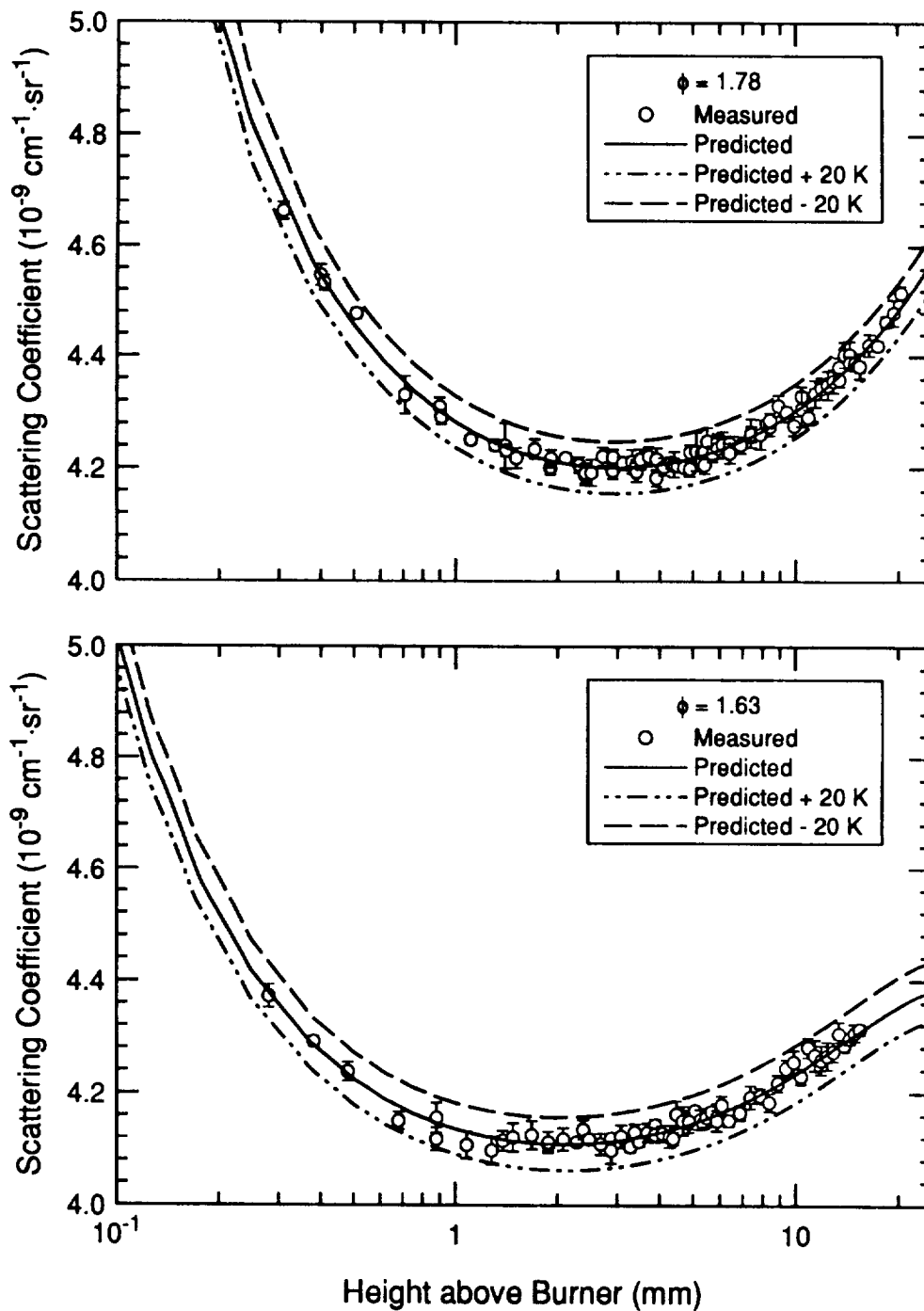


Figure C.2 Comparison of the predicted scattering coefficient profile with the measured scattering coefficient profile for the A-IA-S1 flame ($\phi = 1.78$, upper plot) and the A-IA-R2 flame ($\phi = 1.63$, lower plot). Also shown are the predicted scattering coefficient profiles when the peak temperatures are varied by 20 K.

C.4 Results and Discussion

The temperature profiles estimated from the scattering coefficient profiles are shown in Figures C.4 to C.7 for four atmospheric pressure flames with the same cold flow velocity ($v_c = 7.73 \text{ cm}\cdot\text{sec}^{-1}$) and dilution ratio ($D = 4.16$). The first flame in the sequence, flame A-IA-R2, is a nonsooting flame, while the remainder of the flames are visibly sooting. For each flame, the solid line is the temperature profile obtained by fitting the predicted scattering coefficient profile from the flame code solution to the measured scattering coefficient profile. The dashed line is the temperature profile obtained by the flame code when it solved the energy equation to determine the temperature. The circular symbols correspond to the temperatures calculated using Eq. (C.3) with the measured scattering coefficient and the calculated mean differential scattering cross-section obtained from the flame code solution at the peak of the temperature profile (see Fig. C.3).

The estimated temperature profiles of all four flames rise to a peak temperature closer to the burner surface than the temperature profiles from the flame code solution of the energy equation. In each of the flames, the temperature profile of the energy equation rises rapidly in the first few millimeters above the burner surface and then rises only $\sim 10 \text{ K}$ over the next 20 mm above the burner. The estimated temperature profiles decline steadily with height above the peak of the temperature profile. The temperature decline is caused by radiative losses that are not modelled in the flame code. The estimated temperature profile also peaks at a lower height than the profile of the energy equation solution. The likely cause for this difference is that the boundary conditions applied in the flame code do not accurately model the flame conditions for the honeycomb plug burner used in this experiment. The boundary conditions at the burner surface are specified to be the mass fluxes of the reactants at a fixed temperature, usually 300 K. Since the honeycomb plug burner is not cooled, preheating of the gases may occur so that the initial temperature and reactant composition may differ from the model assumptions.

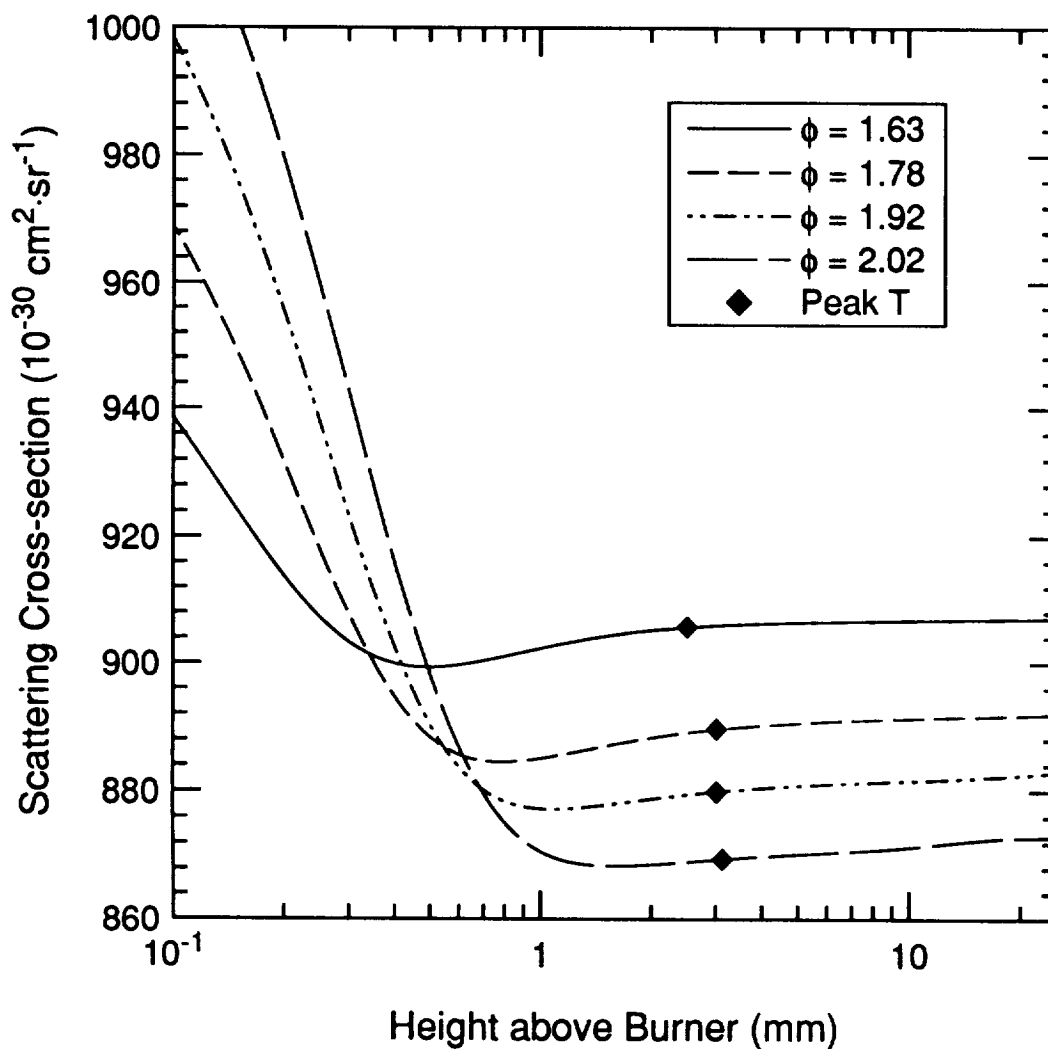


Figure C.3 Variation of the mean differential scattering cross-section with height above the burner for four flames: A-IA-R2 ($\phi = 1.63$), A-IA-S1 ($\phi = 1.78$), A-IA-S2 ($\phi = 1.92$), and A-IA-S3 ($\phi = 2.02$). The mean differential scattering cross-sections at the peak of the temperature profiles are marked with filled diamonds.

Radical species such as the hydrogen atom may also diffuse from the reaction zone back into the burner honeycomb and initiate reactions before the reactants reach the burner surface.

The estimated temperature in the A-IA-R2 flame (Fig. C.4) declines from a peak of 1617 K to 1547 K at 15 mm above the burner, a 60 K difference. The estimated temperature in the lightly sooting A-IA-S1 flame (Fig. C.5) declines from a peak of 1554 K to 1489 K at 15 mm above the burner, a 65 K difference. The scattering coefficient profile of this lightly sooting flame does not show a significant difference from the molecular scattering coefficient background, as evidenced by the similarity of its profile to the nonsooting flame, A-IA-R2. The estimated temperature declines more steeply with height after the peak in the two more heavily sooting flames. The estimated temperature of the A-IA-S2 flame (Fig. C.6) declines from the peak at 1546 K to 1375 K at 15 mm above the burner, while that of the A-IA-S3 flame (Fig. C.7) declines from 1489 K to 1117 K over the same interval. The measured scattering coefficient profiles in these two flames have an inflection point, beginning at about 15 mm in the A-IA-S2 flame and at 12 mm in the A-IA-S3 flame, where the scattering coefficient begins to increase significantly because of scattering from the particles. However, below this inflection point, the height where particle scattering begins to contribute significantly to the overall scattering coefficient is not clear.

The steeper estimated temperature decline in the A-IA-S2 and A-IA-S3 flames could be caused by two factors: (1) an increase in the radiative heat loss caused by emission from soot particles and (2) an increase in the scattered light caused by incipient soot particles and higher molecular weight species such as PAHs that have larger scattering cross-sections than the major combustion products.

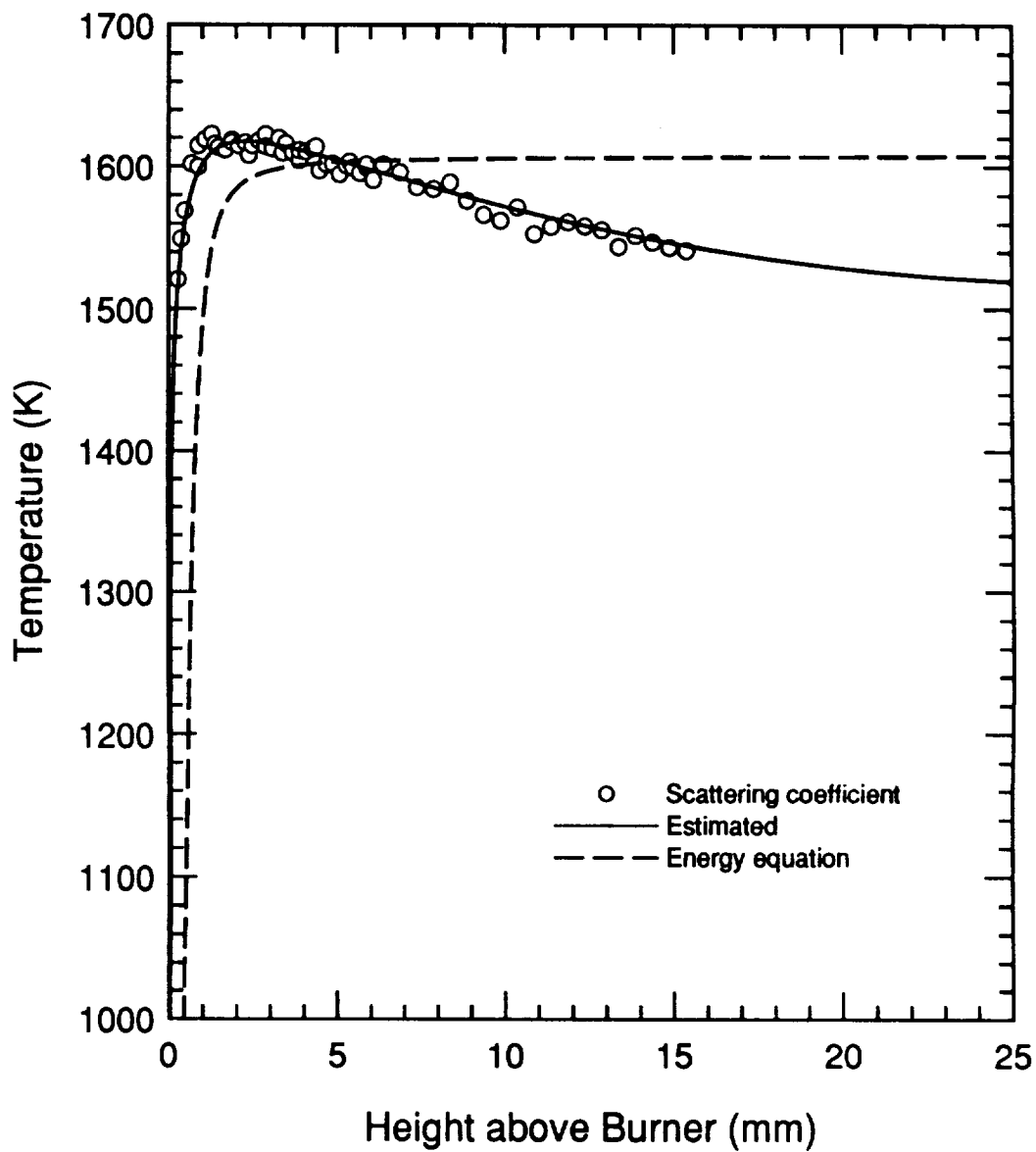


Figure C.4 Calculated temperature profiles for the A-IA-R2 flame ($\phi = 1.63$).

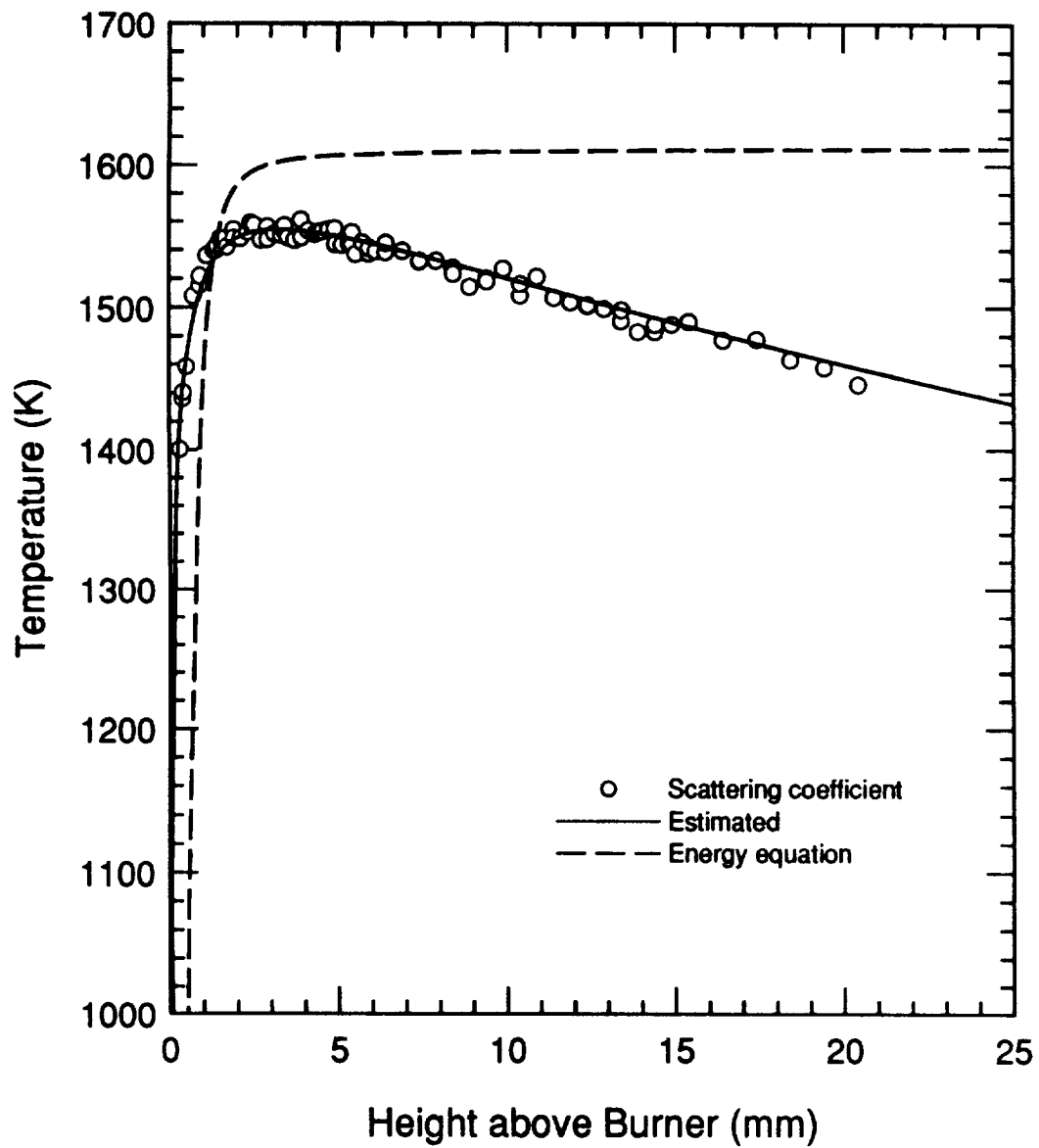


Figure C.5 Calculated temperature profiles for the A-IA-S1 flame ($\phi = 1.78$).

The high molecular weight hydrocarbons will cause an increase in the scattered light only if they are present in relatively large concentrations. For example, a benzene mole fraction in the range of $2.5\text{-}2.9 \times 10^{-4}$ would be required to produce an increase in the scattering coefficient on the order of $4 \times 10^{-11} \text{ cm}^{-1} \cdot \text{sr}^{-1}$, which is the uncertainty estimated for the scattering coefficient in Appendix B. Harris et al. (1986) measured peak concentrations of benzene at 170 ppm for a $\phi = 2.76$ and 5 ppm for a $\phi = 1.68$ atmospheric ethylene/oxygen/argon flame. Thus, the benzene concentrations are not likely to be large enough to produce a significant increase in the scattering coefficient. Harris and Weiner (1988) note that the same will be true for larger aromatics, because, even though their cross-sections are larger than that of benzene, their concentrations are one to two orders of magnitude smaller than that of benzene.

Since their scattering cross-sections are about three orders of magnitude larger than that of benzene, incipient soot particles are more likely to contribute significantly to the scattered signal. Incipient particles 1.5 nm in diameter have a scattering cross-section of $C_{\text{VV}} \sim 1\text{-}2 \times 10^{-23} \text{ cm}^2 \cdot \text{sr}^{-1}$ and would require a number density of $N_p \sim 2\text{-}4 \times 10^{12} \text{ cm}^{-3}$ to increase the scattering coefficient on the order of its uncertainty. Particles 2 nm in diameter ($C_{\text{VV}} \sim 6\text{-}11 \times 10^{-23} \text{ cm}^2 \cdot \text{sr}^{-1}$) would only require a number density of $N_p \sim 4\text{-}7 \times 10^{11} \text{ cm}^{-3}$ to produce a similar increase in the scattering coefficient. These number densities are of the same order of magnitude as the number of incipient particles identified in sooting ethylene/oxygen/argon flames (Harris, Weiner, and Ashcraft, 1986).

Thus, incipient soot particles could increase the scattering coefficient in these flames and their effect would be to produce an apparent temperature decline. Since this same effect is also likely to occur because of the increased emission of soot particles, these two effects will be difficult to separate. Separation would require an independent measure of temperature, such as with a thermocouple or with optical methods, e.g., absorption-emission or two-color emission. Comparison of the measured temperature

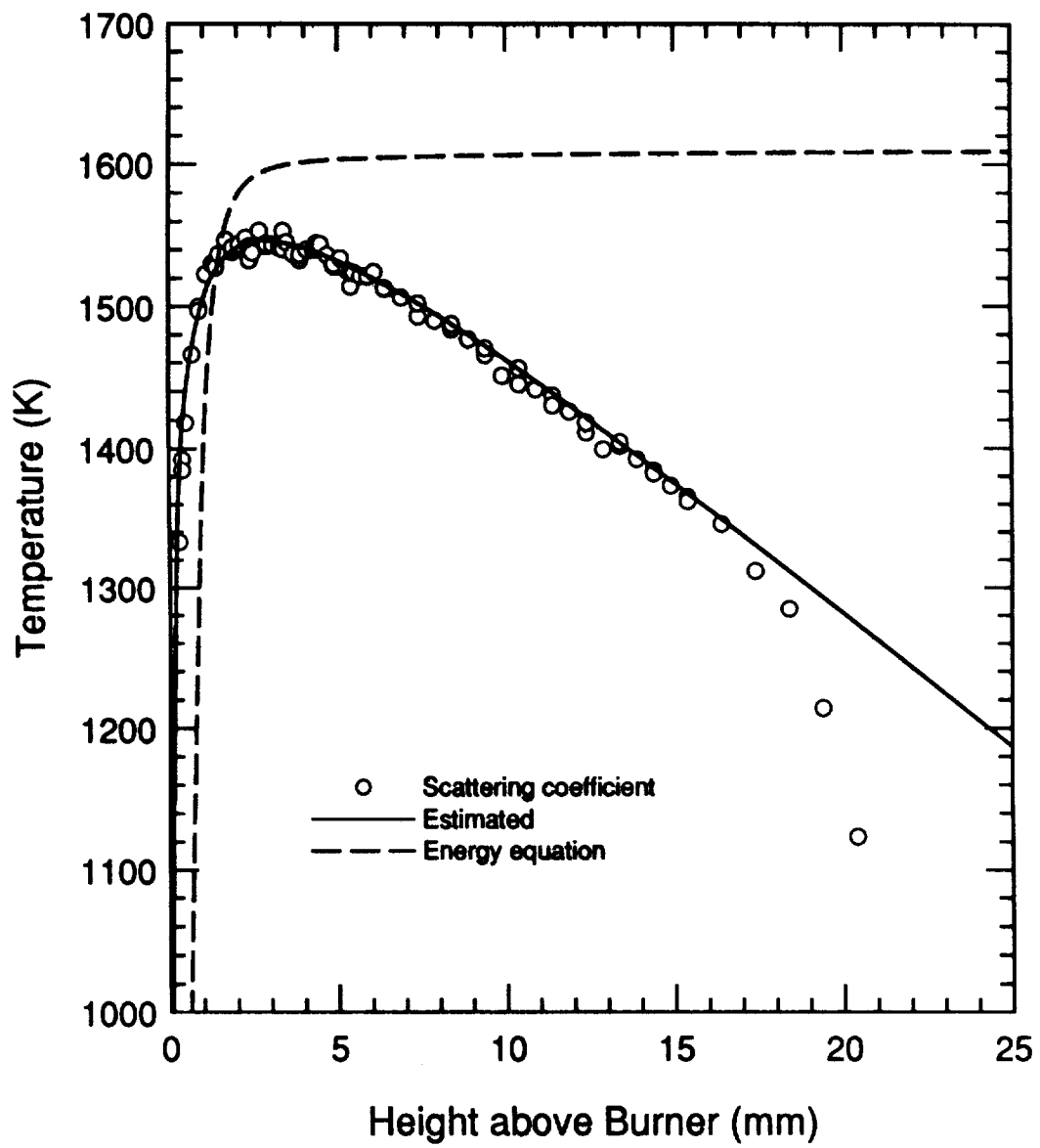


Figure C.6 Calculated temperature profiles for the A-IA-S2 flame ($\phi = 1.92$).

with the estimated temperature would then identify whether the apparent temperature decline is real or not. An independent measure of temperature would also be valuable in verifying this temperature estimation method.

The variation of the mean differential scattering cross-section with height above the burner is shown in Figure C.3 for these four atmospheric pressure flames. Above a 1 mm height, the scattering cross-section remains almost constant within a flame. The variation in scattering cross-section with height from 1 mm to 15 mm above the burner is less than 0.75% for these four atmospheric pressure flames. The validity of assuming a constant cross-section for this range is shown in Figures C.4 to C.7 which testify to the agreement between the temperature profile calculated from the measured scattering coefficient using a constant cross-section and the estimated temperature profile which accounted for the variation in cross-section. The scattering cross-section at the peak of the temperature profile (also, the minimum of the scattering coefficient profile) was chosen for these calculations because it lies in the middle of the range of cross-sections between 1 mm and 15 mm and thus provides a scattering cross-section that is easy to identify and that reduces the error over the cross-section range.

The scattering cross-section remains approximately constant above a height of 1 mm because the concentrations of the major species, N_2 , CO, CO_2 , H_2O , and H_2 , remain approximately constant above this height and these species are responsible for 95% of the molecular scattering cross-section. Table C.4 lists the major species and the percentage fraction of their contribution to the scattering cross-section in the four flames at 3 mm above the burner, the approximate height at which the peak temperature occurs.

Below the height of 1 mm above the burner, the scattering cross-section increases significantly, because the scattering cross-section of the fuel, C_2H_4 , and its pyrolysis products are typically two to three times larger than those of the oxidation products, CO, CO_2 , and H_2O (see Tables C.1 to C.3). Thus, in the reaction zone and below it, the assumption of a constant cross-section fails. This is not critical in the atmospheric

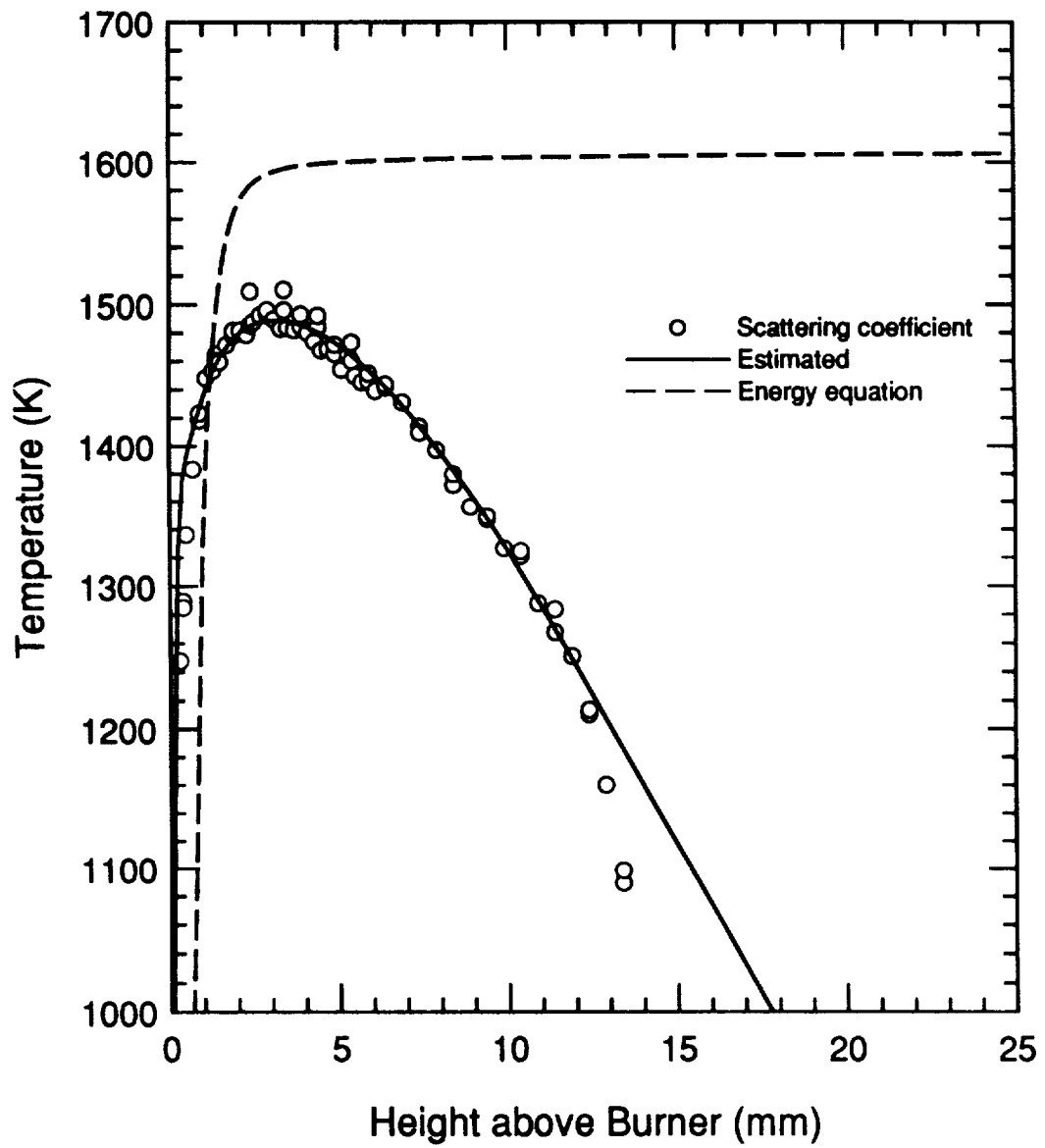


Figure C.7 Calculated temperature profiles for the A-IA-S3 flame ($\phi = 1.92$).

pressure flames, since the reaction zone is close to the burner surface and the scattering coefficient profile cannot be resolved much below 1 mm above the burner because of interference from the burner surface.

However, in the 80-torr flames, the scattering coefficient profile can be resolved through the reaction zone and below it because the flame is lifted off the burner and the reaction zone is expanded because of the low pressure. Thus, the constant cross-section assumption was not valid throughout this region of the low-pressure profiles. An additional factor in the variation of the cross-section is that no nitrogen diluent was used in most of the 80-torr flames. The nitrogen diluent in the atmospheric flames damps out variations in the scattering cross-section because its mole fraction is over 60% and thus it contributes a major fraction of the cross-section. Without this diluent to reduce the variation in cross-section, the temperature profiles in the 80-torr flames were difficult to estimate by matching the predicted to the measured scattering coefficient profiles. In this case, the predicted scattering coefficient becomes more sensitive to how well the flame chemistry model describes the oxidation and pyrolysis of the fuel up to the reaction zone. In the 80-torr flames without nitrogen diluent, the predicted profile could not match the measured profile without assuming an unrealistic temperature profile for the region below the reaction zone (less than 5 mm above the burner). However, similar to the atmospheric pressure flames, the region around the peak of the temperature profile and higher in the flame could be modelled, because then the major combustion products dominate the contributions to the scattering cross-sections. This suggests that the reaction mechanism (Drake and Blint, 1991) does not model well the oxidation and pyrolysis of ethylene for these particular conditions in the pre-reaction zone of the 80-torr flames.

The accuracy of the Rayleigh scattering method depends on how well the flame chemistry model predicts the actual species concentrations. For purposes of temperature measurement, the accuracy of the model could be checked by measuring the major combustion products in the post-flame zone. For the atmospheric-pressure flames, such

Table C.4 Percentage contributions by the principal species to the mean differential scattering cross-section at a height of 3 mm above the burner.

Flame	A-IA-R2 ($\phi = 1.63$)	A-IA-S1 ($\phi = 1.78$)	A-IA-S2 ($\phi = 1.92$)	A-IA-S3 ($\phi = 2.02$)
Species	$\frac{x_k \cdot C_{VV,t}}{\bar{C}_{VV}}$ (%)	$\frac{x_k \cdot C_{VV,t}}{\bar{C}_{VV}}$ (%)	$\frac{x_k \cdot C_{VV,t}}{\bar{C}_{VV}}$ (%)	$\frac{x_k \cdot C_{VV,t}}{\bar{C}_{VV}}$ (%)
N ₂	64.77	64.08	63.17	62.60
CO	15.01	17.82	19.77	21.37
CO ₂	10.66	7.89	6.16	4.92
H ₂ O	7.16	6.96	6.57	6.27
H ₂	1.48	1.78	2.08	2.31
CH ₄	-	0.16	0.31	0.47
C ₂ H ₄	-	-	-	0.10
C ₂ H ₂	0.83	1.24	1.79	1.80
\bar{C}_{VV} (cm ² ·sr ⁻¹)	900.7×10 ⁻³⁰	885.9×10 ⁻³⁰	877.7×10 ⁻³⁰	872.8×10 ⁻³⁰
Temperature (K)	1616	1553	1546	1488

a measurement could be used to calculate a scattering cross-section that, because of the constancy of the cross-section, could be used to calculate the temperature from the scattering coefficient through at least the peak of the profile.

The plot of the predicted and measured scattering coefficient profiles for the two flames shown in Figure C.2 illustrates the sensitivity of the molecular scattering coefficient to temperature. The bracketing of the measured scattering coefficient profile by the predicted scattering coefficient profile when the peak of the temperature profile is varied by ± 20 K indicates the potential resolution of the method. Given the uncertainty of $\delta Q_{sca} = 4.2 \times 10^{-11} \text{ cm}^2 \cdot \text{sr}^{-1}$ estimated for the scattering coefficient measurement in Appendix B, the corresponding uncertainty in the temperature is ± 15 K for the range of temperatures in the four atmospheric pressure flames shown here. This uncertainty does not include any uncertainty in the scattering cross-section. An evaluation of the uncertainty of the Rayleigh scattering method would require a separate measure of the gas composition and a finite-difference approximation approach similar to that in Appendix B.

C.5 Conclusions and Recommendations

We have demonstrated the theory and application of a procedure to determine the temperature profiles of the flames in this study by matching the predicted Rayleigh scattering coefficient profile obtained with the Sandia flame code to the measured Rayleigh scattering coefficient profile. Temperature profiles were estimated for four atmospheric pressure ethylene flames. For these flames, a constant scattering cross-section can be assumed to calculate the temperature from the scattering coefficient for heights greater than 1 mm above the burner. This assumption is sufficient to determine the peak of the temperature profile. Below the reaction zone in the atmospheric-pressure flames and in the 80-torr flames, the variation of the scattering cross-section must be considered when calculating the temperature.

The molecular scattering coefficient has a high sensitivity to temperature and thus the method has the potential for high resolution. The resolution of the temperature measurement is estimated to be ± 15 K for the experimental setup of this study. The accuracy of the method, however, was not evaluated or measured. The technique should be verified by measuring the temperature of the flame with a second method such as with other optical techniques or with a thermocouple. The accuracy of the measurement will also depend on how well the flame chemistry model predicts the actual gas composition. Again, an independent measure of the gas composition in the post-flame zone could be used to verify the accuracy of the flame chemistry model or actually eliminate the need to use the model if a constant scattering cross-section assumption should prove valid. Measurements in flames that have a significant nitrogen diluent mole fraction will be less sensitive to the accuracy of the flame chemistry model.

The interference from particle scattering in sooting flames limits the usefulness of this thermometric method because the contributions from molecular scattering and particle scattering cannot be separated. The temperature can then be estimated only in the regions of the flame that can be identified as nonsooting. Measurement of the temperature profile by a second method would be useful for sooting flames because the molecular scattering coefficient background could be predicted and then subtracted from the measured scattering coefficient profile to obtain the particle scattering coefficient.

Appendix D: Summary of Scattering-Extinction Data for the Atmospheric-Pressure Flames

We present here the data obtained from the scattering-extinction measurements for the atmospheric-pressure flames. The extinction and scattering coefficient profiles presented in Figures 5.1 to 5.11 are tabulated to facilitate their use for modelling. In addition, we tabulate the profiles of the argon-ion laser-induced fluorescence coefficients presented in Figure 5.17. We also list the temperature profiles determined from the scattering coefficient profiles. These temperature profiles were subsequently used for the chemical kinetic modelling.

Tables D.1 to D.14 list the normalized transmittance and extinction coefficient profiles for the atmospheric-pressure flames. The data analysis to determine these profiles is described in Sections 4.4.4 and B.4. The normalized transmittance was calculated using Eqs. (4.4.2) and (4.4.7) from the transmittance signal ratio. The standard deviation of the transmittance was calculated from the measured samples of the transmittance signal ratio as described in Section B.4. The extinction coefficient was calculated from the normalized transmittance using Eq. (4.4.10) with the pathlength, $L = 5.6$ cm. The standard deviation of the extinction coefficient was calculated from the standard deviation of the transmittance using Eq. (B.23) and assuming no error in the pathlength.

Tables D.15 to D.28 list the scattering coefficient profiles for the atmospheric-pressure flames. The total scattering coefficient profiles, $Q_{scd}(z)$, are listed for all the flames. The total scattering coefficient was calculated from the scattering signal ratio using Eq. (4.4.5). The standard deviation was calculated from the measured samples of the scattering signal ratio as described in Section B.4. For the sooting flames, we also list the particle scattering coefficient. The particle scattering coefficient was calculated from the total scattering coefficient by subtracting the molecular scattering

coefficient as described in Sections 4.4.4 and 5.3.1. For the flames in which the argon-ion laser-induced fluorescence background could be determined, the 'corrected' particle scattering coefficient determined by subtracting the fluorescence coefficient is listed.

Tables D.29 to D.32 list the profiles of the argon-ion laser-induced fluorescence detected at both 473 nm and 503 nm. The fluorescence profiles detected at 503 nm are shown in Figure 5.17. The fluorescence profiles detected at 473 nm are not presented in the text because of their similarity to the profiles detected at 503 nm, but are tabulated here for reference. The standard deviation was calculated from the measured samples of the fluorescence signal ratio as described in Section B.4.

Tables D.33 to D.36 list the temperature profiles determined from the scattering coefficient profiles for the atmospheric-pressure flames. The temperature data presented here are shown in Figures 5.29 to 5.31. These temperature profiles were determined using the procedure described in Appendix C. For the sooting flames, the temperatures are listed only up to the height at which particle scattering becomes significant.

Table D.1 Normalized transmittance and extinction coefficient profiles of the A-IA-R2 flame ($\phi = 1.63$, $v_c = 7.73 \text{ cm}\cdot\text{sec}^{-1}$, $D = 4.15$).

	Height (mm)	Transmittance	Standard Deviation	Extinction Coefficient (cm^{-1})	Standard Deviation
1.	0.875	9.9940E-1	1.4056E-4	1.0753E-4	2.5115E-5
2.	1.375	9.9951E-1	1.2549E-4	8.6807E-5	2.2419E-5
3.	1.875	9.9949E-1	7.0418E-5	9.1452E-5	1.2581E-5
4.	2.375	9.9953E-1	8.6276E-5	8.3591E-5	1.5414E-5
5.	2.875	9.9949E-1	1.0796E-4	9.1988E-5	1.9289E-5
6.	3.375	9.9956E-1	9.2893E-5	7.8589E-5	1.6595E-5
7.	3.875	9.9959E-1	1.1276E-4	7.2872E-5	2.0144E-5
8.	4.375	9.9960E-1	1.0181E-4	7.1800E-5	1.8188E-5
9.	4.875	9.9951E-1	9.2506E-5	8.7164E-5	1.6527E-5
10.	5.375	9.9950E-1	1.3316E-4	8.9487E-5	2.3790E-5
11.	5.875	9.9956E-1	6.9957E-5	7.8053E-5	1.2498E-5
12.	6.375	9.9962E-1	1.1207E-4	6.7691E-5	2.0019E-5
13.	6.875	9.9956E-1	1.1086E-4	7.8410E-5	1.9805E-5
14.	7.375	9.9956E-1	1.1786E-4	7.8946E-5	2.1056E-5
15.	7.875	9.9958E-1	1.2722E-4	7.5909E-5	2.2728E-5
16.	8.375	9.9960E-1	1.1004E-4	7.2157E-5	1.9658E-5
17.	8.875	9.9967E-1	1.0079E-4	5.8402E-5	1.8003E-5
18.	9.375	9.9961E-1	1.3642E-4	6.9299E-5	2.4370E-5
19.	9.875	9.9956E-1	8.6347E-5	7.8589E-5	1.5426E-5
20.	10.375	9.9966E-1	1.1869E-4	6.1618E-5	2.1203E-5
21.	10.875	9.9966E-1	8.7938E-5	6.1261E-5	1.5709E-5
22.	11.375	9.9970E-1	5.6357E-5	5.4473E-5	1.0067E-5
23.	11.875	9.9971E-1	1.3241E-4	5.1079E-5	2.3651E-5
24.	12.375	9.9979E-1	9.2706E-5	3.7861E-5	1.6558E-5
25.	12.875	9.9973E-1	8.9632E-5	4.7864E-5	1.6010E-5
26.	13.375	9.9977E-1	9.9963E-5	4.1433E-5	1.7855E-5
27.	13.875	9.9984E-1	1.0755E-4	2.8752E-5	1.9209E-5
28.	14.375	1.0000	1.0008E-4	0.0	--
29.	14.875	9.9982E-1	9.9755E-5	3.2324E-5	1.7817E-5
30.	15.375	9.9986E-1	1.1055E-4	2.4823E-5	1.9744E-5
31.	15.875	9.9985E-1	1.1595E-4	2.6966E-5	2.0708E-5
32.	16.375	9.9984E-1	9.4534E-5	2.8574E-5	1.6884E-5
33.	16.875	9.9994E-1	9.3062E-5	1.0000E-5	1.6619E-5
34.	17.375	9.9995E-1	1.3285E-4	9.8217E-6	2.3725E-5
35.	17.875	9.9992E-1	1.2653E-4	1.3929E-5	2.2596E-5
36.	18.375	9.9996E-1	8.9329E-5	6.6073E-6	1.5952E-5
37.	18.875	1.0000	1.0333E-4	0.0	--
38.	19.375	1.0000	9.4107E-5	0.0	--
39.	19.875	9.9995E-1	8.1275E-5	9.1074E-6	1.4514E-5
40.	20.375	1.0000	1.1642E-4	0.0	--

Table D.2 Normalized transmittance and extinction coefficient profiles of the A-IA-S1 flame ($\phi = 1.78$, $v_c = 7.73 \text{ cm}\cdot\text{sec}^{-1}$, $D = 4.16$).

	Height (mm)	Transmittance	Standard Deviation	Extinction Coefficient (cm^{-1})	Standard Deviation
1.	0.875	9.9961E-1	8.8665E-5	6.9835E-5	1.5839E-5
2.	1.375	9.9982E-1	7.9252E-5	3.1789E-5	1.4155E-5
3.	1.875	9.9985E-1	1.0486E-4	2.6431E-5	1.8727E-5
4.	2.375	9.9983E-1	9.5641E-5	2.9824E-5	1.7082E-5
5.	2.875	9.9984E-1	9.7442E-5	2.7859E-5	1.7403E-5
6.	3.375	9.9978E-1	1.0247E-4	3.9469E-5	1.8302E-5
7.	3.875	9.9990E-1	1.1840E-4	1.8037E-5	2.1145E-5
8.	4.375	9.9984E-1	6.8076E-5	2.7859E-5	1.2158E-5
9.	4.875	9.9987E-1	1.0002E-4	2.3394E-5	1.7863E-5
10.	5.375	9.9974E-1	8.7945E-5	4.7149E-5	1.5709E-5
11.	5.875	9.9992E-1	7.5503E-5	1.4286E-5	1.3484E-5
12.	6.375	9.9985E-1	1.1270E-4	2.7145E-5	2.0128E-5
13.	6.875	9.9998E-1	8.5856E-5	4.2858E-6	1.5332E-5
14.	7.375	9.9994E-1	1.0958E-4	1.0893E-5	1.9569E-5
15.	7.875	9.9988E-1	8.4869E-5	2.1251E-5	1.5157E-5
16.	8.375	9.9982E-1	9.6295E-5	3.2860E-5	1.7199E-5
17.	8.875	1.0000	6.8945E-5	0.0	--
18.	9.375	9.9993E-1	9.8758E-5	1.2143E-5	1.7637E-5
19.	9.875	9.9993E-1	1.0822E-4	1.2322E-5	1.9326E-5
20.	10.375	9.9987E-1	1.0098E-4	2.3037E-5	1.8034E-5
21.	10.875	9.9984E-1	9.2562E-5	2.8217E-5	1.6532E-5
22.	11.375	9.9994E-1	8.9671E-5	1.1429E-5	1.6014E-5
23.	11.875	9.9994E-1	9.0450E-5	1.0536E-5	1.6153E-5
24.	12.375	9.9986E-1	9.3283E-5	2.5002E-5	1.6660E-5
25.	12.875	9.9990E-1	6.4700E-5	1.7501E-5	1.1555E-5
26.	13.375	9.9988E-1	7.4337E-5	2.2144E-5	1.3276E-5
27.	13.875	1.0000	9.0383E-5	0.0	--
28.	14.375	1.0000	1.2001E-4	0.0	--
29.	14.875	9.9997E-1	1.0790E-4	6.0715E-6	1.9269E-5
30.	15.375	1.0000	1.1017E-4	0.0	--
31.	15.875	9.9992E-1	9.3529E-5	1.4465E-5	1.6703E-5
32.	16.375	9.9987E-1	8.8367E-5	2.2680E-5	1.5782E-5
33.	16.875	9.9987E-1	1.1287E-4	2.2859E-5	2.0159E-5
34.	17.375	1.0000	1.2271E-4	0.0	--
35.	17.875	1.0000	1.1226E-4	0.0	--
36.	18.375	9.9991E-1	1.3091E-4	1.6251E-5	2.3379E-5
37.	18.875	9.9999E-1	5.7143E-5	1.0714E-6	1.0204E-5
38.	19.375	1.0000	8.0484E-5	0.0	--
39.	19.875	1.0000	8.2116E-5	0.0	--
40.	20.375	9.9998E-1	1.3908E-4	3.3929E-6	2.4837E-5

Table D.3 Normalized transmittance and extinction coefficient profiles of the A-IA-S2 flame ($\phi = 1.92$, $v_c = 7.75 \text{ cm}\cdot\text{sec}^{-1}$, $D = 4.17$).

	Height (mm)	Transmittance	Standard Deviation	Extinction Coefficient (cm^{-1})	Standard Deviation
1.	0.894	9.9957E-1	8.3502E-5	7.6802E-5	1.4917E-5
2.	1.394	1.0000	6.5712E-5	0.0	--
3.	1.894	9.9994E-1	6.6569E-5	1.0000E-5	1.1888E-5
4.	2.394	1.0000	7.3544E-5	0.0	--
5.	2.894	9.9990E-1	9.0604E-5	1.7501E-5	1.6181E-5
6.	3.394	9.9990E-1	9.2355E-5	1.7501E-5	1.6494E-5
7.	3.894	9.9987E-1	8.2620E-5	2.3216E-5	1.4756E-5
8.	4.394	9.9985E-1	9.3341E-5	2.6966E-5	1.6671E-5
9.	4.894	9.9961E-1	7.7977E-5	7.0371E-5	1.3930E-5
10.	5.394	9.9946E-1	8.6244E-5	9.6633E-5	1.5409E-5
11.	5.894	9.9937E-1	7.4677E-5	1.1289E-4	1.3344E-5
12.	6.394	9.9924E-1	8.2658E-5	1.3505E-4	1.4772E-5
13.	6.894	9.9906E-1	8.6185E-5	1.6794E-4	1.5405E-5
14.	7.394	9.9896E-1	9.7037E-5	1.8599E-4	1.7346E-5
15.	7.894	9.9884E-1	1.0317E-4	2.0691E-4	1.8445E-5
16.	8.394	9.9872E-1	7.4009E-5	2.2800E-4	1.3233E-5
17.	8.894	9.9845E-1	9.2043E-5	2.7700E-4	1.6462E-5
18.	9.394	9.9829E-1	1.0416E-4	3.0490E-4	1.8631E-5
19.	9.894	9.9819E-1	9.5034E-5	3.2279E-4	1.7001E-5
20.	10.394	9.9783E-1	9.6984E-5	3.8828E-4	1.7356E-5
21.	10.894	9.9760E-1	9.3168E-5	4.2927E-4	1.6677E-5
22.	11.394	9.9742E-1	1.0903E-4	4.6059E-4	1.9521E-5
23.	11.894	9.9726E-1	1.3127E-4	4.9014E-4	2.3505E-5
24.	12.394	9.9714E-1	1.2964E-4	5.1127E-4	2.3217E-5
25.	12.894	9.9679E-1	7.4268E-5	5.7467E-4	1.3305E-5
26.	13.394	9.9671E-1	1.0550E-4	5.8793E-4	1.8902E-5
27.	13.894	9.9644E-1	1.2467E-4	6.3685E-4	2.2343E-5
28.	14.394	9.9637E-1	8.7631E-5	6.4886E-4	1.5705E-5
29.	14.894	9.9608E-1	1.3263E-4	7.0227E-4	2.3777E-5
30.	15.394	9.9608E-1	9.5874E-5	7.0138E-4	1.7188E-5
31.	15.894	9.9545E-1	1.1369E-4	8.1382E-4	2.0395E-5
32.	16.394	9.9536E-1	1.3250E-4	8.2978E-4	2.3771E-5
33.	16.894	9.9522E-1	1.4028E-4	8.5508E-4	2.5171E-5
34.	17.394	9.9497E-1	1.6718E-4	9.0084E-4	3.0005E-5
35.	17.894	9.9481E-1	1.4794E-4	9.2974E-4	2.6556E-5
36.	18.394	9.9479E-1	1.7526E-4	9.3225E-4	3.1459E-5
37.	18.894	9.9439E-1	1.7955E-4	1.0046E-3	3.2244E-5
38.	19.394	9.9434E-1	1.4511E-4	1.0132E-3	2.6060E-5
39.	19.894	9.9422E-1	1.7797E-4	1.0351E-3	3.1964E-5
40.	20.394	9.9407E-1	1.3562E-4	1.0617E-3	2.4363E-5

Table D.4 Normalized transmittance and extinction coefficient profiles of the A-IA-S3 flame ($\phi = 2.02$, $v_c = 7.74 \text{ cm}\cdot\text{sec}^{-1}$, $D = 4.16$).

	Height (mm)	Transmittance	Standard Deviation	Extinction Coefficient (cm^{-1})	Standard Deviation
1.	0.875	9.9980E-1	7.8827E-5	3.5897E-5	1.4079E-5
2.	1.375	9.9997E-1	8.7657E-5	5.0001E-6	1.5654E-5
3.	1.875	1.0000	7.9697E-5	0.0	--
4.	2.375	1.0000	6.3190E-5	0.0	--
5.	2.875	9.9986E-1	7.8295E-5	2.5002E-5	1.3983E-5
6.	3.375	9.9971E-1	8.5991E-5	5.1079E-5	1.5360E-5
7.	3.875	9.9934E-1	7.4329E-5	1.1736E-4	1.3282E-5
8.	4.375	9.9902E-1	6.8752E-5	1.7509E-4	1.2289E-5
9.	4.875	9.9878E-1	9.3649E-5	2.1799E-4	1.6743E-5
10.	5.375	9.9836E-1	8.3737E-5	2.9346E-4	1.4978E-5
11.	5.875	9.9792E-1	9.5210E-5	3.7271E-4	1.7037E-5
12.	6.375	9.9731E-1	9.3026E-5	4.8136E-4	1.6657E-5
13.	6.875	9.9691E-1	8.2509E-5	5.5282E-4	1.4780E-5
14.	7.375	9.9625E-1	8.3557E-5	6.7054E-4	1.4977E-5
15.	7.875	9.9568E-1	9.4657E-5	7.7346E-4	1.6976E-5
16.	8.375	9.9507E-1	9.6586E-5	8.8325E-4	1.7333E-5
17.	8.875	9.9434E-1	1.3281E-4	1.0143E-3	2.3851E-5
18.	9.375	9.9385E-1	1.1386E-4	1.1025E-3	2.0459E-5
19.	9.875	9.9287E-1	1.1216E-4	1.2772E-3	2.0172E-5
20.	10.375	9.9234E-1	9.1260E-5	1.3724E-3	1.6422E-5
21.	10.875	9.9182E-1	1.3647E-4	1.4664E-3	2.4570E-5
22.	11.375	9.9097E-1	1.1349E-4	1.6202E-3	2.0451E-5
23.	11.875	9.9018E-1	1.2231E-4	1.7630E-3	2.2059E-5
24.	12.375	9.8964E-1	1.2749E-4	1.8600E-3	2.3005E-5
25.	12.875	9.8921E-1	1.3959E-4	1.9374E-3	2.5199E-5
26.	13.375	9.8839E-1	1.8396E-4	2.0861E-3	3.3235E-5
27.	13.875	9.8789E-1	1.6451E-4	2.1752E-3	2.9736E-5
28.	14.375	9.8729E-1	1.5394E-4	2.2851E-3	2.7844E-5
29.	14.875	9.8669E-1	1.8340E-4	2.3927E-3	3.3191E-5
30.	15.375	9.8611E-1	1.7359E-4	2.4972E-3	3.1435E-5
31.	15.875	9.8524E-1	1.8531E-4	2.6557E-3	3.3587E-5
32.	16.375	9.8492E-1	1.8514E-4	2.7137E-3	3.3568E-5
33.	16.875	9.8437E-1	3.0876E-4	2.8131E-3	5.6012E-5
34.	17.375	9.8374E-1	2.9598E-4	2.9269E-3	5.3728E-5
35.	17.875	9.8305E-1	2.1698E-4	3.0520E-3	3.9413E-5
36.	18.375	9.8291E-1	2.6557E-4	3.0787E-3	4.8248E-5
37.	18.875	9.8240E-1	4.2268E-4	3.1707E-3	7.6830E-5
38.	19.375	9.8153E-1	3.2920E-4	3.3283E-3	5.9891E-5
39.	19.875	9.8092E-1	2.7110E-4	3.4399E-3	4.9351E-5
40.	20.375	9.8054E-1	3.8231E-4	3.5094E-3	6.9624E-5

Table D.5 Normalized transmittance and extinction coefficient profiles of the A-IA-S4 flame ($\phi = 2.17$, $v_c = 7.75 \text{ cm}\cdot\text{sec}^{-1}$, $D = 4.16$).

	Height (mm)	Transmittance	Standard Deviation	Extinction Coefficient (cm^{-1})	Standard Deviation
1.	0.534	9.9867E-1	1.1247E-4	2.3766E-4	2.0111E-5
2.	0.734	9.9928E-1	7.6378E-5	1.2862E-4	1.3649E-5
3.	0.924	9.9942E-1	5.6205E-5	1.0396E-4	1.0043E-5
4.	0.934	9.9985E-1	9.2799E-5	2.7324E-5	1.6574E-5
5.	1.134	9.9984E-1	7.7530E-5	2.8752E-5	1.3847E-5
6.	1.334	1.0000	6.6453E-5	0.0	--
7.	1.424	1.0000	6.2781E-5	0.0	--
8.	1.534	9.9996E-1	5.1396E-5	8.0359E-6	9.1782E-6
9.	1.734	9.9998E-1	6.8689E-5	3.5715E-6	1.2266E-5
10.	1.924	9.9986E-1	7.0044E-5	2.5538E-5	1.2510E-5
11.	1.934	9.9992E-1	5.1711E-5	1.3751E-5	9.2348E-6
12.	2.134	9.9990E-1	7.8277E-5	1.7858E-5	1.3979E-5
13.	2.334	9.9969E-1	1.2373E-4	5.6259E-5	2.2102E-5
14.	2.424	9.9959E-1	5.6647E-5	7.2515E-5	1.0120E-5
15.	2.534	9.9965E-1	9.8180E-5	6.2154E-5	1.7538E-5
16.	2.734	9.9930E-1	5.8013E-5	1.2594E-4	1.0367E-5
17.	2.924	9.9890E-1	1.2134E-4	1.9618E-4	2.1691E-5
18.	2.934	9.9917E-1	5.8653E-5	1.4917E-4	1.0483E-5
19.	3.134	9.9870E-1	7.0525E-5	2.3158E-4	1.2610E-5
20.	3.334	9.9828E-1	5.7023E-5	3.0777E-4	1.0200E-5
21.	3.424	9.9790E-1	4.2732E-5	3.7539E-4	7.6468E-6
22.	3.534	9.9774E-1	7.6355E-5	4.0367E-4	1.3666E-5
23.	3.734	9.9734E-1	4.1571E-5	4.7492E-4	7.4432E-6
24.	3.924	9.9650E-1	6.3641E-5	6.2592E-4	1.1404E-5
25.	3.934	9.9649E-1	6.4795E-5	6.2878E-4	1.1611E-5
26.	4.134	9.9585E-1	8.3662E-5	7.4261E-4	1.5002E-5
27.	4.334	9.9502E-1	7.7981E-5	8.9187E-4	1.3995E-5
28.	4.424	9.9468E-1	7.8293E-5	9.5218E-4	1.4056E-5
29.	4.534	9.9411E-1	1.6110E-4	1.0556E-3	2.8939E-5
30.	4.734	9.9325E-1	7.9472E-5	1.2087E-3	1.4288E-5
31.	4.924	9.9234E-1	7.2603E-5	1.3740E-3	1.3065E-5
32.	4.934	9.9247E-1	5.4137E-5	1.3503E-3	9.7407E-6
33.	5.134	9.9146E-1	8.8787E-5	1.5317E-3	1.5991E-5
34.	5.334	9.9049E-1	4.2311E-5	1.7056E-3	7.6281E-6
35.	5.424	9.8984E-1	6.7275E-5	1.8230E-3	1.2137E-5
36.	5.534	9.8942E-1	9.9261E-5	1.8994E-3	1.7915E-5
37.	5.734	9.8828E-1	5.7448E-5	2.1045E-3	1.0380E-5
38.	5.924	9.8710E-1	8.4662E-5	2.3191E-3	1.5316E-5
39.	5.934	9.8721E-1	8.8927E-5	2.2996E-3	1.6086E-5
40.	6.134	9.8575E-1	6.0667E-5	2.5635E-3	1.0990E-5
41.	6.424	9.8379E-1	1.1769E-4	2.9191E-3	2.1363E-5
42.	6.924	9.8047E-1	1.9075E-4	3.5229E-3	3.4740E-5
43.	7.424	9.7686E-1	2.8232E-4	4.1813E-3	5.1609E-5
44.	7.924	9.7287E-1	3.8501E-4	4.9108E-3	7.0669E-5
45.	8.424	9.6929E-1	2.4206E-4	5.5701E-3	4.4594E-5

Table D.5 continued

	Height (mm)	Transmittance	Standard Deviation	Extinction Coefficient (cm^{-1})	Standard Deviation
46.	8.924	9.6421E-1	2.5656E-4	6.5082E-3	4.7515E-5
47.	9.424	9.6032E-1	1.5232E-4	7.2305E-3	2.8323E-5
48.	9.924	9.5745E-1	1.0144E-3	7.7655E-3	1.8920E-4
49.	10.424	9.5246E-1	4.3860E-4	8.6979E-3	8.2232E-5
50.	10.924	9.4841E-1	9.5512E-4	9.4579E-3	1.7983E-4
51.	11.424	9.4520E-1	1.2038E-3	1.0065E-2	2.2743E-4
52.	11.924	9.4109E-1	4.3974E-4	1.0842E-2	8.3440E-5
53.	12.424	9.3837E-1	6.3632E-4	1.1359E-2	1.2109E-4
54.	12.924	9.3379E-1	5.8298E-4	1.2233E-2	1.1149E-4
55.	13.424	9.2673E-1	1.3776E-3	1.3589E-2	2.6546E-4
56.	13.924	9.2491E-1	1.0176E-3	1.3938E-2	1.9646E-4
57.	14.424	9.1970E-1	1.1114E-3	1.4949E-2	2.1580E-4
58.	14.924	9.1627E-1	1.6763E-3	1.5616E-2	3.2669E-4
59.	15.424	9.1209E-1	2.5267E-3	1.6432E-2	4.9469E-4

Table D.6 Normalized transmittance and extinction coefficient profiles of the A-IA-S5 flame ($\phi = 2.32$, $v_c = 7.75 \text{ cm}\cdot\text{sec}^{-1}$, $D = 4.16$).

	Height (mm)	Transmittance	Standard Deviation	Extinction Coefficient (cm^{-1})	Standard Deviation
1.	0.534	9.9867E-1	1.1247E-4	2.3766E-4	2.0111E-5
2.	0.734	9.9928E-1	7.6378E-5	1.2862E-4	1.3649E-5
3.	0.924	9.9942E-1	5.6205E-5	1.0396E-4	1.0043E-5
4.	0.934	9.9985E-1	9.2799E-5	2.7324E-5	1.6574E-5
5.	1.134	9.9984E-1	7.7530E-5	2.8752E-5	1.3847E-5
6.	1.334	1.0000	6.6453E-5	0.0	--
7.	1.424	1.0000	6.2781E-5	0.0	--
8.	1.534	9.9996E-1	5.1396E-5	8.0359E-6	9.1782E-6
9.	1.734	9.9998E-1	6.8689E-5	3.5715E-6	1.2266E-5
10.	1.924	9.9986E-1	7.0044E-5	2.5538E-5	1.2510E-5
11.	1.934	9.9992E-1	5.1711E-5	1.3751E-5	9.2348E-6
12.	2.134	9.9990E-1	7.8277E-5	1.7858E-5	1.3979E-5
13.	2.334	9.9969E-1	1.2373E-4	5.6259E-5	2.2102E-5
14.	2.424	9.9959E-1	5.6647E-5	7.2515E-5	1.0120E-5
15.	2.534	9.9965E-1	9.8180E-5	6.2154E-5	1.7538E-5
16.	2.734	9.9930E-1	5.8013E-5	1.2594E-4	1.0367E-5
17.	2.924	9.9890E-1	1.2134E-4	1.9618E-4	2.1691E-5
18.	2.934	9.9917E-1	5.8653E-5	1.4917E-4	1.0483E-5
19.	3.134	9.9870E-1	7.0525E-5	2.3158E-4	1.2610E-5
20.	3.334	9.9828E-1	5.7023E-5	3.0777E-4	1.0200E-5
21.	3.424	9.9790E-1	4.2732E-5	3.7539E-4	7.6468E-6
22.	3.534	9.9774E-1	7.6355E-5	4.0367E-4	1.3666E-5
23.	3.734	9.9734E-1	4.1571E-5	4.7492E-4	7.4432E-6
24.	3.924	9.9650E-1	6.3641E-5	6.2592E-4	1.1404E-5
25.	3.934	9.9649E-1	6.4795E-5	6.2878E-4	1.1611E-5
26.	4.134	9.9585E-1	8.3662E-5	7.4261E-4	1.5002E-5
27.	4.334	9.9502E-1	7.7981E-5	8.9187E-4	1.3995E-5
28.	4.424	9.9468E-1	7.8293E-5	9.5218E-4	1.4056E-5
29.	4.534	9.9411E-1	1.6110E-4	1.0556E-3	2.8939E-5
30.	4.734	9.9325E-1	7.9472E-5	1.2087E-3	1.4288E-5
31.	4.924	9.9234E-1	7.2603E-5	1.3740E-3	1.3065E-5
32.	4.934	9.9247E-1	5.4137E-5	1.3503E-3	9.7407E-6
33.	5.134	9.9146E-1	8.8787E-5	1.5317E-3	1.5991E-5
34.	5.334	9.9049E-1	4.2311E-5	1.7056E-3	7.6281E-6
35.	5.424	9.8984E-1	6.7275E-5	1.8230E-3	1.2137E-5
36.	5.534	9.8942E-1	9.9261E-5	1.8994E-3	1.7915E-5
37.	5.734	9.8828E-1	5.7448E-5	2.1045E-3	1.0380E-5
38.	5.924	9.8710E-1	8.4662E-5	2.3191E-3	1.5316E-5
39.	5.934	9.8721E-1	8.8927E-5	2.2996E-3	1.6086E-5
40.	6.134	9.8575E-1	6.0667E-5	2.5635E-3	1.0990E-5
41.	6.424	9.8379E-1	1.1769E-4	2.9191E-3	2.1363E-5
42.	6.924	9.8047E-1	1.9075E-4	3.5229E-3	3.4740E-5
43.	7.424	9.7686E-1	2.8232E-4	4.1813E-3	5.1609E-5
44.	7.924	9.7287E-1	3.8501E-4	4.9108E-3	7.0669E-5
45.	8.424	9.6929E-1	2.4206E-4	5.5701E-3	4.4594E-5

Table D.6 continued

	Height (mm)	Transmittance	Standard Deviation	Extinction Coefficient (cm^{-1})	Standard Deviation
46.	8.924	9.6421E-1	2.5656E-4	6.5082E-3	4.7515E-5
47.	9.424	9.6032E-1	1.5232E-4	7.2305E-3	2.8323E-5
48.	9.924	9.5745E-1	1.0144E-3	7.7655E-3	1.8920E-4
49.	10.424	9.5246E-1	4.3860E-4	8.6979E-3	8.2232E-5
50.	10.924	9.4841E-1	9.5512E-4	9.4579E-3	1.7983E-4
51.	11.424	9.4520E-1	1.2038E-3	1.0065E-2	2.2743E-4
52.	11.924	9.4109E-1	4.3974E-4	1.0842E-2	8.3440E-5
53.	12.424	9.3837E-1	6.3632E-4	1.1359E-2	1.2109E-4
54.	12.924	9.3379E-1	5.8298E-4	1.2233E-2	1.1149E-4
55.	13.424	9.2673E-1	1.3776E-3	1.3589E-2	2.6546E-4
56.	13.924	9.2491E-1	1.0176E-3	1.3938E-2	1.9646E-4
57.	14.424	9.1970E-1	1.1114E-3	1.4949E-2	2.1580E-4
58.	14.924	9.1627E-1	1.6763E-3	1.5616E-2	3.2669E-4
59.	15.424	9.1209E-1	2.5267E-3	1.6432E-2	4.9469E-4

Table D.7 Normalized transmittance and extinction coefficient profiles of the A-IB-C flame ($\phi = 1.67$, $v_c = 7.87 \text{ cm}\cdot\text{sec}^{-1}$, $D = 3.31$).

	Height (mm)	Transmittance	Standard Deviation	Extinction Coefficient (cm^{-1})	Standard Deviation
1.	0.672	9.9954E-1	5.6438E-5	8.1983E-5	1.0083E-5
2.	0.872	9.9977E-1	5.9698E-5	4.0362E-5	1.0663E-5
3.	0.872	9.9942E-1	7.7776E-5	1.0360E-4	1.3897E-5
4.	1.072	1.0000	5.5184E-5	0.0	--
5.	1.272	9.9993E-1	8.7728E-5	1.1965E-5	1.5667E-5
6.	1.372	9.9972E-1	7.1288E-5	4.9293E-5	1.2734E-5
7.	1.472	9.9990E-1	6.2782E-5	1.7679E-5	1.1212E-5
8.	1.672	1.0000	5.4731E-5	0.0	--
9.	1.872	9.9971E-1	9.1027E-5	5.1615E-5	1.6260E-5
10.	1.872	1.0000	9.4202E-5	0.0	--
11.	2.072	9.9991E-1	5.3685E-5	1.6072E-5	9.5874E-6
12.	2.272	1.0000	5.6803E-5	0.0	--
13.	2.372	1.0000	6.4542E-5	0.0	--
14.	2.472	1.0000	5.6848E-5	0.0	--
15.	2.677	1.0000	5.7434E-5	0.0	--
16.	2.872	9.9970E-1	6.6716E-5	5.3222E-5	1.1917E-5
17.	2.872	1.0000	4.7341E-5	0.0	--
18.	3.072	9.9994E-1	5.7410E-5	1.1608E-5	1.0253E-5
19.	3.272	1.0000	8.7050E-5	0.0	--
20.	3.372	9.9994E-1	7.0603E-5	1.1072E-5	1.2609E-5
21.	3.472	9.9998E-1	6.2063E-5	3.9286E-6	1.1083E-5
22.	3.672	1.0000	5.1548E-5	5.3572E-7	9.2051E-6
23.	3.872	9.9979E-1	7.8048E-5	3.7683E-5	1.3940E-5
24.	3.872	9.9992E-1	4.9542E-5	1.3751E-5	8.8475E-6
25.	4.072	1.0000	1.0073E-4	0.0	--
26.	4.272	1.0000	5.7134E-5	0.0	--
27.	4.372	9.9993E-1	7.0234E-5	1.2322E-5	1.2543E-5
28.	4.472	1.0000	6.0041E-5	0.0	--
29.	4.672	9.9999E-1	4.5038E-5	1.6072E-6	8.0425E-6
30.	4.872	9.9991E-1	5.7590E-5	1.5715E-5	1.0285E-5
31.	4.872	9.9967E-1	9.7320E-5	5.8581E-5	1.7384E-5
32.	5.072	9.9993E-1	8.0499E-5	1.3393E-5	1.4376E-5
33.	5.272	9.9999E-1	5.1732E-5	1.6072E-6	9.2379E-6
34.	5.372	1.0000	8.6888E-5	0.0	--
35.	5.472	9.9981E-1	8.9502E-5	3.3217E-5	1.5986E-5
36.	5.672	1.0000	4.6952E-5	0.0	--
37.	5.872	9.9996E-1	8.7016E-5	7.8573E-6	1.5539E-5
38.	5.872	9.9973E-1	1.1861E-4	4.8399E-5	2.1187E-5
39.	6.072	1.0000	8.0526E-5	0.0	--
40.	6.372	9.9991E-1	8.1503E-5	1.6608E-5	1.4556E-5
41.	6.872	9.9982E-1	6.0085E-5	3.1610E-5	1.0731E-5
42.	7.372	9.9985E-1	8.4099E-5	2.6252E-5	1.5020E-5
43.	7.872	9.9960E-1	1.0086E-4	7.1979E-5	1.8017E-5
44.	8.372	9.9976E-1	1.1683E-4	4.3220E-5	2.0868E-5
45.	8.872	9.9989E-1	6.9955E-5	1.8930E-5	1.2493E-5

Table D.7 continued

	Height (mm)	Transmittance	Standard Deviation	Extinction Coefficient (cm^{-1})	Standard Deviation
46.	9.372	9.9989E-1	1.1544E-4	1.9108E-5	2.0617E-5
47.	9.872	9.9988E-1	8.4164E-5	2.1787E-5	1.5031E-5
48.	10.372	9.9995E-1	7.9396E-5	9.8217E-6	1.4179E-5
49.	10.872	9.9977E-1	1.6746E-4	4.1076E-5	2.9910E-5
50.	11.372	9.9998E-1	8.8241E-5	3.2143E-6	1.5758E-5
51.	11.872	9.9981E-1	9.2166E-5	3.3217E-5	1.6461E-5
52.	12.372	9.9988E-1	9.5060E-5	2.1430E-5	1.6977E-5
53.	12.872	9.9998E-1	7.3182E-5	3.3929E-6	1.3069E-5
54.	13.372	9.9993E-1	1.2392E-4	1.3215E-5	2.2130E-5
55.	13.872	9.9997E-1	9.1848E-5	5.5358E-6	1.6402E-5
56.	14.372	9.9995E-1	1.0148E-4	8.7502E-6	1.8121E-5
57.	14.872	1.0000	5.6155E-5	0.0	--
58.	15.372	1.0000	7.1567E-5	0.0	--
59.	16.372	1.0000	9.8789E-5	0.0	--
60.	17.372	1.0000	6.8870E-5	0.0	--
61.	18.372	9.9999E-1	1.2489E-4	1.4286E-6	2.2303E-5
62.	19.372	9.9994E-1	7.6646E-5	1.1250E-5	1.3688E-5
63.	20.372	1.0000	1.2288E-4	0.0	--

Table D.8 Normalized transmittance and extinction coefficient profiles of the A-IB-S2 flame ($\phi = 1.92$, $v_c = 7.78 \text{ cm}\cdot\text{sec}^{-1}$, $D = 3.54$).

	Height (mm)	Transmittance	Standard Deviation	Extinction Coefficient (cm^{-1})	Standard Deviation
1.	0.668	9.9944E-1	8.8539E-5	9.9492E-5	1.5819E-5
2.	0.858	9.9980E-1	1.0093E-4	3.5539E-5	1.8027E-5
3.	0.868	9.9976E-1	6.3965E-5	4.3041E-5	1.1425E-5
4.	1.068	9.9989E-1	6.4947E-5	1.9823E-5	1.1599E-5
5.	1.268	9.9987E-1	6.4693E-5	2.3037E-5	1.1554E-5
6.	1.358	1.0000	8.0432E-5	0.0	--
7.	1.468	9.9972E-1	6.4020E-5	5.0364E-5	1.1435E-5
8.	1.668	1.0000	7.3440E-5	0.0	--
9.	1.858	9.9997E-1	5.3896E-5	5.7144E-6	9.6247E-6
10.	1.868	9.9983E-1	9.5098E-5	3.0360E-5	1.6985E-5
11.	2.068	9.9983E-1	6.9898E-5	3.0717E-5	1.2484E-5
12.	2.268	9.9985E-1	6.4069E-5	2.7324E-5	1.1443E-5
13.	2.358	9.9987E-1	9.1361E-5	2.3216E-5	1.6317E-5
14.	2.468	9.9976E-1	8.5633E-5	4.3398E-5	1.5295E-5
15.	2.668	9.9979E-1	9.4412E-5	3.8040E-5	1.6863E-5
16.	2.858	9.9978E-1	1.4004E-4	3.8933E-5	2.5013E-5
17.	2.868	9.9978E-1	7.8339E-5	3.8576E-5	1.3992E-5
18.	3.068	9.9975E-1	6.2032E-5	4.4113E-5	1.1080E-5
19.	3.268	9.9969E-1	6.6087E-5	5.4830E-5	1.1805E-5
20.	3.358	9.9980E-1	6.5102E-5	3.6611E-5	1.1628E-5
21.	3.468	9.9981E-1	9.8939E-5	3.4468E-5	1.7671E-5
22.	3.668	9.9975E-1	7.2777E-5	4.3755E-5	1.2999E-5
23.	3.858	9.9966E-1	6.8208E-5	6.1261E-5	1.2184E-5
24.	3.868	9.9985E-1	1.2874E-4	2.6252E-5	2.2993E-5
25.	4.068	9.9966E-1	5.7449E-5	6.1082E-5	1.0262E-5
26.	4.268	9.9958E-1	8.0815E-5	7.4301E-5	1.4437E-5
27.	4.358	9.9951E-1	1.0293E-4	8.7879E-5	1.8389E-5
28.	4.468	9.9953E-1	8.4360E-5	8.3948E-5	1.5071E-5
29.	4.668	9.9932E-1	6.9571E-5	1.2183E-4	1.2432E-5
30.	4.858	9.9928E-1	4.4294E-5	1.2790E-4	7.9154E-6
31.	4.868	9.9926E-1	8.3143E-5	1.3183E-4	1.4858E-5
32.	5.068	9.9919E-1	8.4596E-5	1.4524E-4	1.5119E-5
33.	5.268	9.9910E-1	1.9640E-4	1.6150E-4	3.5104E-5
34.	5.358	9.9925E-1	1.0743E-4	1.3434E-4	1.9198E-5
35.	5.468	9.9916E-1	9.5865E-5	1.4935E-4	1.7133E-5
36.	5.668	9.9891E-1	1.3420E-4	1.9421E-4	2.3990E-5
37.	5.858	9.9887E-1	8.2803E-5	2.0136E-4	1.4803E-5
38.	5.868	9.9876E-1	6.7496E-5	2.2139E-4	1.2068E-5
39.	6.068	9.9886E-1	1.2173E-4	2.0387E-4	2.1763E-5
40.	6.358	9.9883E-1	1.3409E-4	2.0977E-4	2.3973E-5
41.	6.858	9.9854E-1	7.9260E-5	2.6073E-4	1.4174E-5
42.	7.358	9.9818E-1	2.0226E-4	3.2548E-4	3.6183E-5
43.	7.858	9.9810E-1	7.0716E-5	3.4015E-4	1.2652E-5
44.	8.358	9.9799E-1	1.5758E-4	3.6001E-4	2.8195E-5
45.	8.858	9.9782E-1	1.2886E-4	3.9025E-4	2.3062E-5

Table D.8 continued

	Height (mm)	Transmittance	Standard Deviation	Extinction Coefficient (cm^{-1})	Standard Deviation
46.	9.358	9.9742E-1	4.9472E-5	4.6131E-4	8.8571E-6
47.	9.858	9.9729E-1	8.1157E-5	4.8405E-4	1.4532E-5
48.	10.358	9.9701E-1	6.4637E-5	5.3509E-4	1.1577E-5
49.	10.858	9.9677E-1	1.6959E-4	5.7862E-4	3.0382E-5
50.	11.358	9.9659E-1	6.8929E-5	6.1051E-4	1.2351E-5
51.	11.858	9.9616E-1	8.2978E-5	6.8757E-4	1.4875E-5
52.	12.358	9.9614E-1	1.0825E-4	6.8990E-4	1.9405E-5
53.	12.858	9.9600E-1	5.1592E-5	7.1572E-4	9.2498E-6
54.	13.358	9.9564E-1	7.9649E-5	7.8045E-4	1.4285E-5
55.	13.858	9.9539E-1	9.3020E-5	8.2494E-4	1.6688E-5
56.	14.358	9.9523E-1	2.0602E-4	8.5382E-4	3.6965E-5
57.	14.858	9.9517E-1	8.4575E-5	8.6441E-4	1.5176E-5
58.	15.358	9.9472E-1	8.6244E-5	9.4571E-4	1.5483E-5

Table D.9 Normalized transmittance and extinction coefficient profiles of the A-IB-S3 flame ($\phi = 2.02$, $v_c = 7.78 \text{ cm}\cdot\text{sec}^{-1}$, $D = 3.54$).

	Height (mm)	Transmittance	Standard Deviation	Extinction Coefficient (cm^{-1})	Standard Deviation
1.	0.877	9.9976E-1	6.6821E-5	4.2684E-5	1.1935E-5
2.	1.377	1.0000	7.9098E-5	0.0	--
3.	1.877	9.9991E-1	7.1341E-5	1.6072E-5	1.2741E-5
4.	2.377	9.9963E-1	5.8814E-5	6.6441E-5	1.0506E-5
5.	2.877	9.9961E-1	4.2103E-5	6.8942E-5	7.5213E-6
6.	3.377	9.9909E-1	5.7092E-5	1.6347E-4	1.0204E-5
7.	3.877	9.9888E-1	7.1468E-5	1.9958E-4	1.2776E-5
8.	4.377	9.9804E-1	6.5566E-5	3.4963E-4	1.1731E-5
9.	4.877	9.9791E-1	6.1347E-5	3.7289E-4	1.0978E-5
10.	5.377	9.9701E-1	5.9115E-5	5.3509E-4	1.0588E-5
11.	5.877	9.9650E-1	7.1463E-5	6.2681E-4	1.2806E-5
12.	6.377	9.9576E-1	9.2408E-5	7.5804E-4	1.6572E-5
13.	6.877	9.9516E-1	6.8182E-5	8.6728E-4	1.2235E-5
14.	7.377	9.9433E-1	8.0768E-5	1.0148E-3	1.4505E-5
15.	7.877	9.9371E-1	7.2526E-5	1.1275E-3	1.3033E-5
16.	8.377	9.9264E-1	8.0753E-5	1.3193E-3	1.4527E-5
17.	8.877	9.9216E-1	5.4636E-5	1.4059E-3	9.8336E-6
18.	9.377	9.9137E-1	7.3692E-5	1.5470E-3	1.3274E-5
19.	9.877	9.9131E-1	1.0357E-4	1.5591E-3	1.8657E-5
20.	10.377	9.9018E-1	1.0403E-4	1.7622E-3	1.8761E-5
21.	10.877	9.8998E-1	1.0047E-4	1.7981E-3	1.8122E-5
22.	11.377	9.8893E-1	9.2837E-5	1.9882E-3	1.6764E-5
23.	11.877	9.8918E-1	9.7624E-5	1.9436E-3	1.7624E-5
24.	12.377	9.8778E-1	7.9266E-5	2.1960E-3	1.4330E-5
25.	12.877	9.8798E-1	7.4096E-5	2.1587E-3	1.3392E-5
26.	13.377	9.8693E-1	6.4234E-5	2.3500E-3	1.1622E-5
27.	13.877	9.8680E-1	1.3772E-4	2.3730E-3	2.4922E-5
28.	14.377	9.8627E-1	1.0614E-4	2.4691E-3	1.9218E-5
29.	14.877	9.8596E-1	2.1439E-4	2.5255E-3	3.8829E-5
30.	15.377	9.8519E-1	1.8323E-4	2.6642E-3	3.3211E-5
31.	16.377	9.8408E-1	2.9081E-4	2.8666E-3	5.2770E-5
32.	17.377	9.8327E-1	1.0847E-4	3.0121E-3	1.9698E-5
33.	18.377	9.8245E-1	7.8115E-5	3.1616E-3	1.4198E-5
34.	19.377	9.8225E-1	1.4952E-4	3.1974E-3	2.7182E-5
35.	20.377	9.8094E-1	2.1338E-4	3.4370E-3	3.8844E-5

Table D.10 Normalized transmittance and extinction coefficient profiles of the A-IB-S4 flame ($\phi = 2.17$, $v_c = 7.77 \text{ cm}\cdot\text{sec}^{-1}$, $D = 3.53$).

	Height (mm)	Transmittance	Standard Deviation	Extinction Coefficient (cm^{-1})	Standard Deviation
1.	0.504	9.9899E-1	5.5604E-5	1.8045E-4	9.9394E-6
2.	0.704	9.9961E-1	5.1981E-5	6.9121E-5	9.2859E-6
3.	0.894	9.9993E-1	5.6015E-5	1.3215E-5	1.0003E-5
4.	0.904	9.9990E-1	9.8934E-5	1.7858E-5	1.7669E-5
5.	1.104	9.9993E-1	7.4278E-5	1.1786E-5	1.3265E-5
6.	1.304	1.0000	6.0483E-5	0.0	--
7.	1.394	1.0000	7.5256E-5	0.0	--
8.	1.504	9.9991E-1	5.6615E-5	1.6429E-5	1.0111E-5
9.	1.704	9.9983E-1	1.3538E-4	2.9645E-5	2.4179E-5
10.	1.894	9.9975E-1	5.4546E-5	4.4648E-5	9.7428E-6
11.	1.904	9.9962E-1	5.9544E-5	6.7156E-5	1.0637E-5
12.	2.104	9.9944E-1	4.4678E-5	1.0039E-4	7.9827E-6
13.	2.304	9.9922E-1	1.0748E-4	1.4023E-4	1.9208E-5
14.	2.394	9.9911E-1	5.5432E-5	1.5846E-4	9.9073E-6
15.	2.504	9.9904E-1	7.6095E-5	1.7205E-4	1.3601E-5
16.	2.704	9.9872E-1	6.7655E-5	2.2836E-4	1.2097E-5
17.	2.894	9.9816E-1	1.2467E-4	3.2870E-4	2.2303E-5
18.	2.904	9.9815E-1	1.0797E-4	3.3138E-4	1.9316E-5
19.	3.104	9.9779E-1	6.4114E-5	3.9562E-4	1.1474E-5
20.	3.304	9.9731E-1	4.9273E-5	4.8083E-4	8.8225E-6
21.	3.394	9.9704E-1	5.4546E-5	5.2900E-4	9.7693E-6
22.	3.504	9.9674E-1	6.0232E-5	5.8381E-4	1.0791E-5
23.	3.704	9.9605E-1	6.2699E-5	7.0747E-4	1.1241E-5
24.	3.894	9.9559E-1	5.5485E-5	7.8870E-4	9.9518E-6
25.	3.904	9.9547E-1	8.3917E-5	8.1166E-4	1.5053E-5
26.	4.104	9.9503E-1	8.2422E-5	8.9061E-4	1.4792E-5
27.	4.304	9.9417E-1	8.5397E-5	1.0450E-3	1.5339E-5
28.	4.394	9.9383E-1	5.7225E-5	1.1047E-3	1.0282E-5
29.	4.504	9.9330E-1	7.1246E-5	1.2006E-3	1.2808E-5
30.	4.704	9.9252E-1	9.5601E-5	1.3415E-3	1.7200E-5
31.	4.894	9.9174E-1	8.1927E-5	1.4806E-3	1.4752E-5
32.	4.904	9.9181E-1	5.7702E-5	1.4678E-3	1.0389E-5
33.	5.104	9.9089E-1	7.8378E-5	1.6350E-3	1.4125E-5
34.	5.304	9.8998E-1	6.7690E-5	1.7978E-3	1.2210E-5
35.	5.394	9.8952E-1	8.8311E-5	1.8806E-3	1.5937E-5
36.	5.504	9.8893E-1	6.9679E-5	1.9884E-3	1.2582E-5
37.	5.704	9.8799E-1	6.6662E-5	2.1582E-3	1.2049E-5
38.	5.894	9.8700E-1	9.1224E-5	2.3367E-3	1.6505E-5
39.	5.904	9.8693E-1	1.0842E-4	2.3500E-3	1.9617E-5
40.	6.104	9.8600E-1	9.8472E-5	2.5173E-3	1.7834E-5
41.	6.394	9.8443E-1	1.5628E-4	2.8024E-3	2.8349E-5
42.	6.894	9.8178E-1	7.9879E-5	3.2841E-3	1.4529E-5
43.	7.394	9.7914E-1	8.4308E-5	3.7646E-3	1.5376E-5
44.	7.894	9.7666E-1	7.5761E-5	4.2171E-3	1.3852E-5
45.	8.394	9.7431E-1	1.7476E-4	4.6478E-3	3.2031E-5

Table D.10 continued

	Height (mm)	Transmittance	Standard Deviation	Extinction Coefficient (cm^{-1})	Standard Deviation
46.	8.894	9.7187E-1	7.9648E-5	5.0945E-3	1.4634E-5
47.	9.394	9.6954E-1	1.9352E-4	5.5248E-3	3.5642E-5
48.	9.894	9.6704E-1	6.8832E-5	5.9858E-3	1.2711E-5
49.	10.394	9.6482E-1	9.5762E-5	6.3948E-3	1.7724E-5
50.	10.894	9.6283E-1	2.5699E-4	6.7640E-3	4.7663E-5
51.	11.394	9.6033E-1	8.0878E-5	7.2279E-3	1.5039E-5
52.	11.894	9.5759E-1	1.4340E-4	7.7391E-3	2.6741E-5
53.	12.394	9.5536E-1	2.3341E-4	8.1552E-3	4.3629E-5
54.	12.894	9.5369E-1	5.1464E-4	8.4671E-3	9.6362E-5
55.	13.394	9.5160E-1	2.6338E-4	8.8588E-3	4.9424E-5
56.	13.894	9.4992E-1	3.8932E-4	9.1749E-3	7.3186E-5
57.	14.394	9.4680E-1	5.7147E-4	9.7615E-3	1.0778E-4
58.	14.894	9.4528E-1	3.9409E-4	1.0049E-2	7.4447E-5
59.	15.394	9.4381E-1	4.6013E-4	1.0327E-2	8.7057E-5

Table D.11 Normalized transmittance and extinction coefficient profiles of the A-IIA-R2 flame ($\phi = 1.63$, $v_c = 10.42 \text{ cm}\cdot\text{sec}^{-1}$, $D = 4.29$).

	Height (mm)	Transmittance	Standard Deviation	Extinction Coefficient (cm^{-1})	Standard Deviation
1.	0.880	9.9943E-1	4.8189E-5	1.0199E-4	8.6101E-6
2.	1.380	9.9965E-1	7.6458E-5	6.2690E-5	1.3658E-5
3.	1.880	9.9966E-1	4.7481E-5	6.1082E-5	8.4817E-6
4.	2.380	9.9972E-1	7.8142E-5	4.9650E-5	1.3958E-5
5.	2.880	9.9974E-1	7.9047E-5	4.6971E-5	1.4119E-5
6.	3.380	9.9981E-1	6.6708E-5	3.3217E-5	1.1914E-5
7.	3.880	9.9970E-1	7.1120E-5	5.4294E-5	1.2704E-5
8.	4.380	9.9983E-1	9.5739E-5	3.1253E-5	1.7099E-5
9.	4.880	9.9968E-1	5.9685E-5	5.6616E-5	1.0661E-5
10.	5.380	9.9983E-1	6.4511E-5	3.0003E-5	1.1522E-5
11.	5.880	9.9967E-1	1.0011E-4	5.8581E-5	1.7883E-5
12.	6.380	9.9979E-1	7.2360E-5	3.7683E-5	1.2924E-5
13.	6.880	9.9990E-1	7.5493E-5	1.8215E-5	1.3482E-5
14.	7.380	9.9985E-1	8.3009E-5	2.6788E-5	1.4825E-5
15.	7.880	9.9981E-1	1.6017E-4	3.3753E-5	2.8607E-5
16.	8.380	9.9964E-1	5.6460E-5	6.4297E-5	1.0086E-5
17.	8.880	1.0000	1.2597E-4	0.0	
18.	9.380	9.9991E-1	1.2438E-4	1.6608E-5	2.2214E-5
19.	9.880	9.9981E-1	9.6087E-5	3.3217E-5	1.7162E-5
20.	10.380	9.9989E-1	9.1737E-5	2.0001E-5	1.6383E-5
21.	10.880	9.9992E-1	8.1910E-5	1.5001E-5	1.4628E-5
22.	11.380	9.9990E-1	1.0600E-4	1.7858E-5	1.8931E-5
23.	11.880	9.9994E-1	8.9582E-5	1.0357E-5	1.5998E-5
24.	12.380	9.9994E-1	8.0365E-5	1.0357E-5	1.4352E-5
25.	12.880	9.9983E-1	1.5766E-4	2.9645E-5	2.8158E-5
26.	13.380	9.9987E-1	1.0104E-4	2.2501E-5	1.8046E-5
27.	13.880	9.9988E-1	9.2832E-5	2.0716E-5	1.6579E-5
28.	14.380	9.9997E-1	7.3384E-5	5.7144E-6	1.3105E-5
29.	14.880	9.9992E-1	6.3020E-5	1.4644E-5	1.1255E-5
30.	15.380	9.9992E-1	7.6695E-5	1.4822E-5	1.3697E-5
31.	16.380	9.9991E-1	7.8823E-5	1.5358E-5	1.4077E-5
32.	17.380	9.9988E-1	6.3918E-5	2.2144E-5	1.1415E-5
33.	18.380	9.9991E-1	7.8245E-5	1.6429E-5	1.3974E-5
34.	19.380	9.9997E-1	1.3066E-4	4.4643E-6	2.3332E-5
35.	20.380	1.0000	8.4895E-5	0.0	--

Table D.12 Normalized transmittance and extinction coefficient profiles of the A-IIA-S1 flame ($\phi = 1.78$, $v_c = 10.45 \text{ cm}\cdot\text{sec}^{-1}$, $D = 4.29$).

	Height (mm)	Transmittance	Standard Deviation	Extinction Coefficient (cm^{-1})	Standard Deviation
1.	0.680	9.9940E-1	6.2721E-5	1.0718E-4	1.1207E-5
2.	0.880	9.9940E-1	8.3683E-5	1.0735E-4	1.4952E-5
3.	0.880	9.9940E-1	8.5160E-5	1.0789E-4	1.5216E-5
4.	1.080	9.9958E-1	5.1623E-5	7.5730E-5	9.2223E-6
5.	1.280	9.9964E-1	9.4772E-5	6.5191E-5	1.6930E-5
6.	1.380	9.9963E-1	7.5304E-5	6.6798E-5	1.3452E-5
7.	1.480	9.9972E-1	7.4799E-5	4.9293E-5	1.3361E-5
8.	1.680	9.9970E-1	1.0325E-4	5.3580E-5	1.8443E-5
9.	1.880	9.9971E-1	8.3275E-5	5.1972E-5	1.4875E-5
10.	1.880	9.9973E-1	6.7302E-5	4.7685E-5	1.2021E-5
11.	2.080	9.9971E-1	7.5628E-5	5.1972E-5	1.3509E-5
12.	2.280	9.9986E-1	6.7593E-5	2.4287E-5	1.2072E-5
13.	2.380	9.9975E-1	6.7220E-5	4.4470E-5	1.2007E-5
14.	2.480	9.9985E-1	9.4682E-5	2.6609E-5	1.6910E-5
15.	2.680	9.9983E-1	5.8579E-5	3.0717E-5	1.0462E-5
16.	2.880	9.9979E-1	5.9985E-5	3.6968E-5	1.0714E-5
17.	2.880	9.9973E-1	7.4251E-5	4.8042E-5	1.3263E-5
18.	3.080	9.9982E-1	6.5804E-5	3.1967E-5	1.1753E-5
19.	3.280	9.9988E-1	7.3044E-5	2.0716E-5	1.3045E-5
20.	3.380	9.9983E-1	7.0921E-5	3.0538E-5	1.2667E-5
21.	3.480	9.9991E-1	8.7016E-5	1.6251E-5	1.5540E-5
22.	3.680	9.9989E-1	6.3359E-5	1.9823E-5	1.1315E-5
23.	3.880	9.9980E-1	1.1066E-4	3.5182E-5	1.9764E-5
24.	3.880	9.9988E-1	6.9891E-5	2.1609E-5	1.2482E-5
25.	4.080	9.9982E-1	9.7488E-5	3.2503E-5	1.7412E-5
26.	4.280	9.9979E-1	6.7201E-5	3.7325E-5	1.2003E-5
27.	4.380	9.9994E-1	6.4189E-5	1.1429E-5	1.1463E-5
28.	4.480	9.9994E-1	5.8673E-5	1.1608E-5	1.0478E-5
29.	4.680	9.9988E-1	9.2703E-5	2.0894E-5	1.6556E-5
30.	4.880	9.9988E-1	8.8128E-5	2.1251E-5	1.5739E-5
31.	4.880	9.9997E-1	5.5413E-5	5.0001E-6	9.8954E-6
32.	5.080	9.9989E-1	8.9044E-5	1.9108E-5	1.5902E-5
33.	5.280	9.9993E-1	6.7347E-5	1.3393E-5	1.2027E-5
34.	5.380	1.0000	7.4337E-5	0.0	--
35.	5.480	9.9999E-1	8.3083E-5	1.6072E-6	1.4836E-5
36.	5.680	9.9999E-1	7.6082E-5	1.6072E-6	1.3586E-5
37.	5.880	9.9997E-1	8.1053E-5	5.1787E-6	1.4474E-5
38.	5.880	1.0000	5.6987E-5	0.0	--
39.	6.080	9.9991E-1	6.4139E-5	1.6608E-5	1.1454E-5
40.	6.380	1.0000	6.5535E-5	0.0	--
41.	6.880	1.0000	1.5504E-4	0.0	--
42.	7.380	9.9997E-1	7.8791E-5	5.0001E-6	1.4070E-5
43.	7.880	1.0000	8.8143E-5	0.0	--
44.	8.380	9.9994E-1	1.1799E-4	1.1250E-5	2.1071E-5
45.	8.880	1.0000	8.8975E-5	0.0	--

Table D.12 continued

	Height (mm)	Transmittance	Standard Deviation	Extinction Coefficient (cm^{-1})	Standard Deviation
46.	9.380	1.0000	6.1532E-5	0.0	--
47.	9.880	9.9996E-1	1.1068E-4	6.6073E-6	1.9765E-5
48.	10.380	9.9994E-1	1.2746E-4	1.0179E-5	2.2762E-5
49.	10.880	9.9984E-1	1.2265E-4	2.8752E-5	2.1905E-5
50.	11.380	1.0000	9.2623E-5	0.0	--
51.	11.880	1.0000	1.0041E-4	0.0	--
52.	12.380	1.0000	1.0746E-4	0.0	--
53.	12.880	1.0000	1.1146E-4	0.0	--
54.	13.380	1.0000	7.0647E-5	0.0	--
55.	13.880	1.0000	1.0297E-4	0.0	--
56.	14.380	1.0000	9.2842E-5	0.0	--
57.	14.880	9.9994E-1	7.3549E-5	1.0000E-5	1.3134E-5
58.	15.380	1.0000	9.3487E-5	0.0	--
59.	16.380	1.0000	1.1191E-4	0.0	--
60.	17.380	1.0000	6.9497E-5	0.0	--
61.	18.380	1.0000	1.1544E-4	0.0	--
62.	19.380	1.0000	9.4148E-5	0.0	--
63.	20.380	1.0000	7.8730E-5	0.0	--

Table D.13 Normalized transmittance and extinction coefficient profiles of the A-IIA-S2 flame ($\phi = 1.92$, $v_c = 10.45 \text{ cm}\cdot\text{sec}^{-1}$, $D = 4.28$).

	Height (mm)	Transmittance	Standard Deviation	Extinction Coefficient (cm^{-1})	Standard Deviation
1.	0.693	9.9892E-1	6.6583E-5	1.9368E-4	1.1903E-5
2.	0.893	9.9929E-1	4.6209E-5	1.2665E-4	8.2575E-6
3.	0.893	9.9910E-1	7.0005E-5	1.6150E-4	1.2512E-5
4.	1.093	9.9952E-1	4.8822E-5	8.5914E-5	8.7224E-6
5.	1.293	9.9963E-1	5.0996E-5	6.5905E-5	9.1099E-6
6.	1.393	9.9960E-1	4.5872E-5	7.1086E-5	8.1947E-6
7.	1.493	9.9972E-1	5.3378E-5	4.9293E-5	9.5343E-6
8.	1.693	9.9976E-1	4.8505E-5	4.2684E-5	8.6638E-6
9.	1.893	9.9967E-1	4.8527E-5	5.9832E-5	8.6684E-6
10.	1.893	9.9981E-1	5.1362E-5	3.4825E-5	9.1737E-6
11.	2.093	9.9971E-1	4.2580E-5	5.1257E-5	7.6058E-6
12.	2.293	9.9978E-1	4.6556E-5	3.9469E-5	8.3154E-6
13.	2.393	9.9972E-1	4.2274E-5	5.0900E-5	7.5510E-6
14.	2.493	9.9988E-1	4.5349E-5	2.2144E-5	8.0991E-6
15.	2.693	9.9991E-1	4.1417E-5	1.5894E-5	7.3965E-6
16.	2.893	9.9985E-1	5.9197E-5	2.6966E-5	1.0572E-5
17.	2.893	1.0000	1.0134E-4	0.0	--
18.	3.093	1.0000	4.3499E-5	0.0	--
19.	3.293	9.9993E-1	7.4085E-5	1.2500E-5	1.3230E-5
20.	3.393	9.9978E-1	6.6941E-5	4.0183E-5	1.1956E-5
21.	3.493	9.9983E-1	5.7527E-5	3.0003E-5	1.0275E-5
22.	3.693	9.9984E-1	7.5532E-5	2.9110E-5	1.3490E-5
23.	3.893	9.9982E-1	7.7927E-5	3.1789E-5	1.3918E-5
24.	3.893	9.9979E-1	4.8690E-5	3.7147E-5	8.6965E-6
25.	4.093	9.9978E-1	5.0340E-5	3.8754E-5	8.9913E-6
26.	4.293	9.9984E-1	7.5184E-5	2.9288E-5	1.3428E-5
27.	4.393	9.9986E-1	5.7698E-5	2.4287E-5	1.0305E-5
28.	4.493	9.9986E-1	7.4255E-5	2.5895E-5	1.3262E-5
29.	4.693	9.9970E-1	5.3027E-5	5.3044E-5	9.4720E-6
30.	4.893	9.9978E-1	8.5891E-5	3.9647E-5	1.5341E-5
31.	4.893	9.9980E-1	6.3038E-5	3.6075E-5	1.1259E-5
32.	5.093	9.9978E-1	1.0015E-4	4.0183E-5	1.7888E-5
33.	5.293	9.9973E-1	5.8263E-5	4.7506E-5	1.0407E-5
34.	5.393	9.9984E-1	5.1814E-5	2.9288E-5	9.2541E-6
35.	5.493	9.9971E-1	6.8789E-5	5.1257E-5	1.2287E-5
36.	5.693	9.9962E-1	4.5112E-5	6.8227E-5	8.0588E-6
37.	5.893	9.9973E-1	7.4827E-5	4.9114E-5	1.3366E-5
38.	5.893	9.9965E-1	7.2825E-5	6.2511E-5	1.3009E-5
39.	6.093	9.9957E-1	7.0772E-5	7.7696E-5	1.2643E-5
40.	6.393	9.9959E-1	5.5469E-5	7.3229E-5	9.9092E-6
41.	6.893	9.9952E-1	4.5230E-5	8.5735E-5	8.0807E-6
42.	7.393	9.9965E-1	1.1163E-4	6.3226E-5	1.9941E-5
43.	7.893	9.9961E-1	1.3509E-4	7.0192E-5	2.4133E-5
44.	8.393	9.9945E-1	1.0638E-4	9.8241E-5	1.9007E-5
45.	8.893	9.9927E-1	1.1338E-4	1.2969E-4	2.0261E-5

Table D.13 continued

	Height (mm)	Transmittance	Standard Deviation	Extinction Coefficient (cm ⁻¹)	Standard Deviation
46.	9.393	9.9931E-1	6.3237E-5	1.2344E-4	1.1300E-5
47.	9.893	9.9930E-1	1.1057E-4	1.2594E-4	1.9758E-5
48.	10.393	9.9926E-1	8.5251E-5	1.3255E-4	1.5235E-5
49.	10.893	9.9920E-1	6.6241E-5	1.4238E-4	1.1838E-5
50.	11.393	9.9904E-1	1.1336E-4	1.7187E-4	2.0262E-5
51.	11.893	9.9902E-1	3.7221E-5	1.7562E-4	6.6532E-6
52.	12.393	9.9887E-1	1.2929E-4	2.0262E-4	2.3113E-5
53.	12.893	9.9894E-1	6.6071E-5	1.8867E-4	1.1811E-5
54.	13.393	9.9882E-1	1.1244E-4	2.1048E-4	2.0102E-5
55.	13.893	9.9865E-1	1.0273E-4	2.4159E-4	1.8370E-5
56.	14.393	9.9860E-1	1.0201E-4	2.5053E-4	1.8242E-5
57.	14.893	9.9893E-1	5.9625E-5	1.9153E-4	1.0659E-5
58.	15.393	9.9877E-1	4.7952E-5	2.2014E-4	8.5734E-6

Table D.14 Normalized transmittance and extinction coefficient profiles of the A-IIA-S3 flame ($\phi = 2.02$, $v_c = 10.45 \text{ cm}\cdot\text{sec}^{-1}$, $D = 4.28$).

	Height (mm)	Transmittance	Standard Deviation	Extinction Coefficient (cm^{-1})	Standard Deviation
1.	0.542	9.9802E-1	4.6934E-5	3.5428E-4	8.3977E-6
2.	0.742	9.9869E-1	4.2824E-5	2.3462E-4	7.6571E-6
3.	0.942	9.9911E-1	5.9972E-5	1.5936E-4	1.0719E-5
4.	0.942	9.9933E-1	5.6101E-5	1.2040E-4	1.0025E-5
5.	1.142	9.9930E-1	4.6396E-5	1.2522E-4	8.2907E-6
6.	1.342	9.9950E-1	8.8684E-5	8.9487E-5	1.5844E-5
7.	1.442	9.9973E-1	6.7800E-5	4.7506E-5	1.2110E-5
8.	1.542	9.9965E-1	6.6947E-5	6.2154E-5	1.1959E-5
9.	1.742	9.9974E-1	5.1062E-5	4.6971E-5	9.1206E-6
10.	1.942	9.9999E-1	8.4067E-5	1.7857E-6	1.5012E-5
11.	1.942	9.9978E-1	7.3612E-5	3.8754E-5	1.3148E-5
12.	2.142	9.9982E-1	7.3542E-5	3.1967E-5	1.3135E-5
13.	2.342	1.0000	5.8816E-5	0.0	
14.	2.442	9.9997E-1	6.3826E-5	5.1787E-6	1.1398E-5
15.	2.542	9.9984E-1	6.2183E-5	2.9467E-5	1.1106E-5
16.	2.742	9.9993E-1	6.1516E-5	1.3215E-5	1.0986E-5
17.	2.942	9.9996E-1	5.7657E-5	6.4287E-6	1.0296E-5
18.	2.942	9.9987E-1	6.2150E-5	2.3216E-5	1.1100E-5
19.	3.142	9.9980E-1	5.0729E-5	3.5718E-5	9.0605E-6
20.	3.342	9.9981E-1	4.6790E-5	3.3932E-5	8.3569E-6
21.	3.442	9.9995E-1	5.7207E-5	9.8217E-6	1.0216E-5
22.	3.542	9.9972E-1	5.4414E-5	4.9293E-5	9.7194E-6
23.	3.742	9.9973E-1	7.5491E-5	4.8757E-5	1.3484E-5
24.	3.942	9.9974E-1	6.0881E-5	4.6971E-5	1.0874E-5
25.	3.942	9.9967E-1	1.1528E-4	5.8938E-5	2.0593E-5
26.	4.142	9.9961E-1	6.7070E-5	6.9121E-5	1.1982E-5
27.	4.342	9.9952E-1	6.2389E-5	8.6271E-5	1.1146E-5
28.	4.442	9.9947E-1	5.9531E-5	9.5561E-5	1.0636E-5
29.	4.542	9.9950E-1	6.7260E-5	8.9844E-5	1.2017E-5
30.	4.742	9.9941E-1	5.6881E-5	1.0557E-4	1.0163E-5
31.	4.942	9.9920E-1	6.8198E-5	1.4363E-4	1.2188E-5
32.	4.942	9.9940E-1	5.6344E-5	1.0646E-4	1.0067E-5
33.	5.142	9.9907E-1	5.8172E-5	1.6615E-4	1.0397E-5
34.	5.342	9.9903E-1	5.8992E-5	1.7330E-4	1.0545E-5
35.	5.442	9.9915E-1	5.5994E-5	1.5131E-4	1.0008E-5
36.	5.542	9.9888E-1	6.8372E-5	2.0029E-4	1.2223E-5
37.	5.742	9.9885E-1	6.1955E-5	2.0583E-4	1.1076E-5
38.	5.942	9.9862E-1	4.5527E-5	2.4749E-4	8.1411E-6
39.	5.942	9.9899E-1	6.5621E-5	1.8063E-4	1.1730E-5
40.	6.142	9.9842E-1	4.7025E-5	2.8183E-4	8.4105E-6
41.	6.442	9.9863E-1	6.5246E-5	2.4499E-4	1.1667E-5
42.	6.942	9.9833E-1	6.8994E-5	2.9882E-4	1.2341E-5
43.	7.442	9.9788E-1	7.0965E-5	3.7915E-4	1.2699E-5
44.	7.942	9.9756E-1	6.6263E-5	4.3553E-4	1.1862E-5
45.	8.442	9.9713E-1	7.1777E-5	5.1413E-4	1.2854E-5

Table D.14 continued

	Height (mm)	Transmittance	Standard Deviation	Extinction Coefficient (cm^{-1})	Standard Deviation
46.	8.942	9.9686E-1	7.0827E-5	5.6213E-4	1.2688E-5
47.	9.442	9.9643E-1	8.5493E-5	6.3954E-4	1.5321E-5
48.	9.942	9.9620E-1	8.8030E-5	6.7915E-4	1.5780E-5
49.	10.442	9.9571E-1	1.0205E-4	7.6790E-4	1.8302E-5
50.	10.942	9.9545E-1	9.8727E-5	8.1435E-4	1.7710E-5
51.	11.442	9.9515E-1	8.3182E-5	8.6854E-4	1.4926E-5
52.	11.942	9.9510E-1	7.3543E-5	8.7715E-4	1.3197E-5
53.	12.442	9.9475E-1	1.0456E-4	9.3961E-4	1.8769E-5
54.	12.942	9.9463E-1	1.2452E-4	9.6079E-4	2.2356E-5
55.	13.442	9.9442E-1	1.1240E-4	9.9886E-4	2.0185E-5
56.	13.942	9.9443E-1	8.2333E-5	9.9742E-4	1.4785E-5
57.	14.442	9.9403E-1	8.4371E-5	1.0695E-3	1.5157E-5
58.	14.942	9.9392E-1	8.2467E-5	1.0887E-3	1.4816E-5
59.	15.442	9.9366E-1	1.0907E-4	1.1363E-3	1.9600E-5
60.	16.442	9.9322E-1	1.2695E-4	1.2154E-3	2.2825E-5
61.	17.442	9.9296E-1	2.8958E-4	1.2618E-3	5.2077E-5
62.	18.442	9.9263E-1	7.7644E-5	1.3218E-3	1.3968E-5
63.	19.442	9.9284E-1	1.1617E-4	1.2837E-3	2.0894E-5
64.	20.442	9.9187E-1	3.1682E-4	1.4586E-3	5.7040E-5

Table D.15 Profile of the total scattering coefficient for the A-IA-R2 flame ($\phi = 1.63$, $v_c = 7.73 \text{ cm}\cdot\text{sec}^{-1}$, $D = 4.15$).

	Height (mm)	Total Scattering Coefficient ($\text{cm}^{-1}\cdot\text{sr}^{-1}$)	Standard Deviation
1.	0.68	4.150E-9	1.585E-11
2.	0.88	4.156E-9	2.709E-11
3.	0.88	4.117E-9	2.097E-11
4.	1.08	4.107E-9	2.442E-11
5.	1.28	4.097E-9	2.552E-11
6.	1.38	4.115E-9	1.786E-11
7.	1.48	4.121E-9	2.552E-11
8.	1.68	4.125E-9	2.545E-11
9.	1.88	4.112E-9	1.889E-11
10.	1.88	4.107E-9	1.051E-11
11.	2.08	4.117E-9	2.037E-11
12.	2.28	4.112E-9	7.357E-12
13.	2.38	4.135E-9	1.747E-11
14.	2.48	4.117E-9	8.985E-12
15.	2.68	4.109E-9	1.913E-11
16.	2.88	4.119E-9	7.755E-12
17.	2.88	4.097E-9	2.318E-11
18.	3.08	4.123E-9	2.024E-11
19.	3.28	4.104E-9	9.317E-12
20.	3.38	4.130E-9	1.466E-11
21.	3.48	4.113E-9	7.963E-12
22.	3.68	4.130E-9	1.640E-11
23.	3.88	4.126E-9	1.335E-11
24.	3.88	4.143E-9	9.949E-12
25.	4.08	4.128E-9	1.464E-11
26.	4.28	4.123E-9	2.001E-11
27.	4.38	4.119E-9	1.223E-11
28.	4.48	4.163E-9	2.375E-11
29.	4.68	4.151E-9	2.556E-11
30.	4.88	4.150E-9	1.982E-11
31.	4.88	4.151E-9	1.449E-11
32.	5.08	4.169E-9	7.701E-12
33.	5.28	4.153E-9	1.796E-11
34.	5.38	4.146E-9	8.589E-12
35.	5.48	4.157E-9	1.677E-11
36.	5.68	4.167E-9	9.207E-12
37.	5.88	4.151E-9	1.867E-11
38.	5.88	4.157E-9	2.483E-11
39.	6.08	4.179E-9	1.615E-11
40.	6.38	4.151E-9	1.052E-11
41.	6.88	4.165E-9	1.321E-11
42.	7.38	4.193E-9	2.044E-11
43.	7.88	4.196E-9	1.317E-11
44.	8.38	4.184E-9	1.593E-11
45.	8.88	4.217E-9	1.489E-11

Table D.15 continued

	Height (mm)	Total Scattering Coefficient ($\text{cm}^{-1}\cdot\text{sr}^{-1}$)	Standard Deviation
46.	9.38	4.244E-9	1.488E-11
47.	9.88	4.255E-9	2.035E-11
48.	10.38	4.230E-9	1.372E-11
49.	10.88	4.281E-9	1.781E-11
50.	11.38	4.267E-9	2.724E-11
51.	11.88	4.258E-9	2.527E-11
52.	12.38	4.266E-9	2.466E-11
53.	12.88	4.273E-9	1.705E-11
54.	13.38	4.306E-9	2.084E-11
55.	13.88	4.284E-9	1.059E-11
56.	14.38	4.297E-9	1.090E-11
57.	14.88	4.307E-9	1.592E-11
58.	15.38	4.314E-9	9.447E-12

Table D.16 Profile of the total scattering coefficient and the corrected scattering coefficient for the A-IA-S1 flame ($\phi = 1.78$, $v_c = 7.73 \text{ cm}\cdot\text{sec}^{-1}$, $D = 4.16$).

	Height (mm)	Total Scattering Coefficient ($\text{cm}^{-1}\cdot\text{sr}^{-1}$)	Standard Deviation	Corrected Scattering Coefficient ($\text{cm}^{-1}\cdot\text{sr}^{-1}$)
1.	0.90	4.310E-9	1.621E-11	4.310E-9
2.	1.41	4.237E-9	4.189E-11	4.237E-9
3.	1.90	4.202E-9	1.274E-11	4.202E-9
4.	2.41	4.190E-9	2.570E-11	4.190E-9
5.	2.90	4.196E-9	1.438E-11	4.196E-9
6.	3.41	4.199E-9	2.098E-11	4.198E-9
7.	3.90	4.183E-9	1.464E-11	4.181E-9
8.	4.41	4.208E-9	2.519E-11	4.204E-9
9.	4.90	4.200E-9	1.400E-11	4.195E-9
10.	5.41	4.219E-9	1.811E-11	4.213E-9
11.	5.90	4.248E-9	1.476E-11	4.241E-9
12.	6.41	4.236E-9	2.249E-11	4.228E-9
13.	6.90	4.243E-9	1.500E-11	4.232E-9
14.	7.41	4.263E-9	2.887E-11	4.250E-9
15.	7.90	4.261E-9	2.648E-11	4.247E-9
16.	8.41	4.281E-9	2.038E-11	4.265E-9
17.	8.90	4.312E-9	1.895E-11	4.295E-9
18.	9.41	4.299E-9	1.612E-11	4.279E-9
19.	9.90	4.277E-9	1.758E-11	4.255E-9
20.	10.41	4.318E-9	3.555E-11	4.294E-9
21.	10.90	4.292E-9	1.350E-11	4.266E-9
22.	11.41	4.334E-9	2.578E-11	4.305E-9
23.	11.90	4.343E-9	1.920E-11	4.312E-9
24.	12.41	4.350E-9	2.649E-11	4.316E-9
25.	12.90	4.356E-9	2.096E-11	4.320E-9
26.	13.41	4.370E-9	2.144E-11	4.331E-9
27.	13.90	4.404E-9	2.300E-11	4.362E-9
28.	14.41	4.396E-9	2.691E-11	4.352E-9
29.	14.90	4.389E-9	1.102E-11	4.341E-9
30.	15.41	4.383E-9	2.495E-11	4.332E-9
31.	16.41	4.421E-9	1.978E-11	4.365E-9
32.	17.41	4.420E-9	8.054E-12	4.357E-9
33.	18.41	4.464E-9	1.005E-11	4.393E-9
34.	19.41	4.480E-9	2.402E-11	4.403E-9
35.	20.41	4.517E-9	1.258E-11	4.432E-9

Table D.17 Profile of the total scattering coefficient, the particle scattering coefficient, and the corrected particle scattering coefficient for the A-IA-S2 flame ($\phi = 1.92$, $v_c = 7.75 \text{ cm}\cdot\text{sec}^{-1}$, $D = 4.17$).

	Height (mm)	Total Scattering Coefficient ($\text{cm}^{-1}\cdot\text{sr}^{-1}$)	Standard Deviation	Particle Scattering Coefficient ($\text{cm}^{-1}\cdot\text{sr}^{-1}$)	Corrected Particle Scattering Coefficient ($\text{cm}^{-1}\cdot\text{sr}^{-1}$)
1.	0.90	4.315E-9	1.355E-11	8.904E-11	1.469E-10
2.	1.40	4.225E-9	1.961E-11	3.431E-11	9.413E-11
3.	1.90	4.190E-9	1.088E-11	1.205E-11	7.196E-11
4.	2.40	4.201E-9	2.656E-11	2.739E-11	8.555E-11
5.	2.90	4.182E-9	1.100E-11	8.707E-12	6.337E-11
6.	3.40	4.176E-9	3.600E-11	0.000	4.948E-11
7.	3.90	4.203E-9	2.051E-11	2.355E-11	6.626E-11
8.	4.40	4.187E-9	1.776E-11	3.169E-12	3.758E-11
9.	4.90	4.222E-9	1.858E-11	3.230E-11	5.695E-11
10.	5.40	4.253E-9	2.383E-11	5.683E-11	7.034E-11
11.	5.90	4.245E-9	1.904E-11	4.312E-11	4.420E-11
12.	6.40	4.270E-9	3.922E-11	6.095E-11	4.837E-11
13.	6.90	4.288E-9	1.232E-11	7.268E-11	4.530E-11
14.	7.40	4.314E-9	2.585E-11	9.104E-11	4.777E-11
15.	7.90	4.335E-9	1.653E-11	1.057E-10	4.557E-11
16.	8.40	4.348E-9	2.514E-11	1.113E-10	3.333E-11
17.	8.90	4.374E-9	1.416E-11	1.298E-10	3.314E-11
18.	9.40	4.401E-9	3.280E-11	1.489E-10	3.276E-11
19.	9.90	4.452E-9	2.661E-11	1.928E-10	5.653E-11
20.	10.40	4.453E-9	3.226E-11	1.862E-10	2.915E-11
21.	10.90	4.482E-9	1.462E-11	2.070E-10	2.862E-11
22.	11.40	4.506E-9	1.904E-11	2.237E-10	2.349E-11
23.	11.90	4.530E-9	2.282E-11	2.403E-10	1.789E-11
24.	12.40	4.566E-9	1.714E-11	2.682E-10	2.323E-11
25.	12.90	4.616E-9	2.756E-11	3.110E-10	4.323E-11
26.	13.40	4.604E-9	2.677E-11	2.907E-10	.000e+000
27.	13.90	4.639E-9	2.086E-11	3.183E-10	4.531E-12
28.	14.40	4.670E-9	2.351E-11	3.413E-10	4.431E-12
29.	14.90	4.703E-9	9.376E-12	3.666E-10	6.731E-12
30.	15.40	4.737E-9	1.960E-11	3.921E-10	9.215E-12
31.	16.40	4.800E-9	2.360E-11	4.395E-10	1.153E-11
32.	17.40	4.923E-9	2.098E-11	5.466E-10	7.474E-11
33.	18.40	5.027E-9	2.548E-11	6.351E-10	1.215E-10
34.	19.40	5.319E-9	5.425E-11	9.114E-10	3.585E-10
35.	20.40	5.748E-9	4.539E-11	1.324E-9	7.351E-10

Table D.18 Profile of the total scattering coefficient, the particle scattering coefficient, and the corrected particle scattering coefficient for the A-IA-S3 flame ($\phi = 2.02$, $v_c = 7.74 \text{ cm}\cdot\text{sec}^{-1}$, $D = 4.16$).

	Height (mm)	Total Scattering Coefficient ($\text{cm}^{-1}\cdot\text{sr}^{-1}$)	Standard Deviation	Particle Scattering Coefficient ($\text{cm}^{-1}\cdot\text{sr}^{-1}$)	Corrected Particle Scattering Coefficient ($\text{cm}^{-1}\cdot\text{sr}^{-1}$)
1.	0.89	4.484E-9	1.679E-11	1.866E-10	2.425E-10
2.	1.39	4.364E-9	3.416E-11	1.025E-10	1.584E-10
3.	1.89	4.308E-9	2.171E-11	5.988E-11	1.157E-10
4.	2.39	4.263E-9	2.999E-11	1.895E-11	7.480E-11
5.	2.89	4.266E-9	1.466E-11	2.225E-11	6.649E-11
6.	3.39	4.246E-9	2.174E-11	0.000e+00	2.796E-11
7.	3.89	4.275E-9	4.395E-11	2.466E-11	3.286E-11
8.	4.39	4.289E-9	2.832E-11	3.423E-11	1.935E-11
9.	4.89	4.337E-9	2.136E-11	7.648E-11	3.538E-11
10.	5.39	4.352E-9	2.298E-11	8.535E-11	1.507E-11
11.	5.89	4.398E-9	1.293E-11	1.250E-10	2.276E-11
12.	6.39	4.424E-9	3.676E-11	1.452E-10	8.355E-12
13.	6.89	4.460E-9	1.781E-11	1.738E-10	0.000e+00
14.	7.39	4.521E-9	3.310E-11	2.281E-10	1.498E-11
15.	7.89	4.569E-9	7.966E-12	2.682E-10	1.375E-11
16.	8.39	4.640E-9	3.308E-11	3.322E-10	3.440E-11
17.	8.89	4.707E-9	1.688E-11	3.920E-10	4.921E-11
18.	9.39	4.734E-9	3.230E-11	4.118E-10	2.244E-11
19.	9.89	4.811E-9	1.035E-11	4.814E-10	4.398E-11
20.	10.39	4.824E-9	3.741E-11	4.870E-10	4.161E-13
21.	10.89	4.956E-9	2.559E-11	6.109E-10	7.407E-11
22.	11.39	5.003E-9	4.593E-11	6.508E-10	6.281E-11
23.	11.89	5.102E-9	2.860E-11	7.412E-10	1.014E-10
24.	12.39	5.267E-9	3.374E-11	8.984E-10	2.063E-10
25.	12.89	5.502E-9	3.243E-11	1.126E-9	3.810E-10
26.	13.39	5.834E-9	4.703E-11	1.450E-9	6.523E-10
27.	13.89	6.447E-9	7.000E-11	2.055E-9	1.205E-9
28.	14.39	7.246E-9	1.484E-10	2.846E-9	1.943E-9
29.	14.89	8.831E-9	2.873E-10	4.423E-9	3.468E-9
30.	15.39	1.129E-8	3.071E-10	6.876E-9	5.869E-9
31.	16.39	2.011E-8	2.982E-10	1.567E-8	1.457E-8
32.	17.39	3.898E-8	6.863E-10	3.453E-8	3.332E-8
33.	18.39	7.122E-8	3.207E-9	6.676E-8	6.546E-8
34.	19.39	1.233E-7	1.287E-8	1.188E-7	1.174E-7
35.	20.39	1.995E-7	3.752E-9	1.950E-7	1.936E-7

Table D.19 Profile of the total scattering coefficient, the particle scattering coefficient, and the corrected particle scattering coefficient for the A-IA-S4 flame ($\phi = 2.17$, $v_c = 7.75 \text{ cm}\cdot\text{sec}^{-1}$, $D = 4.16$).

	Height (mm)	Total Scattering Coefficient ($\text{cm}^{-1}\cdot\text{sr}^{-1}$)	Standard Deviation	Particle Scattering Coefficient ($\text{cm}^{-1}\cdot\text{sr}^{-1}$)	Corrected Particle Scattering Coefficient ($\text{cm}^{-1}\cdot\text{sr}^{-1}$)
1.	0.90	4.629E-9	1.275E-11	2.088E-10	2.371E-10
2.	1.40	4.446E-9	5.205E-11	6.070E-11	8.895E-11
3.	1.90	4.406E-9	3.886E-11	3.407E-11	6.232E-11
4.	2.40	4.408E-9	9.662E-11	4.035E-11	6.860E-11
5.	2.90	4.385E-9	1.472E-11	1.679E-11	3.315E-11
6.	3.40	4.371E-9	5.564E-11	0.000e+00	0.000e+00
7.	3.90	4.411E-9	2.671E-11	3.638E-11	1.655E-11
8.	4.40	4.497E-9	6.709E-11	1.179E-10	7.489E-11
9.	4.90	4.535E-9	3.240E-11	1.501E-10	8.081E-11
10.	5.40	4.602E-9	8.911E-11	2.115E-10	1.130E-10
11.	5.90	4.700E-9	3.325E-11	3.031E-10	1.726E-10
12.	6.40	4.772E-9	1.214E-10	3.680E-10	2.029E-10
13.	6.90	4.909E-9	3.715E-11	4.987E-10	2.965E-10
14.	7.40	4.974E-9	8.890E-11	5.568E-10	3.153E-10
15.	7.90	5.056E-9	4.188E-11	6.310E-10	3.481E-10
16.	8.40	5.220E-9	5.990E-11	7.885E-10	4.623E-10
17.	8.90	5.469E-9	3.975E-11	1.030E-9	6.588E-10
18.	9.40	5.608E-9	1.164E-10	1.162E-9	7.437E-10
19.	9.90	6.140E-9	4.340E-11	1.685E-9	1.219E-9
20.	10.40	6.655E-9	7.687E-11	2.193E-9	1.678E-9
21.	10.90	8.717E-9	1.046E-10	4.247E-9	3.682E-9
22.	11.40	1.220E-8	1.577E-10	7.724E-9	7.107E-9
23.	11.90	2.085E-8	1.924E-10	1.636E-8	1.569E-8
24.	12.40	3.363E-8	1.023E-9	2.914E-8	2.842E-8
25.	12.90	6.212E-8	8.253E-10	5.762E-8	5.685E-8
26.	13.40	1.005E-7	7.070E-9	9.603E-8	9.521E-8
27.	13.90	1.802E-7	3.649E-9	1.757E-7	1.748E-7
28.	14.40	2.762E-7	1.952E-8	2.717E-7	2.707E-7
29.	14.90	4.300E-7	5.260E-9	4.255E-7	4.245E-7
30.	15.40	6.171E-7	1.575E-8	6.126E-7	6.115E-7
31.	16.40	1.127E-6	2.167E-8	1.123E-6	1.122E-6
32.	17.40	2.065E-6	5.842E-8	2.061E-6	2.059E-6
33.	18.40	3.498E-6	2.699E-7	3.494E-6	3.492E-6

Table D.20 Profile of the total scattering coefficient and the particle scattering coefficient for the A-IA-S5 flame ($\phi = 2.32$, $v_c = 7.75 \text{ cm}\cdot\text{sec}^{-1}$, $D = 4.16$).

	Height (mm)	Total Scattering Coefficient ($\text{cm}^{-1}\cdot\text{sr}^{-1}$)	Standard Deviation	Particle Scattering Coefficient ($\text{cm}^{-1}\cdot\text{sr}^{-1}$)
1.	0.53	4.841E-9	2.115E-11	3.309E-10
2.	0.73	4.587E-9	2.778E-11	1.285E-10
3.	0.92	4.614E-9	2.913E-11	1.829E-10
4.	0.93	4.544E-9	2.403E-11	1.138E-10
5.	1.13	4.541E-9	4.770E-11	1.288E-10
6.	1.33	4.491E-9	2.407E-11	8.954E-11
7.	1.42	4.495E-9	3.386E-11	9.768E-11
8.	1.53	4.446E-9	2.234E-11	5.257E-11
9.	1.73	4.428E-9	1.861E-11	3.960E-11
10.	1.92	4.457E-9	1.634E-11	7.159E-11
11.	1.93	4.447E-9	1.561E-11	6.164E-11
12.	2.13	4.393E-9	2.237E-11	1.074E-11
13.	2.33	4.402E-9	1.340E-11	2.015E-11
14.	2.42	4.420E-9	2.066E-11	3.880E-11
15.	2.53	4.395E-9	1.369E-11	1.203E-11
16.	2.73	4.407E-9	1.365E-11	1.936E-11
17.	2.92	4.394E-9	3.104E-11	0.000e+00
18.	2.93	4.406E-9	2.939E-11	1.147E-11
19.	3.13	4.415E-9	1.303E-11	1.428E-11
20.	3.33	4.430E-9	3.685E-11	2.064E-11
21.	3.42	4.427E-9	3.591E-11	1.394E-11
22.	3.53	4.444E-9	1.915E-11	2.610E-11
23.	3.73	4.457E-9	1.901E-11	2.956E-11
24.	3.92	4.506E-9	3.407E-11	6.932E-11
25.	3.93	4.519E-9	1.854E-11	8.128E-11
26.	4.13	4.526E-9	1.932E-11	7.824E-11
27.	4.33	4.552E-9	1.948E-11	9.292E-11
28.	4.42	4.552E-9	7.192E-11	8.748E-11
29.	4.53	4.595E-9	2.731E-11	1.230E-10
30.	4.73	4.647E-9	3.264E-11	1.632E-10
31.	4.92	4.667E-9	3.784E-11	1.706E-10
32.	4.93	4.686E-9	1.663E-11	1.888E-10
33.	5.13	4.708E-9	3.098E-11	1.969E-10
34.	5.33	4.788E-9	2.437E-11	2.627E-10
35.	5.42	4.767E-9	3.665E-11	2.344E-10
36.	5.53	4.828E-9	1.652E-11	2.872E-10
37.	5.73	4.882E-9	3.052E-11	3.259E-10
38.	5.92	4.923E-9	5.426E-11	3.526E-10
39.	5.93	4.963E-9	2.086E-11	3.911E-10
40.	6.13	4.982E-9	3.371E-11	3.947E-10
41.	6.42	5.121E-9	4.882E-11	5.085E-10
42.	6.92	5.348E-9	1.544E-10	6.915E-10
43.	7.42	5.488E-9	9.369E-11	7.851E-10
44.	7.92	5.747E-9	7.281E-11	9.957E-10
45.	8.42	6.089E-9	6.401E-11	1.287E-9

Table D.20 continued

	Height (mm)	Total Scattering Coefficient ($\text{cm}^{-1}\cdot\text{sr}^{-1}$)	Standard Deviation	Particle Scattering Coefficient ($\text{cm}^{-1}\cdot\text{sr}^{-1}$)
46.	8.92	6.613E-9	5.875E-11	1.759E-9
47.	9.42	8.191E-9	5.543E-11	3.283E-9
48.	9.92	1.177E-8	4.489E-10	6.810E-9
49.	10.42	2.320E-8	2.286E-10	1.818E-8
50.	10.92	4.922E-8	1.573E-9	4.414E-8
51.	11.42	1.334E-7	6.230E-8	1.283E-7
52.	11.92	1.972E-7	2.153E-9	1.920E-7
53.	12.42	3.642E-7	1.969E-8	3.590E-7
54.	12.92	6.746E-7	1.171E-8	6.693E-7
55.	13.42	1.162E-6	2.457E-8	1.156E-6
56.	13.92	1.785E-6	1.119E-8	1.779E-6
57.	14.42	2.743E-6	2.921E-8	2.738E-6
58.	14.92	3.919E-6	8.421E-8	3.913E-6
59.	15.42	5.391E-6	1.638E-7	5.386E-6

Table D.21 Profile of the total scattering coefficient for the A-IB-C flame ($\phi = 1.67$, $v_c = 7.87 \text{ cm}\cdot\text{sec}^{-1}$, $D = 3.31$).

	Height (mm)	Total Scattering Coefficient ($\text{cm}^{-1}\cdot\text{sr}^{-1}$)	Standard Deviation
1.	0.87	4.150E-9	2.750E-11
2.	1.37	4.086E-9	2.097E-11
3.	1.87	4.096E-9	8.285E-12
4.	2.37	4.085E-9	1.808E-11
5.	2.87	4.095E-9	1.085E-11
6.	3.37	4.085E-9	2.133E-11
7.	3.87	4.104E-9	1.919E-11
8.	4.37	4.092E-9	1.879E-11
9.	4.87	4.132E-9	1.505E-11
10.	5.37	4.095E-9	2.126E-11
11.	5.87	4.148E-9	2.601E-11
12.	6.37	4.133E-9	2.752E-11
13.	6.87	4.129E-9	1.968E-11
14.	7.37	4.144E-9	1.470E-11
15.	7.87	4.169E-9	1.644E-11
16.	8.37	4.179E-9	3.101E-11
17.	8.87	4.194E-9	1.339E-11
18.	9.37	4.181E-9	3.524E-11
19.	9.87	4.214E-9	1.233E-11
20.	10.37	4.212E-9	2.022E-11
21.	10.87	4.220E-9	2.025E-11
22.	11.37	4.234E-9	2.638E-11
23.	11.87	4.241E-9	3.214E-11
24.	12.37	4.233E-9	2.757E-11
25.	12.87	4.268E-9	1.818E-11
26.	13.37	4.274E-9	3.170E-11
27.	13.87	4.250E-9	1.248E-11
28.	14.37	4.283E-9	2.466E-11
29.	14.87	4.304E-9	1.979E-11
30.	15.37	4.294E-9	2.572E-11
31.	16.37	4.310E-9	2.564E-11
32.	17.37	4.340E-9	1.652E-11
33.	18.37	4.326E-9	1.711E-11
34.	19.37	4.334E-9	2.001E-11
35.	20.37	4.374E-9	1.314E-11

Table D.22 Profile of the total scattering coefficient and the particle scattering coefficient for the A-IB-S2 flame ($\phi = 1.92$, $v_c = 7.78 \text{ cm}\cdot\text{sec}^{-1}$, $D = 3.54$).

	Height (mm)	Total Scattering Coefficient ($\text{cm}^{-1}\cdot\text{sr}^{-1}$)	Standard Deviation	Particle Scattering Coefficient ($\text{cm}^{-1}\cdot\text{sr}^{-1}$)
1.	0.67	4.303E-9	1.370E-11	1.020E-10
2.	0.86	4.218E-9	3.340E-11	5.342E-11
3.	0.87	4.205E-9	2.164E-11	4.255E-11
4.	1.07	4.179E-9	2.362E-11	3.836E-11
5.	1.27	4.184E-9	1.251E-11	5.758E-11
6.	1.36	4.155E-9	1.702E-11	3.364E-11
7.	1.47	4.176E-9	1.279E-11	5.922E-11
8.	1.67	4.144E-9	1.791E-11	3.334E-11
9.	1.86	4.131E-9	1.845E-11	2.502E-11
10.	1.87	4.136E-9	1.785E-11	3.032E-11
11.	2.07	4.128E-9	6.673E-12	2.467E-11
12.	2.27	4.152E-9	2.937E-11	4.996E-11
13.	2.36	4.116E-9	1.975E-11	1.443E-11
14.	2.47	4.102E-9	2.850E-11	1.048E-12
15.	2.67	4.120E-9	1.515E-11	1.945E-11
16.	2.86	4.134E-9	9.029E-12	3.263E-11
17.	2.87	4.106E-9	1.841E-11	4.856E-12
18.	3.07	4.141E-9	8.541E-12	3.872E-11
19.	3.27	4.149E-9	1.761E-11	4.521E-11
20.	3.36	4.117E-9	1.560E-11	1.335E-11
21.	3.47	4.117E-9	1.177E-11	1.242E-11
22.	3.67	4.148E-9	1.807E-11	4.200E-11
23.	3.86	4.156E-9	1.105E-11	4.769E-11
24.	3.87	4.140E-9	1.338E-11	3.161E-11
25.	4.07	4.154E-9	1.643E-11	4.351E-11
26.	4.27	4.155E-9	2.093E-11	4.248E-11
27.	4.36	4.113E-9	1.457E-11	0.000e+00
28.	4.47	4.157E-9	2.150E-11	4.261E-11
29.	4.67	4.148E-9	1.801E-11	3.097E-11
30.	4.86	4.166E-9	1.961E-11	4.641E-11
31.	4.87	4.170E-9	1.959E-11	5.003E-11
32.	5.07	4.194E-9	2.321E-11	7.173E-11
33.	5.27	4.186E-9	1.780E-11	6.178E-11
34.	5.36	4.195E-9	8.304E-12	6.876E-11
35.	5.47	4.220E-9	1.821E-11	9.295E-11
36.	5.67	4.234E-9	2.119E-11	1.040E-10
37.	5.86	4.232E-9	2.170E-11	9.927E-11
38.	5.87	4.216E-9	2.567E-11	8.316E-11
39.	6.07	4.222E-9	2.509E-11	8.626E-11
40.	6.36	4.256E-9	1.739E-11	1.160E-10
41.	6.86	4.257E-9	1.918E-11	1.098E-10
42.	7.36	4.252E-9	1.742E-11	9.726E-11
43.	7.86	4.312E-9	2.330E-11	1.492E-10
44.	8.36	4.343E-9	1.445E-11	1.719E-10
45.	8.86	4.402E-9	1.278E-11	2.236E-10

Table D.22 continued

	Height (mm)	Total Scattering Coefficient ($\text{cm}^{-1}\cdot\text{sr}^{-1}$)	Standard Deviation	Particle Scattering Coefficient ($\text{cm}^{-1}\cdot\text{sr}^{-1}$)
46.	9.36	4.412E-9	1.599E-11	2.256E-10
47.	9.86	4.446E-9	2.516E-11	2.507E-10
48.	10.36	4.491E-9	2.759E-11	2.878E-10
49.	10.86	4.530E-9	2.862E-11	3.185E-10
50.	11.36	4.534E-9	1.517E-11	3.137E-10
51.	11.86	4.622E-9	1.695E-11	3.933E-10
52.	12.36	4.714E-9	1.533E-11	4.778E-10
53.	12.86	4.781E-9	2.151E-11	5.358E-10
54.	13.36	4.971E-9	1.952E-11	7.176E-10
55.	13.86	5.163E-9	3.269E-11	9.010E-10
56.	14.36	5.474E-9	3.416E-11	1.204E-9
57.	14.86	5.981E-9	2.895E-11	1.702E-9
58.	15.36	6.732E-9	8.298E-11	2.444E-9

Table D.23 Profile of the total scattering coefficient and the particle scattering coefficient for the A-IB-S3 flame ($\phi = 2.02$, $v_c = 7.78 \text{ cm}\cdot\text{sec}^{-1}$, $D = 3.54$).

	Height (mm)	Total Scattering Coefficient ($\text{cm}^{-1}\cdot\text{sr}^{-1}$)	Standard Deviation	Particle Scattering Coefficient ($\text{cm}^{-1}\cdot\text{sr}^{-1}$)
1.	0.67	4.445E-9	1.006E-11	1.323E-10
2.	0.87	4.370E-9	1.077E-11	9.480E-11
3.	0.87	4.373E-9	1.317E-11	9.816E-11
4.	1.07	4.338E-9	1.245E-11	8.561E-11
5.	1.27	4.306E-9	1.009E-11	6.787E-11
6.	1.37	4.273E-9	1.246E-11	3.992E-11
7.	1.47	4.287E-9	1.778E-11	5.800E-11
8.	1.67	4.295E-9	2.053E-11	7.192E-11
9.	1.87	4.249E-9	1.763E-11	3.001E-11
10.	1.87	4.264E-9	2.138E-11	4.539E-11
11.	2.07	4.240E-9	2.294E-11	2.420E-11
12.	2.27	4.242E-9	1.660E-11	2.692E-11
13.	2.37	4.241E-9	1.070E-11	2.697E-11
14.	2.47	4.256E-9	2.972E-11	4.162E-11
15.	2.67	4.229E-9	1.953E-11	1.537E-11
16.	2.87	4.214E-9	1.687E-11	0.000e+00
17.	2.87	4.216E-9	2.040E-11	2.090E-12
18.	3.07	4.233E-9	1.295E-11	1.809E-11
19.	3.27	4.241E-9	1.459E-11	2.432E-11
20.	3.37	4.223E-9	1.472E-11	5.867E-12
21.	3.47	4.242E-9	2.143E-11	2.482E-11
22.	3.67	4.257E-9	1.740E-11	3.823E-11
23.	3.87	4.286E-9	1.396E-11	6.453E-11
24.	3.87	4.295E-9	1.461E-11	7.378E-11
25.	4.07	4.298E-9	2.168E-11	7.457E-11
26.	4.27	4.307E-9	1.876E-11	8.184E-11
27.	4.37	4.326E-9	1.464E-11	9.929E-11
28.	4.47	4.283E-9	1.333E-11	5.588E-11
29.	4.67	4.354E-9	1.632E-11	1.238E-10
30.	4.87	4.366E-9	2.798E-11	1.331E-10
31.	4.87	4.362E-9	1.784E-11	1.299E-10
32.	5.07	4.393E-9	3.099E-11	1.576E-10
33.	5.27	4.388E-9	1.765E-11	1.503E-10
34.	5.37	4.390E-9	2.906E-11	1.514E-10
35.	5.47	4.422E-9	1.207E-11	1.819E-10
36.	5.67	4.440E-9	1.807E-11	1.967E-10
37.	5.87	4.461E-9	1.007E-11	2.150E-10
38.	5.87	4.470E-9	1.224E-11	2.244E-10
39.	6.07	4.484E-9	1.120E-11	2.356E-10
40.	6.37	4.509E-9	2.587E-11	2.563E-10
41.	6.87	4.599E-9	1.738E-11	3.388E-10
42.	7.37	4.651E-9	1.243E-11	3.831E-10
43.	7.87	4.761E-9	2.201E-11	4.854E-10
44.	8.37	4.848E-9	2.045E-11	5.639E-10
45.	8.87	5.021E-9	2.242E-11	7.295E-10

Table D.23 continued

	Height (mm)	Total Scattering Coefficient ($\text{cm}^{-1}\cdot\text{sr}^{-1}$)	Standard Deviation	Particle Scattering Coefficient ($\text{cm}^{-1}\cdot\text{sr}^{-1}$)
46.	9.37	5.310E-9	6.202E-11	1.011E-9
47.	9.87	5.827E-9	2.118E-11	1.519E-9
48.	10.37	6.666E-9	2.676E-11	2.350E-9
49.	10.87	8.472E-9	6.200E-11	4.147E-9
50.	11.37	1.136E-8	1.179E-10	7.029E-9
51.	11.87	1.592E-8	1.016E-10	1.158E-8
52.	12.37	2.370E-8	3.661E-10	1.935E-8
53.	12.87	3.324E-8	4.534E-10	2.888E-8
54.	13.37	4.840E-8	5.003E-11	4.403E-8
55.	13.87	7.132E-8	5.391E-10	6.695E-8
56.	14.37	1.136E-7	2.147E-9	1.092E-7
57.	14.87	1.566E-7	2.822E-9	1.523E-7
58.	15.37	2.085E-7	5.224E-9	2.041E-7

Table D.24 Profile of the total scattering coefficient and the particle scattering coefficient for the A-IB-S4 flame ($\phi = 2.17$, $v_c = 7.77 \text{ cm}\cdot\text{sec}^{-1}$, $D = 3.53$).

	Height (mm)	Total Scattering Coefficient ($\text{cm}^{-1}\cdot\text{sr}^{-1}$)	Standard Deviation	Particle Scattering Coefficient ($\text{cm}^{-1}\cdot\text{sr}^{-1}$)
1.	0.50	4.534E-9	1.899E-11	1.922E-10
2.	0.70	4.419E-9	1.875E-11	1.424E-10
3.	0.89	4.364E-9	1.871E-11	1.204E-10
4.	0.90	4.326E-9	1.816E-11	8.408E-11
5.	1.10	4.260E-9	1.773E-11	3.902E-11
6.	1.30	4.243E-9	2.116E-11	3.532E-11
7.	1.39	4.224E-9	3.160E-11	2.065E-11
8.	1.50	4.245E-9	1.835E-11	4.549E-11
9.	1.70	4.238E-9	3.163E-11	4.426E-11
10.	1.89	4.195E-9	1.973E-11	5.561E-12
11.	1.90	4.215E-9	2.011E-11	2.579E-11
12.	2.10	4.187E-9	1.808E-11	0.000e+00
13.	2.30	4.216E-9	1.905E-11	3.029E-11
14.	2.39	4.230E-9	3.259E-11	4.456E-11
15.	2.50	4.209E-9	1.958E-11	2.345E-11
16.	2.70	4.240E-9	1.230E-11	5.503E-11
17.	2.89	4.225E-9	3.318E-11	3.954E-11
18.	2.90	4.256E-9	1.555E-11	7.012E-11
19.	3.10	4.276E-9	1.538E-11	8.977E-11
20.	3.30	4.277E-9	9.626E-12	8.892E-11
21.	3.39	4.317E-9	3.206E-11	1.290E-10
22.	3.50	4.284E-9	1.673E-11	9.487E-11
23.	3.70	4.303E-9	3.294E-11	1.122E-10
24.	3.89	4.352E-9	2.841E-11	1.597E-10
25.	3.90	4.350E-9	3.595E-11	1.569E-10
26.	4.10	4.412E-9	2.484E-11	2.171E-10
27.	4.30	4.414E-9	3.927E-11	2.175E-10
28.	4.39	4.448E-9	2.616E-11	2.503E-10
29.	4.50	4.457E-9	1.614E-11	2.579E-10
30.	4.70	4.506E-9	1.744E-11	3.048E-10
31.	4.89	4.553E-9	4.786E-11	3.488E-10
32.	4.90	4.548E-9	3.031E-11	3.437E-10
33.	5.10	4.594E-9	2.074E-11	3.870E-10
34.	5.30	4.618E-9	3.791E-11	4.087E-10
35.	5.39	4.642E-9	3.940E-11	4.313E-10
36.	5.50	4.728E-9	2.561E-11	5.165E-10
37.	5.70	4.717E-9	2.443E-11	5.020E-10
38.	5.89	4.821E-9	7.401E-11	6.040E-10
39.	5.90	4.813E-9	2.592E-11	5.957E-10
40.	6.10	4.855E-9	2.317E-11	6.347E-10
41.	6.39	5.055E-9	4.674E-11	8.307E-10
42.	6.89	5.221E-9	3.921E-11	9.889E-10
43.	7.39	5.796E-9	4.024E-11	1.557E-9
44.	7.89	7.556E-9	3.819E-11	3.308E-9
45.	8.39	1.198E-8	8.068E-11	7.723E-9

Table D.24 continued

	Height (mm)	Total Scattering Coefficient ($\text{cm}^{-1}\cdot\text{sr}^{-1}$)	Standard Deviation	Particle Scattering Coefficient ($\text{cm}^{-1}\cdot\text{sr}^{-1}$)
46.	8.89	2.296E-8	1.049E-10	1.870E-8
47.	9.39	3.728E-8	3.937E-11	3.301E-8
48.	9.89	9.600E-8	8.232E-10	9.172E-8
49.	10.39	1.821E-7	1.366E-9	1.778E-7
50.	10.89	3.290E-7	4.508E-9	3.247E-7
51.	11.39	5.473E-7	3.186E-9	5.430E-7
52.	11.89	1.124E-6	5.089E-7	1.120E-6
53.	12.39	1.328E-6	1.568E-8	1.324E-6
54.	12.89	1.917E-6	2.108E-8	1.913E-6
55.	13.39	2.685E-6	2.178E-8	2.681E-6
56.	13.89	3.661E-6	3.390E-8	3.657E-6
57.	14.39	4.723E-6	7.753E-8	4.719E-6
58.	14.89	6.051E-6	5.623E-8	6.046E-6
59.	15.39	7.602E-6	2.566E-8	7.598E-6

Table D.25 Profile of the total scattering coefficient for the A-IIA-R2 flame ($\phi = 1.63$, $v_c = 10.42 \text{ cm}\cdot\text{sec}^{-1}$, $D = 4.29$).

	Height (mm)	Total Scattering Coefficient ($\text{cm}^{-1}\cdot\text{sr}^{-1}$)	Standard Deviation
1.	0.88	4.106E-9	9.843E-12
2.	1.38	4.066E-9	2.785E-11
3.	1.88	4.065E-9	1.485E-11
4.	2.38	4.051E-9	1.449E-11
5.	2.88	4.062E-9	1.351E-11
6.	3.38	4.057E-9	2.286E-11
7.	3.88	4.060E-9	1.522E-11
8.	4.38	4.066E-9	2.391E-11
9.	4.88	4.078E-9	7.525E-12
10.	5.38	4.092E-9	2.005E-11
11.	5.88	4.095E-9	1.456E-11
12.	6.38	4.100E-9	1.990E-11
13.	6.88	4.103E-9	1.745E-11
14.	7.38	4.123E-9	2.756E-11
15.	7.88	4.137E-9	1.064E-11
16.	8.38	4.116E-9	2.844E-11
17.	8.88	4.146E-9	3.550E-11
18.	9.38	4.126E-9	2.739E-11
19.	9.88	4.142E-9	1.862E-11
20.	10.38	4.145E-9	2.887E-11
21.	10.88	4.138E-9	1.497E-11
22.	11.38	4.160E-9	2.314E-11
23.	11.88	4.165E-9	1.379E-11
24.	12.38	4.168E-9	2.538E-11
25.	12.88	4.183E-9	1.903E-11
26.	13.38	4.177E-9	2.078E-11
27.	13.88	4.170E-9	6.628E-12
28.	14.38	4.185E-9	1.826E-11
29.	14.88	4.182E-9	1.833E-11
30.	15.38	4.195E-9	2.064E-11
31.	16.38	4.208E-9	1.252E-11
32.	17.38	4.202E-9	1.340E-11
33.	18.38	4.230E-9	8.999E-12
34.	19.38	4.235E-9	1.589E-11
35.	20.38	4.263E-9	7.401E-12

Table D.26 Profile of the total scattering coefficient for the A-IIA-S1 flame ($\phi = 1.78$, $v_c = 10.45 \text{ cm}\cdot\text{sec}^{-1}$, $D = 4.29$).

	Height (mm)	Total Scattering Coefficient ($\text{cm}^{-1}\cdot\text{sr}^{-1}$)	Standard Deviation
1.	0.68	4.092E-9	1.183E-11
2.	0.88	4.056E-9	2.770E-11
3.	0.88	4.090E-9	1.626E-11
4.	1.08	4.062E-9	2.372E-11
5.	1.28	4.052E-9	2.539E-11
6.	1.38	4.052E-9	2.338E-11
7.	1.48	4.059E-9	2.208E-11
8.	1.68	4.079E-9	2.442E-11
9.	1.88	4.082E-9	2.876E-11
10.	1.88	4.072E-9	2.832E-11
11.	2.08	4.061E-9	1.720E-11
12.	2.28	4.065E-9	4.067E-11
13.	2.38	4.048E-9	2.411E-11
14.	2.48	4.058E-9	3.090E-11
15.	2.68	4.043E-9	2.971E-11
16.	2.88	4.075E-9	2.624E-11
17.	2.88	4.074E-9	2.941E-11
18.	3.08	4.051E-9	1.424E-11
19.	3.28	4.065E-9	2.289E-11
20.	3.38	4.059E-9	2.356E-11
21.	3.48	4.072E-9	4.152E-11
22.	3.68	4.078E-9	3.043E-11
23.	3.88	4.076E-9	3.093E-11
24.	3.88	4.068E-9	3.571E-11
25.	4.08	4.075E-9	2.091E-11
26.	4.28	4.059E-9	1.718E-11
27.	4.38	4.060E-9	1.796E-11
28.	4.48	4.063E-9	2.957E-11
29.	4.68	4.062E-9	2.197E-11
30.	4.88	4.089E-9	3.927E-11
31.	4.88	4.072E-9	2.702E-11
32.	5.08	4.076E-9	1.570E-11
33.	5.28	4.074E-9	2.304E-11
34.	5.38	4.072E-9	3.438E-11
35.	5.48	4.070E-9	2.214E-11
36.	5.68	4.078E-9	3.257E-11
37.	5.88	4.084E-9	2.698E-11
38.	5.88	4.081E-9	2.400E-11
39.	6.08	4.070E-9	2.348E-11
40.	6.38	4.091E-9	2.701E-11
41.	6.88	4.093E-9	2.248E-11
42.	7.38	4.094E-9	2.509E-11
43.	7.88	4.106E-9	2.051E-11
44.	8.38	4.091E-9	2.814E-11
45.	8.88	4.109E-9	1.864E-11

Table D.26 continued

	Height (mm)	Total Scattering Coefficient ($\text{cm}^{-1}\cdot\text{sr}^{-1}$)	Standard Deviation
46.	9.38	4.119E-9	2.870E-11
47.	9.88	4.132E-9	2.584E-11
48.	10.38	4.136E-9	3.755E-11
49.	10.88	4.142E-9	2.249E-11
50.	11.38	4.145E-9	2.088E-11
51.	11.88	4.121E-9	2.298E-11
52.	12.38	4.124E-9	3.406E-11
53.	12.88	4.148E-9	1.531E-11
54.	13.38	4.158E-9	3.021E-11
55.	13.88	4.145E-9	2.191E-11
56.	14.38	4.152E-9	2.391E-11
57.	14.88	4.150E-9	2.113E-11
58.	15.38	4.173E-9	2.281E-11
59.	16.38	4.175E-9	1.351E-11
60.	17.38	4.199E-9	1.714E-11
61.	18.38	4.205E-9	1.526E-11
62.	19.38	4.200E-9	1.103E-11
63.	20.38	4.199E-9	1.228E-11

Table D.27 Profile of the total scattering coefficient and the particle scattering coefficient for the A-IIA-S2 flame ($\phi = 1.92$, $v_c = 10.45 \text{ cm}\cdot\text{sec}^{-1}$, $D = 4.28$).

	Height (mm)	Total Scattering Coefficient ($\text{cm}^{-1}\cdot\text{sr}^{-1}$)	Standard Deviation	Particle Scattering Coefficient ($\text{cm}^{-1}\cdot\text{sr}^{-1}$)
1.	0.52	4.366E-9	2.047E-11	2.436E-10
2.	0.72	4.268E-9	1.682E-11	1.790E-10
3.	0.92	4.247E-9	2.027E-11	1.741E-10
4.	0.92	4.224E-9	2.042E-11	1.508E-10
5.	1.12	4.170E-9	1.254E-11	1.058E-10
6.	1.32	4.182E-9	1.245E-11	1.222E-10
7.	1.42	4.139E-9	2.111E-11	8.140E-11
8.	1.52	4.133E-9	1.526E-11	7.669E-11
9.	1.72	4.133E-9	1.400E-11	7.815E-11
10.	1.92	4.114E-9	1.204E-11	6.097E-11
11.	1.92	4.121E-9	2.183E-11	6.786E-11
12.	2.12	4.115E-9	6.061E-12	6.185E-11
13.	2.32	4.101E-9	1.320E-11	4.762E-11
14.	2.42	4.059E-9	2.588E-11	5.655E-12
15.	2.52	4.082E-9	8.756E-12	2.860E-11
16.	2.72	4.101E-9	2.513E-11	4.707E-11
17.	2.92	4.062E-9	1.751E-11	6.472E-12
18.	2.92	4.081E-9	2.846E-11	2.578E-11
19.	3.12	4.090E-9	1.793E-11	3.434E-11
20.	3.32	4.064E-9	6.893E-12	7.088E-12
21.	3.42	4.059E-9	2.786E-11	6.856E-13
22.	3.52	4.092E-9	1.728E-11	3.372E-11
23.	3.72	4.079E-9	1.495E-11	1.885E-11
24.	3.92	4.063E-9	1.997E-11	2.165E-12
25.	3.92	4.087E-9	1.777E-11	2.539E-11
26.	4.12	4.077E-9	7.314E-12	1.436E-11
27.	4.32	4.097E-9	1.553E-11	3.242E-11
28.	4.42	4.074E-9	1.914E-11	8.448E-12
29.	4.52	4.079E-9	3.444E-11	1.273E-11
30.	4.72	4.068E-9	2.106E-11	0.000e+00
31.	4.92	4.113E-9	1.431E-11	4.322E-11
32.	4.92	4.090E-9	2.389E-11	2.116E-11
33.	5.12	4.097E-9	2.087E-11	2.560E-11
34.	5.32	4.105E-9	1.818E-11	3.273E-11
35.	5.42	4.082E-9	2.372E-11	8.007E-12
36.	5.52	4.110E-9	1.199E-11	3.584E-11
37.	5.72	4.108E-9	1.815E-11	3.141E-11
38.	5.92	4.088E-9	3.331E-11	9.474E-12
39.	5.92	4.095E-9	1.546E-11	1.723E-11
40.	6.12	4.109E-9	1.578E-11	2.922E-11
41.	6.42	4.111E-9	3.019E-11	2.830E-11
42.	6.92	4.120E-9	3.003E-11	3.288E-11
43.	7.42	4.105E-9	1.546E-11	1.302E-11
44.	7.92	4.139E-9	1.649E-11	4.226E-11
45.	8.42	4.143E-9	3.980E-11	4.157E-11

Table D.27 continued

	Height (mm)	Total Scattering Coefficient ($\text{cm}^{-1}\cdot\text{sr}^{-1}$)	Standard Deviation	Particle Scattering Coefficient ($\text{cm}^{-1}\cdot\text{sr}^{-1}$)
46.	8.92	4.149E-9	1.297E-11	4.237E-11
47.	9.42	4.178E-9	2.730E-11	6.657E-11
48.	9.92	4.131E-9	1.009E-11	1.498E-11
49.	10.42	4.175E-9	1.812E-11	5.357E-11
50.	10.92	4.186E-9	1.706E-11	5.915E-11
51.	11.42	4.209E-9	2.462E-11	7.779E-11
52.	11.92	4.217E-9	1.918E-11	8.067E-11
53.	12.42	4.227E-9	4.145E-11	8.515E-11
54.	12.92	4.223E-9	2.241E-11	7.638E-11
55.	13.42	4.251E-9	2.213E-11	9.912E-11
56.	13.92	4.241E-9	1.292E-11	8.428E-11
57.	14.42	4.281E-9	3.168E-11	1.197E-10
58.	14.92	4.312E-9	1.557E-11	1.455E-10
59.	15.42	4.349E-9	1.984E-11	1.767E-10
60.	16.42	4.446E-9	1.912E-11	2.635E-10
61.	17.42	4.601E-9	2.487E-11	4.087E-10
62.	18.42	4.814E-9	1.983E-11	6.115E-10
63.	19.42	5.181E-9	2.787E-11	9.686E-10
64.	20.42	5.776E-9	2.492E-11	1.553E-9

Table D.28 Profile of the total scattering coefficient and the particle scattering coefficient for the A-IIA-S3 flame ($\phi = 2.02$, $v_c = 10.45 \text{ cm}\cdot\text{sec}^{-1}$, $D = 4.28$).

	Height (mm)	Total Scattering Coefficient ($\text{cm}^{-1}\cdot\text{sr}^{-1}$)	Standard Deviation	Particle Scattering Coefficient ($\text{cm}^{-1}\cdot\text{sr}^{-1}$)
1.	0.54	4.572E-9	9.049E-12	4.408E-10
2.	0.74	4.395E-9	1.556E-11	2.936E-10
3.	0.94	4.274E-9	1.659E-11	1.879E-10
4.	0.94	4.282E-9	1.981E-11	1.951E-10
5.	1.14	4.248E-9	2.180E-11	1.696E-10
6.	1.34	4.197E-9	1.345E-11	1.237E-10
7.	1.44	4.148E-9	3.559E-11	7.683E-11
8.	1.54	4.163E-9	1.848E-11	9.311E-11
9.	1.74	4.157E-9	1.343E-11	8.877E-11
10.	1.94	4.113E-9	1.032E-11	4.531E-11
11.	1.94	4.129E-9	1.965E-11	6.151E-11
12.	2.14	4.124E-9	1.043E-11	5.692E-11
13.	2.34	4.128E-9	8.948E-12	6.019E-11
14.	2.44	4.068E-9	5.571E-11	0.000e+00
15.	2.54	4.108E-9	6.857E-12	4.027E-11
16.	2.74	4.110E-9	2.505E-11	4.145E-11
17.	2.94	4.090E-9	1.758E-11	2.083E-11
18.	2.94	4.087E-9	9.273E-12	1.799E-11
19.	3.14	4.108E-9	1.883E-11	3.771E-11
20.	3.34	4.120E-9	2.412E-11	4.824E-11
21.	3.44	4.107E-9	2.781E-11	3.480E-11
22.	3.54	4.138E-9	2.612E-11	6.515E-11
23.	3.74	4.104E-9	1.809E-11	3.014E-11
24.	3.94	4.089E-9	1.549E-11	1.349E-11
25.	3.94	4.113E-9	9.947E-12	3.700E-11
26.	4.14	4.109E-9	8.420E-12	3.196E-11
27.	4.34	4.130E-9	1.801E-11	5.137E-11
28.	4.44	4.094E-9	4.054E-11	1.473E-11
29.	4.54	4.122E-9	6.213E-12	4.201E-11
30.	4.74	4.156E-9	1.930E-11	7.369E-11
31.	4.94	4.149E-9	1.698E-11	6.507E-11
32.	4.94	4.133E-9	1.334E-11	4.940E-11
33.	5.14	4.140E-9	1.384E-11	5.449E-11
34.	5.34	4.143E-9	9.633E-12	5.577E-11
35.	5.44	4.163E-9	3.787E-11	7.474E-11
36.	5.54	4.162E-9	1.535E-11	7.265E-11
37.	5.74	4.174E-9	1.331E-11	8.351E-11
38.	5.94	4.184E-9	1.435E-11	9.123E-11
39.	5.94	4.157E-9	2.691E-11	6.434E-11
40.	6.14	4.164E-9	2.167E-11	6.931E-11
41.	6.44	4.204E-9	5.193E-11	1.072E-10
42.	6.94	4.221E-9	2.523E-11	1.192E-10
43.	7.44	4.242E-9	4.375E-11	1.350E-10
44.	7.94	4.272E-9	1.370E-11	1.609E-10
45.	8.44	4.313E-9	3.070E-11	1.972E-10

Table D.28 continued

	Height (mm)	Total Scattering Coefficient ($\text{cm}^{-1}\cdot\text{sr}^{-1}$)	Standard Deviation	Particle Scattering Coefficient ($\text{cm}^{-1}\cdot\text{sr}^{-1}$)
46.	8.94	4.338E-9	1.595E-11	2.165E-10
47.	9.44	4.370E-9	5.006E-11	2.437E-10
48.	9.94	4.447E-9	2.097E-11	3.163E-10
49.	10.44	4.599E-9	3.723E-11	4.635E-10
50.	10.94	4.745E-9	2.775E-11	6.041E-10
51.	11.44	5.079E-9	3.800E-11	9.336E-10
52.	11.94	5.504E-9	1.616E-11	1.353E-9
53.	12.44	6.231E-9	3.926E-11	2.075E-9
54.	12.94	7.287E-9	5.373E-11	3.126E-9
55.	13.44	8.990E-9	1.163E-10	4.824E-9
56.	13.94	1.072E-8	5.981E-11	6.552E-9
57.	14.44	1.474E-8	2.229E-9	1.057E-8
58.	14.94	1.722E-8	2.104E-10	1.304E-8
59.	15.44	2.321E-8	3.525E-10	1.902E-8
60.	16.44	3.883E-8	9.372E-10	3.463E-8
61.	17.44	5.977E-8	9.462E-10	5.556E-8
62.	18.44	9.180E-8	6.864E-10	8.759E-8
63.	19.44	1.258E-7	3.177E-9	1.216E-7
64.	20.44	1.836E-7	1.078E-9	1.794E-7

Table D.29 Profiles of the fluorescence coefficient detected at 503 nm and 473 nm for the A-IA-R2 flame ($\phi = 1.63$, $v_c = 7.73 \text{ cm}\cdot\text{sec}^{-1}$, $D = 4.15$).

	Height (mm)	Fluorescence Coefficient $\lambda = 503 \text{ nm}$ ($\text{cm}^{-1}\cdot\text{sr}^{-1}$)	Standard Deviation	Fluorescence Coefficient $\lambda = 473 \text{ nm}$ ($\text{cm}^{-1}\cdot\text{sr}^{-1}$)	Standard Deviation
1.	0.88	-9.032E-12	2.726E-12	1.141E-11	8.981E-12
2.	1.38	2.270E-13	4.036E-12	-4.553E-12	2.001E-12
3.	1.88	2.199E-12	2.045E-12	2.984E-12	1.960E-12
4.	2.38	7.776E-13	1.107E-12	-2.921E-13	1.158E-12
5.	2.88	1.368E-12	7.735E-13	1.285E-12	7.888E-13
6.	3.38	-8.293E-13	1.422E-12	1.638E-12	1.231E-12
7.	3.88	2.025E-12	1.398E-12	8.350E-13	1.030E-12
8.	4.38	-2.811E-13	1.322E-12	7.309E-13	9.557E-13
9.	4.88	9.785E-13	8.315E-13	1.009E-12	7.476E-13
10.	5.38	1.176E-12	1.495E-12	2.969E-13	1.395E-12
11.	5.88	7.838E-13	1.695E-12	-1.084E-13	7.555E-13
12.	6.38	7.420E-13	1.860E-12	3.701E-13	1.755E-12
13.	6.88	1.193E-12	1.653E-12	9.567E-13	1.564E-12
14.	7.38	1.068E-12	6.306E-13	6.617E-13	7.814E-13
15.	7.88	5.629E-13	1.520E-12	4.559E-13	8.230E-13
16.	8.38	1.563E-12	6.463E-13	2.388E-12	1.298E-12
17.	8.88	1.453E-12	1.674E-12	-4.958E-14	1.235E-12
18.	9.38	1.501E-12	1.343E-12	-6.137E-13	1.002E-12
19.	9.88	1.292E-13	1.551E-12	2.697E-13	1.067E-12
20.	10.38	1.323E-12	6.874E-13	-1.503E-13	1.709E-12
21.	10.88	1.195E-12	2.020E-12	-9.229E-13	2.601E-12
22.	11.38	1.599E-12	7.516E-13	-7.681E-13	9.814E-13
23.	11.88	2.425E-12	1.188E-12	1.521E-12	8.851E-13
24.	12.38	3.357E-12	8.301E-13	1.600E-12	1.554E-12
25.	12.88	2.634E-12	1.298E-12	1.113E-12	1.716E-12
26.	13.38	3.516E-12	1.088E-12	2.553E-13	1.010E-12
27.	13.88	3.891E-12	1.410E-12	9.976E-13	1.439E-12
28.	14.38	2.359E-12	9.966E-13	3.016E-12	6.704E-13
29.	14.88	1.368E-12	1.797E-12	1.226E-12	1.106E-12
30.	15.38	2.705E-12	9.015E-13	7.565E-13	1.103E-12
31.	15.88	3.837E-12	1.543E-12	4.126E-12	1.035E-12
32.	16.38	-1.134E-15	1.242E-12	2.515E-12	7.149E-13
33.	16.88	3.670E-12	7.286E-13	1.152E-12	1.221E-12
34.	17.38	3.620E-12	8.621E-13	3.206E-12	1.029E-12
35.	17.88	3.480E-12	1.689E-12	1.204E-12	1.478E-12
36.	18.38	4.256E-12	1.118E-12	5.092E-12	1.475E-12
37.	18.88	2.224E-12	8.712E-13	1.808E-12	1.304E-12
38.	19.38	3.969E-12	8.623E-13	1.769E-12	4.375E-13
39.	19.88	4.608E-12	1.966E-12	6.176E-13	1.272E-12
40.	20.38	4.501E-12	1.085E-12	3.092E-12	8.382E-13

Table D.30 Profiles of the fluorescence coefficient detected at 503 nm and 473 nm for the A-IA-S1 flame ($\phi = 1.78$, $v_c = 7.73 \text{ cm}\cdot\text{sec}^{-1}$, $D = 4.16$)

	Height (mm)	Fluorescence Coefficient $\lambda = 503 \text{ nm}$ ($\text{cm}^{-1}\cdot\text{sr}^{-1}$)	Standard Deviation	Fluorescence Coefficient $\lambda = 473 \text{ nm}$ ($\text{cm}^{-1}\cdot\text{sr}^{-1}$)	Standard Deviation
1.	0.87	-5.432E-12	4.263E-12	-2.454E-12	7.248E-12
2.	1.37	1.402E-12	3.896E-12	-8.154E-12	3.246E-12
3.	1.87	1.099E-12	3.025E-12	1.744E-12	3.510E-12
4.	2.37	1.600E-12	1.570E-12	9.247E-13	2.203E-12
5.	2.87	3.811E-12	1.639E-12	2.809E-12	2.568E-12
6.	3.37	2.364E-12	1.143E-12	2.747E-12	1.239E-12
7.	3.87	3.592E-12	2.117E-12	4.918E-12	1.679E-12
8.	4.37	1.056E-11	1.640E-12	6.866E-12	1.978E-12
9.	4.87	1.387E-11	1.374E-12	7.369E-12	8.135E-13
10.	5.37	1.615E-11	1.425E-12	9.417E-12	1.401E-12
11.	5.87	2.006E-11	1.973E-12	1.157E-11	1.710E-12
12.	6.37	2.499E-11	9.917E-13	1.556E-11	1.712E-12
13.	6.87	2.906E-11	4.104E-12	1.552E-11	1.869E-12
14.	7.37	3.326E-11	6.138E-13	1.896E-11	1.270E-12
15.	7.87	4.410E-11	2.871E-12	2.426E-11	1.479E-12
16.	8.37	4.156E-11	3.640E-12	2.578E-11	1.815E-12
17.	8.87	5.569E-11	2.554E-12	2.993E-11	2.758E-12
18.	9.37	6.216E-11	2.102E-12	3.372E-11	1.889E-12
19.	9.87	7.188E-11	1.861E-12	3.565E-11	1.380E-12
20.	10.37	7.878E-11	2.985E-12	4.328E-11	3.443E-12
21.	10.87	8.319E-11	2.136E-12	4.626E-11	1.668E-12
22.	11.37	9.446E-11	1.749E-12	4.851E-11	1.315E-12
23.	11.87	9.519E-11	1.680E-12	5.580E-11	1.870E-12
24.	12.37	1.205E-10	3.887E-12	5.727E-11	1.396E-12
25.	12.87	1.146E-10	2.995E-12	6.743E-11	2.675E-12
26.	13.37	1.200E-10	3.235E-12	7.116E-11	1.973E-12
27.	13.87	1.389E-10	1.891E-12	7.593E-11	2.025E-12
28.	14.37	1.350E-10	1.607E-12	8.204E-11	4.081E-12
29.	14.87	1.503E-10	2.536E-12	8.253E-11	2.298E-12
30.	15.37	1.728E-10	1.547E-12	8.795E-11	1.916E-12
31.	15.87	1.779E-10	2.784E-12	9.539E-11	3.403E-12
32.	16.37	1.920E-10	4.957E-12	9.828E-11	5.290E-12
33.	16.87	2.064E-10	3.278E-12	1.081E-10	3.053E-12
34.	17.37	2.175E-10	3.200E-12	1.093E-10	3.560E-12
35.	17.87	2.161E-10	3.899E-12	1.165E-10	2.090E-12
36.	18.37	2.210E-10	3.247E-12	1.211E-10	2.822E-12
37.	18.87	2.428E-10	3.848E-12	1.243E-10	5.205E-12
38.	19.37	2.503E-10	2.831E-12	1.380E-10	2.788E-12
39.	19.87	2.650E-10	6.351E-12	1.340E-10	3.981E-12
40.	20.37	2.765E-10	1.118E-12	1.362E-10	4.101E-12

Table D.31 Profiles of the fluorescence coefficient detected at 503 nm and 473 nm for the A-IA-S2 flame ($\phi = 1.92$, $v_c = 7.75 \text{ cm}\cdot\text{sec}^{-1}$, $D = 4.17$).

	Height (mm)	Fluorescence Coefficient $\lambda = 503 \text{ nm}$ ($\text{cm}^{-1}\cdot\text{sr}^{-1}$)	Standard Deviation	Fluorescence Coefficient $\lambda = 473 \text{ nm}$ ($\text{cm}^{-1}\cdot\text{sr}^{-1}$)	Standard Deviation
1.	0.88	4.198E-12	5.671E-12	9.440E-12	9.937E-12
2.	1.38	3.898E-13	3.491E-12	-1.495E-12	2.573E-12
3.	1.88	3.474E-12	1.687E-12	1.732E-12	3.425E-12
4.	2.38	1.101E-11	2.454E-12	5.595E-12	2.195E-12
5.	2.88	2.226E-11	3.002E-12	1.085E-11	2.251E-12
6.	3.38	3.777E-11	1.892E-12	2.030E-11	1.499E-12
7.	3.88	5.699E-11	3.346E-12	3.250E-11	1.741E-12
8.	4.38	8.333E-11	3.456E-12	4.513E-11	2.359E-12
9.	4.88	1.106E-10	4.020E-12	6.013E-11	3.107E-12
10.	5.38	1.456E-10	8.221E-12	7.422E-11	4.677E-12
11.	5.88	1.894E-10	7.899E-12	9.874E-11	7.010E-12
12.	6.38	2.361E-10	3.834E-12	1.183E-10	4.219E-12
13.	6.88	2.798E-10	1.010E-11	1.507E-10	6.254E-12
14.	7.38	3.412E-10	5.093E-12	1.770E-10	7.801E-12
15.	7.88	3.986E-10	1.345E-11	2.107E-10	2.841E-12
16.	8.38	4.528E-10	3.745E-12	2.333E-10	7.797E-12
17.	8.88	5.276E-10	6.964E-12	2.667E-10	5.306E-12
18.	9.38	5.979E-10	5.123E-12	2.988E-10	2.452E-12
19.	9.88	6.616E-10	7.442E-12	3.326E-10	6.769E-12
20.	10.38	7.320E-10	5.090E-12	3.700E-10	1.192E-11
21.	10.88	7.822E-10	8.464E-12	3.969E-10	6.177E-12
22.	11.38	8.795E-10	1.395E-11	4.362E-10	6.897E-12
23.	11.88	9.591E-10	9.297E-12	4.732E-10	8.802E-12
24.	12.38	9.430E-10	8.229E-12	5.013E-10	4.986E-12
25.	12.88	1.073E-9	9.286E-12	5.473E-10	7.156E-12
26.	13.38	1.140E-9	1.249E-11	5.879E-10	9.146E-12
27.	13.88	1.221E-9	9.112E-12	6.374E-10	5.662E-12
28.	14.38	1.435E-9	1.938E-11	6.470E-10	8.866E-12
29.	14.88	1.413E-9	2.048E-11	6.990E-10	4.334E-12
30.	15.38	1.504E-9	7.943E-12	7.395E-10	5.442E-12
31.	15.88	1.552E-9	4.825E-12	7.758E-10	6.989E-12
32.	16.38	1.650E-9	1.556E-11	7.986E-10	8.552E-12
33.	16.88	1.714E-9	2.009E-11	8.432E-10	1.555E-11
34.	17.38	1.738E-9	3.414E-11	8.980E-10	9.964E-12
35.	17.88	1.853E-9	1.667E-11	9.327E-10	1.577E-11
36.	18.38	1.865E-9	3.388E-12	9.308E-10	1.636E-11
37.	18.88	1.965E-9	3.984E-11	9.858E-10	9.263E-12
38.	19.38	2.087E-9	1.029E-11	9.947E-10	1.634E-11
39.	19.88	2.126E-9	1.833E-11	1.038E-9	1.951E-11
40.	20.38	2.185E-9	1.397E-11	1.098E-9	1.109E-11

Table D.32 Profiles of the fluorescence coefficient detected at 503 nm and 473 nm for the A-IA-S3 flame ($\phi = 2.02$, $v_c = 7.74 \text{ cm}\cdot\text{sec}^{-1}$, $D = 4.16$).

	Height (mm)	Fluorescence Coefficient $\lambda = 503 \text{ nm}$ ($\text{cm}^{-1}\cdot\text{sr}^{-1}$)	Standard Deviation	Fluorescence Coefficient $\lambda = 473 \text{ nm}$ ($\text{cm}^{-1}\cdot\text{sr}^{-1}$)	Standard Deviation
1.	0.88	-7.528E-13	3.541E-12	5.835E-12	4.003E-12
2.	1.38	-3.456E-12	5.236E-12	9.478E-13	2.074E-12
3.	1.88	7.792E-12	2.022E-12	7.067E-12	3.235E-12
4.	2.38	2.264E-11	3.314E-12	1.143E-11	2.455E-12
5.	2.88	5.048E-11	3.245E-12	2.591E-11	3.164E-12
6.	3.38	7.605E-11	6.917E-12	5.366E-11	3.151E-12
7.	3.88	1.283E-10	4.039E-12	7.585E-11	3.962E-12
8.	4.38	2.120E-10	5.524E-12	1.184E-10	5.567E-12
9.	4.88	2.822E-10	5.573E-12	1.556E-10	2.203E-12
10.	5.38	3.844E-10	9.906E-12	2.089E-10	5.546E-12
11.	5.88	4.714E-10	1.296E-11	2.546E-10	6.136E-12
12.	6.38	5.986E-10	1.329E-11	3.132E-10	5.641E-12
13.	6.88	7.332E-10	2.867E-12	3.675E-10	9.516E-12
14.	7.38	8.513E-10	1.490E-11	4.517E-10	8.240E-12
15.	7.88	1.013E-9	1.180E-11	5.322E-10	7.005E-12
16.	8.38	1.136E-9	1.563E-11	6.148E-10	5.827E-12
17.	8.88	1.338E-9	2.320E-11	6.914E-10	1.915E-11
18.	9.38	1.453E-9	1.746E-11	7.330E-10	1.249E-11
19.	9.88	1.672E-9	1.250E-11	8.538E-10	5.287E-12
20.	10.38	1.799E-9	1.041E-11	9.169E-10	1.041E-11
21.	10.88	2.019E-9	1.424E-11	9.757E-10	4.765E-12
22.	11.38	2.182E-9	2.310E-11	1.127E-9	1.329E-11
23.	11.88	2.334E-9	2.981E-11	1.185E-9	7.291E-12
24.	12.38	2.535E-9	6.588E-11	1.266E-9	7.789E-12
25.	12.88	2.715E-9	5.850E-11	1.349E-9	1.379E-11
26.	13.38	2.856E-9	1.432E-11	1.503E-9	2.127E-11
27.	13.88	3.018E-9	1.495E-11	1.512E-9	1.005E-11
28.	14.38	3.224E-9	1.334E-11	1.595E-9	8.256E-12
29.	14.88	3.336E-9	2.472E-11	1.681E-9	1.112E-11
30.	15.38	3.516E-9	1.331E-11	1.785E-9	2.265E-11
31.	15.88	3.719E-9	2.094E-11	1.859E-9	1.834E-11
32.	16.38	3.817E-9	1.990E-11	1.908E-9	2.831E-11
33.	16.88	3.818E-9	2.947E-11	2.002E-9	1.072E-11
34.	17.38	4.243E-9	1.613E-11	2.103E-9	2.006E-11
35.	17.88	4.387E-9	1.999E-11	2.135E-9	2.151E-11
36.	18.38	4.427E-9	2.285E-11	2.289E-9	2.685E-11
37.	18.88	4.663E-9	8.411E-11	2.349E-9	3.115E-11
38.	19.38	4.801E-9	1.778E-11	2.387E-9	1.333E-11
39.	19.88	4.914E-9	4.639E-11	2.472E-9	1.180E-11
40.	20.38	5.093E-9	3.511E-11	2.617E-9	2.449E-11

Table D.33 Temperature profiles determined from the scattering coefficient profiles for the A-IA flames ($v_c = 7.73 \text{ cm}\cdot\text{sec}^{-1}$, $D = 4.15$).

	Height (mm)	Temperature (K)		
		A-IA-R2 ($\phi = 1.63$)	A-IA-S1 ($\phi = 1.78$)	A-IA-S2 ($\phi = 1.92$)
1.	0.250	1507.7	1397.7	1382.7
2.	0.375	1541.3	1438.2	1425.1
3.	0.500	1562.6	1462.3	1446.5
4.	0.625	1577.3	1480.8	1463.3
5.	0.750	1587.9	1495.4	1477.6
6.	0.875	1595.6	1506.9	1489.7
7.	1.000	1601.4	1516.0	1499.7
8.	1.125	--	1523.3	1508.0
9.	1.250	1609.0	1529.1	1514.8
10.	1.500	1613.4	1537.8	1525.2
11.	1.750	1615.9	1543.7	1532.6
12.	2.000	1617.1	1547.8	1537.8
13.	2.250	--	1550.6	1541.1
14.	2.500	1617.4	1552.5	1544.4
15.	3.000	1616.0	1554.5	1547.8
16.	3.500	1613.5	1554.5	1548.7
17.	4.000	1610.9	1554.5	1549.7
18.	4.500	1607.8	1553.2	1549.0
19.	5.000	1604.6	1551.9	1548.4
20.	6.000	1597.9	1548.1	1545.5
21.	7.000	1591.3	1543.7	1541.6
22.	7.500	1588.0	1541.5	1539.7
23.	8.750	1579.9	1535.5	1534.0
24.	10.000	1572.3	1529.5	1528.3
25.	12.500	1558.4	1517.6	1516.2
26.	15.000	1546.5	1506.2	1504.0
27.	17.500	1536.7	1495.6	1492.0
28.	20.000	1528.9	1485.8	--

Table D.34 Temperature profiles determined from the scattering coefficient profiles for the A-IA flames ($v_c = 7.73 \text{ cm}\cdot\text{sec}^{-1}$, $D = 4.15$).

	Height (mm)	Temperature (K)		
		A-IA-S3 ($\phi = 2.02$)	A-IA-S4 ($\phi = 2.17$)	A-IA-S5 ($\phi = 2.32$)
1.	0.250	1323.2	1275.9	1350.5
2.	0.375	1369.1	1338.2	1371.8
3.	0.500	1387.9	1363.4	1376.1
4.	0.625	1401.0	1378.3	1378.1
5.	0.750	1412.5	1390.0	1381.4
6.	0.875	1423.0	1400.4	1385.6
7.	1.000	1432.6	1410.7	1390.4
8.	1.125	1441.0	1419.5	1395.4
9.	1.250	1448.5	1427.5	1400.7
10.	1.500	1460.7	1441.0	1410.3
11.	1.750	1470.2	1451.6	1418.5
12.	2.000	1477.5	1459.5	1424.5
13.	2.250	1483.4	1465.2	1428.5
14.	2.500	1488.0	1469.1	1430.1
15.	3.000	1494.6	1472.1	--
16.	3.125	--	--	1425.2
17.	3.500	1499.2	1469.9	--
18.	3.750	--	1468.2	1408.0
19.	4.000	1501.9	1463.2	--
20.	4.500	1503.4	1453.2	--
21.	5.000	1504.9	1443.1	1375.9
22.	6.000	1502.4	1413.5	--
23.	7.000	1500.0	--	--
24.	7.500	1498.7	--	--
25.	8.750	1489.9	--	--
26.	10.000	1481.1	--	--
27.	12.500	1454.6	--	--

Table D.35 Temperature profiles determined from the scattering coefficient profiles for the A-IB flames ($v_c = 7.87 \text{ cm}\cdot\text{sec}^{-1}$, $D = 3.31$).

	Height (mm)	Temperature (K)			
		A-IB-C ($\phi = 1.67$)	A-IB-S2 ($\phi = 1.92$)	A-IB-S3 ($\phi = 2.02$)	A-IB-S4 ($\phi = 2.17$)
1.	0.250	1496.4	1431.4	1406.8	1361.9
2.	0.375	1530.7	1468.0	1434.3	1416.2
3.	0.500	1553.8	1490.1	1450.4	1441.1
4.	0.625	1570.3	1506.7	1463.5	1453.8
5.	0.750	1582.4	1519.5	1474.8	1461.5
6.	0.875	1591.5	1529.5	1484.5	1467.0
7.	1.000	1598.3	1537.3	1492.8	1472.1
8.	1.125	1603.6	1543.6	1500.0	--
9.	1.250	1607.8	1548.6	1506.1	1483.6
10.	1.500	1613.6	1555.9	1515.8	1493.5
11.	2.000	1619.5	1563.9	1527.9	1505.2
12.	2.250	--	1565.8	1530.4	1506.9
13.	2.500	1621.5	1566.8	1533.0	1506.2
14.	2.750	--	1566.9	1533.0	1503.2
15.	3.000	1621.6	1566.9	1533.0	1497.9
16.	3.250	--	--	--	1489.5
17.	3.500	1620.2	1564.5	1526.7	1481.2
18.	3.750	--	--	--	1469.2
19.	4.000	1618.9	1562.1	1520.4	1457.1
20.	4.500	1616.7	1557.5	1507.3	1424.0
21.	5.000	1614.5	1553.0	1494.1	1390.9
22.	5.500	1611.8	--	--	--
23.	6.000	1609.2	1541.0	1456.5	--
24.	7.000	1603.5	1526.6	1409.6	--
25.	7.500	1600.5	1518.7	1383.4	--
26.	8.750	1592.9	1496.9	--	--
27.	10.000	1585.1	1472.7	--	--
28.	11.25	--	1445.6	--	--
29.	12.500	1569.4	1418.5	--	--
30.	15.000	1553.6	--	--	--
31.	17.500	1538.0	--	--	--
32.	20.000	1522.6	--	--	--

Table D.36 Temperature profiles determined from the scattering coefficient profiles for the A-IIA flames ($v_c = 10.42 \text{ cm}\cdot\text{sec}^{-1}$, $D = 4.29$).

	Height (mm)	Temperature (K)			
		A-IIA-R2 ($\phi = 1.63$)	A-IIA-S1 ($\phi = 1.78$)	A-IIA-S2 ($\phi = 1.92$)	A-IIA-S3 ($\phi = 2.02$)
1.	0.250	1578.0	1566.5	1458.7	1371.8
2.	0.375	1588.0	1577.8	1485.3	1420.5
3.	0.500	1594.5	1585.0	1502.8	1441.9
4.	0.625	1600.2	1590.6	1517.1	1458.9
5.	0.750	1605.7	1595.6	1528.8	1474.7
6.	0.875	1610.3	1600.5	1538.2	1488.9
7.	1.000	1613.9	1604.5	1545.8	1501.1
8.	1.250	1619.1	1610.2	1557.1	1519.9
9.	1.500	1622.3	1613.8	1564.9	1532.9
10.	2.000	1625.7	1617.5	1574.6	1548.1
11.	2.250	1626.5	--	1577.3	1552.2
12.	2.500	1626.9	1618.7	1580.0	1554.8
13.	2.750	1627.0	--	--	1555.8
14.	3.000	1627.0	1618.6	1583.0	1556.7
15.	3.250	--	--	--	1555.6
16.	3.500	1626.4	1617.8	1584.0	1554.5
17.	4.000	1625.4	1616.6	1585.0	1552.3
18.	4.500	1624.2	1615.1	--	1546.7
19.	5.000	1622.7	1613.4	1584.0	1541.1
20.	6.000	1619.5	1609.8	1581.0	1525.6
21.	7.000	1616.1	1605.9	1576.6	1506.8
22.	7.500	1614.3	1604.0	1573.9	1496.4
23.	8.750	1609.6	1599.3	1565.9	1467.9
24.	10.000	1604.9	1594.6	1556.3	1436.5
25.	12.500	1595.3	1586.1	1533.1	--
26.	15.000	1585.7	1578.6	1505.0	--
27.	17.500	1576.1	1572.2	--	--
28.	20.000	1566.7	1567.0	--	--

Appendix E: Scattering Coefficient Profiles for the 80-Torr Flames

In this appendix, we present the scattering coefficient profiles measured in the 80-torr flames. These profiles were shown in Figures 5.12 to 5.15 and are tabulated here to facilitate their use for modelling. Tables E.1 to E.10 list the scattering coefficient profiles for the 80-torr flames. The total scattering coefficient profiles, $Q_{scd}(z)$, are listed for all the flames. The total scattering coefficient was calculated from the scattering signal ratio using Eq. (4.4.5). The standard deviation was calculated from the measured samples of the scattering signal ratio as described in Section B.4. For the sooting flames, the particle scattering coefficient is also listed. The particle scattering coefficient was calculated from the total scattering coefficient by subtracting the molecular scattering coefficient as described in Sections 4.4.4 and 5.3.1.

Table E.1 Profile of the total scattering coefficient for the L-I-R1 flame ($\phi = 2.03$, $v_c = 18.1 \text{ cm}\cdot\text{sec}^{-1}$).

	Height (mm)	Total Scattering Coefficient ($\text{cm}^{-1}\cdot\text{sr}^{-1}$)	Standard Deviation
1.	1.00	5.984E-10	2.982E-13
2.	1.25	6.600E-10	2.125E-13
3.	1.50	6.627E-10	3.325E-13
4.	1.75	6.666E-10	1.892E-13
5.	2.00	6.092E-10	3.902E-13
6.	2.25	6.124E-10	1.709E-13
7.	2.50	5.826E-10	4.121E-13
8.	2.75	5.805E-10	3.161E-13
9.	3.00	5.374E-10	7.154E-13
10.	3.25	5.607E-10	3.009E-13
11.	3.50	5.200E-10	7.148E-13
12.	3.75	5.232E-10	2.195E-13
13.	4.00	5.023E-10	5.217E-13
14.	4.25	5.113E-10	2.372E-13
15.	4.50	4.849E-10	3.191E-13
16.	4.75	4.855E-10	3.693E-13
17.	5.00	4.610E-10	2.992E-13
18.	5.25	4.539E-10	1.894E-13
19.	5.50	4.472E-10	2.410E-13
20.	5.75	4.502E-10	2.275E-13
21.	6.00	4.455E-10	2.238E-13
22.	6.50	4.328E-10	2.447E-13
23.	7.00	4.229E-10	3.048E-13
24.	7.50	4.113E-10	1.035E-13
25.	8.00	4.163E-10	1.125E-13
26.	8.49	4.180E-10	1.194E-13
27.	8.99	4.142E-10	2.503E-13
28.	9.49	4.161E-10	1.312E-13
29.	9.99	4.073E-10	1.588E-13
30.	10.50	4.117E-10	1.186E-13
31.	11.00	4.170E-10	1.657E-13
32.	13.00	4.135E-10	1.768E-13
33.	15.00	4.007E-10	8.327E-14
34.	17.00	3.972E-10	1.345E-13
35.	19.00	4.003E-10	1.067E-13
36.	21.00	4.102E-10	9.427E-14
37.	25.00	4.089E-10	1.723E-13
38.	27.00	4.151E-10	1.924E-13
39.	29.00	4.234E-10	8.917E-14
40.	31.00	4.270E-10	1.803E-13
41.	33.00	4.297E-10	1.304E-13
42.	35.00	4.337E-10	7.265E-14
43.	37.00	4.418E-10	1.488E-13
44.	39.00	4.461E-10	1.484E-13
45.	41.00	4.511E-10	8.779E-14

Table E.1 continued

	Height (mm)	Total Scattering Coefficient ($\text{cm}^{-1}\cdot\text{sr}^{-1}$)	Standard Deviation
46.	43.00	4.576E-10	1.464E-13
47.	45.00	4.687E-10	1.211E-13
48.	47.00	4.703E-10	8.439E-14
49.	49.00	4.783E-10	1.619E-13
50.	51.00	4.916E-10	1.350E-13
51.	53.00	4.994E-10	2.148E-13
52.	55.00	5.087E-10	1.393E-13
53.	57.00	5.082E-10	1.818E-13
54.	59.00	5.219E-10	2.152E-13
55.	61.00	5.265E-10	3.485E-13

Table E.2 Profile of the total scattering coefficient for the L-I-R2 flame ($\phi = 2.17$, $v_c = 18.1 \text{ cm}\cdot\text{sec}^{-1}$).

	Height (mm)	Total Scattering Coefficient ($\text{cm}^{-1}\cdot\text{sr}^{-1}$)	Standard Deviation
1.	1.00	7.583E-10	4.337E-13
2.	1.25	7.228E-10	1.501E-13
3.	1.50	6.739E-10	2.939E-13
4.	1.75	6.440E-10	3.069E-13
5.	2.00	6.262E-10	4.202E-13
6.	2.25	6.066E-10	3.220E-13
7.	2.50	5.854E-10	3.783E-13
8.	2.75	5.785E-10	4.598E-13
9.	3.00	5.618E-10	5.642E-13
10.	3.25	5.615E-10	3.217E-13
11.	3.50	5.331E-10	2.582E-13
12.	3.75	5.293E-10	2.103E-13
13.	4.00	5.162E-10	4.881E-13
14.	4.25	4.936E-10	2.792E-13
15.	4.50	4.813E-10	4.455E-13
16.	4.75	4.898E-10	3.094E-13
17.	5.00	4.762E-10	5.098E-13
18.	5.25	4.765E-10	2.536E-13
19.	5.50	4.616E-10	2.894E-13
20.	6.00	4.415E-10	3.147E-13
21.	6.50	4.454E-10	2.028E-13
22.	7.00	4.416E-10	2.011E-13
23.	7.50	4.304E-10	1.997E-13
24.	8.00	4.226E-10	2.110E-13
25.	8.49	4.265E-10	1.223E-13
26.	8.99	4.209E-10	2.355E-13
27.	9.49	4.216E-10	1.528E-13
28.	9.99	4.240E-10	2.432E-13
29.	10.50	4.258E-10	1.263E-13
30.	11.00	4.294E-10	1.341E-13
31.	13.00	4.255E-10	9.254E-14
32.	15.00	4.142E-10	1.385E-13
33.	17.00	4.131E-10	1.295E-13
34.	19.00	4.183E-10	2.053E-13
35.	21.00	4.232E-10	2.331E-13
36.	25.00	4.252E-10	1.183E-13
37.	27.00	4.305E-10	1.455E-13
38.	29.00	4.363E-10	1.509E-13
39.	31.00	4.391E-10	1.799E-13
40.	33.00	4.450E-10	1.081E-13
41.	35.00	4.519E-10	1.294E-13
42.	37.00	4.575E-10	2.119E-13
43.	39.00	4.626E-10	1.559E-13
44.	41.00	4.750E-10	1.935E-13
45.	43.00	4.760E-10	1.729E-13

Table E.2 continued

	Height (mm)	Total Scattering Coefficient ($\text{cm}^{-1}\cdot\text{sr}^{-1}$)	Standard Deviation
46.	45.00	4.793E-10	2.146E-13
47.	47.00	4.894E-10	1.424E-13
48.	49.00	4.917E-10	1.194E-13
49.	51.00	4.998E-10	1.011E-13
50.	53.00	5.116E-10	2.251E-13
51.	55.00	5.111E-10	1.714E-13
52.	57.00	5.278E-10	1.355E-13
53.	59.00	5.248E-10	1.586E-13
54.	61.00	5.365E-10	3.187E-13

Table E.3 Profile of the total scattering coefficient and the particle scattering coefficient for the L-I-S1 flame ($\phi = 2.32$, $v_c = 18.1 \text{ cm}\cdot\text{sec}^{-1}$).

	Height (mm)	Total Scattering Coefficient ($\text{cm}^{-1}\cdot\text{sr}^{-1}$)	Standard Deviation	Particle Scattering Coefficient ($\text{cm}^{-1}\cdot\text{sr}^{-1}$)
1.	1.00	8.309E-10	3.514E-13	7.374E-11
2.	1.25	7.805E-10	1.366E-13	2.186E-11
3.	1.50	7.332E-10	2.511E-13	1.847E-12
4.	1.75	6.988E-10	2.184E-13	-1.292E-12
5.	2.00	6.668E-10	3.216E-13	-4.181E-12
6.	2.25	6.540E-10	2.111E-13	8.744E-12
7.	2.50	6.305E-10	3.064E-13	7.419E-12
8.	2.75	6.177E-10	1.166E-13	1.374E-11
9.	3.00	5.908E-10	5.141E-13	3.441E-12
10.	3.25	5.708E-10	3.933E-13	-2.211E-12
11.	3.50	5.741E-10	3.329E-13	1.368E-11
12.	3.75	5.568E-10	2.098E-13	7.434E-12
13.	4.00	5.427E-10	2.770E-13	3.032E-12
14.	4.25	5.283E-10	3.603E-13	-2.728E-12
15.	4.50	5.076E-10	3.892E-13	-1.570E-11
16.	4.75	5.033E-10	2.086E-13	-1.319E-11
17.	5.00	4.959E-10	7.431E-13	-1.436E-11
18.	5.25	4.905E-10	1.596E-13	-1.417E-11
19.	5.50	4.920E-10	2.959E-13	-7.736E-12
20.	6.00	4.808E-10	1.801E-13	-1.020E-11
21.	6.50	4.650E-10	1.496E-13	-1.889E-11
22.	7.00	4.623E-10	3.581E-13	-1.558E-11
23.	7.50	4.569E-10	1.887E-13	-1.600E-11
24.	8.00	4.559E-10	5.350E-14	-1.278E-11
25.	8.49	4.502E-10	1.965E-13	-1.492E-11
26.	8.99	4.510E-10	1.729E-13	-1.111E-11
27.	9.49	4.479E-10	1.504E-13	-1.163E-11
28.	9.99	4.432E-10	1.925E-13	-1.426E-11
29.	10.50	4.456E-10	1.451E-13	-1.005E-11
30.	11.00	4.566E-10	3.168E-13	2.414E-12
31.	13.00	4.526E-10	1.651E-13	1.990E-12
32.	15.00	4.515E-10	1.705E-13	1.883E-12
33.	17.00	4.658E-10	1.355E-13	1.540E-11
34.	19.00	4.704E-10	1.521E-13	1.803E-11
35.	21.00	4.911E-10	1.006E-13	3.594E-11
36.	25.00	5.302E-10	2.519E-13	6.760E-11
37.	27.00	5.443E-10	9.083E-14	7.744E-11
38.	29.00	5.668E-10	2.487E-13	9.524E-11
39.	31.00	5.825E-10	1.238E-13	1.061E-10
40.	33.00	6.096E-10	1.097E-13	1.282E-10
41.	35.00	6.255E-10	3.339E-13	1.388E-10
42.	37.00	6.446E-10	1.068E-13	1.527E-10
43.	39.00	6.764E-10	1.479E-13	1.790E-10
44.	41.00	6.923E-10	2.048E-13	1.893E-10
45.	43.00	7.084E-10	1.268E-13	1.997E-10

Table E.3 continued

	Height (mm)	Total Scattering Coefficient ($\text{cm}^{-1}\cdot\text{sr}^{-1}$)	Standard Deviation	Particle Scattering Coefficient ($\text{cm}^{-1}\cdot\text{sr}^{-1}$)
46.	45.00	7.275E-10	1.797E-13	2.131E-10
47.	47.00	7.421E-10	1.274E-13	2.219E-10
48.	49.00	7.634E-10	1.842E-13	2.374E-10
49.	51.00	7.796E-10	1.880E-13	2.477E-10
50.	53.00	8.098E-10	2.690E-13	2.719E-10
51.	55.00	8.272E-10	1.910E-13	2.834E-10
52.	57.00	8.430E-10	4.357E-13	2.931E-10
53.	59.00	8.448E-10	2.169E-13	2.889E-10
54.	61.00	8.554E-10	2.295E-13	2.934E-10

Table E.4 Profile of the total scattering coefficient and the particle scattering coefficient for the L-I-S2 flame ($\phi = 2.46$, $v_c = 18.1 \text{ cm}\cdot\text{sec}^{-1}$).

	Height (mm)	Total Scattering Coefficient ($\text{cm}^{-1}\cdot\text{sr}^{-1}$)	Standard Deviation	Particle Scattering Coefficient ($\text{cm}^{-1}\cdot\text{sr}^{-1}$)
1.	1.00	1.074E-9	4.029E-13	2.033E-10
2.	1.50	9.938E-10	2.235E-13	1.492E-10
3.	2.00	9.718E-10	2.705E-13	1.876E-10
4.	2.50	8.931E-10	1.391E-13	1.568E-10
5.	3.00	8.116E-10	5.058E-13	1.110E-10
6.	3.50	7.505E-10	2.933E-13	7.685E-11
7.	4.00	7.285E-10	2.773E-13	7.559E-11
8.	4.50	6.826E-10	3.993E-13	4.608E-11
9.	5.00	6.586E-10	5.257E-13	3.505E-11
10.	5.50	6.204E-10	2.599E-13	7.440E-12
11.	6.00	5.991E-10	4.119E-13	-5.168E-12
12.	6.50	5.779E-10	1.837E-13	-1.920E-11
13.	7.00	5.679E-10	3.412E-13	-2.320E-11
14.	7.50	5.564E-10	2.430E-13	-2.969E-11
15.	8.00	5.593E-10	1.908E-13	-2.255E-11
16.	8.49	5.630E-10	2.316E-13	-1.536E-11
17.	8.99	5.585E-10	3.932E-13	-1.680E-11
18.	9.49	5.593E-10	1.465E-13	-1.345E-11
19.	9.99	5.702E-10	4.605E-13	-4.223E-13
20.	10.50	5.805E-10	2.044E-13	1.162E-11
21.	11.00	6.293E-10	4.247E-13	1.851E-10
22.	13.00	6.730E-10	4.242E-13	1.091E-10
23.	14.00	6.790E-10	2.154E-13	1.159E-10
24.	15.00	7.022E-10	3.545E-13	1.393E-10
25.	16.00	7.773E-10	2.599E-13	2.142E-10
26.	17.00	8.652E-10	2.007E-13	3.015E-10
27.	18.00	9.622E-10	4.021E-13	3.977E-10
28.	19.00	1.080E-9	5.115E-13	5.143E-10
29.	20.00	1.205E-9	1.525E-13	6.384E-10
30.	21.00	1.369E-9	4.370E-13	8.006E-10
31.	22.00	1.521E-9	3.038E-13	9.505E-10
32.	24.00	1.868E-9	3.792E-13	1.294E-9
33.	25.00	1.941E-9	8.633E-13	1.366E-9
34.	26.00	2.289E-9	6.852E-13	1.711E-9
35.	27.00	2.341E-9	8.574E-13	1.761E-9
36.	28.00	2.957E-9	5.625E-13	2.374E-9
37.	29.00	2.760E-9	5.679E-13	2.175E-9
38.	30.00	3.464E-9	6.829E-13	2.877E-9
39.	31.00	3.221E-9	1.390E-12	2.631E-9
40.	33.00	3.682E-9	5.111E-13	3.087E-9
41.	35.00	4.219E-9	1.624E-12	3.619E-9
42.	37.00	4.706E-9	1.168E-12	4.101E-9
43.	39.00	6.468E-9	3.359E-11	5.858E-9
44.	41.00	6.337E-9	2.963E-12	5.721E-9
45.	43.00	6.915E-9	2.029E-12	6.293E-9

Table E.4 continued

	Height (mm)	Total Scattering Coefficient ($\text{cm}^{-1}\cdot\text{sr}^{-1}$)	Standard Deviation	Particle Scattering Coefficient ($\text{cm}^{-1}\cdot\text{sr}^{-1}$)
46.	45.00	7.351E-9	2.663E-12	6.723E-9
47.	47.00	7.869E-9	2.112E-12	7.236E-9
48.	49.00	8.238E-9	2.542E-12	7.599E-9
49.	51.00	8.891E-9	2.967E-12	8.246E-9
50.	53.00	9.267E-9	6.006E-12	8.615E-9
51.	55.00	9.257E-9	2.266E-12	8.599E-9
52.	57.00	9.520E-9	5.217E-12	8.857E-9
53.	59.00	9.510E-9	4.931E-12	8.840E-9
54.	61.00	9.062E-9	7.376E-12	8.387E-9

Table E.5 Profile of the total scattering coefficient and the particle scattering coefficient for the L-I-S3 flame ($\phi = 2.60$, $v_c = 18.1 \text{ cm}\cdot\text{sec}^{-1}$).

	Height (mm)	Total Scattering Coefficient ($\text{cm}^{-1}\cdot\text{sr}^{-1}$)	Standard Deviation	Particle Scattering Coefficient ($\text{cm}^{-1}\cdot\text{sr}^{-1}$)
1.	1.00	1.004E-9	2.370E-13	1.602E-10
2.	1.28	9.989E-10	2.410E-13	1.573E-10
3.	1.50	8.773E-10	2.673E-13	5.955E-11
4.	1.78	8.839E-10	3.011E-13	1.022E-10
5.	2.00	7.954E-10	2.577E-13	3.807E-11
6.	2.28	8.107E-10	3.949E-13	8.272E-11
7.	2.50	7.299E-10	3.471E-13	2.045E-11
8.	2.78	7.562E-10	3.455E-13	6.868E-11
9.	3.00	6.912E-10	3.982E-13	1.746E-11
10.	3.28	7.194E-10	5.930E-13	6.214E-11
11.	3.50	6.474E-10	2.678E-13	5.953E-13
12.	3.78	6.732E-10	4.416E-13	3.911E-11
13.	4.00	6.217E-10	3.974E-13	-4.332E-12
14.	4.28	6.484E-10	4.194E-13	3.231E-11
15.	4.50	5.816E-10	3.271E-13	-2.805E-11
16.	4.78	6.210E-10	4.371E-13	1.922E-11
17.	5.00	5.972E-10	4.503E-13	5.363E-13
18.	5.28	6.329E-10	3.874E-13	4.258E-11
19.	5.50	5.486E-10	4.435E-13	-3.748E-11
20.	6.00	5.723E-10	4.506E-13	-5.120E-12
21.	6.50	5.295E-10	3.329E-13	-4.069E-11
22.	7.00	5.498E-10	4.145E-13	-1.441E-11
23.	7.50	5.500E-10	3.959E-13	-9.230E-12
24.	8.00	5.609E-10	5.796E-13	5.910E-12
25.	8.49	5.556E-10	2.360E-13	4.174E-12
26.	8.99	5.931E-10	3.849E-13	4.460E-11
27.	9.49	6.152E-10	2.591E-13	6.924E-11
28.	9.99	6.673E-10	5.176E-13	1.235E-10
29.	10.50	7.325E-10	5.155E-13	1.905E-10
30.	11.00	8.160E-10	5.265E-13	2.755E-10
31.	12.00	1.088E-9	4.059E-13	5.500E-10
32.	13.00	1.458E-9	5.169E-13	9.215E-10
33.	14.00	2.021E-9	3.353E-13	1.484E-9
34.	15.00	2.800E-9	5.202E-13	2.264E-9
35.	16.00	3.797E-9	1.301E-12	3.261E-9
36.	17.00	5.026E-9	7.464E-13	4.489E-9
37.	18.00	6.374E-9	8.574E-13	5.836E-9
38.	19.00	7.953E-9	1.160E-12	7.414E-9
39.	20.00	9.746E-9	2.376E-12	9.206E-9
40.	21.00	1.175E-8	2.537E-12	1.121E-8
41.	22.00	1.378E-8	2.542E-12	1.323E-8
42.	23.00	1.626E-8	2.573E-12	1.571E-8
43.	25.00	2.136E-8	3.445E-12	1.795E-8
44.	25.03	2.008E-8	1.858E-12	1.953E-8
45.	26.00	2.414E-8	4.486E-12	2.359E-8

Table E.5 continued

	Height (mm)	Total Scattering Coefficient ($\text{cm}^{-1}\cdot\text{sr}^{-1}$)	Standard Deviation	Particle Scattering Coefficient ($\text{cm}^{-1}\cdot\text{sr}^{-1}$)
46.	27.00	2.677E-8	1.290E-11	2.622E-8
47.	27.03	2.558E-8	6.358E-12	2.503E-8
48.	28.00	2.960E-8	5.958E-12	2.904E-8
49.	29.00	3.268E-8	1.249E-11	3.212E-8
50.	29.03	3.072E-8	2.229E-12	3.016E-8
51.	30.00	3.632E-8	9.838E-12	3.576E-8
52.	31.00	3.998E-8	7.543E-12	3.941E-8
53.	31.03	3.641E-8	3.104E-12	3.585E-8
54.	33.03	4.247E-8	5.342E-12	4.190E-8
55.	35.03	4.873E-8	5.265E-12	4.815E-8
56.	37.03	5.695E-8	4.504E-12	5.637E-8
57.	39.03	6.227E-8	1.994E-11	6.169E-8
58.	41.03	6.878E-8	8.325E-12	6.819E-8
59.	43.03	7.226E-8	5.269E-11	7.167E-8
60.	45.03	7.900E-8	8.311E-12	7.840E-8
61.	47.03	8.358E-8	7.860E-12	8.298E-8
62.	49.03	8.547E-8	8.982E-12	8.486E-8
63.	51.03	9.057E-8	1.222E-11	8.995E-8
64.	53.03	9.754E-8	9.584E-12	9.692E-8
65.	55.03	1.034E-7	1.028E-11	1.028E-7
66.	57.03	1.060E-7	1.914E-11	1.054E-7
67.	59.03	1.142E-7	2.109E-11	1.135E-7
68.	61.03	1.213E-7	5.907E-11	1.206E-7

Table E.6 Profile of the total scattering coefficient for the L-II-R1 flame ($\phi = 2.03$, $v_c = 22.4 \text{ cm}\cdot\text{sec}^{-1}$).

	Height (mm)	Total Scattering Coefficient ($\text{cm}^{-1}\cdot\text{sr}^{-1}$)	Standard Deviation
1.	1.03	6.147E-10	6.691E-13
2.	1.28	5.779E-10	5.473E-13
3.	1.53	5.366E-10	8.662E-13
4.	1.78	5.336E-10	4.571E-13
5.	2.03	5.228E-10	9.455E-13
6.	2.28	4.950E-10	7.233E-13
7.	2.53	4.964E-10	8.401E-13
8.	2.78	4.972E-10	3.284E-13
9.	3.03	4.873E-10	9.829E-13
10.	3.28	4.809E-10	4.613E-13
11.	3.53	4.646E-10	7.072E-13
12.	3.78	4.682E-10	3.019E-13
13.	4.03	4.480E-10	8.580E-13
14.	4.28	4.478E-10	3.758E-13
15.	4.53	4.267E-10	7.066E-13
16.	4.78	4.126E-10	4.787E-13
17.	5.03	4.163E-10	6.369E-13
18.	5.28	4.080E-10	2.687E-13
19.	5.53	4.083E-10	5.094E-13
20.	6.03	3.974E-10	3.259E-13
21.	6.53	3.915E-10	1.361E-13
22.	7.03	3.950E-10	3.624E-13
23.	7.53	3.968E-10	2.232E-13
24.	8.03	3.861E-10	3.353E-13
25.	8.53	3.928E-10	1.099E-13
26.	9.03	3.945E-10	4.262E-13
27.	9.53	3.857E-10	2.894E-13
28.	10.03	3.865E-10	1.705E-13
29.	10.53	3.827E-10	2.147E-13
30.	15.03	3.828E-10	1.299E-13
31.	17.03	3.819E-10	1.647E-13
32.	19.03	3.845E-10	1.299E-13
33.	21.03	3.895E-10	1.887E-13
34.	25.03	3.963E-10	1.676E-13
35.	27.03	3.975E-10	1.651E-13
36.	29.03	3.994E-10	1.357E-13
37.	31.03	4.017E-10	1.116E-13
38.	33.03	4.113E-10	2.208E-13
39.	35.03	4.096E-10	1.793E-13
40.	37.03	4.106E-10	1.417E-13
41.	39.03	4.222E-10	2.035E-13
42.	41.03	4.220E-10	2.006E-13
43.	43.03	4.234E-10	2.168E-13
44.	45.03	4.374E-10	1.831E-13
45.	47.03	4.368E-10	1.855E-13

Table E.6 continued

	Height (mm)	Total Scattering Coefficient ($\text{cm}^{-1} \cdot \text{sr}^{-1}$)	Standard Deviation
46.	49.03	4.451E-10	1.605E-13
47.	51.03	4.441E-10	1.694E-13
48.	53.03	4.493E-10	9.625E-14
49.	55.03	4.517E-10	1.997E-13
50.	57.03	4.588E-10	1.537E-13
51.	59.03	4.596E-10	2.093E-13
52.	61.03	4.589E-10	1.693E-13

Table E.7 Profile of the total scattering coefficient for the L-II-R2 flame ($\phi = 2.16$, $v_c = 22.4 \text{ cm}\cdot\text{sec}^{-1}$).

	Height (mm)	Total Scattering Coefficient ($\text{cm}^{-1}\cdot\text{sr}^{-1}$)	Standard Deviation
1.	1.03	7.757E-10	5.148E-13
2.	1.28	6.959E-10	3.282E-13
3.	1.53	6.696E-10	5.516E-13
4.	1.78	6.332E-10	5.243E-13
5.	2.03	6.111E-10	7.509E-13
6.	2.28	5.803E-10	5.539E-13
7.	2.53	5.925E-10	1.106E-12
8.	2.78	5.452E-10	5.431E-13
9.	3.03	5.738E-10	9.638E-13
10.	3.28	5.377E-10	5.511E-13
11.	3.53	5.413E-10	7.798E-13
12.	3.78	5.096E-10	4.334E-13
13.	4.03	5.313E-10	5.307E-13
14.	4.28	5.044E-10	4.221E-13
15.	4.53	4.924E-10	5.533E-13
16.	4.78	4.981E-10	5.282E-13
17.	5.03	4.879E-10	8.299E-13
18.	5.28	4.756E-10	3.418E-13
19.	5.53	4.750E-10	5.137E-13
20.	6.03	4.817E-10	2.006E-13
21.	6.53	4.584E-10	2.798E-13
22.	7.03	4.667E-10	6.357E-13
23.	7.53	4.489E-10	2.190E-13
24.	8.03	4.520E-10	1.763E-13
25.	8.53	4.364E-10	2.894E-13
26.	9.03	4.414E-10	3.586E-13
27.	9.53	4.337E-10	2.660E-13
28.	10.03	4.392E-10	1.892E-13
29.	10.53	4.430E-10	2.084E-13
30.	15.03	4.176E-10	2.033E-13
31.	17.03	4.128E-10	1.634E-13
32.	19.03	4.033E-10	1.354E-13
33.	21.03	4.142E-10	1.028E-13
34.	25.03	4.089E-10	2.735E-13
35.	27.03	4.150E-10	2.399E-13
36.	29.03	4.138E-10	1.370E-13
37.	31.03	4.190E-10	2.238E-13
38.	33.03	4.158E-10	1.738E-13
39.	35.03	4.246E-10	1.527E-13
40.	37.03	4.308E-10	1.670E-13
41.	39.03	4.303E-10	1.097E-13
42.	41.03	4.337E-10	1.458E-13
43.	43.03	4.380E-10	3.442E-13
44.	45.03	4.456E-10	1.528E-13
45.	47.03	4.518E-10	1.664E-13

Table E.7 continued

	Height (mm)	Total Scattering Coefficient ($\text{cm}^{-1}\text{-sr}^{-1}$)	Standard Deviation
46.	49.03	4.555E-10	1.547E-13
47.	51.03	4.556E-10	1.886E-13
48.	53.03	4.607E-10	1.479E-13
49.	55.03	4.618E-10	1.729E-13
50.	57.03	4.739E-10	1.709E-13
51.	59.03	4.693E-10	1.608E-13
52.	61.03	4.763E-10	1.313E-13

Table E.8 Profile of the total scattering coefficient and the particle scattering coefficient for the L-II-S1 flame ($\phi = 2.32$, $v_c = 22.4 \text{ cm}\cdot\text{sec}^{-1}$).

	Height (mm)	Total Scattering Coefficient ($\text{cm}^{-1}\cdot\text{sr}^{-1}$)	Standard Deviation	Particle Scattering Coefficient ($\text{cm}^{-1}\cdot\text{sr}^{-1}$)
1.	1.03	9.337E-10	5.162E-13	1.434E-10
2.	1.28	8.732E-10	4.295E-13	1.007E-10
3.	1.53	8.161E-10	4.994E-13	7.562E-11
4.	1.78	7.835E-10	4.319E-13	7.509E-11
5.	2.03	7.384E-10	4.889E-13	5.874E-11
6.	2.28	7.189E-10	2.616E-13	6.421E-11
7.	2.53	6.999E-10	6.867E-13	6.681E-11
8.	2.78	6.902E-10	5.476E-13	7.571E-11
9.	3.03	6.602E-10	8.817E-13	6.186E-11
10.	3.28	6.459E-10	3.134E-13	6.162E-11
11.	3.53	6.235E-10	5.933E-13	5.149E-11
12.	3.78	6.185E-10	5.575E-13	5.745E-11
13.	4.03	5.984E-10	6.803E-13	4.693E-11
14.	4.28	5.974E-10	4.039E-13	5.457E-11
15.	4.53	5.786E-10	1.054E-12	4.340E-11
16.	4.78	5.703E-10	3.352E-13	4.198E-11
17.	5.03	5.545E-10	6.718E-13	3.240E-11
18.	5.28	5.498E-10	3.400E-13	3.337E-11
19.	5.53	5.422E-10	5.938E-13	3.087E-11
20.	6.03	5.331E-10	2.825E-13	3.069E-11
21.	6.53	5.180E-10	2.751E-13	2.313E-11
22.	7.03	5.082E-10	4.276E-13	1.967E-11
23.	7.53	5.006E-10	2.982E-13	1.744E-11
24.	8.03	4.993E-10	3.055E-13	2.070E-11
25.	8.53	4.903E-10	2.472E-13	1.565E-11
26.	9.03	4.839E-10	4.241E-13	1.268E-11
27.	9.53	4.936E-10	2.700E-13	2.539E-11
28.	10.03	4.798E-10	2.756E-13	1.414E-11
29.	15.03	4.513E-10	1.843E-13	-2.210E-12
30.	17.03	4.442E-10	1.447E-13	-8.292E-12
31.	19.03	4.447E-10	2.206E-13	-7.966E-12
32.	21.03	4.520E-10	1.990E-13	-1.707E-12
33.	25.03	4.476E-10	2.754E-13	-9.839E-12
34.	27.03	4.558E-10	3.301E-13	-4.162E-12
35.	29.03	4.538E-10	3.037E-13	-9.058E-12
36.	31.03	4.681E-10	2.217E-13	2.157E-12
37.	33.03	4.706E-10	2.808E-13	1.385E-12
38.	35.03	4.735E-10	1.453E-13	9.413E-13
39.	37.03	4.840E-10	1.489E-13	7.864E-12
40.	39.03	4.936E-10	2.471E-13	1.372E-11
41.	41.03	4.898E-10	1.362E-13	6.137E-12
42.	43.03	4.961E-10	2.233E-13	8.579E-12
43.	45.03	4.976E-10	1.593E-13	6.166E-12
44.	47.03	5.042E-10	1.735E-13	8.658E-12
45.	49.03	5.081E-10	2.084E-13	8.501E-12

Table E.8 continued

	Height (mm)	Total Scattering Coefficient ($\text{cm}^{-1}\cdot\text{sr}^{-1}$)	Standard Deviation	Particle Scattering Coefficient ($\text{cm}^{-1}\cdot\text{sr}^{-1}$)
46.	51.03	5.103E-10	1.803E-13	6.564E-12
47.	53.03	5.161E-10	1.496E-13	8.178E-12
48.	55.03	5.164E-10	2.088E-13	4.267E-12
49.	57.03	5.268E-10	3.224E-13	1.044E-11
50.	59.03	5.245E-10	2.674E-13	3.907E-12
51.	61.03	5.354E-10	2.085E-13	1.051E-11

Table E.9 Profile of the total scattering coefficient and the particle scattering coefficient for the L-II-S2 flame ($\phi = 2.46$, $v_c = 22.4 \text{ cm}\cdot\text{sec}^{-1}$).

	Height (mm)	Total Scattering Coefficient ($\text{cm}^{-1}\cdot\text{sr}^{-1}$)	Standard Deviation	Particle Scattering Coefficient ($\text{cm}^{-1}\cdot\text{sr}^{-1}$)
1.	1.03	9.738E-10	5.013E-13	1.431E-10
2.	1.28	9.118E-10	2.086E-13	9.881E-11
3.	1.53	8.609E-10	3.678E-13	7.995E-11
4.	1.78	8.152E-10	2.552E-13	6.623E-11
5.	2.03	7.701E-10	5.664E-13	4.993E-11
6.	2.28	7.380E-10	6.482E-13	4.287E-11
7.	2.53	7.292E-10	5.111E-13	5.557E-11
8.	2.78	6.967E-10	5.065E-13	4.174E-11
9.	3.03	6.695E-10	7.738E-13	3.068E-11
10.	3.28	6.706E-10	4.212E-13	4.581E-11
11.	3.53	6.480E-10	6.091E-13	3.557E-11
12.	3.78	6.461E-10	4.033E-13	4.451E-11
13.	4.03	6.236E-10	6.079E-13	3.170E-11
14.	4.28	6.209E-10	4.834E-13	3.756E-11
15.	4.53	5.836E-10	4.980E-13	7.866E-12
16.	4.78	5.742E-10	4.075E-13	5.445E-12
17.	5.03	5.656E-10	6.286E-13	3.013E-12
18.	5.28	5.685E-10	3.412E-13	1.157E-11
19.	5.53	5.566E-10	5.559E-13	4.804E-12
20.	6.03	5.345E-10	2.693E-13	-8.389E-12
21.	6.53	5.313E-10	2.269E-13	-4.129E-12
22.	7.03	5.166E-10	3.467E-13	-1.245E-11
23.	7.53	5.138E-10	2.524E-13	-9.836E-12
24.	8.03	5.147E-10	2.437E-13	-4.359E-12
25.	8.53	5.052E-10	4.055E-13	-9.869E-12
26.	9.03	4.948E-10	5.240E-13	-1.686E-11
27.	9.53	5.012E-10	2.782E-13	-7.586E-12
28.	10.03	4.847E-10	2.047E-13	-2.151E-11
29.	10.53	5.046E-10	3.187E-13	6.059E-13
30.	15.03	5.093E-10	3.455E-13	1.529E-11
31.	17.03	5.207E-10	1.750E-13	2.767E-11
32.	19.03	5.416E-10	2.792E-13	4.849E-11
33.	21.03	5.723E-10	2.511E-13	7.816E-11
34.	25.03	6.185E-10	3.573E-13	1.205E-10
35.	27.03	6.486E-10	4.501E-13	1.481E-10
36.	29.03	6.902E-10	2.289E-13	1.869E-10
37.	31.03	7.330E-10	2.165E-13	2.266E-10
38.	33.03	7.691E-10	1.593E-13	2.594E-10
39.	35.03	8.178E-10	1.634E-13	3.047E-10
40.	37.03	8.383E-10	2.312E-13	3.216E-10
41.	39.03	8.783E-10	2.505E-13	3.580E-10
42.	41.03	9.097E-10	1.811E-13	3.856E-10
43.	43.03	9.501E-10	2.710E-13	4.221E-10
44.	45.03	9.783E-10	2.254E-13	4.463E-10
45.	47.03	1.026E-09	3.912E-13	4.904E-10

Table E.9 continued

	Height (mm)	Total Scattering Coefficient ($\text{cm}^{-1}\cdot\text{sr}^{-1}$)	Standard Deviation	Particle Scattering Coefficient ($\text{cm}^{-1}\cdot\text{sr}^{-1}$)
46.	49.03	1.045E-09	2.201E-13	5.053E-10
47.	51.03	1.062E-09	2.917E-13	5.175E-10
48.	53.03	1.090E-09	3.711E-13	5.420E-10
49.	55.03	1.119E-09	2.341E-13	5.665E-10
50.	57.03	1.140E-09	4.431E-13	5.827E-10
51.	59.03	1.149E-09	4.459E-13	5.875E-10
52.	61.03	1.152E-09	1.240E-13	5.870E-10

Table E.10 Profile of the total scattering coefficient and the particle scattering coefficient for the L-II-S3 flame ($\phi = 2.60$, $v_c = 22.4 \text{ cm}\cdot\text{sec}^{-1}$).

	Height (mm)	Total Scattering Coefficient ($\text{cm}^{-1}\cdot\text{sr}^{-1}$)	Standard Deviation	Particle Scattering Coefficient ($\text{cm}^{-1}\cdot\text{sr}^{-1}$)
1.	1.03	1.035E-09	5.371E-13	1.349E-10
2.	1.28	9.989E-10	2.410E-13	1.163E-10
3.	1.53	9.376E-10	4.636E-13	8.708E-11
4.	1.78	8.839E-10	3.011E-13	6.544E-11
5.	2.03	8.308E-10	5.172E-13	4.111E-11
6.	2.28	8.107E-10	3.949E-13	4.601E-11
7.	2.53	7.819E-10	3.607E-13	3.874E-11
8.	2.78	7.562E-10	3.455E-13	3.172E-11
9.	3.03	7.100E-10	8.460E-13	1.651E-12
10.	3.28	7.194E-10	5.930E-13	2.508E-11
11.	3.53	6.971E-10	7.129E-13	1.513E-11
12.	3.78	6.732E-10	4.416E-13	2.126E-12
13.	4.03	6.597E-10	7.851E-13	-1.833E-12
14.	4.28	6.484E-10	4.194E-13	-4.477E-12
15.	4.53	6.236E-10	5.762E-13	-2.158E-11
16.	4.78	6.210E-10	4.371E-13	-1.729E-11
17.	5.03	6.027E-10	8.424E-13	-2.942E-11
18.	5.28	6.329E-10	3.874E-13	6.408E-12
19.	5.53	6.010E-10	5.728E-13	-2.034E-11
20.	6.03	5.869E-10	6.715E-13	-2.547E-11
21.	6.53	5.730E-10	3.612E-13	-3.194E-11
22.	7.03	5.684E-10	7.448E-13	-3.014E-11
23.	7.53	5.767E-10	4.089E-13	-1.649E-11
24.	8.03	5.798E-10	6.840E-13	-8.758E-12
25.	8.53	5.641E-10	4.558E-13	-2.057E-11
26.	9.03	5.542E-10	8.809E-13	-2.701E-11
27.	9.53	5.792E-10	4.395E-13	9.591E-13
28.	10.03	5.831E-10	5.508E-13	7.397E-12
29.	10.53	5.819E-10	3.475E-13	8.370E-12
30.	11.03	6.062E-10	7.242E-13	3.456E-11
31.	13.03	6.248E-10	4.232E-13	5.856E-11
32.	14.03	6.340E-10	5.444E-13	6.940E-11
33.	15.03	6.815E-10	5.961E-13	1.179E-10
34.	16.03	7.192E-10	2.792E-13	1.564E-10
35.	17.03	7.783E-10	6.133E-13	2.158E-10
36.	18.03	8.355E-10	3.965E-13	2.731E-10
37.	19.03	9.144E-10	4.070E-13	3.517E-10
38.	20.03	9.874E-10	2.346E-13	4.243E-10
39.	21.03	1.075E-09	6.179E-13	5.113E-10
40.	22.03	1.142E-09	3.339E-13	5.778E-10
41.	24.03	1.318E-09	4.828E-13	7.519E-10
42.	25.03	1.462E-09	5.947E-13	8.945E-10
43.	26.03	1.540E-09	5.483E-13	9.716E-10
44.	27.03	1.695E-09	5.254E-13	1.125E-09
45.	28.03	1.775E-09	2.373E-13	1.203E-09

Table E.10 continued

	Height (mm)	Total Scattering Coefficient ($\text{cm}^{-1}\cdot\text{sr}^{-1}$)	Standard Deviation	Particle Scattering Coefficient ($\text{cm}^{-1}\cdot\text{sr}^{-1}$)
46.	29.03	1.962E-09	5.712E-13	1.389E-09
47.	30.03	2.027E-09	3.398E-13	1.453E-09
48.	31.07	2.313E-09	4.186E-13	1.737E-09
49.	33.07	2.595E-09	6.581E-13	2.016E-09
50.	35.07	2.929E-09	5.405E-13	2.346E-09
51.	37.07	3.273E-09	6.098E-13	2.687E-09
52.	39.07	3.577E-09	4.869E-13	2.987E-09
53.	41.07	3.888E-09	5.319E-13	3.294E-09
54.	43.07	4.248E-09	8.412E-13	3.651E-09
55.	45.07	4.555E-09	1.001E-12	3.953E-09
56.	47.07	4.837E-09	6.118E-13	4.231E-09
57.	49.07	5.184E-09	6.929E-13	4.575E-09
58.	51.07	5.477E-09	7.924E-13	4.863E-09
59.	53.07	5.769E-09	8.952E-13	5.151E-09
60.	55.07	6.004E-09	1.354E-12	5.382E-09
61.	57.07	6.194E-09	6.648E-13	5.568E-09
62.	59.07	6.397E-09	8.528E-13	5.766E-09
63.	61.07	6.517E-09	8.559E-13	5.882E-09

Appendix F: OH Fluorescence Profiles for the Atmospheric and 80-Torr Flames

In this appendix, we present the the OH fluorescence profiles for both the 80-torr and atmospheric-pressure flames. These data sets, tabulated here to facilitate their use in modelling, are the basis for the OH number density profiles of the atmospheric flames presented in Figures 6.1 and 6.2 and for the relative OH fluorescence profiles of the 80-torr flames presented in Figure 6.3.

Tables F.1 to F.3 list the normalized OH fluorescence profiles measured on three days for the lean atmospheric-pressure flame, A-0-L ($\phi = 0.97$). These profiles were used to calibrate the fluorescence profiles of the rich atmospheric flames to obtain their respective number density profiles. The OH fluorescence profiles are normalized to the fluorescence signal at the height $z = 5.30$ mm. Tables F.4 to F.7 list the normalized OH fluorescence profiles for the four rich atmospheric flames. These fluorescence profiles were normalized to the fluorescence signal measured in the lean flame, A-0-L, at the height $z = 5.30$ mm. Tables F.8 to F.11 list the normalized OH fluorescence profiles for the four 80-torr flames. These profiles were normalized to the fluorescence signal voltage measured in the leanest rich nonsooting flame (L-II-R1, $\phi = 2.03$) at a height of 10 mm. In all the tables, the standard deviations were calculated from the measured samples of the fluorescence signal at each height.

Table F.1 Normalized OH fluorescence profile measured on Day 1 for the lean atmospheric-pressure flame, A-0-L ($\phi = 0.97$, $v_c = 8.86 \text{ cm}\cdot\text{sec}^{-1}$, $D = 5.42$).

	Height (mm)	Fluorescence Signal	Standard Deviation
1.	0.55	1.037E+0	1.389E-2
2.	0.55	9.719E-1	1.350E-2
3.	0.80	1.375E+0	1.593E-2
4.	1.05	1.594E+0	1.701E-2
5.	1.30	1.646E+0	1.695E-2
6.	1.55	1.587E+0	1.712E-2
7.	1.55	1.523E+0	1.669E-2
8.	1.80	1.572E+0	1.735E-2
9.	2.05	1.491E+0	1.658E-2
10.	2.30	1.449E+0	1.559E-2
11.	2.55	1.397E+0	1.617E-2
12.	2.55	1.318E+0	1.571E-2
13.	2.80	1.323E+0	1.631E-2
14.	3.05	1.296E+0	1.561E-2
15.	3.05	1.330E+0	1.638E-2
16.	3.05	1.300E+0	1.491E-2
17.	3.05	1.316E+0	1.530E-2
18.	3.05	1.337E+0	1.570E-2
19.	3.05	1.362E+0	1.550E-2
20.	3.30	1.265E+0	1.532E-2
21.	3.55	1.219E+0	1.534E-2
22.	3.55	1.159E+0	1.487E-2
23.	3.80	1.195E+0	1.437E-2
24.	4.05	1.161E+0	1.481E-2
25.	4.30	1.120E+0	1.501E-2
26.	4.55	1.075E+0	1.459E-2
27.	4.55	1.081E+0	1.471E-2
28.	4.80	1.048E+0	1.415E-2
29.	5.05	1.031E+0	1.498E-2
30.	5.30	1.015E+0	1.443E-2
31.	5.55	9.936E-1	1.426E-2
32.	5.55	9.350E-1	8.617E-3
33.	6.55	8.345E-1	7.767E-3
34.	7.55	7.699E-1	7.485E-3
35.	8.55	7.041E-1	7.472E-3
36.	9.55	6.598E-1	7.384E-3
37.	10.55	6.090E-1	7.140E-3
38.	11.55	5.518E-1	6.473E-3
39.	12.55	5.410E-1	6.536E-3
40.	13.55	5.017E-1	6.228E-3
41.	14.55	4.778E-1	5.930E-3
42.	15.55	4.561E-1	6.281E-3
43.	16.55	4.309E-1	5.937E-3
44.	17.55	4.083E-1	5.403E-3
45.	18.55	3.856E-1	5.533E-3
46.	19.55	3.768E-1	5.272E-3
47.	20.55	3.606E-1	5.463E-3

Table F.2 Normalized OH fluorescence profile measured on Day 2 for the lean atmospheric-pressure flame, A-0-L ($\phi = 0.97$, $v_c = 8.86 \text{ cm}\cdot\text{sec}^{-1}$, $D = 5.42$).

	Height (mm)	Fluorescence Signal	Standard Deviation
1.	0.53	1.640E+0	2.162E-2
2.	0.53	1.393E+0	1.866E-2
3.	0.78	1.756E+0	2.123E-2
4.	0.78	1.475E+0	1.835E-2
5.	1.03	1.737E+0	2.098E-2
6.	1.03	1.597E+0	1.879E-2
7.	1.28	1.696E+0	2.107E-2
8.	1.28	1.647E+0	1.862E-2
9.	1.53	1.620E+0	2.041E-2
10.	1.53	1.565E+0	1.757E-2
11.	1.78	1.554E+0	2.010E-2
12.	1.78	1.529E+0	1.812E-2
13.	2.03	1.530E+0	1.968E-2
14.	2.03	1.481E+0	1.764E-2
15.	2.28	1.465E+0	1.829E-2
16.	2.28	1.413E+0	1.725E-2
17.	2.53	1.454E+0	1.909E-2
18.	2.53	1.386E+0	1.628E-2
19.	2.78	1.375E+0	1.845E-2
20.	2.78	1.318E+0	1.599E-2
21.	3.03	1.285E+0	1.336E-2
22.	3.03	1.295E+0	1.641E-2
23.	3.28	1.266E+0	1.299E-2
24.	3.28	1.236E+0	1.543E-2
25.	3.53	1.213E+0	1.265E-2
26.	3.53	1.209E+0	1.606E-2
27.	3.78	1.183E+0	1.223E-2
28.	3.78	1.147E+0	1.567E-2
29.	4.03	1.130E+0	1.272E-2
30.	4.03	1.160E+0	1.593E-2
31.	4.28	1.120E+0	1.269E-2
32.	4.28	1.107E+0	1.276E-2
33.	4.53	1.088E+0	1.234E-2
34.	4.53	1.107E+0	1.326E-2
35.	4.78	1.051E+0	1.196E-2
36.	4.78	1.046E+0	1.297E-2
37.	5.03	1.041E+0	1.152E-2
38.	5.03	1.049E+0	1.322E-2
39.	5.28	1.007E+0	1.198E-2
40.	5.28	1.010E+0	1.266E-2
41.	5.53	9.977E-1	1.145E-2
42.	5.53	1.002E+0	1.214E-2

Table F.3 Normalized OH fluorescence profile measured on Day 3 for the lean atmospheric-pressure flame, A-0-L ($\phi = 0.97$, $v_c = 8.86 \text{ cm}\cdot\text{sec}^{-1}$, $D = 5.42$).

	Height (mm)	Fluorescence Signal	Standard Deviation
1.	0.51	1.598E+0	1.794E-2
2.	0.51	9.438E-1	9.992E-3
3.	0.76	1.774E+0	1.926E-2
4.	0.76	1.277E+0	1.203E-2
5.	1.01	1.740E+0	1.943E-2
6.	1.01	1.530E+0	1.408E-2
7.	1.26	1.690E+0	1.921E-2
8.	1.26	1.547E+0	1.380E-2
9.	1.51	1.650E+0	1.913E-2
10.	1.51	1.526E+0	1.307E-2
11.	1.76	1.596E+0	1.828E-2
12.	1.76	1.565E+0	1.643E-2
13.	2.01	1.512E+0	1.724E-2
14.	2.01	1.521E+0	1.589E-2
15.	2.26	1.459E+0	1.716E-2
16.	2.26	1.460E+0	1.615E-2
17.	2.51	1.409E+0	1.696E-2
18.	2.51	1.407E+0	1.482E-2
19.	2.76	1.382E+0	1.745E-2
20.	2.76	1.399E+0	1.562E-2
21.	3.01	1.356E+0	1.568E-2
22.	3.01	1.363E+0	1.457E-2
23.	3.26	1.289E+0	1.611E-2
24.	3.26	1.299E+0	1.487E-2
25.	3.51	1.267E+0	1.641E-2
26.	3.51	1.287E+0	1.374E-2
27.	3.76	1.208E+0	1.596E-2
28.	3.76	1.253E+0	1.440E-2
29.	4.01	1.182E+0	1.601E-2
30.	4.01	1.215E+0	1.463E-2
31.	4.26	1.131E+0	1.525E-2
32.	4.26	1.117E+0	1.152E-2
33.	4.51	1.111E+0	1.493E-2
34.	4.51	1.116E+0	1.163E-2
35.	4.76	1.078E+0	1.504E-2
36.	4.76	1.082E+0	1.170E-2
37.	5.01	1.069E+0	1.430E-2
38.	5.01	1.081E+0	1.142E-2
39.	5.26	1.032E+0	1.428E-2
40.	5.26	1.004E+0	1.090E-2
41.	5.51	9.901E-1	1.404E-2
42.	5.51	1.010E+0	1.108E-2

Table F.4 Normalized OH fluorescence profile of the A-IA-R1 flame ($\phi = 1.49$, $v_c = 7.73 \text{ cm}\cdot\text{sec}^{-1}$, $D = 4.15$).

	Height (mm)	Fluorescence Signal	Standard Deviation
1.	0.55	8.793E-2	1.664E-3
2.	0.80	1.083E-1	1.855E-3
3.	1.05	1.075E-1	1.860E-3
4.	1.30	9.212E-2	1.777E-3
5.	1.55	7.518E-2	1.537E-3
6.	1.80	5.742E-2	1.178E-3
7.	2.05	4.578E-2	1.030E-3
8.	2.30	3.676E-2	9.477E-4
9.	2.55	3.024E-2	8.534E-4
10.	2.80	2.501E-2	7.901E-4
11.	3.07	2.038E-2	4.865E-4
12.	3.30	1.739E-2	4.353E-4
13.	3.55	1.525E-2	4.299E-4
14.	3.80	1.350E-2	4.009E-4
15.	4.05	1.194E-2	3.731E-4
16.	4.30	1.077E-2	2.610E-4
17.	4.55	9.495E-3	2.435E-4
18.	4.80	8.818E-3	2.381E-4
19.	5.05	8.235E-3	2.350E-4
20.	5.30	7.649E-3	2.251E-4
21.	5.55	7.237E-3	2.262E-4
22.	6.55	5.224E-3	1.507E-4
23.	7.55	4.608E-3	1.440E-4
24.	8.55	3.955E-3	1.118E-4
25.	9.55	3.510E-3	1.054E-4
26.	10.55	3.191E-3	1.066E-4
27.	11.55	2.943E-3	1.024E-4
28.	12.55	2.744E-3	1.027E-4
29.	13.55	2.629E-3	9.976E-5
30.	14.55	2.504E-3	1.008E-4
31.	15.55	2.276E-3	1.006E-4
32.	16.55	1.861E-3	5.123E-5
33.	17.55	1.698E-3	5.274E-5
34.	18.55	1.518E-3	5.282E-5
35.	19.55	1.453E-3	5.153E-5
36.	20.55	1.394E-3	5.247E-5

Table F.5 Normalized OH fluorescence profile of the A-IA-R2 flame ($\phi = 1.63$, $v_c = 7.73 \text{ cm}\cdot\text{sec}^{-1}$, $D = 4.15$).

	Height (mm)	Fluorescence Signal	Standard Deviation
1.	0.55	4.375E-2	9.015E-4
2.	0.80	5.659E-2	1.042E-3
3.	1.05	5.747E-2	1.043E-3
4.	1.30	4.952E-2	9.715E-4
5.	1.55	4.037E-2	8.710E-4
6.	1.80	3.280E-2	7.123E-4
7.	2.05	2.653E-2	6.726E-4
8.	2.30	2.163E-2	6.059E-4
9.	2.55	1.721E-2	5.569E-4
10.	2.80	1.486E-2	4.985E-4
11.	3.05	1.233E-2	2.829E-4
12.	3.30	1.089E-2	2.679E-4
13.	3.55	9.249E-3	2.630E-4
14.	3.80	8.620E-3	2.464E-4
15.	4.05	7.863E-3	2.368E-4
16.	4.30	7.325E-3	2.054E-4
17.	4.55	6.473E-3	2.096E-4
18.	4.80	6.276E-3	2.028E-4
19.	5.05	6.013E-3	1.978E-4
20.	5.30	5.699E-3	1.965E-4
21.	5.55	5.354E-3	1.983E-4
22.	6.55	4.036E-3	1.261E-4
23.	7.55	3.510E-3	1.235E-4
24.	8.55	2.989E-3	1.068E-4
25.	9.55	2.789E-3	1.087E-4
26.	10.55	2.563E-3	1.056E-4
27.	11.55	2.401E-3	9.866E-5
28.	12.55	2.267E-3	9.380E-5
29.	13.55	1.996E-3	9.143E-5
30.	14.55	2.127E-3	9.551E-5
31.	15.55	1.844E-3	8.123E-5
32.	16.55	1.667E-3	6.095E-5
33.	17.55	1.594E-3	6.035E-5
34.	18.55	1.465E-3	6.387E-5
35.	19.55	1.425E-3	6.177E-5
36.	20.55	1.391E-3	5.833E-5

Table F.6 Normalized OH fluorescence profile of the A-IA-S1 flame ($\phi = 1.78$, $v_c = 7.73 \text{ cm}\cdot\text{sec}^{-1}$, $D = 4.16$).

	Height (mm)	Fluorescence Signal	Standard Deviation
1.	0.53	2.695E-2	5.660E-4
2.	0.78	3.255E-2	6.211E-4
3.	1.03	3.332E-2	6.299E-4
4.	1.28	3.042E-2	5.774E-4
5.	1.53	2.440E-2	5.541E-4
6.	1.78	2.067E-2	4.061E-4
7.	2.03	1.685E-2	3.865E-4
8.	2.28	1.363E-2	3.659E-4
9.	2.53	1.098E-2	3.289E-4
10.	2.78	9.625E-3	3.115E-4
11.	3.03	8.526E-3	2.087E-4
12.	3.28	7.475E-3	2.092E-4
13.	3.54	6.135E-3	2.069E-4
14.	3.78	6.039E-3	1.862E-4
15.	4.03	5.438E-3	1.862E-4
16.	4.28	4.933E-3	1.680E-4
17.	4.53	4.691E-3	1.610E-4
18.	4.78	4.273E-3	1.652E-4
19.	5.03	3.986E-3	1.679E-4
20.	5.28	4.055E-3	1.653E-4
21.	5.53	3.270E-3	1.413E-4
22.	6.54	2.594E-3	1.284E-4
23.	7.54	2.167E-3	1.225E-4
24.	8.54	1.975E-3	1.225E-4
25.	9.54	1.748E-3	1.264E-4
26.	10.54	1.549E-3	1.220E-4
27.	11.54	1.581E-3	1.231E-4
28.	12.54	1.345E-3	1.154E-4
29.	13.54	1.274E-3	1.171E-4
30.	14.54	1.056E-3	1.146E-4
31.	15.54	1.011E-3	1.148E-4
32.	16.54	1.363E-3	9.817E-5
33.	17.54	1.465E-3	1.036E-4
34.	18.54	1.317E-3	9.902E-5
35.	19.54	1.299E-3	1.099E-4

Table F.7 Normalized OH fluorescence profile of the A-IA-S2 flame ($\phi = 1.92$, $v_c = 7.75 \text{ cm}\cdot\text{sec}^{-1}$, $D = 4.17$).

	Height (mm)	Fluorescence Signal	Standard Deviation
1.	0.53	1.759E-2	3.885E-4
2.	0.78	2.000E-2	4.075E-4
3.	1.03	2.078E-2	4.208E-4
4.	1.28	1.902E-2	4.126E-4
5.	1.53	1.578E-2	3.876E-4
6.	1.78	1.369E-2	3.308E-4
7.	2.03	1.142E-2	3.171E-4
8.	2.28	9.638E-3	2.802E-4
9.	2.53	7.897E-3	2.365E-4
10.	2.78	7.180E-3	2.185E-4
11.	3.03	6.002E-3	1.871E-4
12.	3.28	5.410E-3	1.945E-4
13.	3.53	4.499E-3	1.716E-4
14.	3.78	4.466E-3	1.741E-4
15.	4.03	3.950E-3	1.681E-4
16.	4.28	3.675E-3	1.613E-4
17.	4.53	3.284E-3	1.224E-4
18.	4.78	3.316E-3	1.403E-4
19.	5.03	3.236E-3	1.447E-4
20.	5.28	3.004E-3	1.455E-4
21.	5.53	3.242E-3	1.468E-4
22.	6.53	2.179E-3	1.256E-4
23.	7.53	1.846E-3	1.227E-4
24.	8.53	1.727E-3	1.242E-4
25.	9.53	1.545E-3	1.214E-4
26.	10.53	1.365E-3	1.286E-4
27.	11.53	1.337E-3	1.189E-4
28.	12.53	1.236E-3	1.221E-4
29.	13.53	1.247E-3	1.238E-4
30.	14.53	1.214E-3	1.216E-4
31.	15.53	1.125E-3	1.232E-4
32.	16.53	1.333E-3	1.061E-4
33.	17.53	1.361E-3	1.080E-4
34.	18.53	1.225E-3	1.082E-4
35.	19.53	1.250E-3	1.173E-4
36.	20.53	1.314E-3	1.221E-4

Table F.8 Normalized OH fluorescence profile of the L-II-R1 flame ($\phi = 2.03$, $v_c = 22.4 \text{ cm}\cdot\text{sec}^{-1}$, $P = 80 \text{ torr}$).

	Height (mm)	Fluorescence Signal	Standard Deviation
1.	0.440	2.886E-1	5.195E-3
2.	0.505	3.002E-1	6.908E-3
3.	0.840	5.321E-1	7.288E-3
4.	0.940	4.845E-1	1.118E-2
5.	1.005	6.363E-1	1.008E-2
6.	1.005	5.699E-1	1.326E-2
7.	1.240	7.968E-1	8.791E-3
8.	1.505	9.788E-1	1.244E-2
9.	1.640	1.086E+0	1.012E-2
10.	1.940	1.258E+0	1.864E-2
11.	2.005	1.341E+0	1.429E-2
12.	2.005	1.409E+0	1.981E-2
13.	2.040	1.361E+0	1.819E-2
14.	2.440	1.550E+0	1.940E-2
15.	2.505	1.617E+0	1.601E-2
16.	2.840	1.710E+0	2.056E-2
17.	2.940	1.816E+0	2.113E-2
18.	2.950	1.828E+0	2.134E-2
19.	2.950	1.813E+0	2.039E-2
20.	2.950	1.805E+0	2.139E-2
21.	2.950	1.835E+0	2.018E-2
22.	2.950	1.771E+0	2.195E-2
23.	3.005	1.894E+0	2.436E-2
24.	3.005	1.861E+0	2.463E-2
25.	3.240	1.802E+0	2.033E-2
26.	3.505	1.923E+0	2.360E-2
27.	3.640	1.816E+0	2.044E-2
28.	3.940	1.933E+0	2.183E-2
29.	4.005	1.950E+0	2.490E-2
30.	4.005	1.931E+0	2.314E-2
31.	4.040	1.827E+0	2.055E-2
32.	4.440	1.768E+0	2.035E-2
33.	4.505	1.876E+0	2.364E-2
34.	4.840	1.719E+0	1.965E-2
35.	4.940	1.744E+0	2.086E-2
36.	5.005	1.845E+0	2.415E-2
37.	5.005	1.811E+0	2.366E-2
38.	5.240	1.630E+0	1.697E-2
39.	5.505	1.646E+0	1.581E-2
40.	5.640	1.556E+0	1.640E-2
41.	5.940	1.582E+0	1.957E-2
42.	6.005	1.570E+0	1.906E-2
43.	6.005	1.548E+0	1.458E-2
44.	6.040	1.479E+0	1.639E-2
45.	6.440	1.442E+0	1.641E-2

Table F.8 continued

	Height (mm)	Fluorescence Signal	Standard Deviation
46.	6.505	1.458E+0	1.499E-2
47.	6.840	1.338E+0	1.512E-2
48.	6.940	1.353E+0	1.836E-2
49.	7.005	1.383E+0	1.443E-2
50.	7.005	1.357E+0	1.684E-2
51.	7.240	1.289E+0	1.439E-2
52.	7.505	1.307E+0	1.380E-2
53.	7.640	1.219E+0	1.423E-2
54.	7.940	1.194E+0	1.781E-2
55.	8.005	1.222E+0	1.302E-2
56.	8.005	1.219E+0	1.744E-2
57.	8.040	1.184E+0	1.454E-2
58.	8.440	1.183E+0	1.214E-2
59.	8.505	1.171E+0	1.206E-2
60.	8.840	1.118E+0	1.232E-2
61.	8.940	1.102E+0	1.392E-2
62.	9.005	1.113E+0	1.214E-2
63.	9.005	1.097E+0	1.583E-2
64.	9.240	1.065E+0	1.238E-2
65.	9.505	1.082E+0	1.151E-2
66.	9.640	1.060E+0	1.203E-2
67.	9.940	1.015E+0	1.339E-2
68.	10.005	9.935E-1	1.554E-2
69.	10.005	1.006E+0	1.154E-2
70.	10.040	1.000E+0	1.165E-2
71.	10.440	9.608E-1	1.170E-2
72.	10.505	9.369E-1	1.068E-2
73.	10.840	9.323E-1	1.140E-2
74.	10.940	9.250E-1	1.305E-2
75.	11.005	8.699E-1	8.995E-3
76.	11.240	9.129E-1	1.151E-2
77.	11.640	8.704E-1	1.061E-2
78.	11.940	8.347E-1	1.210E-2
79.	12.005	8.006E-1	8.918E-3
80.	12.040	8.530E-1	1.092E-2
81.	12.440	8.129E-1	1.046E-2
82.	12.940	7.317E-1	9.642E-3
83.	13.005	7.493E-1	8.609E-3
84.	13.940	6.877E-1	9.286E-3
85.	14.005	6.922E-1	8.566E-3
86.	14.940	6.448E-1	9.223E-3
87.	15.005	6.374E-1	7.667E-3
88.	15.940	6.110E-1	9.120E-3
89.	16.005	5.688E-1	7.282E-3
90.	16.940	5.477E-1	7.689E-3

Table F.8 continued

	Height (mm)	Fluorescence Signal	Standard Deviation
91.	17.005	5.397E-1	7.522E-3
92.	17.940	5.094E-1	7.212E-3
93.	18.005	5.145E-1	6.867E-3
94.	18.940	4.824E-1	7.165E-3
95.	19.005	4.723E-1	6.860E-3
96.	19.940	4.334E-1	6.759E-3
97.	20.005	4.326E-1	6.445E-3
98.	20.940	4.110E-1	5.561E-3
99.	21.005	3.974E-1	4.215E-3
100.	21.940	3.942E-1	5.342E-3
101.	22.005	3.698E-1	4.249E-3
102.	22.940	3.545E-1	5.069E-3
103.	23.005	3.415E-1	3.801E-3
104.	23.940	3.256E-1	4.919E-3
105.	24.005	3.247E-1	3.995E-3
106.	24.940	2.939E-1	3.832E-3
107.	25.005	3.036E-1	3.709E-3
108.	25.940	2.741E-1	3.773E-3
109.	26.005	2.710E-1	3.652E-3
110.	26.940	2.494E-1	3.410E-3
111.	27.005	2.539E-1	3.728E-3
112.	27.940	2.338E-1	3.344E-3
113.	28.005	2.323E-1	3.354E-3
114.	28.940	2.104E-1	3.321E-3
115.	29.005	2.185E-1	3.098E-3
116.	29.940	1.966E-1	3.356E-3
117.	30.005	2.043E-1	3.116E-3
118.	30.940	1.751E-1	3.246E-3
119.	31.005	1.905E-1	2.700E-3

Table F.9 Normalized OH fluorescence profile of the L-II-R2 flame ($\phi = 2.16$, $v_c = 22.4 \text{ cm}\cdot\text{sec}^{-1}$, $P = 80 \text{ torr}$).

	Height (mm)	Fluorescence Signal	Standard Deviation
1.	0.43	2.038E-1	3.601E-3
2.	0.83	3.228E-1	4.534E-3
3.	0.94	3.426E-1	6.837E-3
4.	1.23	4.901E-1	5.560E-3
5.	1.63	6.547E-1	6.324E-3
6.	1.94	8.179E-1	1.047E-2
7.	2.03	8.623E-1	1.187E-2
8.	2.43	1.026E+0	1.306E-2
9.	2.83	1.158E+0	1.444E-2
10.	2.94	1.204E+0	1.287E-2
11.	3.23	1.252E+0	1.425E-2
12.	3.63	1.315E+0	1.457E-2
13.	3.94	1.354E+0	1.240E-2
14.	4.03	1.343E+0	1.450E-2
15.	4.43	1.307E+0	1.489E-2
16.	4.83	1.296E+0	1.491E-2
17.	4.94	1.290E+0	1.407E-2
18.	5.23	1.270E+0	1.496E-2
19.	5.63	1.232E+0	1.411E-2
20.	5.94	1.207E+0	1.410E-2
21.	6.03	1.170E+0	1.462E-2
22.	6.43	1.112E+0	1.380E-2
23.	6.83	1.053E+0	1.279E-2
24.	6.94	1.060E+0	1.412E-2
25.	7.23	1.013E+0	1.233E-2
26.	7.63	9.619E-1	1.286E-2
27.	7.94	9.355E-1	1.264E-2
28.	8.03	9.086E-1	1.251E-2
29.	8.43	8.850E-1	1.058E-2
30.	8.83	8.228E-1	1.063E-2
31.	8.94	8.316E-1	9.066E-3
32.	9.23	8.293E-1	1.075E-2
33.	9.63	7.663E-1	9.678E-3
34.	9.94	7.483E-1	9.107E-3
35.	10.03	7.532E-1	8.005E-3
36.	10.43	7.317E-1	8.432E-3
37.	10.83	6.925E-1	7.850E-3
38.	10.94	6.756E-1	8.495E-3
39.	11.23	6.609E-1	7.552E-3
40.	11.63	6.554E-1	7.325E-3
41.	11.94	6.107E-1	8.425E-3
42.	12.03	6.245E-1	7.634E-3
43.	12.43	6.030E-1	7.457E-3
44.	12.94	5.621E-1	7.788E-3
45.	13.94	5.235E-1	7.139E-3

Table F.9 continued

	Height (mm)	Fluorescence Signal	Standard Deviation
46.	14.94	4.734E-1	7.064E-3
47.	15.94	4.427E-1	6.980E-3
48.	16.94	4.191E-1	5.333E-3
49.	17.94	3.908E-1	5.493E-3
50.	18.94	3.578E-1	5.406E-3
51.	19.94	3.291E-1	4.963E-3
52.	20.94	3.106E-1	3.769E-3
53.	21.94	2.750E-1	3.894E-3
54.	22.94	2.659E-1	3.447E-3
55.	23.94	2.428E-1	3.412E-3
56.	24.94	2.307E-1	2.876E-3
57.	25.94	2.143E-1	2.783E-3
58.	26.94	2.019E-1	2.838E-3
59.	27.94	1.842E-1	2.557E-3
60.	28.94	1.681E-1	2.595E-3
61.	29.94	1.534E-1	2.424E-3
62.	30.94	1.465E-1	2.351E-3

Table F.10 Normalized OH fluorescence profile of the L-II-S1 flame ($\phi = 2.32$, $v_c = 22.4 \text{ cm}\cdot\text{sec}^{-1}$, $P = 80 \text{ torr}$).

	Height (mm)	Fluorescence Signal	Standard Deviation
1.	0.460	2.202E-1	3.940E-3
2.	0.515	1.358E-1	5.062E-3
3.	0.860	2.221E-1	4.035E-3
4.	0.940	2.134E-1	5.003E-3
5.	1.005	2.484E-1	7.257E-3
6.	1.015	2.497E-1	6.610E-3
7.	1.260	3.317E-1	4.998E-3
8.	1.515	3.976E-1	7.879E-3
9.	1.660	4.443E-1	5.289E-3
10.	1.940	5.434E-1	7.528E-3
11.	2.005	5.737E-1	1.020E-2
12.	2.015	5.307E-1	9.033E-3
13.	2.060	5.610E-1	8.806E-3
14.	2.460	7.039E-1	9.537E-3
15.	2.515	7.237E-1	1.035E-2
16.	2.860	8.335E-1	1.132E-2
17.	2.940	7.999E-1	8.988E-3
18.	3.005	8.963E-1	1.288E-2
19.	3.015	8.458E-1	1.149E-2
20.	3.260	9.144E-1	1.126E-2
21.	3.515	9.626E-1	1.153E-2
22.	3.660	9.778E-1	1.190E-2
23.	3.940	9.648E-1	9.760E-3
24.	4.005	1.036E+0	1.420E-2
25.	4.015	9.886E-1	1.205E-2
26.	4.060	1.011E+0	1.220E-2
27.	4.460	1.026E+0	1.152E-2
28.	4.515	1.023E+0	1.254E-2
29.	4.860	1.000E+0	1.168E-2
30.	4.940	9.983E-1	1.268E-2
31.	5.005	1.022E+0	1.399E-2
32.	5.015	9.999E-1	1.254E-2
33.	5.260	1.011E+0	1.151E-2
34.	5.515	9.808E-1	1.224E-2
35.	5.660	9.832E-1	1.132E-2
36.	5.940	9.176E-1	1.071E-2
37.	6.005	9.289E-1	9.493E-3
38.	6.015	9.211E-1	1.209E-2
39.	6.060	9.380E-1	1.118E-2
40.	6.460	9.143E-1	1.072E-2
41.	6.515	8.785E-1	1.173E-2
42.	6.860	8.676E-1	1.079E-2
43.	6.940	8.212E-1	1.057E-2
44.	7.005	8.452E-1	8.588E-3
45.	7.015	8.125E-1	1.069E-2

Table F.10 continued

	Height (mm)	Fluorescence Signal	Standard Deviation
46.	7.260	8.227E-1	1.046E-2
47.	7.515	7.695E-1	1.092E-2
48.	7.660	7.806E-1	1.002E-2
49.	7.940	7.471E-1	9.919E-3
50.	8.005	7.344E-1	8.511E-3
51.	8.015	7.277E-1	7.748E-3
52.	8.060	7.419E-1	1.041E-2
53.	8.460	7.050E-1	7.741E-3
54.	8.515	6.886E-1	7.464E-3
55.	8.860	6.961E-1	8.120E-3
56.	8.940	6.502E-1	8.336E-3
57.	9.005	6.665E-1	8.503E-3
58.	9.015	6.442E-1	6.806E-3
59.	9.260	6.549E-1	7.566E-3
60.	9.515	6.167E-1	7.392E-3
61.	9.660	6.245E-1	7.884E-3
62.	9.940	5.886E-1	7.712E-3
63.	10.005	6.032E-1	7.485E-3
64.	10.015	5.870E-1	6.781E-3
65.	10.060	6.021E-1	7.856E-3
66.	10.460	5.664E-1	7.463E-3
67.	10.515	5.605E-1	6.979E-3
68.	10.860	5.569E-1	7.142E-3
69.	10.940	5.434E-1	7.365E-3
70.	11.005	5.475E-1	7.213E-3
71.	11.260	5.358E-1	7.320E-3
72.	11.660	5.227E-1	7.525E-3
73.	11.940	5.011E-1	7.710E-3
74.	12.005	5.082E-1	7.243E-3
75.	12.060	5.016E-1	6.606E-3
76.	12.460	5.078E-1	7.176E-3
77.	12.940	4.633E-1	5.521E-3
78.	13.005	4.601E-1	7.137E-3
79.	13.940	4.320E-1	5.765E-3
80.	14.005	4.261E-1	6.965E-3
81.	14.940	3.978E-1	5.183E-3
82.	15.005	3.881E-1	6.354E-3
83.	15.940	3.701E-1	5.207E-3
84.	16.005	3.606E-1	4.208E-3
85.	16.940	3.362E-1	4.279E-3
86.	17.005	3.347E-1	4.103E-3
87.	17.940	3.109E-1	3.866E-3
88.	18.005	3.114E-1	3.792E-3
89.	18.940	2.943E-1	3.834E-3
90.	19.005	2.905E-1	3.817E-3

Table F.10 continued

	Height (mm)	Fluorescence Signal	Standard Deviation
91.	19.940	2.741E-1	3.710E-3
92.	20.005	2.726E-1	3.508E-3
93.	20.940	2.547E-1	3.711E-3
94.	21.005	2.444E-1	3.299E-3
95.	21.940	2.310E-1	3.491E-3
96.	22.005	2.317E-1	3.212E-3
97.	22.940	2.204E-1	3.347E-3
98.	23.005	2.132E-1	3.374E-3
99.	23.940	2.016E-1	3.266E-3
100.	24.005	1.923E-1	3.147E-3
101.	24.940	1.965E-1	2.711E-3
102.	25.005	1.747E-1	3.029E-3
103.	25.940	1.745E-1	2.705E-3
104.	26.005	1.628E-1	2.705E-3
105.	26.940	1.579E-1	2.722E-3
106.	27.005	1.576E-1	2.733E-3
107.	27.940	1.457E-1	2.433E-3
108.	28.005	1.385E-1	2.427E-3
109.	28.940	1.360E-1	2.519E-3
110.	29.005	1.321E-1	2.366E-3
111.	29.940	1.269E-1	2.458E-3
112.	30.005	1.199E-1	2.339E-3
113.	30.940	1.140E-1	2.271E-3
114.	31.005	1.078E-1	2.236E-3

Table F.11 Normalized OH fluorescence profile of the L-II-S2 flame ($\phi = 2.46$, $v_c = 22.4 \text{ cm}\cdot\text{sec}^{-1}$, $P = 80 \text{ torr}$).

	Height (mm)	Fluorescence Signal	Standard Deviation
1.	0.440	1.471E-1	3.415E-3
2.	0.515	5.943E-2	3.296E-3
3.	0.940	1.744E-1	3.581E-3
4.	0.950	1.566E-1	4.980E-3
5.	1.005	1.411E-1	3.793E-3
6.	1.015	1.696E-1	4.266E-3
7.	1.440	2.837E-1	4.679E-3
8.	1.515	2.671E-1	5.223E-3
9.	1.940	3.889E-1	5.099E-3
10.	1.950	3.713E-1	6.145E-3
11.	2.005	3.594E-1	5.294E-3
12.	2.015	3.854E-1	6.195E-3
13.	2.440	5.050E-1	8.621E-3
14.	2.515	5.080E-1	9.368E-3
15.	2.940	6.192E-1	8.900E-3
16.	2.950	5.994E-1	8.079E-3
17.	3.005	5.831E-1	6.621E-3
18.	3.015	6.064E-1	9.785E-3
19.	3.440	7.020E-1	1.018E-2
20.	3.515	7.149E-1	1.108E-2
21.	3.940	7.679E-1	1.050E-2
22.	3.950	7.652E-1	9.220E-3
23.	4.005	7.128E-1	7.097E-3
24.	4.015	7.654E-1	1.212E-2
25.	4.440	8.449E-1	1.017E-2
26.	4.515	7.958E-1	8.275E-3
27.	4.940	8.487E-1	1.067E-2
28.	4.950	7.996E-1	8.738E-3
29.	5.005	7.811E-1	1.026E-2
30.	5.015	7.793E-1	8.162E-3
31.	5.440	8.282E-1	1.019E-2
32.	5.515	7.696E-1	8.151E-3
33.	5.940	8.167E-1	1.007E-2
34.	5.950	7.540E-1	8.647E-3
35.	6.005	7.146E-1	9.923E-3
36.	6.015	7.372E-1	7.830E-3
37.	6.440	7.824E-1	9.578E-3
38.	6.515	6.915E-1	7.982E-3
39.	6.940	7.252E-1	1.016E-2
40.	6.950	6.951E-1	8.664E-3
41.	7.005	6.498E-1	9.247E-3
42.	7.015	6.633E-1	8.000E-3
43.	7.440	6.998E-1	9.473E-3
44.	7.515	6.179E-1	7.032E-3
45.	7.940	6.527E-1	8.995E-3

Table F.11 continued

	Height (mm)	Fluorescence Signal	Standard Deviation
46.	7.950	6.167E-1	7.944E-3
47.	8.005	5.872E-1	9.060E-3
48.	8.015	5.909E-1	7.175E-3
49.	8.440	6.082E-1	8.146E-3
50.	8.515	5.563E-1	7.433E-3
51.	8.940	5.752E-1	7.471E-3
52.	8.950	5.542E-1	7.134E-3
53.	9.005	5.175E-1	5.698E-3
54.	9.015	5.183E-1	6.697E-3
55.	9.440	5.413E-1	7.070E-3
56.	9.515	4.924E-1	6.751E-3
57.	9.940	5.183E-1	7.352E-3
58.	9.950	5.121E-1	7.241E-3
59.	10.005	4.661E-1	5.620E-3
60.	10.015	4.688E-1	6.816E-3
61.	10.440	4.992E-1	6.988E-3
62.	10.515	4.538E-1	6.551E-3
63.	10.950	4.670E-1	6.744E-3
64.	11.005	4.301E-1	5.656E-3
65.	11.950	4.369E-1	6.806E-3
66.	12.005	3.949E-1	5.573E-3
67.	12.950	3.836E-1	4.414E-3
68.	13.005	3.698E-1	5.294E-3
69.	13.950	3.529E-1	4.181E-3
70.	14.005	3.363E-1	5.325E-3
71.	14.950	3.171E-1	3.863E-3
72.	15.005	3.085E-1	4.885E-3
73.	15.950	2.990E-1	3.960E-3
74.	16.005	2.807E-1	4.965E-3
75.	16.950	2.759E-1	3.794E-3
76.	17.005	2.622E-1	3.795E-3
77.	17.950	2.594E-1	3.713E-3
78.	18.005	2.425E-1	3.687E-3
79.	18.950	2.333E-1	3.438E-3
80.	19.005	2.215E-1	3.386E-3
81.	19.950	2.145E-1	3.295E-3
82.	20.005	2.079E-1	3.363E-3
83.	20.950	2.116E-1	2.787E-3
84.	21.005	1.974E-1	2.989E-3
85.	21.950	1.967E-1	2.796E-3
86.	22.005	1.813E-1	2.955E-3
87.	22.950	1.746E-1	2.667E-3
88.	23.005	1.644E-1	2.610E-3
89.	23.950	1.611E-1	2.673E-3
90.	24.005	1.545E-1	2.565E-3

Table F.11 continued

	Height (mm)	Fluorescence Signal	Standard Deviation
91.	24.950	1.479E-1	2.461E-3
92.	25.005	1.379E-1	2.659E-3
93.	25.950	1.371E-1	2.566E-3
94.	26.005	1.264E-1	2.419E-3
95.	26.950	1.298E-1	2.664E-3
96.	27.005	1.189E-1	2.326E-3
97.	27.950	1.167E-1	2.404E-3
98.	28.005	1.033E-1	2.329E-3
99.	28.950	1.056E-1	2.272E-3
100.	29.005	9.662E-2	2.054E-3
101.	29.950	9.358E-2	2.306E-3
102.	30.005	8.337E-2	1.831E-3
103.	30.950	8.954E-2	2.172E-3
104.	31.005	8.181E-2	1.804E-3



REPORT DOCUMENTATION PAGE

Form Approved
OMB No. 0704-0188

Public reporting burden for this collection of information is estimated to average 1 hour per response, including the time for reviewing instructions, searching existing data sources, gathering and maintaining the data needed, and completing and reviewing the collection of information. Send comments regarding this burden estimate or any other aspect of this collection of information, including suggestions for reducing this burden, to Washington Headquarters Services, Directorate for Information Operations and Reports, 1215 Jefferson Davis Highway, Suite 1204, Arlington, VA 22202-4302, and to the Office of Management and Budget, Paperwork Reduction Project (0704-0188), Washington, DC 20503.

1. AGENCY USE ONLY (Leave blank)	2. REPORT DATE March 1993	3. REPORT TYPE AND DATES COVERED Final Contractor Report	
4. TITLE AND SUBTITLE Measurements of Soot Formation and Hydroxyl Concentration in Near-Critical Equivalence Ratio Premixed Ethylene Flame		5. FUNDING NUMBERS WU-537-02-20 G-NAG3-1038	
6. AUTHOR(S) Michael Andrew Inbody		8. PERFORMING ORGANIZATION REPORT NUMBER E-7696	
7. PERFORMING ORGANIZATION NAME(S) AND ADDRESS(ES) Purdue University West Lafayette, Indiana 47907		10. SPONSORING/MONITORING AGENCY REPORT NUMBER NASA CR-191099	
9. SPONSORING/MONITORING AGENCY NAMES(S) AND ADDRESS(ES) National Aeronautics and Space Administration Lewis Research Center Cleveland, Ohio 44135-3191		11. SUPPLEMENTARY NOTES Project Manager, Valerie J. Lyons, Propulsion Systems Division, NASA Lewis Research Center, (216) 433-5970. A similar version of this report was submitted by Michael Andrew Inbody as a thesis in partial fulfillment of the requirements for the degree Doctor of Philosophy to Purdue University, West Lafayette, Indiana 47907.	
12a. DISTRIBUTION/AVAILABILITY STATEMENT Unclassified - Unlimited Subject Category		12b. DISTRIBUTION CODE	
13. ABSTRACT (Maximum 200 words) The testing and development of existing global and detailed chemical kinetic models for soot formation requires measurements of soot and radical concentrations in flames. A clearer understanding of soot particle inception relies upon the evaluation and refinement of these models in comparison with such measurements. We present measurements of soot formation and hydroxyl (OH) concentration in sequences of flat premixed atmospheric-pressure C ₂ H ₄ /O ₂ /N ₂ flames and 80-torr C ₂ H ₄ /O ₂ flames for a unique range of equivalence ratios bracketing the critical equivalence ratio (ϕ_c) and extending to more heavily sooting conditions. Soot volume fraction and number density profiles are measured using a laser scattering-extinction apparatus capable of resolving a 0.1% absorption. Hydroxyl number density profiles are measured using laser-induced fluorescence (LIF) with broadband detection. Temperature profiles are obtained from Rayleigh scattering measurements. The relative volume fraction and number density profiles of the richer sooting flames exhibit the expected trends in soot formation. In near- ϕ_c visibly sooting flames, particle scattering and extinction are not detected, but an LIF signal due to polycyclic aromatic hydrocarbons (PAHs) can be detected upon excitation with an argon-ion laser. A linear correlation between the argon-ion LIF and the soot volume fraction implies a common mechanistic source for the growth of PAHs and soot particles. The peak OH number density in both the atmospheric and 80-torr flames declines with increasing equivalence ratio, but the profile shape remains unchanged in the transition to sooting, implying that the primary reaction pathways for OH remain unchanged over this transition. Chemical kinetic modelling is demonstrated by comparing predictions using two current reaction mechanisms with the atmospheric flame data. The measured and predicted OH number density profiles show good agreement. The predicted benzene number density profiles correlate with the measured trends in soot formation, although anomalies in the benzene profiles for the richer and cooler sooting flames suggest a need for the inclusion of benzene oxidation reactions.			
14. SUBJECT TERMS		15. NUMBER OF PAGES 468	16. PRICE CODE A20
17. SECURITY CLASSIFICATION OF REPORT Unclassified	18. SECURITY CLASSIFICATION OF THIS PAGE Unclassified	19. SECURITY CLASSIFICATION OF ABSTRACT Unclassified	20. LIMITATION OF ABSTRACT

National Aeronautics and
Space Administration

Lewis Research Center
Cleveland, Ohio 44135

Official Business
Penalty for Private Use \$300

FOURTH CLASS MAIL

ADDRESS CORRECTION REQUESTED



Postage and Fees Paid
National Aeronautics and
Space Administration
NASA 451

NASA
